Czech Technical University in Prague

Faculty of Electrical Engineering

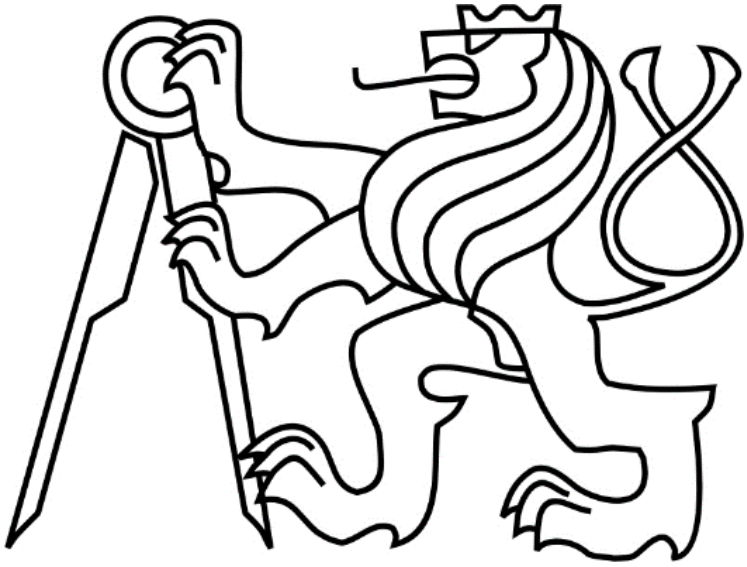

Doctoral thesis

August 2020 **Mehran Mirzaei**

Czech Technical University in Prague

Faculty of Electrical Engineering
Department of Measurement

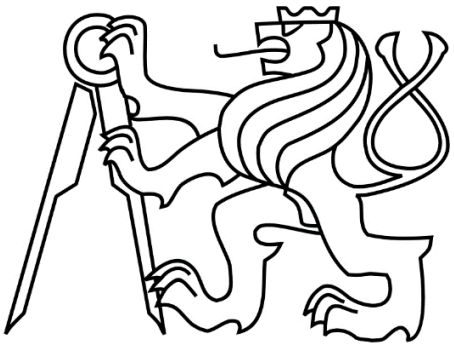

Magnetic Material Modeling and Simulations for Magnetic Sensors

Doctoral thesis

Author: Ing. Mehran Mirzaei

Supervisor: Prof. Ing. Pavel Ripka, CSc.

PhD Programme: P2612, Electrical Engineering and Information Technology

Branch of study: 2601V006, Measurement and Instrumentation

Prague, August 2020

Declaration

I declare that this thesis was completely performed by myself and I have mentioned and cited all sources in the bibliography and references.

Prague, 27.08.2020

Prohlašuji, že jsem tuto práci kompletně vypracoval a uvedl jsem v seznamu literatury odkazy na všechny použité prameny.

V Praze, 27.08.2020

Acknowledgements

I would like to express my gratitude to Prof. Pavel Ripka, my supervisor, for his technical help and support, scientific guidance during my PhD study. I am also grateful of my colleagues in MAGLAB for their supports in experiments of my thesis. I would like to thank my mother for her inspiring me to study, and moral support throughout my life and whole study. This thesis becomes realizable with the patience and support of my wife and my daughter, which I am very much grateful.

Abstract

In this thesis, new magnetic materials models are presented and applied for the design of the magnetic sensors. The following main topics are covered both in theory and in applications.

Mathematical models for *B-H* curves and magnetic hysteresis loops are developed in the first part. The proposed mathematical models are based on novel combined rational and power functions.

The effect of magnetic permeability of solid iron rectangular conductor on field distribution around conductors is measured and studied in the second part. The impedance analysis of solid iron conductors of circular shape and rectangular shape and solid iron railway rails are considered at different frequencies for various irons *B-H* curves and electrical conductivities. Finite element method (FEM) and newly developed analytical method which take into account material non-linearity and eddy currents are used to analyze impedance of solid iron conductors and the calculations are compared with experimental results.

Third part of the thesis is devoted to the analysis of position sensor for pneumatic cylinder. The effect of magnetic iron rod material characteristics on the performance of position sensor is evaluated. Thermal stability of the position sensor is also studied in this thesis. In addition, a flat type position sensor is presented with rectangular shape solid iron and laminated silicon steel moving parts. The effects of magnetic materials are calculated to optimize the flat type position sensor. 2D and 3D FEM together with finite difference method are used for the calculations.

Fourth part of the thesis is about eddy current speed sensors. The proposed speed sensors are designed for solid conductive moving part. Translational and rotational configurations of the eddy current speed sensors are analyzed and optimized. The effects of magnetic permeability and electrical conductivity of the moving part iron are evaluated for the speed sensors performance. 2D and 3D analytical models are developed and compared with FEM results and measurements. Static and dynamic performance of speed sensors are both calculated. Also the effect of magnetic shielding and yoke is taken into the account.

Keywords: Magnetic materials, *B-H* curve and hysteresis loop modeling, magnetic sensors, impedance analysis, position sensor, speed sensor, analytical and numerical calculations, 2D and 3D FEM

Abstrakt

V této práci jsou prezentovány nové matematické modely magnetických materiálů a tyto modely jsou následně použity pro návrh magnetických senzorů. Jedná se jak o teoretické analýzy, tak praktické aplikace

V první části jsou uvedeny matematické modely pro křivky *B-H* a hysterezní smyčky. Navrhované matematické modely jsou založeny na nových kombinacích racionálních a mocninných funkcích.

Druhá část práce se týká měření a studiu vlivu magnetické permeability pravoúhlého masivního železného vodiče na distribuci magnetického pole v jeho okolí. Impedanční analýza vodičů kruhového a pravoúhlého tvaru a železničních kolejnic je v této části práce provedena pro různé frekvence a různé magnetizační charakteristiky a elektrické vodivosti. Metoda konečných prvků (FEM) a nově vyvinutá analytická metoda přihlížející k nelinearitě materiálu a vířivým proudům se používají k analýze impedance železných vodičů, výpočty jsou porovnány s experimentálními výsledky.

Třetí část práce je věnována analýze polohového senzoru pro pneumatický válec. Je vyhodnocen vliv magnetické charakteristiky pístní tyče z masivní oceli na chování polohového senzoru. V této části práce je rovněž studována teplotní stabilita polohového senzoru. Kromě toho je zde prezentován plochý polohový senzor pro pravoúhlou pohyblivou část z masivního železa nebo laminovaných plechů z křemíkové oceli. Při optimalizaci polohového snímače plochého typu se vyhodnocuje vliv použitého magnetického material. Pro výpočty byly použity metody 2D a 3D FEM spolu s metodou konečných diferencí.

Čtvrtá část práce se zabývá senzory rychlosti založených na vířivých proudech. Navrhované snímače rychlosti jsou konstruovány pro pohyblivé masivní vodivé součásti. Translační a rotační konfigurace snímačů rychlosti využívající vířivých proudů jsou analyzovány a optimalizovány. Efekt magnetické permeability a elektrické vodivosti materiálu pohyblivé části je hodnocen z hlediska optimalizace parametrů těchto snímačů. Byly vyvinuty 2D a 3D analytické modely a porovnávány s výsledky FEM analýzy a měření. Dále byly vypočteny jak statické, tak i dynamické parametry vyvinutých snímačů rychlosti. Zohledněn je také
účinek magnetického stínění a jha.

Klíčová slova: Magnetické materiály, *B-H* křivka, modelování hysterezní smyčky, magnetické senzory, analýza impedance, polohový senzor, senzor rychlosti, analytické výpočty, numerické výpočty, 2D a 3D FEM.

Table of Contents

1- State of Art

1-1 Modeling

In this part of thesis, mathematical models for *B-H* and magnetization curves and hysteresis loops for soft magnetic materials are addressed.

1-1-1 *B-H* Curve Modeling

Metallic magnetic materials are mostly iron alloys families such as cast iron and steels, low carbon steels, silicon steels, nickel based iron alloy and cobalt based iron alloy [1]. Analytical representations of the magnetization and *B-H* curve of magnetic materials are used for magnetic modeling, numerical analysis and design process. Using approximated mathematical *B-H* curve could help for first design step of magnetic devices [2]-[3]. It gives simple and fast picture of maximum magnetic relative permeability and magnetic saturation without *B-H* data table.

B-H curve can be represented by different closed-form formulae [4]. Rational functions have been presented for *B-H* curve modeling, in [5] - [7] and exponential functions are used in [8] - [10]. The modeled magnetic materials for *B-H* functions were silicon steel laminations and solid irons and steels in [4] - [10], which have small magnetic permeability especially at low magnetic fields. Papers [5] and [7] are mostly devoted to optimization of curve fitting. Piecewise modeling of *B-H* curve with high precision is also presented [11] but it does not obtain one closed-form equation. Power functions could precisely model a fraction part of *B-H* curve but not the whole *B-H* curve from low field part to highly saturated part [12]-[14].

1-1-2 Hysteresis Loops Modeling

Jiles-Atherton and Mel'gui methods [15] – [16] were used for the magnetic hysteresis modeling in [17] - [19]. Preisach method and Energetic model method were described for hysteresis modeling in [20] - [21]. Magnetic hysteresis was analytically modeled in [22] using simplified Jiles-Atherton model. Pure analytical hysteresis model was presented in [23]. A piecewise approximation method for hysteresis modeling was used in [24]. The approaches in [15]-[24] need time-consuming procedure to calculate the constants and parameters and a large number of experiments, which are not suitable for fast calculations and design process and optimization. Straightforward and uncomplicated analytical equations and procedures were implemented in [6] and [25]. However, these methods did not show generality of the proposed analytical functions for different magnetic materials. Detailed analyses of hysteresis loops for high magnetic permeability materials and grain-oriented steel laminations were presented in [26]-[28], in which multi-form mathematical functions are used to fit analytical hysteresis loops for various magnetic field strength ranges.

1-2 Applications

In this part of thesis, applications of modeling for impedance analysis of solid iron conductors, position sensors and eddy current speed sensors are addressed.

1-2-1 Analysis of Solid Iron Conductors and Impedance Analysis

The impedance of a solid iron conductor is not only dependent on frequency, but is also affected by the nonlinearity of the *B-H* curves of solid irons and steels. The main challenge for impedance analysis of solid iron conductors is how to take into account the effect of the eddy currents in the solid iron together with nonlinearity and hysteresis effects.

An analytical model for impedance analysis restricted to circular conductors, using an innovative analysis for saturation consideration in the solid iron was performed in [29]. A detailed linear analysis of the impedances of rectangular and circular solid iron conductors is presented in [30], using analytical calculations, but measurements were made only at 50 Hz. Approximate analytical calculations of circular solid iron conductors are shown in [31] with considering nonlinearity, but in that work only resistances were measured and calculated. The same authors claimed to present impedance results for rectangular conductors, in [32]. References [33] and [34] calculated the impedances of the solid iron rails with considering nonlinearity and rail material effects on the impedances.

Analytical and numerical calculations for linear and nonlinear magnetic analysis have been performed to evaluate the eddy current and its effect on electromagnetic devices [13] and [35]. Although numerical calculations using the finite difference method (FDM) and the finite element method (FEM) are well developed, and free software and commercial software are accessible, a fast and easy analytical method for impedance calculations is still very desirable. The earliest precise eddy current analysis in a nonlinear model for solid iron was performed in [12], using the power function for *B-H* curve modeling, which was later also used in [13], [36] - [37]. A rectangular function was used in [38] - [40] for saturation and nonlinearity modeling in the *B-H* curve, but it is less precise than the method in [12]. Eddy current loss analysis and analytical modeling for nonlinearity consideration for solid and laminated iron parts exposed to non-sinusoidal alternating fields were described in [41], using the extended works of [38]. Only tangential component of magnetic field was considered in all above mentioned references. Recent work on analytical modeling of the eddy current in a nonlinear magnetic material was presented in [42], which both tangential and normal components of magnetic fields were considered.

1-2-2 Position Sensors

Contactless linear and angular position detection of target objects in industrial conditions is a challenging issue [43]-[45]. Piston position detection in a pneumatic aluminum cylinder and in a hydraulic solid iron cylinder is a problematic task, because the piston is shielded by conductive and magnetic covers [43]-[44]. The position of the piston in the cylinder is not symmetric as LVDT sensors [2].

Various internal and external sensors for pneumatic and hydraulic cylinders are implemented for detecting piston positions. In the case of a pneumatic cylinder, internal sensors are inserted into the piston rod. This is mechanically complicated, and the sensors are not cost-effective and they are unreliable. Microwave and optical sensors implemented inside the cylinder display the same problems [46]-[49]. For an aluminum cylinder, a permanent magnet on the piston can be used in external sensors. However, this approach has some disadvantages. Firstly, it is necessary to use an expensive non-magnetic stainless steel rod. Stainless non-magnetic steel must be used to cancel out the distortion of the permanent magnet fields caused by the magnetic iron rod. Secondly, mounting a permanent magnet on the piston is a complicated procedure. In

addition, the temperature dependency of the remanence flux density of a permanent magnet is a major weakness in a harsh environment.

The recent works presented an AC-excited contactless piston position transducer with axial excitation and detection of the radial magnetic field related to the end of a magnetically soft iron rod [44]. A moving ferromagnetic piston rod causes changes in the magnetic field, which are sensed by an array of integrated fluxgate sensors mounted on the outside of the aluminum cylinder. The uncorrected maximum static error was ±3 mm with achievable 0.1 mm resolution. The dynamic performance is a limiting factor for this sensor: the dynamic error is ±3 mm even at a speed of 0.2 m/s. Complex signal processing of the sensor array is required for this type of sensor. Similar limitations were faced when radial excitation by saddle coils was used [50].

A simpler method is to use a variable inductance sensor. This was presented for a hydraulic cylinder with a non-metallic shell [51]. A modified inductance method as a position sensor of a power cylinder with a carbon steel shell was employed in [43], using a differential coils configuration [52]. Measuring the pick-up voltage for a position sensor is a well-known method for LVDT sensors with various cylindrical and flat shape configurations [53]-[56]. An alternative to the configuration for the variable inductance sensor in [43] and [51] is to implement coils around the iron rod instead of the cylinder. However, this is a cumbersome task, because of the long coil that is used for pneumatic and hydraulic cylinders [57]. Moving coils have problems with reliability in a harsh environment.

Recent works on alternative configurations of position sensors using an ironless inductive position sensor [58], and a variable reluctance differential solenoid transducer [59], cannot be applied to pneumatic cylinders and hydraulic cylinders with a large stroke.

1-2-3 Eddy Current Speed Sensors

Sensorless speed measurement methods for rotating electrical machines are well developed, although their signal processing is complex and time-consuming, and may not be rapid enough for control purposes [60]-[61]. Optical sensors are also widely used for speed measurements, but they may not be appropriate for harsh and dusty environments, and they often need maintenance to clean out dust and dirt [2]. The use of an external magnetic field sensor mounted on the housing of a machine was presented in [62]. Since it is not non-destructive, it needs magnetic shielding against external magnetic fields. Implementing a Hall sensor in the stator or inside the end windings to measure the speed of the rotating rotor was presented in [63]-[64]. However, this may be unreliable, e. g. in conditions where the winding becomes overheated. Variable reluctance (VR) or saliency-based speed measurements with pick-up coils or Hall sensors have also been used in industry for rotating machines. However, a non-salient magnetic surface needs to be built for operating reluctance variations or for changing the induced eddy current [65]-[68]. Recent works using electrostatic phenomena to measure speed were published in [69]-[70]. However, these sensors will be quite sensitive to dirt and dust, and they therefore need to be capsulated.

Utilizing the speed component of an induced eddy current, means going back to the principles of the Faraday generator, unipolar generator and eddy current brake [71]-[72]. A non-destructive testing method for metals utilizes the same principle, as has been reported in [73]-[74].

Magnetic flow meters are used to measure the speed of fluids by reading the voltage caused by speed effects with electrodes in contact with the fluid across the fluid flowing in

magnetic fields perpendicular to the direction of the flowing fluid [2] and [75]. A speed sensor using the fluxgate effect in an amorphous ring core to measure the field of eddy currents was presented in [76]. This rather complicated sensor has a poor linearity error of approx. 5%. A rotating permanent magnet rotor for contactless eddy current speed sensing was tested and analyzed in [77]; this type of sensor is not easy to manufacture and use because of the moving part. A Hall sensor with permanent magnet excitation was presented in [78]; however, this sensor shows poor offset stability.

Parallel and perpendicular types of eddy current-based speed sensors with air coils for excitation and pick-up voltage were analyzed and measured in detail in [74] and in [79]-[83]. The same parallel configuration as in [83], with one excitation coil and two pick-up coils using a ferrite magnetic yoke, was measured in [84]. These sensors use only aluminum for the moving part, though iron is a material typically used for shafts and rails.

2- Thesis Objectives

From the fact mentioned in the previous chapter emerged the following objectives:

To increase the quality of models mentioned in 1-1,

- the development of novel mathematical models for nonlinear magnetization curves and hysteresis loops should be designed,
- the assessment of analytical and numerical modeling of impedances of solid iron rectangular bars, cylindrical rods, and iron rails using mathematical models of magnetization curves should be done.

Concerning applications mentioned in 1-2, the following goals emerged:

- To develop new types of a position sensor for a pneumatic cylinder with aluminum shell and solid iron rod and axisymmetric coils wound around aluminum shell or iron rod using 2D axisymmetric time-harmonic finite element method (FEM).
- To design and analyze a flat type position sensor with solid iron and steel lamination armatures using developed finite difference method (FDM).
- To evaluate magnetic materials effects on the position sensors performance.
- To develop different types of eddy current speed sensors with translational and rotational motions using 2D and 3D computational models.
- To model magnetic materials in the design process with various magnetic permeabilities and electrical conductivities in the conductive moving part.

3- The Results

The results and outcomes of this thesis were presented in the journal and conference papers, which include 13 published journal papers and 3 conference papers. Two unpublished under review papers are also presented. The presented papers are categorized in two groups of modeling and applications.

3-1 Soft Magnetic Materials Modeling and Analysis

In this section, two papers describe new methods for analytical modeling of *B-H* curves and hysteresis loops for different magnetic materials, respectively. Novel combined rational and power functions were used for the magnetization modeling.

3-1-1 Analytical Functions of Magnetization Curves for High Magnetic Permeability Materials [J3]

In this work, combined rational and power functions are used to represent magnetization curves of high magnetic permeability ferromagnetic materials. The proposed functions cover much wider range of magnetic fields than functions currently used in simulation software packages. The objective is to present simple functions for approximation of magnetization curves with minimum number of unknown constants. The calculated functions are finally compared with measured magnetization curves to validate the precision in a wide field range from 10^{-2}A/m to 10^{6} A/m.

New analytical function has been presented, which can precisely model *B–H* curve and relative permeability. The selected materials were high magnetic permeability Ni-Fe alloys but the presented analytical function could also be used for other magnetic materials. The main advantages of presented function are its compact format and high precision even with low number of unknowns for curve fitting. The typical value of rms error ranges from 0.3% to 1.6 %. Standard rational function was compared with the proposed analytical function, which has the disadvantage of probable zeros in denominator and discontinuities in the modeled curve. Exponential functions for *B–H* curve modeling are not as precise as rational functions. The unknowns of the proposed analytical function could be calculated with simple curve fitting function. Compatibility of the proposed analytical function has been presented for modified *B–H* curve corresponding to fundamental component of flux density, which also shows high precision.

Analytical Functions of Magnetization Curves for High Magnetic Permeability Materials

Mehran Mirzaei and Pavel Ripka

Faculty of Electrical Engineering, Czech Technical University, 16627 Prague, Czech Republic

In this paper, combined rational and power functions are used to represent magnetization curves of high magnetic permeability ferromagnetic materials. The proposed functions cover much wider range of magnetic fields than functions currently used in simulation software packages. The objective is to present simple functions for approximation of magnetization curves with minimum number of unknown constants. The calculated functions are finally compared with measured magnetization curves to validate the precision in a wide field range from 10^{-2} to 10^{6} A/m.

Index Terms— **Analytical functions, curve fitting, high magnetic permeability materials, magnetization curves.**

I. Introduction

THE most industrial used ferromagnetic materials could be categorized into two major groups of metallic and non-metallic magnetic materials. Non-metallic magnetic materials are composed of Ferrite families. Metallic magnetic materials are mostly iron alloys families such as cast iron and steels, low carbon steels, silicon steels, nickel-based iron alloy, and cobalt-based iron alloy [1].

The nickel-based iron alloys (Ni-Fe) have special industrial applications because of very high maximum permeability with small hysteresis losses and considerably high electrical resistivity. The high magnetic permeability is caused by small hysteresis loop and very low-magnetic coercive force, which makes sharp changing of magnetic flux density at low-magnetic field strength. These characteristics show suitable applications of Ni-Fe alloy for telecommunication functions. They have also numerous industrial applications such as magnetic sensors, high efficiency transformers, magnetic recording heads, and magnetic shields [1]–[3].

Analytical representations of the magnetization and B–H curve of magnetic materials are used for magnetic modeling, numerical analysis, and design process. Using approximated mathematical B–H curve could help for first design step of magnetic devices [3]. It gives apparent and fast picture of maximum magnetic relative permeability and magnetic saturation without B–H data table. B–H curve could be represented by different closed-form formulas [4]. Several publications have presented detailed analysis for B–H curve modeling, for example, rational function [4]–[7] and exponential function [8]–[10]. The modeled magnetic materials for B–H functions were silicon steel laminations and solid irons and steels in [4]–[10], which have a small magnetic permeability especially at low-magnetic fields. References [5] and [7] are mostly devoted to optimization of curve fitting. Piecewise modeling of B–H curve with high precision is also presented [11] but it does not obtain one closed-form equation. Power functions could precisely model a fraction part of B–H curve but not the whole B–H curve from low field part to highly saturated part [12]–[14].

In this paper, rational function and power function are combined for modeling very high permeability B–H curves. The constants of the proposed function are calculated by curve fitting tool. It is shown that the proposed function can accurately fit the measured B–H curve despite its non-complicated equation. Finally, the proposed function is used for curve fitting of modified B–H curve corresponding to fundamental component of flux density for ac analysis.

II. Basic Study

A. Assumptions

Magnetization parameter, J versus magnetic field strength and relative magnetic permeabilities are represented as follows:

$$\begin{aligned} J &= B - \mu_0 . H \\ \mu_{r,a} &= \frac{1}{\mu_0} \cdot \frac{B}{H} \\ \mu_{r,d} &= \frac{1}{\mu_0} \cdot \frac{dB}{dH} = \frac{1}{\mu_0} \cdot \frac{d(\mu_0.\mu_{r,a} \cdot H)}{dH} \\ &= \mu_{r,a} + H \cdot \frac{d\mu_{r,a}}{dH} \end{aligned} \tag{1}$$

where μ_0, $\mu_{r,a}$, and $\mu_{r,d}$ are free space magnetic permeability, apparent relative permeability, and differential relative permeability. In order to calculate the analytical function, it must be considered that magnetization, J, is becoming constant when magnetic field strength, H is moving toward infinite and apparent and differential relative permeabilities must have one maxima between magnetic field strength, $H = 0$ until $H = \infty$. The former condition is necessary to model Rayleigh region of the B–H curve.

B. Basic Function

First-order rational function is a simple analytical function, which could match with B–H curve from low field to highly saturation. The main disadvantage of the first-order rational

Manuscript received March 9, 2018; accepted April 10, 2018. Date of publication May 8, 2018; date of current version October 17, 2018. Corresponding author: M. Mirzaei (e-mail: mirzameh@fel.cvut.cz).

Color versions of one or more of the figures in this paper are available online at http://ieeexplore.ieee.org.

Digital Object Identifier 10.1109/TMAG.2018.2827932

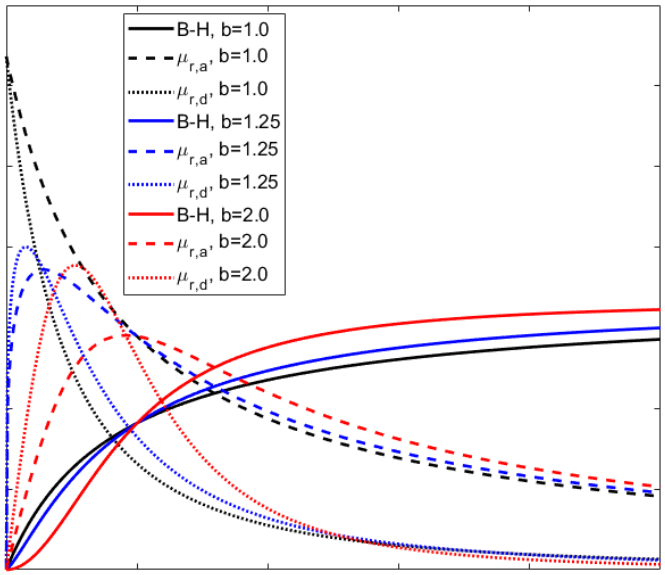

Fig. 1. Schematic B–H curve based on (2)—parameters a and a' are the same for all curves.

function is that it is not able to model Rayleigh region and relative permeability maxima could not be reproduced. In order to improve it, power of parameter, x, must be adjusted to value above 1

$$f(x) = \frac{a \cdot x^b}{1 + a' \cdot x^b}, (f(x) = J, x = H) \tag{2}$$

where a, a', and b are constants. The relative magnetic permeability for basic function (2) is as follows:

$$\begin{aligned} f(x) &= \frac{a \cdot x^b}{1 + a' \cdot x^b}, \quad (J = f(x), x = H) \\ \mu_{r,a} &= 1 + \frac{1}{\mu_0} \cdot \frac{a \cdot x^{b-1}}{1 + a' \cdot x^b} \\ \mu_{r,d} &= \mu_{r,a} + \frac{1}{\mu_0} \cdot \frac{(b-1) - a' \cdot x^b}{(1 + a' \cdot x^b)^2} \cdot a \cdot x^{b-1} \\ &= 1 + \frac{1}{\mu_0} \cdot \frac{a \cdot b \cdot x^{b-1}}{(1 + a' \cdot x^b)^2}. \end{aligned} \tag{3}$$

Maximum values for relative magnetic permeability is given in (4). It is shown that smaller non-integer b less than 2 makes it possible increase maximum relative magnetic permeability and decrease corresponding field strength, H without changing parameters a and a', which is required for high permeability magnetic materials modeling. Parameters a and a' could be adjusted for matching formula for the modeling of the saturation and knee of B–H curve. Fig. 1 shows schematic view of B–H curves and relative magnetic permeabilities versus magnetic field strength, which maximum value of differential relative permeability is always bigger than maximum value of apparent relative permeability

$$\begin{aligned} \mu_{r,a}\left(x = \sqrt[b]{\frac{b-1}{a'}}\right) &= \mu_{r,a}^{\max} = 1 + \frac{1}{\mu_0} \frac{a\left(\frac{b-1}{a'}\right)^{\frac{b-1}{b}}}{b} \\ \mu_{r,d}\left(x = \sqrt[b]{\frac{b-1}{a' \cdot (b+1)}}\right) &= \mu_{r,d}^{\max} = 1 + \frac{1}{\mu_0} \frac{a\left(\frac{b-1}{a'(b+1)}\right)^{\frac{b-1}{b}}}{\frac{4 \cdot b}{(b+1)^2}}. \end{aligned} \tag{4}$$

III. Proposed Function

One possible form of the proposed function for combined rational function and power function could be as follows:

$$f(x) = \frac{\sum\limits_{i=1,2,\ldots} a_i \cdot x^{b_i}}{1 + \sum\limits_{i=1,2,\ldots} a_i' \cdot x^{b_i}}, \quad (f(x) = J^m, x = H^n) \tag{5}$$

where a_i, a_i', b_i, m, and n are constants.

The big range of magnetic field strength between the small values for maximum relative permeability and large values for high saturation make to choose m and n values not equal to one. The parameters m and n are adjusted to improve curve fitting process; they have positive values less than 1. The relative apparent permeability and relative differential permeability are analytically calculated as

$$\begin{aligned} \mu_{r,a} &= 1 + \frac{1}{\mu_0} \cdot \left(\frac{\sum\limits_{i=1,2,\ldots} a_i \cdot H^{n \cdot b_i - m}}{1 + \sum\limits_{i=1,2,\ldots} a_i' \cdot H^{n \cdot b_i}} \right)^{\frac{1}{m}} \\ \mu_{r,d} &= 1 + \frac{1}{\mu_0} \cdot \frac{1}{m} \cdot \left(\frac{\sum\limits_{i=1,2,\ldots} a_i \cdot H^{n \cdot b_i}}{1 + \sum\limits_{i=1,2,\ldots} a_i' \cdot H^{n \cdot b_i}} \right)^{\frac{1-m}{m}} \\ &\quad \times \frac{C_1 - C_2}{\left(1 + \sum\limits_{i=1,2,\ldots} a_i' \cdot H^{n \cdot b_i}\right)^2} \\ C_1 &= \sum_{i=1,2,\ldots} a_i \cdot n \cdot b_i \cdot H^{n \cdot b_i - 1} \cdot \left(1 + \sum_{i=1,2,\ldots} a_i' \cdot H^{n \cdot b_i}\right) \\ C_2 &= \sum_{i=1,2,\ldots} a_i \cdot H^{n \cdot b_i} \cdot \sum_{i=1,2,\ldots} a_i' \cdot n \cdot b_i \cdot H^{n \cdot b_i - 1}. \end{aligned} \tag{6}$$

Different high permeability materials are used from two material data resources [15]–[17] to validate the analytical functions.

A. First Group of Materials

In this section, three Ni-Fe magnetic materials are used for curve fitting [15], [16]. The number of power functions is limited to maximum three in the numerator and denominator of rational function

$$f(x) = \frac{a_1 \cdot x^{b_1} + a_2 \cdot x^{b_2} + a_3 \cdot x^{b_3}}{1 + a_1' \cdot x^{b_1} + a_2' \cdot x^{b_2} + a_3' \cdot x^{b_3}}. \tag{7}$$

The number of unknowns in (7) is 9 with other unknown parameters m and n, which will be totally 11. The curve fitting process is used to find the unknowns [18]. The parameters m and n are adjusted by trial and error and they are not calculated by curve fitting to decrease the complexity of curve fitting.

The results are presented in Figs. 2–4 for three high permeability magnetic materials with relative permeability between 50 000 and 500 000. The unknowns are calculated with curve fitting.

1) *Moly Permalloy:* $a_1 = -2.679$, $a_1' = -0.8315$, $a_2 = 2.758$, $a_2' = 0.9487$, $a_3 = 0.08104$, $a_3' = 0.09077$,

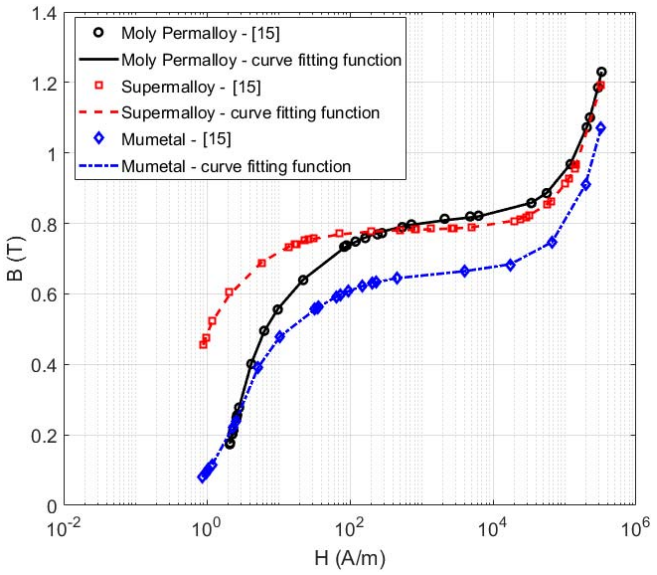

Fig. 2. Curve fitting for B–H curve.

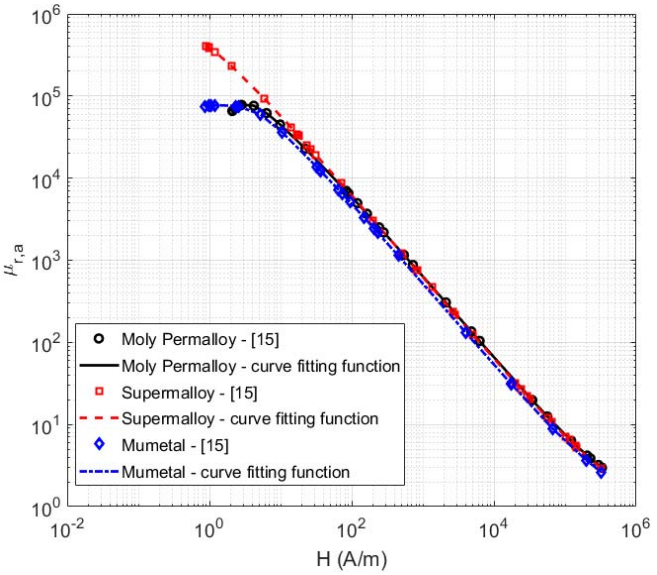

Fig. 3. Curve fitting for $\mu_{r,a}$–H curve—-apparent relative permeability.

$b_1 = 28$, $b_2 = 27.74$, $b_3 = 39.48$, $m = 0.56$, and $n = 0.07$.

2) *Supermalloy:* $a_1 = 17.37$, $a_1' = 19.92$, $a_2 = 0.52$, $a_2' = 0.2364$, $a_3 = 0.8789$, $a_3' = 6.982$, $b_1 = 85.01$, $b_2 = 11.73$, $b_3 = 73.74$, $m = 0.56$, and $n = 0.07$.
3) *Mumetal:* $a_1 = 0.04578$, $a_1' = 0.0576$, $a_2 = 0.617$, $a_2' = 0.469$, $a_3 = -0.3419$, $a_3' = -0.3305$, $b_1 = 33.42$, $b_2 = 15.65$, $b_3 = 22.79$, $m = 0.56$, and $n = 0.07$.

B. Second Group of Materials

Two Ni-Fe magnetic materials are used for curve fitting from material data resource [17]. The calculated curves and analytical functions unknown are presented in Figs. 5–7.

1) *Metglas:* $a_1 = 219.2$, $a_1' = 6661$, $a_2 = 722.9$, $a_2' = 770.4$, $a_3 = 0.2055$, $a_3' = 0.1705$, $b_1 = 5.941$, $b_2 = 7.817$, $b_3 = 11.3$, $m = 0.56$, and $n = 0.63$.
2) *Nickel-Steel:* $a_1 = 0.05361$, $a_1' = 0.04131$, $a_2 = 0.1532$, $a_2' = 0.09216$, $a_3 = -0.04524$, $a_3' = -0.02018$, $b_1 = 3.961$, $b_2 = 1.069$, $b_3 = 3.552$, $m = 0.56$, and $n = 0.63$.

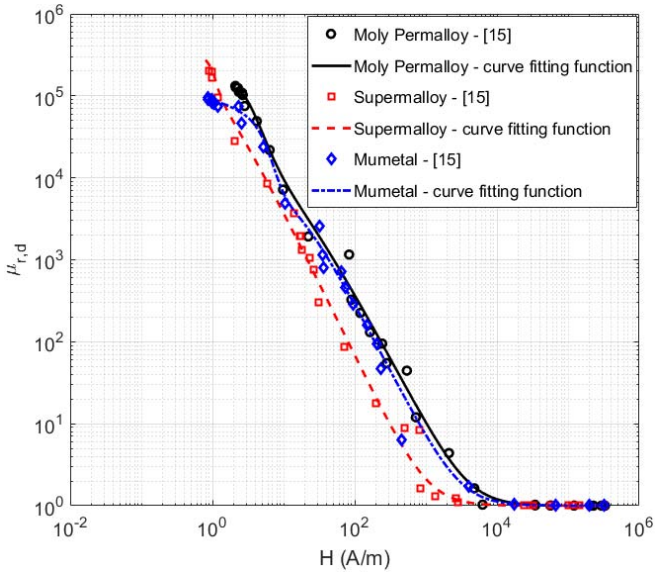

Fig. 4. Curve fitting for $\mu_{r,d}$–H curve—-differential relative permeability.

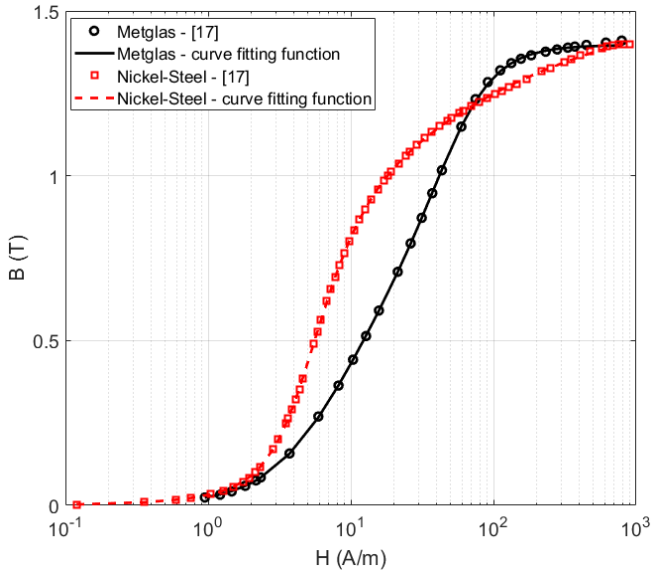

Fig. 5. Curve fitting for B–H curve.

TABLE I
NORMALIZED RMS ERROR AND NORMALIZED MAXIMUM ERROR

Material	Normalized rms error (%)		Max error (%)	
	B	μ_r	B	μ_r
Moly permalloy	0.27	0.55	0.60	0.60
Supermalloy	0.28	1.55	1.53	1.53
Mumetal	0.20	0.64	0.90	0.90
Metglas	0.45	0.87	2.1	2.1
Nickel-Steel	0.29	1.20	13.21	13.21

Table I presents maximum and rms errors for five analyzed materials. The large value for maximum errors is due to mismatching between the curve fitting function and measured data at one point.

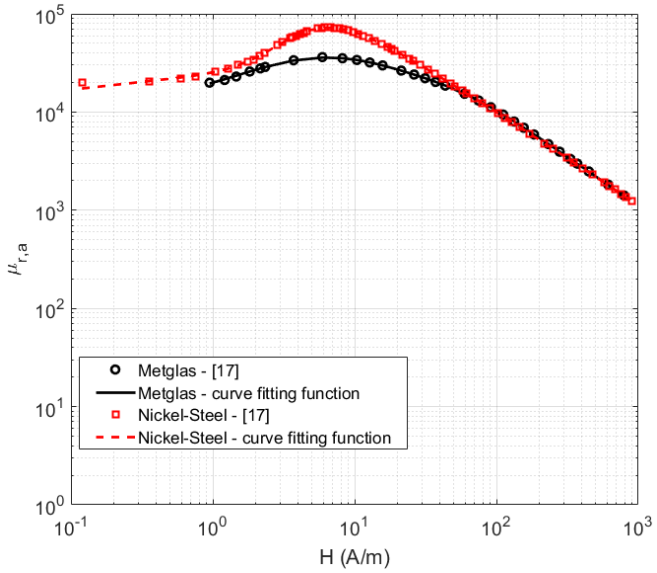

Fig. 6. Curve fitting for $\mu_{r,a}$–H curve—-apparent relative permeability.

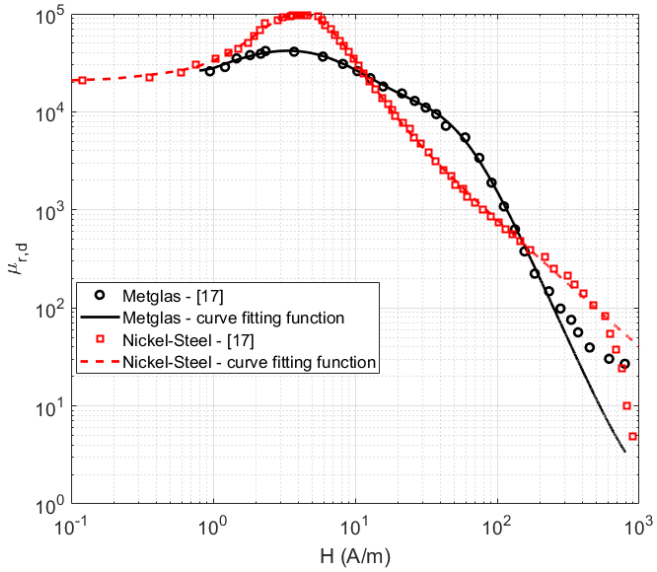

Fig. 7. Curve fitting for $\mu_{r,d}$–H curve—-differential relative permeability.

TABLE II
NORMALIZED RMS ERROR AND NORMALIZED MAXIMUM ERROR—FUNCTION WITH LESS UNKNOWNS

Material	Normalized rms error (%)		Max error (%)	
	B	μ_r	B	μ_r
Moly permalloy	0.59	2.06	2.62	2.62
Supermalloy	0.26	0.684	1.32	1.32
Mumetal	1.26	3.15	6.63	6.63
Metglas	3.32	6.56	8.6	8.6
Nickel-Steel	1.0	15.35	98.9	98.9

IV. ALTERNATIVE FUNCTIONS

Shorter form of the proposed analytical function and standard rational function, (8) and (9), is also evaluated. Table II shows corresponding errors for using (8), which are totally increased in comparison with the longer form function in (7).

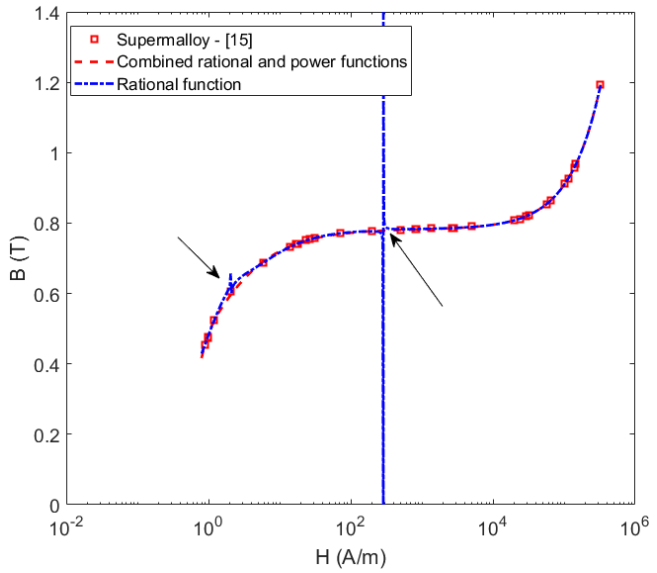

Fig. 8. Curve fitting for B–H curve—calculated rational function (9) unknowns: $a_1 = 0.7828$, $a_2 = -228.1$, $a_3 = 969.1$, $a_4 = -2581$, $a_5 = 3194$, $a_1' = -290.6$, $a_2' = 937.9$, $a_3' = -1792$, $a_4' = 634$, and $a_5' = 3323$.

The rational function with fifth-order and 10 unknown results are presented in Fig. 8. Two discontinuities are observed due to the zeros in the denominator of rational function, which is common for rational function curve fitting. It needs complicated algorithm to remove zeros [5], [7]. This phenomenon has less probability to happen in the proposed analytical function because powers of parameter, x, is not an integer number as in (9)

$$f(x) = \frac{a_1 \cdot x^{b_1} + a_2 \cdot x^{b_2}}{1 + a_1' \cdot x^{b_1} + a_2' \cdot x^{b_2}}, \quad (f(x) = J^m, x = H^n) \tag{8}$$

$$f(x) = \frac{a_1 \cdot x + a_2 \cdot x^2 + a_3 \cdot x^3 + a_4 \cdot x^4 + a_5 \cdot x^5}{1 + a_1' \cdot x + a_2' \cdot x^2 + a_3' \cdot x^3 + a_4' \cdot x^4 + a_5' \cdot x^5}$$
$$(f(x) = J, x = H). \tag{9}$$

The unknowns are calculated for (8) with curve fitting as follows.

1) *Moly Permalloy:* $a_1 = 4.256$, $a_1' = 4.894$, $a_2 = -4.337$, $a_2' = -5.592$, $b_1 = 2.527$, $b_2 = 1.222$, $m = 0.56$, and $n = 0.07$.
2) *Supermalloy:* $a_1 = 0.6312$, $a_1' = 0.7258$, $a_2 = -0.4198$, $a_2' = -1.408$, $b_1 = 4.737$, $b_2 = 0.1899$, $m = 0.56$, and $n = 0.07$.
3) *Mumetal:* $a_1 = 0.4232$, $a_1' = 0.5815$, $a_2 = 0.003329$, $a_2' = 0.004199$, $b_1 = 15.23$, $b_2 = 30.72$, $m = 0.56$, and $n = 0.07$.
4) *Metglas:* $a_1 = 0.000468$, $a_1' = 0.0004867$, $a_2 = -0.0002592$, $a_2' = -0.9988$, $b_1 = 0.6358$, $b_2 = 0.000674$, $m = 0.56$, and $n = 0.63$.
5) *Nickel-Steel:* $a_1 = 0.1039$, $a_1' = 0.09879$, $a_2 = 0.001024$, $a_2' = 0.0008324$, $b_1 = 2.629$, $b_2 = 4.219$, $m = 0.56$, and $n = 0.63$.

Comparison of other functions such as exponential functions or closed-form trigonometric functions is skipped to be

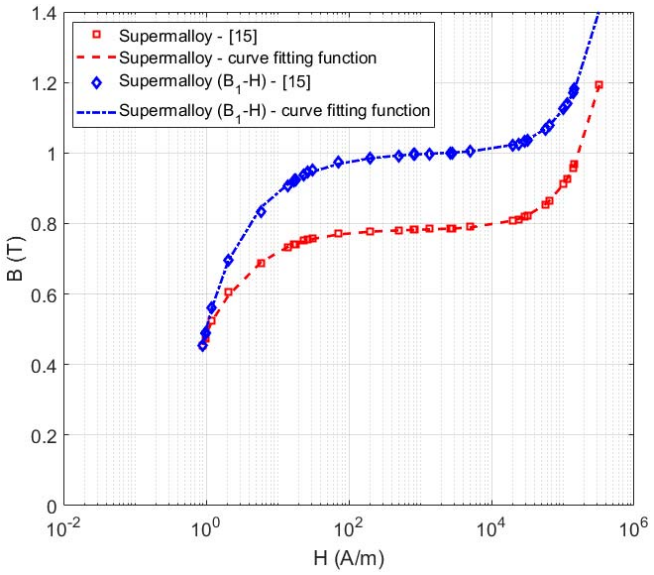

Fig. 9. Curve fitting for B_1–H curve.

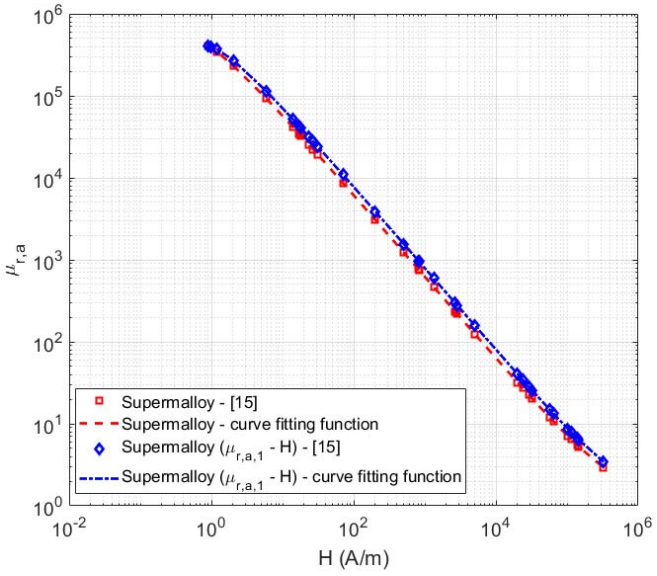

Fig. 10. Curve fitting for $\mu_{r,a,1}$–H curve–apparent relative permeability.

presented in this paper, which could give less precision rather than rational function.

V. Modified B–H Curve

A modified B–H curve is used when magnetic materials are involved in ac or time harmonic analysis especially with high non-linearity. The B–H curve is modified to B_1–H, which B_1 is the fundamental component of flux density when field strength changes in sinusoidal form [14], [15].

Figs. 9 and 10 show the B_1–H curve from measured values and curve fitting function. The results are promising for B_1–H curve. The calculated results for maximum error of flux density and relative permeability, rms error of flux density and relative permeability are 1.41% and 1.41%, 0.29% and 0.70%, respectively.

VI. Conclusion

New analytical function has been presented, which could precisely model B–H curve and relative permeability. The selected materials were high magnetic permeability Ni-Fe alloys but the presented analytical function could also be used for other magnetic materials. The main advantages of presented function are its compact format and high precision even with low number of unknowns for curve fitting. The typical value of rms error ranges from 0.3% to 1.6 %.

Standard rational function was compared with the proposed analytical function, which has the disadvantage of probable zeros in denominator and discontinuities in the modeled curve. Exponential functions for B–H curve modeling are not as precise as rational functions. The unknowns of the proposed analytical function could be calculated with simple curve fitting function.

Compatibility of the proposed analytical function has been presented for modified B–H curve corresponding to fundamental component of flux density, which also shows high precision.

References

[1] C.-W. Chen, *Magnetism and Metallurgy of Soft Magnetic Materials*. Amsterdam, The Netherlands: North Holland, Jan. 1977.
[2] P. Ripka, *Magnetic Sensors and Magnetometers*. Norwood, MA, USA: Artech House, Jan. 2001, p. 494.
[3] S. Tumanski, *Handbook of Magnetic Measurements*. Boca Raton, FL, USA: CRC Press, Jun. 2011, p. 404.
[4] F. C. Trutt, E. A. Erdélyi, and R. E. Hopkins, "Representation of the magnetization characteristic of DC machines for computer use," *IEEE Trans. Power App. Syst.*, vol. PAS-87, no. 3, pp. 665–669, Mar. 1968.
[5] G. F. T. Widger, "Representation of magnetisation curves over extensive range by rational-fraction approximations," *Proc. Inst. Elect. Eng.*, vol. 116, no. 1, pp. 156–160, Jan. 1969.
[6] J. Rivas, J. M. Zamarro, E. Martín, and C. Pereira, "Simple approximation for magnetization curves and hysteresis loops," *IEEE Trans. Magn.*, vol. 17, no. 4, pp. 1498–1502, Jul. 1981.
[7] P. Diez and J. P. Webb, "A rational approach to $B-H$ curve representation," *IEEE Trans. Magn.*, vol. 52, no. 3, Mar. 2016, Art. no. 7203604.
[8] M. El-Sherbiny, "Representation of the magnetization characteristic by a sum of exponentials," *IEEE Trans. Magn.*, vol. MAG-9, no. 1, pp. 60–61, Mar. 1973.
[9] W. K. Macfadyen, R. R. S. Simpson, R. D. Slater, and W. S. Wood, "Representation of magnetisation curves by exponential series," *Proc. Inst. Elect. Eng.*, vol. 120, no. 8, pp. 902–904, 1973.
[10] J. R. Brauer, "Simple equations for the magnetization and reluctivity curves of steel," *IEEE Trans. Magn.*, vol. 11, no. 1, p. 81, Jan. 1975.
[11] P. Diez, "Symmetric invertible $B-H$ curves using piecewise linear rationals," *IEEE Trans. Magn.*, vol. 53, no. 6, Jun. 2017, Art. no. 2001103.
[12] L. R. Nejman, *Skin Effect in Ferromagnetic Bodies*. Moscow, Russia: GEI, 1949.
[13] J. Lammeraner and M. Stafl, *Eddy Currents*. London, U.K.: Iliffe, 1967.
[14] S. A. Nasar, G. Y. Xiong, and Z. X. Fu, "Eddy-current losses in a tubular linear induction motor," *IEEE Trans. Magn.*, vol. 30, no. 4, pp. 1437–1445, Jul. 1994.
[15] *FEMM Software*. Accessed: Mar. 2, 2018. [Online]. Available: http://www.femm.info/wiki/Documentation/
[16] *Metals Handbook*, vol. 1, Amer. Soc. Met., Materials Park, OH, USA, 1966.
[17] *Free BH Curves*. Accessed: Mar. 2, 2018. [Online]. Available: http://www.magweb.us/free-bh-curves/
[18] *MATLAB Curve Fitting Toolbox Help*. Accessed: Mar. 2, 2018. [Online]. Available: https://www.mathworks.com/products/curvefitting.html

3-1-2 Hysteresis Loops Modeling using Combined Rational and Power Functions [S2] (Paper submitted for publication in Journal of Magnetism and Magnetic Materials)

Simple and precise hysteresis models with a small number of parameters allowing fast calculation are required for the magnetic analysis, as the field is calculated in a very large number of points. This paper presents a new simple method for modeling the hysteresis loops of soft magnetic materials using combined rational and power functions. Three approaches are used to model the hysteresis loops analytically. In the first approach, the upper and lower curves of the hysteresis loops are estimated and are calculated separately, using combined rational and power functions. In the second approach, the hysteresis loops are calculated using the DC magnetization curve and combined rational and power functions, applying a phase shift in the magnetic field strength variations relative to the magnetic flux density. The third approach presents a novel method for modeling hysteresis loops: first, the model is fitted to the "mean curve", which is in the middle of the measured hysteresis curve, and as a second step the phase shift is calculated as in the second approach. A solid iron sample with a rectangular cross section is used for the measurements and the hysteresis modeling. The proposed method is also applied to model the hysteresis loops of a magnetic material with high magnetic permeability and grain oriented steel, to show the generality of the proposed methods.

The proposed analytical methods for hysteresis loop modeling utilize a single closed-form equation for the entire *B*-*H* loop, which is simpler to implement than multi-function modeling of hysteresis loops. It has been shown that the methods presented for hysteresis modeling are a good compromise between simplicity and high accuracy. The third approach to model hysteresis loops is the most precise method, and it is very suitable for fast hysteresis modeling. The generality of the proposed method for various magnetically soft materials has been demonstrated on construction iron, grain-oriented steel and high-permeability amorphous alloy magnetic materials. Greater precision could be obtained with higher order combined rational and power functions, but this would increase the computational time. Calculating the phase shift between magnetic flux density B and magnetic field strength H is essential for resistance and inductance analysis of solid iron busbars in power systems, as it has a big influence on the phase angle of the impedance.

Modeling of Hysteresis Loops using Rational and Power Functions

Mehran Mirzaei, Pavel Ripka, Jan Vyhnanek, Andrey Chirtsov and Vaclav Grim

Faculty of Electrical Engineering, Czech Technical University
Prague 16627, Czech Republic, e-mail: mirzameh@fel.cvut.cz

***Abstract*—Simple and precise hysteresis models with a small number of parameters allowing fast calculation are required for the magnetic analysis, as the field is calculated in a very large number of points. This paper presents a new simple method for modeling the hysteresis loops of soft magnetic materials using combined rational and power functions. Three approaches are used to model the hysteresis loops analytically. In the first approach, the upper and lower curves of the hysteresis loops are estimated and are calculated separately, using combined rational and power functions. In the second approach, the hysteresis loops are calculated using the DC magnetization curve and combined rational and power functions, applying a phase shift in the magnetic field strength variations relative to the magnetic flux density. The third approach presents a novel method for modeling hysteresis loops: first, the model is fitted to the "mean curve", which is in the middle of the measured hysteresis curve, and as a second step the phase shift is calculated as in the second approach. A solid iron sample with a rectangular cross section is used for the measurements and the hysteresis modeling. The proposed method is also applied to model the hysteresis loops of a magnetic material with high magnetic permeability and grain-oriented steel, to show the generality of the proposed methods.**

***Keywords*—Hysteresis loops, modeling, combined rational and power functions, analytical**

I. Introduction

Analyzing the magnetic characteristics of soft magnetic materials is the key to the evaluation and design of electromagnetic devices. For example, the hysteresis loop effects in the impedance of solid irons and steels for current carrying busbars and high-permeability magnetic materials are critical for the performance of magnetic sensors, and they should be considered and analyzed in the design process [1]-[3]. Hysteresis loop models are used to analyze electromagnetic devices in transient and steady state analysis [4]-[5].

Various methods for hysteresis loop modeling of magnetic materials have been presented and their appropriateness are compared [6]. Preisach method for hysteresis modeling is well described in [7].It is based on the phenomenological and mathematical modeling methodand not a physical based method. Itcan accurately model major and minor hysteresis loops with high accuracy.Jiles-Atherton method and energetic model are physical based and they depend on micromagnetic characteristics of the magnetic materials [8]-[10].For example, a comparison between Preisach and Jiles-Atherton for hysteresis modeling was presented in [11], which showsextensive measurements requirements for parameters identifications using Preisach model with less problems for precise fitting with measurements. Jiles-Atherton method has opposite properties. However, time-consuming proceduresare required to calculate the constants and parameters in [6]-[15], and they are not easy handling for fast design and analysis process and optimization of the magnetic devices.Straightforward and uncomplicated analytical equations and procedures were implemented in [16]-[18]. However, these methods did not show generality of the proposed analytical functions for different magnetic materials. Detailed analyses of hysteresis loops for high magnetic permeability materials and grain-oriented steel laminations were presented in [19]-[21], in which multi-form mathematical functions are used to fit analytical hysteresis loops for various magnetic field strength ranges.

Combined rational and power functions were used in [22] to model magnetization characteristics without hysteresis. In this paper, we present three methods for introducing hysteresis into such a model. The aim is to keep the approximation very simple, so that the model has only minimum parameters and is suitable for design and calculation. The measured hysteresis loops of construction solid iron sample with a rectangular cross section are modeled and shown. The calculated phase shift between the magnetic flux density and the magnetic field strength is applied to calculate the phase angle of the solid iron impedance. The hysteresis loops of a high-permeability magnetic material and grain-oriented steel are also modeled in this paper to show the generality of the proposed method.

II. Measurement of Hysteresis Loops

A compensated permeameter is used to measure DC magnetization and the *B-H* curve and hysteresis loops for a rectangular solid iron sample (Fig. 1). A compensated permeameter is an instrument for measuring hysteresis loops for an open sample at DC and low frequency [23]. A solid iron sample with a rectangular cross section (5 mm · 30 mm) is used for the measurements and for hysteresis modeling. Four hysteresis loop measurements are presented with maximum magnetic field strengths of 500 A/m, 1000 A/m, 3000 A/m and 6000 A/m, respectively. The measured DC magnetization

curve for a solid iron sample is shown in Fig. 2.

III. Mathematical Approach

The analytical function of the magnetization or magnetic flux density B versus the magnetic field strength H curve in (1) can be represented as in (2) and (3), using combined rational and power functions [22]:

$$B = J + \mu_0 . H \tag{1}$$

$$f(x) = \left(\left(\sum_{i=1,2,\dots} a_i \cdot x^{b_i} \right) \Big/ \left(1 + \sum_{i=1,2,\dots} c_i \cdot x^{b_i} \right) \right)^{b_0},$$
$$J = f(x), x = H \tag{2}$$

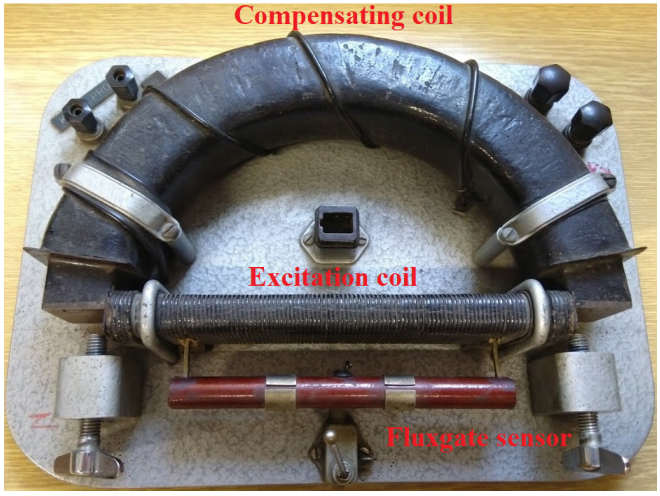

Fig. 1. A DC compensated permeameterand its elements (compensating coil, excitation coil, Fluxgate sensor)

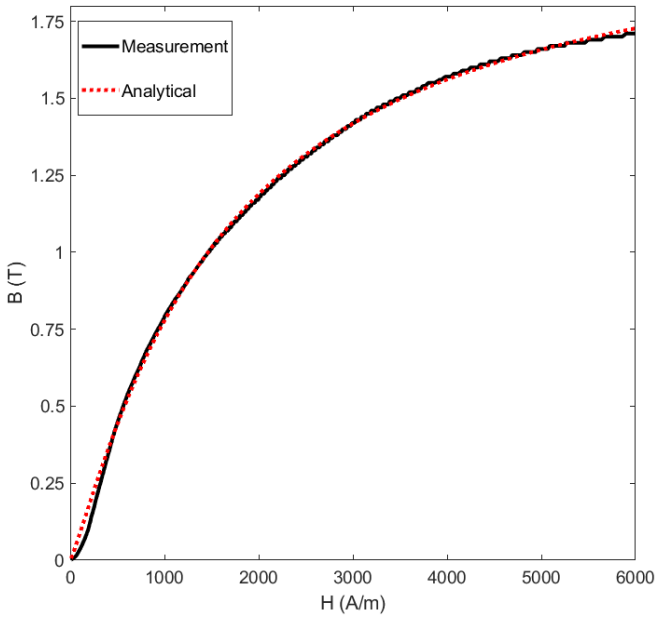

Fig. 2. DC magnetization curve for solid iron - Measurements using permeameter and analytical curve fit using function in (4)

$$f(x) = \left(\sum_{i=1,2,\dots} a_i \cdot x^{b_i} / (1 + c_i \cdot x^{b_i}) \right)^{b_0}, J = f(x), x = H$$
$$f(x) = \left(\sum_{i=1,2,\dots} a_i \cdot x^{b_i} / (1 + c_i \cdot x)^{b_i} \right)^{b_0}, J = f(x), x = H \tag{3}$$

Where a_i, c_i and b_i are constants which are calculated using curve fitting, and μ_0 is the magnetic permeability of the free space. Parameter $b_0$is considered to be equal to 1 in this paper. Term $\mu_0 \cdot H$ in (1)-(3) is negligible and it is not considered for the curve fitting because of the low magnetic fields (< 10000 A/m) in modeling the hysteresis loops.

IV. Modeling of Hysteresis Loops

In this paper, first order combined rational and power functions for modeling a DC magnetization curve are only used as follows in two forms of (4) and (5), which also take into account the change in the polarity of the magnetization curve for positive and negative values of the magnetic flux density and the magnetic field strength.

$$B = a_1 \cdot H \cdot |H|^{b_1 - 1} / (c_1 \cdot |H|^{b_1} + 1) \tag{4}$$

$$B = a_1 \cdot H \cdot |H|^{b_1 - 1} / (c_1 \cdot |H| + 1)^{b_1} \tag{5}$$

A. *First approach*

In the first approach to the modeling of hysteresis loops, the upper and lower curves of the hysteresis loops are calculated separately as described in appendix A, using the proposed functions in (6) - (9). Four parameters, a_1, a'_1, b_1 and c_1, are constants, and they are calculated by curve fitting.

$$B_a = a_1 \cdot H \cdot |H|^{b_1 - 1} / (c_1 \cdot |H|^{b_1} + 1) - a'_1 \cdot (|H_m|^{b_1} - |H|^{b_1}) / (c_1 \cdot |H|^{b_1} + 1) \tag{6}$$

$$B_a = a_1 \cdot H \cdot |H|^{b_1 - 1} / (c_1 \cdot |H|^{b_1} + 1) + a'_1 \cdot (|H_m|^{b_1} - |H|^{b_1}) / (c_1 \cdot |H|^{b_1} + 1) \tag{7}$$

$$B_a = a_1 \cdot H \cdot |H|^{b_1 - 1} / (c_1 \cdot |H| + 1)^{b_1} - a'_1 \cdot (|H_m|^{b_1} - |H|^{b_1}) / (c_1 \cdot |H| + 1)^{b_1} \tag{8}$$

$$B_a = a_1 \cdot H \cdot |H|^{b_1 - 1} / (c_1 \cdot |H| + 1)^{b_1} + a'_1 \cdot (|H_m|^{b_1} - |H|^{b_1}) / (c_1 \cdot |H| + 1)^{b_1} \tag{9}$$

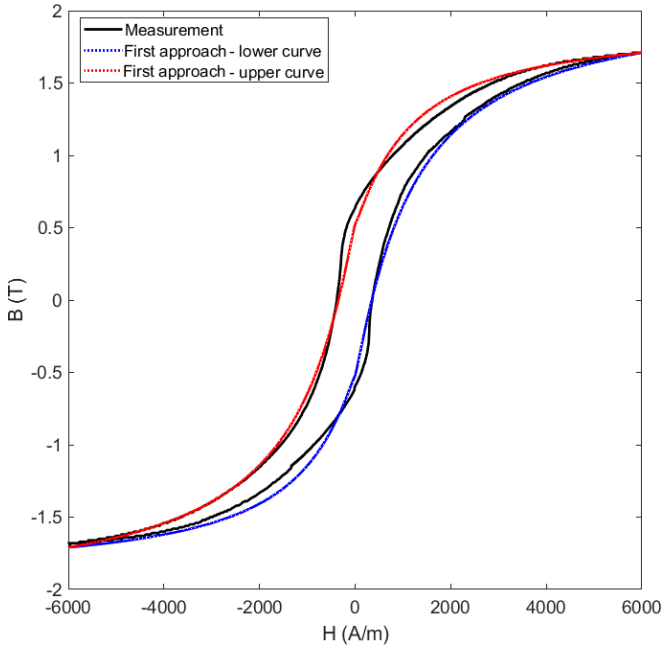

Fig. 3. Hysteresis loop modeling for solid iron (H_m = 6000 A/m) - Measurements using permeameter and analytical curve using second approach in (6) and (7)

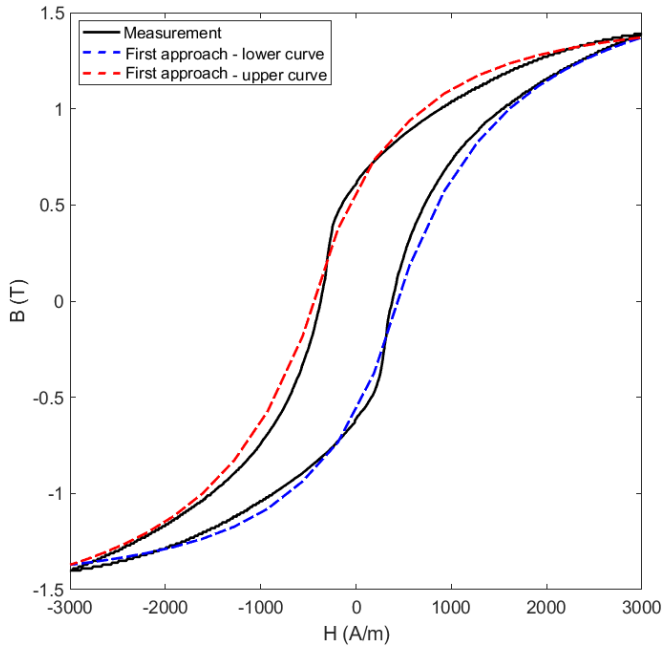

Fig. 4. Hysteresis loop modeling for solid iron (H_m = 3000 A/m) Measurements using permeameter and analytical curve using first approach in (6) and (7)

TABLE I. HYSTERESIS LOOPS PARAMTERS FOR THE FIRST APPROACH USING (6) AND (7)

Parameter	Value
$a_1 - H_m = 6000$ A/m	$7.021 \cdot 10^{-4}$
$b_1 - H_m = 6000$ A/m	1.122
$c_1 - H_m = 6000$ A/m	$3.531 \cdot 10^{-4}$
$a'_1 - H_m = 6000$ A/m	$3.013 \cdot 10^{-5}$
$a_1 - H_m = 3000$ A/m	$1.999 \cdot 10^{-4}$
$b_1 - H_m = 3000$ A/m	1.319
$c_1 - H_m = 3000$ A/m	$1.199 \cdot 10^{-4}$
$a'_1 - H_m = 3000$ A/m	$1.653 \cdot 10^{-5}$

Fig. 3 and Fig. 4 show a comparison between measurements and analytical model using the first approach. The results of the first approach for hysteresis loop modeling are as much as necessaryprecise and the results approximately fit with the measurements. The constants of the upper and lower curves in the first approach, using (6) and (7) could be calculated (Table I) using the curve fitting tool and alsothe iterative method described in appendix B.

B. *Second approach*

Parameter x in (2) and (3) can be replaced by function $H_m \cdot \cos(\theta - \theta_o)$ to model hysteresis loops, where H_m is the maximum magnetic field strength (Fig. 5), and θ_o is the phase shift. Fig. 5 presents a schematic model of the hysteresis loops using the first order function in (2) or (3) for different phase shifts θ_o and parameter $b_{i=1}$ in (2) or (3). A higher value for parameter b_1 makes the magnetization curve and the hysteresis loops sharper, and a change to phase shift θ_o makes the hysteresis loops wider or narrower.In the second approach, the DC magnetization curve is used as the method shown in Fig. 6, replacing parameter H with the use of$H_m \cdot \cos(\theta - \theta_o)$ in (4) and (5) to obtain (10) and (11). The phase shift θ_o is calculated to minimize the difference between the analytical model of the hysteresis loops and the measurements.

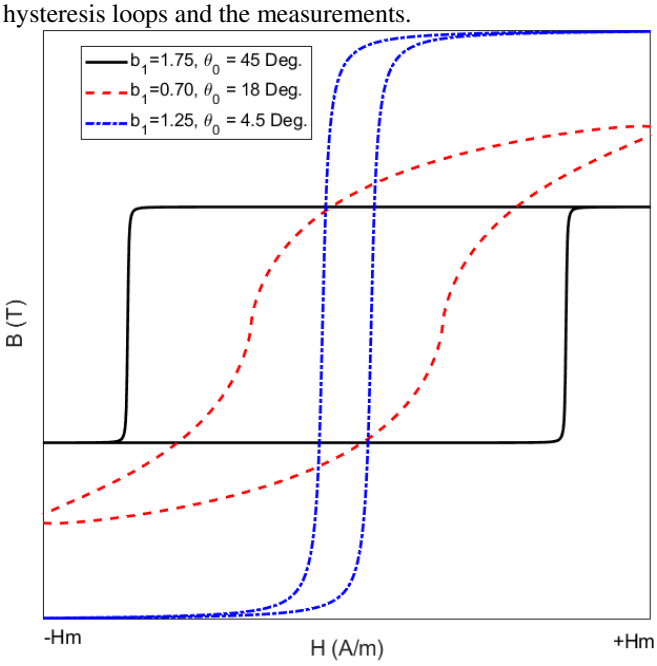

Fig. 5. Schematic models of hysteresis loops for different phase shifts, $\theta_o$modeled by analytical function in (4)

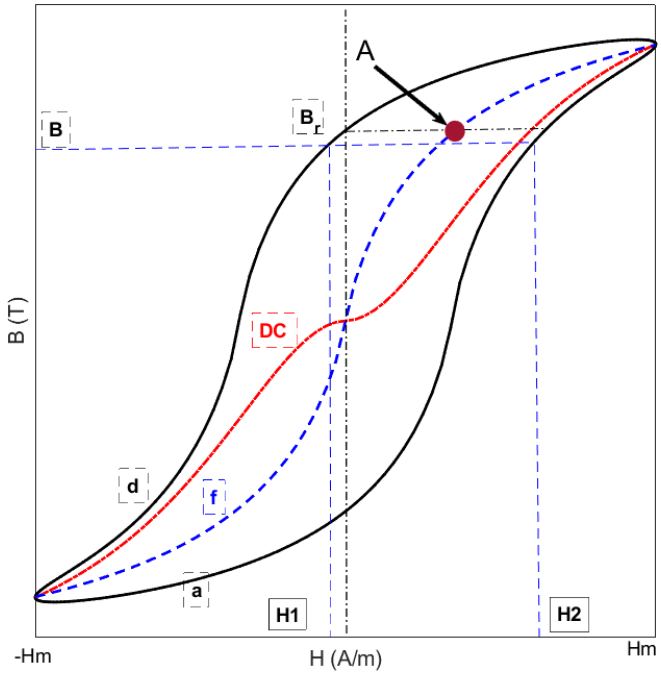

Fig. 6. Schematic model of the hysteresis loop and DC magnetization curvemodeled by analytical function in (4)

$$B = a_1 \cdot H_m \cdot \cos(\theta - \theta_o) \cdot |H_m \cdot \cos(\theta - \theta_o)|^{b_1 - 1} / (c_1 \cdot |H_m \cdot \cos(\theta - \theta_o)|^{b_1} + 1) \quad -\pi \le \theta \le \pi \tag{10}$$

$$B = a_1 \cdot H_m \cdot \cos(\theta - \theta_o) \cdot |H_m \cdot \cos(\theta - \theta_o)|^{b_1 - 1} / (c_1 \cdot |H_m \cdot \cos(\theta - \theta_o)| + 1)^{b_1} \tag{11}$$

Constants a_1, b_1 and c_1 in (4) for the DC magnetization curve (analytical), shown in Fig. 2, are calculated as $4.528 \cdot 10^{-4}$, 1.145 and $2.150 \cdot 10^{-4}$, respectively. The constants in a_1, b_1 and c_1 in (5) are calculated to be equal to $9.827 \cdot 10^{-5}$, 1.439 and $9.556 \cdot 10^{-4}$, respectively. An excellent fit between the measurements and the analytical model for the DC magnetization curve is shown in Fig. 2, except where the field values are very low.The results for hysteresis modeling are shown in Fig. 7 and Fig. 8. The phase shift angle θ_o in the second approach is calculated as 4.0 Deg. and 7.5 Deg. for the maximum magnetic field strength, 6000 A/m and 3000 A/m, respectively. The hysteresis loops for lower fields have bigger phase shifts between the magnetic flux density and the strength of the magnetic field.Both the first approach and the second approach have limited precision, especially for hysteresis loops at lower magnetic field strengths.

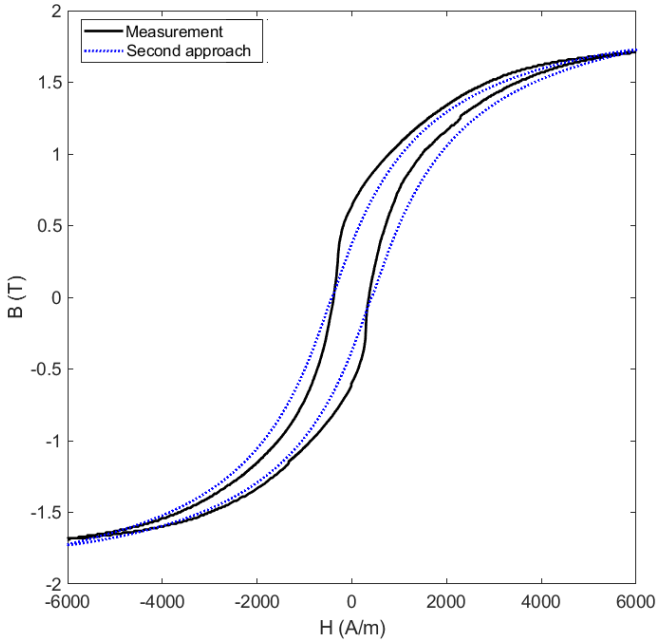

Fig. 7. Hysteresis loop modeling for solid iron (H_m = 6000 A/m) - Measurements using permeameter and analytical curve using second approach in (10)

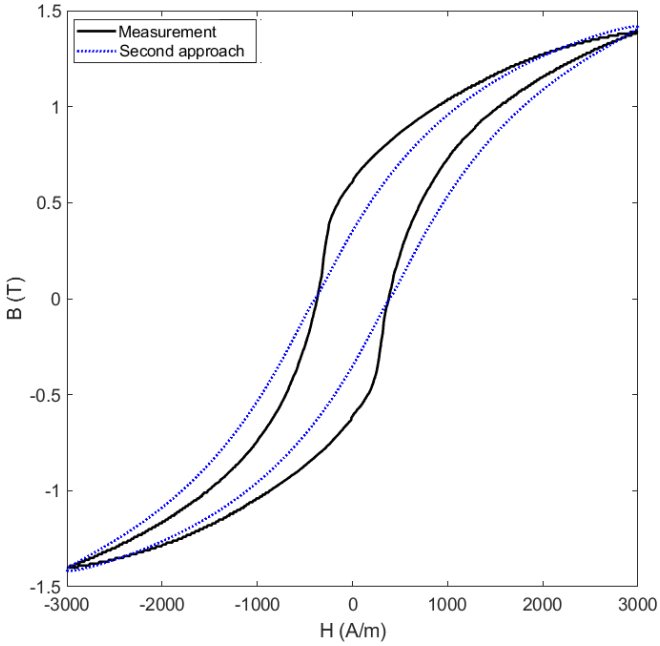

Fig. 8. Hysteresis loop modeling for solid iron (H_m = 3000 A/m) - Measurements using permeameter and analytical curve using second approach in (10)

C. *Third approach*

The third approach to hysteresis loop modeling in this paper uses "mean curve f", which is the average of the rising and falling branches of the hysteresis curve $H_f(B) = (H_a(B) + H_d(B))/2$, as shown in Fig. 6. As a second step, an analytical function in (4) or (5) is fitted to curve f; and finally the phase shift is calculated to this curve to model the hysteresis:

$$B_f = B_a = B_d$$
$$H_f = (H_a + H_d)/2 \quad (12)$$

Fig. 9 - Fig. 12 show a comparison between measurements and third approach models for different maximum values of the strength of the magnetic field. The third approach provides more precise models than the first and second approaches. The calculated constants of (10) and the phase shift angles are presented in Table II for different maximum values of the magnetic field strength, using curve fitting and minimizing the difference between the measurements and the models of hysteresis loops. The hysteresis loop modeling fits better with the measurements at higher maximum magnetic field strengths, H_m = 6000 A/m and 3000 A/m (Fig. 9 and Fig. 10).

The measurements are less symmetric at lower H_m = 1000 A/m and 500 A/m, which causes the greater visual difference in Fig. 9 and Fig. 10. Equation (13) replaces parameter $H_m \cdot \cos(\theta - \theta_o)$ in (10) with parameter $H = H_m \cdot \cos(\theta)$, which is easier to handle for the analysis. The upper and lower curves of the hysteresis loops can be distinguished: the plus sign (+) in (13) corresponds to the upper curve of the hysteresis loop (downward magnetization), and the minus sign (-) corresponds to the lower curve (upward magnetization). Calculations of hysteresis losses can be made using (13), as the upward and downward magnetization curves are separated.

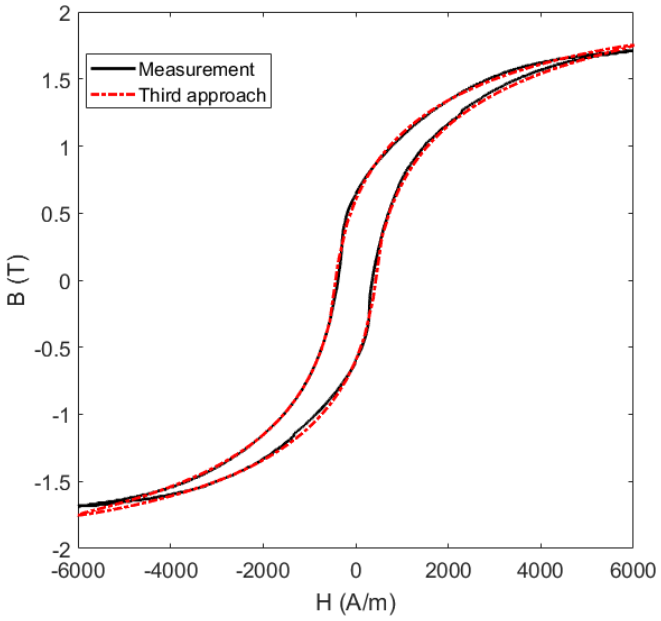

Fig. 9. Hysteresis loop modeling for solid iron (H_m = 6000 A/m) - Measurements using permeameter and analytical curve using third approach in (10)

$$H_m \cdot \cos(\theta - \theta_o) = H_m \cdot (\cos(\theta) \cdot \cos(\theta_o) + \sin(\theta) \cdot \sin(\theta_o)) = H_m \cdot \left(\cos(\theta) \cdot \cos(\theta_o) \pm \sqrt{1 - (\cos(\theta))^2} \cdot \sin(\theta_o)\right) = H \cdot \cos(\theta_o) \pm \sqrt{H_m^2 - H^2} \cdot \sin(\theta_o),\ H = H_m \cdot \cos(\theta),\ -H_m \le H \le +H_m \quad (13)$$

Appendix B shows simple iterative methods to calculate parameters of the hysteresis models for first and third approaches.

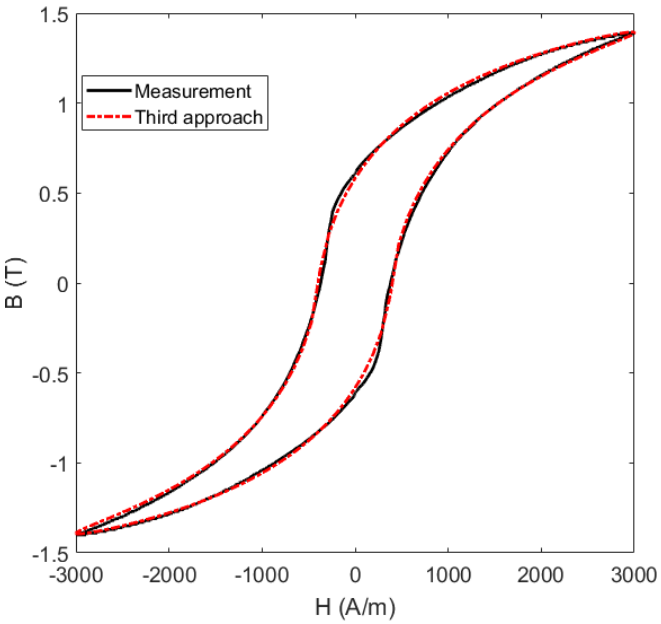

Fig. 10. Hysteresis loop modeling for solid iron (H_m = 3000 A/m) - Measurements using permeameter and analytical curve using third approach in (10)

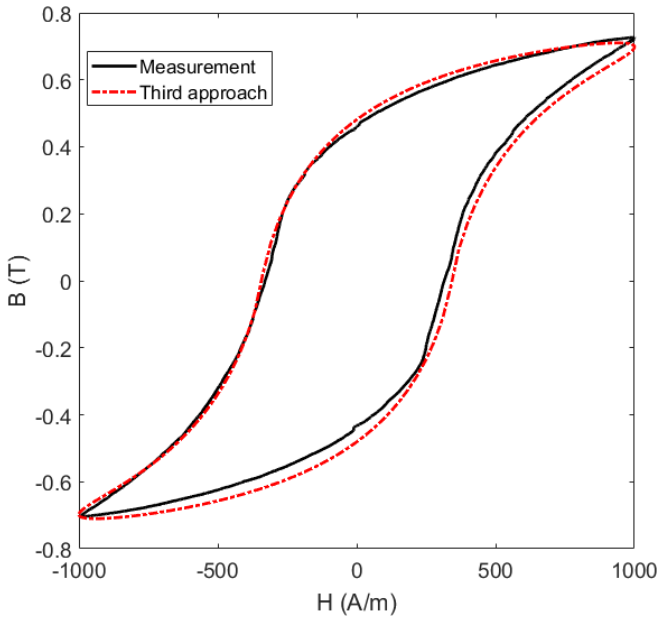

Fig. 11. Hysteresis loop modeling for solid iron (H_m = 1000 A/m) - Measurements using permeameter and analytical curve using third approach in (10)

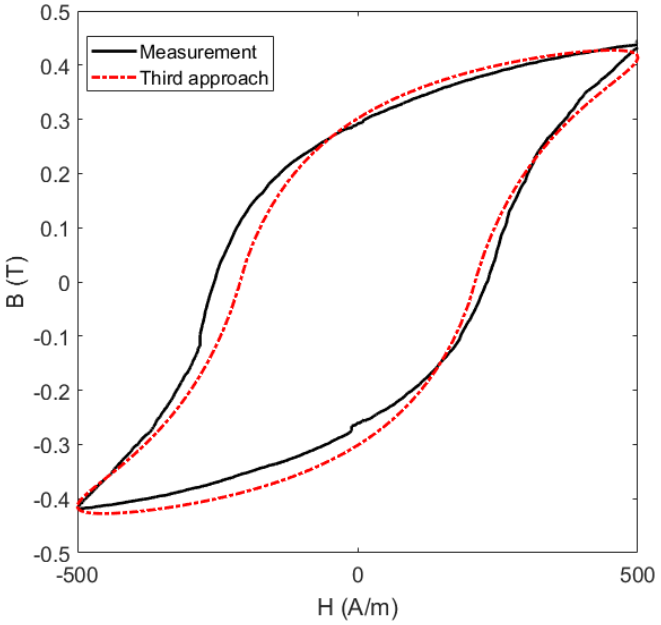

Fig. 12. Hysteresis loop modeling for solid iron (H_m = 500 A/m) - Measurements using permeameter and analytical curve using third approach in (10)

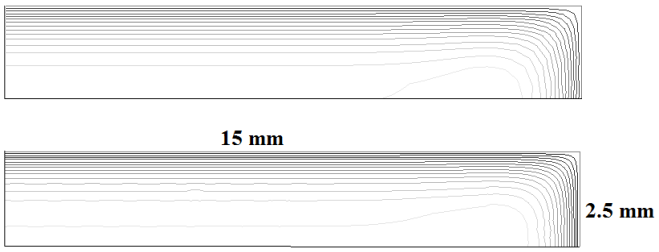

Fig. 13. Magnetic flux distribution in one quarter of a rectangular solid conductor- without hysteresis (above)and with hysteresis (below)

The first and third approach for hysteresis modeling showbetter accuracy than the second approach. However, more hysteresis loop input data are required for the first and third approaches. The first approach can be used when there is no access to hysteresis loop data.

TABLE II. HYSTERESIS LOOPS PARAMTERS FOR THE THIRD APPROACH USING (10)

Parameter	Value
$a_1 - H_m$ = 6000 A/m	$9.472 \cdot 10^{-3}$
$b_1 - H_m$ = 6000 A/m	0.7315
$c_1 - H_m$ = 6000 A/m	$3.678 \cdot 10^{-3}$
$\theta_o - H_m$ = 6000 A/m	4.0 Deg.
$a_1 - H_m$ = 3000 A/m	$1.04 \cdot 10^{-2}$
$b_1 - H_m$ = 3000 A/m	0.7211
$c_1 - H_m$ = 3000 A/m	$4.347 \cdot 10^{-3}$
$\theta_o - H_m$ = 3000 A/m	7.5 Deg.
$a_1 - H_m$ = 1000 A/m	$6.104 \cdot 10^{-3}$
$b_1 - H_m$ = 1000 A/m	0.855
$c_1 - H_m$ = 1000 A/m	$5.872 \cdot 10^{-3}$
$\theta_o - H_m$ = 1000 A/m	20 Deg.
$a_1 - H_m$ = 500 A/m	$4.044 \cdot 10^{-3}$
$b_1 - H_m$ = 500 A/m	0.9236
$c_1 - H_m$ = 500 A/m	$6.245 \cdot 10^{-3}$
$\theta_o - H_m$ = 500 A/m	24.8

V. IMPEDANCE ANALYSIS OF SOLID IRON BUSBAR

The effect of hysteresis on the internal impedances of a solid iron conductor is considerable and it must be taken into account, as shown in [1] and [24]. Impedance angle θ_z in (14) is dependent on the phase shift angle θ_o between B and H. Table III shows a comparison of the impedance angles between measurements and simulations. H_o is the strength of the magnetic field on the circumference of a rectangular solid iron conductor, which is calculated by the applied current I, the rectangular conductor cross section thickness t, and the width w, in (15).

The magnetic flux distribution in one quarter of a rectangular solid conductor is shown in Fig. 13, with and without taking hysteresis into consideration, showing the difference, especially in the middle of the conductor.

$$Z = R + jX, \theta_z = arctan(X/R) \quad (14)$$

$$H_o = 0.5\, I/(t + w) \quad (15)$$

TABLE III. IMPEDANCE PHASE ANGLE

Parameter	Value
$\theta_Z - H_o$ = 500 A/m (Exp.)	31.66 Deg.
$\theta_Z - H_o$ = 500 A/m (FEM without hysteresis)	43.58 Deg.
$\theta_Z - H_o$ = 500 A/m (FEM with hysteresis)	30.78 Deg.
$\theta_Z - H_o$ = 1000 A/m (Exp.)	31.43 Deg.
$\theta_Z - H_o$ = 1000 A/m (FEM without hysteresis)	43.49 Deg.
$\theta_Z - H_o$ = 1000 A/m (FEM with hysteresis)	32.92 Deg.

It is essential to take the hysteresis angle into consideration in internal impedance calculations, as presented in Table III. The impedance angle θ_z in (14) decreases by about 12 Deg., which causes a lower inductive part or inductance, and a higher resistive part or resistance.

VI. HIGH MAGNETIC PERMEABILITY MATERIAL

A highly magnetic permeability material, Vitrovac 6025X [25], is also considered for hysteresis modeling. The calculated constants of (10) and (11) are presented in Table IV and Table V. The phase shift angle is calculated as 10.9 Deg. The modeled hysteresis loop shows noteworthy accuracy (Fig. 14) for high magnetic permeability materials, despite the less-than-perfect symmetrical measured hysteresis loop. The values of parameter b_1 in Tables IV and V are higher than for solid iron in Table II, due to the higher permeability. The phase shift angle is considerably smaller than for solid iron at the same maximum magnetic flux density value of about 0.5 T, as high-quality magnetic materials have narrow hysteresis loops in order to have lower iron and hysteresis losses.

TABLE IV. HYSTERESIS LOOP PARAMTERS FOR THE THIRD APPROACH – USING (10)

Parameter	Value
a_1	0.2439
b_1	1.103
c_1	0.4363
θ_o	10.9 Deg.

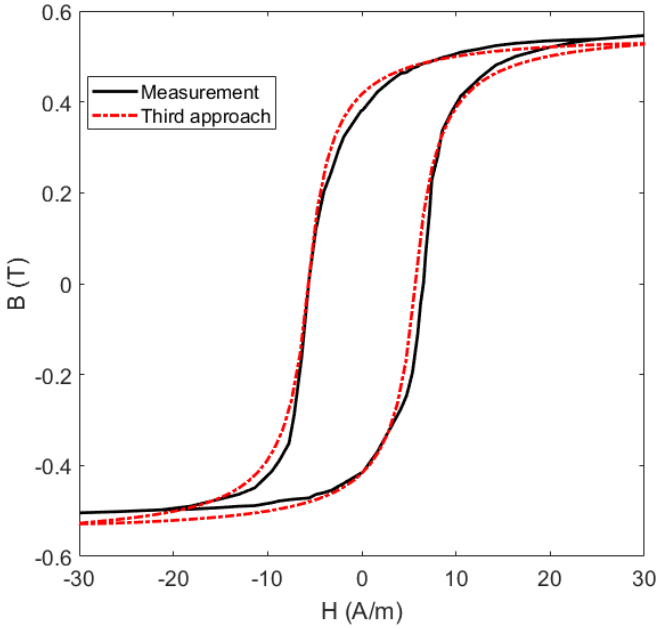

Fig. 14. Hysteresis loops modeling for high magnetic permeability material (H_m = 30 A/m) - Measurements [25] and analytical curve using third approach in (10)

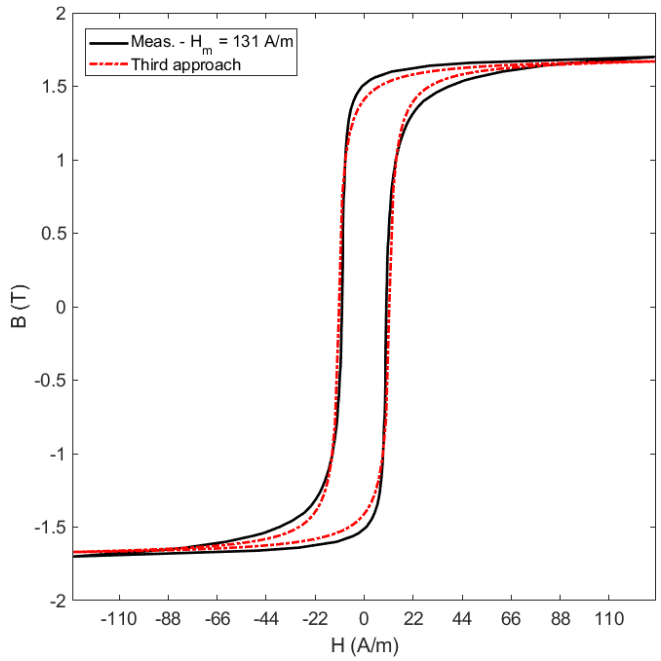

Fig. 15. Hysteresis loops modeling for grain oriented steel(H_m = 131 A/m) - Measurements [26] and analytical curve using third approach in (10)

TABLE V. HYSTERESIS LOOP PARAMTERS FOR THE THIRD APPROACH – USING (11)

Parameter	Value
a_1	0.2963
b_1	1.212
c_1	0.5783
θ_o	10.9 Deg.

VII. GRAIN ORIENTED STEEL

Hysteresis loops of grain-oriented steel are modeled using the third approach. Table VI presents the calculated parameters of hysteresis loops at various values of H_m. Fig. 15- Fig. 18 show modeled hysteresis loops in comparison with the values presented in [26]. Modeled hysteresis loops could be better fitted with the use of higher order combined rational and power functions, but this would substantially increase the computation time.

TABLE VI. HYSTERESIS LOOPS PARAMTERS FOR THE THIRD APPROACH USING (10)

Parameter	Value
$a_1 - H_m$ = 131 A/m	0.9282
$b_1 - H_m$ = 131 A/m	0.8899
$c_1 - H_m$ = 131 A/m	0.5429
$\theta_o - H_m$ = 131 A/m	5.0 Deg.
$a_1 - H_m$ = 38 A/m	0.312
$b_1 - H_m$ = 38 A/m	1.349
$c_1 - H_m$ = 38 A/m	0.2006
$\theta_o - H_m$ = 38 A/m	13.9 Deg.
$a_1 - H_m$ = 21 A/m	0.2124
$b_1 - H_m$ = 21 A/m	1.378
$c_1 - H_m$ = 21 A/m	0.1438
$\theta_o - H_m$ = 21 A/m	20 Deg.
$a_1 - H_m$ = 14 A/m	0.1519
$b_1 - H_m$ = 14 A/m	1.403
$c_1 - H_m$ = 14 A/m	0.1257
$\theta_o - H_m$ = 14 A/m	24.0

The maximum differences are seen for the hysteresis loop with H_m = 131 A/m. This is because of the different phase shift in the hysteresis loops for low value fields, for medium value field ranges and for high value field ranges. The differences could be reduced by using a variable phase shift instead of a constant phase shift for the hysteresis loop for high fields, which is planned for future work. The value of parameter b_1 goes down from low fields to high fields because the magnetization curve has sharper changes in the low fields.

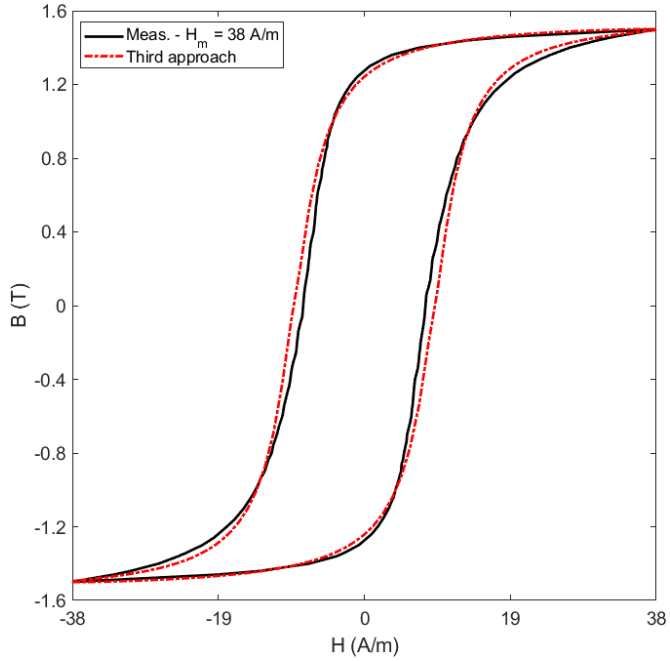

Fig. 16. Hysteresis loops modeling for grain oriented steel(H_m = 38 A/m) - Measurements [26] and analytical curve using third approach in (10)

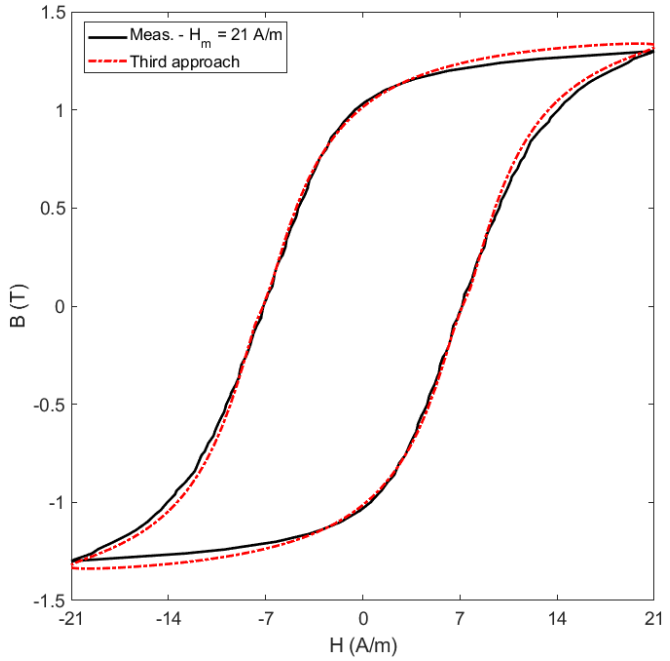

Fig. 17. Hysteresis loops modeling for grain oriented steel(H_m = 21 A/m) - Measurements [26] and analytical curve using third approach in (10)

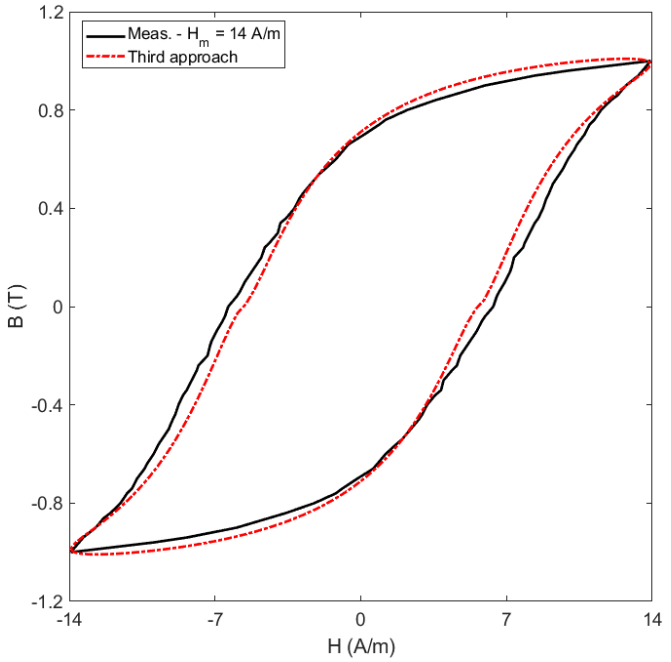

Fig. 18. Hysteresis loops modeling forgrain oriented steel (H_m = 14 A/m) - Measurements [26] and analytical curve using third approach in (10)

VIII. Discussions

Calculated phase shift, θ_o (Tables II and VI) curve versus magnetic field strength, H for solid iron and grain-oriented steel are shown in Fig. 19 and Fig. 20. They show the maximum phase shift corresponds to the maximum relative magnetic permeability, which confirms same conclusion in [24], [27].

The presented hysteresis modeling using third approach is fast and precise, which is crucial for electromagnetic devices analysis [28]-[33] with less time-consuming process.

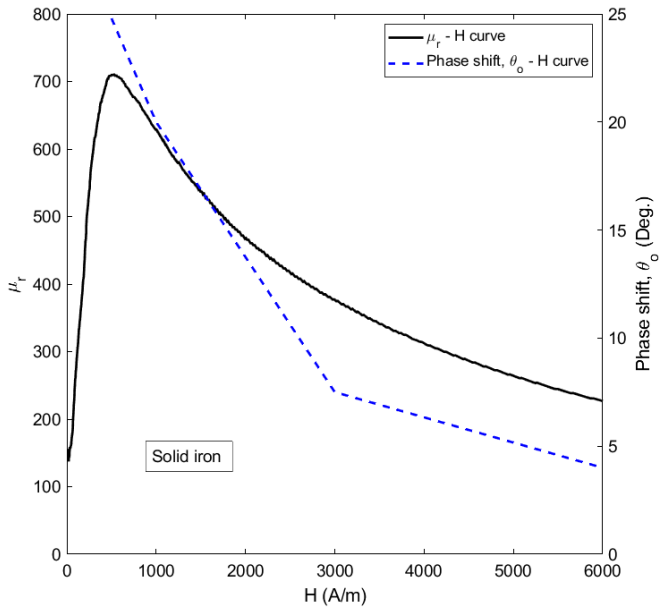

Fig. 19. Relative magnetic permeability, μ_r curve versus magnetic field strength, H and phase shift angle, θ_o curve versus H– solid iron

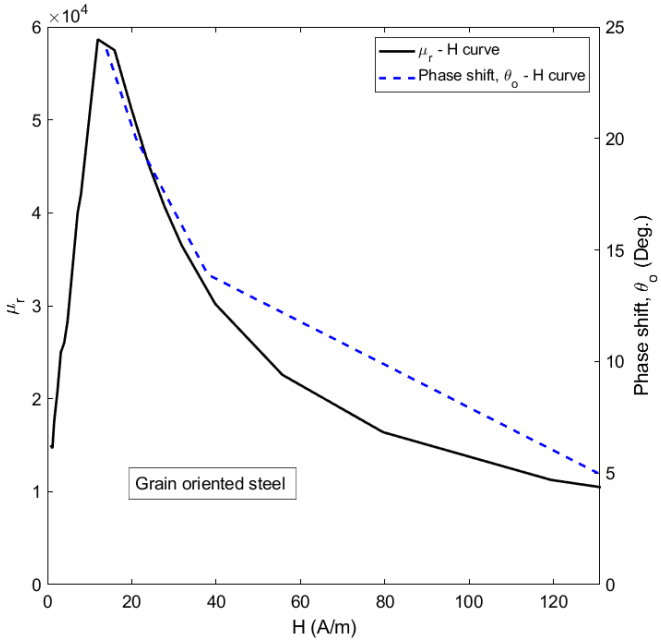

Fig. 20. Relative magnetic permeability, μ_r curve versus magnetic field strength, H and phase shift angle, θ_o curve versus H– Grain oriented steel

Micromagnetic models can simulate soft and hard magnetic materials [34]-[35] at very small scale and find magnetic domains with exact physical basis.

Hysteresis loop models including micromagnetic and physical parameters are ideal for understanding of the magnetization processes [36]-[37]. Such models are available, but they have complicated curve fitting [38]. The disadvantage of these methods is that they are very time consuming and therefore less practical for magnetic materials in macroscopic range [39].

IX. Conclusions

The proposed analytical methods for hysteresis loop modeling utilize a single closed-form equation for the entire *B-H* loop, which is simpler to implement than multi-function modeling of hysteresis loops. It has been shown that the methods presented for hysteresis modeling are a good compromise between simplicity and high accuracy. The third approach to modeling hysteresis loops is the most precise method, and it is very suitable for fast hysteresis modeling. Modeling can be made also using known physical parameters H_c,B_r, H_m and B_m as shown in Appendix B.The generality of the proposed method for various magnetically soft materials has been demonstrated on construction iron, grain-oriented steel and high-permeability amorphous alloy magnetic materials. Greater precision could be obtained with higher order combined rational and power functions, but this would increase the computational time.

Calculating the phase shift between magnetic flux density B and magnetic field strength H is essential for resistance and inductance analysis of solid iron busbars in power systems, as it has a big influence on the phase angle of the impedance.

X. Appendix A

Two auxiliary curves, p and m(Fig. 21) in (16) are extracted from curves corresponding to rising (lower) and falling (upper) curves, a and d of hysteresis loops [16]. Functions in (17) – (20) are assumed for the mathematical modeling of the curves p and m.

$$H_p = H_m = H_a = H_d$$
$$B_p = (B_d + B_a)/2$$
$$B_m = (B_d - B_a)/2$$
$$B = B_p \pm B_m \quad (16)$$

$$B_p = a_1 \cdot H \cdot |H|^{b_1-1}/(c_1 \cdot |H|^{b_1} + 1) \quad (17)$$

$$B_m = a_1' \cdot (|H_m|^{b_1} - |H|^{b_1})/(c_1 \cdot |H|^{b_1} + 1) \quad (18)$$

$$B_p = a_1 \cdot H \cdot |H|^{b_1-1}/(c_1 \cdot |H| + 1)^{b_1} \quad (19)$$

$$B_m = a_1' \cdot (|H_m|^{b_1} - |H|^{b_1})/(c_1 \cdot |H| + 1)^{b_1} \quad (20)$$

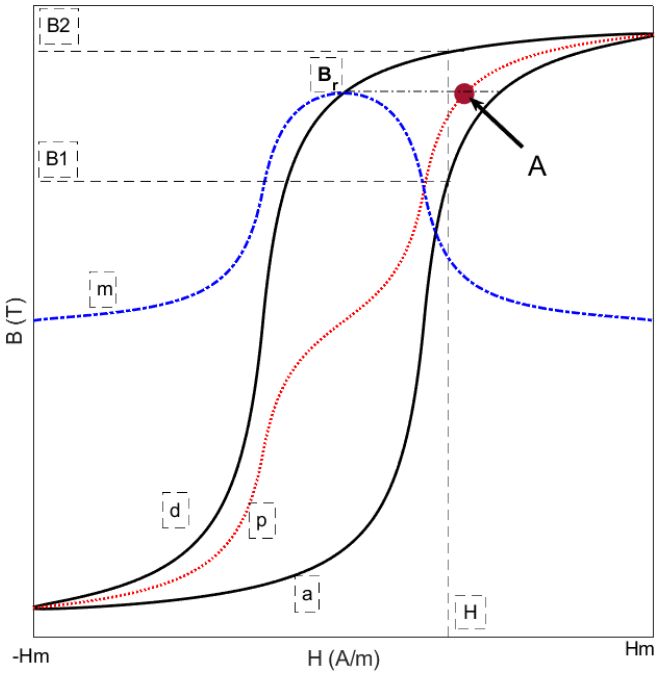

Fig. 21. Schematic model of the hysteresis loop used in first approachmodeled by analytical function in (6) and (7)

XI. Appendix B

An alternative method for calculating of the constants of the first approach in (6) and (7) is using equations in (21)-(24). Equations (21)-(23) correspond to the three points (0, $\pm B_r$), ($\pm H_c$, 0) and ($\pm B_m$, $\pm H_m$) in a hysteresis loop, which are obvious points in any hysteresis loop. H_c, B_r and B_m are coercivity force, remanence and the maximum flux density of the hysteresis loop corresponding to the maximum magnetic field strength,H_m, respectively. Another equation is required to calculate four constants,a_1, b_1, c_1 and a'_1, which corresponds to the differential permeability, $\mu_{r\text{-}d\text{-}A}$ inpoint A,(H_A, B_r) of Fig.

21. Point (H_A, B_r) in the curve p corresponds to the remanence magnetic flux density, B_r.

A simple numerical procedure is used to calculate constants, a_1, b_1, c_1 and a'_1. Firstly, initial value 1 is considered for the constant, b_1. Constant, a'_1 is calculated using (21) in second step. Equation (22) is used to obtain constant, a_1 in third step with calculated value, a'_1 from second step. Calculated constant, a_1 from (22) is replaced in (23) to obtain constant, c_1 in fourth step. Constant, b_1 is recalculated using (24) and calculated constants, a_1, c_1 and a'_1 in previous steps. The final and converged values of constants, a_1, b_1, c_1 and a'_1 could be calculated after 10 to 20 iterations, which takes less than 1 second time for the calculations. Fig. 22 shows hysteresis loop modeling of solid iron using first approach with calculated constants, a_1, b_1, c_1 and a'_1in Table VII as described in (21)-(24).

$$(0, \pm B_r) \rightarrow B_r = a_1' \cdot |H_m|^{b_1}, a_1' = B_r / |H_m|^{b_1} \quad (21)$$

$$(\pm H_c, 0) \rightarrow 0 = a_1 \cdot |H_c|^{b_1}/(c_1 \cdot |H_c|^{b_1} + 1) - a_1' \cdot (|H_m|^{b_1} - |H_c|^{b_1})/(c_1 \cdot |H_c|^{b_1} + 1)$$
$$a_1 = a_1' \cdot (|H_m|^{b_1}/|H_c|^{b_1} - 1) \quad (22)$$

$$(\pm H_m, \pm B_m) \rightarrow B_m = a_1 \cdot |H_m|^{b_1}/(c_1 \cdot |H_m|^{b_1} + 1)$$
$$c_1 = a_1 \cdot 1/B_m - 1/|H_m|^{b_1} \quad (23)$$

$$B_p = a_1 \cdot H \cdot |H|^{b_1 - 1}/(c_1 \cdot |H|^{b_1} + 1)$$
$$\mu_{r-d}\mu_0 = dB_p/dH = a_1 \cdot b_1 \cdot |H|^{b_1 - 1}/(c_1 \cdot |H|^{b_1} + 1)^2$$
$$b_1 = \mu_{r-d-A}\mu_0 \cdot (c_1 \cdot |H_A|^{b_1} + 1)^2/(a_1 \cdot |H_A|^{b_1 - 1}) \quad (24)$$

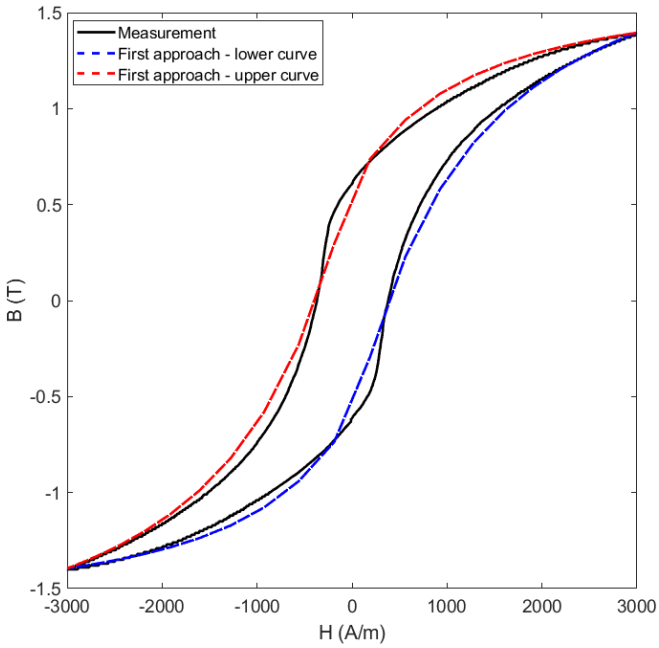

Fig. 22. Hysteresis loop modeling for solid iron (H_m = 3000 A/m) - Measurements using permeameter and analytical curve using first approach in (21) -(24)

TABLE VII. HYSTERESIS LOOPS PARAMTERS FOR THE FIRST APPROACH USING (21) AND (24) -FIG. 22

Parameter	Value
$a_1 - H_m$ = 3000 A/m	$7.0134 \cdot 10^{-4}$
$b_1 - H_m$ = 3000 A/m	1.1222
$c_1 - H_m$ = 3000 A/m	$3.7749 \cdot 10^{-4}$
$a'_1 - H_m$ = 3000 A/m	$7.6792 \cdot 10^{-5}$

Also the alternative approach to the curve fitting method for calculating four constants a_1, b_1, c_1 and $\theta_o$of third approach in (10) has similar numerical procedure as first method in (21)-(24), which are presented in four equations in (25) - (28).In order to calculate the phase shift, θ_o, the phase angle, θ_c is calculated according to (25). The phase shift, θ_o is obtained with condition in (26). The initial values of the parameters a_1 and c_1 are calculated from (27) with consideration of initial value 1 for b_1, which correspond to two points (H_m, B_m) and (H_A, B_r) in Fig. 6. Constant, b_1 is recalculated using (28) and calculated constants, $a_1$and $c_1$in previous steps. The differential permeability, $\mu_{r\text{-}d\text{-}A}$corresponds to point A, (H_A, B_r) of Fig. 6. The final and converged values of constants, a_1, $b_1$and $c_1$could be calculated after 10 to 20 iterations. Fig. 23 and Fig. 24 show hysteresis loop modeling of solid iron and grain oriented steel using third approach with calculated constants, a_1, b_1, c_1 and $\theta_o$in Tables VIII and IX as described in (25)-(28).

$$H = H_c = H_m \cdot cos(\theta_c), \theta_c = -\cos^{-1}(H_c/H_m), -\pi \leq \theta \leq 0$$
$$H = -H_c = H_m \cdot cos(\theta_c), \theta_c = \pi - \cos^{-1}(H_c/H_m), 0 \leq \theta \leq \pi \quad (25)$$

$$B(H = H_c) = 0$$
$$B = a_1 \cdot H_m \cdot cos(\theta_c - \theta_o) \cdot |H_m \cdot \cos(\theta_a - \theta_o)|^{b_1 - 1}/(c_1 \cdot |H_m \cdot \cos(\theta_a - \theta_o)|^{b_1} + 1) = 0$$
$$\rightarrow \theta_c - \theta_o = -\pi/2 \rightarrow \theta_o = \pi/2 + \theta_c = \pi/2 - \cos^{-1}(H_c/H_m) \quad (26)$$

$$B_m = a_1 \cdot |H_m|^{b_1}/(c_1 \cdot |H_m|^{b_1} + 1)$$
$$B_r = a_1 \cdot |H_A|^{b_1}/(c_1 \cdot |H_A|^{b_1} + 1)$$
$$a_1 = B_m \cdot B_r/(B_r - B_m) \cdot (1/|H_m|^{b_1} - 1/|H_A|^{b_1})$$
$$c_1 = 1/(B_r - B_m) \cdot (B_m/|H_m|^{b_1} - B_r/|H_A|^{b_1}) \quad (27)$$

$$B_f = a_1 \cdot H \cdot |H|^{b_1 - 1}/(c_1 \cdot |H|^{b_1} + 1)$$
$$\mu_{r-d}\mu_0 = dB_f/dH = a_1 \cdot b_1 \cdot |H|^{b_1 - 1}/(c_1 \cdot |H|^{b_1} + 1)^2$$
$$b_1 = \mu_{r-d-A} \cdot \mu_0 \cdot (c_1 \cdot |H_A|^{b_1} + 1)^2/(a_1 \cdot |H_A|^{b_1 - 1}) \quad (28)$$

TABLE VIII. HYSTERESIS LOOPS PARAMTERS FOR THE THIRD APPROACH USING (25)-(28) – FIG. 23

Parameter	Value
$a_1 - H_m$ = 500 A/m	$5.728 \cdot 10^{-3}$
$b_1 - H_m$ = 500 A/m	0.8407
$c_1 - H_m$ = 500 A/m	$8.017 \cdot 10^{-3}$
$\theta_o - H_m$ = 500 A/m	28.8

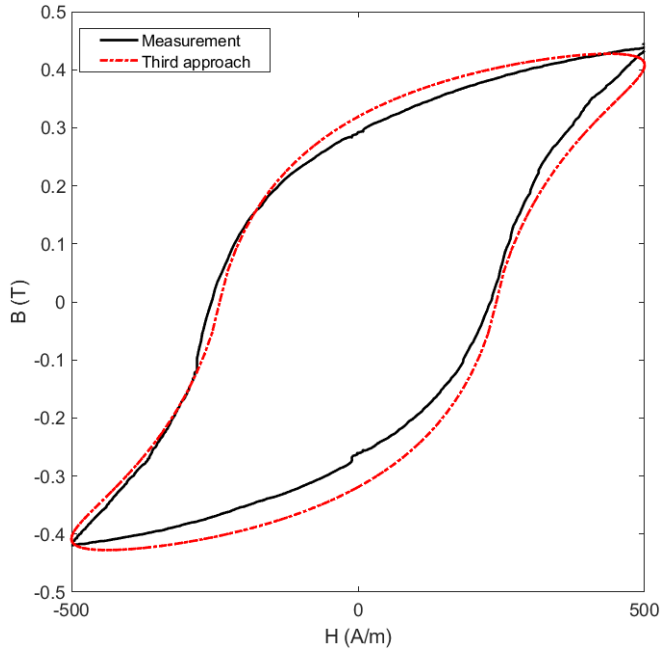

Fig. 23. Hysteresis loop modeling for solid iron (H_m = 500 A/m) - Measurements using permeameter and analytical curve using third approach in (25) - (28)

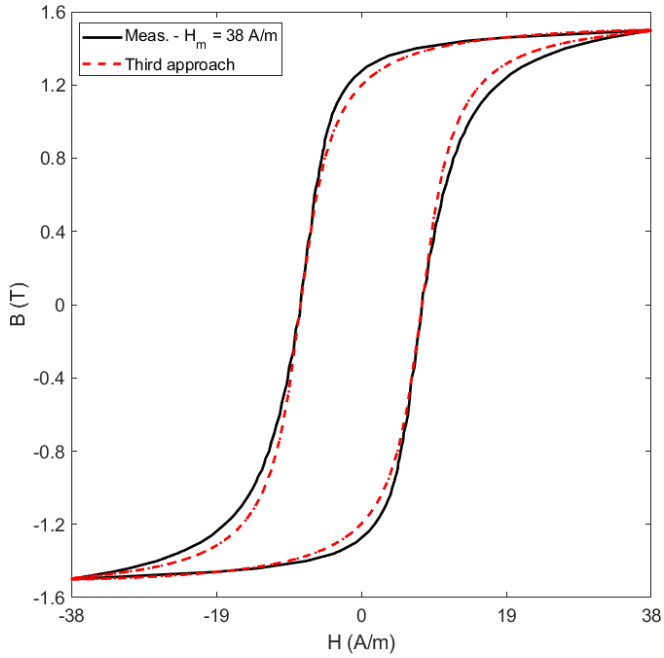

Fig. 24. Hysteresis loops modeling for grain oriented steel (H_m = 38 A/m) - Measurements [26] and analytical curve using third approach in (25) -(28)

TABLE IX. HYSTERESIS LOOPS PARAMTERS FOR THE THIRD APPROACH USING (10) -FIG. 24

Parameter	Value
$a_1 - H_m = 38$ A/m	0.3774
$b_1 - H_m = 38$ A/m	1.2581
$c_1 - H_m = 38$ A/m	0.2414
$\theta_o - H_m = 38$ A/m	12.0 Deg.

References

[1] M. Mirzaei, P. Ripka, A. Chirtsov, J. Vyhnanek, "Impedance of iron conductors with circular and rectangular shapes," Proceedings of the IECON 2018 - 44th Annual Conference of the IEEE Industrial Electronics Society, Washington, DC, USA, 21-23 October, 2018.

[2] M. Nowicki, R. Szewczyk, T. Charubin, A. Marusenkov, A. Nosenko, V. Kyrylchuk, "Modeling the hysteresis loop of ultra-high permeability amorphous alloy for space applications," Materials (11) (2018) 1-10.

[3] P. Ripka, "Sensors based on bulk soft magnetic materials: Advances and challenges," J. Magn. Magn. Mater. 320 (20) (2008) 2466-2473.

[4] C. Carrander, S. A. Mousavi, G Engdahl, "An application of the time-step topological model for three-phase transformer no-load current calculation considering hysteresis," J. Magn. Magn. Mater., 423, (2017), 241-243.

[5] A. A. Adly and H. H. Hanafy, "Incorporating core hysteresis properties in three-dimensional computations of transformer inrush current forces, " J. Appl. Phys. 105, 07A329 (2009).

[6] A. Ivany, *Hysteresis models in electromagnetic computation*, Akademiai Kiado, Budapest, 1997

[7] I. D. Mayergoyz, *Mathematical models of hysteresis*, New York: Springer-Verlag, 1991.

[8] D.C Jiles and D.L. Atherton, "Theory of ferromagnetic hysteresis," Journal of Applied Physics , vol. 55, no. 6, (1984), 2115-2120

[9] D.C Jiles and D.L. Atherton, "Theory of ferromagnetic hysteresis," J. Magn. Magn. Mater., vol. 61, no. 1-2, (1986), 48-60

[10] H. Hauser, "Energetic model of ferromagnetic hysteresis: Isotropic magnetization," Journal of Applied Physics, vol.96, no.5, (1984), 2753-2767

[11] D. A. Philips, L. R. Dupre, and J. A. Melkebeek, "Comparison of Jiles and Preisach hysteresis models in magnetodynamics," IEEE Trans. Magn., vol. 31, no. 6, (1995), 3551–3553

[12] A. Skarlatos, A. Martínez-de-Guerenu, R. Miorelli, A. Lasaosa, C. Reboud, "Use of meta-modelling for identification and interpolation of parametric hysteresis models applied to the characterization of carbon steels," Physica B: Condensed Matter, 549, (2018), 122–126

[13] S. E. Zirka, Y. I. Moroz, R. G. Harrison, and K. Chwastek, "On physical aspects of the Jiles-Atherton hysteresis models," J. Appl. Phys. 112, 043916 (2012)

[14] A. P. S. Baghel and S. V. Kulkarni, "Hysteresis modeling of the grain-oriented laminations with inclusion of crystalline and textured structure in a modified JilesAtherton model, " J. Appl. Phys. 113, 043908 (2013)

[15] B. Sai Ram, S.V. Kulkarni, "An isoparametric approach to model ferromagnetic hysteresis including anisotropy and symmetric minor loops," J. Magn. Magn. Mater., 474, (2019), 574–584.

[16] J. Rivas, J. M. Zamarro, E. Martin, C. Pereira, "Simple approximation for magnetization curves and hysteresis loops," IEEE Trans. Mag. 17 (4) (1983) 1498-1502.

[17] L. Battistelli, G. Gentile, A. Piccolo, "Representation of hysteresis loops by rational fraction approximations," Physica Scripta. 40, (1989), 502-507.

[18] Z. Wlodarski, "Analytical description of magnetization curves," Physica B, 373, (2006), 323–327.

[19] I. Nova, V. Havlicek, I. Zemanek, "Dynamic hysteresis loops modeling by means of extended hyperbolic model," IEEE Trans. Mag. 49 (1) (2013) 148-151.

[20] I. Nova, I. Zemanek, "Analytical model with flexible parameters for dynamic hysteresis loops modeling," J. of Elec. Eng., 61, (7/s), (2010), 46-49.

[21] I. Nova, I. Zemanek, "Analytical inverse model with flexible parameters for dynamic hysteresis loops modelling,"Prz. Elek. (9b), (2011), 89-92.

[22] M. Mirzaei, P. Ripka, "Analytical functions of magnetization curves for high magnetic permeability materials," IEEE Trans. Mag. 54 (11) (2018).

[23] P. Kaspar, P. Ripka. J. Vyhnanek, "DC compensated permeameter – the accuracy study," J. of Elec. Eng., 69, (6), (2018), 415-417.

[24] D. O'Kelly, "Hysteresis and eddy current losses in steel plates with nonlinear magnetization characteristics," Proc. IEE, 119 (11) (1972) 1675-1676.

[25] J. Kubik, L. Pavel, P. Ripka, P. Kaspar, “Low-power printed circuit board fluxgate sensor,” IEEE SENS. J., 7 (2) (2007), 179-183.

[26] D-C Hysteresis loops - M-2 Mill – Anneal GOES 0.007 in. Thick, AK Steel, Available online on 11.09.2018: https://www.aksteel.com › sites › default › files › lite-carlite-and-mill-anneal

[27] D. O’Kelly, “Flux penetration and core loss in solid iron,” IEEE Trans. Mag. 11 (1) (1975) 55-60.

[28] Z. Q. Wu, G. H. Shirkoohi, J. Z. Ca, “Simple dynamic hysteresis modelling of three phase power transformer,” J. Magn. Magn. Mater., 160, (1996), 79-80.

[29] Z. Sigut, T. Zemcik, “Hysteresis loop analytical approximation,” J. Magn. Magn. Mater., 73, (1988), 193-198.

[30] J. Zhao, S. E. Zirka, Y. I. Moroz, T. Matsuo, “Physical Cauer circuits in nonlinear eddy-current modeling,” J. Magn. Magn. Mater., 508, (2020), 166850.

[31] Y. Liu, D. Zhang, Z. Li, J. Li, L. Wu, S. Zhang, and H. Tang,“Study of the stray losses calculation in structural parts for HVDC converter transformers based on the TEAM problem 21 family,” IEEE Trans. Power. Delivery.31 (2) (2016) 605-612.

[32] J. He, L. Yu, X. Wang, and X. Song,“Simulation of transient skin effect of DC railway system based on MATLAB/Simulink,” IEEE Trans. Power. Delivery.28 (2) (2013) 145-152.

[33] H. Lu, A. Bokhari, T. Hong, and F. de Leon, “Experimental evaluation of available computational methods for eddy current and hysteresis losses for cables installed in steel pipes,” IEEE Trans. Power. Delivery.33 (4) (2018) 1777-1786.

[34] G. P. Zhao and X. L. Wang, “Nucleation, pinning, and coercivity in magnetic nanosystems: An analytical micromagnetic approach,” Phys. Rev. B 74, 012409 (2006)

[35] G. P. Zhao,X. L. Wang, C. Yang, L. H. Xie and G. Zhou, “Self-pinning: Dominant coercivity mechanism in exchange-coupled permanent/composite magnets,” J. of App. Phys. 101, 09K102 (2007)

[36] A. Furuya, J. Fujisaki, Y. Uehara, K. Shimizu, H. Oshima, and T. Matsuo, “Micromagnetic hysteresis model dealing with magnetization flip motion for grain-oriented silicon steel,” IEEE Trans. Mag., vol. 50, no. 11, (2014)

[37] M. Hofmann, H. Naumoski, U. Herr, and H.-G. Herzog, “Magnetic properties of electrical steel sheets in respect of cutting: micromagnetic analysis and macromagnetic modeling,” IEEE Trans. Mag., vol. 52, no. 2, (2016)

[38] D. C. Jiles, J. B. Thoelke. and M. K. Devine, “Numerical determination of hysteresis parameters the modeling of magnetic properties using the theory of ferromagnetic hysteresis,” IEEE Trans. Mag., vol. 28, no. 1 (1992), 27-35

[39] F. Liorzou, B. Phelps, and D. L. Atherton, “Macroscopic models of magnetization,” IEEE Trans. Mag., vol. 36, no. 2, (2000), 418-428

3-2 Applications

In this section, 16 papers describe applications of magnetic material modeling. Firstly, 4 papers concerning analysis of solid iron conductors are presented. Secondly, 6 papers are concerned about different types of position sensors. And finally, 6 papers present the results about linear and rotational eddy current speed sensors.

3-2-1 Solid Iron Conductors Analysis

3-2-1-1 The Effect of Conductor Permeability on Electric Current Transducers [J1]

In this work, experimental works and theoretical analysis are presented to analyze the influence of the conductor permeability on the precision of yokeless current sensors. The results of finite-element method (FEM) fit well the measured field values around the conductor. Finally we evaluate the difference in magnetic fields distribution around non-magnetic and magnetic conductor. The calculated values show that the permeability of the ferromagnetic conductor significantly affects the reading of the electric current sensors even at DC.

In this work, measurements and calculations of magnetic flux densities around a rectangular conductor were presented. Solid iron and copper were used for conductor material. We measured the material properties to be used for FEM simulations and verified the fit with measured field values around the conductor. General conclusion is that yokeless current sensors cannot be used for iron busbars without recalibration. Maximum error caused by the busbar permeability is 33% at DC and in minimum distance between the sensor and the busbar. If the distance is increased to 6 mm, the error drops to 10 %. The error is slightly decreasing with frequency, indicating that the difference in resistivity between copper and iron is not the dominant source of the error.

AIP ADVANCES **8**, 047506 (2018)

The effect of conductor permeability on electric current transducers

M. Mirzaei,[1] P. Ripka,[1,a] A. Chirtsov,[1] P. Kaspar,[1] and J. Vyhnanek[1]
[1]*Faculty of Electrical Engineering, Czech Technical University, Technicka 2, 166 27 Praha 6, Czech Republic*

(Received 4 July 2017; accepted 31 July 2017; published online 7 November 2017)

In this paper, experimental works and theoretical analysis are presented to analyze the influence of the conductor permeability on the precision of yokeless current sensors. The results of finite-element method (FEM) fit well the measured field values around the conductor. Finally we evaluate the difference in magnetic fields distribution around non-magnetic and magnetic conductor. The calculated values show that the permeability of the ferromagnetic conductor significally affects the reading of the electric current sensors even at DC. https://doi.org/10.1063/1.4994195

I. INTRODUCTION

Large electric currents are often measured by yokeless current transducers, which have small size and low price and also do not suffer from yoke saturation.[1,2] In the case that the measured current has DC component, Rogowski coil cannot be used and a differential magnetic sensor on the surface of the measured conductor[3] or inside the conductor[4] is typical solution. While for large currents individual discrete sensors are used, small currents up to typically 5 A can be measured by integrated sensors.[5] The main problem of using only two sensors in differential configuration can suppress external homogeneous field, but this configuration has large sensitivity to external currents in any direction.[6] Circular array of DC magnetic sensors is much more effective in this respect.[7] Circular arrays use Hall sensors,[8,9] but these suffer from poor DC stability. AMR sensors have small offset and drift, but due to their small range they can be used only for current sensors up to tens of Amps.[10] Using microfluxgate sensors, the DC stability is good and the current range can be increased to hundreds of Amps.[11]

To our knowledge all published papers on current sensors consider non-magnetic conductor. However, in some applications such as grounding conductors, iron busbars are used for their low price and high robustness. In this paper we study the effect of the busbar permeability on the accuracy of the current transducers. The calculations are done by Finite Element Modeling (FEM). This can be used to optimize the location and number of magnetic sensors to achieve minimum frequency dependence and also minimum influence of external currents. Finite element method (FEM) results are compared with measurements.

II. MODEL CONDUCTOR

In this paper we consider rectangular 30 × 5 mm conductor from soft iron. The conductor hysteresis curve was measured using compensated permeameter. This is an old method which is very useful for this type of materials. For massive soft magnetic materials permeameter gives more precise results than methods using H-coils. The complete hysteresis loop is shown in FIG. 1. The measured electrical conductivity of solid iron rectangular conductor is 5.07 MS/m.

[a]Author to whom correspondence should be addressed. Electronic mail: ripka@fel.cvut.cz

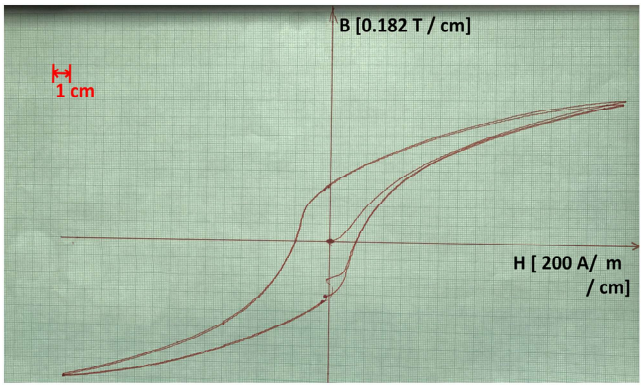

FIG. 1. Measured hysteresis B-H curve.

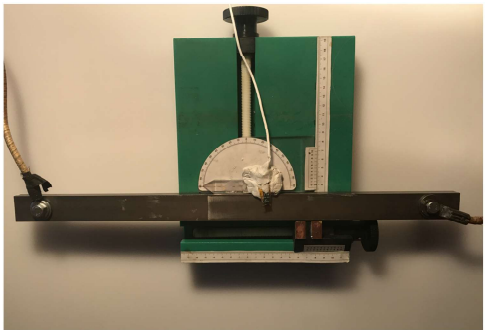

FIG. 2. Experimental setup.

FIG. 2 shows experimental setup for magnetic flux density measurement around solid iron rectangular conductor. Integrated fluxgate sensor DRV425[12] is used for the measurement.

Measurements and calculations of magnetic field around the conductor are done on two paths, which is shown in FIG. 3 as well as conductor dimensions. The distance between x and y paths and the surface of conductor is 1.5 mm. The amplitude of applied current is 23 A for all measurements and simulations.

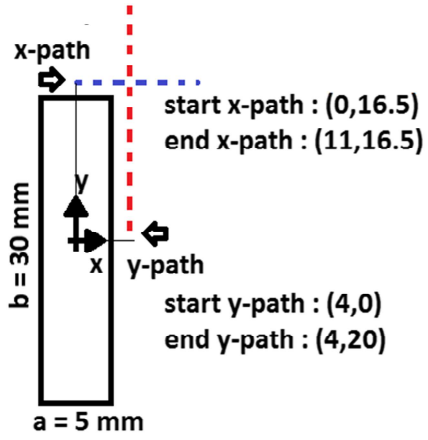

FIG. 3. Considered paths for magnetic flux densities measurement - center of coordinate is located in the center of rectangular conductor.

III. FEM SIMULATIONS AND MEASUREMENTS

FIG. 4 shows DC B-H curve and magnetic relative permeability. The maximum relative magnetic permeability is about 700. The FEM calculations are time harmonic method (FIG. 5), using FEMM package.[13]

Calculated and measured values of magnetic field in the 1.5 mm distance from the conductor are shown in FIGs. 6 and 7. The field sensors will be positioned in the range -2.5 < x < 2.5 mm and -7.5 < y < 7.5 mm. In this range the deviation between the measured and simulated values is below 10%.

The current density distribution in the conductor and magnetic field strength in the conductor and around the conductor are shown in FIGs. 8–10. For DC the current density is constant, while for AC it is affected by the skin effect. Skin effect is increased at higher frequency. Magnetic field distribution is affected both by the current distribution and by the busbar permeability, which is field dependent.

The effects of replacing solid iron conductor with copper conductor on magnetic fields on different paths (FIG. 11) are shown in FIGs. 12–14. It can be seen that largest difference between copper and iron conductors is observed by the sensor located at x=0, which is in the middle of the short side

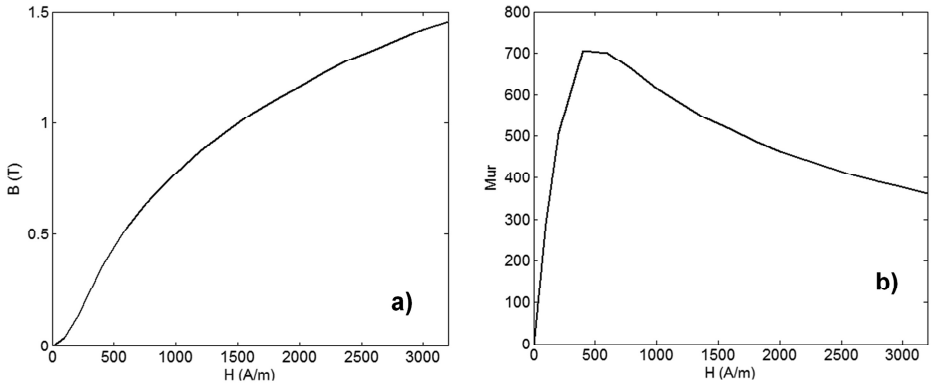

FIG. 4. DC B-H curve (a) and relative magnetic permeability curve (b) extracted from measurement (FIG. 1).

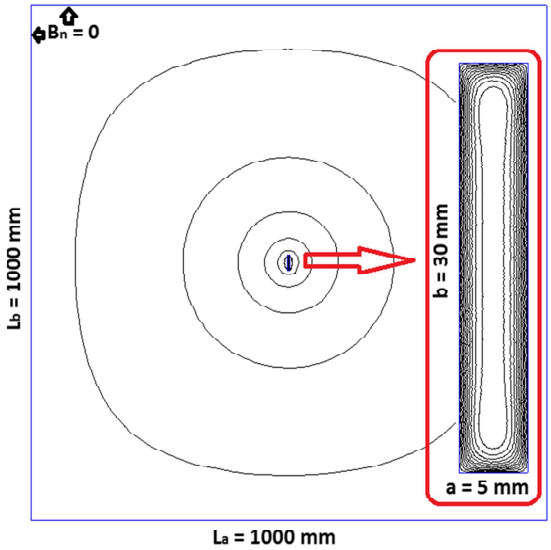

FIG. 5. Magnetic flux distribution using FEM[13] for solid iron rectangular conductor at 50 Hz and boundary conditions with applied current amplitude 23 A.

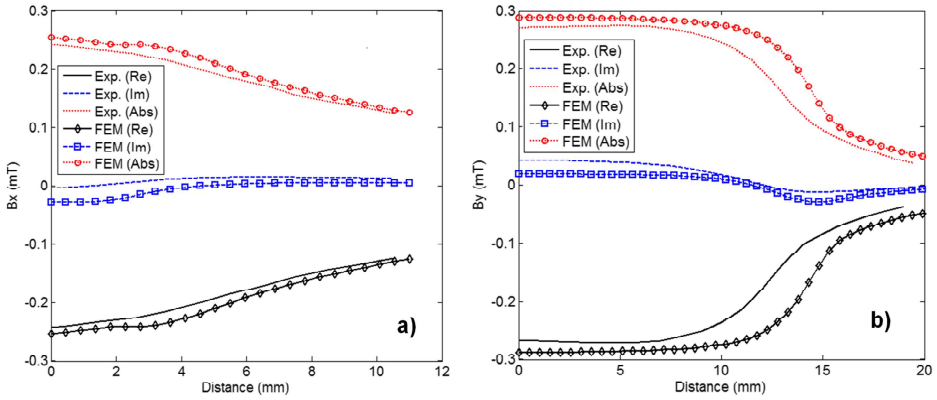

FIG. 6. Measured (Exp.) and FEM calculated magnetic flux density (tangential component) values on x-path (a) and on y-path (b) at 50 Hz - (Real values (Re), Imaginary values (Im) and absolute values (Abs)).

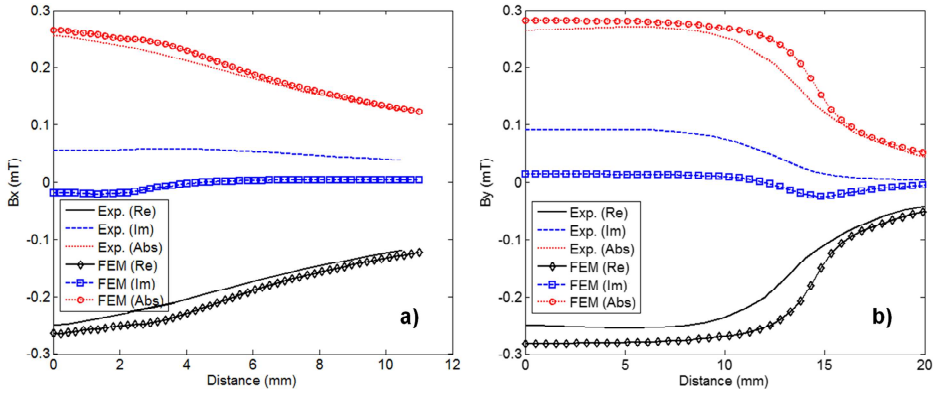

FIG. 7. Measured (Exp.) and FEM calculated magnetic flux density (tangential component) values on x-path (a) and on y-path (b) at 100 Hz - (Real values (Re), Imaginary values (Im) and absolute values (Abs)).

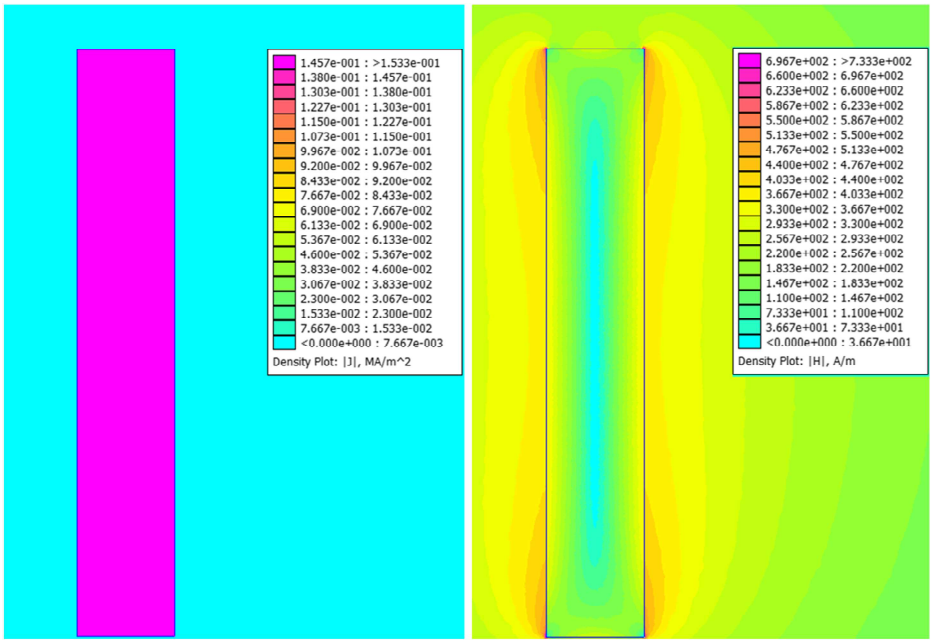

FIG. 8. Current density distribution in the conductor (left) and magnetic field strength distribution (right) at DC (I_{DC} = $23/\sqrt{2}$) A).

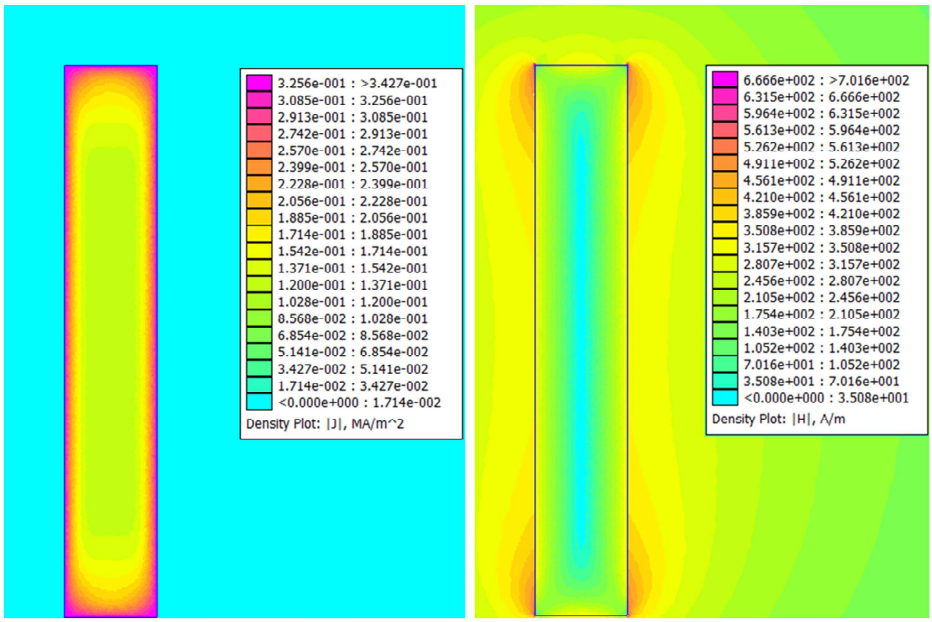

FIG. 9. Eddy current distribution in the conductor (left) and magnetic field strength distribution (right) at 50 Hz (I_{AC}=23 A).

of the busbar. This difference is increasing with reducing the distance and surprisingly it is slightly decreasing with frequency. The maximum difference of 33 % is observed at DC and in the minimum technically achievable distance of 1.5 mm. Increasing the distance to 6 mm reduces the maximum difference to 10%.

From the observed dependencies we may estimate that the main factor influencing the difference is busbar permeability, not the change between resistivity. The difference is decreasing with frequency, which indicates again that the effect of conductor permeability is stronger than the effect of eddy currents.

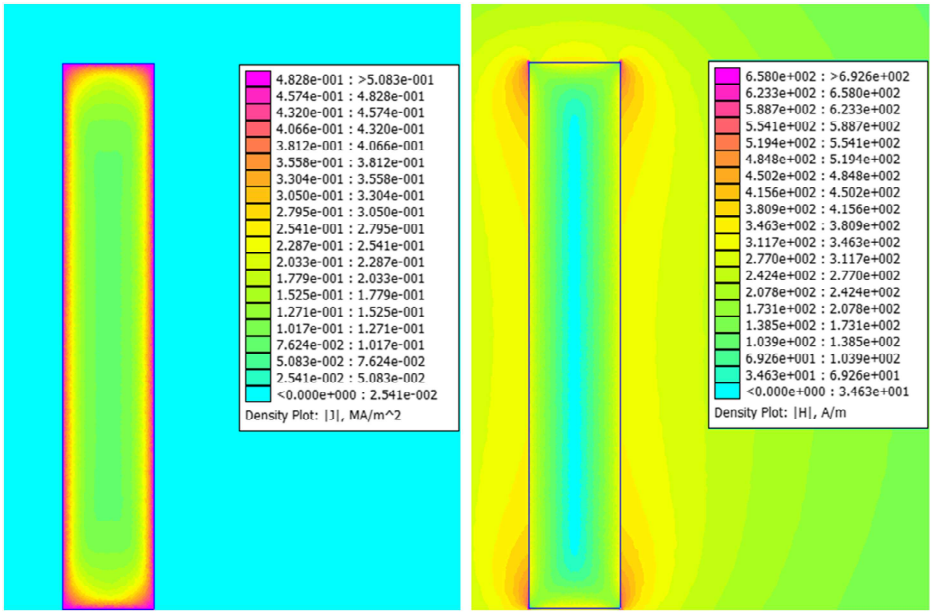

FIG. 10. Eddy current distribution in the conductor (left) and magnetic field strength distribution (right) at 100 Hz (I_{AC}=23 A).

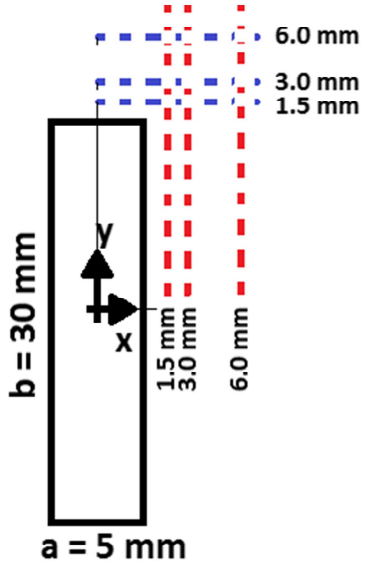

FIG. 11. Considered paths for magnetic flux densities (1.5 mm, 3 mm and 6 mm distances from the surface of conductor) - center of coordinate is located in the center of rectangular conductor.

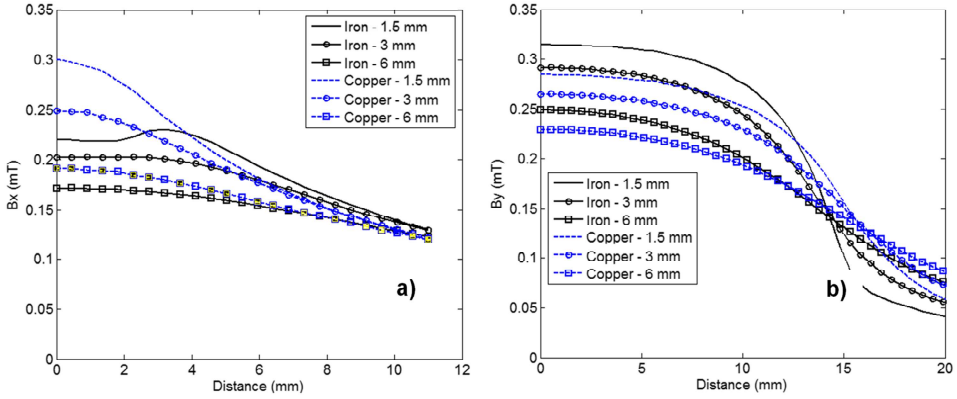

FIG. 12. Magnetic flux density (absolute value of tangential component) values at different paths (FIG. 11) using FEM at DC ($I_{DC} = 23/\sqrt{2}$ A) - x-directions (a) and y-directions (b).

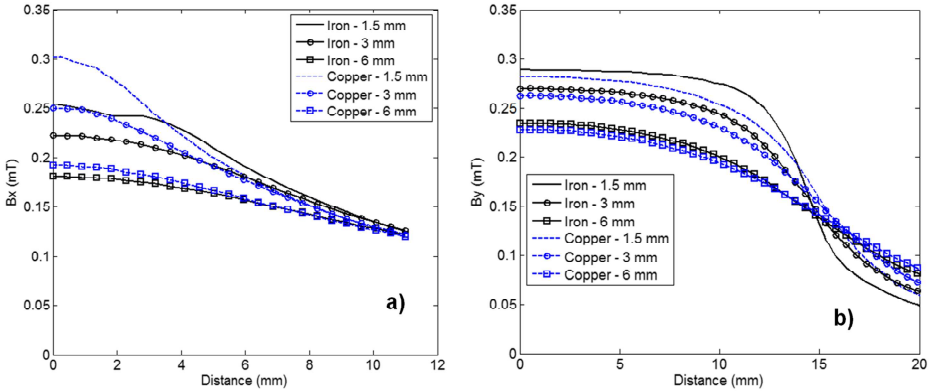

FIG. 13. Magnetic flux density (absolute value of tangential component) values at different paths (FIG. 11) using FEM at 50 Hz- x-directions (a) and y-directions (b).

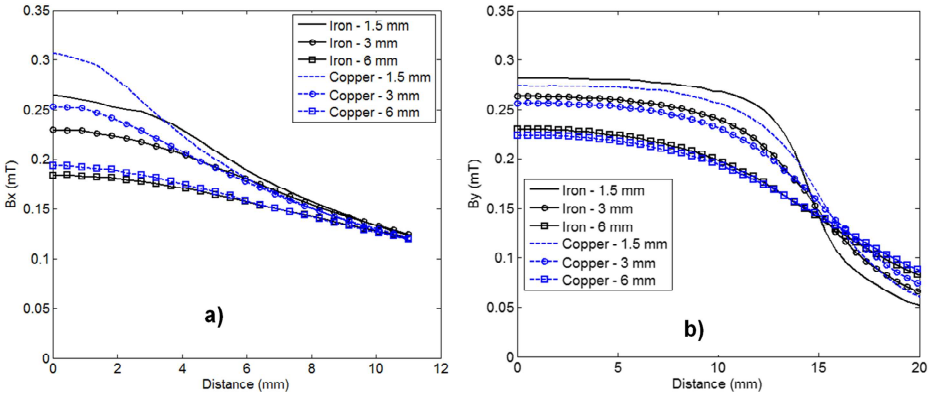

FIG. 14. Magnetic flux density (absolute value of tangential component) values at different paths (FIG. 11) using FEM at 100 Hz- x-directions (a) and y-directions (b).

IV. CONCLUSIONS

In this paper, measurement and calculations of magnetic flux densities around a rectangular conductor were presented. Solid iron and copper were used for conductor material. We measured the material properties to be used for FEM simulations and verified the fit with measured field values around the conductor. General conclusion is that yokeless current sensors cannot be used for iron busbars without recalibration. Maximum error caused by the busbar permeability is 33% at DC and in minimum distance between the sensor and the busbar. If the distance is increased to 6 mm, the error drops to 10 %. The error is slightly decreasing with frequency, indicating that the difference in resistivity between copper and iron is not the dominant source of the error.

ACKNOWLEDGMENTS

This work was supported by the Grant agency of the Czech Republic through the project "New methods for the measurement of electric currents" (GACR 17-19877S).

[1] P. Ripka, "Electric current sensors: A review," Meas. Science and Technology **21**(11), 1–23 (2010).
[2] Y.-P. Tsai, K.-L. Chen, Y.-R. Chen, and N. Chen, "Multifunctional coreless Hall-effect current transformer for the protection and measurement of power systems," IEEE Trans. Magn **63**, 557–565 (2014).
[3] M. Blagojevič, U. Jovanovič, I. Jovanovič, D. Mančič, and R. S. Popovič, "Realization and optimization of bus bar current transducers based on Hall effect sensors," Meas. Sci. Technol. **27**, 065102 (2016).
[4] P. Ripka, V. Grim, and V. Petrucha, "A busbar current sensor with frequency compensation," IEEE Trans. Magn. **53**(4) (2017), paper # 4000505.
[5] V. Frick, L. Hebrard, P. Poure, F. Anstotz, and F. Braun, "CMOS microsystem for AC current measurement with galvanic isolation," IEEE Sensors J. **3**, 752–760 (2003).
[6] P. Ripka and A. Chirtsov, Influence of External Current on Yokeless Electric Current Transducers, proc. Intermag 2017, accepted for IEEE Trans. Magn.
[7] L. Di Rienzo, R. Bazzocchi, and A. Manara, "Circular arrays of magnetic sensors for current measurement," IEEE Trans. Instrum. Meas. **50**(5), 1093–1096 (2001).
[8] K. L. Chen and N. Chen, "A new method for power current measurement using a coreless Hall effect current transformer," IEEE Trans. Instrum. Meas. **60**, 158–169 (2011).
[9] G.-J. Huang, N. Chen, and K.-L. Chen, "Self-calibration method for coreless Hall effect current transformer," 2016 IEEE Power and Energy Society General Meeting (PESGM), Boston, MA, 2016, pp. 1–5. Subm. To IEEE Trans. On Power Delivery.
[10] P. Mlejnek, M. Vopalensky, and P. Ripka, "AMR current measurement device," Sensors and Actuators A **141**, 649–653 (2008).
[11] R. Weiss, R. Makuch, A. Itzke, and R. Weigel, "Crosstalk in circular arrays of magnetic sensors for current measurement," IEEE Transactions on Industrial Electronics **64**(6) 4903–4909 (2017).
[12] D. Lee, M. Eissa, A. Gabrys, B. Shulver, E. Mazotti, S. Lavangkul, S. Chevacharoenkul, N. Murphy, F. Wang, Y. Zhang, W. French, M. Jenson, and R. Jackson, Fabrication and Performance of Integrated Fluxgate for Current Sensing Applications, Intermag 2017, in press IEEE Trans. Magn.,
[13] http://www.femm.info/wiki/Documentation/, accessed 2017/07/02.

3-2-1-2 Analysis of Material Effect on Rail Impedance [C1]

In this work, two different solid iron materials are used for two different size rails. The internal impedances, resistances and inductances of the rails are evaluated and analyzed with time harmonic and time stepping finite element methods. Two solid iron materials have different *B-H* curves and electrical conductivities. The analysis will be presented for different currents at different frequencies, 10 Hz - 10 kHz. The inductance analysis using finite element method is also performed under simultaneous large DC signal and small AC signal.

Different solid iron materials effects on the impedance of rails were presented. Analytical methods and FEM were used for the simulations. Presented analytical methods are quite precise in comparison with FEM, which could be used for fast analysis of rails impedances. Approximate analytical methods were presented for two approximated models, circular and rectangular solid conductors. Inductances and resistances were calculated at DC and AC currents with and without iron non-linearity effects. The material effects such as different electrical conductivities and *B-H* curves are not negligible at low and high frequencies. The hysteresis effects have considerable influences on the resistances and the inductances of the rails.

Analysis of Material Effect on Rail Impedance

Mehran Mirzaei
faculty of electrical engineering, department of measurement
czech technical university
Prague, Czech Republic
mirzameh@fel.cvut.cz

Pavel Ripka
faculty of electrical engineering, department of measurement
czech technical university
Prague, Czech Republic
ripka@fel.cvut.cz

***Abstract*—In this paper, two different solid iron materials are used for two different size rails. The internal impedances, resistances and inductances of the rails are evaluated and analyzed with time harmonic and time stepping finite element methods. Two solid iron materials have different *B-H* curves and electrical conductivities. The analysis will be presented for different currents at different frequencies, 10 Hz - 10 kHz. The inductance analysis using finite element method is also performed under simultaneous large DC signal and small AC signal.**

Keywords—rail, material, impedance, analysis

I. Introduction

The rails are electrically used for traction power currents and signaling circuits. Therefore impedance analyses of the rails are critical for power system analysis and accurate control signaling. The rail inductance value is required for signaling circuit analysis. Rail impedance and earth impedance is used in the power system dynamic analysis during unbalanced conditions.

AC and DC analysis of rail impedance are both required for AC and DC systems. Using power electronics switching in DC traction systems causes both DC signals and AC signals simultaneously in the rail, which means that incremental permeability is required for impedance analysis for AC component. Same phenomena are happening for impedance analysis of the rail for signaling circuits when power currents exist in the rails. Impedance of iron rails are highly dependent on the current and the frequency, which is caused by nonlinear *B-H* curve and high electrical conductivity of the solid iron rail.

Several papers were presented for impedance analysis of the iron rails [1]-[11]. Few papers presented detailed analysis of the rails impedances [8] - [10], which lack rail material effect on the rails impedances. References [8] - [10] study non-linearity and hysteresis effects on the rail impedances but they do not precisely illustrate different materials effects on the rails impedances.

Two materials with different *B-H* curves and electrical conductivities are used for simulations in this paper. Two iron rails are used with different dimensions. Two simplified circular and rectangular shapes equivalent models will be presented for each rail, which will be analyzed with finite element method (FEM) and analytical method for using as equivalent models of the complicated shapes of the rails.

II. Dimensions and Materials

A. Dimensions and Material data

The rails dimensions are shown in Fig. 1 for two rail models, A and B.

Two different solid iron materials 1 and 2 are used, with corresponding μ_r-H curves (relative magnetic permeability versus magnetic field strength) shown in Fig. 2. Electrical conductivities for materials 1 and 2 are 4.45 MS/m and 5.07 MS/m, respectively.

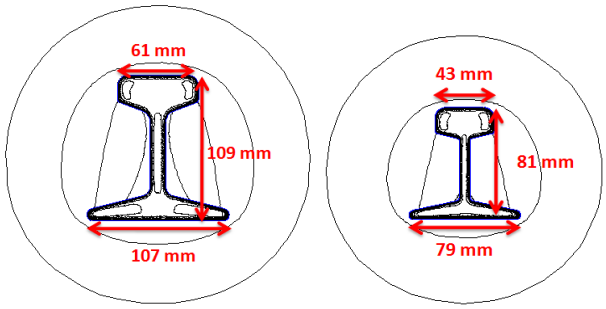

Fig. 1. Rails dimensions and corresponding magnetic flux distribution at 50 Hz - Model A (left) and Model B (right)

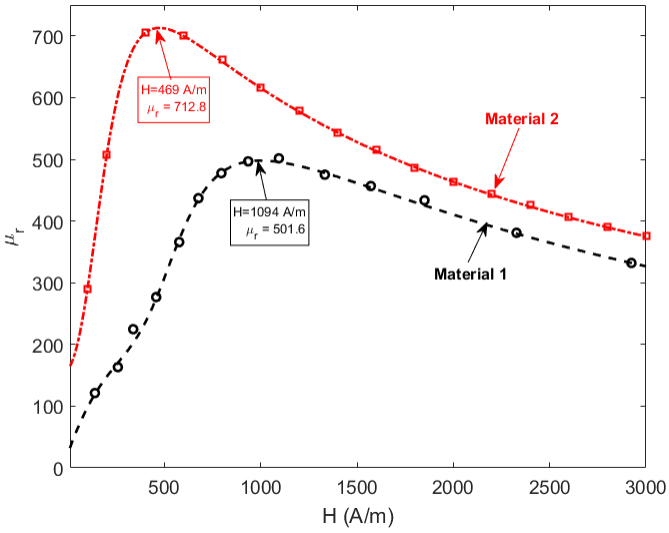

Fig. 2. Materials 1 and 2 - μ_r - H

978-1-5386-2910-9/18/$31.00 ©2018 IEEE

III. Approximate Equivalent Modles

Two equivalent models are considered for the rails configuration in Fig. 1. First equivalent model is circular shape and second equivalent model is square shape, for which edge and corner effects could be seen unlike circular shape model. The dimensions of equivalent models are calculated from circumferences and areas of the rails. Rail area value is used for equivalent models dimensions calculations when skin effect is low and current is smoothly distributed in the rail cross section. Rail circumference value is applied for high skin effect to calculate equivalent models dimensions. Equivalent radius, r_e and edge, a_e sizes for circular shape and square shape models are as following in (1) and (2):

$$r_{e,S} = \left(\frac{S}{\pi}\right)^{0.5} \qquad r_{e,C} = \frac{C}{2\pi} \tag{1}$$

$$a_{e,S} = S^{0.5} \qquad a_{e,C} = \frac{C}{4} \tag{2}$$

where, S and C are area and circumference of the rails cross section.

Cross section area and circumference of rails A and B are 3837.3 mm^2, 473.77 mm, 2070.8 mm^2 and 356.41 mm. Only rails models are considered in the internal impedance calculations and surrounding air region is neglected due to the high permeability of the solid iron.

A. Circular shape models

Equivalent radii, $r_{e,S}$, $r_{e,C}$ for rails A and B are calculated using (1), equal to 34.95 mm, 75.4 mm, 25.67 mm and 56.72 mm, respectively. Fig. 3 shows equivalent circular models with half model configuration for rails A and B.

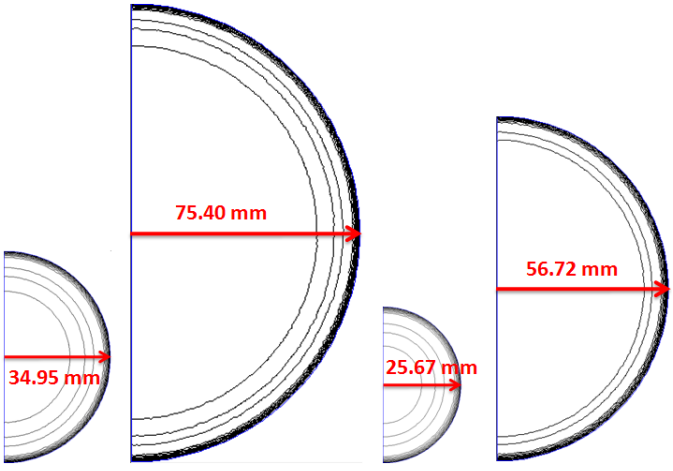

Fig. 3. Equiavlent circular models radius and magnetic flux distribution at 50 Hz- from left to right, equivalent area to rail A, equivalent circumference to rail A, equivalent area to rail B and equivalent circumference to rail B

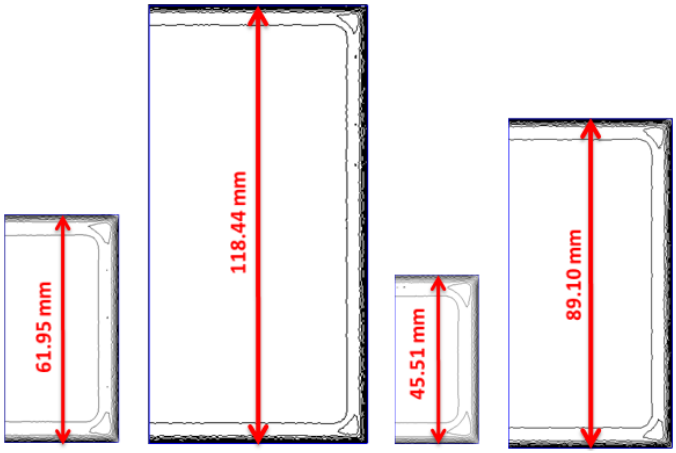

Fig. 4. Equivalent square models edge and magnetic flux distribution at 50 Hz- from left to right, equivalent area to rail A, equivalent circumference to rail A, equivalent area to rail B and equivalent circumference to rail B

B. Square shape models

Equivalent edges, $a_{e,S}$, $a_{e,C}$ for rails A and B are calculated using (2), equal to 61.95 mm, 118.44 mm, 45.51 mm and 89.10 mm, respectively. Fig. 4 shows equivalent square models with half model configuration for rails A and B.

Table I shows finite element analysis of the resistances and the inductances of the rails with relative magnetic permeability, $\mu_r = 250$ and two different conductivities. The conductivities have 12% difference, which has significant influence about 3.5% - 9% on resistances and inductances at 10 Hz and 50 Hz.

TABLE I. Resistance and Inductance per Meter Resuls for Real Models using FEM

μ_r= 250	Rail A		Rail B	
	4.45 MS/m	*5.07 MS/m*	*4.45 MS/m*	*5.07 MS/m*
R,DC	58.6 μΩ	51.4 μΩ	108.5 μΩ	95.3 μΩ
L,DC	2.61 μH	2.61 μH	2.73 μH	2.73 μH
R,10Hz	101.7 μΩ	94.2 μΩ	154.0 μΩ	140.1 μΩ
L,10Hz	1.41 μH	1.36 μH	1.63 μH	1.57 μH
R,50Hz	226.1 μΩ	211.8 μΩ	296.3 μΩ	278.8 μΩ
L,50Hz	0.71 μH	0.66 μH	0.93 μH	0.88 μH

TABLE II. Resistance and Inductance per Meter Resuls for Equivalent Circular Models using FEM

σ_i= 4.45 MS/m μ_r= 250	Rail A		Rail B	
	Equi. Area	*Equi. circu.*	*Equi. area*	*Equi. circu.*
R,DC	58.6 μΩ	12.6 μΩ	108.6 μΩ	22.2 μΩ
L,DC	12.5 μH	12.5 μH	12.5 μH	12.5 μH
R,10Hz	230.0 μΩ	102.9 μΩ	321.4 μΩ	137.9 μΩ
L,10Hz	3.40 μH	1.58 μH	4.61 μH	2.10 μH
R,50Hz	496.5 μΩ	228.7 μΩ	684.8 μΩ	301.5 μΩ
L,50Hz	1.52 μH	0.70 μH	2.06 μH	0.94 μH

TABLE III. RESISTANCE AND INDUCTANCE PER METER RESULS FOR EQUIVALENT SQUARE MODELS USING FEM

σ_i= 4.45 MS/m μ_r= 250	Rail A		Rail B	
	Equi. area	*Equi. circu.*	*Equi. area*	*Equi. circu.*
R,DC	58.6 μΩ	16.0 μΩ	108.5 μΩ	28.3 μΩ
L,DC	11.04 μH	11.04 μH	11.04 μH	11.04 μH
R,10Hz	209.7 μΩ	104.7 μΩ	295.6 μΩ	141.5 μΩ
L,10Hz	3.01 μH	1.58 μH	4.07 μH	2.10 μH
R,50Hz	444.6 μΩ	227.7 μΩ	614.7 μΩ	305.0 μΩ
L,50Hz	1.35 μH	0.71 μH	1.84 μH	0.94 μH

The FEM results for equivalent circular and square models are presented in Tables II and III. The approximate models equivalent to cross section areas of the rails are not suitable for resistance and inductance analysis for AC currents, because the currents and fields are mostly located near the skin of the models. Therefore, the models equivalent to circumferences of the rail are more practical.

The approximate models equivalent to rails circumference show promising results in Table II and III for higher frequencies in comparison with real rail impedance analysis in Table I. Fig. 5 shows magnetic flux distributions in the rail models and equivalent models at DC and 50 Hz currents. Magnetic flux distributions at 50 Hz are located close to the rail wall and magnetic fields intensities are independent of rail shape unlike DC field model. Therefore the approximate models results are coinciding well with real rail results at AC currents.

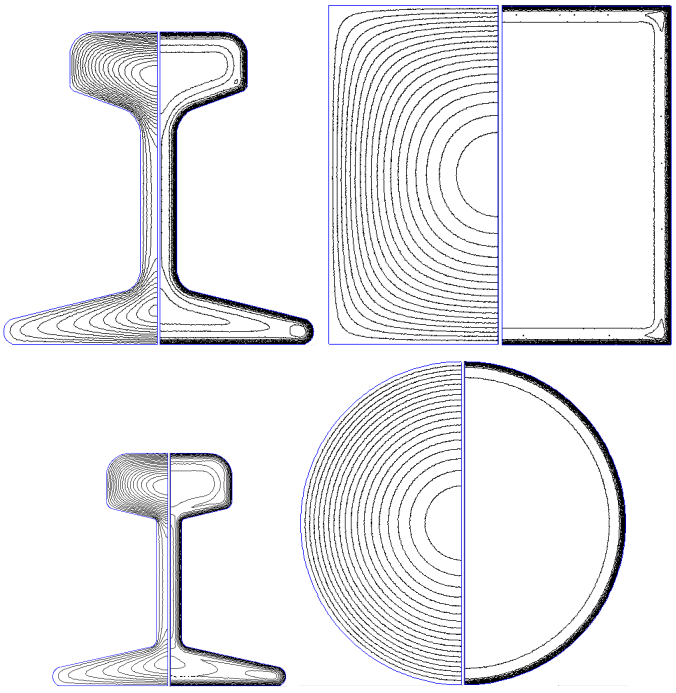

Fig. 5. Magnetic flux distribution at DC (left) and 50 Hz (right) in real model of rail A and equivalent models of rail A (up with square equivalent) and rail B (bottom with circular equivalent) for equal circumferences

C. *Analytical Formulations*

The electric field, E_z in the circular conductor and resulting internal impedance, Z_{in} for the circular conductor with outer radius r are given as following [12]:

$$Z_{in} = \frac{E_z(r)}{I} = \frac{\alpha}{\sigma_i \cdot 2 \cdot \pi \cdot r} \cdot \frac{\text{Besseli}(0, \alpha \cdot r)}{\text{Besseli}(1, \alpha \cdot r)}$$
$$\alpha = \sqrt{j\omega\sigma_i\mu} = \frac{1+j}{\delta},\ (\delta = \sqrt{\frac{2}{\omega\sigma_i\mu}}) \quad (3)$$
$$\mu = \mu_r \cdot \mu_0,\ \omega = 2 \cdot \pi \cdot f$$

where, I , σ_i, μ_0, μ_r and f are applied current, solid iron electrical conductivity, free space permeability, relative magnetic permeability and frequency, respectively. δ is the classical skin depth formula.

The simpler formula for equivalent circular model impedance could be as following [12]:

$$Z_{in} = R + j\omega L,\ R_{dc} = \frac{1}{\sigma_i \cdot \pi r^2}$$
$$R = R_{dc} \cdot \left(\frac{r}{2\delta} + \frac{1}{4} + \frac{3\delta}{32r} \right) \quad (4)$$
$$L = \frac{R_{dc}}{\omega} \cdot \left(\frac{r}{2\delta} - \frac{3\delta}{32r} \right)$$

It is assumed that magnetic field is tangential to outer surface of solid iron equivalent square model because of high magnetic permeability of solid iron relative to the surrounding air region [12]. The approximate formula for internal impedance, Z_{in} is given in (5) with square edge value, a, which is the average integral of electric field on the outer surface of the rectangular conductor:

$$Z_{in} = \frac{\oint E_z \cdot dl}{4 \cdot a \cdot I} = \frac{1}{\sigma_i} \cdot (2 + a \cdot \coth\left(\alpha \cdot \frac{a}{2} \right) \cdot \alpha) / (4 \cdot a^2) \quad (5)$$

The simpler formula for the equivalent square model impedance could be as following:

$$Z_{in} = R + j\omega L,\ R_{dc} = \frac{1}{\sigma_i \cdot a^2}$$
$$R = R_{dc} \cdot \left(\frac{1}{2} + \frac{a}{4\delta} \right) \quad (6)$$
$$L = \frac{R_{dc}}{\omega} \cdot \frac{a}{4\delta}$$

The analytical results for resistances and inductances of approximate circular and square models are presented in Tables IV and V. They coincide well with FEM results, which show high precision of analytical models. The simpler formulas in (4) and (6) are also precise despite their simple function form. The FEM and analytical results for simplified models match better with FEM results for real rail models at higher frequencies due to the higher skin effects.

TABLE IV. RESISTANCE AND INDUCTANCE PER METER RESULS FOR EQUIVALENT CIRCULAR MODELS USING ANALYTICAL

σ_i= 4.45 MS/m μ_r= 250	Rail A		Rail B	
	Using (3)	*Using (4)*	*Using (3)*	*Using (4)*
R,10Hz	102.6 μΩ	102.6 μΩ	137.9 μΩ	137.9 μΩ
L,10Hz	1.58 μH	1.58 μH	2.10 μH	2.10 μH
R,50Hz	225.5 μΩ	225.5 μΩ	301.1 μΩ	301.1μΩ
L,50Hz	0.71 μH	0.71 μH	0.94 μH	0.94 μH

TABLE V. RESISTANCE AND INDUCTANCE PER METER RESULS FOR EQUIVALENT SQUARE MODELS USING ANALYTICAL

σ_i= 4.45 MS/m μ_r= 250	Rail A		Rail B	
	Using (5)	*Using (6)*	*Using (5)*	*Using (6)*
R,10Hz	107.5 μΩ	107.5 μΩ	146.3 μΩ	146.3 μΩ
L,10Hz	1.58 μH	1.58 μH	2.10 μH	2.10 μH
R,50Hz	230.4 μΩ	230.4 μΩ	309.6 μΩ	309.6 μΩ
L,50Hz	0.71 μH	0.71 μH	0.94 μH	0.94 μH

IV. NONLINEAR ANALYSIS

A. DC Current

Fig. 6 shows inductances at DC currents. The inductances profile versus current is similar to μ_r-H curves in Fig. 2 because the internal inductance is proportional to relative magnetic permeability at very low frequencies and DC. The corresponding curve fitting function is as following for inductance versus current:

$$L_{DC} = \frac{p_1 \cdot x^2 + p_2 \cdot x + p_3}{x^2 + q_1 \cdot x + q_2} (\mu H),\ x = \frac{I_{DC} - 476.7}{436.3} \qquad (7)$$

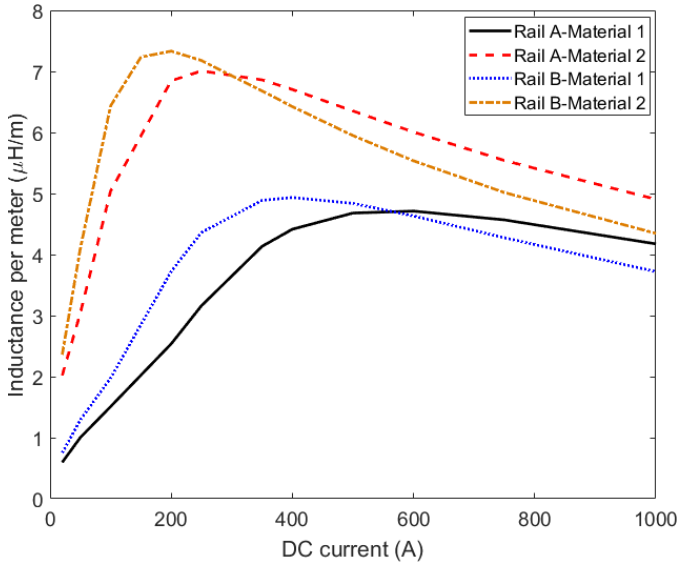

Fig. 6. DC inductance of the rails versus DC current (curve fitting function parameters: RailA Material 1 (p_1=1.825,p_2=7.608,p_3=6.733,q_1=1.324,q_2=1.447),Rail A Material 2 (p_1=2.393,p_2=11.62,p_3=10.17,q_1=2.24,q_2=1.575),Rail B Material 1 (p_1=1.492,p_2=7.264,p_3=6.474,q_1=1.657,q_2=1.315), Rail B Material 2 (p_1=1.734,p_2=11.26,p_3=10.34,q_1=2.489,q_2=1.708))

B. AC Current

The time stepping FEM is required to calculate accurately nonlinear eddy current analysis. For example, the resistance can be calculated from time stepping analysis as following:

$$R = \frac{P_L}{0.5 \cdot I^2} \qquad (8)$$

where, P_L is the average of power losses of the rail with AC current. Time stepping FEM is time consuming, which could be replaced by nonlinear time harmonic FEM with some approximations. Magnetic flux density, B and magnetic field strength, H cannot be sinusoidal in the same time because B-H curve is nonlinear. It is assumed that H is sinusoidal and B is not sinusoidal. In order to compute magnetic fields in time harmonic domain, only fundamental component of B is considered and other harmonics are ignored due to the negligible effect on the eddy current losses [13]. Fig. 7 shows losses for rail A with material 1 at 50 Hz and current amplitude 500 A. The average value for losses is 32.66 W, which means resistance of the rail equal to 261 $\mu\Omega$/m. The calculated resistance from time harmonic FEM is almost the same value as 261 $\mu\Omega$/m from time stepping FEM. Fig. 8-Fig. 11 show resistances and inductances of the rails A and B with two materials 1 and 2 using time harmonic FEM [13]. The resistances increase and inductances decrease with increasing frequency due to the skin effect. The resistances and inductances values and their maxima are highly dependent on the materials. The corresponding currents for maximum values of resistances and inductances are independent of frequencies and they are almost the same for the rails A and B. The rail B is smaller and its resistance and inductance are larger than resistance and inductance of rail A. The effects of materials decrease at higher currents because of saturation effects on the relative permeability. The permeabilities differences are decreasing with increasing currents and corresponding magnetic fields.

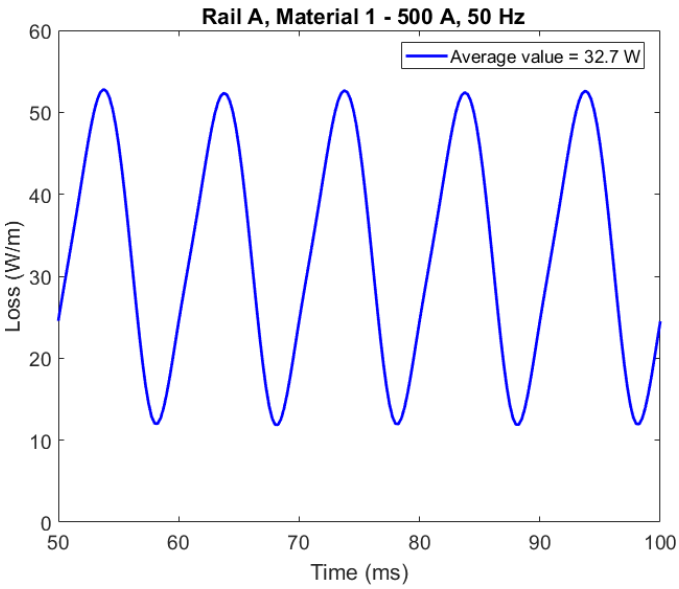

Fig. 7. Losses versus time for rail A with material 1 at 50 Hz and current amplitude 500 A - time stepping finite element method

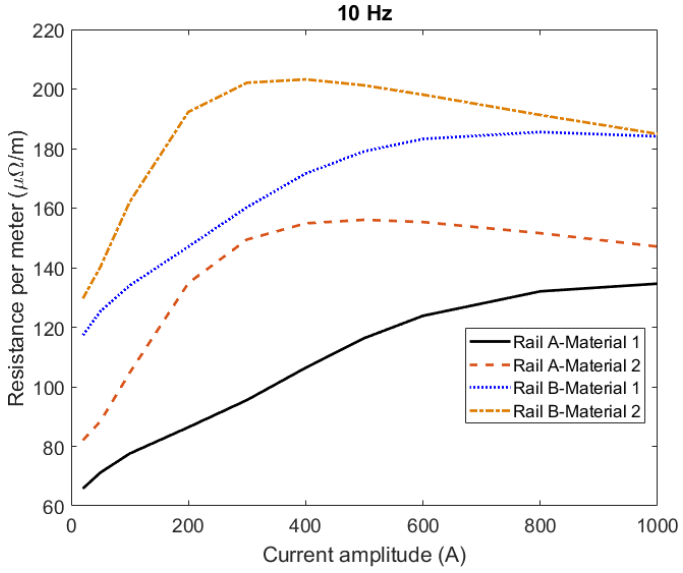

Fig. 8. AC resistance of the rails at 10 Hz

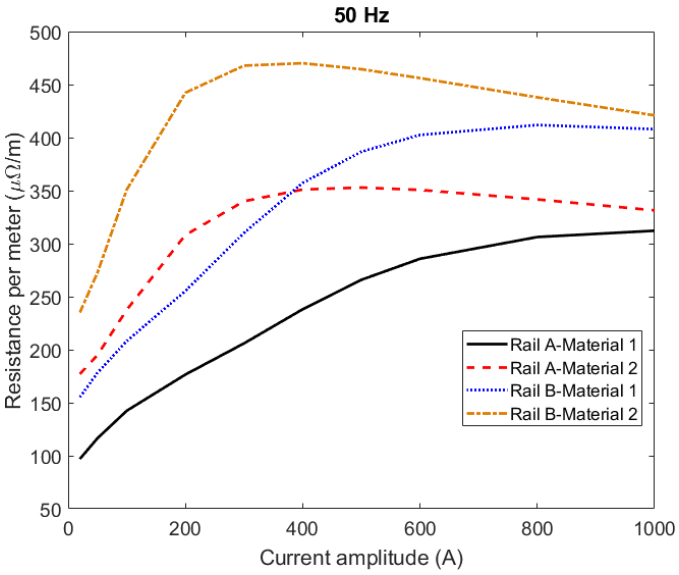

Fig. 10. AC resistance of the rails at 50 Hz

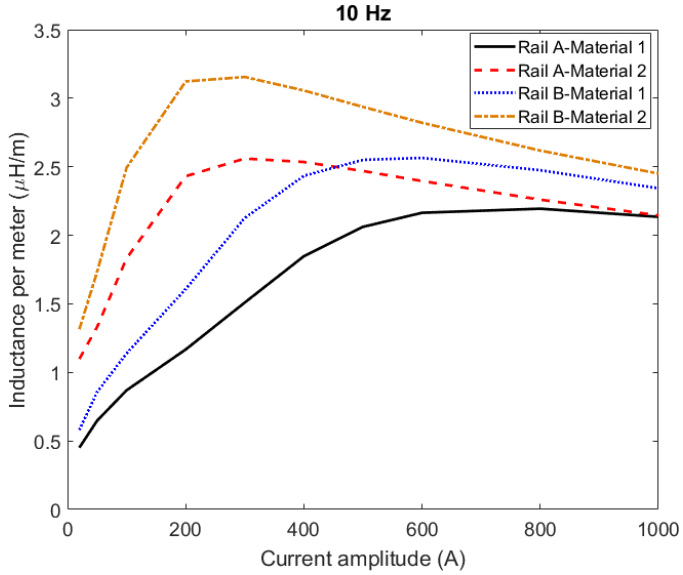

Fig. 9. AC internal inductance of the rails at 10 Hz

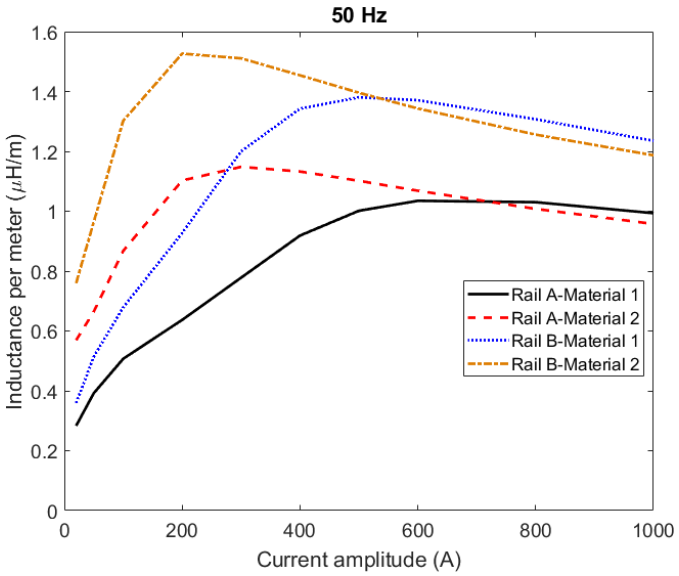

Fig. 11. AC internal inductance of the rails at 50 Hz

In order to consider hysteresis effects, hysteresis angle is taken into account in time harmonic FEM as following [13]-[14]:

$$\varphi_h(B) = \frac{\mu_e(B)}{\mu_{e-\max}} \cdot \varphi_{h-\max} \tag{9}$$

where, $\varphi_h(B)$, $\mu_e(B)$, $\mu_{e\text{-}max}(B)$ and $\varphi_{h\text{-}max}$ are flux density dependent hysteresis angle, flux density dependent efficient relative permeability, maximum efficient relative permeability and maximum hysteresis angle.

The calculated resistances and inductances at 500 A are shown in Table VI when maximum hysteresis angle, $\varphi_{h\text{-}max}$ = 30 Deg. is considered.

TABLE VI. RESISTANCE AND INDUCTANCE PER METER RESULS USING FEM WITH HYSTERESIS EFFECTS - 500 A

500 A	**Rail A**		**Rail B**	
	Material 1	***Material 2***	***Material 1***	***Material 2***
R,10Hz	148.6 μΩ	189.0 μΩ	223.5 μΩ	247.3 μΩ
L,10Hz	1.60 μH	1.77 μH	1.91 μH	2.17 μH
R,50Hz	323.8 μΩ	422.6 μΩ	473.2 μΩ	548.9 μΩ
L,50Hz	0.77 μH	0.80 μH	1.01 μH	1.03 μH

The resistances increase and inductances decrease with consideration of hysteresis effects.

V. Small Signal Analysis

Impedance analysis of the rail for signaling circuits when DC power currents exist in the rails are evaluated. Signaling currents in comparison with power currents for railways is negligible, which small signal analysis could be used for impedance analysis of the rails at high frequencies [8]. Differential or incremental magnetic permeability, μ_d ($1/\mu_0 dB/dH$) is calculated for resistance and inductance analysis in the simulations (Fig. 12). It could be assumed that magnetic fields are mostly concentrated on the very small region on the skin of the rail due to the very high frequency of signaling circuits. Therefore magnetic permeability is considered constant in the skin depth and it is equal to the differential permeability corresponding to the magnetic field strength on the surface of rail. In order to obtain differential permeability from μ_d-H curve, surface magnetic field strength of the rail, H_o must be calculated:

$$H_o = \frac{I}{C} \tag{10}$$

Table VII presents resistances and inductances at 10 kHz with different differential permeabilities using (4) or (6). The resistances are much higher and inductances are much lower in comparison with low frequencies, 10 Hz and 50 Hz.

TABLE VII. Resistance and Inductance per Meter Resuls using Analytical Method at 10 kHz

500 A	**Rail A**		**Rail B**	
	Material 1	***Material 2***	***Material 1***	***Material 2***
R, μ_d=250	3151.5 μΩ	2952.0 μΩ	4192.8 μΩ	3927.2 μΩ
L, μ_d=250	0.050 μH	0.047 μH	0.067 μH	0.062 μH
R, μ_d=750	5452.7 μΩ	5107.9 μΩ	7251.7 μΩ	6793.0 μΩ
L, μ_d=750	0.087 μH	0.081 μH	0.115 μH	0.108 μH

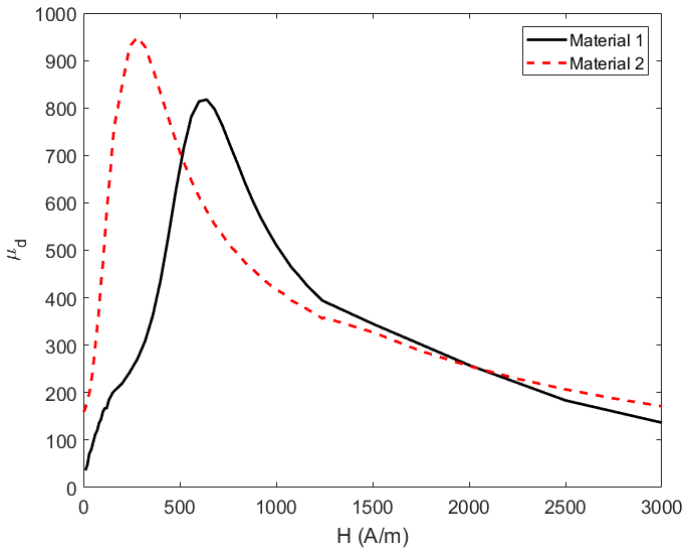

Fig. 12. Materials 1 and 2 - μ_d - H

VI. Conclusions

Different solid iron materials effects on the impedance of rails were presented. Analytical methods and FEM were used for the simulations.

Presented analytical methods are quite precise in comparison with FEM, which could be used for fast analysis of rails impedances. Approximate analytical methods were presented for two approximated models, circular and rectangular solid conductors.

Inductances and resistances were calculated at DC and AC currents with and without iron non-linearity effects. The material effects such as different electrical conductivities and B-H curves are not negligible at low and high frequencies.

The hysteresis effects have considerable influences on the resistances and the inductances of the rails.

References

[1] A. Alberto Dolara and Sonia Leva, "Calculation of rail internal impedance by using finite elements methods and complex magnetic permeability," International Journal of Vehicular Technology Volume 2009, Article ID 505246, 10 pages

[2] V. Kolar , P. Bojko , R. Hrbac, "Measurement of current flowing through a rail with the use of Ohm's method; determination of the impedance of a rail," Przeglad Elektrotechniczny, R. 89 NR 6/2013

[3] J.C. Brown ; J. Allan ; B. Mellitt, "Calculation and measurement of rail impedances applicable to remote circuit fault currents," IEE Proceedings B - Electric Power Applications , Volume: 139, Issue: 4, Jul 1992

[4] A. Mariscotti, P. Pozzobon, "Measurement of the internal impedance of traction rails at 50 Hz," IEEE Transactions on Instrumentation and Measurement, vol. 49, pp. 294-299, 2000

[5] A. Mariscotti, P. Pozzobon, "Measurement of the internal impedance of traction rails at audiofrequency", IEEE Transactions on Instrumentation and Measurement, vol. 53, pp. 792-797, 2004

[6] A. Mariscotti, P. Pozzobon, "Resistance and internal inductance of traction rails at power frequency: a survey," IEEE Transactions on Vehicular Technology, vol. 53, pp. 1069-1075, 2004

[7] F. Filippone, A. Mariscotti, P. Pozzobon, "The Internal impedance of traction rails for DC railways in the 1–100 kHz frequency range," IEEE Transactions on Instrumentation and Measurement, vol. 55, pp. 1616-1619, 2006

[8] R. J. Hill, D. C. Carpenter, "Determination of rail internal impedance for electric railway traction system simulation," IEE Proc. B, vol. 138, no. 6, pp. 311-321, November 1991.

[9] D. C. Carpenter; R. J. Hill, "The effects of magnetic saturation, hysteresis and eddy currents on rail track impedance," Proceedings., Technical Papers Presented at the IEEE/ASME Joint Railroad Conference, Year: 1989, Pages: 73 - 79

[10] R. J. Hill; D. C. Carpenter, "Modelling of nonlinear rail impedance in AC traction power systems," IEEE Transactions on Power Delivery, Year: 1991, Volume: 6, Issue: 4. Pages: 1755 - 1761

[11] H. M. Trueblood, G. Wascheck, "Investigation of rail impedances," Electr. Eng., pp. 898-907, 1933.

[12] R. L. Stoll, Analysis of Eddy Currents, Published by Oxford University Press, 1974

[13] http://www.femm.info/wiki/Documentation/

[14] D. O'Kelly, "Hysteresis and eddy current losses in steel plates with nonlinear magnetization characteristics," Proceedings of the IEE, 119(11):1675-1676, November 1972

3-2-1-3 Impedance of Iron Conductors with Circular and Rectangular Shapes [C2]

The impedance of rectangular and circular shape solid iron conductors is studied in this paper. 2D analytical model is presented for linear iron materials with different relative magnetic permeability and the results are compared with finite element method (FEM). Experiments are performed to measure the impedances. Nonlinear time harmonic FEM results are compared with experimental results for detailed evaluations. Different solid irons are considered for the measurement and the simulations.

The impedances of circular and rectangular conductors are presented. Analytical method and FEM are used for the evaluations. The experimental results prove the validity of calculations for different currents for circular and rectangular conductors with solid iron materials. Considering hysteresis angle for *B-H* curve in the analysis shows better results for impedance phase angle in comparison with measurement. The *B-H* curve shape has strong influence on the solid conductors impedances as it has been shown in the analytical modeling for different values of relative permeability.

Impedance of Iron Conductors with Circular and Rectangular Shapes

Mehran Mirzaei
Faculty of Electrical Engineering
Czech Technical University
Prague, Czech Republic
mirzameh@fel.cvut.cz

Pavel Ripka
Faculty of Electrical Engineering
Czech Technical University
Prague, Czech Republic
ripka@fel.cvut.cz

Andrey Chirtsov
Faculty of Electrical Engineering
Czech Technical University
Prague, Czech Republic
chirtand@fel.cvut.cz

Jan Vyhnanek
Faculty of Electrical Engineering
Czech Technical University
Prague, Czech Republic
vyhnajan@fel.cvut.cz

***Abstract*—The impedance of rectangular and circular shape solid iron conductors is studied in this paper. 2D analytical model is presented for linear iron materials with different relative magnetic permeability and the results are compared with finite element method (FEM). Experiments are performed to measure the impedances. Nonlinear time harmonic FEM results are compared with experimental results for detailed evaluations. Different solid irons are considered for measurement and simulations.**

Keywords— Impedance, iron, conductor, FEM, analytical

I. Introduction

Solid iron conductor is rarely used in comparison with copper and aluminum conductor in the large electrical systems because of higher electrical resistivity. Nevertheless solid iron conductor could be utilized when mechanical stability and robustness is vital. For example, earthing systems often use solid iron conductors for mechanical reasons (Fig. 1). The calculation of earth conductor impedance is needed for dynamic analysis of electrical systems under overload or fault conditions [1]-[2]. AC resistance or impedance using analytical formulas for copper and aluminum materials of various conductor shapes and dimensions could be approximately calculated [3]-[5]. But it would be complicated to obtain general formula for solid iron conductor because AC resistance and impedance of conductor is highly dependent on *B-H* characteristics of solid iron conductor and its shape. The analysis of the solid iron conductor must be differently treated than non-magnetic conductors [6]-[7].

Several analytical studies have been published for rectangular and circular conductors in order to calculate AC losses and resistance and impedance using complex formulations. The analytical calculations show precise results with linear permeability [8]-[9], but the analytical results with consideration of nonlinear *B-H* curve is less precise [10]-[11]. Regardless of the high accuracy of FEM, it is complicated and time consuming especially with nonlinearity and skin effects in the solid iron conductor. Modeling solid iron parts for different electromagnetic devices with taking into account eddy currents is always a challenging issue [12]-[14].

In this paper, simple analytical methods with linear permeability for solid iron conductor with circular and rectangular shapes are presented. 2D time harmonic FEM using FEMM package is used for simulations too. Experimental works are performed to measure impedance of conductors. Five conductors with rectangular and circular shapes are selected for measurement and simulations. They have different *B-H* curves and electrical resistivities. The simulations results and measurement results are finally compared for detailed evaluations of impedances at different AC currents. The excitation current frequency is 50 Hz for all cases.

II. Modeling

A. Conductor Models

Fig. 2 shows rectangular shape and circular shape solid iron conductors, dimensions and magnetic flux distribution, which caused by AC current in z-direction.

The round conductors have 7 mm, 10 mm and 15 mm radius, *r* and rectangular conductors have 10 mm and 5 mm width, *a* and 16 mm and 30 mm length, *b*, respectively. It is assumed that the conductors are long, i.e. the third dimension (z-direction) has negligible effect on conductor impedance per unit length.

Fig. 1. Iron solid iron conductor, which used for earthing in power station [7]

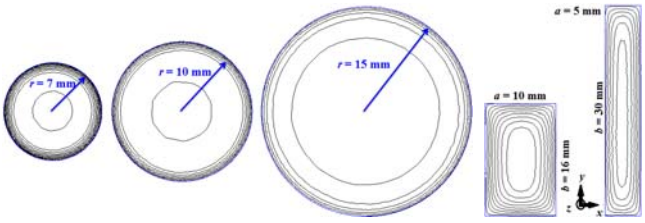

Fig. 2. Rectangular shape and circular shape solid iron conductors, dimensions and magnetic flux distribution calculůated by FEM

B. Material Data

The *B-H* curves for different solid iron conductors are measured with double E-shape yoke method [15].

The measured *B-H* curve is usually available at the limited number of points and ranges of magnetic flux density, B and magnetic field strength, H values. In order to estimate *B-H* curve at all points, a rational curve fitting function is used. Equation (1) shows the proposed rational function with constants, p_1, p_2, p_3, p_4, q_1, q_2, q_3, q_4 and q_5 for relative magnetic permeability, μ_r. μ_0 is the permeability of open space.

Approximated μ_r-*H* curves are shown in Fig. 3 and Fig. 4 in comparison with measurement. The comparison between the curve fitting functions and the measured *B-H* curves shows high precision of the proposed function.

$$\mu_r = \frac{B}{\mu_0 \cdot H} = \\ = \frac{p_1 \cdot x^3 + p_2 \cdot x^2 + p_3 \cdot x + p_4}{q_1 \cdot x^4 + q_2 \cdot x^3 + q_3 \cdot x^2 + q_4 \cdot x + q_5} + 1 \qquad (1)$$
$$x = \frac{H - H_{m,1}}{H_{m,2}}$$

where, $H_{m,1}$ and $H_{m,2}$ are constant parameters for curve fitting functions. Table I presents rational functions constants.

The electrical conductivities, σ_i of circular conductors with radius 7 mm, 10 mm and 15 mm are 4.605 MS/m, 4.45 MS/m and 5.54 MS/m, respectively and rectangular conductor with edges dimensions 10mm*16mm and 5mm*30mm are 5.0 MS/m and 5.07 MS/m, respectively.

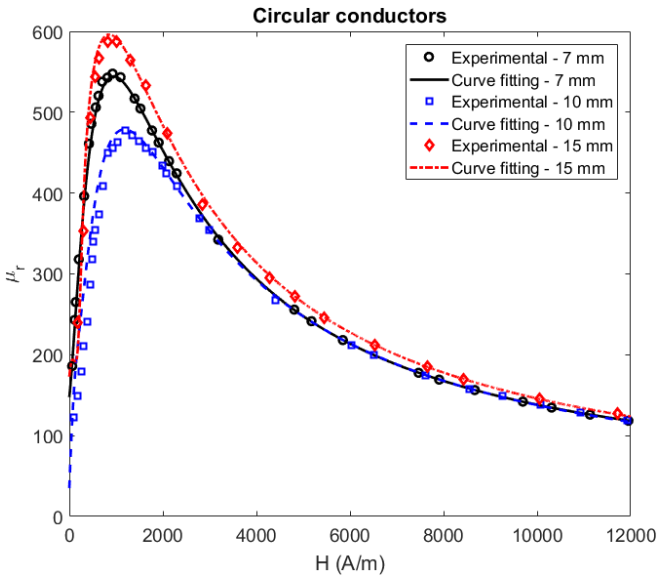

Fig. 3. Relative magnetic permeability, μ_r-H curve - curve fitting function versus measurement for iron conductor with circular shape, 7 mm radius ($H_{m,1}$=3571, $H_{m,2}$=3828), 10 mm radius ($H_{m,1}$=3098, $H_{m,2}$=3571) and 15 mm radius ($H_{m,1}$=3335, $H_{m,2}$=3506)

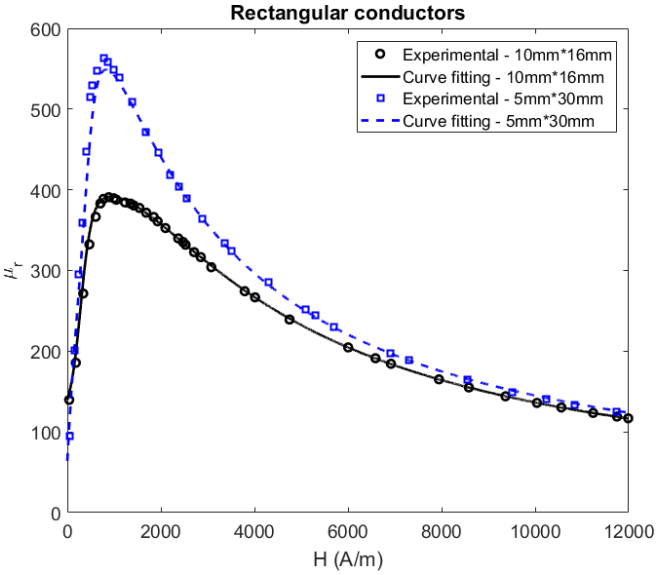

Fig. 4. Relative magnetic permeability, μ_r-H curve - curve fitting function versus measurement for iron conductor with rectangular shape, edges dimension 10 mm*16 mm ($H_{m,1}$=3913, $H_{m,2}$=3725) and edges dimension 5 mm*30 mm ($H_{m,1}$=3068, $H_{m,2}$=3261)

TABLE I. PARAMETERS OF RELATIVE PERMEABILITY

	Parameters				
	Circ. 7 mm	***Circ. 10 mm***	***Circ. 15 mm***	***Rect. 10mm* 16mm***	***Rect. 5mm* 30mm***
p_1	380.1	419.4	450.9	410.15	506.9
p_2	-687.8	1068	1264	1333	1339.5
p_3	-2365	907.8	1180	1440	1182.5
p_4	-1302	257.6	366.9	517.85	349.15
q_1	1	1	1	1	1
q_2	-0.603	3.643	3.985	4.54	4.0125
q_3	-8.065	5.058	6.013	8.0085	6.0305
q_4	-10.55	3.159	4.056	6.387	4.0105
q_5	-4.09	0.7463	1.029	1.922	0.9957

III. LINEAR PERMEABILITY ANALYSIS

A. Circular Conductor

The electric field in the circular conductor, E_z and resulting internal impedance for circular conductor is given as following [5]:

$$Z_{in} = \frac{E_z(r)}{I} = \frac{\alpha}{\sigma_i \cdot 2 \cdot \pi \cdot r} \cdot \frac{\text{Besseli}(0, \alpha \cdot r)}{\text{Besseli}(1, \alpha \cdot r)}$$
$$\alpha = \sqrt{j\omega\sigma_i\mu} = \frac{1+j}{\delta}, \ (\delta = \sqrt{\frac{2}{\omega\sigma_i\mu}}) \qquad (2)$$
$$\mu = \mu_r \cdot \mu_0, \ \omega = 2 \cdot \pi \cdot f$$

where, f and δ are frequency and the classical skin depth, respectively.

The simplified form of (2) for the case of small skin depth in comparison with conductor radius, r is presented in (3):

$$Z_{in} = R + j\omega L, \quad R_{\mathrm{dc}} = \frac{1}{\sigma_i \cdot \pi r^2}$$
$$R = R_{\mathrm{dc}} \cdot \left(\frac{r}{2\delta} + \frac{1}{4} + \frac{3\delta}{32r} \right) \tag{3}$$
$$\omega L = R_{\mathrm{dc}} \cdot \left(\frac{r}{2\delta} - \frac{3\delta}{32r} \right)$$

B. Rectangular Conductor

Equation (4) presents integral of electric field, E_z and calculated internal impedance, Z_{in} in the rectangular conductor. It is assumed that magnetic field is tangential to outer surface of solid iron conductor because of high magnetic permeability of solid iron relative to the surrounding air region [5]. The approximate formula for internal impedance, Z_{in} in (4) is the average of integral of electric field around outer surface of rectangular conductor. The simplified form of (4) is also presented in (5).

$$Z_{in} = \frac{\oint E_z \cdot dl}{2 \cdot (a+b) \cdot I} = \frac{1}{\sigma_i} \cdot (2 + \frac{b}{2} \cdot \coth\left(\alpha \cdot \frac{a}{2} \right) \cdot \alpha + \frac{a}{2} \cdot \coth\left(\alpha \cdot \frac{b}{2} \right) \cdot \alpha) / (a+b)^2 \tag{4}$$

$$Z_{in} = R + j\omega L, \quad R_{\mathrm{dc}} = \frac{1}{\sigma_i \cdot a \cdot b}$$
$$R = R_{\mathrm{dc}} \cdot \frac{a \cdot b}{(a+b)^2} \cdot \left(2 + \frac{a+b}{2\delta} \right) \tag{5}$$
$$\omega L = R_{\mathrm{dc}} \cdot \frac{a \cdot b}{a+b} \cdot \frac{1}{2\delta}$$

Fig. 5 shows the internal impedance results for circular conductor, which exhibit high accuracy of simplified analytical formula in (3). Fig. 6 presents the internal impedance for rectangular conductors. The impedance increases with increasing magnetic permeability because of higher skin effects.

Fig. 7 and Fig. 8 show impedance phase angles versus permeability, which is increasing to the angle 45 deg. at higher permeabilities.

C. Hysteresis effects

Hysteresis effects on the impedances and phase angle could be considered in (6) and (7) using (3) and (5):

$$\mu_{\text{r-h}} = \mu_{\mathrm{r}} \cdot e^{-j\theta}$$
$$R = R_{\mathrm{dc}} \cdot \left(\left(\frac{r}{2\delta} + \frac{3\delta}{32r} \right) \cdot \left(\cos\left(\frac{\theta}{2} \right) + \sin\left(\frac{\theta}{2} \right) \right) + \frac{1}{4} \right) \tag{6}$$
$$\omega L = R_{\mathrm{dc}} \cdot \left(\frac{r}{2\delta} - \frac{3\delta}{32r} \right) \cdot \left(\cos\left(\frac{\theta}{2} \right) - \sin\left(\frac{\theta}{2} \right) \right)$$

$$R = R_{\mathrm{dc}} \cdot \frac{a \cdot b}{(a+b)^2} \cdot \left(2 + \frac{a+b}{2\delta} \cdot \left(\cos\left(\frac{\theta}{2} \right) + \sin\left(\frac{\theta}{2} \right) \right) \right) \tag{7}$$
$$\omega L = R_{\mathrm{dc}} \cdot \frac{a \cdot b}{a+b} \cdot \frac{1}{2\delta} \cdot \left(\cos\left(\frac{\theta}{2} \right) - \sin\left(\frac{\theta}{2} \right) \right)$$

Considering hysteresis effects using a phase shift between B and H causes higher resistance and lower inductance. The absolute value of impedance shows very small changes by hysteresis effects but phase angle decreases.

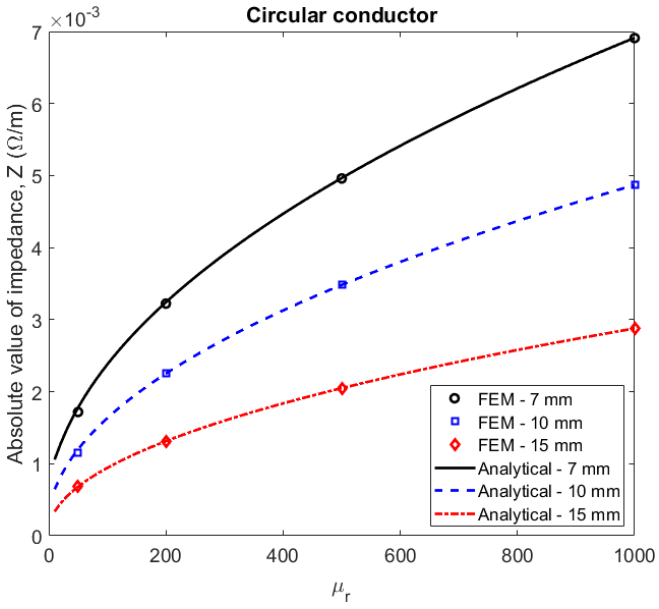

Fig. 5. Internal impedance versus relative magnetic permeability at 50 Hz for circular conductor - approximate equation (3) and FEM simulations

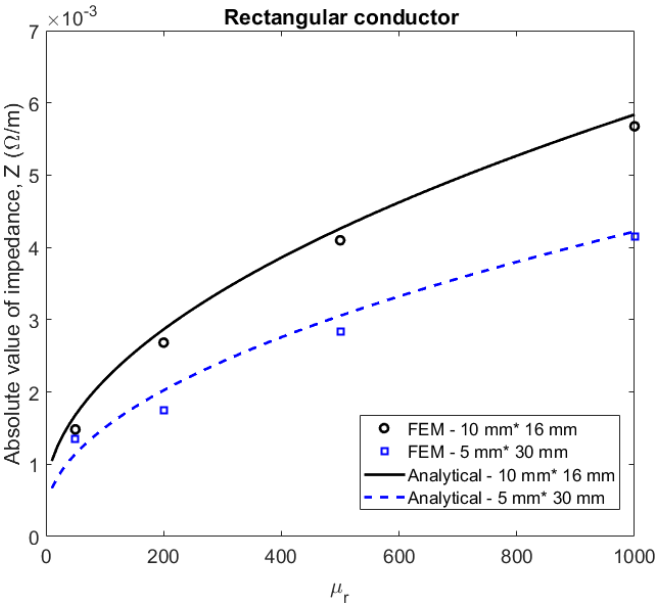

Fig. 6. Internal impedance versus relative magnetic permeability at 50 Hz for rectangular conductor- approximate equation (5)

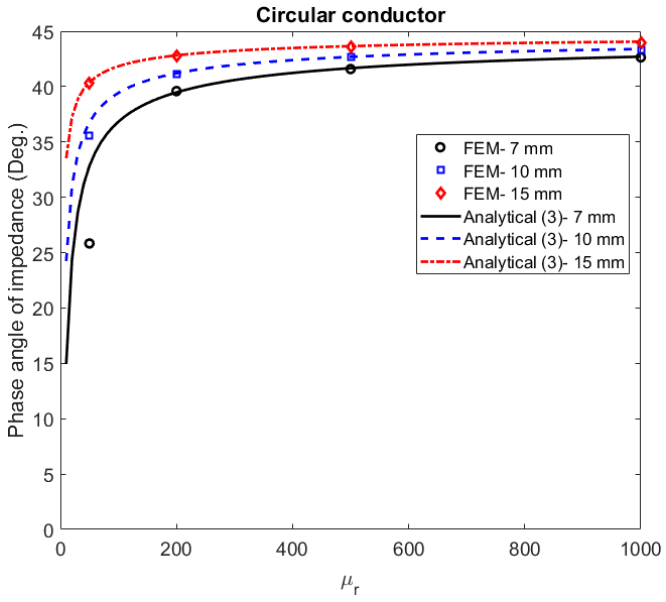

Fig. 7. Internal impedance phase angle versus relative magnetic permeability at 50 Hz for circular conductor - using analytical equation (3) and FEM simulation

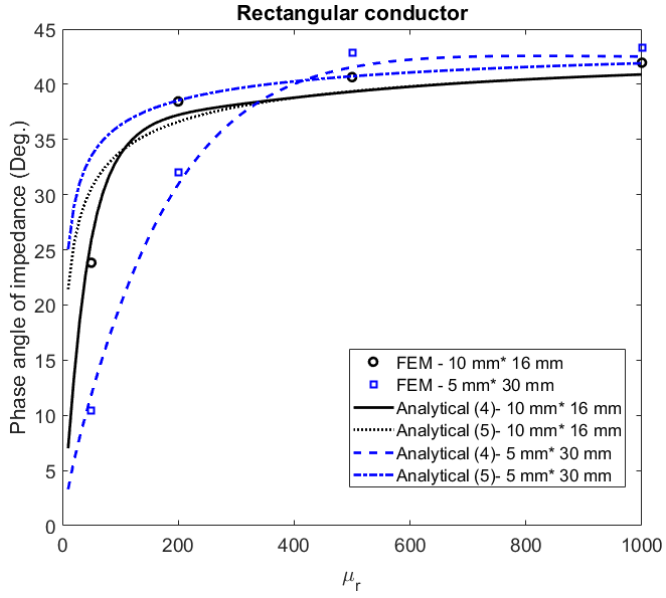

Fig. 8. Internal impedance phase angle versus relative magnetic permeability at 50 Hz for rectangular conductor - using analytical equations (4) and (5)

The analytical and FEM [16] results coincide with higher accuracy for circular conductor in comparison with rectangular conductor due to the absence of edge effect.

IV. Nonlinear Analysis

The nonlinear *B-H* curve is considered for higher field amplitudes. In our analysis we consider that I and thus *H* is sinusoidal and B is non-sinusoidal. In order to compute magnetic fields in harmonic time domain, only fundamental component of *B* is considered and other harmonics are ignored due to the negligible effect on the eddy current losses [16].

The relative magnetic permeability versus radial distance from the conductor center, μ_r are shown in Fig. 9 -Fig. 10. The depicted relative magnetic permeability is calculated using normal component of *B* and *H* to the paths, which is shown in Fig. 9 and Fig. 10 with red color.

The relative magnetic permeability curves are different for circular and rectangular conductors mainly because of different μ_r-H curve according to Fig. 3 and Fig. 4.

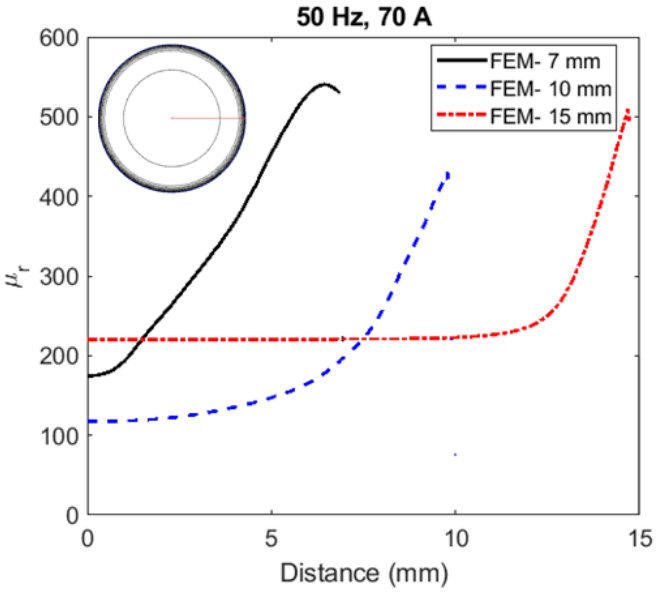

Fig. 9. Relative magnetic permeability, μ_r versus radial distance form the conductor center for circular conductors

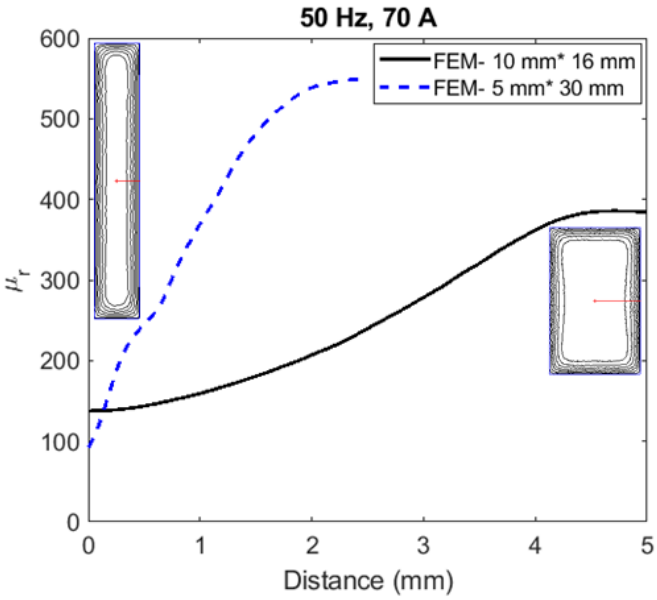

Fig. 10. Relative magnetic permeability, μ_r versus distance from center for rectangular conductors

The relative permeability curve starts from initial permeability of solid irons and increase to maximum permeability. The magnetic fields are zero in the center of conductor and increasing to maximum value at the outer circumference of the conductor.

V. Experimental Results

In order to validate the calculations, five conductors (Fig. 2) were tested at different currents. A sinusoidal current was applied in the rectangular and circular conductors. An oscilloscope was used to read voltage between two points on the conductors. The voltage was measured at 30 cm distance on the conductors.

The measured voltages for circular and rectangular conductors and fundamental component are shown in Fig. 11 at current amplitude 100 A and frequency 50 Hz. The voltages are not sinusoidal at 100 A due to the iron nonlinearity. The impedances are calculated using fundamental component of voltages, V_1 divided by applied current:

$$Z\angle\theta = \frac{V_1}{I} \tag{8}$$

The measured impedances and phase angles are presented in Fig. 12 and Fig. 13. In order to improve accuracy of calculations, hysteresis angle is taken into account as following [16]-[17]:

$$\varphi_h(B) = \frac{\mu_e(B)}{\mu_{e-\max}} \cdot \varphi_{h-\max} \tag{9}$$

where, $\varphi_h(B)$, $\mu_e(B)$, $\mu_{e\text{-max}}(B)$ and $\varphi_{h\text{-max}}$ are flux density dependent hysteresis angle, flux density dependent efficient relative permeability, maximum efficient relative permeability and maximum hysteresis angle.

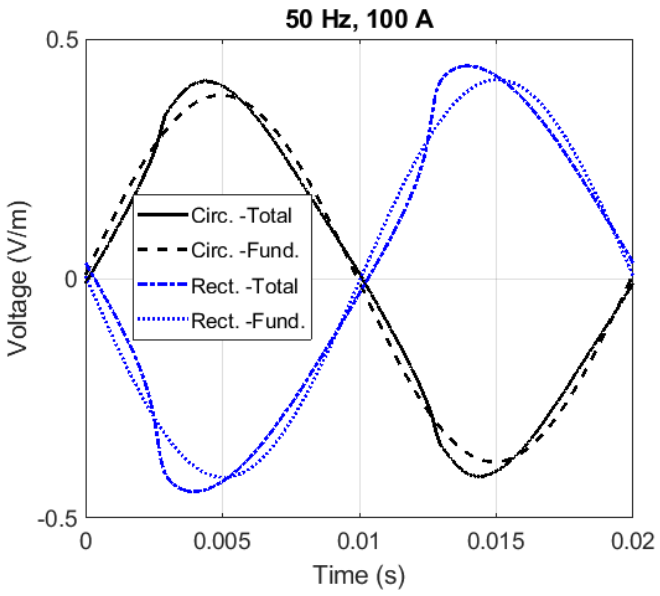

Fig. 11. Experimental voltages versus time for current amplitude 100 A

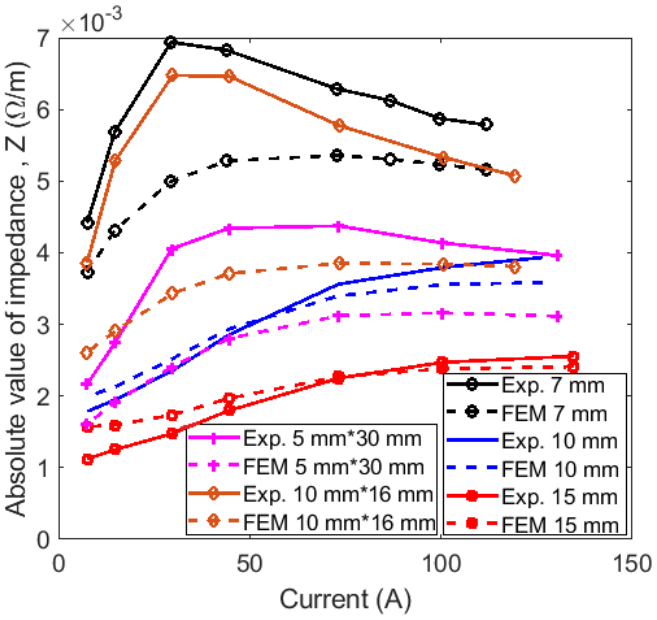

Fig. 12. Absolute value of impedance - measurement and FEM (hysteresis angle = 30 Deg.)

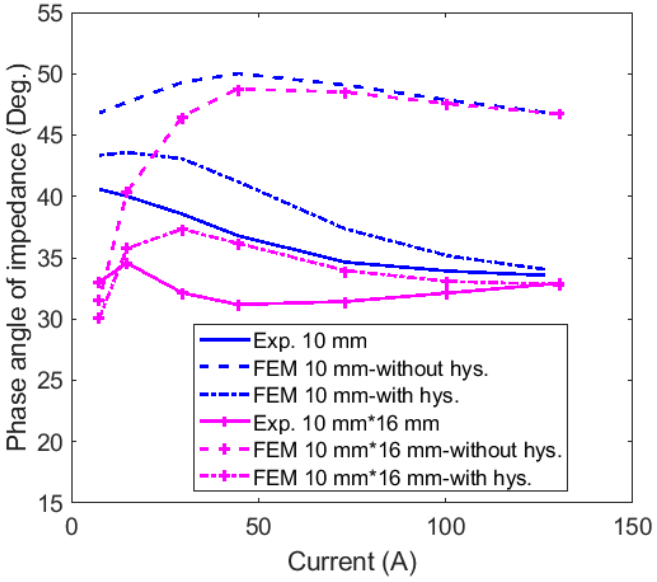

Fig. 13. Phase angle of impedance - measurement and FEM (hysteresis angle = 30 Deg.)

The calculated phase angles for the impedances are matching better with measurement when maximum hysteresis angle 30 Deg., $\varphi_{h\text{-max}}$ is considered. The impedance phase angle is around 33 Deg. at highest current and saturation.

Precise nonlinear FEM calculations are more practical to calculate solid iron conductors impedance, which is complicated for analytical methods [18]-[19]. The edge effects and finite dimensions effects of conductors are easily to be considered in FEM despite the longer simulations time. Exact implementing nonlinearity of solid irons with taking into account exact μ_r curve is rather complicated.

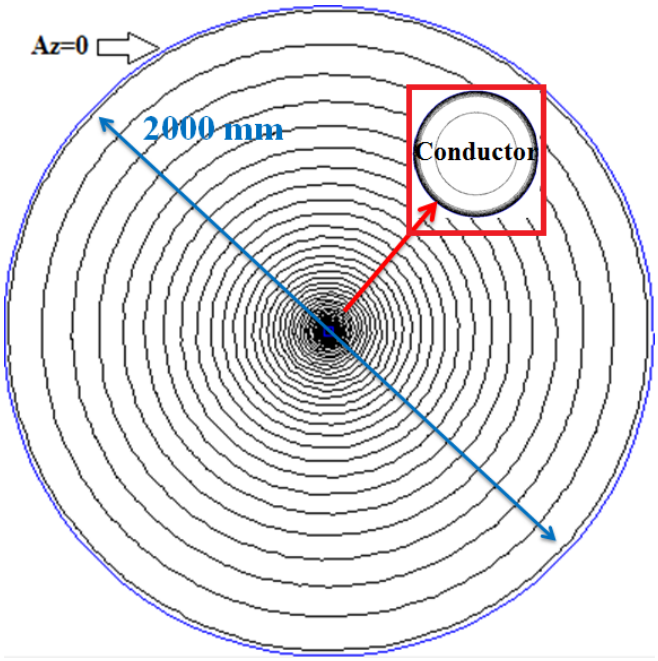

Fig. 14. Conductor model with boundray conditions and magnetic flux distribution – magnetic vector potential, A_z=0

VI. Discussions of Boundary Conditions Effects

Fig. 14 shows the computational model with boundary conditions. Table II shows resistances and reactances of solid conductors with and without external inductances. Without external inductances means that the boundary conditions, A_z=0 is exactly on the outer surface of the conductor and surrounding air region is removed. Table II presents the results, which show small influence of external inductance on the whole impedance of the solid conductors.

TABLE II. Resistances and Reactances with and without External Inductances at 100 A using FEM

***R* (mΩ/m) *ωL* (mΩ/m)**	**Parameters**				
	Circ. 7 mm	***Circ. 10 mm***	***Circ. 15 mm***	***Rect. 10mm* 16mm***	***Rect. 5mm* 30mm***
R, with ext.	3.803	2.383	1.517	2.777	2.136
ωL, with ext.	3.593	2.637	1.833	2.656	2.332
R, without ext.	3.803	2.383	1.517	2.776	2.132
ωL, without ext.	3.283	2.350	1.570	2.349	2.035

VII. Conclusions

The impedances of circular and rectangular conductors are presented. Analytical method and FEM are used for evaluations. The experimental results prove the validity of calculations for different currents for circular and rectangular conductors with solid iron materials. Taking into account hysteresis angle for *B-H* curve in the analysis shows better results for impedance phase angle in comparison with measurement.

The *B-H* curve has influential effects on the solid conductors impedances as it has been shown in the analytical modeling for different relative permeability.

References

[1] B. Nekhoul; P. Labie; F. X. Zgainski; G. Meunier; F. Morillon; S. Bourg, Calculating the impedance of a grounding system , IEEE Transactions on Magnetics Year: 1996, Volume: 32, Issue: 3 Pages: 1509 - 1512

[2] Theofilos A. Papadopoulos; Andreas I. Chrysochos; Grigoris K. Papagiannis, Analytical study of the frequency-dependent earth conduction effects on underground power cables IET Generation, Transmission & Distribution Year: 2013, Volume: 7, Issue: 3 Pages: 276 - 287

[3] J. Lammeraner and M. Stafl, "Eddy Currents", Iliffe Books Ltd 1966

[4] M. Stafl, "Electrodynamics of Electrical Machines", Iliffe Books Ltd 1967

[5] Stoll, R. L., Analysis of Eddy Currents", Published by Oxford University Press, 1974

[6] P. Ripka, and A. Chirtsov, "Influence of External Current on Yokeless Electric Current Transducers", IEEE Transactions on Magnetics Year: 2017, Volume: 53, Issue: 11

[7] M. Mirzaei, P. Ripka, A. Chirtsov1, P. Kaspar, and J. Vyhnanek, The effect of conductor permeability on electric current transducers, AIP Advances 8, 047506 (2018); https://doi.org/10.1063/1.4994195

[8] A. Press., "Resistance and Reactance of Massed Rectangular Conductors", Phys. Rev. 8, 417-422 – Published 1 October 1916

[9] J. L. Daley, "Current Distribution in a Rectangular Conductor", Transactions of the American Institute of Electrical Engineers, Year: 1939, Volume: 58, Issue: 12, Pages: 687 - 691

[10] M. K. Gohar, "The A-C resistance of solid magnetic wires", Transactions of the American Institute of Electrical Engineers, Part I: Communication and Electronics , Volume: 78, Issue: 6, Jan. 1960 ,Page(s): 912 - 916

[11] P.K. Rajagopalan , D.V.S. Murty, "Internal impedance of solid ferromagnetic conductors", Proceedings of the Institution of Electrical Engineers ,Volume: 112, Issue: 7, July 1965 , Page(s): 1449 - 146

[12] A. Mahmood Mohammed, T. Cox, M. Galea, and C. Gerada, "A new method for determining the magnetic properties of solid materials employed in unconventional magnetic Circuits", IEEE Transactions on Industrial Electronics, Year: 2017, Volume: 64, Issue: 3, Pages: 2468 - 2475

[13] G. Lv, D. Zeng, T. Zhou, and Z. Liu, "Investigation of Forces and Secondary Losses in Linear Induction Motor With the Solid and Laminated Back Iron Secondary for Metro", IEEE Transactions on Industrial Electronics, Year: 2017, Volume: 64, Issue: 6, Pages: 4382 - 4390

[14] H. Lu, A. Bokhari, T. Hong, and F. de Leon, "Experimental evaluation of available computational methods for eddy current and hysteresis losses for cables installed in steel pipes", IEEE Transactions on Power Delivery, Year: 2018, Volume: 33, Issue: 4, Pages: 1777 - 1786

[15] S. Tumanski, Handbook of Magnetic Measurements, June 23, 2011 by CRC Press Reference - page 303

[16] http://www.femm.info/wiki/Documentation/

[17] D. O'Kelly, "Hysteresis and eddy current losses in steel plates with nonlinear magnetization characteristics," Proceedings of the IEE, 119(11):1675-1676, November 1972

[18] B. Béland and D. Gamache, "Impedance and Losses in Magnetic Cylindrical Conductors", Electromagnetic Fields in Electrical Engineering, pp 39-43

[19] B. Beland and D. Gamache, "The Impedance of Flat Plate Steel Conductors", Proceedings of the International Conference on Electrical Machines, Part I, Lausanne, Suisse, 18-21, septembre 1984, pp. 5-8.

3-2-1-4 Impedance of Solid Iron Conductors at High Frequencies [S1]
(Paper submitted for publication in International Journal of Electrical Power & Energy Systems)

Impedance analyses of a number of solid iron conductors at high frequencies are presented in this paper. The impedance of solid nonmagnetic conductors is well documented. However, there have been fewer studies of solid magnetic conductors, because of complications caused by strong nonlinearity. Nevertheless, some industrial applications require ferromagnetic conductors, and a simple method for expressing their impedance is desirable. Solid iron conductors of various shapes are considered here. Analytical methods are developed that take into the account the eddy currents in the solid iron and its magnetic nonlinearity. Magnetization curves of solid iron conductors were measured using the yoke method and using a permeameter. The nonlinear time harmonic finite element method is used for impedance calculations of solid iron conductors. The impedance measurement results are compared with the calculations using analytical method and with finite element calculations. Hysteresis effects on resistance and inductance are also taken into consideration. The calculated results are compared with measurements at different currents and frequencies.

Impedance measurements of solid iron conductors of various cross section shapes at high frequencies have been presented in this paper. 2D time harmonic FEM and a 1D time harmonic analytical method were utilized for the analysis of solid iron conductor impedances. The solid iron conductors with different magnetization characteristics and electrical conductivities were considered in order to evaluate the effects of the materials on the impedances. Analytical functions for modeling the *B-H* curves and the magnetic permeability curves were developed for all types of soft magnetic materials for fast analytical analysis of the impedances. Neglecting the hysteresis effects causes a large error in the resistance and internal inductance calculations. However, the absolute value of the impedance is almost unchanged. Solid iron conductors with higher permeability have larger impedances, because the skin depth is smaller. It is therefore recommended to use solid iron conductors with lower permeabilities. The impedance increases with the current until the maximum magnetic permeability point, and it decreases at higher currents because of saturation and decreasing magnetic permeability. The measured *B-H* curves were obtained using a yoke device and using a permeameter. A permeameter provides more accurate *B-H* results than a yoke at low magnetic field strength. The magnetic fields operate at low values inside solid iron conductors, as the applied current is low at the higher frequencies presented in this paper.

Impedance Analysis of Solid Iron Conductors at High Frequencies for Power Systems

Mehran Mirzaei and Pavel Ripka

Faculty of Electrical Engineering, Czech Technical University, Prague 16627, Czech Republic
(e-mail: mirzameh@fel.cvut.cz).

***Abstract*—Impedance analyses of a number of solid iron conductors at high frequencies is presented in this paper. The impedance of solid nonmagnetic conductors is well documented. However, there have been fewer studies of solid magnetic conductors, because of complications caused by strong nonlinearity. Nevertheless, some industrial applications require ferromagnetic conductors, and a simple method for expressing their impedance is desirable. Solid iron conductors of various shapes are considered here. Analytical methods are developed that take into the account the eddy currents in the solid iron and its magnetic nonlinearity. Magnetization curves of solid iron conductors were measured using the yoke method and using a permeameter. The nonlinear time harmonic finite element method is used for impedance calculations of solid iron conductors. The impedance measurement results are compared with the analytical method and with finite element calculations. Hysteresis effects on resistance and inductance are also taken into consideration. The calculated results are compared with measurements at different currents and frequencies.**

***Index Terms*—Impedance, high frequencies, solid iron conductors, eddy currents, nonlinearity, saturation**

I. Introduction

Electric power lines use highly conductive copper, or they use aluminum when mass minimization of the electrical conductor is a critical issue. Solid iron and steel conductors are rarely used for power currents, except in railways, where the iron rails are utilized for carrying AC and DC power current for the electricity requirements and for the traction of trains and locomotives. Signaling currents in the kHz frequency range flow simultaneously with power DC and AC current in the iron rails [1]-[5], and this makes it necessary to analyze the impedance of iron conductors in high frequency operations. Solid iron and steel conductors could be utilized in cases when mechanical strength is critical, e.g. for grounding a power station [6]. Impedance analyses of magnetic solid iron conductors are less known than impedance analyses of nonmagnetic copper and aluminum conductors [7].

This work was supported in part by the Czech Technical University in Prague under Grant SGS18/187/OHK3/3T/1.

The impedance of a solid iron conductor is not only dependent on frequency, but is also affected by the nonlinearity of the *B-H* curves of solid irons and steels. The main challenge for impedance analysis of solid iron conductors is how to take into account the effect of the eddy currents in the solid iron together with nonlinearity and hysteresis effects.

Studies and analyses of eddy currents in solid iron and steels have a long history in the design of electromagnetic devices [8]-[11]. Analytical and numerical calculations for linear and nonlinear magnetic analysis have been performed to evaluate the eddy current and its effect on electromagnetic devices [12]-[13]. Although numerical calculations using the finite difference method (FDM) and the finite element method (FEM) are well developed, and free software and commercial software are accessible, a fast and easy analytical method for impedance calculations is still very desirable. The earliest precise eddy current analysis in a nonlinear model for solid iron was performed in [14], using the power function for *B-H* curve modeling, which was later also used in [12], [15] - [16]. A rectangular function is used in [17] - [19] for saturation and nonlinearity modeling in the *B-H* curve, but it is less precise than the method in [14]. Eddy current loss analysis and analytical modeling for nonlinearity consideration for solid and laminated iron parts exposed to non-sinusoidal alternating fields are described in [20], using the extended works of [17]. Recent work on analytical modeling of the eddy current in a nonlinear magnetic material was presented in [21], but it is complicated to implement and it was not proved for a practical application.

An analytical model for impedance analysis of circular conductors only, using an innovative analysis for saturation consideration in the solid iron was performed in [22]. A detailed linear analysis of the impedances of rectangular and circular solid iron conductors is presented in [23], using analytical calculations, but measurements were made only at 50 Hz. Approximate analytical calculations of circular solid iron conductors are shown in [24], but in that work only resistances were measured and calculated. The same authors claimed to present impedance results for rectangular conductors, in [25]. The authors measured and calculated impedances for circular and rectangular solid iron conductors at 50 Hz in [6]. However, no detailed analysis of the impedances for solid iron conductors at higher frequencies is

available in the literature.

Measurements and theoretical analyses for resistance and inductance calculations of solid iron conductors with various magnetic characteristics are presented in this paper. Various dimensions of circular, rectangular and hexagonal conductors are considered. Magnetic devices for measuring *B-H* curves for solid iron conductors are also shown. A fast analytical method is presented that takes into the account the eddy currents and nonlinearity, and the results for impedance analyses of solid iron conductors are compared with measurements and with 2D time harmonic finite element results. The major objective of this paper is to measure and analyze the impedances of solid iron conductors at high frequencies of 400 Hz and 1000 Hz. In addition, the results of impedances for a rectangular conductor at 50 Hz are presented for a comparison between low frequency and high frequency.

II. Impedance Measurements

Fig. 1 shows a schematic model [26] and the experimental set up for impedance measurements of solid iron conductors. Six different solid iron conductors with circular, rectangular and hexagonal cross sections (Fig. 2) with various cross section areas, were tested at various currents. A sinusoidal current, I, was applied to the solid conductors. An oscilloscope was used to read the voltage between two points on the conductors, as shown in Fig. 1. The voltage, U, was measured at l = 30cm distance on the conductors. The current was also measured with an oscilloscope, using a current probe.

Only the fundamental component of the voltage, U_1, is considered for calculating the impedance, Z, of solid iron conductors with nonlinear magnetization:

$$U_1 = U_{m,1}\angle\theta_U \ , \ I = I_m\angle\theta_I$$
$$Z = |Z|\angle\theta_Z, \ |Z| = \frac{U_{m,1}}{I_m}, \ \theta_Z = \theta_U - \theta_I \quad (1)$$

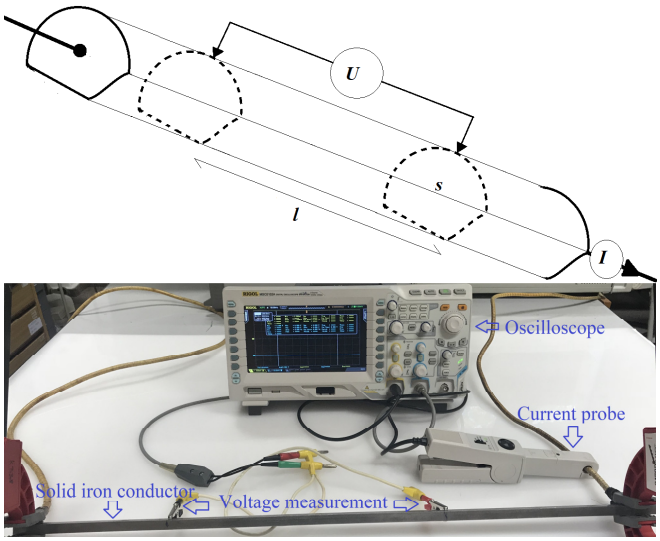

Fig. 1. A schematic model for impedance measurements, and the experimental set up for impedance measurements, using an oscilloscope

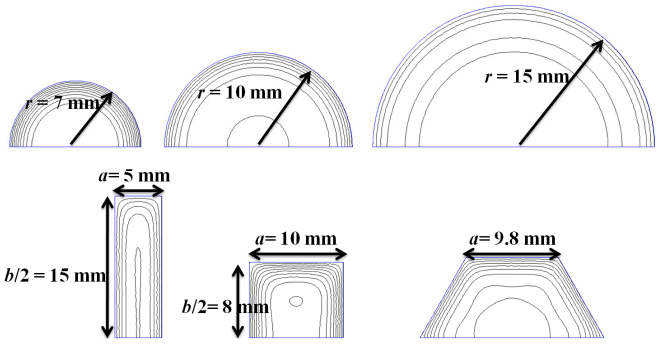

Fig. 2. The circular, rectangular and hexagonal-shaped solid iron conductors: dimensions and magnetic flux distribution calculated by FEM for a half model

The impedance phase angle, θ_Z is dependent on the *B-H* curve of solid iron conductor, its hysteresis loop and external fields of conductor, which are investigated in detail in the next sections.

III. Magnetic Measurements

Firstly, the *B-H* curves for the different solid iron conductors are measured with the double E-shape yoke method, see Fig. 3 [27]. The *B-H* curves of all solid iron conductors in Fig. 2 are measured using 6 cm-long samples from all solid conductors. The magnetic field strength, H, is measured using a Gaussmeter, and magnetic flux density is measured using a fluxmeter [27].

A compensated permeameter is also utilized for measuring DC magnetization and the *B-H* curve, and for measuring the hysteresis loops for the rectangular-shaped solid iron sample, (Fig. 4). The compensated permeameter can measure the hysteresis loops for an open magnetic sample at DC and low frequency [27] - [28]. Only the rectangular solid iron conductor with dimensions of 5×30 mm was measured with a permeameter to compare the results with the yoke method.

Combined rational and power functions [29] for fitting the function curve are used to model analytically the *B-H* curve in appendix I. This will subsequently be used for fast analytical calculations in appendix II for precise interpolation within the measured *B-H* data and for precise extrapolation outside the measured *B-H* data.

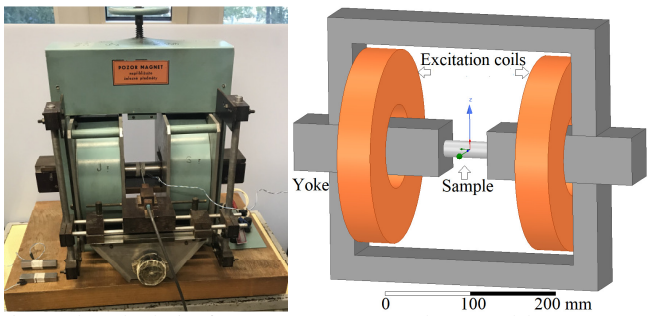

Fig. 3. The yoke device for *B-H* measurements and a 3D model

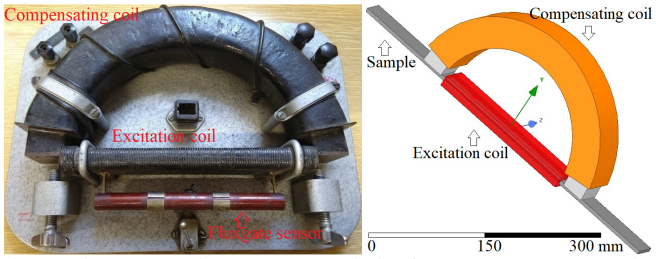

Fig. 4. The compensating permeameter device for *B-H* measurements and a 3D model

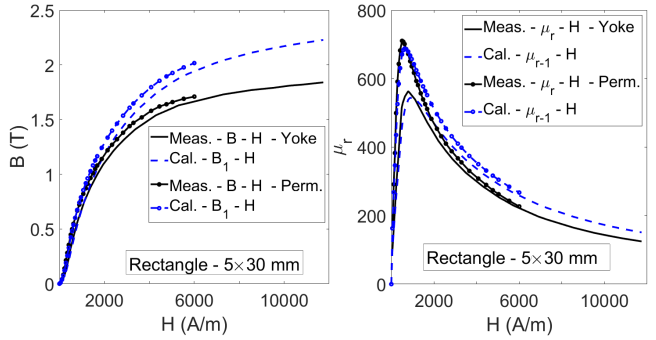

Fig. 5. a) The measured *B-H* curves using a yoke and using a permeameter, and the calculated curves (left) and the B_1-*H* b) μ_r-H curves and the calculated B_1-*H* curves and $\mu_{r\text{-}1}$-*H* curves (right) corresponding to the fundamental component of the magnetic flux density, $B_1(\mu_0 \cdot \mu_{r\text{-}1}=B_1/H)$

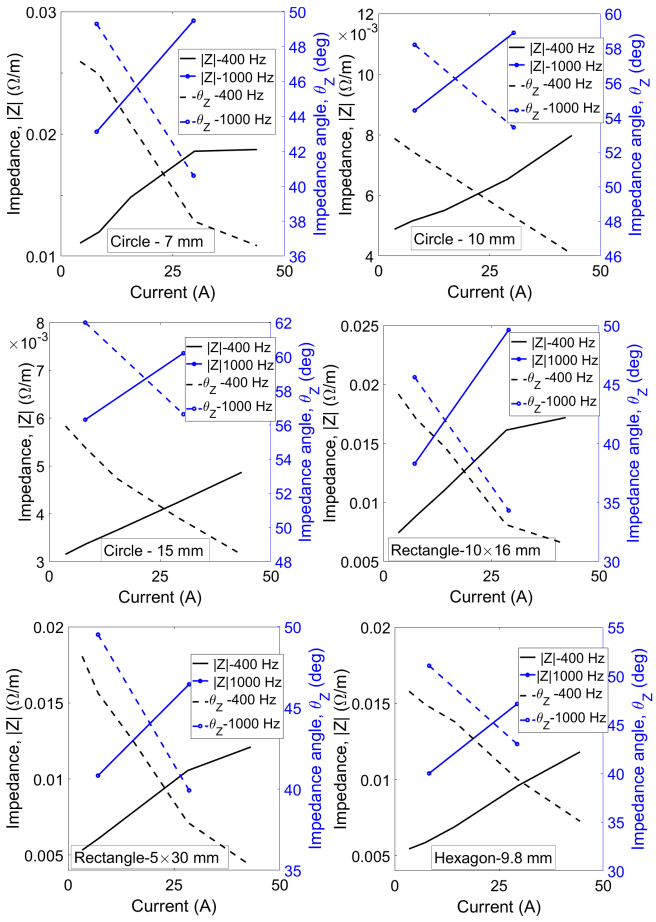

Fig. 6. Measured impedances and impedance angles at 400 Hz and at 1000 Hz

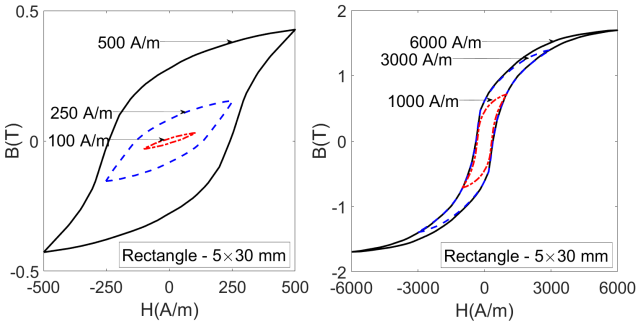

Fig. 7. Measured hysteresis loops, using the permeameter

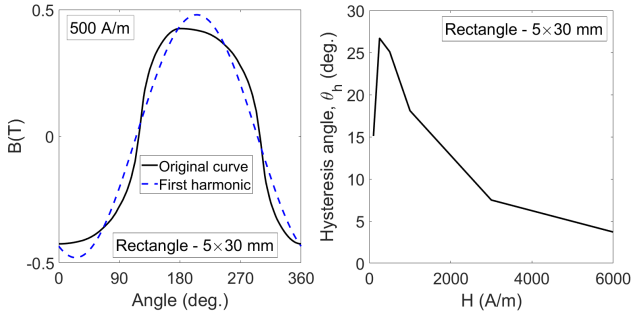

Fig. 8. a) Fundamental component of the magnetic flux density in comparison with the original non-sinusoidal curve corresponding to the hysteresis loop with the sinusoidal magnetic field strength of maximum, 500 A/m (left), b) the hysteresis angle caused by the hysteresis effect at different maximum magnetic field strengths

In time harmonic FEM and analytical calculations [16], [30] for an analysis of magnetic saturation, the conventional method takes into consideration the fundamental component of flux density, B_1. B_1-*H* and the corresponding relative magnetic permeability curve, $\mu_{r\text{-}1}$-*H*, are therefore calculated and are obtained from *B-H*. Fig. 5 shows *B-H*, B_1-*H*, μ_r-*H* and $\mu_{r\text{-}1}$-*H* for a rectangular 5×30 mm conductor measured by a yoke and by a permeameter. The two measurements match less well in low fields, as is shown more clearly in the μ_r-*H* and $\mu_{r\text{-}1}$-*H* curves.

IV. Impedance Results

The measured impedances and phase angles are presented in Fig. 6 for various solid iron conductors at 400 Hz and 1000 Hz. The solid conductors have different circumferences (Fig. 2) and magnetization curves, as shown in appendix I, which affect the impedances and their phase angle. The impedances are proportional to the inverse of the circumference of the solid conductor at high frequencies, as the magnetic flux is concentrated near the circumferences of the conductors (appendix II). The impedances increase with increasing current as the relative magnetic permeability increases. However, the phase angles of the impedances decrease with increasing current. The measured impedances include the external inductance, which is difficult to measure or subtract.

Fig. 7 shows the measured hysteresis loops of a solid 5×30 mm conductor in various magnetic field strength ranges, using

a permeameter. The phase shift between B and H caused by hysteresis can be calculated by the phase difference of the assumed sinusoidal magnetic field strength, H, and the fundamental component of the resulting magnetic flux density, as shown in Fig. 8. The hysteresis phase shift, θ_h , has its maximum value above 26 deg.

The results of 2D time harmonic FEM, neglecting the external inductance and measurement, are compared for the rectangular solid 5×30 mm conductor shown in Fig. 9. In order to improve the accuracy of the FEM calculations, the hysteresis angle is taken into the account as follows [30]-[31]:

$$\theta_h(B) = \frac{\mu_e(B)}{\mu_{e-\max}} \cdot \theta_{h-\max} \tag{2}$$

where $\theta_h(B)$, $\mu_e(B)$, $\mu_{e\text{-max}}(B)$ and $\theta_{h\text{-max}}$ are the flux density dependent hysteresis angle, the flux density dependent efficient relative permeability, the maximum efficient relative permeability, and the maximum hysteresis angle. The influence of hysteresis is negligible on absolute value impedance. The phase angle of the impedance calculated by FEM coincides better with measurement when the hysteresis angle, 30 deg, is taken into consideration.

The calculations with the measured B-H curve using a permeameter provide a better match with the measurement, as the B-H curve has higher values especially at low fields. It can be mentioned here that a permeameter is more precise than a yoke device for low fields. The B-H curves measured by a yoke and by a permeameter are almost the same for high fields (Fig. 5).

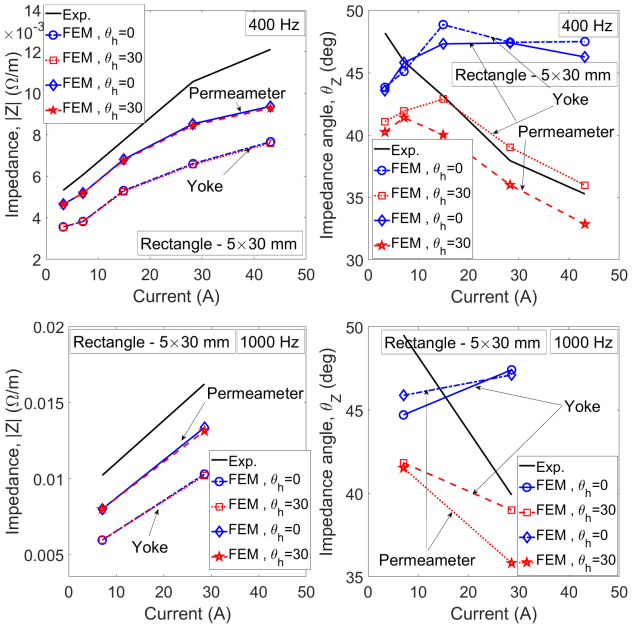

Fig. 9. Measured and FEM-calculated impedances and impedance angles

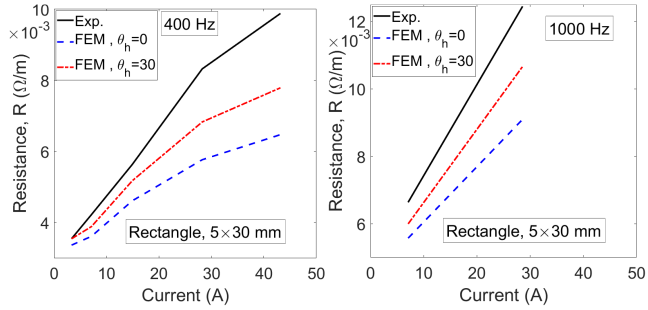

Fig. 10. Measured resistances and FEM calculated resistances

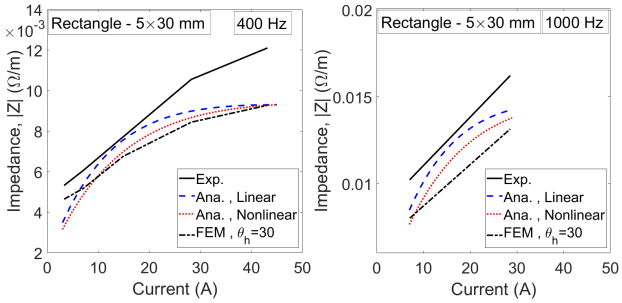

Fig. 11. Measured impedances and FEM and analytical calculated values

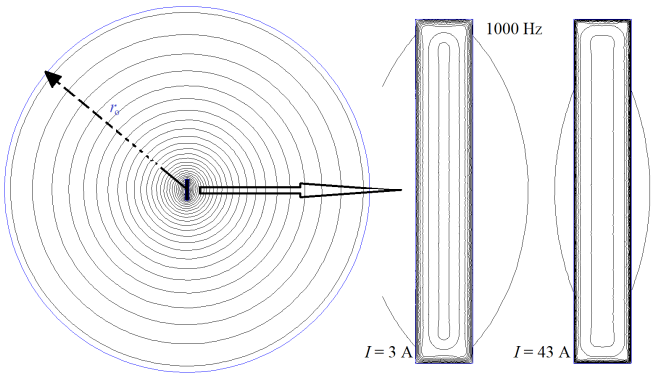

Fig. 12. Magnetic flux distribution with an external boundary condition

Fig. 10 presents a comparison between measured resistances and FEM results with the B-H curve measured by a permeameter. The resistance increases when the hysteresis angle is taken into consideration. The analytical calculation of impedances presented in appendix II takes the nonlinearity into account and provides a closer match with the FEM results (Fig. 11). This shows the high accuracy of the analytical method presented here and the corresponding assumptions in the analytical calculations.

The contribution of the external inductance is given by the size of the external boundary condition. Table I presents the effects of the size of the external boundary condition on the impedance, the impedance phase angle and the resistance of the solid iron conductors, using the FEM model, see Fig. 12. This shows that the resistance is almost the same for all external boundary conditions.

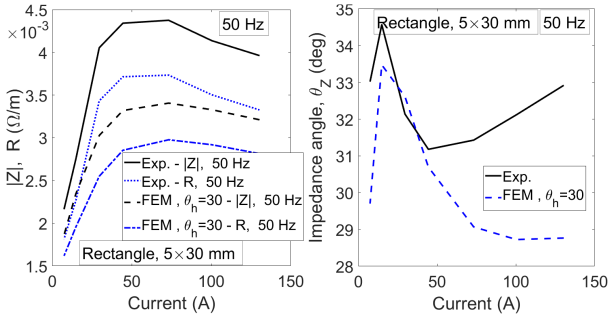

Fig. 13. Measured and calculated FEM impedances, resistance and impedance angles at 50 Hz

TABLE I EFFECT OF APPLYING AN EXTERNAL BOUNDARY CONDITION (FIG. 12)

$\|Z\|$, R (mΩ) θ_Z (deg)	Parameters, Rect. 5×30mm, I = 20 A					
	400 Hz			1000 Hz		
	R	$\|Z\|$	θ_Z	R	$\|Z\|$	θ_Z
No ext.	5.1	7.6	47.6	8.0	11.8	47.5
r_o=50 mm	5.1	8.3	51.7	8.0	13.5	53.8
r_o=100 mm	5.1	8.5	53.1	8.0	14.2	55.8
r_o=200 mm	5.1	8.8	54.5	8.0	15.0	57.7
r_o=500 mm	5.1	9.2	56.1	8.0	15.9	59.9
r_o=1000 mm	5.1	9.5	57.2	8.0	16.6	61.3

The impedance phase angle increases when the external boundary condition becomes bigger. Theoretically, the phase angle of impedance with linear magnetic characteristics is 45 deg, and it is less than 45 deg with non-linear magnetic characteristics and hysteresis effects (appendix II). It can be concluded that the phase angle higher than 45 deg in Fig. 6 is partially caused by external inductance. The measured and FEM calculated impedance, impedance phase angle and resistance of a rectangular solid iron conductor at 50 Hz is shown in Fig. 13 for higher currents. The impedance and the resistance have their maximum value at about 50 A, which corresponds to the maximum permeability, as mentioned in Table I4 (appendix I).

V. CONCLUSION

Impedance measurements of solid iron conductors of various cross section shapes at high frequencies have been presented in this paper. 2D time harmonic FEM and a 1D time harmonic analytical method were utilized for the analysis of solid iron conductor impedances. The solid iron conductors have different magnetization characteristics and electrical conductivities, in order to evaluate the effects of the materials on the impedances. Analytical functions for modeling the *B-H* curves and the magnetic permeability curves were developed for all types of soft magnetic materials for fast analytical analysis of the impedances.

Neglecting the hysteresis effects causes a large error in the resistance and internal inductance calculations. However, the absolute value of the impedance is almost unchanged.

Solid iron conductors with higher permeability have larger impedances, because the skin depth is smaller. It is therefore recommended to use solid iron conductors with lower permeabilities. The impedance curve versus current increases with the current until the maximum magnetic permeability point, and it decreases at higher currents because of saturation and decreasing magnetic permeability.

The measured *B-H* curves were obtained using a yoke device and using a permeameter. A permeameter provides more accurate *B-H* results than a yoke at low magnetic field strength. The magnetic fields operate at low values inside solid iron conductors, as the applied current is low at the higher frequencies presented in this paper.

Despite their high impedance, especially at high frequencies, in comparison with copper and aluminum conductors, solid iron conductors are a suitable option for electricity and signal transmission lines with high mechanical tension and low magnetic reluctance [32]-[37].

VI. APPENDIX I

A measured *B-H* curve is usually available at a limited number of points and ranges of magnetic flux density, B, values and magnetic field strength, H , values. In order to estimate the *B-H* curve at all points for analytical calculations, combined rational and power functions for fitting the function curve are used. Equation (I1) shows the proposed function with constants, a, a_1, c, c_1, b, and d for relative magnetic permeability, μ_r , which are calculating using curve fitting. μ_0 is the permeability of an open space. Equation (I2) presents the calculated magnetic permeability corresponding to the fundamental component of the magnetic flux density, B_1 , when the field strength, H changes in a sinusoidal form. The constants, a', a'_1, c, c'_1, b', and d' are calculated using curve fitting.

Approximated μ_r-H and $\mu_{r\text{-}1}$-H curves in comparison with measurement are shown in Fig. I1. The comparison between the curve fitting functions and the measured *B-H* curves shows the high precision of the proposed function. Tables I1-I3 present the parameters and constants of (I1) and (I2).

$$\mu_r = \frac{B}{\mu_0 \cdot H} = \frac{a \cdot H^{b-1} + c \cdot H^{d-1}}{a_1 \cdot H^b + c_1 \cdot H^d + 1} + 1 \quad \text{(I1)}$$

$$\mu_{r\text{-}1} = \frac{B_1}{\mu_0 \cdot H} = \frac{a' \cdot H^{b'-1} + c' \cdot H^{d'-1}}{a'_1 \cdot H^{b'} + c'_1 \cdot H^{d'} + 1} + 1 \quad \text{(I2)}$$

TABLE I1 PARAMETERS OF RELATIVE PERMEABILITY USING A YOKE

	Parameters					
	Circ. 7 mm	Circ. 10 mm	Circ. 15 mm	Rect. 10×16 mm	Rect. 5×30 mm	Hex. 9.8 mm
a	9.48e-7	1.55e-6	7.13e-8	3.78e-6	6.19e-8	2.42e-7
a_1	3.96e-7	1.64e-6	3.47e-8	8.68e-3	3.07e-8	1.15e-7
b	1.946	1.846	2.542	1.222	2.722	2.354
c	1.85e-5	8.61e-8	8.88e-6	4.55e-7	1.5e-8	2.54e-5
c_1	1.79e-5	2.92e-8	5.43e-5	2.38e-7	1.51e-4	1.25e-3
d	1.515	2.24	1.524	2.589	1.571	1.153

TABLE I2 PARAMETERS OF RELATIVE PERMEABILITY USING A YOKE

	Parameters					
	Circ. 7 mm	Circ. 10 mm	Circ. 15 mm	Rect. 10×16 mm	Rect. 5×30 mm	Hex. 9.8 mm
a'	1.79e-7	1.87e-6	3.86e-8	2.3e-6	5.57e-7	1.81e-7
a'_1	7.09e-8	4.62e-6	1.47e-8	7.33e-4	2.23e-7	6.61e-8
b'	2.254	1.668	2.563	1.40	2.409	2.301
c'	3.64e-5	1.19e-7	1.06e-5	7.25e-8	1.05e-7	3.27e-5
c'_1	6.35e-5	4.08e-8	3.43e-5	2.98e-8	2.38e-3	4.42e-4
d'	1.373	2.264	1.551	2.669	1.199	1.211

TABLE I3PARAMETERS OF RELATIVE PERMEABILITY USING A YOKE AND A PERMEAMETER

	Parameters	
	yoke/ Rect. 5×30mm	Permeameter/ Rect. 5×30mm
a / a'	6.19e-8 / 5.57e-7	1.0e-6 / 5.11e-6
a_1 /a'_1	3.07e-8 / 2.23e-7	2.42e-5 / 4.56e-5
b / b'	2.722 / 2.409	1.971 / 1.745
c / c'	1.5e-8 / 1.05e-7	2.47e-8 / 5.97e-8
c_1 /c'_1	1.51e-4 / 2.38e-3	1.12e-8 / 2.058e-8
d / d'	1.571 / 1.199	2.997 / 2.722

TABLE I4 MAXIMUM RELATIVE MAGNETIC PERMEABILITY AND THE CORRESPONDING MAGNETIC FIELD STRENGTH (USING A YOKE)

	Parameters					
	Circ. 7 mm	Circ. 10 mm	Circ. 15 mm	Rect. 10×16 mm	Rect. 5×30 mm	Hex. 9.8 mm
H_m	924	1351	1010	994	819	1133
$\mu_{r\text{-}m}$	548	472	588	389	552	390

Table I4 presents the maximum relative magnetic permeability and the corresponding magnetic field strength (Fig. II1).

The electrical conductivities, σ , of circular conductors with a radius of 7 mm, 10 mm and 15 mm are 4.605 MS/m, 4.45 MS/m and 5.54 MS/m, respectively. The values are 5.0 MS/m and 5.07 MS/m for rectangular conductors with edge dimensions of 10mm·16mm and 5mm·30mm, respectively. And it is 5.56 MS/m for the hexagonal conductor.

VII. APPENDIX II

The one dimensional (1D) field solution is considered using the Maxwell equations [12]. The magnetic flux density is directly solved and used in this paper for the impedance calculations of the solid iron conductor. The shape and form of the solid conductor is neglected, and the analysis is performed using a simplified model in Cartesian coordinates. The rationale behind this approach is that the magnetic flux concentrates mostly near the surface of a solid iron conductor. The circumference of the conductor is therefore essential for the impedance analysis.

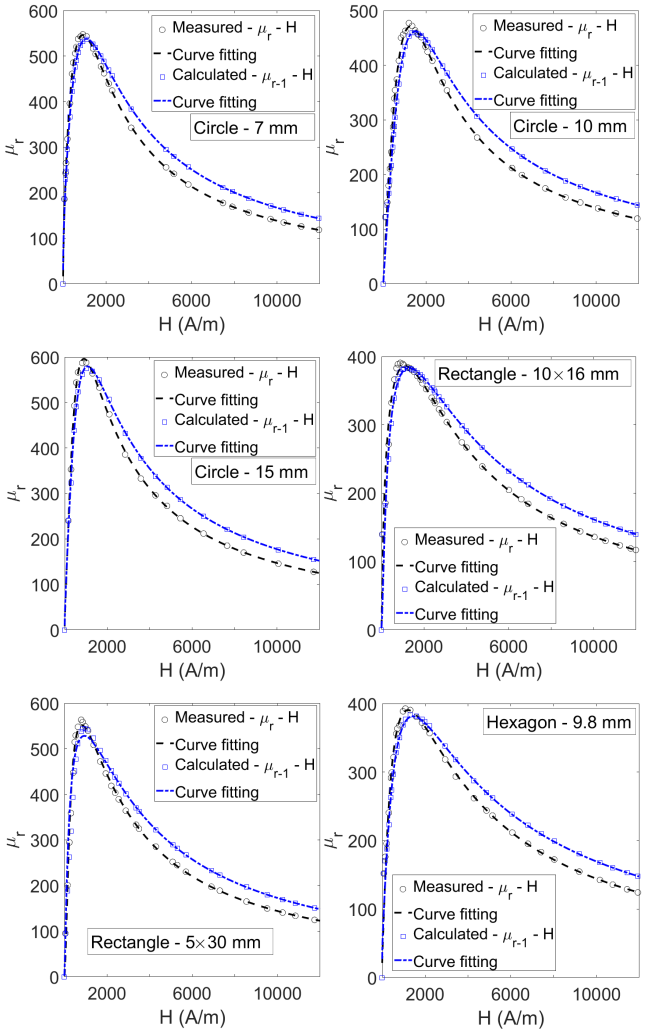

Fig. I1. μ_r-H curves and $\mu_{r\text{-}1}$-H curves corresponding to the fundamental component of magnetic flux density, B_1 – measured using the yoke method

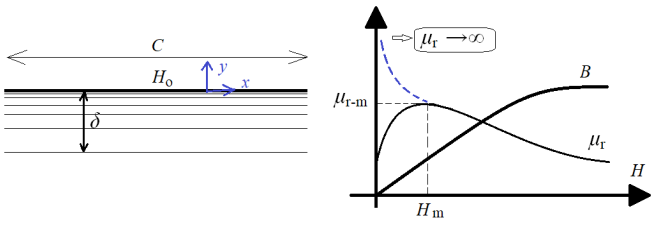

Fig. II1. a) The schematic flux distribution within the skin depth, δ , of the conductor (left) and b) a schematic model of *B-H* curve and the relative magnetic permeability curve, μ_r-*H* (right)

The 1D model is shown in Fig. II1 a). Only the *x* component of the magnetic flux density, B_x , and the magnetic field strength, H_x are used in the magnetic field solutions.

The impedance of the conductor, *Z*, the resistance, *R*, and the inductance, *L,* with circumference length, *C,* are calculated as follows [13]:

$$Z = R + j\omega L = \omega \cdot \frac{\mu_0 \cdot \mu_r \cdot (1+j)}{C \cdot \sqrt{2 \cdot \lambda}} = \frac{(1+j)}{\sigma \cdot \delta \cdot C}$$
$$R = \frac{1}{\sigma \cdot \delta \cdot C}, \quad \omega L = \frac{1}{\sigma \cdot \delta \cdot C} \tag{II1}$$

$$\delta = \sqrt{\frac{2}{\lambda}}, \quad H_o = \frac{I}{C}, \lambda = \omega \cdot \sigma \cdot \mu_0 \cdot \mu_r, \quad \omega = 2\pi f \tag{II2}$$

where, σ, I, μ_r and f are iron conductivity, amplitude of the current, relative magnetic permeability and frequency, respectively. δ is skin depth. H_o is the magnetic field strength on the surface of conductor.

Skin depth, δ is smaller at higher frequencies, and the magnetic flux penetrates less in solid irons and steels. The impedance and resistance are higher with higher magnetic permeability, but they decrease with higher conductivity.

The hysteresis effect is the phase difference between B and H. B lags H by an angle, θ, to model the hysteresis in a linear magnetic material which, the hysteresis loop becomes an ellipse [13]. Complex permeability is used in (II3) to model the hysteresis effects [13]. The resistance increases and the inductance decreases when the hysteresis angle is introduced in (II1), as shown in (II4) in a linear magnetic material. The absolute value of the impedance, |Z|, is unchanged.

$$\mu_{r,h} = \frac{B \cdot e^{-j\theta}}{\mu_0 \cdot H} = \mu_r \cdot e^{-j\theta} \tag{II3}$$

$$R = \frac{\cos(\frac{\theta}{2}) + \sin(\frac{\theta}{2})}{\sigma \cdot \delta \cdot C}, \omega L = \frac{(\cos(\frac{\theta}{2}) - \sin(\frac{\theta}{2})}{\sigma \cdot \delta \cdot C}$$

(II4)

In order to consider analytically the nonlinearity in the analytical calculations of the impedance, the assumption in (II5) for B-H curve modeling is made [14], [16]. The constants a and b are obtained by curve fitting.

$$B_x = a \cdot H_x^b \quad , \mu_x = \frac{B_x}{H_x} = a \cdot H_x^{b-1} \tag{II5}$$

The first assumption in (II5) is the approximate function for the B-H curve. The second assumption in nonlinear solution is that the magnetic permeability varies in proportion to the inverse of the square of the distance from the surface of solid iron part, and the magnetic field vanishes to zero at penetration depth δ_o [14], [16]. The disadvantage of the assumption for function μ_x versus y is that μ_x is infinite at $y = \delta_o$ or H=0 (dashed line in Fig. II2 b)), which is not realistic. However, it does not significantly change the accuracy of analytical method. Therefore, the impedance, the resistance and the inductance of solid iron conductors are calculated in (II6) by substituting equivalent relative permeability, $\mu_{r\text{-}e}$ of (II7) in (II1):

$$Z_o(y=0) = \frac{\alpha' + j \cdot \alpha''}{\sigma \cdot \delta_o \cdot C}$$
$$R = \frac{\alpha'}{\sigma \cdot \delta_o \cdot C}, \quad \omega L = \frac{\alpha''}{\sigma \cdot \delta_o \cdot C} \tag{II6}$$

$$\mu_{r\text{-}e} = \frac{\mu_{x,0}}{\mu_0} \cdot \sqrt{2} \cdot \frac{(1-b)^2}{(3+b) \cdot \sqrt{(1+b)}} \cdot \left(\alpha' \cdot \alpha'' - \frac{\alpha'^2 - \alpha''^2}{2} \cdot j \right) \tag{II7}$$

$\mu_{x,0}$ is magnetic permeability on the surface of the conductor. The unknowns α', α'' and δ_o are calculated as follows [14], [16]:

$$\alpha' = \frac{2}{1-b}, \quad \alpha'' = \frac{1}{1-b} \cdot \sqrt{2.(b+1)}$$
$$\delta_o = \frac{1}{\sqrt{\sigma \cdot \omega \cdot \mu_{x,0}}} \cdot \frac{\sqrt[4]{2 \cdot (1+b) \cdot (3+b)^2}}{1-b} \tag{II8}$$

The impedance angle changes from 45 deg. in linear model of (II1) to smaller values in nonlinear model of (II6), which depends on parameter, b in (II5). The parameter, b is less than 1 for high fields and it could be close to zero in highly saturation conditions, while it is close to 2 at low fields [15]. Therefore, impedance phase angle changes between 35 deg. and 51 deg. for nonlinear model.

Fig. II2 a) shows a comparison between the analytical and FEM impedance results for linear magnetic materials, and a comparison for nonlinear magnetic materials is shown in Fig. II2 b). The comparisons show that the analytical methods are highly accurate. The nonlinearity effects are well modelled in the analytical calculations. The surface impedances versus surface magnetic field strength with different B-H curves corresponding to the different solid iron conductors (Fig. 2) are compared in Fig. II3. The surface impedance for the circular solid iron conductor with a 15 mm radius is the highest, because of the higher relative magnetic permeability.

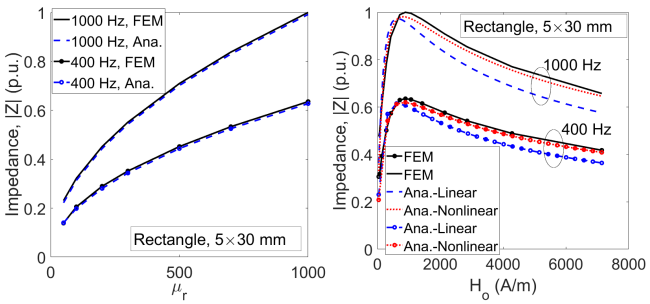

Fig. II2. a) Impedance variation versus the relative magnetic permeability curve, μ_r , for a linear magnetic material (left), b) impedance variation versus magnetic field strength on the surface of the conductor, H_o , for a non-linear magnetic material (right)

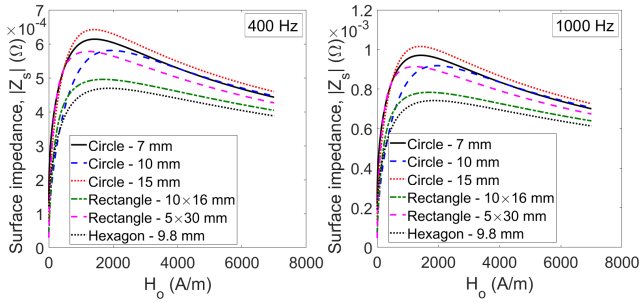

Fig. II3. Surface impedance variation versus magnetic field strength on the surface of the conductor, H_o , for a non-linear magnetic material

ACKNOWLEDGMENT

The authors thank Mr. A. Chirtsov and Dr. J. Vyhnanek, from the Department of Measurement for the measurements. This work was supported by the Czech Technical University within the framework of Grant SGS18/187/OHK3/3T/1.

REFERENCES

[1] R. J. Hill, D. C. Carpenter, "Modeling of nonlinear rail impedance in AC traction power systems," *IEEE Transactions on Power Delivery*, vol. 6, no. 4, pp. 1755 – 1761, 1991

[2] Y. J. Wang, and J.-H. Wang, "Modeling of frequency-dependent impedance of the third rail used in traction power systems," *IEEE Transactions on Power Delivery*, vol. 15, no. 2, pp. 750– 755, 2000

[3] Y.-J. Wang, and Y.-L. Tsai, "Calculation of the frequency-dependent impedance of rail tracks using a four-parameter equivalent tubular conductor model," *IEEE Transactions on Power Delivery*, vol. 19, no. 3, pp. 1142– 1147, 2004

[4] A. Alberto Dolara and S. Leva, "Calculation of rail internal impedance by using finite elements methods and complex magnetic permeability," *International Journal of Vehicular Technology*, pp. 1-10, 2009

[5] M. Mirzaei, P. Ripka, "Analysis of material effect on rail impedance," *53rd International Universities Power Engineering Conference (UPEC),* UK, 4-7 Sept. 2018

[6] M. Mirzaei, P. Ripka, A. Chirtsov, J. Vyhnanek, "Impedance of iron conductors with circular and rectangular shapes," *IECON 2018 - 44th Annual Conference of the IEEE Industrial Electronics Society*, Washington, DC, USA, 21-23 October, 2018.

[7] V. T. Morgan, "The current distribution, resistance and internal inductance of linear power system conductors—A review of explicit equations," *IEEE Transactions on Power Delivery*, vol. 28, no. 3, pp. 1252– 1262, 2013

[8] Y. Liu, D. Zhang, Z. Li, J. Li, L. Wu, S. Zhang, and H. Tang, "Study of the stray losses calculation in structural parts for HVDC converter transformers based on the TEAM problem 21 family," *IEEE Transactions on Power Delivery*, vol. 31, no. 2, pp. 605 – 612, 2016

[9] S. Maximov, R. Escarela-Perez, J. C. Olivares-Galvan, J. Guzman, and E. Campero-Littlewood "New analytical formula for temperature assessment on transformer tanks," *IEEE Transactions on Power Delivery*, vol. 31, no. 3, pp. 1122 – 1131, 2016

[10] L. Susnjic, Z. Haznadar, and Z. Valkovic, "3D finite-element determination of stray losses in power transformer," *Electric Power Systems Research*, vol. 78, pp. 1814–1818, 2008

[11] C. C. Hwang, "Numerical computation of eddy currents induced in structural steel due to a three-phase current," *Electric Power Systems Research*, vol. 43, pp. 143-148, 1997

[12] J. Lammeraner and M. Stafl, *Eddy Currents*, Iliffe Books Ltd 1966

[13] Stoll, R. L., *Analysis of Eddy Currents*, Oxford University Press, 1974

[14] Nejman, L.R., *Skin effect in ferromagnetic bodies*, GEI, Moscow-Leningrad, 1949

[15] J. F. Gieras, "Analytical method of calculating the electromagnetic field and power losses in ferromagnetic halfspace, taking into account saturation and hysteresis," *Proc. of the Institution of Electrical Engineers*, vol. 124, pp. 1098 – 1104, 1977

[16] A.L. Bowden, E.J. Davies, "Analytic separation of the factors contributing to the eddy-current loss in magnetically nonlinear steel," *Proc. of the Institution of Electrical Engineers*, vol. 130, pp. 364-372, 1983

[17] P. D. Agarwal, "Eddy current losses in solid and laminated iron," *Transactions of the American Institute of Electrical Engineers, Part I: Communication and Electronics*, vol. 78, pp. 169-181, 1959

[18] J. Penman, B. J. Chalmers, A. M. A. Kamar, R. N. Tuncay, "The performance of solid steel secondary linear induction machines," *IEEE Trans. on Power Apparatus and Systems*, vol. 100, no. 6, pp. 2927-2935, 1981

[19] J. Penman and A. M. A. Kamar, "Linearization of saturable magnetic field problems, including eddy currents," *IEEE Trans. Mag.* vol.18, no. 2, pp. 563-566, 1982

[20] A. E. Emanuel, "The effect of nonsinusoidal excitation on eddy current losses in saturated iron," *IEEE Transactions on Power Delivery*, vol. 3, no. 2, pp. 662– 671, 1988

[21] R. Escarela-Perez, S. Maximov, J. C. Olivares-Galvan1, E. Melgoza, and M. A. Arjona, "Effective nonlinear surface impedance of conductive magnetic slabs," *IEEE Trans. Mag.* vol.53, no. 5, pp. 563-566, 6300212, 2017

[22] M. K. Gohar, "The A-C resistance of solid magnetic wires", *Transactions of the American Institute of Electrical Engineers, Part I: Communication and Electronics* , vol. 78, no. 6,pp. 912 - 916, 1960

[23] P.K. Rajagopalan , D.V.S. Murty, "Internal impedance of solid ferromagnetic conductors," *Proceedings of the Institution of Electrical Engineers* , vol. 112, no. 7, pp. 1449 - 146, 1965

[24] B. Béland and D. Gamache, "Impedance and losses in magnetic cylindrical conductors", *Electromagnetic Fields in Electrical Engineering*, pp. 39-43, Springer-Verlag US, 1988

[25] B. Beland and D. Gamache, "The impedance of flat plate steel conductors," *Proceedings of the International Conference on Electrical Machines*, Part I, Lausanne, Switzerland, 18-21, pp. 5-8, 1984

[26] P. Ripka, *Magnetic Sensors and Magnetometers*, Artech House, Jan. 1, 2001

[27] S. Tumanski, *Handbook of Magnetic Measurements*, June 23, 2011 by CRC Press Reference - page 303

[28] P. Kaspar, P. Ripka. J. Vyhnanek, "DC compensated permeameter – the accuracy study," *J. of Elec. Eng*., vol. 69, no. 6, pp. 415-417, 2018

[29] M. Mirzaei, P. Ripka, "Analytical functions of magnetization curves for high magnetic permeability materials," *IEEE Trans. Mag.,*vol.54, 2018

[30] FEMM, finite element software, http://www.femm.info/wiki/Documentation/

[31] D. O'Kelly, "Hysteresis and eddy current losses in steel plates with nonlinear magnetization characteristics," *Proceedings of the IEE*, vol. 119, pp. 1675-1676, 1972

[32] M. Sanada, S. Morimoto, "Experimental verification of thrust improvement in voice coil linear actuator using combined wire of copper and iron," *2007 IEEE Industry Applications Annual Meeting*, 23-27 Sept. 2007

[33] A. Nysveen, H. Kullbotten, J. K. Lervik, A. H. Bornes, M. Hoyer-Hansen and J. J. Bremnes, "Direct electrical heating of subsea pipelines—technology development and operating experience", *IEEE Transactions on Industry Applications*, vol. 43, no.1, Jan/Feb. 2007

[34] B. C. W. McGee and F. E. Vermeulen, "Power losses in steel pipe delivering very large currents", *IEEE Trans. Power Del.* vol.17, no.1, pp. 25-32, Jan.2002

[35] A. Chen, A. Nysveen, M. Hoyer-Hansen, J. Lervik, "Analytical and FEM calculation of electrical parameters of carbon steel pipe in DEH systems," *Magnetics Conference (INTERMAG) 2018 IEEE International*, pp. 1-5, 2018.

[36] A. Chen, A. Nysveen, J. Lervik, M. Høyer-Hansen, "Prediction of heating power in magnetic pipe conducting large AC current with high frequencies up to 200Hz,", *Magnetics Conference (INTERMAG) 2018 IEEE International*, pp. 1-1, 2018.

[37] J. M. Miller, *Effective Resistance and Inductance of Iron and Bimetallic Wires*, (Classic Reprint) Paperback – February 1, 2019

3-2-2 Position Sensors

3-2-2-1 Inductance Position Sensor for Pneumatic Cylinder [J2]

The position of the piston in pneumatic cylinder with aluminum wall can be measured by external inductance sensor without modifications of the aluminum piston and massive iron piston rod. The inductance coil is solenoid wound around the cylinder. For frequencies below 20 Hz the inductance is increasing with inserting rod due to the rod permeability. This mode has disadvantage of slow response to piston movement and also high temperature sensitivity. At the frequency of 45 Hz the inductance is position independent, as the permeability effect is compensated by the eddy current effect. At higher frequencies eddy current effects in the rod prevail, the inductance is decreasing with inserting rod. In this mode the sensitivity is smaller but the sensor response is fast and temperature stability is better. We show that FEM simulation of this sensor using measured material properties gives accurate results, which is important for the sensor optimization such as designing the winding geometry for the best linearity and compensation of the temperature dependence. The best temperature stability of 0.03%/K was found at 70 Hz, where the inductance change with position 1.5 mH is still high. We also show that the parameter important for the performance is induced voltage rather than inductance.

Inductance position sensor for pneumatic cylinder

Pavel Ripka,[a] Andrey Chirtsov, Mehran Mirzaei, and Jan Vyhnanek
Faculty of Electrical Engineering, Czech Technical University, Prague 166 27, Czech Republic

(Received 29 June 2017; accepted 3 August 2017; published online 12 October 2017)

The position of the piston in pneumatic cylinder with aluminum wall can be measured by external inductance sensor without modifications of the aluminum piston and massive iron piston rod. For frequencies below 20 Hz the inductance is increasing with inserting rod due to the rod permeability. This mode has disadvantage of slow response to piston movement and also high temperature sensitivity. At the frequency of 45 Hz the inductance is position independent, as the permeability effect is compensated by the eddy current effect. At higher frequencies eddy current effects in the rod prevail, the inductance is decreasing with inserting rod. In this mode the sensitivity is smaller but the sensor response is fast and temperature stability is better. We show that FEM simulation of this sensor using measured material properties gives accurate results, which is important for the sensor optimization such as designing the winding geometry for the best linearity. https://doi.org/10.1063/1.4993559

I. INTRODUCTION

Measurement of the piston position is required for precise control. Inserting sensors into the piston rod[1] is expensive and brings mechanical problems. Inserting sensors inside the piston brings problem with reliability.[2] The same problem applies for the optical sensors.[2–5] Magnetic scale on the piston rod is only incremental sensor.[6]

External position monitoring is simple and cheap, but the existing solutions are limited to non-magnetic cylinders. For cylinders with composite shell inductance displacement sensor was reported in Ref. 7. For aluminum shell (which is typical for pneumatic cylinders) magnetic sensors are used together with permanent magnet attached to the piston. The position of this permanent magnet is traditionally measured by a linear array of magnetic sensors. More elegant solution is to use magnetostrictive delay line[8] outside the cylinder to precisely measure the magnet attached to the piston. Using the magnetostrictive delay line, position can be measured with extreme precision of 10 μm.[9] However, sensors with permanent magnet have two drawbacks. The first drawback is that sensors with permanent magnet use expensive stainless steel piston rod, which is non-magnetic and does not distort the field from the magnet. Compensating these effects for ferromagnetic rod would be very complex.[10] The second drawback is that the permanent magnet cannot be easily mounded on the piston of existing cylinders.

Using piston remanence instead of permanent magnets[11] is also not a practical solution, as it leads to problems with long-term stability and we do not recommend such approach, as remanence of soft iron changes with time, temperature and magnetic history. The problem with AC methods is that the frequency should be small so that the magnetic field penetrates through the conductive wall. This in general brings problems with the sensor response to fast movements. We recently developed AC contactless piston position transducer with axial excitation and detection of radial magnetic field associated with the end of rod made of magnetically soft iron.[12] The disadvantage of this sensor is its short linear stroke which leads to the necessity of using linear sensor array, making the device rather complicated.

[a]Corresponding author: ripka@fel.cvut.cz

In this paper we return to the simple concept of variable inductance sensor and we show that such sensor can be used to measure position of the piston in pneumatic cylinder with aluminum shell, if position accuracy of 1 mm is acceptable, which is the case for many industrial devices. The inductance of the solenoid wound on top of the cylinder is changing with piston position even though the cylinder is made of conducting material, which partly shields the AC field. While at low frequencies the inductance is increased by inserting the ferromagnetic rod, at high frequencies the effect of eddy currents in the solid rod prevails and the inductance is decreasing. We have studied these dependencies by FEM modelling and verified the simulations by measurement. We also studied the temperature dependence of the sensor output and an influence of the temperature dependence of permeability and conductivity.

II. THE MODEL CYLINDER

The 500 mm model cylinder has 60 mm diameter with 2 mm thick aluminum wall. The aluminum piston is 10 mm thick and it is moved by 20 mm diameter iron piston rod, which is 700 mm long, so that with the piston at the end position still 20 cm of the rod is outside the cylinder. The single-layer solenoid coil has 808 turns is wound directly on top of the cylinder. Its 5 mH inductance at 20 Hz increases with inserted rod by 6 mH. The device is shown in FIG. 1 together with potentiometric positions sensor which was used as position standard for the verification measurements. FIG. 2 shows the rod and piston.

FEM model of the cylinder was built by FEMM software. Due to the rotational symmetry the problem is only two-dimensional and analysis is simple and fast. For the FEM model we measured material characteristics of the used components. The results are in Table I. Electrical conductivity was measured using 4-terminal method with the measuring current of 50 A. The voltage terminals were positioned in the region of homogeneous current density, which was verified by measuring potential at several positions. The effective permeability was measured using the same excitation solenoid: the rod flux Φ_{rod} was measured using 10-turn coil wound on the rod surface. After that the air flux Φ_{air} was measured in the same coil when the rod was removed. The voltages V_{rod} and V_{air} induced into the coil were measured by SR830 Lock-in amplifier using tracking filter setting. The effective permeability was calculated as

$$\mu_{eff} = \Phi_{rod}/\Phi_{air} = V_{rod}/V_{air} = 51$$

FIG. 1. Model cylinder attached to standard position sensor.

FIG. 2. Piston and piston rod of the model cylinder.

TABLE I. Material parameters for the FEM, model.

rod effective permeability	measured	(-)	51
rod relative permeability	estimated by FEM	(-)	77.5
rod conductivity	measured	(MS/m)	4.45
cylinder conductivity	measured	(MS/m)	30

at 10 Hz. This value is lower than material permeability estimated by FEM, which was 77.5. There are two reasons for this difference: 1. demagnetisation effect, 2. eddy current effect in the solid bar even at the low frequency of 10 Hz.

III. ATTENUATION OF THE EXCITATION FIELD

In order to observe the shielding effect for the excitation field we measured the field in the middle of the cylinder without the piston. The measurement was made using DRV425 microfluxgate sensor manufactured by Texas Instruments. The field versus excitation frequency measured for constant source voltage of 10 V as a function of frequency is shown in FIG. 3. The excitation current is shown in the same figure. It is clear that the 2 mm thick aluminum cylinder barrel has only small attenuation for the frequencies below 100 Hz, where the attenuation is 150/180 = 0.83.

Next step was observation of the effect of eddy currents inside the piston rod. We fully inserted the piston and rod inside the barrel and measured the field inside the rod using induced voltage into the 10-turn coil around the rod. The measured results are shown in FIG. 4 again for constant source voltage of 10 V. Magnetic field inside the bar decreases with frequency much faster than the field in

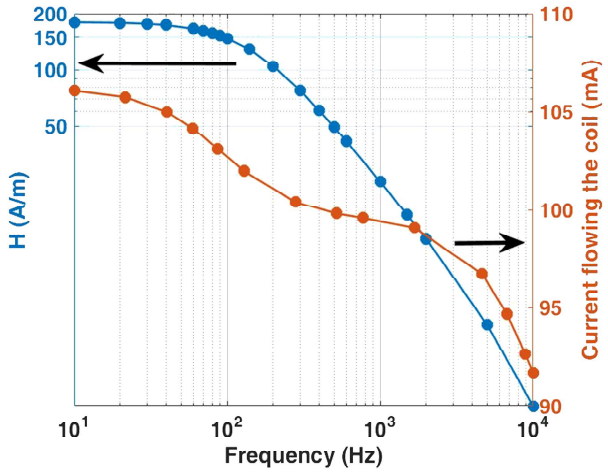

FIG. 3. Field in the center of the cylinder without rod for constant source voltage of 10 V as a function of frequency. Measured values. The DC field was 180.8 A/m.

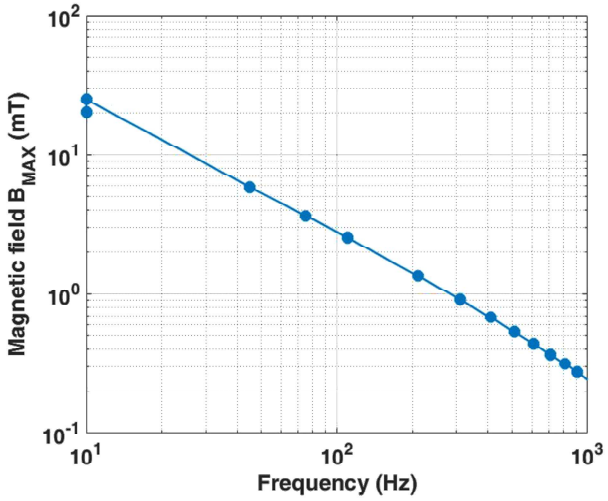

FIG. 4. Field inside the iron rod positioned in the center of the cylinder for constant source voltage of 10 V as a function of frequency. Measured values. The DC field was 180.8 A/m.

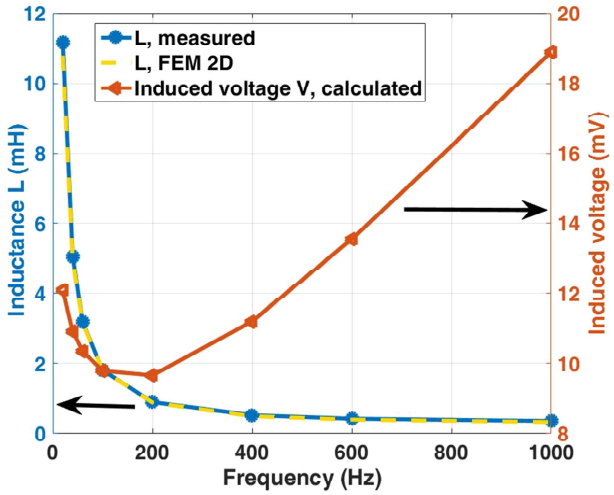

FIG. 5. Piston is completely inside. Dependence of the inductance (measured value) and induced voltage on the excitation frequency for maximum value of the excitation frequency I_m= 8.61 mA.

the air - this shows that the eddy current effect inside the massive rod is much significant than the effect of the eddy currents inside the barrel wall.

Next measurement was the inductance of the coil with fully inserted rod with piston as a function of frequency and amplitude of the measuring current. Rapid inductance decrease with frequency (FIG. 5) is caused by eddy currents in the rod, piston and cylinder wall. However, inductance is not the parameter best describing the performance of the future sensor. The sensor output can be the imaginary part of the voltage across the excitation coil, or voltage induced into the separate sensing winding. The frequency dependence of the induced voltage $2\pi fLI$ drops with frequency less rapidly, as shown in the same FIG. 5. At higher frequencies the induced voltage is even increasing with frequency. This shows that finding optimum excitation parameters is complex task which cannot be solved using just engineering intuition and higher frequencies cannot be taken from the considerations.

IV. VERIFICATION OF THE FEM MODEL

FEM model is relatively simple and it can help in the sensor design. Complicated tasks such as design of non-uniform winding density in order to optimize the sensor linearity cannot be solved experimentally without FEM modelling. FIG. 6 shows frequency dependence of the coil inductance with fully inserted piston. For FEM modelling we used the measured values of conductivity of iron and aluminum. We also found the permeability value of 77.5 giving the best fit between inductance modelling and measurement. This permeability corresponds well with the previously measured value.

We extended the FEM model also to calculate temperature effects. First of all we measured conductivity as a function of frequency and used these values to estimate inductance. TAB. II shows comparison between experimental results and FEM results, which shows well excellent fit (in one piston position).

V. RESPONSE TO MOVING PISTON

The inductance response to piston movement was calculated by FEM at different frequencies and later verified by measurements. Calculated values for low frequencies are shown in FIG. 7 and for the higher frequencies in FIG. 8. Using low frequency brings high sensitivity, but also high temperature dependence and slow response to fast moving piston. At the frequency of 20 Hz the inductance is increasing with piston position towards the end (fully inserted) position.

At the frequency of 45 Hz the inductance is position independent, as the permeability effect is compensated by eddy current effect. At higher frequencies eddy current effects prevail, the

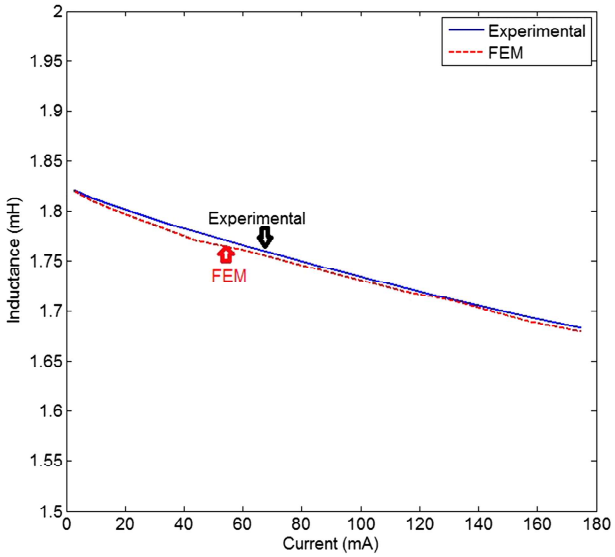

FIG. 6. Piston is completely inside, dependence the inductance on the amplitude of the excitation current through the coil at 100 Hz. The measured and FEM modelled values give the best fit for permeability value of 77.5.

TABLE II. Comparison between experimental results and FEM results for inductances.

		Frequency (Hz)			
		20	60	100	200
Exp.	Room temp.	10.934 (mH)	3.156 (mH)	1.826 (mH)	0.912 (mH)
	47 °C	11.455 (mH)	3.206 (mH)	1.833 (mH)	0.914 (mH)
FEM	Room temp.	10.780 (mH)	3.163 (mH)	1.814 (mH)	0.890 (mH)
	47 °C	11.312 (mH)	3.303 (mH)	1.892 (mH)	0.919 (mH)

sensitivity is smaller, but temperature stability is better. For f=100 Hz the inductance decreasing almost linearly with inserting rod. As already mentioned the induced voltages are large enough for precise measurement.

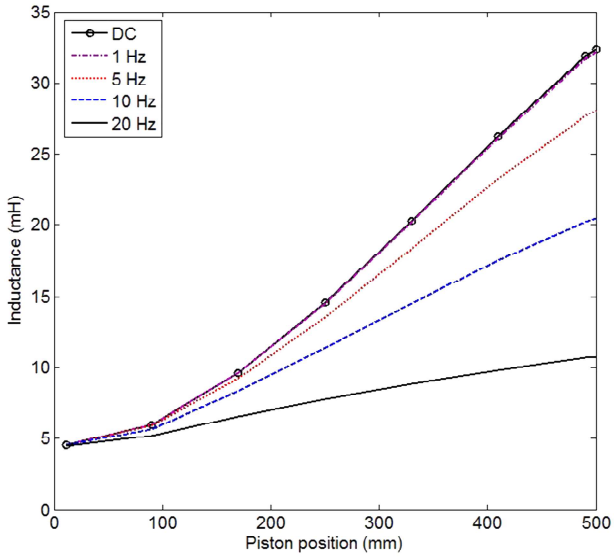

FIG. 7. Inductance vs position for low frequencies - FEM simulation.

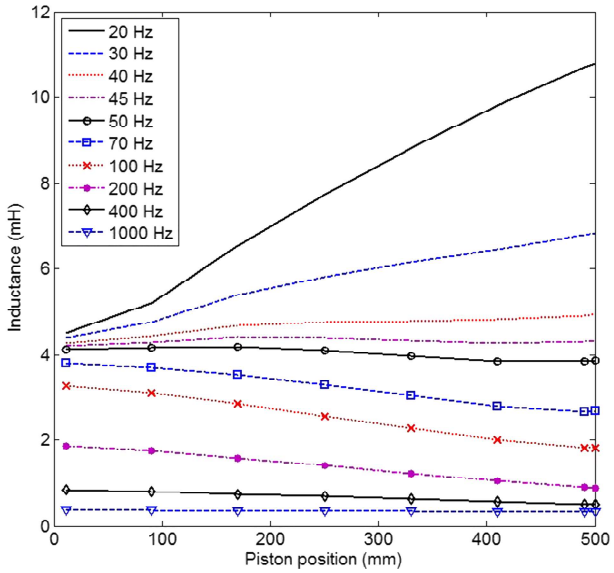

FIG. 8. Inductance vs position for high frequencies – FEM simulation.

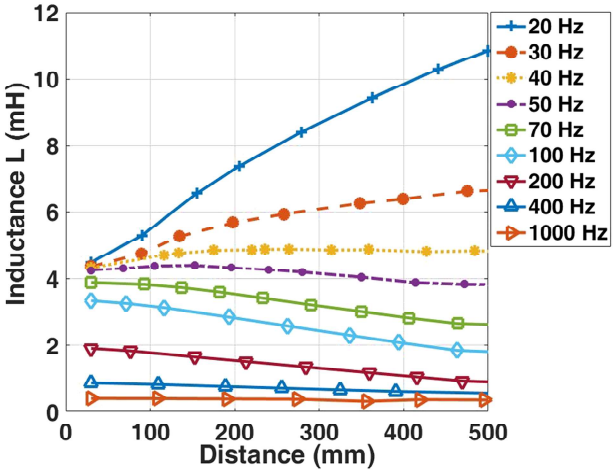

FIG. 9. Measured inductance of the coil (Ls) as the function of the piston position.

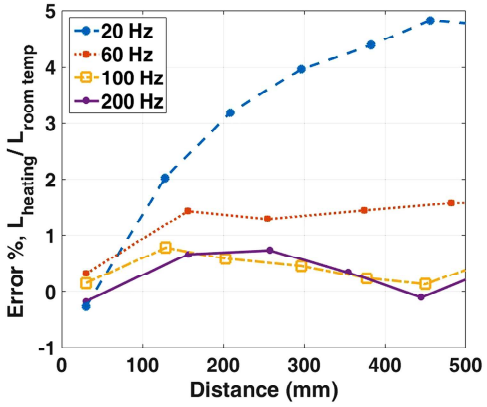

FIG. 10. Error (%) in comparing the coil inductance at a high temperature (47°C) with respect to the usual temperature. L_heating/L_room_temp.

The simulated values shown in FIGs. 7 and 8 predict well the measured characteristics shown in FIG. 9. FIG. 10 shows the results of the preliminary tests at elevated temperature. The best temperature stability (0.02%/K to 0.03%/K depending on the position) was found ad 70 Hz, where the inductance change with position is still 1.5 mH.

VI. CONCLUSIONS

We have developed position sensor for pneumatic cylinder with aluminum wall using solenoid coil on top of the cylinder barrel. For frequencies below 45 Hz the coil inductance is increasing with inserting rod due to the rod permeability. This mode has disadvantage of slow response to piston movement and also high temperature sensitivity. At the frequency of 45 Hz the inductance is position independent, as the permeability effect is compensated by the eddy current effect. At higher frequencies eddy current effects in the rod prevail, the inductance is decreasing with inserting rod. In this mode the sensitivity is smaller but the sensor response is fast and temperature stability is better. We show that simple FEM simulation of this sensor gives excellent fit with the measured results, if we use measured conductivity and estimated permeability. This will allow to use FEM simulation for the optimization of the sensor geometry to improve the linearity and also find ways how to compensate for the temperature dependence. The best temperature stability of 0.03%/K was found at 70 Hz, where the inductance change with position 1.5 mH is still high. We also show that the parameter important for the performance is induced voltage rather than inductance.

[1] I. Herceg, "Taking a position on hydraulic cylinder sensors," Hydraulics & Pneumatics 24–27 (2015).
[2] S. Fericean, A. Hiller-Brod, A. D. Dorneich, and M. Fritton, "Microwave displacement sensor for hydraulic devices," IEEE Sensors Journal **13**(12) (2013).
[3] L. Shih-Yuan, L. Jyun, and S. S. Lee, "The study of the piston driving and position sensing for a linearly moving piston pump," Automatic Control Conference (CACS), 2014 CACS International, Kaohsiung, 2014, pp. 287–291.
[4] K. Suzumori, J. Tanaka, and T. Kanda, "Development of an intelligent pneumatic cylinder and its application to pneumatic servo mechanism," Proceedings, 2005 IEEE/ASME International Conference on Advanced Intelligent Mechatronics., Monterey, CA, 2005, pp. 479–484.
[5] A. A. M. Faudzi, K. Suzumori, and S. Wakimoto, "Design and control of new intelligent pneumatic cylinder for intelligent chair tool application," 2009 IEEE/ASME International Conference on Advanced Intelligent Mechatronics, Singapore, 2009, pp. 1909–1914.
[6] S. Y. Yang, M. C. Lee, M. H. Lee, and S. Arimoto, "Measuring system for development of stroke-sensing cylinder for automatic excavator," IEEE Transactions on Industrial Electronics **45**(3), 376–384 (1998).
[7] H. Sumali, E. P. Bystrom, and G. W. Krutz, "A displacement sensor for nonmetallic hydraulic cylinders," IEEE Sensors Journal **3**(6), 818–826 (2003).
[8] E. Hristoforou, "Magnetostrictive delay lines and their applications," Sens. Actuators A **59**, 183–191 (1997).
[9] E. Hristoforou, P. D. Dimitropoulos, and J. Petrou, "A new position sensor based on the MDL technique," Sensors and Actuators A-physical **132**, 112–121 (2006).
[10] Y. Wang, R. Madson, and R. Rajamani, "Nonlinear observer design for a magnetic position estimation technique," 2015 54th IEEE Conference on Decision and Control (CDC), Osaka, 2015, pp. 6986–6991.
[11] S. Taghvaeeyan, R. Rajamani, and Z. Sun, "Non-intrusive piston position measurement system using magnetic field," IEEE Sensors Journal **13**(8), 3106–3114 (2013).
[12] P. Ripka, A. Chirtsov, V. Grim: Contactless Piston Position Transducer with Axial Excitation, proc. Intermag 2017, accepted for IEEE Trans. Magn.

3-2-2-2 Temperature Influence on Position Transducer for Pneumatic Cylinder [C3]

In this paper, temperature sensitivity of inductance position transducer of a pneumatic cylinder system is presented. The magnetic solid iron rod and aluminum piston position changes the inductance of the tubular coil around the aluminum pneumatic cylinder. The measurement and finite element method are used to evaluate inductances versus piston position at different frequencies. Temperature effect on the coil inductance is analyzed. Temperature of the iron rod and the aluminum cylinder are changed for the temperature sensitivity analysis. The measured iron rod temperature dependence is in the order of 0.45 %/°C at 100 Hz and 0.27 %/°C at 200 Hz. Finally a small compensating solenoid coil is used at one side of the cylinder (entrance side for piston) to compensate temperature dependency effects.

We evaluated temperature dependence of inductive position transducer for piston in pneumatic cylinder. The electrical conductivity temperature dependence is the main factor in the inductance variation versus temperature. The iron rod magnetic permeability variation effects versus temperature are negligible. The sensor is less temperature dependent for higher excitation frequencies, but the temperature dependence of sensitivity is high in the order of 0.45 %/°C at 100 Hz and 0.27 %/°C at 200 Hz. The main coil inductance variation versus temperature can be corrected using compensating coil because compensating coil inductance is less dependent on the iron rod and piston position and depends linearly on the temperature.

Temperature Influence on Position Transducer for Pneumatic Cylinder

Mehran Mirzaei , Pavel Ripka , Andrey Chirtsov and Jan Vyhnanek
Faculty of Electrical Engineering, Czech Technical University, Prague, Czech Republic
mirzameh@fel.cvut.cz, ripka@fel.cvut.cz

***Abstract*—In this paper, temperature sensitivity of inductance position transducer of a pneumatic cylinder system is presented. The magnetic solid iron rod and aluminum piston position changes the inductance of the tubular coil around the aluminum pneumatic cylinder. The measurement and finite element method are used to evaluate inductances versus piston position at different frequencies. Temperature effect on the coil inductance is analyzed. Temperature of the iron rod and the aluminum cylinder are changed for the temperature sensitivity analysis. The measured iron rod temperature dependence is in the order of 0.45 %/°C at 100 Hz and 0.27 %/°C at 200 Hz. Finally a small compensating solenoid coil is used at one side of the cylinder (entrance side for piston) to compensate temperature dependency effects.**

Keywords—temperature; transducer; pneumatic; cylinder

I. INTRODUCTION

Different methods for the piston position sensing are used with internal and external sensors for pneumatic cylinder. Internal sensors inserted into the piston rod are mechanically complicated and expensive and not reliable. The same problem applies for the microwave and optical sensors inside the cylinder [1]. External sensors with permanent magnet on the piston can be used for aluminum cylinder. Using permanent magnets has disadvantages. The first disadvantage is that these sensors require non-magnetic stainless steel rod, which is expensive. The non-magnetic iron rod is used to avoid distorting of permanent magnet fields. Second disadvantage is difficult mounting of permanent magnet on the piston. Third disadvantage is high temperature dependency of permanent magnets remanence flux density. We recently developed AC contactless piston position transducer with axial excitation and detection of radial magnetic field associated with the end of rod made of magnetically soft iron. The disadvantage of this sensor is its short linear stroke which leads to the necessity of using linear sensor array, making the device rather complicated [2]. In order to improve previous method, we returned to the simple concept of variable inductance sensor. This type of sensor was already used for hydraulic cylinders with composite non-conductive shell [3]. We have shown that variable inductance sensors can also be used to measure position of the piston in pneumatic cylinder with aluminum shell. The inductance of the solenoid wound on outer surface of the cylinder is changing with piston position even though the cylinder is made of conducting material, which partly shields the AC field [4]. Improving magnetic position sensor sensitivity and decrease environmental effects such as stray fields and temperature are important topics [5]-[9].

In this paper, theoretical analysis and experimental results of piston position transducer for pneumatic cylinder are presented. The inductance of axisymmetric wound solenoid around cylinder is used for piston position measurement. Temperature dependency of inductance is investigated at different piston positions and solenoid excitation frequencies. 2D axisymmetric time harmonic finite element method (FEM) is used for theoretical inductance analysis of solenoid coil on the outer surface of the conducting cylinder. The FEM inductance calculations and comparison with experimental results could help for better understanding of physics of inductance analysis. The calculations and measurement are performed at different temperatures of cylinder-piston system components to analyze sensitivity of inductance versus temperature and to select optimum excitation frequency.

II. INDUCTANCE TRANSDUCER OF PNEUMATIC CYLINDER

Fig. 1 shows the schematic model of inductance transducer for pneumatic cylinder. It shows that magnetic iron rod and piston movement changes magnetic reluctance for the coil flux, which affects inductance of the coil. Iron rod length, iron rod diameter, aluminum cylinder length, aluminum cylinder outer diameter, aluminum cylinder thickness, aluminum piston thickness and number of turns of main coil are 700 mm, 20 mm, 500 mm, 60 mm, 2 mm, 10 mm and 800, respectively. The electrical resistivities of iron rod and aluminum cylinder versus temperature are given as follows:

$$\begin{aligned}
&\rho_{\mathrm{i}}(\theta^{\mathrm{o}}\mathrm{C}) = \rho_{\mathrm{i}}(20^{\mathrm{o}}\mathrm{C})\cdot(1+c_{\mathrm{i}}\cdot(\theta-20))\\
&\rho_{\mathrm{i}}(20^{\mathrm{o}}\mathrm{C}) = 22.18\cdot10^{-8} \rightarrow \sigma_{\mathrm{i}}(20^{\mathrm{o}}\mathrm{C}) = 4.509\,\mathrm{MS/m}\\
&c_{\mathrm{i}} = 0.0027356\\
&\rho_{\mathrm{Al}}(\theta^{\mathrm{o}}\mathrm{C}) = \rho_{\mathrm{Al}}(20^{\mathrm{o}}\mathrm{C})\cdot(1+c_{\mathrm{Al}}\cdot(\theta-20))\\
&\rho_{\mathrm{Al}}(20^{\mathrm{o}}\mathrm{C}) = 3.28\cdot10^{-8} \rightarrow \sigma_{\mathrm{Al}}(20^{\mathrm{o}}\mathrm{C}) = 30.5\,\mathrm{MS/m}\\
&c_{\mathrm{Al}} = 0.0041
\end{aligned} \tag{1}$$

The relative magnetic permeability of the soft iron used for the piston rod at low magnetic fields was estimated between 50 and 100, but the precise measurement would be affected by necessary machining during the preparation of the sample. More precise evaluation of permeability can be made by measuring the inductance as shown in the next section.

978-1-5386-4707-3/18/$31.00 ©2018 IEEE

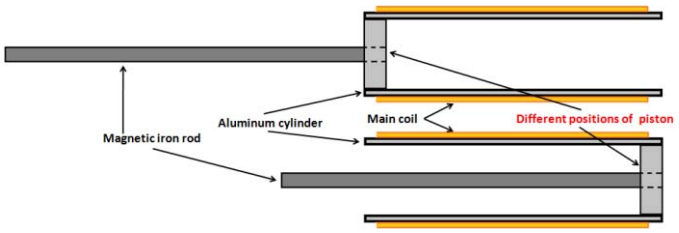

Fig. 1. Schematic model of inductance transducer for pneumatic cylinder

III. One Preliminary Example

In order to evaluate iron rod permeability, one preliminary example is analyzed before main topic of inductance transducer is presented. The model is a simple structure with short coil shown in Fig. 2 and Fig. 3. First we measured and calculated inductance value of the coil without the iron rod (case 1). Then we adjusted the value of permeability so that the FEM results [10] fit the measured values of room-temperature inductance (Case 2). The resulting relative permeability was 77.5. We calculated and measured inductance at elevated temperature (case 3) with the same value of permeability (Table. I). The FEM results coincide well with experimental results for all three cases and showing the validity of the model and evaluated permeability. The measurements suggest that the temperature dependence of permeability plays minor role. The inductance measurements are done by LCR meter.

TABLE I. Inductances Basic Model - Case 1 : without Iron Rod, Case 2: with Iron Rod at Room Temperature and Case 3 : with Iron Rod at 68 °C

Cases	f = 100 Hz	
	Experimental (μH)	*FEM* (μH)
1	257.5	253.0 (98.3%)
2	407.0	385.0 (94.6%)
3	415.5	390.0 (93.9%)

IV. Temperature Dependence

The inductance of the long solenoid coil sensor is increasing with inserting the rod due to its permeability at very low frequencies, below 30 Hz. However, the dependence is opposite for higher excitation frequencies: with inserting the rod, the coil inductance is decreasing due to the eddy currents [4]. Fig. 4 shows the magnetic field distribution in the piston rod. Low field values allow using magnetic model with constant permeability as Fig. 3. Despite lower sensitivity, the inductances at 100 Hz and 200 Hz are most relevant for the intended application because the values linearly change with iron rod and piston position and the response of position sensor excited at these frequencies would be fast enough to detect fast movements of the iron rod and piston position. We will show that the iron rod temperature dependence of the sensor is lower at higher frequencies. In order to understand temperature dependence of the sensor the pneumatic aluminum cylinder and iron rod were heated up separately to evaluate temperature dependency of sensor inductances. Fig. 5 and Fig. 6 show that pneumatic aluminum cylinder temperature has much higher influence on sensor inductances than the temperature of the piston rod at 100 Hz and 200 Hz. The FEM results for inductances show same tendency versus temperature using precise and correct material parameters in FEM model. Only cylinder and iron rod electrical resistivity have been changed in FEM, which shows iron relative magnetic permeability has not been affected by changing temperature.

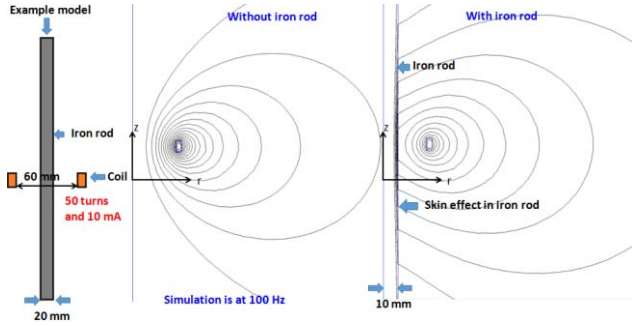

Fig. 2. The model (left), magnetic flux distribution without iron rod (middle) and magnetic flux distribution with iron rod (right)

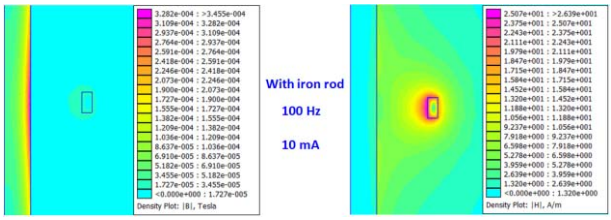

Fig. 3. Magnetic flux density distribution (left) and magnetic field strength distribution (right), which shows low magnetic field

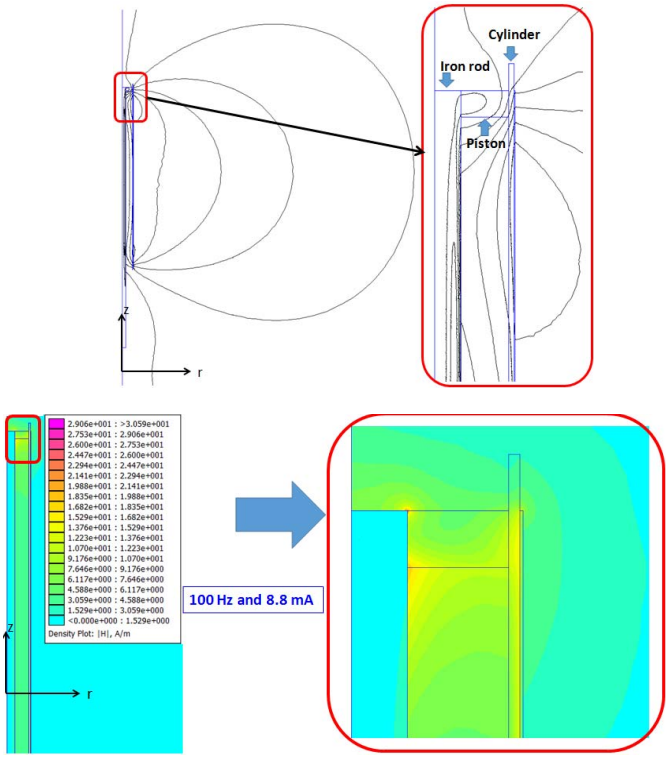

Fig. 4. Magnetic flux distribution (up) and magnetic field strength distribution (bottom) in inductance transducer of pneumatic cylinder

The signal from the short axisymmetric compensation coil (Fig. 7) located at the beginning of the cylinder can be used to compensate for the temperature effects. Fig. 7 shows that with the exception of the beginning area, the inductance of this coil does not depend on the piston position. The number of turns in the compensating coil is 10 and inductances values are in μH. The compensating coil inductance versus iron rod temperature is shown in Fig. 8, when iron rod and piston position is at end of cylinder. The compensating coil inductances linearly increase with temperature in the order of 0.45 %/°C at 100 Hz and 0.27 %/°C at 200 Hz (Fig. 8). The linear changing of compensating coil inductance versus temperature helps to find iron rod temperature and compensate main coil inductance error at higher temperatures.

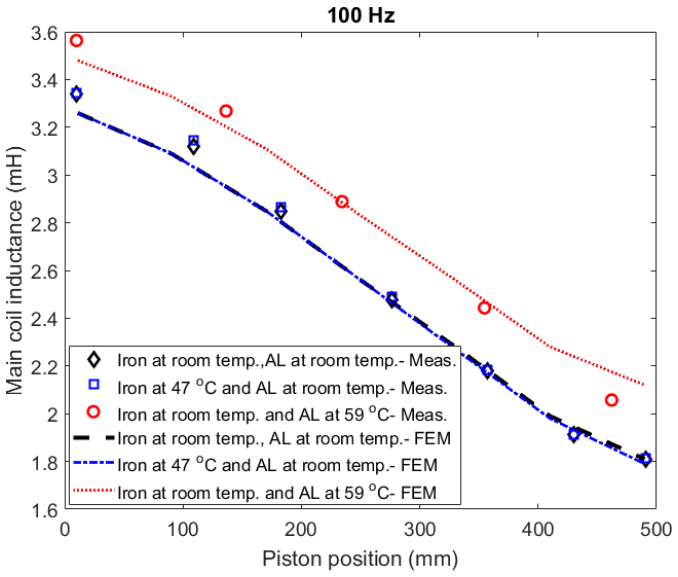

Fig. 5. Inductances at different temperatures for main coil - 100 Hz

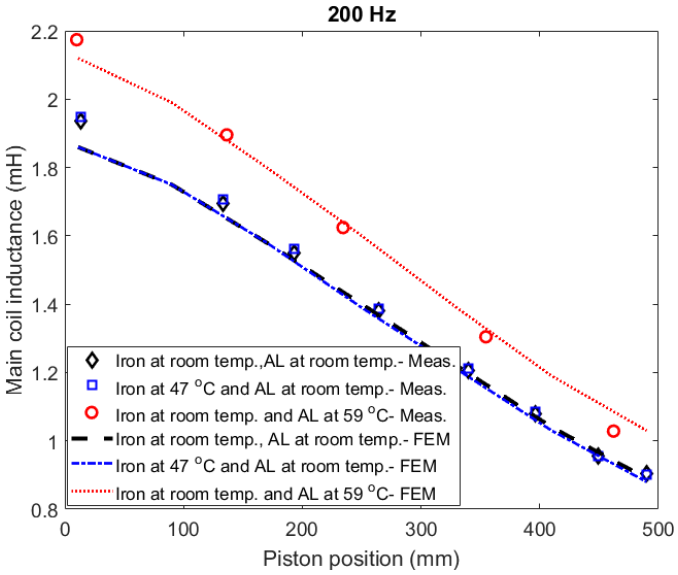

Fig. 6. Inductances at different temperatures for main coil - 200 Hz

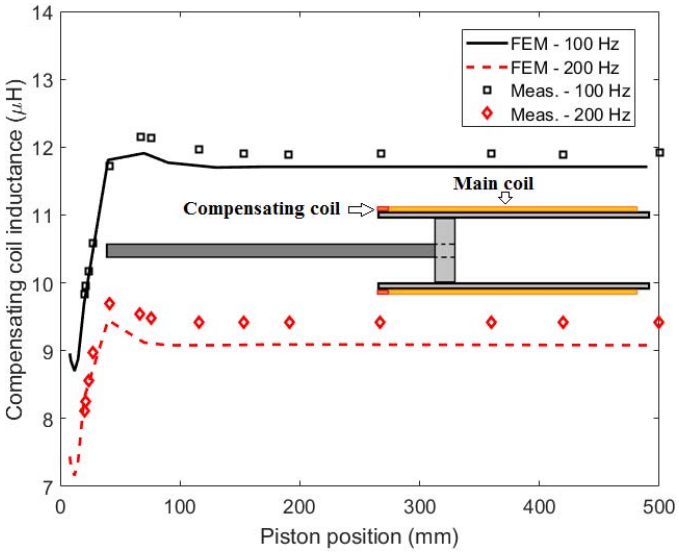

Fig. 7. Inductances versus piston position for compensating coil

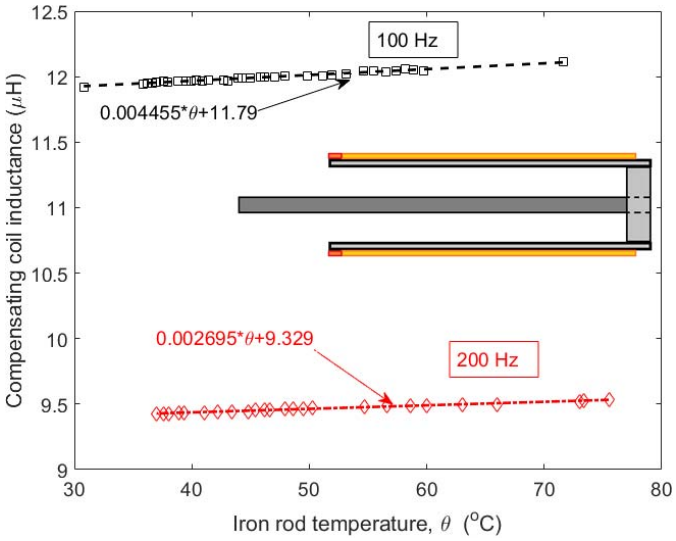

Fig. 8. Inductances versus iron rod temperature for compensating coil – measurement, only iron rod has been heated

V. CONCLUSIONS

We evaluated temperature dependence of inductive position transducer for piston in pneumatic cylinder. The electrical conductivity temperature dependence is the main factor in the inductance variation versus temperature. The iron rod magnetic permeability variation effects versus temperature are negligible. The sensor is less temperature dependent for higher excitation frequencies, but the temperature dependence is high in the order of 0.45 %/°C at 100 Hz and 0.27 %/°C at 200 Hz. The main coil inductance variation versus temperature can be corrected using compensating coil because compensating coil inductance is less dependent on the iron rod and piston position and depends linearly on the temperature.

REFERENCES

[1] S. Fericean, A. Hiller-Brod, A. Daniel Dorneich, and M. Fritton, "Microwave displacement sensor for hydraulic devices," IEEE Sensors Journal, vol. 13, 12, December 2013

[2] P. Ripka, A. Chirtsov and V. Grim, "Contactless piston position transducer with axial excitation, " IEEE Transactions on Magnetics, vol. 53, 2017

[3] H. Sumali, E. P. Bystrom, and G. W. Krutz, "A displacement sensor for non-metallic hydraulic cylinders, " IEEE Sensors Journal, vol. 3, no. 6, pp. 818-826, Dec. 2003

[4] P. Ripka, A. Chirtsov, and M. Mirzaei, "Inductance position sensor for pneumatic cylinder, " AIP Advances 8, 048001, 2018

[5] S. Y. Yang, M. C. Lee, M. Hyung Lee, and S. Arimoto, "Measuring system for development of stroke-sensing cylinder for automatic excavator, " IEEE Transactions on Industrial Electronics, vol. 45, no. 3, pp. 376-384, Jun 1998.

[6] H. Evangelos , P.D. Dimitropoulos, and J. Petrou, "A new position sensor based on the MDL technique, " Sensors and Actuators A-physical - 132. 112-121. 10.1016, 2006

[7] S. Taghvaeeyan, R. Rajamani, and Z. Sun "Non-intrusive piston position measurement system using magnetic field, " IEEE Sensors Journal, vol. 13, 2013

[8] S. Yang , K. Hirata, T. Ota, and Y. Kawase, "Impedance linearity of contactless magnetic-type position sensor, " IEEE Transactions on Magnetics, vol. 53, 6, 2017

[9] Adrian Grima, Mario Di Castro, Alessandro Masi, and Nicholas Sammut, "Electrical metrological characterization of ironless inductive position sensors with long cables, " IEEE Sensors Journal, vol. 18, 17, 2018

[10] http://www.femm.info/wiki/Documentation/, accessed 2017/09/24

3-2-2-3 Transformer Position Sensor for A Pneumatic Cylinder [J6]

A novel transformer-based sensor for a pneumatic cylinder enables measurements of the piston position to be made through a thick conductive cylinder. Unlike existing industrial solutions, which are mainly based on a moving magnet, our sensors do not require modifications to the parts inside the cylinder. Finite element analysis results are compared with measurements at various piston positions and excitation frequencies. Using a suitable model for the magnetic properties of the iron piston rod, we achieved good agreement between the model and reality. When the sensor is operated at 100 Hz, the sensitivity is 200 mV/FS and the raw linearity error is 1.6% of the full 400 mm stroke.

FEM modeling and experimental results for a transformer position sensor for a pneumatic cylinder have been presented. The results show the feasibility of using the principle of a linear transformer with a moving core for measuring the position of the piston in a pneumatic cylinder. Compared to conventional LVDT, our sensor has a highly asymmetric core which moves inside the conducting cylinder. The sound match between FEM results and measurements shows that FEM can be used for optimizing a position sensor of this type. The temperature sensitivity of the secondary coil voltage has been calculated for various iron and aluminum temperatures. The effect of the change in the electrical resistivity of an aluminum cylinder is clearly dominant at 100 Hz excitation frequency. Temperature compensation can be easily made by using the voltage across the excitation coil. Using only fixed copper coils for excitation and pick up make the proposed position sensor for pneumatic cylinder more cost effective than position sensor using rare earth NdFeB permanent magnets and an array of Hall sensors. In industrial applications, single-chip synchronous detector such as AD630 can be used for the output voltage processing. Due to its simplicity the proposed position sensor is suitable for harsh environment such as high temperature and vibrations.

Sensors and Actuators A 294 (2019) 91–101

Contents lists available at ScienceDirect

Sensors and Actuators A: Physical

journal homepage: www.elsevier.com/locate/sna

Transformer position sensor for a pneumatic cylinder

Pavel Ripka*, Mehran Mirzaei, Andrey Chirtsov, Jan Vyhnanek

Faculty of Electrical Engineering, Czech Technical University, Prague, 16627, Czech Republic

ARTICLE INFO

Article history:
Received 14 January 2019
Received in revised form 12 April 2019
Accepted 28 April 2019
Available online 11 May 2019

Keywords:
Position sensor
Transformer
Pneumatic
Cylinder
Finite element method

ABSTRACT

A novel transformer-based sensor for a pneumatic cylinder enables measurements of the piston position to be made through a thick conductive cylinder. Unlike existing industrial solutions, which are mainly based on a moving magnet, our sensors do not require modifications to the parts inside the cylinder.

Finite element analysis results are compared with measurements at various piston positions and excitation frequencies. Using a suitable model for the magnetic properties of the iron piston bar, we achieved good agreement between the model and reality.

When the sensor is operated at 100 Hz, the sensitivity is 200 mV/FS and the raw linearity error is 1.6% of the full 400 mm stroke.

1. Introduction

Sensing the position of a piston inside a pneumatic aluminium cylinder is a challenging task which is necessary for controlling the piston. The piston is shielded by the aluminium cylinder, which makes piston position measurements difficult. Various techniques are used for piston sensing transducers. Direct mounting of sensors inside the piston rod requires a gun-drilled long precise hole, which is expensive and may reduce the mechanical stability of the rod [1]. The use of microwave sensors on the piston is not reliable, and it is also mechanically complicated [2]. An optical scale [3] or a magnetic scale [4] on the piston rod allows only incremental position sensing. Using of magnetostrictive delay line principle is not suitable for harsh environment [5–7]. Remanent field of ferromagnetic piston was used in [8] for position measurement. This approach is not practical, as the remanent field changes with time and temperature and can also be significantly changed by external magnetic fields.

The method currently used by industry is external sensing of the piston position using a permanent magnet mounted on the piston with a non-magnetic stainless-steel rod. Permanent magnet fields are measured by an array of magnetic field sensors to detect the piston position. Although this method is robust and reliable, it requires a piston rod made of non-magnetic stainless steel, which is expensive. The authors recently developed an AC-excited contactless piston position transducer with axial excitation [9]. The field changes caused by a moving ferromagnetic piston rod are sensed by an array of integrated fluxgate sensors. While 0.1 mm resolution is achievable, the uncorrected maximum static error was ±3 mm. Limiting factor for this transducer is the dynamic performance: the maximum dynamic error is ±3 mm even at speed of 0.2 m/s. This type of sensor also requires complex signal processing of the sensor array. Similar results were obtained using radial excitation by saddle coils [10].

A much simpler solution is to evaluate the inductance of a solenoid coil around an aluminium cylinder and sensing piston. This type of sensor was developed by Sumali et al. [11], but only for cylinder made of non-conducting composite. Later simulations have shown that the linearity error of such sensor can be decreased by proper design of the coil [12]. We have experimentally verified the performance of a transducer of this kind even for the conducting cylinder within the industrial temperature range [13,14]. However, the dynamic performance of a sensor based on measured inductance is problematical. Measuring the voltage induced into the secondary coil is a faster solution for dynamic position sensing of the piston. The transformer-based position transducer is a well-known solution [15–22]. One excitation coil and several pick-up coils are implemented in the transformer type of the position transducer. While the moving coil type [15,18,19] is not practical for our application, however, the conventional LVDT transducer, which uses a ferromagnetic core instead, is more suitable [16,17]. Our aim was to adopt the LVDT principle for cases with a highly asymmetric core that moves inside the conducting cylinder.

In this paper, a transformer-based position sensor for a pneumatic cylinder with an aluminium shell, an aluminium piston and a ferromagnetic steel rod is analysed, designed and evaluated. A 2D axisymmetric finite element method (FEM) is used for the mod-

* Corresponding author.
E-mail address: ripka@fel.cvut.cz (P. Ripka).

https://doi.org/10.1016/j.sna.2019.04.046
0924-4247/

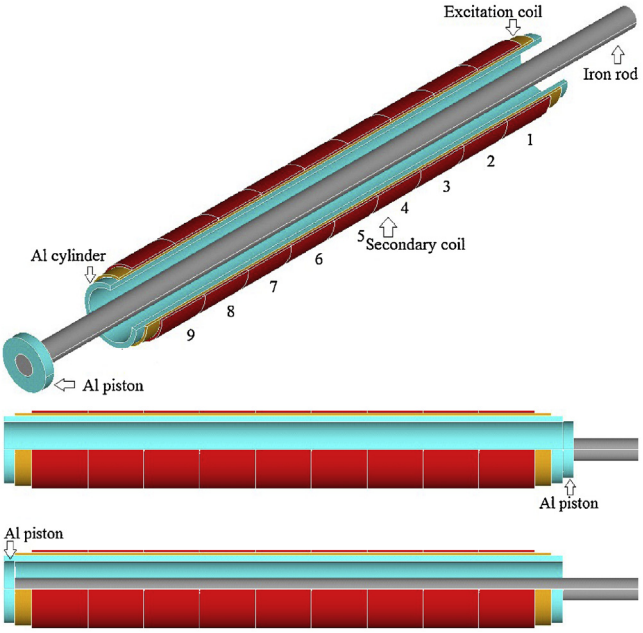

Fig. 1. A model of the transformer position sensor for a pneumatic cylinder – the full model (above), the axisymmetric model at the zero position of the piston (middle), and the axisymmetric model at the end position of the piston (below).

Table 1
Dimensions and Material Data.

Parameter	Value
Cylinder outer diameter, D_{co}	60 (mm)
Cylinder inner diameter, D_{ci}	56 (mm)
Cylinder axial length, L_c	500 (mm)
Piston outer diameter, D_{po}	56 (mm)
Piston inner diameter, D_{pi}	20 (mm)
Piston axial length, L_p	10 (mm)
Iron rod diameter, D_i	20 (mm)
Iron rod axial length, L_i	700 (mm)
Number of turns for the excitation coil, N_e	800
Number of turns for each pick up coil, N_{pc}	77
Number of pick up coils, n_p	9
Wire diameter, D_w	0.56 (mm)
Aluminium electrical conductivity at 20 °C, σ_{Al}	30.5 (MS/m)
Iron electrical conductivity at 20 (°C), σ_i	4.51 (MS/m)

elling. A frequency analysis with and without the iron rod and piston is performed in order to find proper operational conditions for the best precision. We also discuss how to read the secondary coils voltages to achieve the best sensor characteristics.

2. Model of pneumatic cylinder

Fig. 1 shows the pneumatic cylinder model at different piston positions. Two sets of coils are used for the position sensor.

The model has an axisymmetric configuration, which reduces the model to a 2D configuration for the simulations. The first layer is the excitation coil, which is wound around the aluminium cylinder. The second layer coil is divided into 9 sections of pick-up coils.

Table 1 shows the dimensions of the pneumatic cylinder and the material data.

3. Magnetic properties of the iron rod

The correct relative magnetic permeability is important for FEM simulations and analysis. It is difficult to estimate the relative magnetic permeability of the iron rod, because the magnetic fields are low [13]. The relative magnetic permeability can therefore be

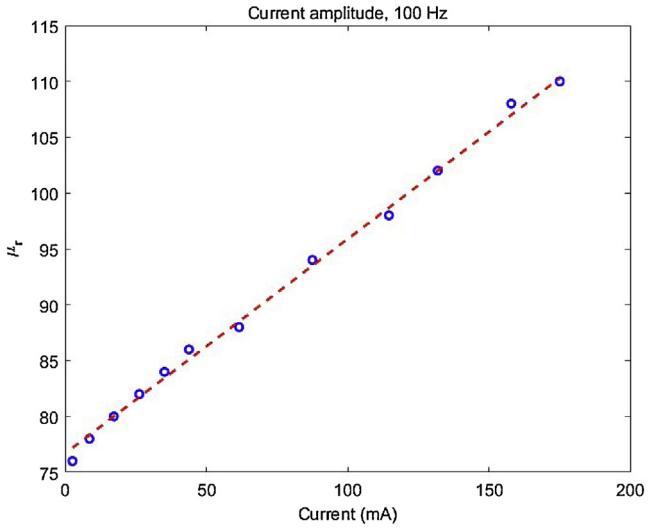

Fig. 2. Relative magnetic permeability, μ_r-I_m curve when the piston is in the end position - (estimated from the inductance [13]).

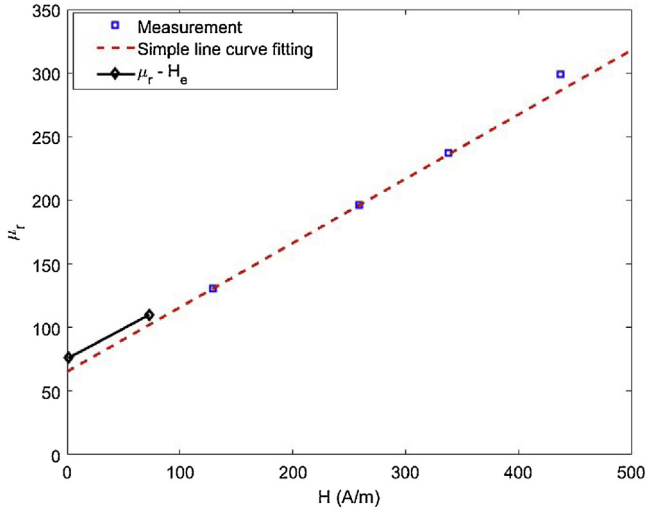

Fig. 3. Relative magnetic permeability, the μ_r-H curve - measured from yoke, and μ_r-H_e, calculated from Fig. 2 (H_e is effective H on the surface of the iron rod).

considered as the initial permeability. Solid irons and steels have different initial permeability, depending on the chemical composition and the processing [23].

One method for finding the relative magnetic permeability is to use the excitation coil inductance. We measured this inductance for a fully-inserted rod, and we estimated the permeability iteratively using the FEM model. Fig. 2 shows the relative magnetic permeability versus the excitation current amplitude evaluated by this method. The relative magnetic permeability increases with increasing current, because the operating points are in the Rayleigh region of the B–H curve.

A second method for estimating the relative magnetic permeability for low fields is to extrapolate the B–H curve for small field values. In standard material models, the measured B–H curve is usually available only for fields above 50 m T [24]. The simplest method for estimating the relative magnetic permeability for lower fields is a simple line, which is calculated on the basis of the first two points from the measured B and H values. The simple equivalent line curve fitting function estimates initial permeability around 70 (Fig. 3). The estimated values from the B–H curve are compatible with the estimated value from the measured inductance, $\mu_r = 77.5$

(Fig. 2). The increasing relative magnetic permeability for a higher excitation coil current and higher magnetic field strength should be taken into account for precise simulations of a position sensor.

4. Operation theory

4.1. Inductances of air core solenoid coils

The magnetic vector potential of a finite-length solenoid coil is calculated as follows [25,26] at an arbitrary point with cylindrical coordinates r and z:

$$A_\phi = \frac{\mu_0 \cdot N \cdot I \cdot r_w}{\pi} \cdot \int_{-0.5L_w}^{0.5L_w} \frac{2 - k_1^2 \cdot K(k_1^2) - 2 \cdot E(k_1^2)}{\beta \cdot k_1^2} dl$$
$$\alpha = \sqrt{r_w^2 + r^2 + (z+l)^2 - 2 \cdot r_w \cdot r} \quad (1)$$
$$\beta = \sqrt{r_w^2 + r^2 + (z+l)^2 + 2 \cdot r_w \cdot r}$$
$$k_1 = \sqrt{1 - \frac{\alpha^2}{\beta^2}}$$

where, μ_0 is the permeability of the open space, N is the number of turns of the solenoid coil, I is the current, r_w is the mean radius of the solenoid coil, L_w is coil length, K are the complete elliptic integrals of the first kind, and E are the complete elliptic integrals of the second kind.

Fig. 4 shows the magnetic flux distribution for various finite length solenoid coils. The end effects are more visible in a shorter coil, which changes the inductance considerably, than when an infinite length solenoid coil is used.

The self inductance of the air core solenoid coil L, and of the induced voltage U are as follows with negligible wires diameters:

$$U = L \cdot \frac{dI}{dt}, \quad L = C \cdot \frac{N^2}{\Re}, \quad \Re = \frac{L_w}{\mu_0 \cdot \pi \cdot r_w^2} \quad (2)$$

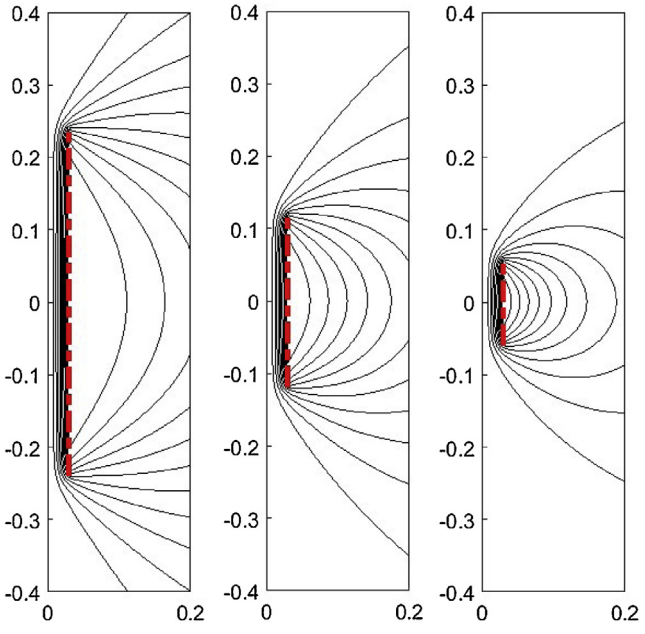

Fig. 4. Magnetic flux distribution in a solenoidal coil (the red dashed line shows the solenoid coil) using (1), which depicted sizes are in meter unit - solenoid length 480 mm (left), solenoid length 240 mm (middle), and solenoid length 120 mm (right) with coil radius 30 mm (For interpretation of the references to colour in this figure legend, the reader is referred to the web version of this article.).

Table 2
Field End Effect C.

L_{ew} (mm)	C – using (3)	C – using (4)
480	0.949	0.947
240	0.902	0.894
120	0.818	0.788

where C is the end effect factor caused by the finite length of the solenoid coil. Parameter C is equal to 1 for a solenoid coil of infinite length. Parameter C can be computed [27] using the exact formula in (3) or using the approximate formula in (4):

$$C = \frac{8}{3 \cdot \pi} \cdot \frac{r_w}{L_w} \cdot \left[\frac{1 - k_2^2}{k_2^3} \cdot K\left(k_2^2\right) + \frac{2k_2^2 - 1}{k_2^3} \cdot E\left(k_2^2\right) - 1 \right]$$
$$k_2 = \sqrt{\frac{\left(\frac{r_w}{L_w}\right)^2}{\left(\frac{r_w}{L_w}\right)^2 + 0.25}} \quad (3)$$

$$C = 1 - \frac{8}{3 \cdot \pi} \cdot \frac{r_w}{L_w} \quad (4)$$

The resulting mutual inductance between the excitation coil with axial length, L_{ew} and the pick up coil with axial length L_{pw} (Fig. 1) and induced voltage U_m can be presented as follows:

$$U_m = M \cdot \frac{dI}{dt}, \quad M = C \cdot \frac{N_e \cdot N_p}{\Re} = \frac{N_p}{N_e} \cdot L \quad (5)$$

where, N_e (=800) is the number of turns for the exciting coil, and N_p ($n_e \cdot N_{pc}$ = 693), is the total number of turns for the pick-up coil. For simplicity, the effects of the wires diameters are neglected when computing (3)-(5) as the wires diameters are very small in comparison with coil radius.

Table 2 shows parameter C for various solenoid coil lengths. It decreases with decreasing coil length, L_{ew}. The smaller r_w/L_{ew} ratio causes the smaller field end effects of a solenoid coil of finite length.

4.2. Real inductances

A conductive aluminium cylinder and piston and a conductive solid iron rod cause a change in the self-inductance of the exciting coil, and also mutual inductance between the exciting coil and the pick-up coil, because of the induced eddy currents in the solid parts and the high permeability of iron.

A 2D axisymmetric finite element method is used to calculate the self-inductance and the mutual inductance, taking into account the solid aluminium cylinder and the solid iron rod [24]. Eqs. (6) and (7) present the governing equations extracted from the Maxwell equations for a 2D axisymmetric model [25]. The first term of (7) is for the excitation coil region, and the second term is for the solid conductive parts of the cylinder and the iron rod (Fig. 1).

$$B_r = \mu \cdot H_r, \; B_z = \mu \cdot H_z$$
$$\frac{1}{r}\frac{\partial}{\partial r}\left(r\frac{\partial A_\phi}{\partial r}\right) - \frac{A_\phi}{r^2} + \frac{\partial^2 A_\phi}{\partial z^2} = -\mu \cdot J_\phi \quad (6)$$
$$B_r = -\frac{\partial A_\phi}{\partial z}, \; B_z = \frac{1}{r}\frac{\partial}{\partial r}\left(rA_\phi\right)$$

$$J_\phi = J_s$$
$$J_\phi = -\sigma\frac{\partial A_\phi}{\partial t} = -j\omega\sigma A_\phi, \quad \omega = 2\pi f \quad (7)$$

where, B_r is the radial component of the magnetic flux density, H_r is the radial component of the magnetic field strength, B_z is the axial component of the magnetic flux density, H_z is the axial

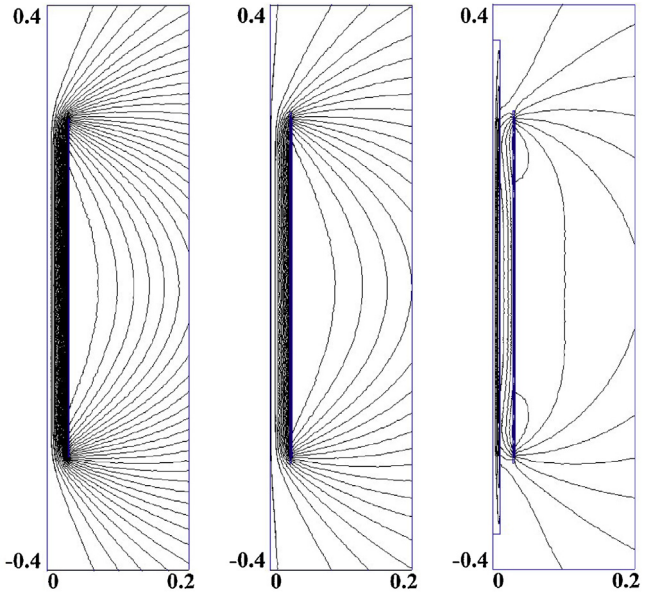

Fig. 5. Magnetic flux distribution using FEM at 100 Hz in a solenoidal coil without an iron rod and without an aluminium cylinder (left), with only an aluminum cylinder (centre), and with an iron rod and with an aluminium cylinder - solenoid length 480 mm with a coil radius of 30 mm.

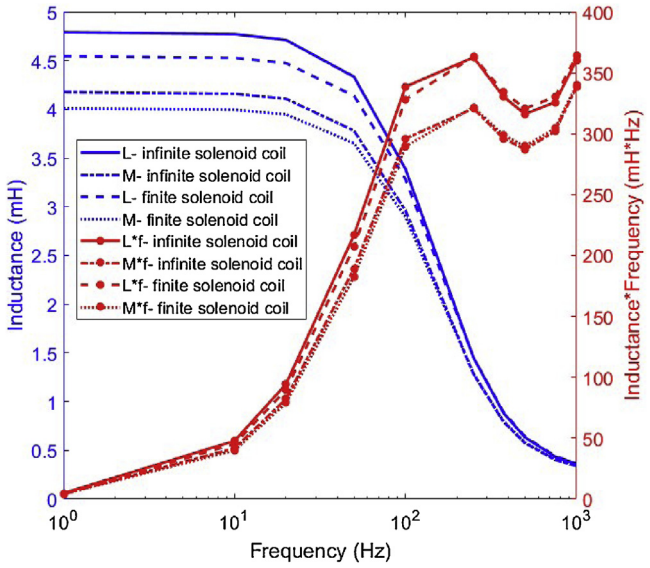

Fig. 6. Inductance versus frequency using FEM - with an aluminium cylinder and without an iron rod - solenoid coil length 480 mm.

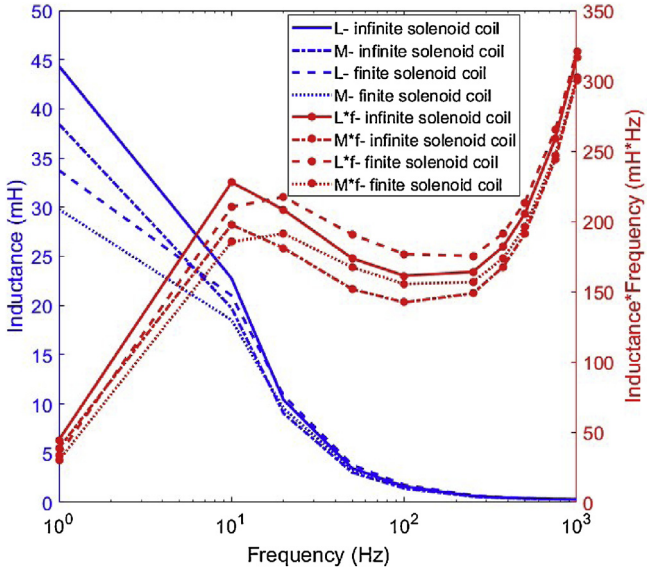

Fig. 7. Inductance versus frequency, using FEM - with an aluminum cylinder and with an iron rod - solenoid coil length 480 mm ($\mu_r = 77.5$).

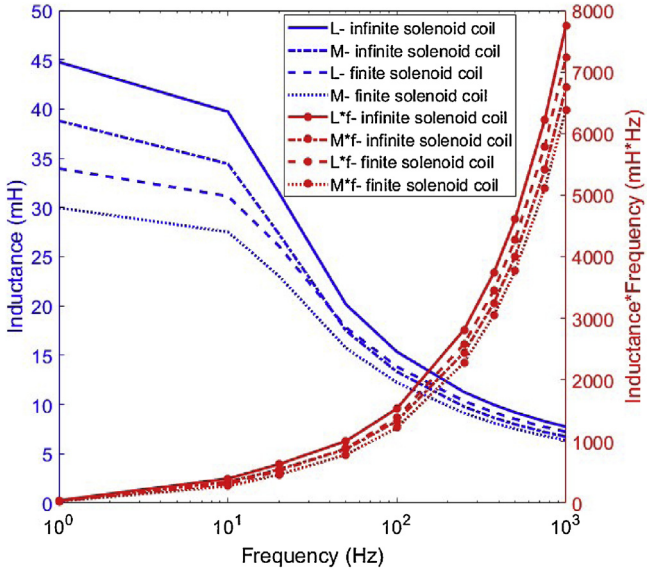

Fig. 8. Inductance versus frequency, using FEM - without an aluminum cylinder and with an iron rod - solenoid coil length 480 mm ($\mu_r = 77.5$).

component of the magnetic field strength, μ is the relative magnetic permeability, A_φ is the magnetic vector potential, J_φ is the azimuthal-angle component of the current density, J_s is the source current density (excitation coil), and σ is the electrical conductivity of the solid parts (the aluminium cylinder and the iron rod). f is electrical frequency.

Fig. 5 shows the magnetic flux distribution with and without an iron rod and an aluminium cylinder, calculated by FEM. It is clear that the conductive parts have a significant influence on the distribution of the magnetic flux. The self-inductance of the exciting coil and the mutual inductance are shown in Figs. 6–8. The ratio between self inductance and mutual inductance in Figs. 6–8 follows the correspondence in (5), which is related to the number of turns of the exciting coil N_e and the pick-up coil N_p.

The self inductances at low frequencies in Fig. 6 are 4.7 mH for an infinite solenoid and 4.5 mH for a finite solenoid coil, which correspond to (2) - (4). The inductances decrease due to the skin effect in the conductive parts at higher frequencies f. A stronger skin effect reduces the effective area for magnetic flux inside the solenoid coil, which results in decreased self-inductances and mutual inductances.

The aluminium cylinder has a dominant effect on the inductances in the high frequency range above 100 Hz, compare Figs. 6 - 8. The resistive part is caused mainly by the induced eddy currents in the conductive parts of the iron rod and the aluminium cylinder. The curves for parameters $L{\cdot}f$ and $M{\cdot}f$ in Figs. 6–8 are proportional to the induced voltages in the excitation coil and in the secondary coil. Local maxima occur at about 100 Hz–200 Hz in Fig. 6 and at 10 Hz in Fig. 7. In Fig. 8, parameters $L{\cdot}f$ and $M{\cdot}f$ versus frequency increase continuously until 1000 Hz. This shows that the eddy cur-

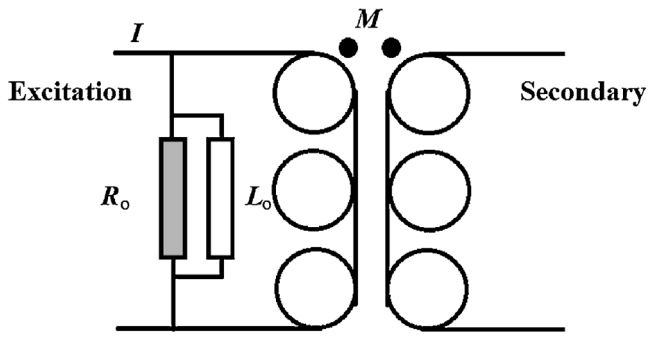

Fig. 9. Equivalent circuit for a pneumatic cylinder with the transformer model – the excitation coil is in the primary side.

rents in the cylinder have a stronger effect than the eddy currents in the piston rod.

Fig. 9 shows the equivalent circuit of a pneumatic cylinder with an open secondary transformer model. Inductance L_o represents the standard equivalent circuit components in parallel connection related to the total magnetic energy, and resistance R_o represents the standard equivalent circuit components in parallel connection related to the total eddy current losses. The hysteresis losses are neglected, because the magnetic fields in the iron are very small. The excitation coil resistance is 13.7 Ω. Resistance R_o is very large when the eddy current losses and the coil resistance are negligible – this is true only at very low frequencies. Inductance L_o changes dramatically from 4.5 mH to 34 mH when the ferromagnetic rod is inserted – compare Fig. 7 with Fig. 6.

All measured and calculated inductances L in this paper are for series connection. However the equivalent circuit corresponding to core losses (R_o) and magnetic energy (L_o) for transformer is usually shown in parallel connection. The components in the equivalent series connections, L and R, are calculated:

$$L = \frac{R_2^o}{\omega^2 L_2^o + R_2^o} \cdot L_o$$
$$R = \frac{\omega^2 L_2^o}{\omega^2 L_2^o + R_2^o} \cdot R_o \quad (8)$$

The first term concerning inductances is shown in Figs. 6–8. It is obvious that inductance L always decreases versus frequency. Eq. (9) shows the excitation coil induced voltage, V_e and the secondary or pick-up coil induced voltage, V_p. The induced voltages have real parts ($V_{e\text{-}r}$ and $V_{p\text{-}r}$) and imaginary parts ($V_{e\text{-}i}$ and $V_{p\text{-}i}$) referred to applied current I as a reference.

$$V_e = (R + j\omega L) \cdot I,\ V_{e-r} = R \cdot I,\ V_{e-i} = \omega L \cdot I$$
$$V_p = \frac{N_p}{N_e} V_e,\ V_{p-r} = \frac{N_p}{N_e} R \cdot I,\ V_{p-i} = \frac{N_p}{N_e} \omega L \cdot I \quad (9)$$

4.3. Inductances versus Iron rod and piston position

Fig. 10 presents the inductances versus the position of the iron rod, without an aluminium cylinder, and Fig. 11 presents the inductances versus the position of the iron rod, with an aluminium cylinder. The inductances increase at DC and AC with greater penetration of the iron rod inside the solenoid coil without an aluminium cylinder, because the magnetic flux reluctance decreases as the high-permeability iron rod penetrates further inside the solenoid coil. The reverse occurs when an aluminium cylinder is added to the model, due to the high reaction fields of the induced eddy currents in the aluminium cylinder shell and the lower resistance R_o in (8) and the lower corresponding equivalent inductance L.

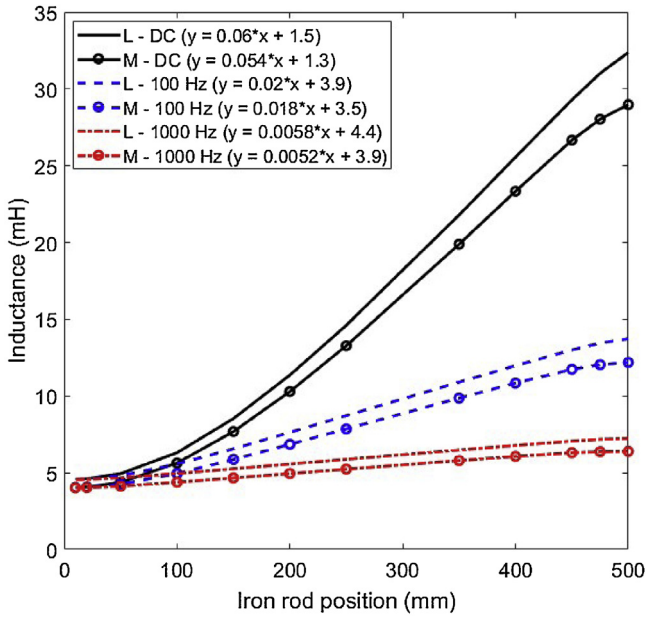

Fig. 10. Inductance versus iron rod position using FEM (with a linear curve fit equation) - without an aluminum cylinder - solenoid coil length 480 mm - $\mu_r = 77.5$.

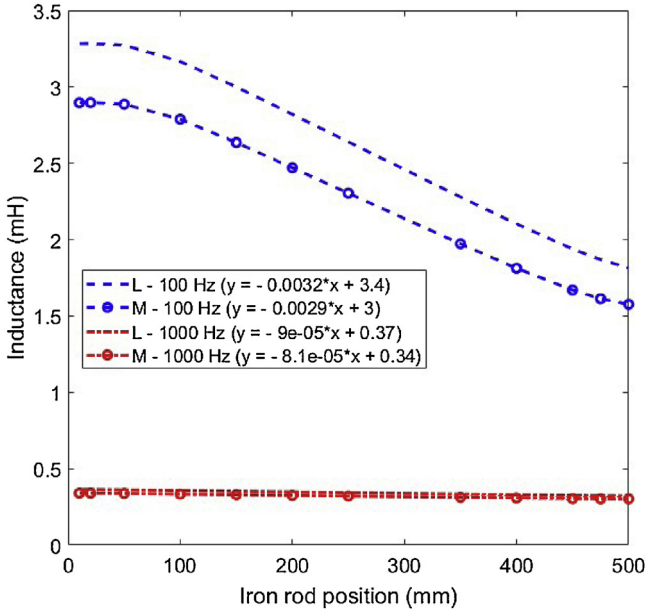

Fig. 11. Inductance versus iron rod position using FEM (with a linear curve fit equation) - with an aluminum cylinder - solenoid coil length 480 mm- $\mu_r = 77.5$.

5. Experimental results

Fig. 12 shows the experimental set-up for a pneumatic position sensor. A reference position sensor is used, which is connected to the iron rod. All the design data of the position sensor are presented in Table I [13]. We used a Senpos MRTM500 type potentiometric linear position sensor with a measurement range of 500 mm and a linearity error of 0.05%. Lock-in amplifier is used for the measurement of the output voltage of our sensor. The power supply for excitation coil is a Keithley 3390 50-MHz signal generator with internal impedance 50 Ω.

The magnetic field strength distributions in the pneumatic cylinder for various positions of the iron rod and the piston are presented in Fig. 13 at 100 Hz and at exciting current amplitude of 116 mA. The magnetic fields are higher in the model with the pis-

Fig. 12. Measurement set-up for a pneumatic position sensor.

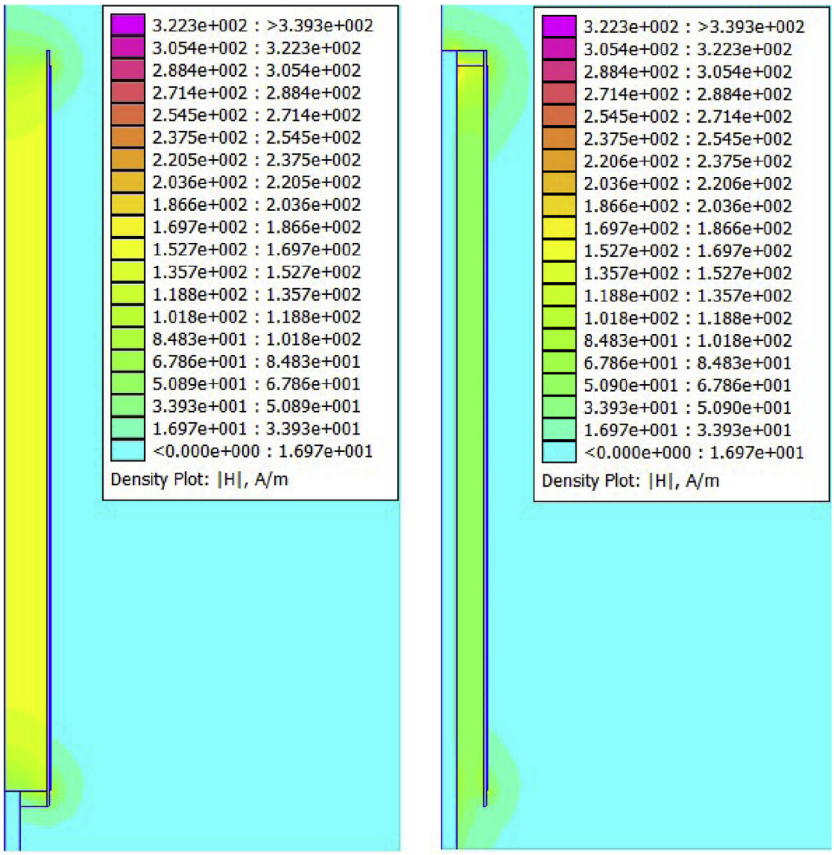

Fig. 13. Magnetic field strength distribution using FEM [24] at 100 Hz for the piston at the begining of the cylinder (left) and for the piston at the end of the cylinder (right) - $\mu_r = 100$.

ton at the beginning of the cylinder, which causes higher magnetic energy in the system and higher self-inductance and mutual inductance than when the piston and the iron rod are at the end of the pneumatic cylinder.

The current of the exciting coil decreases slightly with increasing piston position and iron rod position (Fig. 14). The total impedance of the exciting coil increases, as shown in the circuit in Fig. 14.

The voltage source with amplitude of 10 V is in series with 70 Ω resistances, which causes small changes in the current with the position of the iron rod and the piston.

5.1. Secondary voltage versus the position of the piston and the iron rod

Figs. 15–17 show the experimental and FEM results for the secondary coils-induced voltage. The change in the current with the position of the piston is taken into consideration in the simulations. The FEM results for the induced voltages coincide well with the measurements. The relative permeability μ_r is considered to be equal to 100 (Figs. 2 and 3) in the simulations, based on the exciting current in Fig. 14. The real part and the imaginary part of the secondary coil-induced voltage change almost linearly with the position of the piston in Fig. 17, which can be considered as a position meter for the pneumatic cylinder. The curve fit linear function for iron rod position X versus induced voltage V is presented in (10):

$$X = X_0 + K \cdot V \tag{10}$$

The constant X_0 (mm) and the constant K (mm/mV) are presented in Fig. 18 for 400 mm stroke. The root mean square error (RMSE) values as an indicator [11] for showing the closeness for 11 measured values to the curve fit linear function in (10) are 5.03 mm for the real part of the voltage and 6.31 mm for the imaginary part

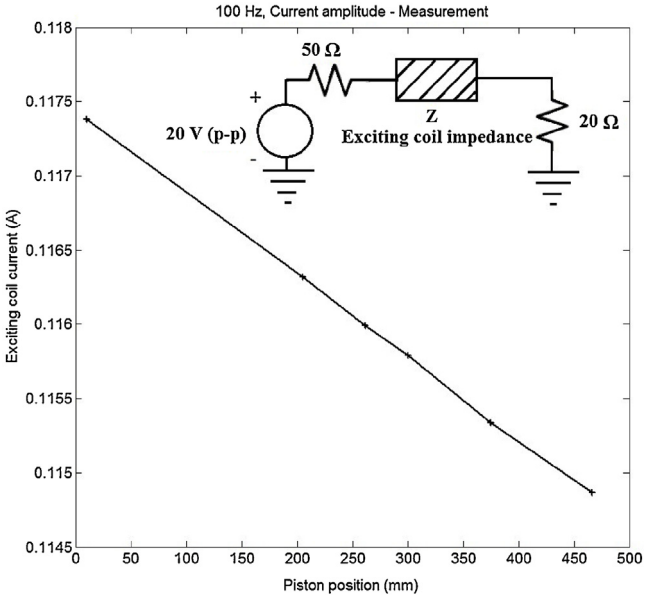

Fig. 14. Measured current of the excitation coil versus piston position, with schematics of the excitation circuit - the resistance of 20 Ω is for the current measurement.

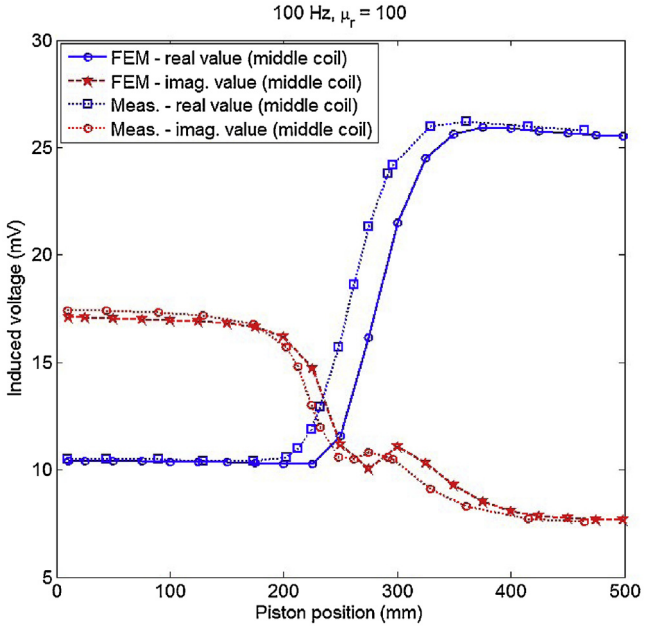

Fig. 15. Induced voltages for secondary coil number 5 - middle coil.

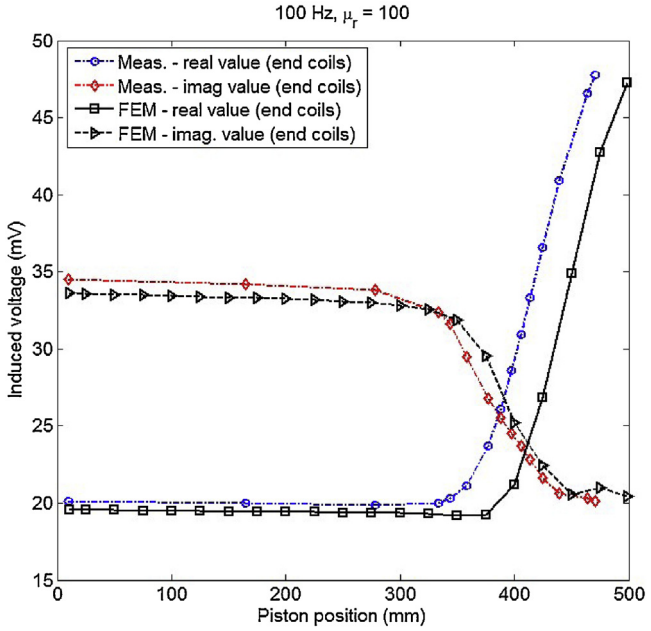

Fig. 16. Induced voltages for secondary coils numbers 8 and 9 in series (end coils).

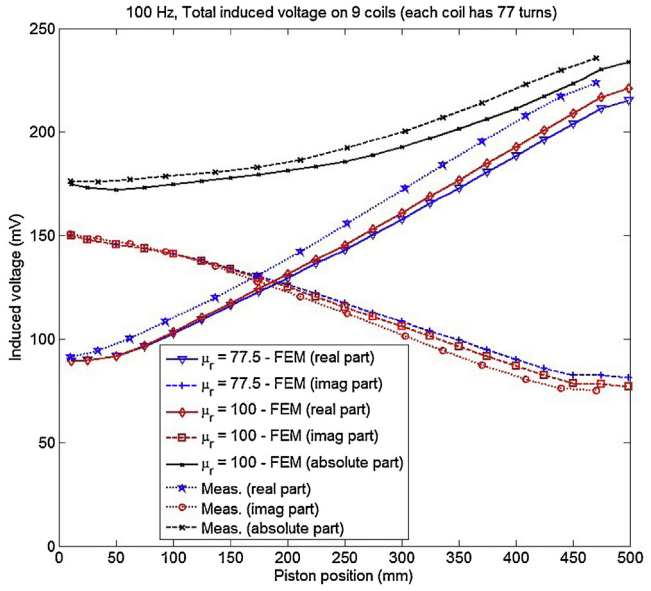

Fig. 17. Induced voltages for all secondary coils connected serially.

of voltage. The real part of the induced voltage shows more linear characteristics than the imaginary part of the induced voltage, based on RMSE.

Another indication for linearity of the position sensor is the correlation coefficient R^2. It is 0.9984 for the real part of the voltage and 0.9974 for the imaginary part of the voltage, which shows that the real part of the voltage is a more linear curve. Fig. 19 shows position errors versus piston position

The sensor characteristics deviate from linear at both ends of the cylinder. This can be partly compensated by increasing the number of turns for the peripheral coil sections or via calibration, but it should be noted that, for real pneumatic cylinders, the piston stroke is always shorter than the cylinder length. We therefore evaluate linearity error for 400 mm stroke.

5.2. Secondary voltage versus frequency

The excitation coil current changes with frequency (Fig. 20) because of the increase in coil impedance at higher frequencies.

The secondary induced voltages at various excitation coil frequencies are shown in Figs. 21–23. The changes in current with frequency are taken into account in the simulations.

The results for different frequencies without an iron rod and with a fully-inserted iron rod and piston in the cylinder show the sensitivity of the position sensor versus frequency.

For the real part, the sensitivity maximum is 150 mV at 100 Hz and the sensitivity decreases rapidly at higher frequencies. However, the maximum sensitivity for the imaginary part is 100 mV at 200 Hz and at higher frequencies it may therefore be preferable to use the imaginary part of the induced voltage for fast moving cylinders.

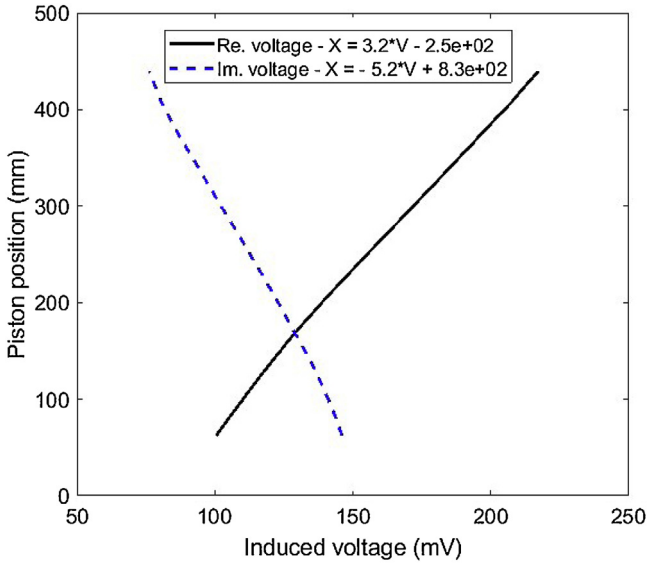

Fig. 18. Piston position versus induced voltage and corresponding curve fit line functions.

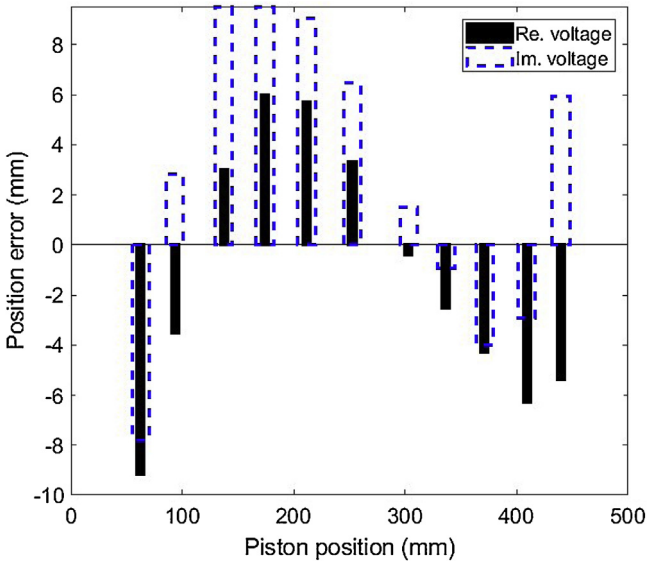

Fig. 19. Position error versus piston position.

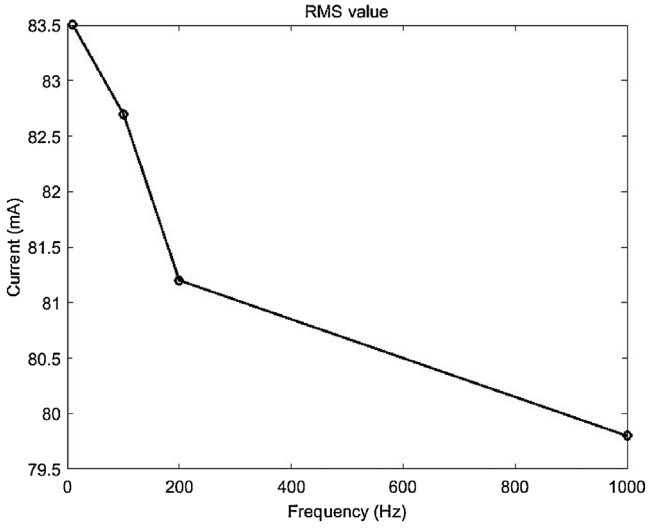

Fig. 20. Measured current of the excitation coil versus frequency – the piston position is at the end of the cylinder.

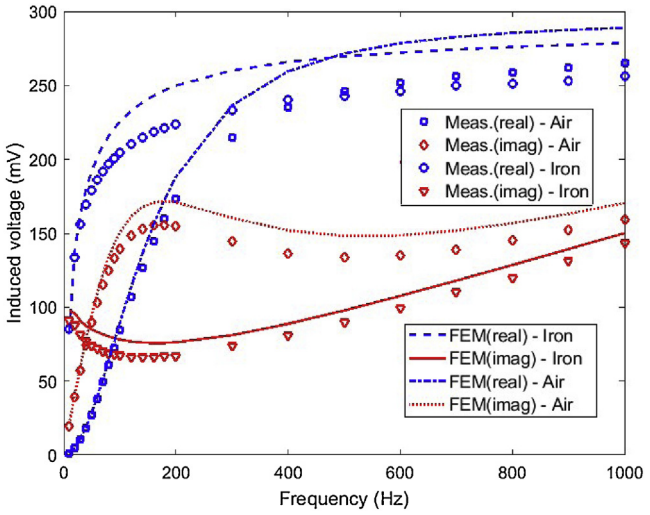

Fig. 21. Induced voltage for the full secondary coil with and without a piston iron rod - Air means without an iron rod, and iron means with a fully-inserted iron rod.

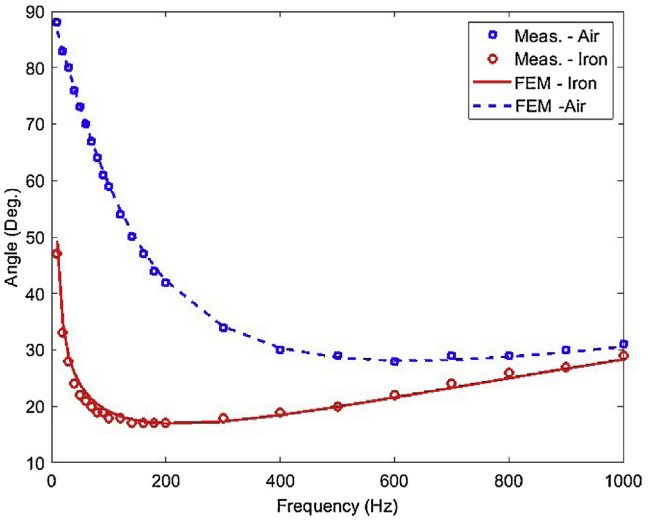

Fig. 22. Phase angle of the induced voltage for the full secondary coil with and without a piston iron rod.

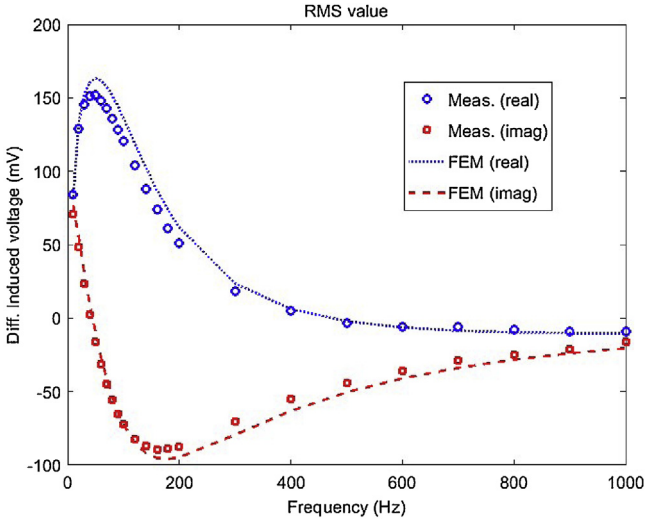

Fig. 23. Difference in induced voltage between two extreme positions of the piston.

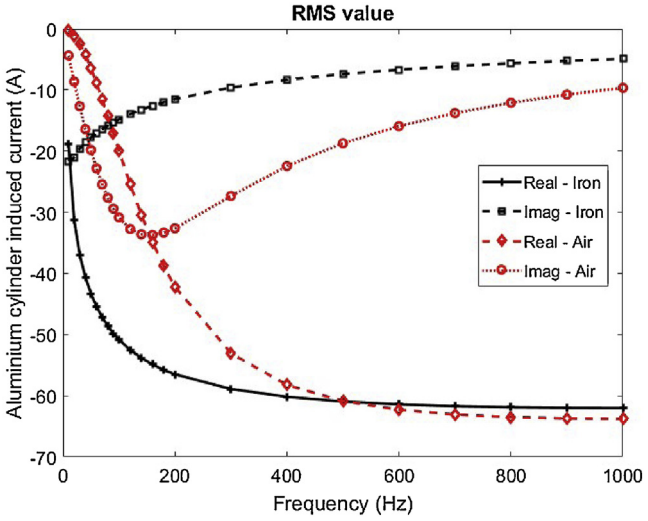

Fig. 24. The induced eddy current in the aluminium cylinder with and without an iron rod.

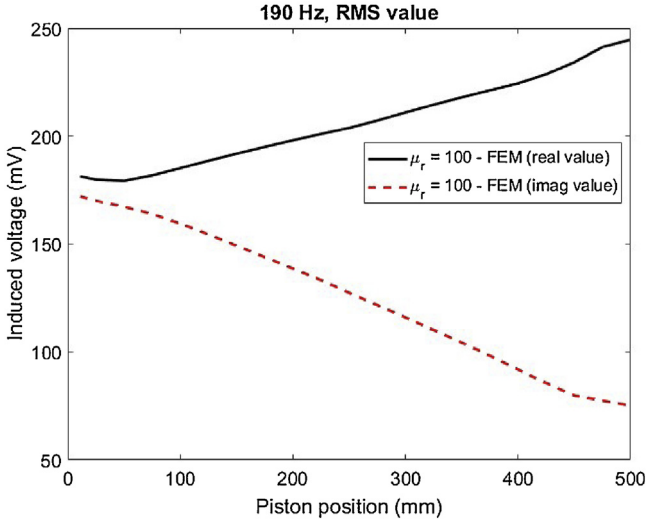

Fig. 26. Induced voltages for a full secondary coil at 190 Hz (FEM simulation).

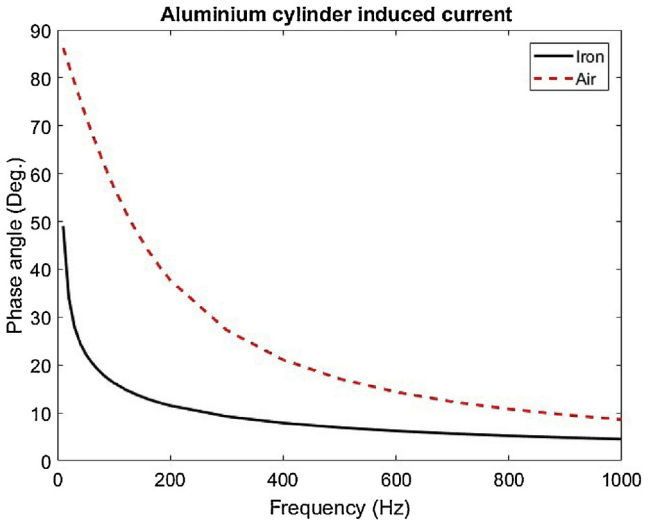

Fig. 25. Phase angle of the induced current in the aluminium cylinder.

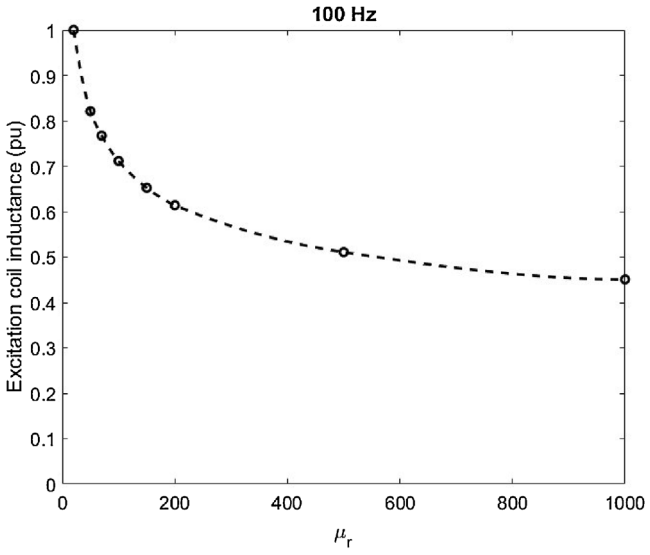

Fig. 27. Excitation coil inductance for various iron rod permeabilities – the piston position is at cylinder end position.

The amplitude and the phase of the induced current in the aluminium cylinder are shown in Figs. 24 and 25. The phase angle without an iron rod (air) is about 90 deg. (Fig. 25) at low frequency, 10 Hz, which shows negligible resistance of the aluminium cylinder at a low frequency. The same phenomenon is shown in Fig. 22 with an inserted iron rod: the ferromagnetic material of the rod causes a phase shift even at small frequencies. The imaginary part of the induced current without an iron rod (Air) in Fig. 24 shows a maximum absolute value similar to Fig. 21 at about 190 Hz. From the measurements and simulations shown in Fig. 23, we can identify two prospective working frequencies for the position sensor: for the real part of the induced voltage, maximum sensitivity is around 80 Hz, and for the imaginary part the sensitivity maximum is at 190 Hz. The secondary induced voltage is therefore also recalculated at 190 Hz, see Fig. 26. The difference between the maximum voltage and the minimum voltage (imaginary parts) are higher at 190 Hz than at 100 Hz, which means higher sensitivity to piston position or less source power consumption at the same sensitivity as 100 Hz. To improve the dynamic performance, the excitation frequency can be raised to 400 Hz.

6. Iron permeability effect

Figs. 27 and 28 show the excitation coil inductance and the secondary coil induced voltages versus the iron permeability. The negative slope is caused by the aluminium shell, and corresponds with the results shown in Fig. 11 and discussed in section IV. It is clear that iron permeability has a high impact on the position sensor outputs. It has to be measured, as various magnetic irons and magnetic steels could be used for the piston iron rod [23].

7. Temperature dependency

Fig. 29 shows temperature effects on the induced voltage in the secondary coil. The electrical conductivity temperature

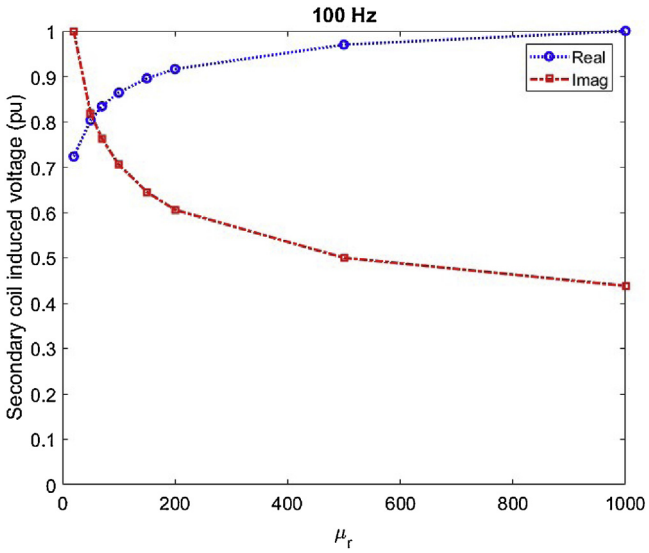

Fig. 28. Induced voltages for a full secondary coil for various iron rod permeabilities – the piston position is at cylinder end position.

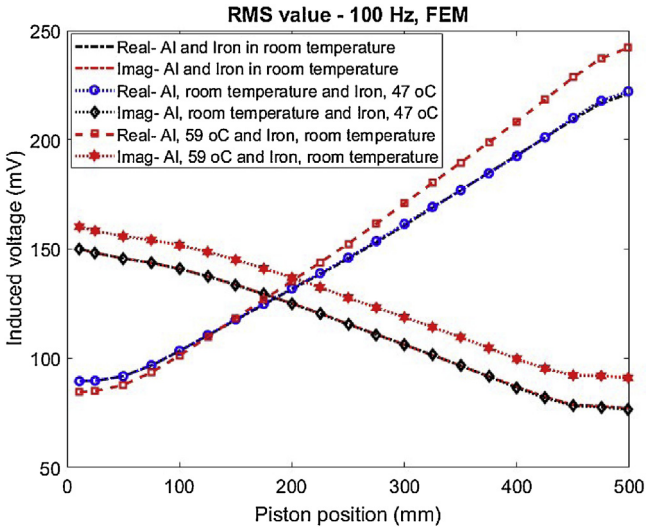

Fig. 29. Induced voltages for a full secondary coil at various iron and alumium temperatures (μ_r =100)- the excitation frequency was 100 Hz.

dependency coefficient for iron, c_i and for aluminium, c_{Al} are as follows:

$$\begin{aligned}
&\sigma_i(\theta^oC) = \sigma_i(20^oC)/(1 + c_i \cdot (\theta - 20))\\
&\sigma_i(20^oC) = 4.509\,MS/m, c_i = 0.0027356\\
&\sigma_{Al}(\theta^oC) = \sigma_{Al}(20^oC) \cdot (1 + c_{Al} \cdot (\theta - 20))\\
&\sigma_{Al}(20^oC) = 30.5\,MS/m, \quad c_{Al} = 0.0041
\end{aligned} \tag{11}$$

where σ is electrical conductivity.

It is shown that an increase in the temperature of the iron rod has a negligible effect on the induced voltage, but the temperature of the aluminium changes the induced voltage of the secondary coil considerably. The imaginary part of the induced voltage increases 6%–10% for a higher temperature of aluminium cylinder. This is similar to the change in the exciting coil inductance reported in [13]. The effect of temperature on iron rod permeability is negligible [14].

8. Conclusions

FEM modelling and experimental results for a transformer position sensor for a pneumatic cylinder have been presented. The results show the feasibility of using the principle of a linear transformer with a moving core for measuring the position of the piston in a pneumatic cylinder. Compared to conventional LVDT, our sensor has a highly asymmetric core which moves inside the conducting cylinder.

The sound match between FEM results and measurements shows that FEM can be used for optimizing a position sensor of this type.

The linearity rms error is maximum 1.6% of the full 400 mm stroke without any compensation.

The temperature sensitivity of the secondary coil voltage has been calculated for various iron and aluminium temperatures. The effect of the change in the electrical resistivity of an aluminium cylinder is clearly dominant at 100 Hz excitation frequency. Temperature compensation can be clearly made by using the voltage across the excitation coil. However, this topic lies beyond the scope of the present paper.

Using only fixed copper coils for excitation and pick up make the proposed position sensor for pneumatic cylinder more cost effective than position sensor using rare earth NdFeB permanent magnets and an array of Hall sensors. In industrial applications, single-chip synchronous detector such as AD630 can be used for the output voltage processing. Due to its simplicity the proposed position sensor is suitable for harsh environment such as high temperature and vibrations.

References

[1] Herceg, Taking a position on hydraulic cylinder sensors, Hydraul. Pneum. (2015) 24–27.
[2] S. Fericean, A. Hiller-Brod, A.D. Dorneich, M. Fritton, Microwave displacement sensor for hydraulic devices, IEEE Sens. J. 13 (12) (2013) 4682–4689.
[3] A.A.M. Faudzi, K. Suzumori, S. Wakimoto, Design and control of new intelligent pneumatic cylinder for intelligent chair tool application, 2009 IEEE/ASME International Conference on Advanced Intelligent Mechatronics (2009) 1909–1914.
[4] S.Y. Yang, M.C. Lee, M.H. Lee, S. Arimoto, Measuring system for development of stroke-sensing cylinder for automatic excavator, IEEE Trans. Ind. Electron. 45 (3) (1998) 376–384.
[5] E. Hristoforou, Magnetostrictive delay lines and their applications, Sens, Actuators A-Phys. 59 (1997) 183–191.
[6] E. Hristoforou, P.D. Dimitropoulos, J. Petrou, A new position sensor based on the MDL technique, Sens, Actuators A-Phys. 132 (2006) 112–121.
[7] Y. Wang, R. Madson, R. Rajamani, Nonlinear observer design for a magnetic position estimation technique, 2015 54th IEEE Conference on Decision and Control (CDC) (2015) 6986–6991.
[8] S. Taghvaeeyan, R. Rajamani, Z. Sun, Non-intrusive piston position measurement system using magnetic field, IEEE Sens. J. 13 (8) (2013) 3106–3114.
[9] P. Ripka, A. Chirtsov, V. Grim, Contactless piston position transducer with axial excitation, IEEE Trans. Magn. 53 (11) (2017), 4002504.
[10] J. Vyhnanek, P. Ripka, A. Chirtsov, Linear position sensing through conductive wall without permanent magnet, Proceedings 1 (4) (2017) 390.
[11] H. Sumali, E.P. Bystrom, G.W. Krutz, A displacement sensor for nonmetallic hydraulic cylinders, IEEE Sens. J. 3 (6) (2003) 818–826.
[12] Seung-Ho Yang, K. Hirata, T. Ota, Y. Kawase, Impedance linearity of contactless magnetic-type position sensor, IEEE Trans. Magn. 53 (June (6)) (2017), 8001204.
[13] P. Ripka, A. Chirtsov, M. Mirzaei, Inductance position sensor for pneumatic cylinder, AIP Adv. 8 (2018), 048001.
[14] M. Mirzaei, P. Ripka, A. Chirtsov, J. Vyhnanek, Temperature influence on position transducer for pneumatic cylinder, in: IEEE Sensors Conference, 2018, India paper #1638.
[15] Y. Kano, S. Hasebe, C. Huang, T. Yamada, New type linear variable differential transformer position transducer, IEEE Trans. Instrum. Meas. 38 (1989) 407–409.
[16] M. Kilani, S. Taifour, L. Al-Sharif, Effect of design geometry on the performance characteristics of linear variable differential transformers, Sens. Transducers 150 (March (3)) (2013) 66–71.
[17] J.K. Sykulski, E. Sykulska, S.T. Hughes, Application of finite element modeling in LVDT design, COMPEL 11 (1) (1992) 73–76.

[18] M. Martino, A. Danisi, R. Losito, A. Masi, G. Spiezia, Design of a linear variable differential transformer with high rejection to external interfering magnetic field, IEEE Trans. Magn. 46 (February (2)) (2010) 674–677.
[19] Alessandro Masi, Alessandro Danisi, Roberto Losito, Yves Perriard, Characterization of magnetic immunity of an ironless inductive position sensor, Sens. J. IEEE 13 (3) (2013) 941–948.
[20] Anish Babu, Boby George, Design and development of a new non-contact inductive displacement sensor, Sens. J. IEEE 18 (3) (2018) 976–984.
[21] Narendiran Anandan, Boby George, Design and development of a planar linear variable differential transformer for displacement sensing,, Sens. J. IEEE 17 (16) (2017) 5298–5305.
[22] Adrian Grima, Alessandro Danisi, Alessandro Masi, Nicholas Sammut, Influence of external conductive objects on the performance of an ironless inductive position sensor, Sens. J. IEEE 17 (14) (2017) 4500–4507.
[23] J.F. Gieras, Analytical method of calculating the electromagnetic field and power losses in ferromagnetic halfspace, taking into account saturation and hysteresis, Electr. Eng., Proc. Inst. 124 (1977) 1098–1104.
[24] FEMM info, [Online]. Available: http://www.femm.info/wiki/HomePage.
[25] John David Jackson, Classical Electrodynamics, John Wiley & Sons, 1999.
[26] Edmund E. Callaghan, Stephen H. Maslen, "The magnetic field of a finite solenoid," NASA, Oct 01, 1960) [Online]. Available: https://ntrs.nasa.gov/search.jsp?R=19980227402.
[27] A. C. M. de Queiroz., "Mutual inductance and inductance calculations by Maxwell's method,") [Online]. Available: http://www.coe.ufrj.br/ãcmq/papers/papers.html.

Biographies

Pavel Ripka received an Engineering degree in 1984, a CSc (equivalent to PhD) in 1989, Docent degree in 1996 and in 2002 Professor degree at the Czech Technical University, Prague, Czech Republic. His main research interests are Magnetic Measurements and Magnetic Sensors, especially Fluxgate.

Mehran Mirzaei is PhD student in Faculty of Electrical Engineering, Czech Technical University. He works on magnetic material modelling and magnetic position sensor simulations and design.

Andrey Chirtsov is Master student in Faculty of Electrical Engineering, Czech Technical University. He works on yokeless current sensor, magnetic position sensor and electronic design and measurements.

Jan Vyhnanek received PhD in Electrical Engineering, Czech Technical University in 2018. His main research fields are magnetometers, electronic design and measurements.

3-2-2-4 Temperature Stability of the Transformer Position Transducer for Pneumatic Cylinder [J10]

This paper presents the analysis and design of a transformer position sensor for pneumatic cylinder considering temperature stability. Two solenoid coils as excitation coil and pick up coil around cylinder are used for position transducer. The effects of temperature of aluminum cylinder and iron rod with different ferromagnetic materials on position sensor performance are analyzed and measured. We found that the effect of temperature dependence of shell resistivity is dominant, while the effect of permeability change is negligible. Based on the simulations and measurement, we suggest simple method of temperature compensation.

Thermal stability of transformer position sensor for a pneumatic sensor has been presented. Temperature of the aluminum cylinder has highest impact on the induced voltage; both real and imaginary components change considerably. Using different solid iron rods with different relative magnetic permeabilities and conductivities has negligible effect on the measured induced voltage of the pick up coil especially at 200 Hz. Excitation frequency 200 Hz is also more suitable for position sensing in dynamic conditions. The effects of temperature on the induced voltage of pick up coil could be corrected using a compensating ring coil in the beginning of pneumatic cylinder as it would not be dependent on iron rod position. Another possibility is to measure the cylinder temperature and make compensation by calculations. Imaginary part of the induced voltage is more suitable for the temperature compensation, as the error is constant with position and the temperature position error can be expressed by single coefficient.

Journal of Magnetism and Magnetic Materials 503 (2020) 166636

Contents lists available at ScienceDirect

Journal of Magnetism and Magnetic Materials

journal homepage: www.elsevier.com/locate/jmmm

Research articles

Temperature stability of the transformer position transducer for pneumatic cylinder

Mehran Mirzaei*, Pavel Ripka, Andrey Chirtsov, Vaclav Grim

Faculty of Electrical Engineering, Czech Technical University, Prague 16627, Czech Republic

ARTICLE INFO

Keywords:
Transformer position transducer
Pneumatic cylinder
Temperature stability
Ferromagnetic iron rods

ABSTRACT

This paper presents the analysis and design of a transformer position sensor for pneumatic cylinder considering temperature stability. Two solenoid coils as excitation coil and pick up coil around cylinder are used for position transducer. The effects of temperature of aluminum cylinder and iron rod with different ferromagnetic materials on position sensor performance are analyzed and measured. We found that the effect of temperature dependence of shell resistivity is dominant, while the effect of permeability change is negligible. Based on the simulations and measurement we suggest simple method of temperature compensation.

1. Introduction

Position sensors are key components for the industrial automation [1–3]. Detection of piston position inside aluminum shell of pneumatic cylinder is not easy task. Different methods were introduced, such as direct mounting of sensors inside the piston rod, microwave sensors mounted on the piston, optical or magnetic scales, which are not reliable and are mechanically complicated. The most popular method used in the industry is using external sensors, which measure magnetic field of permanent magnet mounted on the piston. It needs large number of sensors with complicated signal processing and expensive non ferromagnetic iron rod. A simpler method is to measure inductance of solenoid coil around cylinder [4–6]. The problem of this solution is slow response and large temperature dependence [5–6]. Therefore, we designed novel position sensor based on transformer configuration [7].

In this paper, temperature stability of a transformer-based position sensor for a pneumatic cylinder with an aluminum shell, an aluminum piston and different ferromagnetic iron rods is analyzed and measured. A simplified and fast 2D axisymmetric analytical method and 2D time harmonic axisymmetric finite element method (FEM) are utilized for simulations and analysis. Four iron rods with different magnetic characteristics are considered.

2. Model

The model and dimensions and parameters of a pneumatic cylinder with transformer position sensor are presented in Table I and Fig. 1. The iron rod and aluminum piston and cylinder are parts of the pneumatic cylinder. Two layers of windings with axisymmetric configuration are used for transformer position transducer: the first layer is excitation coil and second layer is pick up coil. The electrical conductivity temperature dependency are measured and presented in Table II for aluminum cylinder and iron rods using (1).

$$\sigma(\theta^{o}C) = \sigma(20^{o}C)/(1 + c(\theta - 20)) \quad (1)$$

3. Simplified model

A simple model without finite length effects of pneumatic cylinder is developed for fast evaluations of iron rod and aluminum cylinder materials and excitation current frequency. The general governing differential equation [8] is in (2) for 5 regions of computational model (Fig. 2). Region 1 is for iron rod (zero to radius r_1), region 2 is air region (radius r_1 to r_2), region 3 is aluminum cylinder (radius r_2 to r_3), region 4 is excitation coil (radius r_3 to r_4) and region 5 is pick up coil and air region beyond pick up coil (radius r_4 to infinite).

$$\frac{\partial^2 A_{\varphi,n}}{\partial r^2} + \frac{1}{r}\frac{\partial A_{\varphi,n}}{\partial r} - \frac{A_{\varphi,n}}{r^2} - j\omega\sigma\mu A_{\varphi,n} = -\mu J_s, (\omega = 2\pi f) \quad (2)$$

where, $A_{\varphi,n}$ is azimuthal magnetic vector potential in region n, σ is conductivity, μ is magnetic permeability, J_s is current density in the excitation coil region and f is frequency. The solutions of (2) for 5 regions are as follows:

$$A_{\varphi,1} = C_{11}\bullet\text{Besseli}(1, \lambda_i\bullet r),\ \lambda_i = \sqrt{j\omega\sigma\mu_{i,r}\mu_0}$$

* Corresponding author.
E-mail addresses: mirzameh@fel.cvut.cz (M. Mirzaei), ripka@fel.cvut.cz (P. Ripka).

https://doi.org/10.1016/j.jmmm.2020.166636
Received 14 August 2019; Received in revised form 18 February 2020; Accepted 18 February 2020
Available online 21 February 2020

Table 1
Transformer position transducer parameters.

Parameter	Value
Cylinder outer diameter, D_{co}	60 (mm)
Cylinder inner diameter, D_{ci}	56 (mm)
Cylinder axial length, L_c	500 (mm)
Piston outer diameter, D_{po}	56 (mm)
Piston inner diameter, D_{pi}	20 (mm)
Piston axial length, L_p	10 (mm)
Iron rod diameter, D_i	20 (mm)
Iron rod axial length, L_i	700 (mm)
Number of turns for the excitation coil, N_e	800
Number of turns for pick up coil, N_{pc}	693
Wire diameter, D_w	0.56 (mm)

Table 2
Temperature dependency coefficients- conductivity.

Materials	σ (20 °C) – MS/m	c
Al cylinder	30.5	0.0041
Iron rod 1	6.31	0.0069
Iron rod 2	4.11	0.0051
Iron rod 3	4.59	0.0049
Iron rod 4	5.69	0.0051

Table 3
Temperature dependency coefficients- permeability.

Materials	μ_r (25 °C)	μ_r (50 °C)
Iron rod 1	119.42 (100%)	124.35 (104.1%)
Iron rod 2	83.41 (100%)	87.04 (104.4%)
Iron rod 3	90.66 (100%)	95.38 (105.2%)
Iron rod 4	114.83 (100%)	116.64 (101.6%)

Table 4
Induced voltages (mV) comparison for different iron rods at 100 Hz-Measurement.

Piston position		Iron Rod 1 25/50 °C	Iron Rod 2 25/50 °C	Iron Rod 3 25/50 °C	Iron Rod 4 25/50 °C
250 mm	Re	37.93/38.35	37.9/38.6	38.05/38.55	38.1/-
	Im	28.53/28.48	28.65/28.8	28.68/28.68	28.41/28.52
450 mm	Re	51.9/52.7	52.0/52.97	51.92/53.1	51.8/52.42
	Im	19.76/19.61	20.22/20.22	20.35/20.2	19.98/19.92

Table 5
Induced voltages (mV) comparison at different iron rod 3 temperatures at 100 Hz-FEM.

Piston position	μ_r = 90.66 σ = 4.48 MS/m 25 °C		μ_r = 95.36 σ = 4.0 MS/m 50 °C		μ_r = 90.66 σ = 4.0 MS/m 50 °C	
	Re	Im	Re	Im	Re	Im
250 mm	37.43	28.46	37.85	28.23	37.72	28.32
	100%	100%	101%	99%	101%	100%
450 mm	52.17	19.98	52.96	19.47	52.71	19.67
	100%	100%	102%	98%	101%	99%

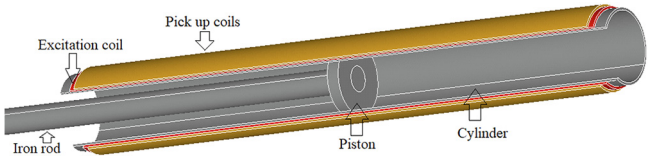

Fig. 1. Pneumatic cylinder with transformer position sensor.

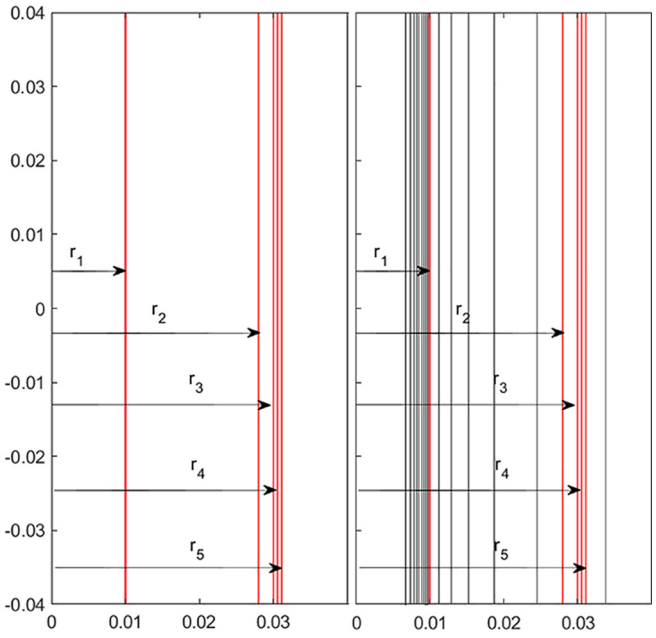

Fig. 2. Analytical model for pneumatic cylinder (left) and magnetic flux distribution in partial model of pneumatic cylinder (right).

$$A_{\varphi,2} = C_{21}\bullet r + C_{22}\bullet\frac{1}{r}$$

$$A_{\varphi,3} = C_{31}\bullet\text{Besseli}(1, \lambda_a\bullet r) + C_{32}\bullet\text{Besselk}(1, \lambda_a\bullet r),\ \lambda_a = \sqrt{j\omega\sigma\mu_0}$$

$$A_{\varphi,4} = C_{41}\bullet r + C_{42}\bullet\frac{1}{r} - \frac{\mu_0 J_s}{3}r^2$$

$$A_{\varphi,5} = C_{52}\bullet\frac{1}{r} \tag{3}$$

C_{11}, C_{21}, C_{22}, C_{31}, C_{32}, C_{41}, C_{42} and C_{52} are constants which are calculated using boundary conditions between regions 1–5 [8]. μ_0 and $\mu_{i,r}$ are air permeability and iron rod relative permeability, respectively.

The self inductance of excitation coil with current amplitude I_m, L_s, induced voltage in the pick up coil, U_M and mutual inductance, M are calculated in (4) [8]. The variations of mutual inductance versus iron rod conductivity and relative permeability are shown in Fig. 3, which shows mutual inductance and induced voltage is less sensitive to iron rod conductivity and relative permeability at higher frequencies because of big reaction fields of induced eddy currents in the aluminum cylinder [7].

$$L_s = \frac{N_e 2\pi}{(r_4 - r_3)I_m}\left(C_{41}\bullet\frac{(r_4^3 - r_3^3)}{3} + C_{42}\bullet(r_4 - r_3) - \frac{\mu_0 J_s}{12}\bullet(r_4^4 - r_3^4)\right)$$

$$U_M = -j\omega M\bullet I_m,\ M = \frac{N_{pc}2\pi}{I_m}C_{52} \tag{4}$$

4. Iron rod relative permeability estimation

Fig. 4 shows setup for measurement to estimate relative magnetic permeability and evaluate temperature effect as presented in Table III. The relative magnetic permeability values are estimated for the best fit between induced voltage in the pick up coil calculated by FEM and measured.

The magnetic permeability increases with increasing temperature, which was expected for solid irons and ferromagnetic materials [9,10].

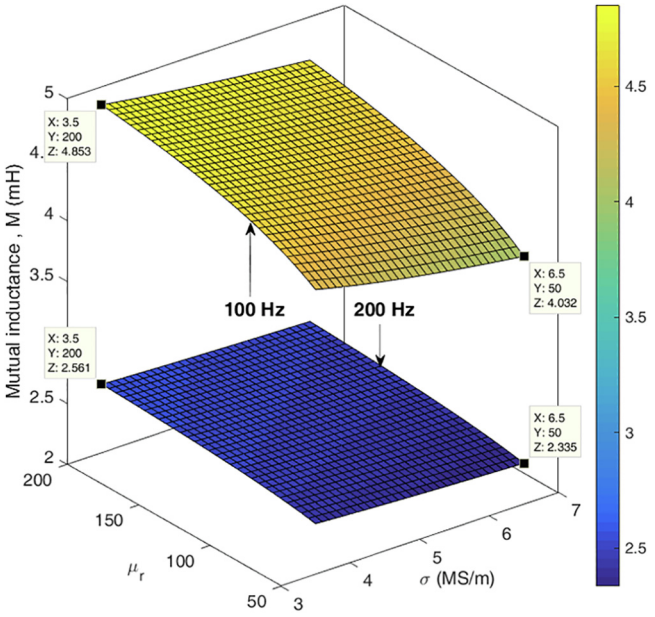

Fig. 3. Variation of mutual inductance between excitation coil and pick up coil versus iron rod conductivity and iron rod permeability at 100 Hz and 200 Hz.

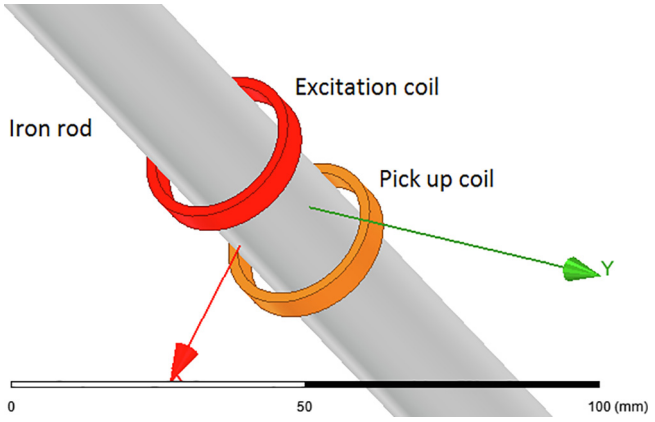

Fig. 4. Proposed model for relative permeability measurement.

5. Experimental results

The experimental set-up for a pneumatic position sensor and reference potentiometric position sensor with 500 mm range is shown in Fig. 5. Induced voltage is measured using a Lock-in amplifier.

5.1. At room temperature

Measured induced voltages in the pick up coil at 100 Hz and 200 Hz are shown in Fig. 6. Excitation coil is connected to a signal generator with 50 Ω internal resistance with voltage amplitude 2.5 V. Excellent linearity of 0.65% is noticed especially at 200 Hz between 50 mm and 450 mm of piston positions for real part (Re) and imaginary part (Im) of the induced voltage, which shows suitability of proposed position sensor for pneumatic cylinder, as the piston stroke is shorter than the cylinder length for real pneumatic cylinders [7]. Effects of different iron rods with different conductivities and relative permeabilities are slightly distinguishable in the imaginary part of the induced voltage at 100 Hz. Fig. 7 shows bigger magnetic field strengths using FEM at starting point of piston position in the pneumatic cylinder, which causes higher imaginary part of induced voltages at starting point in comparison with end position of piston.

Fig. 5. Pneumatic cylinder and reference position sensor.

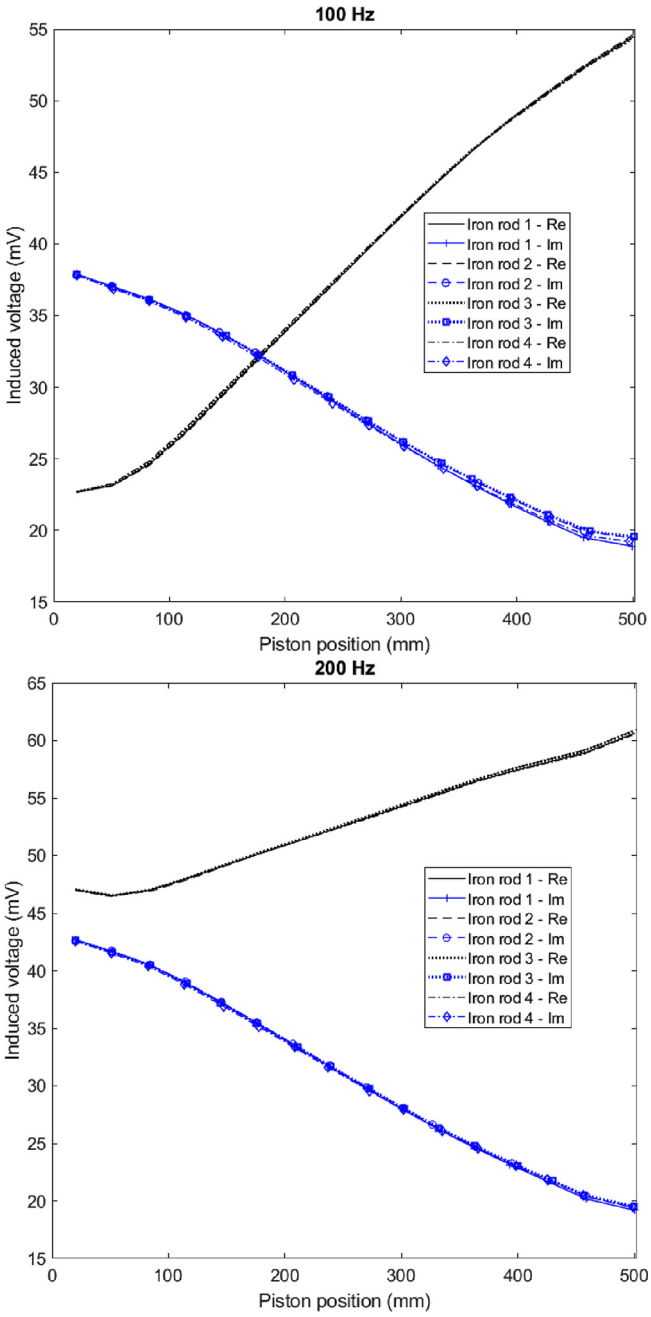

Fig. 6. Measured induced voltage in pick up coil versus iron rod and piston position- real (Re) and imaginary (Im) components of voltages are obtained relative to the excitation coil current as a reference signal.

5.2. At 50 °C

Iron rods temperature effects on the induced voltages are presented in Table IV, which shows small effects on the induced voltage especially in imaginary part of voltage. Only iron rods were heated for higher

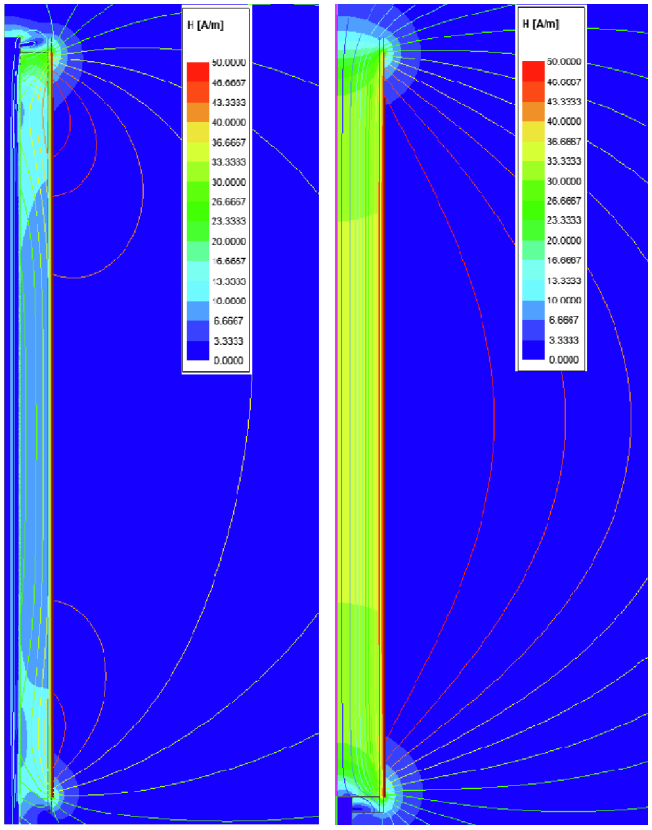

Fig. 7. Magnetic field strength distribution at end position of piston and iron rod (left) and starting position of piston and iron rod (right) at 100 Hz-FEM.

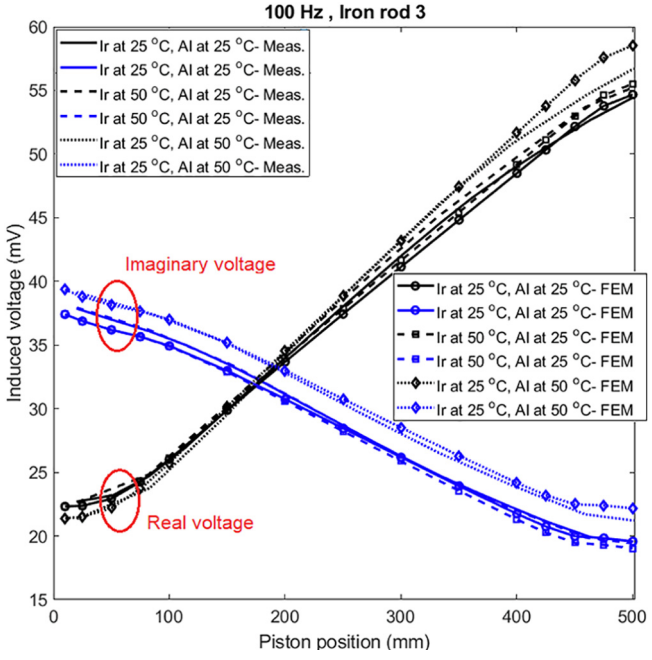

Fig. 8. Induced voltage of pick up coil versus iron rod and piston position at different temperatures of iron rod (Ir) and aluminum cylinder (Al).

temperature, 50 °C. The corresponding maximum position temperature error was 0.4 mm/K for real part and 0.1 mm/K for imaginary part.

Temperature rise in the aluminum cylinder has the main impact on the induced voltage of pick up coil in comparison with temperature rise in the iron rod as shown in Fig. 8. The resulting total position temperature error is 2 mm/K for Im part, while for Re part the temperature dependence is more complex and cannot be described by simple coefficient.

FEM analyses show the same tendency as measurements. FEM analysis also shows that changing of relative permeability and conductivity of the iron rod has equal influence on the induced voltage (Table V).

6. Conclusion

Thermal stability of transformer position sensor for a pneumatic sensor has been presented. Temperature of the aluminum cylinder has highest impact on the induced voltage; both real and imaginary components change considerably.

Using different solid iron rods with different relative magnetic permeabilities and conductivities has negligible effect on the measured induced voltage of the pick up coil especially at 200 Hz. Excitation frequency 200 Hz is also more suitable for position sensing in dynamic conditions.

The effects of temperature on the induced voltage of pick up coil could be corrected using a compensating ring coil in the beginning of pneumatic cylinder as it would not be dependent on iron rod position. Another possibility is to measure the cylinder temperature and make compensation by calculations. Imaginary part of the induced voltage is more suitable for the temperature compensation, as the error is constant with position and the temperature position error can be expressed by single coefficient.

CRediT authorship contribution statement

Mehran Mirzaei: Conceptualization, Formal analysis, Investigation, Methodology, Resources, Software, Validation, Visualization, Writing - original draft, Writing - review & editing. **Pavel Ripka:** Conceptualization, Investigation, Methodology, Project administration, Resources, Software, Supervision, Writing - review & editing. **Andrey Chirtsov:** Formal analysis, Investigation, Methodology, Resources, Software, Supervision, Validation. **Vaclav Grim:** Formal analysis, Investigation, Methodology, Resources, Software, Supervision, Validation.

Declaration of Competing Interest

The authors declare that they have no known competing financial interests or personal relationships that could have appeared to influence the work reported in this paper.

References

[1] P. Ripka, Improved fluxgate for compasses and position sensors, J. Magn. Magn. Mater. 83 (1990) 543–544.
[2] E. Hristoforou, H. Chiriac, Position measuring system for applications in field sports, J. Magn. Magn. Mater. 249 (2002) 407–410.
[3] J.J. Beato-Lopez, I. Royo-Silvestre, C. Gomez-Polo, Micrometric non-contact position magnetoimpedance sensor, J. Magn. Magn. Mater. 465 (2018) 489–494.
[4] H. Sumali, E.P. Bystrom, G.W. Krutz, A displacement sensor for nonmetallic hydraulic cylinders, IEEE Sens. J. 3 (6) (2003) 818–826.
[5] P. Ripka, A. Chirtsov, M. Mirzaei, Inductance position sensor for pneumatic cylinder, AIP Adv. 8 (2018) 048001.
[6] M. Mirzaei, P. Ripka, A. Chirtsov, and J. Vyhnanek, “Temperature influence on position transducer for pneumatic cylinder”, IEEE Sensors Conference 2018, India paper #1638.
[7] P. Ripka, M. Mirzaei, A. Chirtsov, J. Vyhnanek, Transformer position sensor for a pneumatic cylinder, Sens. Actuators, A 294 (2019) 91–101.
[8] M. Mirzaei, P. Ripka, A. Chirtsov, J. Vyhnanek, Eddy current linear speed sensor, IEEE Trans. Mag. 55 (1) (2018) 1–4.
[9] R. L. Sanford, “Temperature coefficient of magnetic permeability within the working range,” Dept. of Commerce, Bureau of Standards, 1915.
[10] M. Sridhar, Y. Aparna, J. Kishore Babu, G. Patrick, Studies on conversion of thermal energy into electrical energy using ferromagnetic mild steel, cobalt and nickel as core materials: comparative study, AIP Conf. Proc. 2104 (2019).

3-2-2-5 Design of A Flat-Type Magnetic Position Sensor using A Finite-Difference Method [J8]

This study presents an analysis and the design of a new flat-type position sensor with an external armature. One excitation coil and two antiserially connected pickup coils are used in the stationary part. Solid iron segments or steel lamination segments are used for the moving armature. The proposed position sensor was modeled using linear movement. A two dimensional finite-difference method was developed and was used for fast analysis and for optimizing the sensor. The induced eddy currents in the solid armature were taken into account in the finite-difference analysis. The finite-difference calculations were compared with 2D and 3D finite-element method simulations and with experimental results. Unlike previous designs, the authors' new sensor has no moving coil. Various dimensions of the armature and the gaps have been taken into account in the modeling and in experiments at two frequencies. We have verified by 3D FEM and experiments that 2D FDM analysis is reasonably precise and reasonably fast for flat type position sensor design and optimization. 3D effects are notable, but they can be neglected to save simulation time in the first step in optimizing the design of a flat-type magnetic position sensor.

The magnetic fields in the armature are low. It is, therefore, preferable to use a thin or laminated armature and to operate the sensors at high frequencies, if the application allows. A magnetic position sensor with a steel lamination armature at 400 Hz shows superior results, as the eddy currents are minimized even at 400 Hz, thanks to the lamination. The sensor that has been developed has a total error of 0.23 mm RMS for 36 mm range without any compensation for non-linearity. This is acceptable for applications such as an elevator cabin landing position sensor. The power consumption at 50 Hz and 400 Hz is 10 mW. The analysis presented here was limited to a simple sensor with antiserially connected pickup coils. Advanced LVDTs often compensate temperature effects and air-gap variations by more complicated processing of the sensor output. The simulation procedures presented here can also be utilized in the analysis of such schemes. Both compensations would be necessary for this practical application. A weak point in the flat-type LVDT is its sensitivity to the movement of ferromagnetic bodies in the vicinity of the sensor.

IET Science, Measurement & Technology

Research Article

IET Journals
The Institution of Engineering and Technology

Design of a flat-type magnetic position sensor using a finite-difference method

ISSN 1751-8822
Received on 25th April 2019
Revised 20th October 2019
Accepted on 8th January 2020
E-First on 4th March 2020
doi: 10.1049/iet-smt.2019.0197
www.ietdl.org

Mehran Mirzaei[1] ✉, Jan Machac[1], Pavel Ripka[1], Andrey Chirtsov[1], Jan Vyhnanek[1], Vaclav Grim[1]

[1]*Faculty of Electrical Engineering, Czech Technical University, Prague 16627, Czech Republic*

✉ *E-mail: mirzameh@fel.cvut.cz*

Abstract: This study presents an analysis and the design of a new flat-type position sensor with an external armature. One excitation coil and two antiserially connected pickup coils are used in the stationary part. Solid iron segments or steel lamination segments are used for the moving armature. The proposed position sensor was modelled using linear movement. A two-dimensional finite-difference method was developed and was used for fast analysis for optimising the sensor. The induced eddy currents in the solid armature were taken into account in the finite-difference analysis. The finite-difference calculations were compared with 2D and 3D finite-element method simulations and with experimental results. The sensor has a total error of 0.23 mm root-mean-square for 36 mm range without any compensation. Unlike previous designs, the authors' new sensor has no moving coil.

Nomenclature

A_z	z-axis component of the magnetic vector potential
f	frequency
μ	magnetic permeability = $\mu_r\mu_0$
σ	electrical conductivity
J_s	source current density
R	μ_m/μ_n
μ_m	magnetic permeability of region m
μ_n	magnetic permeability of region n
w_c	coils width
h_c	coils height
d_e	excitation coil inner distance
d_p	pickup inner coil distance
t	distance between coils sides
w_i	armature width
h_i	armature iron height
g	distance and gap between coils and armature
L	square box edge length for boundary conditions
μ_{r-i}	initial relative magnetic permeability of the armature
σ_i	electrical conductivity of the armature
M	mutual inductance between coils
Ψ	mutual flux linkage between coils
V	induced voltage in the pickup coils
X	armature position
N	number of turns of the pickup and excitation coils
I	current amplitude
L_i	armature width in the z-direction

1 Introduction

The linear variable differential transformer (LVDT) is a very popular magnetic position sensor because of its non-contact nature and its high precision [1]. Owing to its simple and robust structure, it is suitable for industrial applications. The conventional LVDT sensor is cylindrical with an axially symmetric configuration [2–4]. A flat-shaped LVDT is more suitable for harsh environments because the stationary parts and the moving parts (the armature) can be completely physically isolated, unlike in the case of the cylindrical LVDT [5–10]. LVDT sensors can be constructed with an armature (magnetic core) [2, 3, 7, 8] or can be coreless [4–6, 9, 10]. Despite its high brittleness, ferrite is a widely used material for LVDT sensors with magnetic cores. LVDT sensors with nickel–iron and cobalt–iron alloys show enhanced performance, but these alloys are more expensive [11]. The influences of magnetic materials must be taken into account in the design of position sensors [11, 12]. A cylindrical LVDT is usually highly immune to interference, e.g. from movements of ferromagnetic objects in the close vicinity. It often even has magnetic shielding around the coil.

However, for some installations, the flat design of the LVDT is required with physically separated stationary and moving parts. An example of such an application is an elevator cabin landing position sensor, which may have a single armature connected to the cabin and one coil system in each floor. Magnetic sensors would be better resistant to dust and oil than the optical sensors, which are currently used for this application. A flat-type coreless LVDT sensor was presented in [5–6, 9–10], with a moving excitation coil or pickup coils. This solution with moving coils is impractical, and sensors with a large stroke suffer from low reliability.

We address this problem by introducing a novel type of flat LVDT sensor with an external armature made of solid iron (SI) and steel lamination (SL). The advantage of this design compared with existing solutions is the absence of a moving coil, and thus high robustness and reliability. A two-dimensional (2D) finite-difference method (FDM) [13, 14] description has been developed for a flat-type LVDT sensor, taking into account the eddy currents in the armature [15, 16]. The design of the position sensor could be optimised by using the FDM presented here to provide improved precision and performance [17–19]. The 3D finite-element method (FEM) was also used to evaluate 3D effects on the flat-type position sensor [20]. The main purpose of this paper is to present the design and analysis of a new flat-type position sensor with an SI armature using fast and precise FDM. For comparison, an SL armature is also used to evaluate the material effects. We compare the efficiency and the precision of the 2D FDM model with 2D and 3D FEM models. The modelling results are verified by measurements on the sensor demonstrator. We limit our analysis to a simple sensor with antiserially connected pickup coils. We do not take into consideration the shielding against external DC fields that also suppresses the influence of nearby ferromagnetic bodies.

2 Model

Fig. 1 shows the flat LVDT sensor and its equivalent electric circuit. The magnetic shield or yoke is not considered in this paper. The performance of an LVDT sensor is similar to the performance

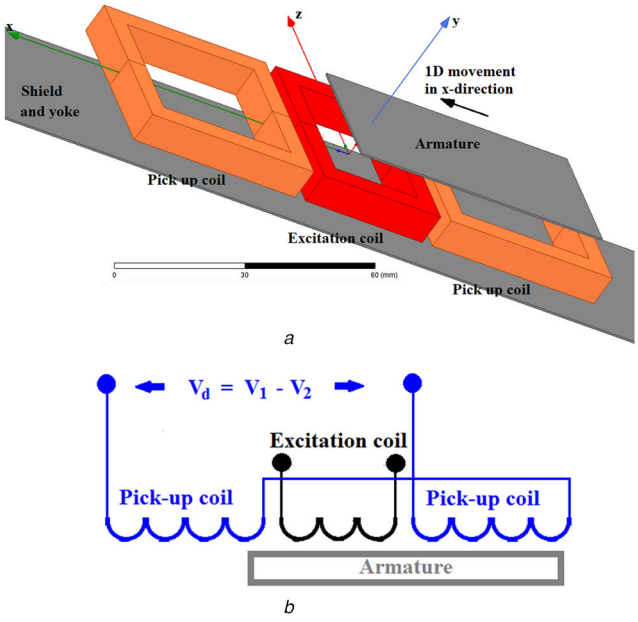

Fig. 1 *Model*
(a) Flat-type position sensor with a magnetic armature (top), ***(b)*** Equivalent electric circuit model (bottom)

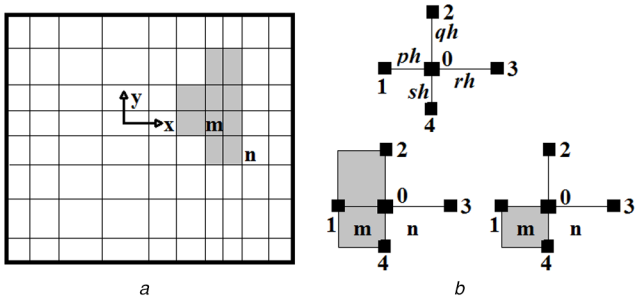

Fig. 2 *FDM*
(a) Schematic model of finite-difference meshed elements for adjacent regions *m* and *n* (left), ***(b)*** For a finite-difference mesh element (right) – region *m* with the grey colour is surrounded by region *n* with white colour

of a transformer with an open-circuit secondary coil. The primary coil and the secondary coils are the excitation coil and pickup coils in the LVDT sensor, respectively. The pickup coils are connected in series anti-phase (antiserial), which gives zero output voltage for the null (centre) position of the armature.

3 Finite-difference method

The general partial differential equation in the 2D *x*–*y*-plane using Maxwell equations is as follows [16]:

$$\frac{\partial^2 A_z}{\partial x^2} + \frac{\partial^2 A_z}{\partial y^2} - \mathrm{j}\omega\mu\sigma A_z + \mu J_\mathrm{s} = 0$$
$$\omega = 2\pi f \tag{1}$$

Only linear magnetic modelling using the initial permeability is considered here, due to the low magnetic fields in the sensor, and non-linearity and hysteresis effects are neglected. Third term in (1) is zero for non-conductive (no eddy current effects) coils and air regions. Fourth term in (1) is zero in armature and air regions. Fig. 2 shows a schematic finite-difference meshed model for two regions *m* (grey colour) and *n* (white colour), and a 5-node finite-difference mesh element. The two adjacent regions *m* and *n* could have a common edge or common vertices at the corners and boundaries. Parameters $p{\cdot}h$, $q{\cdot}h$, $r{\cdot}h$ and $s{\cdot}h$ are the mesh dimensions in the *x* and *y* directions in Fig. 2*b*. The finite-difference equation of (1) for either region *m* or region *n* is presented in (2), using Taylor expansions [14]

$$\frac{A_{z,1}}{p\cdot(p+r)} + \frac{A_{z,2}}{q\cdot(q+s)} + \frac{A_{z,3}}{r\cdot(p+r)} + \frac{A_{z,4}}{s\cdot(q+s)} - \left(\left(\frac{1}{p\cdot r} + \frac{1}{q\cdot s}\right) + \mathrm{j}\omega\mu\sigma\cdot\frac{h^2}{2}\right)\cdot A_{z,0} + \mu J_\mathrm{s}\cdot\frac{h^2}{2} = 0 \tag{2}$$

The centre point 0 in the element has magnetic vector potential $A_{z,0}$, and the magnetic vector potential at nearby node 1 is $A_{z,1}$, at node 2 the magnetic vector potential is $A_{z,2}$, at node 3 it is $A_{z,3}$ and at node 4 it is $A_{z,4}$. Equation (3) presents the finite-difference equation when node 0 with magnetic vector potential $A_{z,0}$ is on the boundary edge between regions *m* and *n* [15, 16]

$$\frac{A_{z,1}}{p} + \frac{(p\cdot R + r)}{q\cdot(q+s)}\cdot A_{z,2} + \frac{R}{r}\cdot A_{z,3} + \frac{(p\cdot R + r)}{q\cdot(q+s)}\cdot A_{z,4} - \left(\left(\frac{1}{p\cdot r} + \frac{1}{q\cdot s}\right)\cdot(p\cdot R + r) + \mathrm{j}\omega\mu\sigma\cdot p\cdot\frac{h^2}{2}\right)\cdot A_{z,0} + \mu J_\mathrm{s}\cdot p\cdot\frac{h^2}{2} = 0$$
$$R = \frac{\mu_m}{\mu_n} \tag{3}$$

Equations (2) and (3) can be simplified further when the mesh element has the same sizes for the element edges ($p = q = r = s = 1$), which are presented in (4) and (5), respectively

$$A_{z,1} + A_{z,2} + A_{z,3} + A_{z,4} - \left(4 + \mathrm{j}\omega\mu\sigma\cdot h^2\right)\cdot A_{z,0} + \mu J_\mathrm{s}\cdot h^2 = 0 \tag{4}$$

$$A_{z,1}+\frac{(R+1)}{2}\cdot A_{z,2}+R\cdot A_{z,3}+\frac{(R+1)}{2}\cdot A_{z,4} -\left(2\cdot(R+1)+\mathrm{j}\omega\mu\sigma\cdot\frac{h^2}{2}\right)\cdot A_{z,0}+\mu J_s\cdot\frac{h^2}{2}=0 \tag{5}$$

The finite-difference equation for a node on the corner located on the boundary between regions m and n is [14–16]:

$$\frac{(R+1)}{2}\cdot A_{z,1}+R\cdot A_{z,2}+R\cdot A_{z,3}+\frac{(R+1)}{2}\cdot A_{z,4} -\left(3\cdot R+1+\mathrm{j}\omega\mu\sigma\cdot\frac{h^2}{4}\right)\cdot A_{z,0}+\mu J_s\cdot\frac{h^2}{4}=0 \tag{6}$$

It is considered that region m contains the source current, and it is the conductive region in (3), (5) and (6) [15, 16].

Fig. 3 presents a computational model for a flat-type position sensor for FDM modelling.

The solution space is limited to ±160 mm and the condition $A_z = 0$ is applied at the solution space boundary (Fig. 3). The magnetic flux densities are calculated at the centre point of each element inside any region in (7), using the approximations in (8)

$$B_{x,0}=\frac{\partial A_z}{\partial y}=\frac{A_{z,2}-A_{z,4}}{h\cdot(q+s)} \qquad B_{y,0}=-\frac{\partial A_z}{\partial x}=\frac{A_{z,1}-A_{z,3}}{h\cdot(p+r)} \tag{7}$$

$$A_{z,0}=\frac{s\cdot A_{z,2}+q\cdot A_{z,4}}{q+s}\rightarrow(B_{x,0}) \qquad A_{z,0}=\frac{r\cdot A_{z,1}+p\cdot A_{z,3}}{p+r}\rightarrow(B_{y,0}) \tag{8}$$

The magnetic flux densities at the common edge boundary, and the common corner boundaries between regions m and n, for example, in Fig. 2*b* could be approximately written as in the equations below, respectively:

$$B_{x,0}=\frac{A_{z,2}-A_{z,4}}{h\cdot(q+s)} \qquad B_{y,0}=0.5\cdot\left(\frac{A_{z,1}-A_{z,0}}{h\cdot p}+\frac{A_{z,0}-A_{z,3}}{h\cdot r}\right) \tag{9}$$

$$B_{x,0}=0.5\cdot\left(\frac{A_{z,2}-A_{z,0}}{h\cdot q}+\frac{A_{z,0}-A_{z,4}}{h\cdot s}\right) \qquad B_{y,0}=0.5\cdot\left(\frac{A_{z,1}-A_{z,0}}{h\cdot p}+\frac{A_{z,0}-A_{z,3}}{h\cdot r}\right) \tag{10}$$

Fig. 2 shows a simplified FDM mesh model to explain the FDM used in this paper. Each node is adjacent to four nodes, which is totally five nodes for each mesh inside the model, except the nodes on the boundary with determined zero magnetic vector potential. Each node can be inside a region or on the boundary between different regions, as shown in Fig. 2.

4 FDM simulations

Table 1 presents flat-type position sensor dimensions and properties. The other dimensions are defined in Fig. 3. The initial relative magnetic permeability μ_{r-i} (which is 100 for SI and 1000 for SL) and the electrical conductivity σ_i of the SI and SL armature are also presented in Table 1. The initial permeability is used because the magnetic fields in the position sensor are very small.

Two source frequencies 50 and 400 Hz were selected for the first analysis of the flat-type position sensor. The corresponding skin depths for SI are calculated for the mesh size at these frequencies, using the following equation [1]:

$$\delta_i=\sqrt{\frac{2}{\omega\mu_{r-i}\mu_0\sigma_i}} \tag{11}$$

The skin depths are 3.2 mm at 50 Hz and 1.1 mm at 400 Hz.

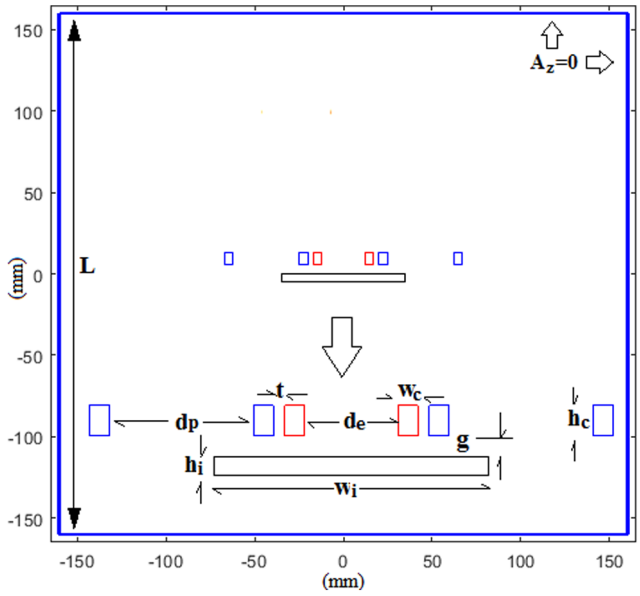

Fig. 3 *Computational model for finite-difference analysis of a flat-type position sensor with boundary conditions*

Table 1 Flat-type position sensor parameters

Parameter	Value
N	70
I	0.165 A
L	320 mm
w_c	5 mm
h_c	8 mm
w_i	50 and 70 mm
h_i	5 and 0.5 mm
d_e	24 mm
d_p	37 mm
g	5.4 mm
t	3 mm
σ_i	5.07, 3.14 MS/m
μ_{r-i}	100 and 1000
L_i	30 mm

Figs. 4 and 5 show the magnetic flux distribution. The length of square box L for the boundary conditions is considered to be 320 mm, which is a satisfactory value for precision and speed of simulation. The effect of the induced eddy current in the SI armature is obvious at 400 Hz (Fig. 5). Figs. 6 and 7 present the magnetic flux distribution for different heights of the SI armature and different coils and armature gap g to evaluate the sensitivity and the performance of the magnetic position sensor.

Fig. 8 presents the magnetic vector potential versus distance on the line in the middle of the coils. The difference between the DC and 50 Hz values is negligible, while the magnetic vector potential results vary considerably and are reduced on one side at 400 Hz. The x component of the magnetic flux density curve at 1 mm below the surface of the moving iron part is presented in Fig. 9. The field values are in the mT range, which confirms the use of the constant initial relative magnetic permeability in the magnetic modelling. Only AC models are used for the design of the position sensor, as there is no induction component at DC.

The centre position for the armature is that the vertical symmetry lines of the coils and the armature align (Fig. 4). The relations between the magnetic vector potential and induced voltage V and mutual inductance M are [21]

$$V = -\frac{\mathrm{d}\Psi}{\mathrm{d}t} = -\mathrm{j}\omega N \oint A_z \,\mathrm{d}l \tag{12a}$$

$$M = \frac{-N \oint A_z \,\mathrm{d}l}{I} \tag{12b}$$

where Ψ is the mutual flux linkage between the excitation coil and pickup coils.

The induced voltage V in the pickup coils and mutual inductance M between the excitation coil and pickup coils are particularly influenced by the induced eddy current in the SI at higher frequencies.

The induced voltage V and the mutual inductance M are numerically calculated from the relations

$$V = -\mathrm{j}\omega N L_i \frac{\sum_{k=1,2,\ldots}^{K} \left(A^{\mathrm{l}}_{z,k} - A^{\mathrm{r}}_{z,k}\right)}{K} \tag{13a}$$

$$M = \frac{-N L_i}{I} \frac{\sum_{k=1,2,\ldots}^{K} \left(A^{\mathrm{l}}_{z,k} - A^{\mathrm{r}}_{z,k}\right)}{K} \tag{13b}$$

Equations (13a) and (13b) are calculated using (12a) and (12b) for FDM by averaging on the coil sides cross-section and subtracting the left (l) and right (r) of the coil sides [21]. The integral path in (12a) and (12b) is only in the z-direction, as only the z component of the magnetic vector potential A_z is considered in 2D FDM analysis (Fig. 10). Parameter K is the number of nodes of FDM on the cross-section of the coil sides.

Mutual inductances with different armature widths and heights are presented in Table 2, for DC and 400 Hz for the zero position of the armature. The width of the armature has a substantial effect on mutual inductance M. A change in the height of the armature from 5 to 3 mm gives 1% less influence on the mutual inductance. However, the mutual inductance decreases by about 5% for 1 mm in height. A larger gap g causes less influence of the height and width of the armature on the mutual inductances. The increasing gap from 5.4 to 10.8 mm has a larger influence than other parameters.

The influence of the induced eddy current in the SI armature on the mutual inductance is evident in a comparison between 400 Hz and DC. Reducing the height of the armature has less influence on the mutual inductance at 400 Hz independent of gap values g because skin depth is smaller and the magnetic flux is concentrated on the surface of the SI armature. This can be used for applications measuring the positions of changing targets.

The induced eddy current in the armature causes the self-inductance of the excitation coil and mutual inductances between excitation coil and pickup coils to be complex value. It can be explained that the phase angle shift between flux linkage and excitation coil current is non-zero or phase angle shift between induced voltage and excitation coil current is not 90°. Therefore, the inductance values calculated by (13b) are complex numbers because of the induced eddy currents in the SI armature.

The mutual inductances between the excitation coil and pickup coils for the right ($M1$) and left ($M2$) pickup coils and their difference, $M1$–$M2$ (differential inductance) versus the positions of the armature, are shown in Figs. 11 and 12, which are almost sinusoidal in shape [22]. Only the real parts are shown, and the imaginary part of the mutual inductance is not considered as in Table 2. The differential inductances change linearly from the zero position of the armature to close to maximum values.

They are odd symmetric functions relative to the zero position. The gradient of the differential inductance curve is higher for an armature 50 mm in width than for an armature 70 mm. The maximum differential inductance values are about 14 μH, at 25 and 20 mm for armatures of 70 and 50 mm length, respectively.

5 Experimental results

Fig. 13 shows experimental elements, coils and armatures, and also the Stanford Research SR 830 lock-in amplifier and the Keithley 3390 signal generator. The armatures are of SI 5 mm in thickness and electrical steel 0.5 mm in thickness.

The experimental results and the FDM results for the differential voltage amplitudes of the pickup coils for the SI armatures are presented in Fig. 14, for 400 Hz, and in Fig. 15 for 50 Hz. The polarity of the differential voltages is determined based on the phase angles. They contain both inductive and resistive components.

The linear region of the differential voltage curves is used for the magnetic position sensor. The magnetic sensor shows better sensitivity or higher voltage at a smaller distance with the 50 mm armature, and better sensitivity at a longer distance with the 70 mm armature in the linear region of the curves. The maximum values of the differential voltages are located at the same position as the maximum values of the differential mutual inductances curves $M1$–$M2$ in Figs. 11 and 12. Also, Figs. 16 and 17 show the differential voltages for an armature of SLs. The maximum values are higher, especially at higher frequencies, due to the higher initial permeability 1000 and the smaller height (Fig. 18). The main sources of the differences between the experimental results and FDM results for differential voltages are the effects of the 3D, which are not taken into account in the 2D finite-difference analysis.

6 Numerical analysis evaluations

Table 3 shows comparisons between FDM results, 2D FEM calculations and 3D FEM calculations [20] for differential voltages for different positions of an SI armature 70 mm in width. The 3D FEM results agree better with the experimental results, because 3D FEM takes into account the 3D effect, which is not negligible for rectangular coil fields [23] in a magnetic position sensor. The 2D FDM and 2D FEM results are both higher than the experimental results and 3D FEM results. Taking 3D effects into account reduces the differential voltages and the corresponding mutual inductances between the exciting coil and pickup coils. The 2D FDM calculations that have been developed agree well with 2D FEM at 50 Hz.

Reducing the height of the armature reduces the high-frequency effects of the induced eddy currents in the SI (see Fig. 19). The results for differential voltage with and without taking into account the electrical conductivity of the armature show small differences for an SI armature 1 mm in height. The maximum value of the differential voltage for an SI armature 1 mm in height is almost unchanged in comparison with an SI armature 5 mm in height at 400 Hz (Fig. 14).

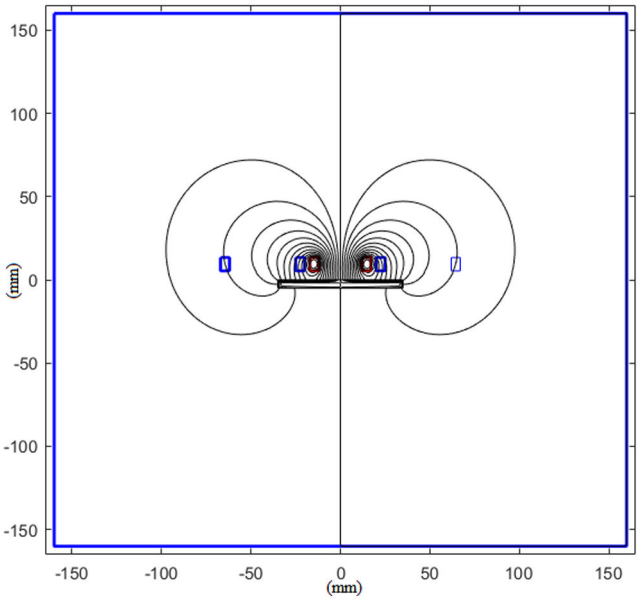

Fig. 4 *Magnetic flux distribution at 400 Hz with zero position armature – SI armature width and height = 70 and 5 mm (the boundary edge is 320 mm in length)*

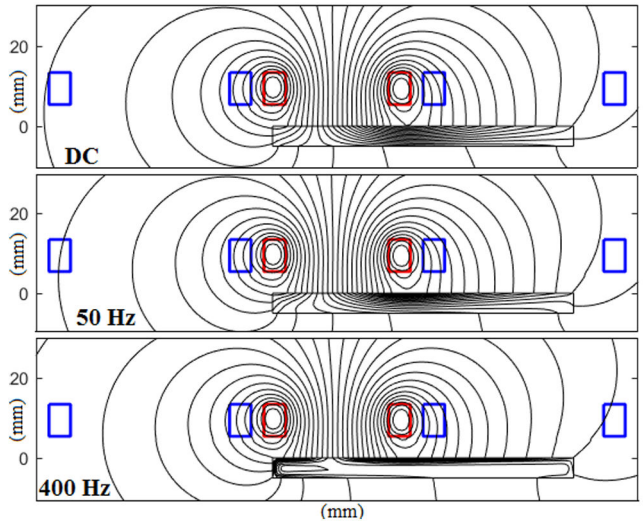

Fig. 5 *Magnetic flux distribution at DC (top), at 50 Hz (middle) and 400 Hz (bottom) – SI armature shifted 20 mm from the centre (armature width = 70 mm and height = 5 mm)*

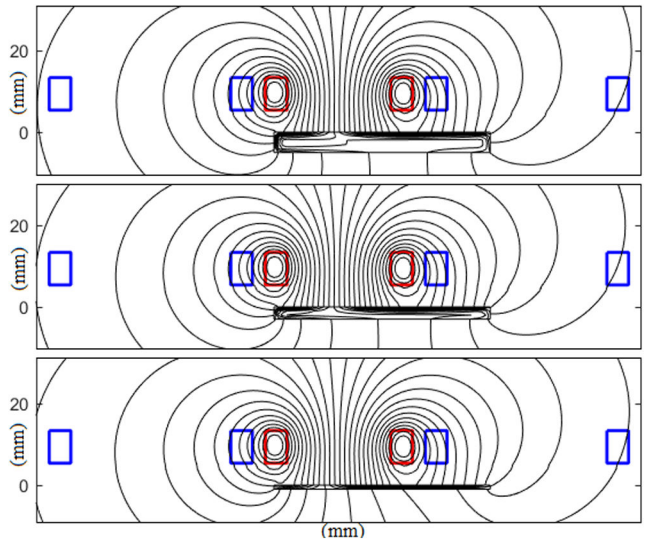

Fig. 6 *Magnetic flux distribution at 400 Hz for SI armature height = 5 mm (top), 3 mm (middle) and 1 mm (bottom) – armature shifted 10 mm from the centre (armature width = 50 mm)*

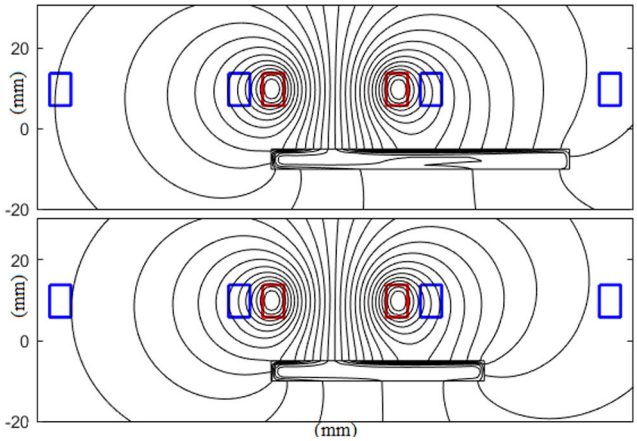

Fig. 7 *Magnetic flux distribution at 400 Hz with the SI armature shifted 20 mm from the centre and armature width = 70 mm (top) and the armature shifted 10 mm from the centre and armature width = 50 mm (bottom) – the gap between the coils and armature, g, is doubled and is equal to 10.8 mm*

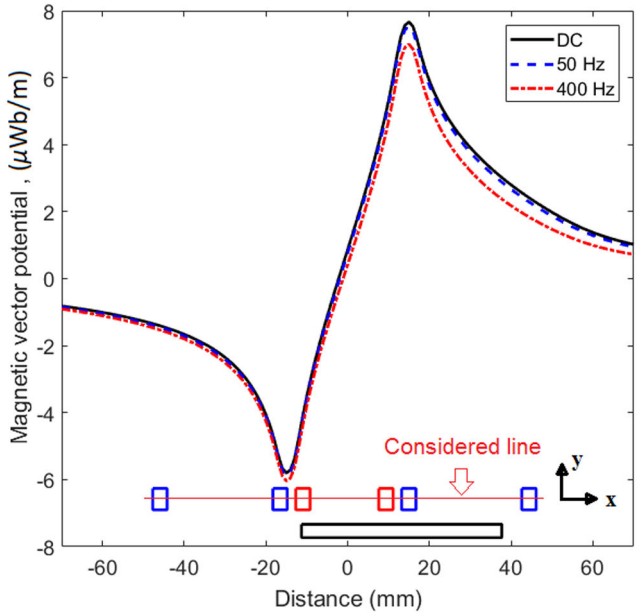

Fig. 8 *Real part of the magnetic vector potential versus distance on the red line in the middle of the coils – SI armature 70 mm width and 5 mm height (armature shifted 20 mm from the centre)*

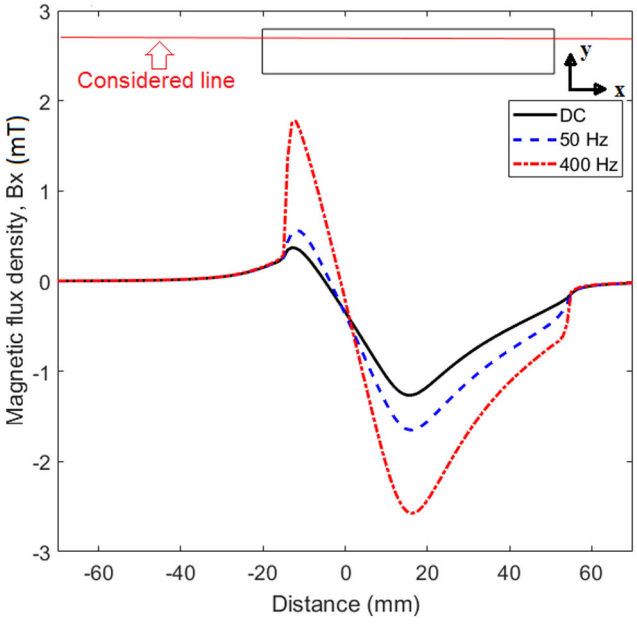

Fig. 9 *Real part of the x component of magnetic flux density versus distance on the red line 1 mm below the surface of the armature – SI armature 70 mm width and 5 mm height (armature shifted 20 mm from the centre)*

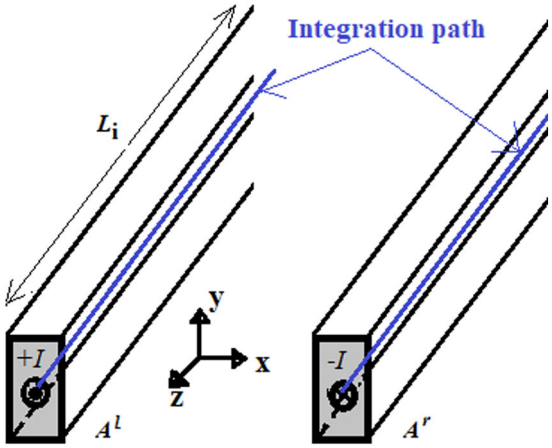

Fig. 10 *Coil model with coil sides In (A^r) and Out (A^l)*

Table 2 Mutual inductance between the excitation coil and pickup coil at zero position of the armature

	Height, mm	Width, mm	Inductance, μH	Gap, *g*, mm
DC	5	70	43.5	5.4
400 Hz	—	—	41.3	—
DC	3	70	43.1	5.4
400 Hz	—	—	41.3	—
DC	1	70	41.4	5.4
400 Hz	—	—	41.1	—
DC	5	50	39.0	5.4
400 Hz	—	—	37.6	—
DC	3	50	38.6	5.4
400 Hz	—	—	37.4	—
DC	1	50	37.4	5.4
400 Hz	—	—	37.3	—
DC	5	70	37.0	10.8
400 Hz	—	—	36.0	—
DC	1	70	36.0	10.8
400 Hz	—	—	35.9	—
DC	5	50	34.7	10.8
400 Hz	—	—	34.1	—

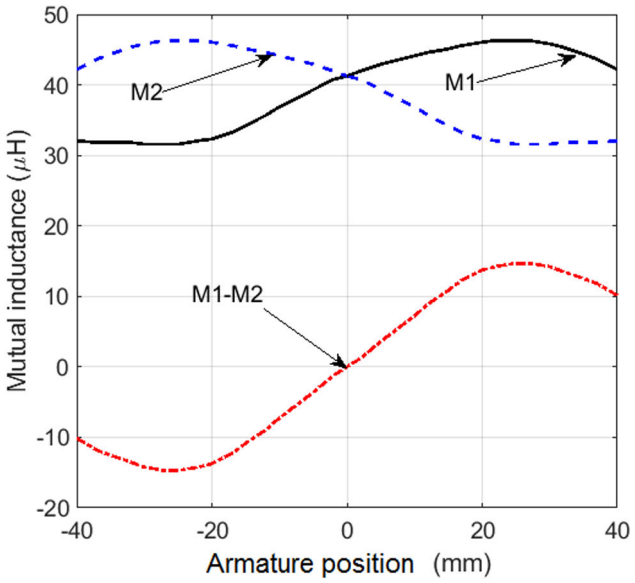

Fig. 11 *Mutual inductance versus armature position – the SI armature is 70 mm in width (400 Hz) – FDM*

7 Linearity

A linear approximation of the relation between the differential voltage V and armature position X is

$$X = C \cdot V \tag{14}$$

Constant C depends on the width of the armature and the frequency of the excitation coil (Table 4). Table 5 presents the root-mean-

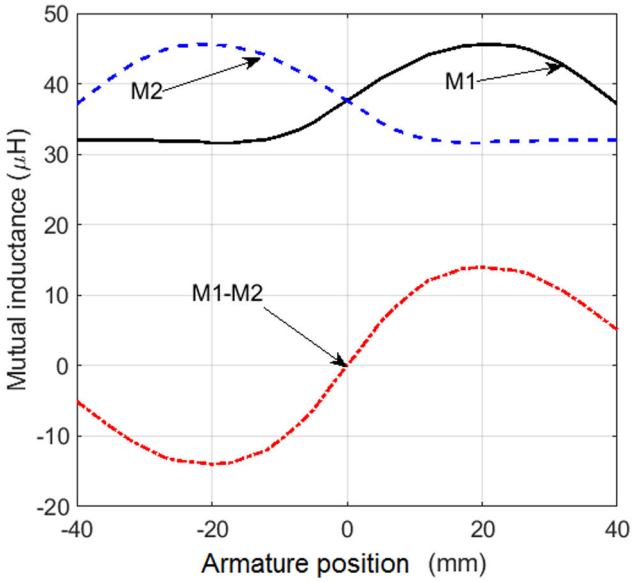

Fig. 12 *Mutual inductance versus armature position – the SI armature is 50 mm in width (400 Hz) – FDM*

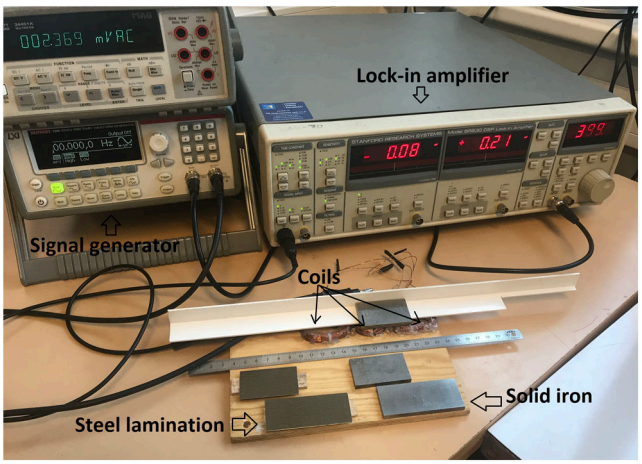

Fig. 13 *Experiment elements – coils and SI and SL armatures – lock-in amplifier and signal generator*

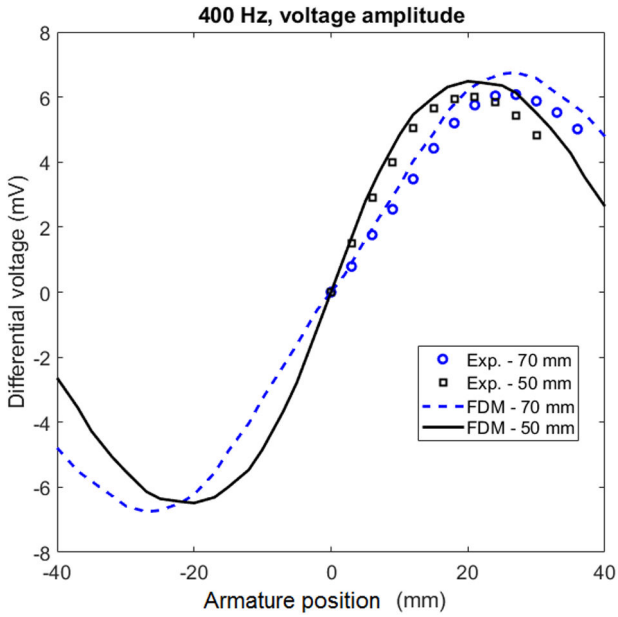

Fig. 14 *Differential voltage versus SI armature position – 400 Hz (experimental versus FDM)*

square error (RMSE) values as an indicator [12] to show the closeness of the Q measured values to the linear curve fit in (14).

The linear ranges considered here are -12 to $+12$ mm for an armature 50 mm in width and -18 to $+18$ mm for an armature 70 mm in width. Reducing the manufacturing tolerance of the magnetic sensor and induced eddy currents in the SI could reduce the RMSE in Table 5.

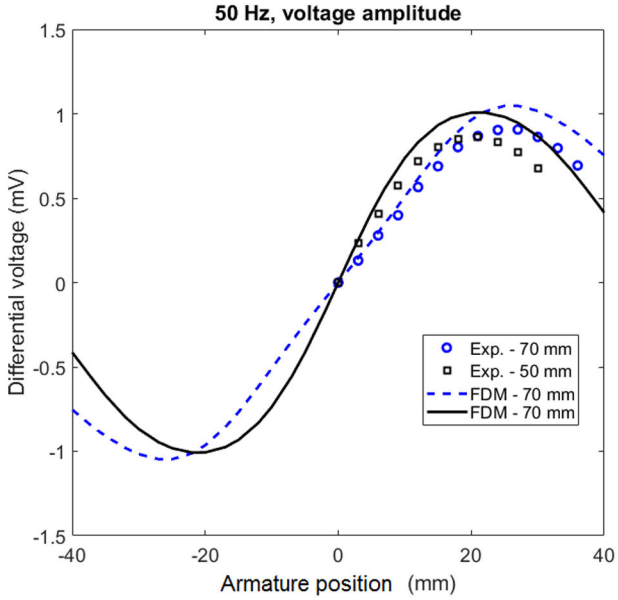

Fig. 15 *Differential voltage versus SI armature position – 50 Hz (experimental versus FDM)*

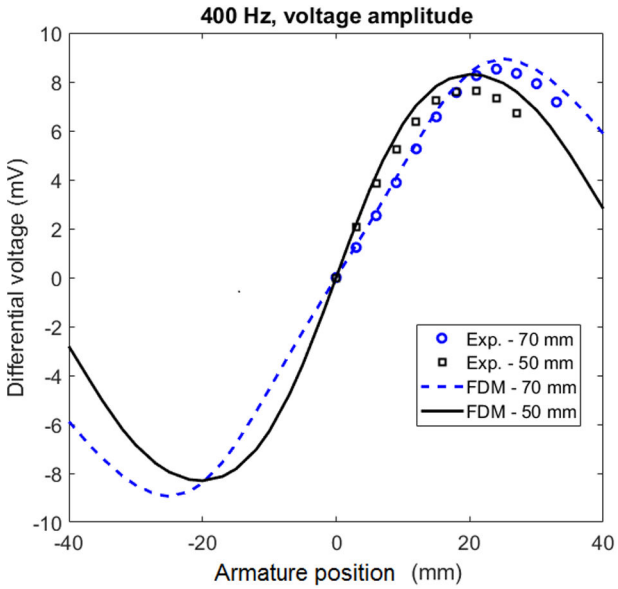

Fig. 16 *Differential voltage versus SL armature position – 400 Hz (experimental versus FDM)*

8 Discussion

Although non-commercial and commercial finite-element software for 2D and 3D electromagnetic analyses for magnetic devices and sensors is highly accessible and has high precision [24–30], fast and sufficiently precise in-house analytical and numerical approaches to the design and optimisation of electromagnetic devices [31–36] are always in demand in industry and academic. Easy post-processing of magnetic analysis, fast parametric analysis and flexible optimisation are major advantages of in-house analytical and numerical computational tools for all types of electromagnetic devices such as magnetic sensors and actuators.

3D numerical calculations are more time-consuming, as they have more unknowns to solve. 3D finite-difference equations have three components of the magnetic vector potential, in comparison with only one component of the magnetic vector potential in the 2D FDM presented in this paper. It is not economical or efficient to use 3D computation in the whole design process of our sensor, as the difference between 2D simulations and 3D simulations is only 10%, as shown in Table 2.

SI and steel maybe a fundamental component of magnetic position sensors [24]. If this is the case, induced eddy currents should be considered. It is essential to take into consideration the magnetic permeabilities and electrical conductivities of magnetic materials [37] in the design of magnetic position sensors.

The effects of the magnetic shield and the yoke in Fig. 1*a* are not considered in this paper. These parts will provide improved sensitivity.

9 Conclusion

We have developed a novel flat LVDT sensor with an external armature and without moving coils. Finite-difference analysis and experimental results have been presented for SI and electrical SL armatures. Various dimensions of the armature and the gaps have been taken into account in the modelling and in experiments at two frequencies. We have verified by 3D FEM and experiments that 2D FDM analysis is reasonably precise and reasonably fast for flat-type position sensor design and optimisation. 3D effects are notable, but they can be neglected to save simulation time in the first step in optimising the design of a flat-type magnetic position sensor.

The magnetic fields in the armature are low. It is, therefore, preferable to use a thin or laminated armature and to operate the sensors at high frequencies, if the application allows. A magnetic position sensor with an SL armature at 400 Hz shows superior results, as the eddy currents are minimised even at 400 Hz, thanks

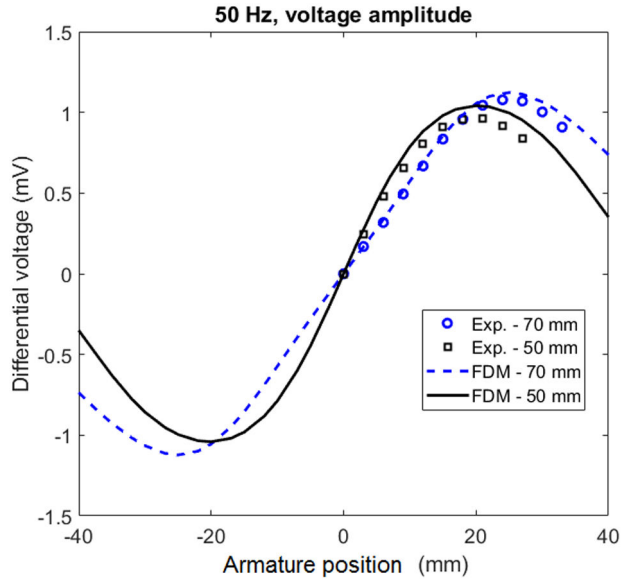

Fig. 17 *Differential voltage versus SL armature position – 50 Hz (experimental versus FDM)*

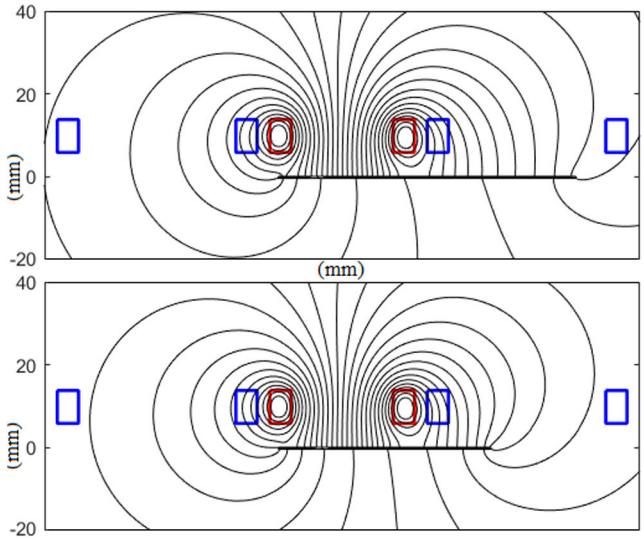

Fig. 18 *Magnetic flux distribution at 50 Hz with the SL armature shifted 20 mm from the centre and armature width = 70 mm (top) and with the armature shifted 10 mm from the centre and armature width = 50 mm (bottom) – the gap, g = 5.4 mm*

to the lamination. High operational frequency also improves the dynamic performance of the sensor. The sensor that has been developed has a total error of 0.23 mm RMS for 36 mm range without any compensation for non-linearity. This is acceptable for applications such as an elevator cabin landing position sensor. The power consumption at 50 and 400 Hz is 10 mW. For the final design, the operation frequency maybe further increased and the number of turns of the coils should be optimised taking into account the sensitivity and the power consumption.

The analysis presented here was limited to a simple sensor with antiserially connected pickup coils. Advanced LVDTs often compensate temperature effects and air-gap variations by more complicated processing of the sensor output. The simulation procedures presented here can also be utilised in the analysis of such schemes. Both compensations would be necessary for this practical application.

A weak point in the flat-type LVDT is its sensitivity to the movement of ferromagnetic bodies in the vicinity of the sensor. If this situation is anticipated, the FDM simulation method presented here can be used to estimate the influence on the precision of the sensor and to evaluate the efficiency of the magnetic shielding.

Table 3 Differential voltage versus SI armature position at 50 Hz – comparison between experimental, FDM, FEM 2D and FEM 3D

Position, mm	Experiment, mV	FDM, mV	FEM 2D, mV	FEM 3D, mV
9	0.40	0.45	0.46	0.42
18	0.80	0.90	0.89	0.80
27	0.91	1.04	1.04	0.90

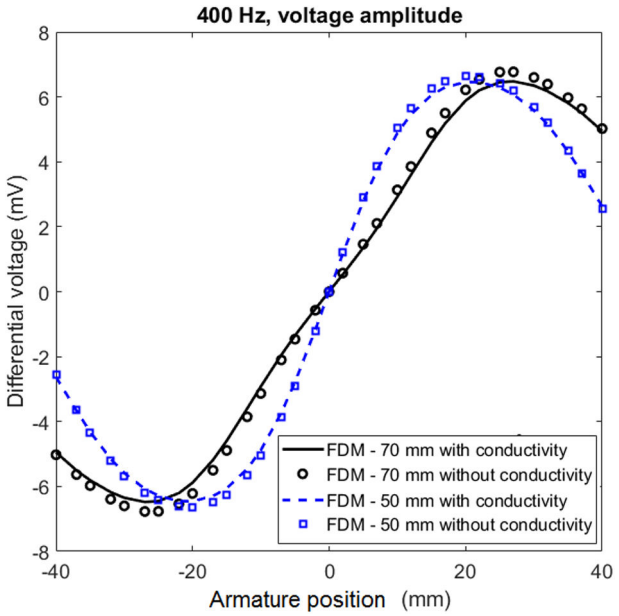

Fig. 19 *Differential voltage versus SI armature position with a moving part 1 mm in height (FDM)*

Table 4 Constant *C* for various SI and SL armature widths and frequencies

	70 mm 400 Hz	70 mm 50 Hz	50 mm 400 Hz	50 mm 50 Hz
C, SI, mm/mV	3.4	22	2.3	16
C, SL, mm/mV	2.3	18	1.8	14

Table 5 RMSE for various SI and SL armature widths and frequencies

	70 mm 400 Hz	70 mm 50 Hz	50 mm 400 Hz	50 mm 50 Hz
RMSE, SI, mm	0.23	0.26	0.43	0.48
RMSE, SL, mm	0.26	0.33	0.64	0.50

10 References

[1] Ripka, P.: '*Magnetic sensors and magnetometers*' (Artech House, USA, 2001)

[2] Kilani, M., Taifour, S., Al-Sharif, L.: 'Effect of design geometry on the performance characteristics of linear variable differential transformers', *Sens. Trans.*, 2013, **150**, (3), pp. 66–71

[3] Sykulski, J.K., Sykulska, E., Hughes, S.T.: 'Application of finite-element modelling in LVDT design', *Int. J. Comput. Math. Electr. Electron. Eng.*, 1992, **11**, (1), pp. 73–76

[4] Martino, M., Danisi, A., Losito, R., *et al.*: 'Design of a linear variable differential transformer with high rejection to external interfering magnetic field', *IEEE Trans. Magn.*, 2010, **46**, (2), pp. 674–677

[5] Sydenham, P.H., Taing, V., Mounsey, D.J., *et al.*: 'Low-cost, precision, flat inductive sensor', *Measurement*, 1995, **15**, (3), pp. 179–188

[6] Kano, Y., Hasebe, S., Huang, C., *et al.*: 'New type linear variable differential transformer position transducer', *IEEE Trans. Instrum. Meas.*, 1989, **38**, (2), pp. 407–409

[7] Kano, Y., Hasebe, S., Miyaji, H.: 'New linear variable differential transformer with square coils', *IEEE Trans. Magn.*, 1990, **26**, (5), pp. 2020–2022

[8] Babu, A., George, B.: 'Design and development of a new non-contact inductive displacement sensor', *IEEE Sens. J.*, 2018, **18**, (3), pp. 976–984

[9] Djuric, S.M.: 'Performance analysis of a planar displacement sensor with inductive spiral coils', *IEEE Trans. Magn.*, 2014, **50**, (4), pp. 1–4

[10] Anandan, N., George, B.: 'Design and development of a planar linear variable differential transformer for displacement sensing', *IEEE Sens. J.*, 2017, **17**, (16), pp. 5298–5305
[11] Yañez-Valdez, R., Alva-Gallegos, R., Caballero-Ruiz, A., *et al.*: 'Selection of soft magnetic core materials used on an LVDT prototype', *J. Appl. Res. Technol.*, 2012, **10**, (2), pp. 195–205
[12] Sumali, H., Bystrom, E.P., Krutz, G.W.: 'A displacement sensor for non-metallic hydraulic cylinders', *IEEE Sens. J.*, 2003, **3**, (6), pp. 818–826
[13] Erdelyi, E.A., Ahamed, S.V., Burtness, R.D.: 'Flux distribution in saturated DC machines at no-load', *IEEE Trans. Power Appl. Syst.*, 1965, **84**, (5), pp. 375–381
[14] Binns, K.J., Lawrenson, P.J.: '*Analysis and computation of electric and magnetic field problems*' (Pergamon International Library of Science, Technology, Engineering and Social Studies, UK, 1973, 2nd edn.)
[15] Nasar, S.A., Boldea, I.: '*Linear motion electric machines*' (John Wiley & Sons, Inc., USA, 1976, 1st edn.)
[16] Stoll, R.L.: '*Analysis of eddy currents*' (Clarendon Press, UK, 1974)
[17] Weissinger, C., Oswald, A., Herzog, H.-G.: 'Design of a position sensor using finite-element analysis based on the effect of local magnetic saturation', *IET Sci. Meas. Technol.*, 2012, **6**, (5), pp. 364–368
[18] Yang, S.-H., Hirata, K., Ota, T., *et al.*: 'Impedance linearity of contactless magnetic-type position sensor', *IEEE Trans. Magn.*, 2017, **53**, (6), pp. 1–4
[19] Singh, W.S., Mukhopadhyay, C.K., Chandra Rao, B.P.: 'Development of a high sensitive magnetic flux leakage instrument for imaging of localised flaws in small diameter ferromagnetic steel tubes', *IET Sci. Meas. Technol.*, 2018, **12**, (7), pp. 932–936
[20] 'ANSYS-Maxwell software'. Available at https://www.ansys.com/products/electronics/ansys-maxwell, accessed 23 January 2019
[21] Salon, S.: '*Finite-element analysis of electrical machines*' (Springer-Verlag (New York) Inc., USA, 1995)
[22] Ripka, P., Tipek, A.: '*Modern sensors handbook*' (Wiley-ISTE, UK, 2013)
[23] Clayton, R.P.: '*Inductance: loop and partial*' (Wiley-IEEE Press, USA, 2009, 1st edn.)
[24] Ripka, P., Mirzaei, M., Chirtsov, A., *et al.*: 'Transformer position sensor for a pneumatic cylinder', *Sens. Actuators A*, 2019, **294**, pp. 91–101
[25] Talaat, M., Mostafa, N.H.: 'Use of finite-element method for the numerical analysis of eddy current brake'. 15th Int. Workshop on Research and Education in Mechatronics (REM), Elgouna, Egypt, 9–11 September 2014
[26] Talaat, M., Metwally, H.M.B., Arafa, I.: 'Experimental and simulation study of wireless power transfer using resonators with coupled electric fields', *IEEE Trans. Plasma Sci.*, 2018, **46**, (7), pp. 2480–2487
[27] Reinholz, B., Seethaler, R.J.: 'Design and validation of a variable reluctance differential solenoid transducer', *IEEE Sens. J.*, 2019, **19**, 11063–11071
[28] Grima, A., Castro, M.D., Masi, A., *et al.*: 'Design enhancements of an ironless inductive position sensor', *IEEE Trans. Instrum. Meas.*, 2019 (Early access on https://ieeexplore.ieee.org/document/8693550, 17 April 2019)
[29] Lesniewska, E., Rajchert, R.: 'Behaviour of measuring current transformers with cores composed from different magnetic materials at non-rated loads and overcurrents', *IET Sci. Meas. Technol.*, 2019, **13**, (7), pp. 944–948
[30] Abu-Siada, A., Radwan, I., Abdou, A.F.: '3D approach for fault identification within power transformers using frequency response analysis', *IET Sci. Meas. Technol.*, 2019, **13**, (6), pp. 903–911
[31] Saxena, S.C., Seksena, S.B.L.: 'A self-compensated smart LVDT transducer', *IEEE Trans. Instrum. Meas.*, 1989, **38**, (3), pp. 748–753
[32] Bera, S.C., Sarkar, R., Bhowmick, M.: 'Study of a modified differential inductance measurement circuit as position transducer of a power cylinder', *IEEE Trans. Instrum. Meas.*, 2012, **61**, (2), pp. 530–538
[33] Tian, G.Y., Zhao, Z.X., Baines, R.W., *et al.*: 'Computational algorithms for linear variable differential transformers (LVDTs)', *IEE Proc. Sci. Meas. Technol.*, 1997, **144**, (4), pp. 189–192
[34] Mishra, S.K., Panda, G., Das, D.P.: 'A novel method of extending the linearity range of linear variable differential transformer using artificial neural network', *IEEE Trans. Instrum. Meas.*, 2010, **59**, (4), pp. 947–953
[35] Yin, S., Ma, X.: 'Analytical model for the equivalent impedances of the domestic induction heating system with rectangular cross-sectional windings', *IET Sci. Meas. Technol.*, 2019, **13**, (7), pp. 1026–1032
[36] Nagel, J.R.: 'Fast finite-difference calculation of eddy currents in thin metal sheets', *ACES J.*, 2018, **33**, (6), pp. 575–584
[37] Gieras, J.F.: 'Analytical method of calculating the electromagnetic field and power losses in ferromagnetic half space, taking into account saturation and hysteresis', *Proc. Inst. Electr. Eng.*, 1977, **124**, (11), pp. 1098–1104

3-2-2-6 A Novel Position Sensor with Conical Iron Core [J12]

A novel position sensor for pneumatic and hydraulic cylinder applications is presented in this paper. The solid iron core conical in shape surrounded by axisymmetric coils is an essential part of the proposed position sensor. The axisymmetric coils are used for excitation and voltage measurements. The conical solid iron core is annealed to homogenize the magnetic properties and to increase its permeability. This improves the performance of the position sensor in terms of sensitivity and linearity. Analytical and finite element analyses are utilized along with measurements in order to analyze the performance of the position sensor. The position sensor performs measurements of excitation coil inductance and pick-up coil voltages. Various frequencies are considered for the analysis and for the measurements. The measurement results show that the maximum linearity error is about 4% for the manufactured sensor, and it is calculated to have a maximum value of 1% for the theoretical model. The achievable resolution of the proposed sensor is about 0.4 mm.

Experimental results and theoretical calculations have been presented for a position sensor with a conical solid iron core. Despite its simplicity, the proposed position sensor shows promising performance. The main purpose of the position sensor is for detecting the position of the piston in pneumatic cylinders and in hydraulic cylinders. However, it could be operated for a wide range of industrial applications. A 2D axisymmetric analytical method and 2D axisymmetric FEM were used to evaluate and analyze the performance of the position sensor. An analytical method is preferred in the design and optimization stages rather than 2D FEM, as a parametric analysis of the position sensor is easier and faster. It is preferable to operate the position sensor at high frequencies; 400 Hz and above is preferable, as the dynamic performance is better. High precision of large range position measurements can be achieved with the conical iron rod configuration, without the use of a long excitation coil and pick-up coils. The linearity of the results presented here can be improved by an iron rod with a smoother conical surface, as the angle of the conical surface slope must be constant in whole range of the conical part. Optimizing the conical iron rod and the size and the positions of the coils could improve the linearity and could reduce the linearity error to considerably below 1%. It has been shown that proper annealing of the iron rod has a considerable impact on the performance of a position sensor in terms of increasing the sensitivity and the linearity, as the magnetic permeability is increased and is homogenized especially in the machined conical surface.

A Novel Position Sensor with Conical Iron Core

Mehran Mirzaei, Pavel Ripka and Vaclav Grim

Faculty of Electrical Engineering, Czech Technical University, Prague 16627, Czech Republic
(e-mail: mirzameh@fel.cvut.cz).

***Abstract*— A novel position sensor for pneumatic and hydraulic cylinder applications is presented in this paper. The solid iron core conical in shape surrounded by axisymmetric coils is an essential part of the proposed position sensor. The axisymmetric coils are used for excitation and voltage measurements. The conical solid iron core is annealed to homogenize the magnetic properties and to increase the permeability of the conical solid iron core. This improves the performance of the position sensor in terms of sensitivity and linearity. Analytical and finite element analyses are utilized along with measurements in order to analyze the performance of the position sensor. The position sensor performs measurements of excitation coil inductance and pick-up coil voltages. Various frequencies are considered for the analysis and for the measurements. The measurement results show that the maximum linearity error is about 4% for the manufactured sensor, and is calculated to have a maximum value of 1% for the theoretical model. The achievable resolution of the proposed sensor is about 0.4 mm.**

***Index Terms*—Novel position sensor, conical iron core, annealing, eddy current, measurements, analytical and finite element analysis**

I. Introduction

Contactless linear and angular position detection of target objects is always a challenging issue [1]-[3]. Piston position detection in a pneumatic aluminum cylinder and in a hydraulic solid iron cylinder is a problematic task, because the piston is shielded by conductive and magnetic covers [1]-[2]. The position of the piston in the cylinder is not symmetric. In addition, it is a one-sided movement, whereas LVDT position sensors [4] are two-sided moving armature budges.

Various internal and external sensors for pneumatic and hydraulic cylinders are implemented for detecting piston positions. In the case of a pneumatic cylinder, internal sensors are inserted into the piston rod. This is mechanically complicated, and the sensors are not cost-effective and are unreliable. Microwave and optical sensors implemented inside the cylinder display the

This work was supported in part by the Czech Technical University in Prague under Grant SGS18/187/OHK3/3T/1.

same problems [5]-[8]. For an aluminum cylinder, a permanent magnet on the piston can be used in external sensors. However, this approach has some disadvantages. Firstly, it is necessary to use an expensive non-magnetic stainless steel rod. Stainless non-magnetic steel must be used to cancel out the distortion of the permanent magnet fields caused by the magnetic iron rod. Secondly, mounting a permanent magnet on the piston is a complicated procedure. In addition, the temperature dependency of the remanence flux density of a permanent magnet is a major weakness in a harsh environment.

The authors recently presented an AC-excited contactless piston position transducer with axial excitation and detection of the radial magnetic field related to the end of a magnetically soft iron rod [2]. A moving ferromagnetic piston rod causes changes in the magnetic field, which are sensed by an array of integrated fluxgate sensors mounted on the outside of the aluminum cylinder. The uncorrected maximum static error was ±3 mm with achievable 0.1 mm resolution. The dynamic performance is a limiting factor for this sensor: the dynamic error is ±3 mm even at a speed of 0.2 m/s. Complex signal processing of the sensor array is required for this type of sensor. Similar limitations were faced when radial excitation by saddle coils was used [9].

A simpler method is to use a variable inductance sensor. This was presented for a hydraulic cylinder with a non-metallic shell [10]. A modified inductance method as a position sensor of a power cylinder with a carbon steel shell was employed in [1], using a differential coils configuration [11]. We have presented an analysis and experimental results confirming that variable inductance sensors can also be utilized for detecting the piston position in pneumatic cylinder with an aluminum shell [12]. The inductance of solenoid coils wound around an aluminum cylinder changes with the position of the magnetic iron rod and the position of the piston, which is affected by the induced eddy current in the aluminum shell. The temperature stability of a variable inductance sensor for a pneumatic cylinder was studied in [13]. The dynamic performance of the variable inductance position sensor is problematic. A faster and more reliable solution, especially for dynamic performance, is to read and measure the voltage, e.g. the pick-up coil voltage of a second coil wound around the first layer of the coil on the aluminum cylinder [14]. Measuring the pick-up voltage for a position sensor is a well-known method for LVDT sensors with various cylindrical and flat types shape configurations [15]-[18]. An alternative to the configuration for the variable inductance sensor in [1], [10] and [12]-[14] is to implement coils around the iron rod instead of the cylinder. However, this is a cumbersome task, because of the long coil that is used for pneumatic and hydraulic cylinders [19]. Moving coils have problems with reliability in a harsh environment.

In this paper, we present a novel position sensor with a conical solid iron rod. It has one excitation coil and two pick-up coils with axisymmetric configurations. The novel position sensor in this paper is simple, cost effective, compact and free of expensive materials, for example, permanent magnets and stainless steel. The new idea of conical iron rod used as piston iron rod could be constructed from any mechanical stable construction iron steel and it is no need to use special steel, for example, stainless steel. The concept of proposed position sensor is nondestructive for hydraulic and pneumatic cylinders. And no additional elements and sensor are added in cylinders, which are the main disadvantage of previous industrial concepts for the

position sensor in hydraulic and pneumatic cylinders. Compared to existing designs, our sensor has no moving coils, compact size and simple design.. Because of that it is very robust against external harsh environment. Unlike DC sensors based on magnet attached to the piston, which require expensive stainless-steel piston rod material, the conical piston rod used in our sensor can be made of ordinary steel, which is cost effective.

The inductance of the excitation coil and the induced voltage in the serially connected pick-up coils change with the displacement of the conical iron rod. The proposed position sensor is short and has small coils, which makes it appropriate and easy to mount in hydraulic and pneumatic cylinders. The inductance measurements are performed with an LCR meter, and precise measurements of the voltage of the pick-up coils voltage are made with a lock-in amplifier. 2D axisymmetric analytical and finite element analyses with an eddy current solver are performed in order to evaluate the performance of a position sensor with a conical solid iron core at different frequencies, along with the measurements.

II. Model of the Position Sensor

A. Structure

A 3D model of the proposed position sensor with a conical solid iron rod with an axisymmetric configuration is shown in Fig. 1. One excitation coil and two serially connected pick-up coils on the left and right sides of the excitation coil are used for the position sensor. Fig. 2(a) shows the 2D schematic side view for the position sensor with a conical iron rod. The iron is solid, and the induced eddy current in the iron rod is investigated in this paper. The full-scale moving range of the position sensor is 500 mm.

B. Dimensions and parameters

The dimensions and the parameters of the position sensor are presented in Table I, according to Fig. 2 (a).

TABLE I

DIMENSIONS AND PARAMETERS OF THE POSITION SENSOR

Parameter	Value
N_e	100
N_p	50
I_a	65.12 (mA)
L	700 (mm)
L_1	0 (mm)
L_2	40 (mm)
D_1	19.7 (mm)
D_2	30 (mm)
D_w	40 (mm)
l_e	10.4 (mm)
l_p	5.35 (mm)
d_w	1.75 (mm)
h_w	0.5 (mm)
σ_i	5.54 (MS/m)
$\mu_{r\text{-}i}$	115

where N_e is the number of turns in the excitation coil, and N_p is the number of turns in the pick-up coil, I_a is the rms value of current in the excitation coil, σ_i is the conductivity of the iron rod at room temperature, and $\mu_{r\text{-}i}$ is the relative magnetic permeability of the iron rod.

III. PERFORMANCE ANALYSIS OF THE POSITION SENSOR

An analytical method is used for fast analysis and parametric calculations of a position sensor with a conical iron rod using the simplified model in Fig. 2 (b). The conical iron rod is replaced by the equivalent cylindrical model in order to compute the magnetic and electric parameters analytically. Diameter D_m in Fig. 2 (b) is calculated equal to the diameter of the conical iron rod corresponding to the position of the midpoint of the excitation coil. The effective diameter, D_m, in the analytical model of the equivalent cylindrical rod is adjusted for each position of the coils. The self-inductance of the excitation coil and the pick-up coil voltage with an air core and an iron core in (A5) – (A6) are calculated using appendix A.

This article has been accepted for publication in a future issue of this journal, but has not been fully edited. Content may change prior to final publication. Citation information: DOI 10.1109/TIM.2020.2999691, IEEE Transactions on Instrumentation and Measurement

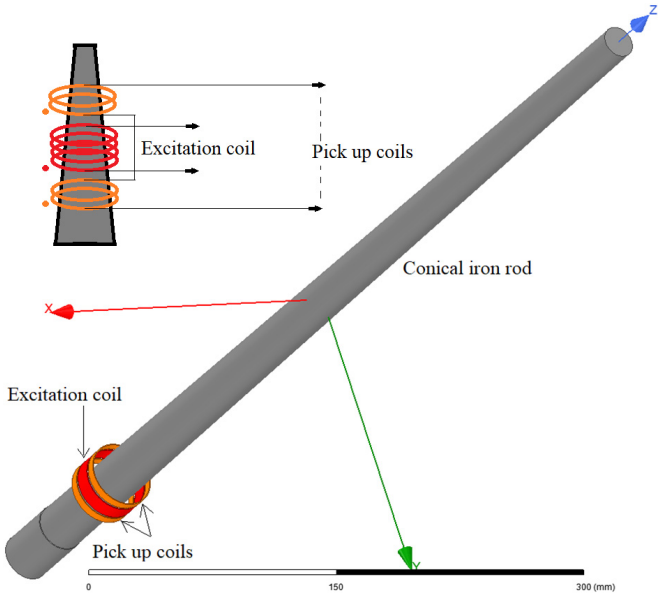

Fig. 1. 3D model of a position sensor with a conical iron rod with an excitation coil and two serially connected pick-up coils

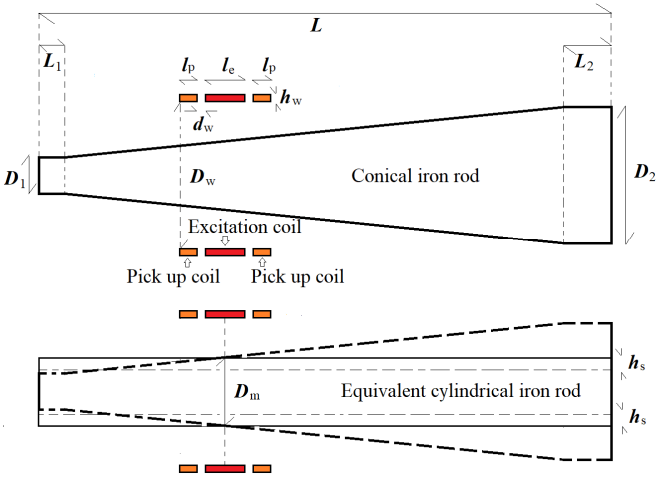

Fig. 2. Schematic model of the side view of the position sensor with a conical iron rod, (a) the real conical model (top), (b) the equivalent cylindrical model for a conical iron rod (bottom)

The relative initial magnetic permeability is considered in this paper, as the magnetic fields of the excitation coil are very small. The *B-H* curve and the relative magnetic permeability curve are presented in appendix B for the iron rod material. The typical value, 115, is estimated for the relative magnetic permeability of a solid iron structure, in Table I. The relative initial magnetic permeability of typical construction steels can vary between 50 and 200 without annealing [20]. This will be measured and analyzed in the sections below.

Firstly, the inductance of the excitation coil and the voltage of the pick-up coils are calculated and are compared with measurements with an air core and with a cylindrical (non-conical) iron core, in order to validate the analytical formulas in (A5)-

(A8). A comparison between analytical calculations and the measurement results is presented in Table II and III. This comparison shows the high precision of the analytical method. The cylindrical iron rod (non-conical) is 520 mm in length and 30 mm in diameter. The coils are located in the middle of the axial length of the iron rod, in order to minimize finite axial length effects.

Fig. 3 shows analytical calculations of the excitation coil inductance and the pick-up coil voltages of a position sensor with a conical iron core (parameters and dimensions as in Table I at 100 Hz, 200 Hz, 400 Hz and 1000 Hz). Excellent linearity is observed. The excitation coil inductance decreases with frequency due to the smaller skin and flux penetration depth in the solid iron core and the higher magnetic reluctance. The pick-up coil voltage increases with frequency. The sensitivity of the imaginary component of the voltage is higher than the real component of the voltage. The zero position in the graphs corresponds to the point at a distance of 100 mm from the head of the conical iron rod (a smaller diameter, D_1, in Fig. 2). The imaginary component (Im) and the real component (Re) of the voltage are calculated based on the excitation coil current as a reference signal.

TABLE II

A COMPARISON BETWEEN ANALYTICAL AND EXPERIMENTAL RESULTS WITH AN AIR CORE

Parameter	Exp./Ana.
$L_{s\text{-}air}$	577 (μH)/570(μH)
$U_{p\text{-}air}$– 100 Hz	10.71 (mV)/10.45(mV)

TABLE III

A COMPARISON BETWEEN ANALYTICAL AND EXPERIMENTAL RESULTS WITH AN IRON CYLINDRICAL CORE

Parameter	Experiment /Analytical (μ_r=115)
$L_{s\text{-}iron}$-20 Hz	2.28 (mH) / 2.25(mH)
$L_{s\text{-}iron}$-100 Hz	1.62 (mH)/ 1.66(mH)
$L_{s\text{-}iron}$-200 Hz	1.40 (mH) / 1.44(mH)
$L_{s\text{-}iron}$-400 Hz	1.22 (mH) / 1.26(mH)
$U_{p\text{-}iron}$– 1 Hz	0.25+i·1.14 (mV) / 0.04+i·1.09 (mV)
$U_{p\text{-}iron}$– 20 Hz	5.88+i·15.80 (mV) / 4.78+i·15.17 (mV)
$U_{p\text{-}iron}$– 100 Hz	23.11+i·52.02 (mV) / 20.04+i·51.66 (mV)
$U_{p\text{-}iron}$– 200 Hz	39.90+i·85.83 (mV) / 35.53+i·86.41 (mV)
$U_{p\text{-}iron}$– 400 Hz	67.56+i·141.12 (mV) / 61.93+i·143.58 (mV)

This article has been accepted for publication in a future issue of this journal, but has not been fully edited. Content may change prior to final publication. Citation information: DOI 10.1109/TIM.2020.2999691, IEEE Transactions on Instrumentation and Measurement

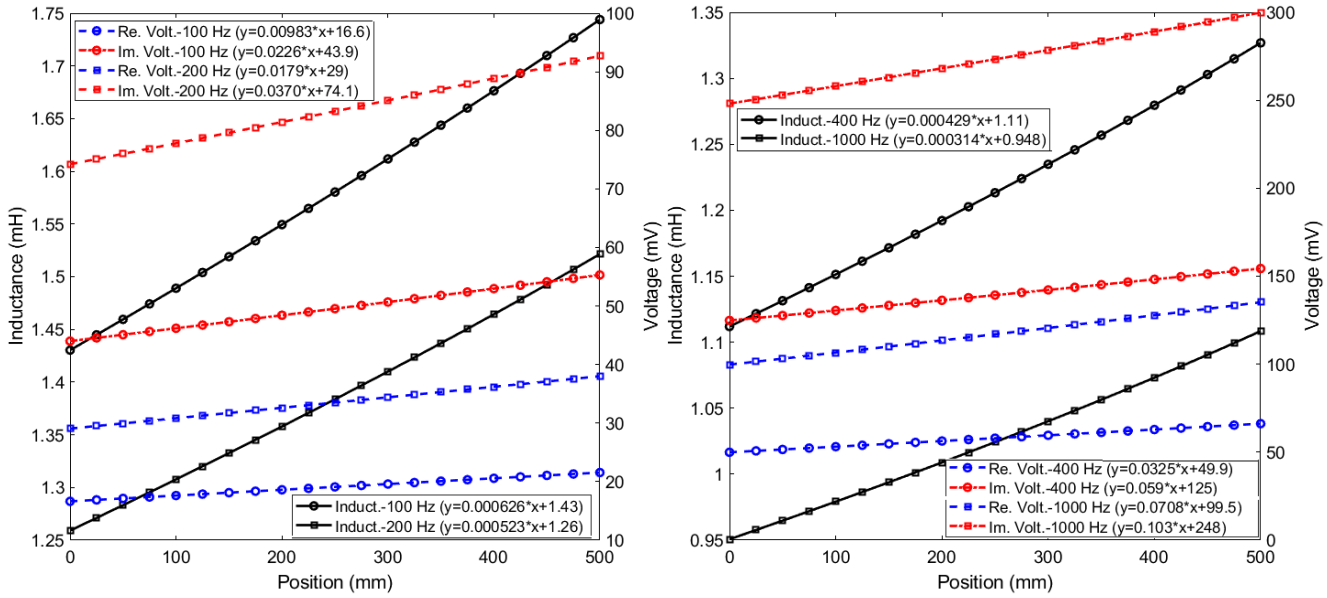

Fig. 3. Variation of the excitation coil self-inductance and the pick-up coil voltage at 100 Hz, 200 Hz, 400 Hz and 1000 Hz (μ_r=150) - analytical

IV. Experiments

Fig. 4 shows the experimental setup and elements for a position sensor with a conical iron rod. A SR865 2 MHz DSP lock-in amplifier (LIA) and an HP 4263B LCR meter are used for the voltage and inductance measurements. The excitation coil is connected to a Keithley 3390 50-MHz signal generator with internal resistance of 50 Ω. The serially connected pick-up coils are directly connected to the input terminal IN-A of the LIA without any interface. The terminal for the reference signal of the LIA is connected in parallel with small resistance, which is serially connected with the excitation coil. Therefore, the excitation coil current is the reference signal and the real and imaginary components of the pick-up coil voltage can be measured relative to the excitation coil current. The excitation and pick-up coils are electrically connected for grounding via the LIA. The maximum output voltage of the signal generator is selected as 10 V (amplitude) to get the maximum excitation current and the maximum sensor output and sensitivity. The conical iron rod was manufactured using a machine tool from a cylindrical iron rod 700 mm in axial length and 30 mm in diameter. The surface of the conical iron part was not faultlessly smooth, which can affect the linearity of the proposed position sensor.

A. Without Annealing

Fig. 5 shows the magnetic flux distribution using 2D axisymmetric FEM [21], using a time harmonic (eddy current) solver at different positions of the coils relative to the conical iron rod. An ideal shape and surface are considered for the conical iron rod model in the FEM simulations according to Table I. The simulations and measurements range is 500 mm from 100 mm of conical iron rod head to 600 mm as shown in Fig. 5.

This article has been accepted for publication in a future issue of this journal, but has not been fully edited. Content may change prior to final publication. Citation information: DOI 10.1109/TIM.2020.2999691, IEEE Transactions on Instrumentation and Measurement

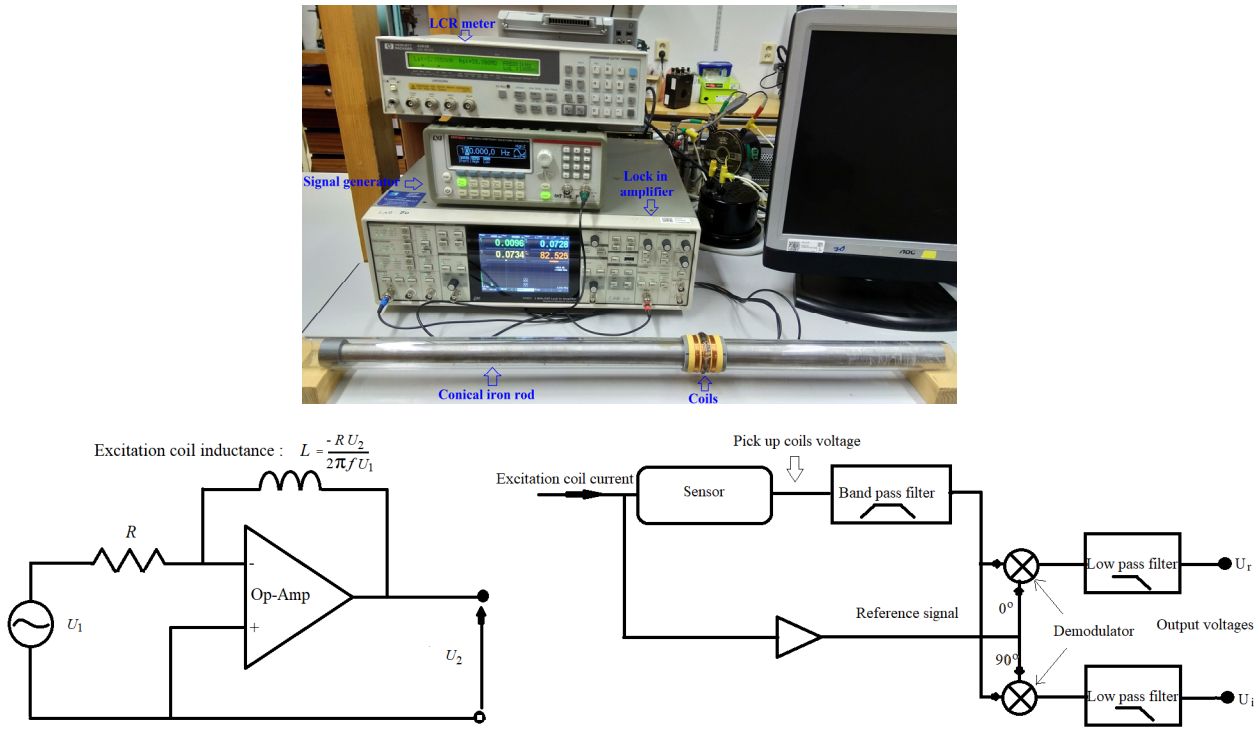

Fig. 4. Measurement elements for the position sensor, the LCR meter, the signal generator, the lock-in amplifier, the coils and the conical iron rod and schematic diagram of inductance meter and lock in amplifier

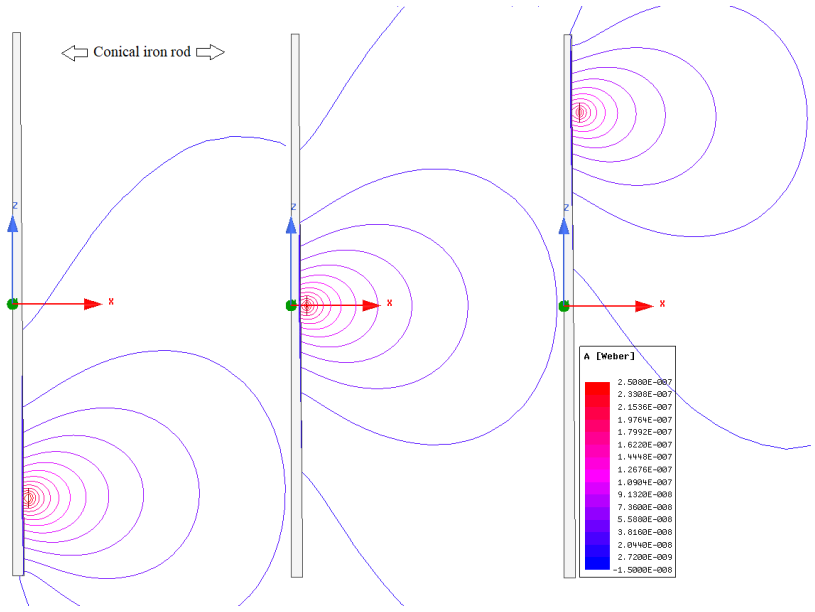

Fig. 5. Distribution of the magnetic flux lines for different positions of the coils using FEM, (left) coil position at 500 mm, (middle) coil position at 250 mm, (right) coil position at 0 mm (f=100 Hz) – the total axial length of the iron is 700 mm

The measured and simulated self-inductance and pick-up voltage values versus the coil position are depicted in Fig. 6, without annealing at 100 Hz and 400 Hz. The analytical results correspond very well with FEM, which shows negligible effects of the approximations used in the analytical method.

This article has been accepted for publication in a future issue of this journal, but has not been fully edited. Content may change prior to final publication. Citation information: DOI 10.1109/TIM.2020.2999691, IEEE Transactions on Instrumentation and Measurement

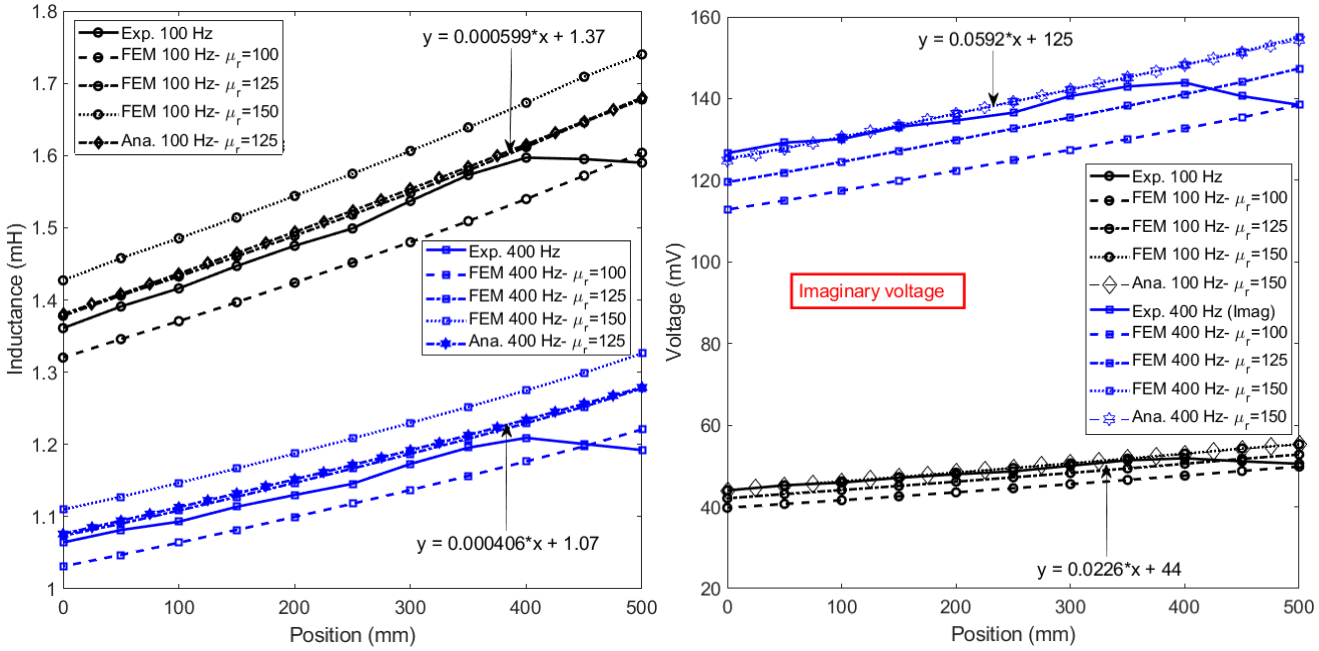

Fig. 6. Variation of the excitation coil self-inductance and the pick-up coil voltage at 100 Hz and at 400 Hz – non-annealed

The estimated relative magnetic permeability is about 125 using the inductance measurement, and it is estimated to be about 150 using the measured pick-up voltage. The excitation coil current is smaller for the inductance measurement using the LCR meter than the current for pick-up coil voltage measurement using a lock-in amplifier. The magnetic field that is produced is therefore lower in the iron rod for the inductance measurements because the current is lower. The magnetic permeability is higher for a high current or for the equivalent magnetic field strength in the iron rod, as the operating point is in the Rayleigh region of the *B-H* curve.

The inductances and the pick-up voltages increase monotonically until position 400 mm, and then they decrease until position 500 mm, which is not expected for the FEM and analytical calculations. The first reason for this is the non-smooth conical surface near the end position, 500 mm due to machining. The second reason is presumed to be a non-homogenized magnetic permeability distribution, again due to machining. This could be minimized with proper annealing [22]. With more precise machining or casting, the non-straight measured curves and their fluctuations in the whole range of measured positions, in comparison with the straight curve of the simulated values, could also be improved by annealing and removing the salient parts in the conical surface.

B. With Annealing

The relaxation and homogenization annealing process is performed in order to improve the magnetic properties of the conical iron rod. The rod was annealed in vacuum, for 2 hours at 800 ^{o}C, was slowly (8 hours) cooled down to 500 ^{o}C, and was rapidly cooled (1h) to room temperature (appendix C). In order to evaluate the annealing effect, firstly two small samples (annealed and

This article has been accepted for publication in a future issue of this journal, but has not been fully edited. Content may change prior to final publication. Citation information: DOI 10.1109/TIM.2020.2999691, IEEE Transactions on Instrumentation and Measurement

non-annealed) 70 mm in axial length and 30 mm in diameter, from the same material as the conical iron rod, were used for the measurements and the simulations, as shown in Fig. 7.

TABLE IV

A COMPARISON BETWEEN ANALYTICAL AND EXPERIMENTAL RESULTS WITH AN IRON CORE-NON-ANNEALED

Parameter	Experiment / FEM (μ_r=115)
$L_{s\text{-}iron}$-20 Hz	1.61 (mH) / 1.62 (mH)
$L_{s\text{-}iron}$-100 Hz	1.44 (mH) / 1.47(mH)
$L_{s\text{-}iron}$-200 Hz	1.33 (mH) / 1.37 (mH)
$L_{s\text{-}iron}$-400 Hz	1.21 (mH) / 1.25 (mH)
$U_{p\text{-}iron}$– 1 Hz	0.09+i·0.51 (mV) / 0.01+i·0.52 (mV)
$U_{p\text{-}iron}$– 20 Hz	1.0+i·9.87 (mV) / 0.85+i·9.86 (mV)
$U_{p\text{-}iron}$– 100 Hz	8.57+i·43.22 (mV) / 7.51 +i·43.41 (mV)
$U_{p\text{-}iron}$– 200 Hz	19.92+i·77.88 (mV) / 17.72+i·79.21 (mV)
$U_{p\text{-}iron}$– 400 Hz	42.4+i·136.1 (mV) / 39.41+i·140.4 (mV)

TABLE V

A COMPARISON BETWEEN ANALYTICAL AND EXPERIMENTAL RESULTS WITH AN IRON CORE-ANNEALED

Parameter	Experiment / FEM (μ_r=400)
$L_{s\text{-}iron}$-20 Hz	1.70 (mH) / 1.70 (mH)
$L_{s\text{-}iron}$-100 Hz	1.61 (mH) / 1.61(mH)
$L_{s\text{-}iron}$-200 Hz	1.53 (mH) / 1.54 (mH)
$L_{s\text{-}iron}$-400 Hz	1.44 (mH) / 1.46(mH)
$U_{p\text{-}iron}$– 1 Hz	0.09+i·0.55 (mV) / 0.01+i·0.54 (mV)
$U_{p\text{-}iron}$– 20 Hz	0.68+i·10.60 (mV) / 0.53+i·10.46 (mV)
$U_{p\text{-}iron}$– 100 Hz	5.63+i·49.80 (mV) / 5.13+i·48.75 (mV)
$U_{p\text{-}iron}$– 200 Hz	13.80+i·95.02 (mV) / 13.05+i·92.52 (mV)
$U_{p\text{-}iron}$– 400 Hz	32.60+i·178.65 (mV) / 31.89+i·172.05 (mV)

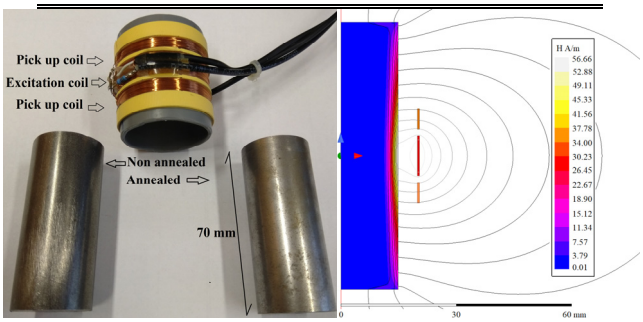

Fig. 7. Annealed and non-annealed iron rods 70 mm in length (left), and the magnetic flux distribution and the magnetic field strength at f= 100 Hz with μ_r=115 (right)

This article has been accepted for publication in a future issue of this journal, but has not been fully edited. Content may change prior to final publication. Citation information: DOI 10.1109/TIM.2020.2999691, IEEE Transactions on Instrumentation and Measurement

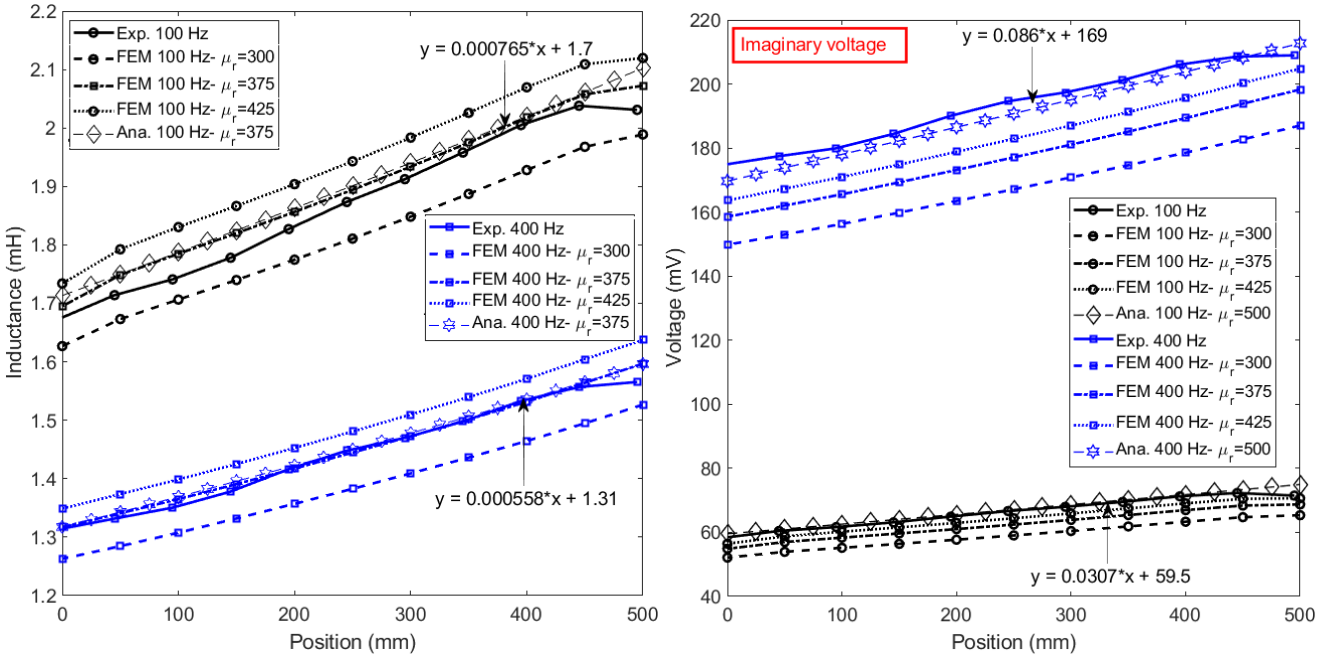

Fig. 8. The variation in the excitation coil self-inductance and the pick-up coil voltage at 100 Hz and 400 Hz –annealed

Tables IV and V present a comparison of measurement results with and without annealing. The estimated relative magnetic permeability is increased 3.5 times (400/115) in the annealed sample relative to the non-annealed sample. The maximum change in the results due to annealing occurred at 400 Hz, where there was a change of about 20%.

A monotonic increase in the measured inductances and voltages continued until 450 mm in the annealed conical iron rod (Fig. 8). This shows a larger linear range and values closer to the simulations results. It can be assumed that the break point in the measurement curves at 450 mm was caused by imperfect machining of the conical surface. Annealing increases the sensitivity of the position sensor between 25% in the inductance values at 100 Hz and 45% in the voltage values at 400 Hz due to the higher magnetic permeability.

The simulated voltages and inductances (Fig. 8) after annealing of the conical iron rod at 100 Hz is less linear, especially after the start point and before the end point in the annealed iron core. This could be caused by the increased relative magnetic permeability and higher finite length effects.

Magnetic yoke around the coils using thin permalloy tape or silicon steel lamination increases the sensitivity of the position sensor and shields it against external magnetic fields. This phenomenon will be investigated in our future work to evaluate the increasing sensitivity and the improving linearity.

V. Linearity Analysis

The piston stroke and the realistic range of movement of the piston are typically shorter than the cylinder length for a real

pneumatic cylinder, as reported by our team in [14]. The linearity analysis was therefore performed between 50 mm and 450 mm. The range of movement of the piston was reported to be practically 400 mm in [14]. The linear curve function between the relative position of the coils and conical iron rod, X (mm) versus the inductance or the voltage, Y (mH or mV) is presented as follows:

$$X = C \cdot Y + X_0 \quad (1)$$

Table VI presents the values of the parameters in (1). The linearity error is calculated from the linear curve function values, X_l, in (1) and the experimental values, X_m, for a 400 mm stroke using as follows:

$$Error\ (\%) = (X_l - X_m)/400 \cdot 100 \quad (2)$$

TABLE VI

THE LINEAR CURVE FUNCTION BETWEEN THE RELATIVE POSITION OF THE COILS AND THE CONICAL IRON ROD, X, VERSUS THE MEASURED INDUCTANCE OR VOLTAGE, Y

Curves	$X=C\cdot Y+X_0$
$L_{s\text{-}iron}$-100 Hz	1181·Y-1966
$L_{s\text{-}iron}$-200 Hz	1411·Y-2072
$L_{s\text{-}iron}$-400 Hz	1717·Y-2232
$L_{s\text{-}iron}$-1000 Hz	2249·Y-2498
$U_{p\text{-}iron}$– 100 Hz	32.56·Y-1918
$U_{p\text{-}iron}$– 400 Hz	12.24·Y-2121

The error calculations are shown in Fig. 9, which has maximum values of about 4% for the experimental results. The overall linearity using the measured inductance at 200 Hz (Fig. 10) is the finest results in terms of linearity. The error results for the analytical calculations show a maximum error of 1% for a 400 mm stroke, which can be achieved for a precisely machined rod. It should be noted that these results were obtained without any corrections.

The linearity errors using the analytical model increase at extreme positions of 25 mm and 475 mm, because of the finite length effects (end effects) of the conical iron rod. The first suggestion is to increase the axial length of the conical iron rod in order to reduce the finite length effect errors. The second suggestion is to optimize the dimensions of the coils and of the conical surface in order to minimize the linearity error caused by the finite length of the iron rod. However, this topic lies beyond the scope of our paper.

This article has been accepted for publication in a future issue of this journal, but has not been fully edited. Content may change prior to final publication. Citation information: DOI 10.1109/TIM.2020.2999691, IEEE Transactions on Instrumentation and Measurement

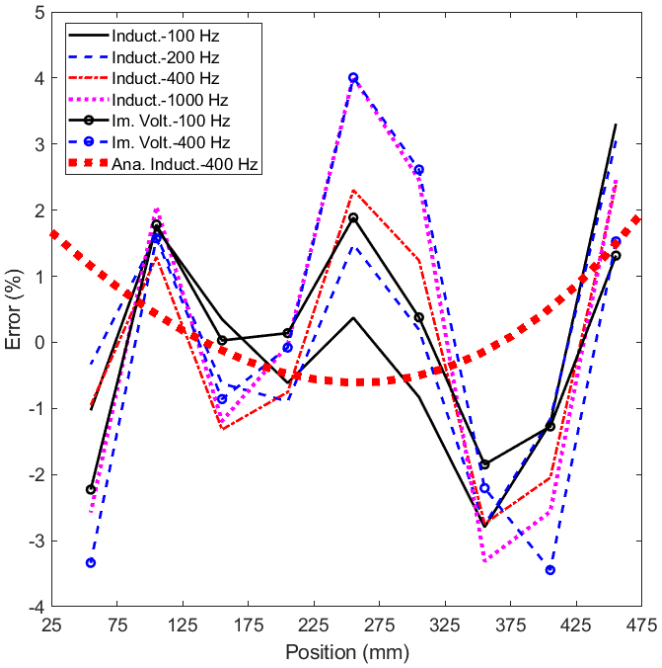

Fig. 9. Error calculations for a 400 mm stroke based on the inductance and voltage values– using an annealed conical iron rod

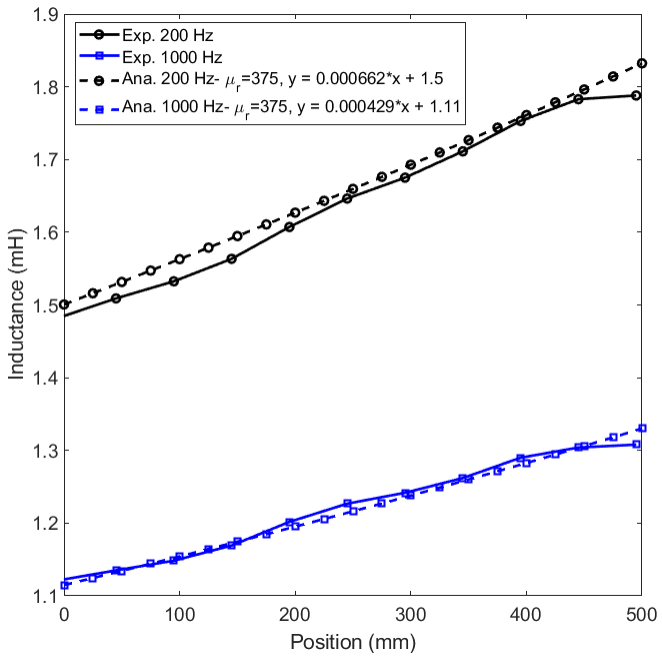

Fig. 10. Variation of the excitation coil self-inductance at 200 Hz and at 1000 Hz –annealed

The conical iron rod diameters were measured at each distance of 1 cm for precise modeling of the real surface of the manufactured conical iron rod in the FEM environment. A comparison of the FEM results between a more precise model of the manufactured conical iron surface and the smooth (perfect) surface of the conical iron rod is shown in Fig. 11. It confirms that some nonlinearities in the measurement results are caused by the non-uniform and non-smooth surface of the manufactured conical iron rod.

This article has been accepted for publication in a future issue of this journal, but has not been fully edited. Content may change prior to final publication. Citation information: DOI 10.1109/TIM.2020.2999691, IEEE Transactions on Instrumentation and Measurement

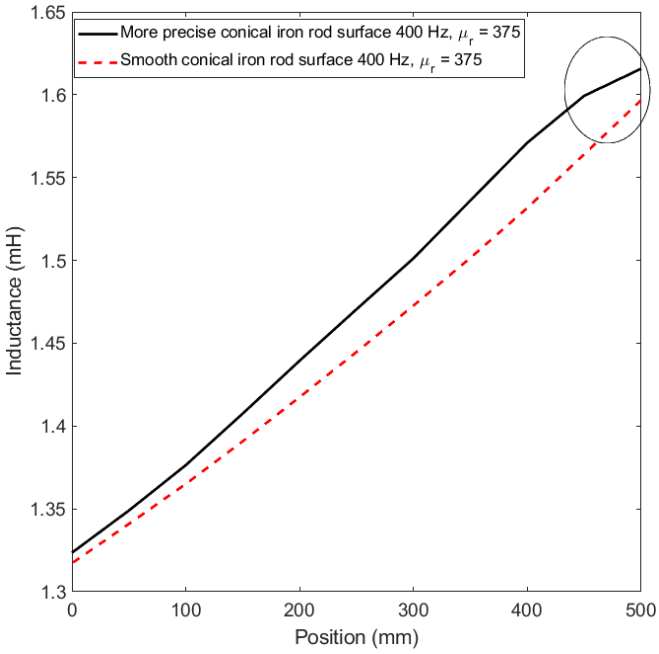

Fig. 11. A comparison between the FEM results for the smooth ideal surface and for more precise surface modeling of the manufactured conical iron rod

VI. Discussion

A potential method for compensating the temperature, the material effects of the solid iron rod, and the changes in eccentricity is the multi-frequency sensor technique and the pulsed eddy current method [23]-[24], which will be investigated in future work. The temperature of the iron rod changes the electrical conductivity and the magnetic permeability, which affect the reluctance of the magnetic flux path and the magnetic flux penetration depth, h_s (Fig. 2 b), and the skin effect depth, δ.

The non-uniformity of the depth on the surface of the conical iron rod strongly affects the measurement accuracy in terms of fluctuations of the results if it is greater than the skin depth [4]:

$$\delta = \sqrt{\frac{2}{\omega\mu\sigma_i}}, \qquad \omega = 2\pi f \tag{3}$$

where, μ, σ_i and f are the magnetic permeability, the electrical conductivity and the frequency, respectively. In addition, the use of artificial neural networks to make the conical surface as perfect as possible can prevent fluctuations of the results, and can improve the linearity by about one order of magnitude [18].

Recent works on alternative configurations of position sensors using an ironless inductive position sensor [25], and a variable reluctance differential solenoid transducer [26], cannot be applied to pneumatic cylinders and hydraulic cylinders with a large

range of operating positions.

Despite its simplicity, the analytical method developed here has almost the same accuracy as 2D FEM, because the effects of the finite length of the iron rod are negligible at frequencies above 400 Hz, even with high relative magnetic permeability of about 400-500. Analytical methods are always preferable to numerical calculations [27], if their accuracy is within a satisfactory range [24].

Voltage measurements are more dynamic, are preferable, and are suitable for position measurements relative to the inductance measurement. Two serially connected pick-up coils on the left and right sides of the excitation coil is preferred to a single pick-up on one side of the excitation coil, in order to avoid end effects (the finite axial length effect of conical iron) by vectorial summation or by averaging the voltages of the two pick-up coils. The pick-up voltage can be on top of the excitation coil if the excitation coil inductance is required for position measurements. The induced voltage will be proportional to the inductance of the excitation coil because of the high coupling between the excitation coil and the pick-up coils. The use of fast rms measurements of voltages is not recommended, as rms or the absolute value is the vectorial summation of the real and imaginary components of the voltage. This will be less linear than the linearity of the individual real and imaginary components. The main drawback of measuring a real or imaginary component could be less dynamic performance of the sensor because of more time-consuming signal processing. However, it is more tolerant to noise than a simple rms reading.

The proposed position sensor is cost effective, small compact for structure of excitation and pick up and measurement system and it can be easily shielded and protected against external magnetic elements and fields, which is its main advantage to previous academic and industrial position sensors for hydraulic and pneumatic cylinders [1], [5] and [10]. The proposed position sensor has simple signal processing unit, which is a merit to reduce cost and increase fault tolerant capability of the sensor in the harsh environment.

One possible limitation of the proposed position sensor is when it operates in variable temperature environments without temperature compensation: temperature affects the magnetic permeability, the conductivity and the performance of the sensor. Real or imaginary component can be evaluated by single-chip LIA such as AD630, so that the cost is not significantly higher than evaluation rms. Another advantage of using LIA is that the sensor is less sensitive to noise and interference in comparison with simple rms reading.

VII. Conclusion

Experimental results and theoretical calculations have been presented for a position sensor with a conical solid iron core. Despite its simplicity, the proposed position sensor shows promising performance. The main purpose of the position sensor is for detecting the position of the piston in pneumatic cylinders and in hydraulic cylinders. However, it could be operated for a wide

range of industrial applications.

A 2D axisymmetric analytical method and 2D axisymmetric FEM were used to evaluate and analyze the performance of the position sensor. An analytical method is preferred in the design and optimization stages rather than 2D FEM, as a parametric analysis of the position sensor is easier and faster. It is preferable to operate the position sensor at high frequencies; 400 Hz and above is preferable, as the dynamic performance is better.

High precision of large range position measurements can be achieved with the conical iron rod configuration, without the use of a long excitation coil and pick-up coils. The linearity of the results presented here can be improved by an iron rod with a smoother conical surface, as the angle of the conical surface slope must be constant in whole range of the conical part. The maximum linearity error was shown to be 4% for the measurement results of the manufactured model, and the maximum error was 1% for the theoretical model. Optimizing the conical iron rod and the size and the positions of the coils could improve the linearity and could reduce the linearity error to considerably below 1%. This is a topic for investigation in future work. The effect of the iron rod materials must be taken into consideration and must be compensated, as construction steels and irons have different initial permeability and electrical conductivity.

It has been shown that proper annealing of the iron rod has a considerable impact on the performance of a position sensor in terms of increasing the sensitivity and the linearity, as the magnetic permeability is increased and is homogenized especially in the machined conical surface.

Using proposed position sensor in this paper for pneumatic and hydraulic cylinders simplify signal processing unit of the sensor and avoid using destructive methods on the cylinders unlike previous concepts. It has merits in terms of simplicity, cost effective and compactness, which is always demanded in industrial applications with mass productions.

In order to provide increased sensitivity and improved linearity for future work on this topic, it is necessary to achieve precise manufacturing of the conical iron rod in order to have a faultless conical surface; to optimize the dimensions and the relative positions of the coils; to calculate the optimum axial length of the conical iron; and to use a magnetic yoke and shielding. A dynamic analysis of the performance of the sensor in transient conditions and an evaluation of thermal stability are also required in order to present the proposed sensor for industrial applications.

APPENDIX A: ANALYTICAL EQUATIONS

A sketch of the conical iron rod is transformed into an equivalent cylindrical rod with diameter D_{m} (Fig. 2). The diameter, D_{m}, is calculated equal to the diameter of the conical iron rod corresponding to the midpoint position of the coils, as shown in Fig. 2.

The governing differential equations versus the magnetic vector potential for three regions ($A_{\phi,1}$ the part of the air beyond the coils in region 1, $A_{\phi,2}$ for region 2 in the part of the air between the iron rod and the coil, and $A_{\phi,3}$ for the iron rod in region 3) in

This article has been accepted for publication in a future issue of this journal, but has not been fully edited. Content may change prior to final publication. Citation information: DOI 10.1109/TIM.2020.2999691, IEEE Transactions on Instrumentation and Measurement

the computational model of Fig. A1 are extracted from the Maxwell equations in the cylindrical coordinates [28] – [31]. The coil area regions are transformed into line regions to simplify the computational model, as the radial thickness of the coils is just 0.5 mm (Fig. A1). Only the azimuthal component of the magnetic vector potential, A_ϕ, is considered, because of the axisymmetric structure [28]:

$$1/r\,\partial/\partial r\left(r\,\partial A_{\phi,1}/\partial r\right)+\partial^2 A_{\phi,1}/\partial z^2-A_{\phi,1}/r^2=0$$

$$1/r\,\partial/\partial r\left(r\,\partial A_{\phi,2}/\partial r\right)+\partial^2 A_{\phi,2}/\partial z^2-A_{\phi,2}/r^2=0$$

$$1/r\,\partial/\partial r\left(r\,\partial A_{\phi,3}/\partial r\right)+\partial^2 A_{\phi,3}/\partial z^2-A_{\phi,3}/r^2=\sigma_i\cdot\mu_3\cdot\partial A_{\phi,3}/\partial t$$

(A1)

The method of separation of variables (the Fourier method) is used to solve (A1) [27]-[31]. It is assumed that magnetic fields change sinusoidal versus time and periodically in z-direction with period length $2L$. Therefore derivations versus z and t (time) could be replaced as following:

$$A_\emptyset=R(r)\cdot Z(z)\cdot T(t) \qquad \text{(A2-1)}$$

$$Z(z)\propto\exp(-jm\cdot z),\quad m=\frac{n\pi}{L},\quad T(t)=\exp(j\omega\cdot t),\quad \omega=2\pi f$$
$$\frac{\partial A_\emptyset}{\partial t}=j\omega A_\emptyset,\quad \frac{\partial A_\emptyset}{\partial z}=-j|m|A_\emptyset,\quad \frac{\partial^2 A_\emptyset}{\partial z^2}=-m^2A_\emptyset \qquad \text{(A2-2)}$$

where, $\omega=2\pi f$ is angular frequency in rad/s. The solutions versus radius as follows:

$$A_{\phi,1}=\sum_{n=\pm1,\pm3,\cdots}\left(C_{11}I_1(|m|\cdot r)+C_{12}K_1(|m|\cdot r)\right)\cdot e^{j(\omega t-mz)}$$

$$A_{\phi,2}=\sum_{n=\pm1,\pm3,\cdots}\left(C_{21}I_1(|m|\cdot r)+C_{22}K_1(|m|\cdot r)\right)\cdot e^{j(\omega t-mz)}$$

$$A_{\phi,3}=\sum_{n=\pm1,\pm3,\cdots}\left(C_{31}J_1(\gamma\cdot r)+C_{32}Y_1(\gamma\cdot r)\right)\cdot e^{j(\omega t-mz)}$$

$$\gamma=\sqrt{-m^2-j\omega\mu_3\sigma_i}$$

(A2-3)

where I_1, J_1, $K_1$and Y_1 are Bessel functions with order 1 [32]. n is the space harmonic order. L is the axial length of the iron rod. C_{11}, C_{12}, C_{21}, C_{22}, C_{31} and C_{32} are constants that are obtained by the following boundary conditions between regions 1, 2 and 3:

$$A_{\phi,1}\left(\frac{D_w'}{2}\right)=A_{\phi,2}\left(\frac{D_w'}{2}\right),\qquad A_{\phi,2}\left(\frac{D_m}{2}\right)=A_{\phi,3}\left(\frac{D_m}{2}\right)$$

This article has been accepted for publication in a future issue of this journal, but has not been fully edited. Content may change prior to final publication. Citation information: DOI 10.1109/TIM.2020.2999691, IEEE Transactions on Instrumentation and Measurement

$$H_{z,1}\left(\frac{D'_w}{2}\right) - H_{z,2}\left(\frac{D'_w}{2}\right) = J_s, \qquad H_{z,2}\left(\frac{D_m}{2}\right) = H_{z,3}\left(\frac{D_m}{2}\right)$$

$$D'_w = D_w + h_w$$

$$J_s = \sum_{n=\pm1,\pm3,\cdots} J_{sn} \cdot e^{j(\omega t - mz)}, \qquad J_{sn} = \frac{2}{n\pi} sin\left(m\frac{l_e}{2}\right) \cdot \frac{N_e \cdot I_a}{l_e}$$

$$H_z = 1/r\,\partial/\partial r\left(rA_\phi\right)/\mu$$

(A3)

where, H_z is the magnetic field strength.

The self-inductance of the excitation coil, L_s and the pick-up coil voltage, U_p are calculated using following equations:

$$L_s = \frac{\Psi}{I_a} = \frac{N_e \cdot \int A_\phi ds}{I_a \cdot l_e},\ U_p = -j\omega\Psi = -j\omega\frac{N_p \cdot \int A_\phi ds}{l_p}, \qquad ds = rd\phi dz = 2\pi r dz = \pi D'_w dz$$

(A4)

Parameter A_ϕ in (A4) is the magnetic vector potential on the boundary between regions 1 and 2. We used $A_{\phi,3}$ in (A2-3) for integration in (A4). The integral in (A4) is performed on the boundary between regions 1 and 2, where the surface regions of the coils are simplified as a line region between regions 1 and 2 in Fig. A1 in 2D view, and they are cylindrical surfaces as shown in Fig. A1. The integration in (A4) is performed on the cylindrical surface of the coils as shown in Fig. A1. The integrations for the voltage of the two pick-up coils are summed, as they are serially connected.

The self-inductance of the excitation coil with an air core, $L_{\text{s-air}}$, and with an iron core, $L_{\text{s-core}}$, and the pick-up coil voltage with an air core, $U_{\text{p-air}}$, and with an iron core, $U_{\text{p-core}}$, are calculated in (A5) – (A8), using (A4).

$$L_{s-air} = \sum_{n=\pm1,\pm3,\cdots} C_a \frac{2\pi \cdot D'_w}{m \cdot I_a \cdot l_e} N_e \cdot \sin\left(\frac{m \cdot l_e}{2}\right), C_a$$

$$= \frac{\mu_0 \cdot J_{sn}}{m \cdot C'_a}, C'_a = \left(I_0\left(m\frac{D'_w}{2}\right)/I_1\left(m\frac{D'_w}{2}\right) + K_0\left(m\frac{D'_w}{2}\right)/K_1\left(m\frac{D'_w}{2}\right)\right)$$

(A5)

$$U_{p-air} = j\omega \cdot \sum_{n=\pm1,\pm3,\cdots} C_a \frac{4\pi \cdot D'_w}{m \cdot l_p} N_p \cdot \sin\left(\frac{m \cdot l_p}{2}\right) \cdot \cos\left(\frac{m \cdot \left(l_e + l_p + 2d_w\right)}{2}\right)$$

This article has been accepted for publication in a future issue of this journal, but has not been fully edited. Content may change prior to final publication. Citation information: DOI 10.1109/TIM.2020.2999691, IEEE Transactions on Instrumentation and Measurement

(A6)

$$L_{s-iron} = \sum_{n=\pm1,\pm3,\cdots} C_i \frac{2\pi \cdot D'_w}{m \cdot I_a \cdot l_e} N_e \cdot \sin\left(\frac{m \cdot l_e}{2}\right), C_i$$

$$= \frac{\mu_0 \cdot J_{sn}}{m \cdot C'_i}, C'_i$$

$$= \left(I_0\left(m\frac{D'_w}{2}\right) \cdot C''_{i-12} - K_0\left(m\frac{D'_w}{2}\right)\right)$$

$$/\left(I_1\left(m\frac{D'_w}{2}\right) \cdot C''_{i-12} + K_1\left(m\frac{D'_w}{2}\right)\right) + K_0\left(m\frac{D'_w}{2}\right)/K_1\left(m\frac{D'_w}{2}\right), C''_{i-12} = C''_{i-1}/C''_{i-2}, C''_{i-1}$$

$$= m \cdot K_0\left(m\frac{D_m}{2}\right) \cdot J_1\left(\lambda\frac{D_m}{2}\right) + \frac{\lambda}{\mu_{r-i}} \cdot K_1\left(m\frac{D_m}{2}\right)$$

$$\cdot J_0\left(\lambda\frac{D_m}{2}\right), C''_{i-2} = m \cdot I_0\left(m\frac{D_m}{2}\right) \cdot J_1\left(\lambda\frac{D_m}{2}\right)$$

$$-\frac{\lambda}{\mu_{r-i}} \cdot I_1\left(m\frac{D_m}{2}\right) \cdot J_0\left(\lambda\frac{D_m}{2}\right)$$

(A7)

$$U_{p-iron} = j\omega \cdot \sum_{n=\pm1,\pm3,\cdots} C_i \frac{4\pi \cdot D'_w}{m \cdot l_p} N_p \cdot \sin\left(\frac{m \cdot l_p}{2}\right) \cdot \cos\left(\frac{m \cdot \left(l_e + l_p + 2d_w\right)}{2}\right)$$

(A8)

where I_0, J_0 and K_0 are Bessel functions with order of 0 [32].

Fig. A2 shows the magnetic flux distribution calculated using an analytical method for different equivalent iron rod radiuses, which correspond to different positions of the coils relative to the conical iron rod, 500 mm, 250 mm and 0 mm.

This article has been accepted for publication in a future issue of this journal, but has not been fully edited. Content may change prior to final publication. Citation information: DOI 10.1109/TIM.2020.2999691, IEEE Transactions on Instrumentation and Measurement

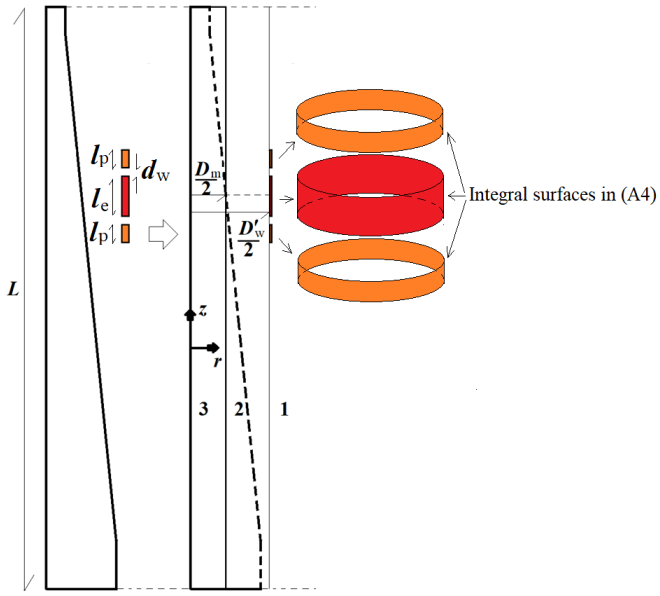

Fig. A1. Computational 2D axisymmetric model for a position sensor with a conical iron rod – transformation of the real shape of the conical iron rod to a cylindrical iron rod with the equivalent diameter, D_m, which changes with the position of the coils

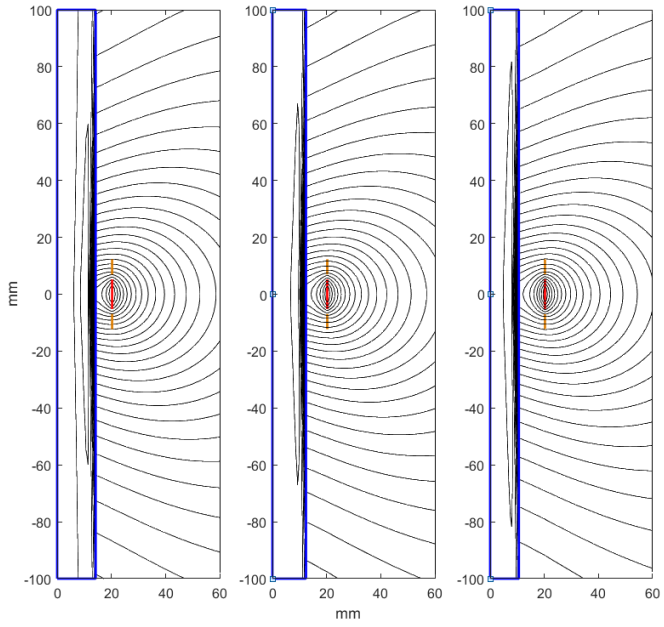

Fig. A2. The magnetic flux distribution for different positions of the coils, using an analytical method, equivalent iron rod radius = 14.2 mm (left) corresponding to coils position at 500 mm,, equivalent iron rod radius = 12.4 mm (middle) corresponding to coils position at 250 mm, equivalent iron rod radius = 10.6 mm (right) corresponding to coils position at zero position (0 mm) - (f=100 Hz, $\mu_{r\text{-}i}$= 125)

APPENDIX B: *B-H* CURVE AND MAGNETIC RELATIVE PERMEABILITY CURVE

Fig. B1 presents the *B-H* curve and the magnetic relative permeability curve of a solid iron conical rod [33]. The initial relative magnetic permeability is extrapolated. It is estimated to be about 100 to 150, as it would be problematic to make direct measurements of the *B-H* curve and of the relative magnetic permeability at low magnetic fields.

This article has been accepted for publication in a future issue of this journal, but has not been fully edited. Content may change prior to final publication. Citation information: DOI 10.1109/TIM.2020.2999691, IEEE Transactions on Instrumentation and Measurement

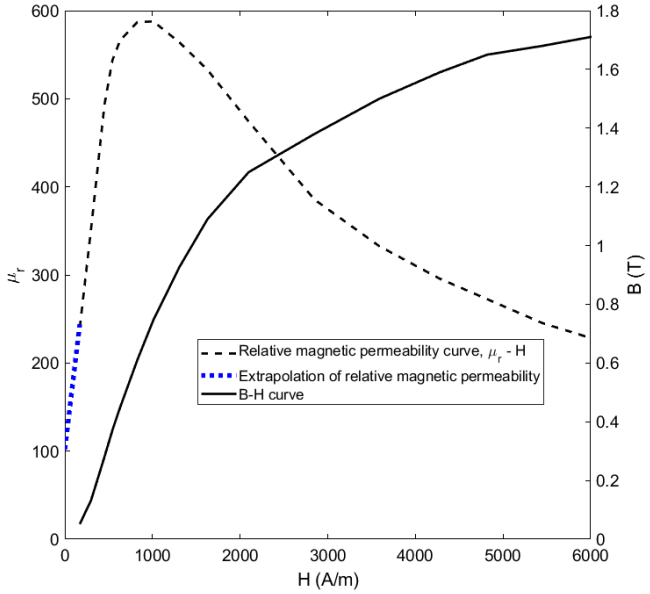

Fig. B1. The *B-H* curve and the relative magnetic permeability curve for material of conical iron rod – non-annealed

The hysteresis effects in conical iron rod are neglected in this paper as sensor operates at low magnetic fields less than 75 A/m, which equivalent hysteresis angle is below 10 Deg. [34].

APPENDIX C: ANNEALING PROCESS AND TEMPERATURE CURVE

The graph for the annealing process is shown in Fig. C1. It was performed at MEDUNA vakuova kalirna, s.r.o. (https://www.kalirna.cz). Two temperatures are shown, one of which is for the air temperature, and the other is from the temperature meter inside a sample located in close proximity to the conical iron rod.

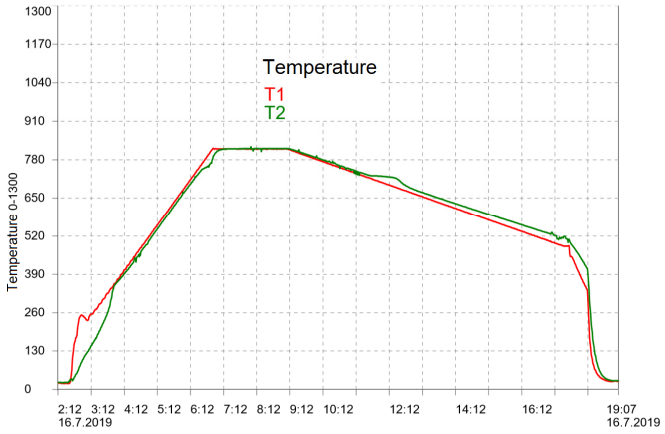

Fig. C1. Temperature profile of the annealing process versus time (hour)

REFERENCES

[1] S. C. Bera, R. Sarkar, M. Bhowmick, "Study of a modified differential inductance measurement circuit as position transducer of a power cylinder," *IEEE Trans. Instr. & Meas.*, vol. 61, no. 2, pp. 530-538, 2012

[2] P. Ripka, A. Chirtsov V. Grim, "Contactless piston position transducer with axial excitation," *IEEE Trans. Mag.*, vol. 53, no. 11, 4002504, 2017

[3] A. Kumar A. S., B. George, "A noncontact angle sensor based on eddy current technique," *IEEE Trans. Instr.& Meas.*, vol. 69, no. 4, pp. 1275-1283, 2020

[4] P. Ripka, *Magnetic Sensors and Magnetometers*, Artech House, Jan. 1,2001

[5] S. Fericean, A. Hiller-Brod, A. D. Dorneich, M. Fritton, "Microwave Displacement Sensor for Hydraulic Devices," *IEEE Sens. J.*, vol. 13, no. 12, pp. 4682 - 4689, 2013

[6] L. Shih-Yuan, L. Jyun, S. S. Lee, "The study of the piston driving and position sensing for a linearly moving piston pump," *Automatic Control Conference (CACS), 2014 CACS International, Kaohsiung*, pp. 287-291, 2014

[7] K. Suzumori, J. Tanaka, T. Kanda, ""Development of an intelligent pneumatic cylinder and its application to pneumatic servo mechanism," *Proceedings, 2005 IEEE/ASME International Conference on Advanced Intelligent Mechatronics*., Monterey, CA, pp. 479-484, 2005

[8] A. A. M. Faudzi, K. Suzumori, S. Wakimoto, "Design and control of new intelligent pneumatic cylinder for intelligent chair tool application," 2009 *IEEE/ASME International Conference on Advanced Intelligent Mechatronics*, Singapore, pp. 1909-1914, 2009

[9] J. Vyhnanek, P.Ripka, A. Chirtsov, "Linear position sensing through conductive wall without permanent magnet," *Proceedings*, vol. 1, no. 4, 390, 2017

[10] H. Sumali, E.P. Bystrom, G.W. Krutz, "A displacement sensor for nonmetallic hydraulic cylinders," *IEEE Sens. J.*, vol. 3, no. 6, pp. 818 – 826, Dec. 2003

[11] B. Legrand, Y. Dordet, J. Y. Voyant, J.P. Yonnet, "Contactless position sensor using magnetic saturation," *Sens. &Act. A, Phys*., vol. 106, no. 1–3, pp. 149–154, Sep. 2003

[12] P. Ripka, A. Chirtsov, M. Mirzaei, "Inductance position sensor for pneumatic cylinder," *AIP Advances*, 8, 048001, 2018

[13] M. Mirzaei, P. Ripka, A. Chirtsov, J. Vyhnanek, "Temperature influence on position transducer for pneumatic cylinder," *IEEE Sensors Conference,* India, 2018

[14] P. Ripka, M. Mirzaei, A. Chirtsov, J. Vyhnanek, "Transformer position sensor for a pneumatic cylinder," *Sens.& Act. A: Phys.*, vol. 294, pp. 91–101, 2019

[15] Y. Kano, S. Hasebe, C. Huang, and T. Yamada, "New type linear variable differential transformer position transducer," *IEEE Trans. Instr.& Meas.,* vol. 38, no. 2, pp. 407 - 409, April 1989

[16] S. C. Saxena, S. B. L. Seksena, "A self-compensated smart LVDT transducer," *IEEE Trans. Instr.& Meas.,* vol. 38, no. 3, pp. 748-753, 1989

[17] G .Y. Tian, Z.X. Zhao, R.W. Baines, N. Zhang, "Computational algorithms for linear variable differential transformers (LVDTs)," *IEE Proc.-Scie. Meas. Technol.*, vol. 144, no. 4, pp. 189-192, 1997

[18] S. K. Mishra, G. Panda, D. P. Das, "A novel method of extending the linearity range of linear variable differential transformer using artificial neural network," *IEEE Trans. Instr. & Meas.*, vol. 59, no. 4, pp. 947-953, 2010

[19] S.-H. Yang, K. Hirata, T. Ota, and Y. Kawase, "Impedance linearity of contactless magnetic-type position sensor," *IEEE Trans. Mag.,* vol. 53, no. 6, pp. 1-4, June 2017

[20] J. F.Gieras, "Analytical method of calculating the electromagnetic field and power losses in ferromagnetic half space, taking into account saturation and hysteresis," *Proc. of the Inst. of Elec. Eng.*, vol. 124, no. 11, pp. 1098 -1104, 1977

[21] ANSYS / Maxwell, Low Frequency Electromagnetic Field, V. 2019 R3, https://www.ansys.com/products/electronics/ansys-maxwell

[22] A. Sumner, C. Gerada, N. Brown, A. Clare, "Controlling DC permeability in cast steels," *J. of Mag.& Mag. Mat.,* vol. 429, pp. 79-85, 1 May 2017

[23] M. Lu, W. Zhu, L. Yin, A.J. Peyton, W. Yin, Z. Qu, "Reducing the lift-off effect on permeability measurement for magnetic plates from multi frequency induction data," *IEEE Trans. Instr. & Meas.*, vol. 67, no. 1, pp. 167 - 174, 2018

[24] P. Yang, M. Fan, B. Cao, S. Gao, "Investigation on Time-to-Peak Feature Insensitive to Liftoff Effect for Pulsed Eddy Current Evaluation," *IEEE Trans. Instr.& Meas.,* 2019 (Early Access)

[25] A. Grima, M. D. Castro, A. Masi, N. Sammut, "Design enhancements of an ironless inductive position sensor," *IEEE Trans. Instr. & Meas.,* vol. 69, no. 4, pp. 1362-1369, 2020

[26] B. Reinholz, R. J. Seethaler, "Design and validation of a variable reluctance differential solenoid transducer," *IEEE Sens. J.*, vol 19, no. 23, pp. 11063-11071, 2019

[27] K. J. Binns, P. J. Lawrenson, C. W. Trowbridge, *The Analytical and Numerical Solution of Electric and Magnetic Fields*, Wiley, 1 edition, December 1992

[28] M. Mirzaei, P. Ripka, A. Chirtsov, J. Vyhnanek, "Eddy current linear speed sensor," *IEEE Trans. Mag.*, vol. 55 , no. 1, pp. 1-4, 2018

[29] A. D. Polyanin, *Handbook of Linear Partial Differential Equations for Engineers and Scientists*, Chapman & Hall/CRC, 2002

[30] Y. Amara and G. Barakat, "Analytical modeling of magnetic field in surface mounted permanent-magnet tubular linear machines," *IEEE Trans. Mag.*, vol. 46 , no. 11 , pp. 3870-3884, 2010

[31] A. Musolino, R. Rizzo, and E. Tripodi, "Tubular linear induction machine as a fast actuator: Analysis and design criteria," *Prog. in Electromag. Research,* vol. 132, pp. 603–619, 2012

[32] M. Abramowitz and I. Stegun, *Handbook of Mathematical Functions with Formulas, Graphs, and Mathematical Tables*, National Bureau of Standards Applied Mathematics Series - 55, Ninth printing, 1970

[33] M. Mirzaei, P. Ripka, A. Chirtsov, J. Vyhnanek, "Impedance of iron conductors with circular and rectangular shapes," *IECON 2018 - 44th Annual Conference of the IEEE Industrial Electronics Society,* Washington, DC, USA, pp. 194-199, 2018

[34] D. O'Kelly, "Hysteresis and eddy-current losses in steel plates with nonlinear magnetisation characteristics," *Proc. of the Inst. of Elec. Eng.*, vol. 119, no. 11, pp. 1675 - 1676,1972

3-2-3 Eddy Current Speed Sensors

3-2-3-1 Eddy Current Linear Speed Sensor [J4]

Novel eddy current speed sensor with axisymmetric coils and solid iron rod as moving part is presented. The analysis is performed for both dc and ac coil currents and for variable iron rod translational speed. The coil inductance and induced voltage results using the analytical method and finite-element method calculation are compared with the measured values. Two different coil configurations are used for simulations and measurement.

Analytical model results coincide well with FEM results and experimental results. The analytical model could be used for speed sensor optimization. Inductances of excitation coils linearly change with the speed at dc currents and low frequencies in model B, which could be used as a speed meter. Pickup coils voltage versus speed has linear dependence. The presented speed sensor could be used for linear machines and pneumatic and hydraulic cylinders.

Eddy Current Linear Speed Sensor

Mehran Mirzaei, Pavel Ripka, Andrey Chirtsov, and Jan Vyhnanek

Faculty of Electrical Engineering, Czech Technical University, 166 36 Prague, Czech Republic

Novel eddy current speed sensor with axisymmetric coils and solid iron rod as moving part is presented. The analysis is performed for both dc and ac coil currents and for variable iron rod translational speed. The coil inductance and induced voltage results using the analytical method and finite-element method calculation are compared with the measured values. Two different coil configurations are used for simulations and measurement.

***Index Terms*—Analysis, eddy current, linear, speed sensor.**

I. Introduction

THE speed sensors are used for rotating and translational objects in many applications. Different types of sensors such as a non-magnetic optical sensor or variable reluctance, eddy current based and Hall effect magnetic sensors could be utilized for speed sensing. Magnetic sensor principles are based on magnetic properties of sensing material or change of parameters of the magnetic circuit [1]. Magnetic sensors are more reliable and robust to dust and dirt, which is a common problem in many applications. Magnetic sensors could have moving or stationary permanent magnet or electric circuit as a magnetic source. They are contactless and have high possibility to be implemented in dirty and high-temperature environment [2]. Contactless translational speed and position sensors are required for the pneumatic and hydraulic cylinders, flat-type or tubular linear motors and actuators and generators for free piston engine and other industrial applications [3], [4]. Available contactless magnetic sensors require non-smooth moving metallic part or permanent magnets for excitation. Another disadvantage of the existing solution is a strong dependence on the distance. Speed probe based on eddy currents in the metallic body moving in the field of permanent magnet was using a Hall sensor, which has poor offset stability [5]. Using speed effects on the induced eddy currents of permanent magnet fields in the moving part was also studied in [6] for metal part defect detection. Speed sensor based on linear variable differential transformer operation with ferrite yoke is presented in [7], which was presented for flat-type moving part. A speed sensor based on the high sensitivity of an amorphous core with ring shape mounted on solid iron E shape core for magnetic field excitation was shown in [8], which has the disadvantage of the necessity of using amorphous core with zero-magnetostriction and sharp rectangular B–H curve.

Our solution for linear speed measurement is based on a single coil and coil pair with dc and ac excitations. We present fast and precise analytical method to calculate coil inductance and induced voltages in the pickup coils taking into account eddy currents in the iron rod caused by alternating current and iron rod speed for an axisymmetric model. Finite-element method (FEM) simulations and experimental results are also presented.

Manuscript received July 14, 2018; revised September 9, 2018; accepted September 17, 2018. Date of publication October 10, 2018; date of current version December 18, 2018. Corresponding author: M. Mirzaei (e-mail: mirzameh@fel.cvut.cz).

Color versions of one or more of the figures in this paper are available online at http://ieeexplore.ieee.org.

Digital Object Identifier 10.1109/TMAG.2018.2872123

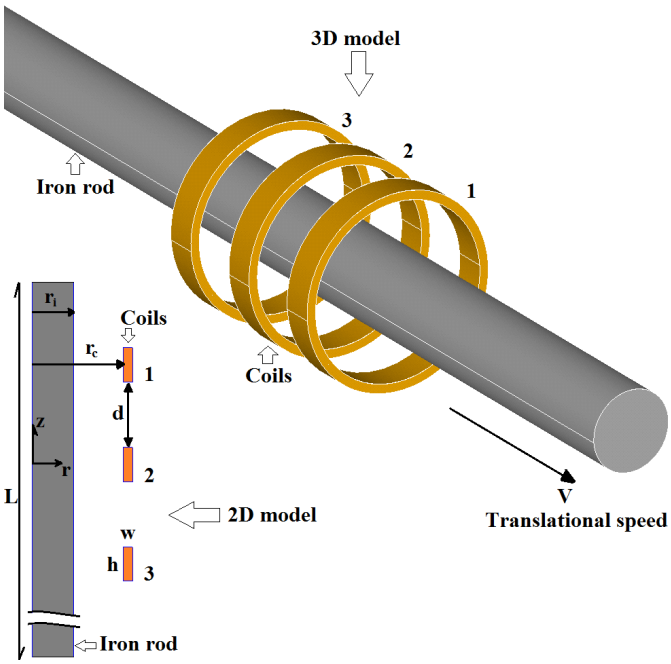

Fig. 1. Speed sensor coils and iron rod—3-D model and 2-D model.

II. Model and Material Data

Fig. 1 shows axisymmetric 3-D model and 2-D model with concentric stationary coils and moving the iron rod. Three coils are implemented for magnetic field excitations and measurements for two different configurations. The first configuration, model A has one excitation coil (number 2 in Fig. 1) and two antiserially connected pickup coils for measurement (numbers 1 and 3). The second configuration, model B has one pickup coil (number 2) and two excitation coils (numbers 1 and 3), which are antiserially connected. The speed of moving iron rod is in the axial direction. Parameters L, r_i, r_c, d, w, and h are the axial length of the iron rod, the outer radius of the iron rod, the inner radius of coils, coils distance, coils thickness, and coils height, respectively.

Solid iron is used for moving the iron rod. Initial relative magnetic permeability is only considered for magnetic analysis because of low magnetic fields, which is estimated to be about 77.5 [9]. The electrical conductivity of solid iron rod is 4.45 MS/m at room temperature.

III. Analytical Modeling

The Maxwell equations are used to compute speed sensor performance [10]. Final differential equations in cylindrical

coordinate have only azimuthal angle component of the magnetic vector potential, A_φ and current density, J_φ because of 2-D axisymmetric configuration. The magnetic flux density and the magnetic field strength have only radial and axial components, B_r, B_z, H_r, and H_z, respectively,

$$\begin{aligned}
&\begin{bmatrix} B_r \\ B_z \end{bmatrix} = \begin{bmatrix} \mu & 0 \\ 0 & \mu \end{bmatrix} \begin{bmatrix} H_r \\ H_z \end{bmatrix}, \quad \frac{\partial H_r}{\partial z} - \frac{\partial H_z}{\partial r} = J_\varphi \\
&\frac{1}{r}\frac{\partial (r B_r)}{\partial r} + \frac{\partial B_z}{\partial z} = 0 \\
&\begin{bmatrix} -\dfrac{\partial J_\varphi}{\partial z} \\ \dfrac{1}{r}\dfrac{\partial (r J_\varphi)}{\partial r} \end{bmatrix} = \begin{bmatrix} -\sigma \dfrac{dB_r}{dt} \\ -\sigma \dfrac{dB_z}{dt} \end{bmatrix}, \quad \begin{bmatrix} B_r \\ B_z \end{bmatrix} = \begin{bmatrix} -\dfrac{\partial A_\varphi}{\partial z} \\ \dfrac{1}{r}\dfrac{\partial (r A_\varphi)}{\partial r} \end{bmatrix}
\end{aligned} \tag{1}$$

where μ and σ are the magnetic permeability and the electrical conductivity, respectively.

The induced eddy current in the iron rod with the electrical conductivity, σ_i due to the iron rod speed, V must be considered in the equations

$$\begin{aligned}
J_\varphi &= -\sigma_i \frac{dA_\varphi}{dt} = -\sigma_i \left(\frac{\partial A_\varphi}{\partial t} + \frac{dz}{dt} \cdot \frac{\partial A_\varphi}{\partial z} \right) \\
&= -\sigma_i \left(\frac{\partial A_\varphi}{\partial t} + V \cdot \frac{\partial A_\varphi}{\partial z} \right).
\end{aligned} \tag{2}$$

The computational model is divided into four parts. Parts 1–4 are iron rod region, air region between the iron rod and coils, coils region, and air region beyond coils, respectively,

$$\begin{aligned}
&\frac{1}{r}\frac{\partial}{\partial r}\left(r \frac{\partial A_{\varphi,1}}{\partial r} \right) + \frac{\partial^2 A_{\varphi,1}}{\partial z^2} - \frac{A_{\varphi,1}}{r^2} \\
&\quad = \sigma_i \cdot \mu_1 \cdot \left(\frac{\partial A_{\varphi,1}}{\partial t} + V \cdot \frac{\partial A_{\varphi,1}}{\partial z} \right)
\end{aligned} \tag{3}$$

$$\begin{aligned}
&\frac{1}{r}\frac{\partial}{\partial r}\left(r \frac{\partial A_{\varphi,3}}{\partial r} \right) + \frac{\partial^2 A_{\varphi,3}}{\partial z^2} - \frac{A_{\varphi,3}}{r^2} \\
&\quad = -\mu_3 \cdot J_s
\end{aligned} \tag{4}$$

$$\begin{aligned}
&\frac{1}{r}\frac{\partial}{\partial r}\left(r \frac{\partial A_{\varphi,2,4}}{\partial r} \right) + \frac{\partial^2 A_{\varphi,2,4}}{\partial z^2} - \frac{A_{\varphi,2,4}}{r^2} \\
&\quad = 0
\end{aligned} \tag{5}$$

where J_s is the source current density in the coils.

The method of separation of variables (method of Fourier) is used to solve (3)–(5) [10].

They are assumed that magnetic fields change sinusoidally versus time and periodically in the z-direction with the period length $2L$. Therefore, derivations could be replaced as following:

$$A_\varphi = R(r) \cdot Z(z) \cdot T(t) \tag{6}$$

$$\begin{aligned}
&Z(z) \propto \exp(-jm \cdot z), \quad m = \frac{n\pi}{L} \\
&T(t) \propto \exp(j\omega \cdot t) \\
&\frac{\partial A_{\varphi,1}}{\partial t} = j\omega \cdot A_{\varphi,1} \\
&\frac{\partial A_{\varphi,1}}{\partial z} = -jm \cdot A_{\varphi,1}, \quad \frac{\partial^2 A_{\varphi,1}}{\partial z^2} = -m^2 \cdot A_{\varphi,1}
\end{aligned} \tag{7}$$

where ω is the angular frequency in rad/s.

The solutions versus radius, r are as follows:

$$\begin{aligned}
A_{\varphi,1} &= \sum_{n=\pm1,\pm3,\ldots} (C_{11} \cdot J_1(\gamma \cdot r) + C_{12} \cdot Y_1(\gamma \cdot r)) \\
\gamma &= \sqrt{-m^2 - j\mu_1\sigma_i(\omega - m \cdot V)} \\
A_{\varphi,2} &= \sum_{n=\pm1,\pm3,\ldots} (C_{21} \cdot I_1(m \cdot r) + C_{22} \cdot K_1(m \cdot r)) \\
A_{\varphi,3} &= \sum_{n=\pm1,\pm3,\ldots} \left(C_{31} \cdot I_1(m \cdot r) + C_{32} \cdot K_1(m \cdot r) - \frac{\mu_3 J_m \pi}{2m^2} \cdot L_1(m \cdot r) \right) \\
A_{\varphi,4} &= \sum_{n=\pm1,\pm3,\ldots} (C_{41} \cdot I_1(m \cdot r) + C_{42} \cdot K_1(m \cdot r))
\end{aligned} \tag{8}$$

where J_1, Y_1, I_1, and K_1 are Bessel functions and L_1 is Struve function. C_{11}, C_{12}, C_{21}, C_{22}, C_{31}, C_{32}, C_{41}, and C_{42} are constants, which are obtained by the following boundary conditions:

$$\begin{aligned}
A_{\varphi,1}(r = 0) &= 0 \\
A_{\varphi,1}(r = r_i) &= A_{\varphi,2}(r = r_i) \\
H_{z,1}(r = r_i) &= H_{z,2}(r = r_i) \\
A_{\varphi,2}(r = r_c) &= A_{\varphi,3}(r = r_c) \\
H_{z,2}(r = r_c) &= H_{z,3}(r = r_c) \\
A_{\varphi,3}(r = r_c + w) &= A_{\varphi,4}(r = r_c + w) \\
H_{z,3}(r = r_c + w) &= H_{z,4}(r = r_c + w) \\
A_{\varphi,3}(r = \infty) &= 0.
\end{aligned} \tag{9}$$

Parameter J_m in (8) for coils region for single-coil excitation and two antiserially connected coils could be calculated as follows, respectively,

$$\begin{aligned}
J_m &= \frac{2}{n\pi} \cdot \sin\left(m \cdot \frac{h}{2} \right) \cdot J_s \\
J_m &= -\frac{2}{jn\pi} \cdot \left(\cos\left(m \cdot \left(d + 3 \cdot \frac{h}{2} \right) \right) - \cos\left(m \cdot \left(d + \frac{h}{2} \right) \right) \right) \cdot J_s \\
J_s &= \frac{NI}{h \cdot w}
\end{aligned} \tag{10}$$

where N and I are the number of turns per coil and current, respectively. Struve function L_1 is complicated for calculation and shows instability. An approximation is used to replace Struve function, L_1 with a simpler one. It is assumed that the current density change is directly proportional or inversely proportional with the radius and it is not constant in the coil cross section. Therefore, solutions of (4) for magnetic vector potentials, $A_{\varphi,3}$, are as following for linear current change and inversely current change with radius, respectively,

$$\begin{aligned}
&\frac{1}{r}\frac{\partial}{\partial r}\left(r \frac{\partial A_{\varphi,3}}{\partial r} \right) + \frac{\partial^2 A_{\varphi,3}}{\partial z^2} - \frac{A_{\varphi,3}}{r^2} \\
&\quad = -\mu_3 J_s r, \; J_s = \frac{2NI}{h(w^2 + 2wr_c)} \\
&A_{\varphi,3} = \sum_{n=\pm1,\pm3,\ldots} \left(C_{31} \cdot I_1(m \cdot r) + C_{32} \cdot K_1(m \cdot r) + \frac{\mu_3 J_m}{m^2} \cdot r \right)
\end{aligned}$$

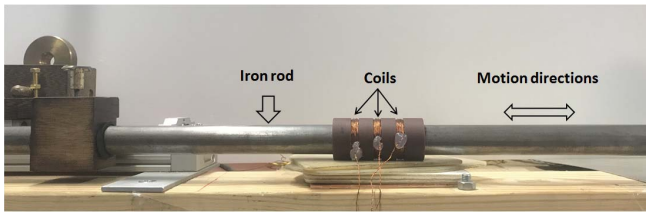

Fig. 2. Experimental set up.

TABLE I
PARAMETERS OF SPEED SENSOR

Parameters	w	h	r_c	d	r_i	L
unit (mm)	1.8	5.0	12.0	10.0	10.0	700.0

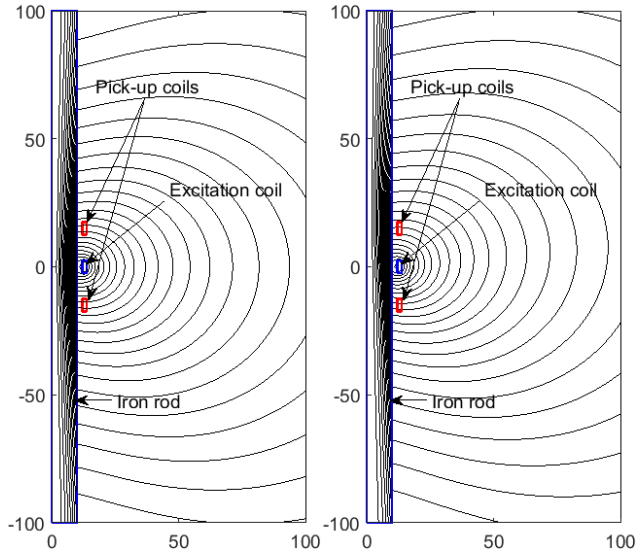

Fig. 3. Magnetic flux distribution in model A at dc current [0 m/s (left) and +5 m/s (right)].

$$\frac{1}{r}\frac{\partial}{\partial r}\left(r\frac{\partial A_{\varphi,3}}{\partial r}\right)+\frac{\partial^2 A_{\varphi,3}}{\partial z^2}-\frac{A_{\varphi,3}}{r^2}=-\mu_3\frac{J_s}{r},\ J_s=\frac{NI}{h\cdot\ln\left(1+\frac{w}{r_c}\right)}$$

$$A_{\varphi,3}=\sum_{n=\pm1,\pm3,\ldots}\left(C_{31}\cdot I_1(m\cdot r)+C_{32}\cdot K_1(m\cdot r)+\frac{\mu_3 J_m}{m^2\cdot r}\right). \quad (11)$$

IV. EXPERIMENTAL AND SIMULATION RESULTS

Fig. 2 and Table I show the experimental setup for eddy current linear speed sensor and parameters. The axial length of the iron rod is considered large enough to decrease end effects caused by the finite length of the iron rod. The number of turns per coil, N is 47. Figs. 3 and 4 show the magnetic flux distribution in models A and B at dc current and iron rod speed 0 and 5 m/s, which are calculated by the analytical method. The effect of speed on the flux distribution could be more distinguished in the iron rod region and in the air region end parts. The induced eddy current due to the iron rod speed causes unsymmetrical magnetic flux distribution.

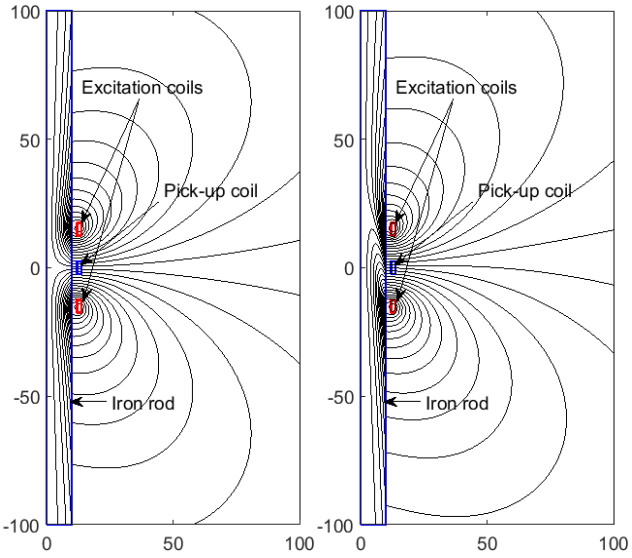

Fig. 4. Magnetic flux distribution in model B at dc current—two excitation coils are connected antiserially [0 m/s (left) and +5 m/s (right)].

TABLE II
COMPARISON BETWEEN EXPERIMENTAL AND ANALYTICAL RESULTS—MODEL A (EXCITATION CURRENT AMPLITUDE = 0.165 A)

	Experimental	Analytical
$L_{\text{S-air}}$	85.0 (μH)	79.8 (μH)
$L_{\text{M-air}}$	12.4 (μH)	11.5 (μH)
$L_{\text{S-iron, 100 Hz}}$	312.0 (μH)	291.1 (μH)
$L_{\text{M-iron,100 Hz}}$	209.3 (μH)	181.8 (μH)
$L_{\text{S-iron, 1000 Hz}}$	195.0 (μH)	185.0 (μH)
$L_{\text{M-iron,1000 Hz}}$	98.6 (μH)	85.4 (μH)

Self-inductance, L_S and mutual inductance, L_M could be calculated as follows [11]:

$$L_S, L_M=\frac{\Psi}{I}=\frac{N\int A_\varphi\cdot dV}{I\cdot h\omega} \quad (12)$$

where Ψ is the total average flux linkage or mutual flux linkage over coils cross-sectional area. The integration is applied on each coil volume. Table II gives the experimental and analytical results for self-inductance and mutual inductance between the adjacent coils at zero speed, which present appropriate precision for the analytical method. The self-inductance has only inductive component in Table II and the mutual inductance has inductive and resistive components, where the resistive component is caused by induced eddy currents in the iron rod. Eddy currents are only generated in the regions where the excitation field has a radial component. Fig.5 shows the analytical and FEM results for the coils inductances and induced voltages of models A and B.

The inductances changes versus speed are negligible in model A at dc current and 100 Hz ac current. The variations of inductances are more obvious in model B, which could be used as a speed meter. The induced voltages amplitude changes linearly with the speed in Fig. 5. The induced voltage amplitude—speed ratio is about 150 μV/ (m/s). The experimental and analytically calculated results for induced voltage of model A versus time at different speeds are shown in Fig. 6. The experimental voltage results are recorded by

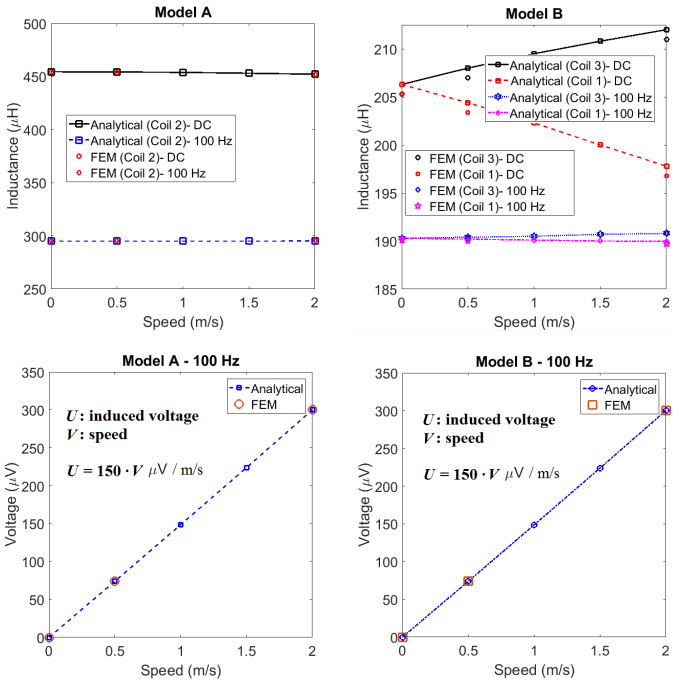

Fig. 5. Coils inductances (top) and induced voltages (bottom)—induced voltage in model A is the difference voltage between pick up coils 1 and 3.

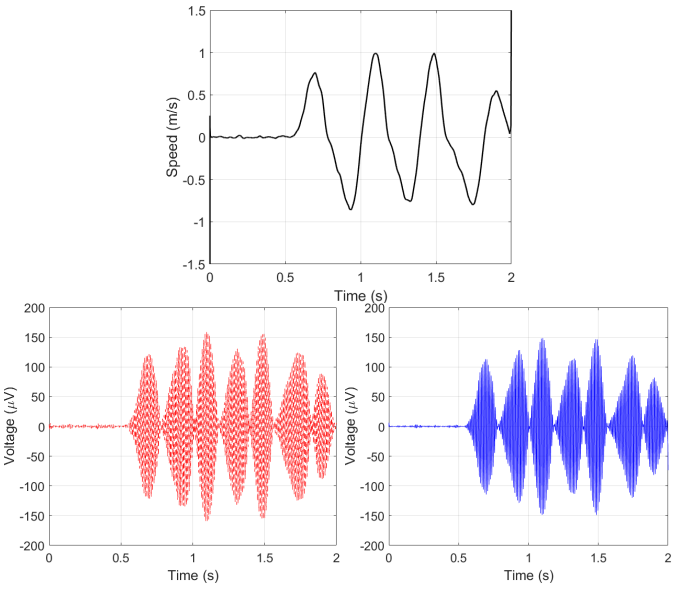

Fig. 6. Measured speed (top), measured voltage (bottom left), and analytical calculated voltage (bottom right)—model A with current amplitude 165 mA.

oscilloscope for a time range. The analytical induced voltages coincide well with the experimental results, which show the accuracy of the proposed analytical method. The acceleration effects are neglected in the analytical modeling and only pure inductive effects are considered. The sign of speed could not be observed from the amplitude of induced voltage but it could be computed by relative phase angle to excitation current.

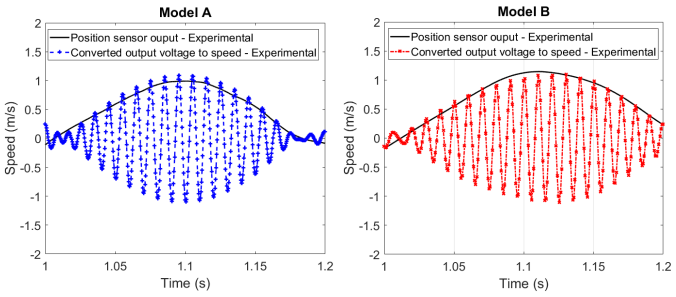

Fig. 7. Comparison between the estimated speed and the measured speed.

The comparison between the estimated speed and the measured speed (Fig. 6) is shown in Fig. 7, which presents an appropriate accuracy. The induced voltage amplitude—speed ratio, 150 μV/ (m/s) is used to convert induced voltages to the speed. The estimated speed results could be obtained using voltage peaks or voltage rms or rectified dc value in each half period.

V. Conclusion

A translational speed sensor for an axisymmetric moving part was presented. Analytical model results coincide well with FEM results and experimental results. The analytical model could be used for speed sensor optimization. Inductances of excitation coils linearly change with the speed at dc currents and low frequencies in model B, which could be used as a speed meter. Pickup coils voltage versus speed is a linear curve. The presented speed sensor could be used for linear machines and pneumatic and hydraulic cylinders.

References

[1] P. Ripka, *Magnetic Sensors and Magnetometers*. Norwood, MA, USA: Artech House, 2001, p. 494.
[2] S. Tumański, *Handbook of Magnetic Measurements*. Boca Raton, FL, USA: CRC Press, 2011, p. 404.
[3] P. Zheng *et al.*, "Research on the magnetic characteristic of a novel transverse-flux PM linear machine used for free-piston energy converter," *IEEE Trans. Magn.*, vol. 47, no. 5, pp. 1082–1085, May 2011.
[4] Y. Sui, P. Zheng, B. Yu, L. Cheng, and Z. Liu, "Research on a tubular yokeless linear PM machine," *IEEE Trans. Magn.*, vol. 51, no. 11, Nov. 2015, Art. no. 8204904.
[5] E. Cardelli, A. Faba, and F. Tissi, "Contact-less speed probe based on eddy currents," *IEEE Trans. Magn.*, vol. 49, no. 7, pp. 3897–3900, Jul. 2013.
[6] T. J. Rocha, H. G. Ramos, A. L. Ribeiro, and D. J. Pasadas, "Evaluation of subsurface defects using diffusion of motion-induced eddy currents," *IEEE Trans. Instrum. Meas.*, vol. 65, no. 5, pp. 1182–1187, May 2016.
[7] A. Tuysuz, M. Flankl, J. W. Kolar, and A. Mutze, "Eddy-current-based contactless speed sensing of conductive surfaces," in *Proc. IEEE 2nd Annu. Southern Power Electron. Conf. (SPEC)*, Dec. 2016, pp. 1–6.
[8] T. Sonoda, R. Ueda, K. Fujitani, T. Irisa, and S. Tatata, "DC magnetic field type eddy current speed sensor detecting cross magnetization field with amorphous core," *IEEE Trans. Magn.*, vol. MAG-21, no. 5, pp. 1732–1734, Sep. 1985.
[9] P. Ripka, A. Chirtsov, and M. Mirzaei, "Inductance position sensor for pneumatic cylinder," *AIP Adv.*, vol. 8, no. 4, p. 048001, 2018.
[10] M. N. O. Sadiku, *Numerical Techniques in Electromagnetics*, 2nd ed. Boca Raton, FL, USA: CRC Press, 2000, p. 760.
[11] K. R. Davey, "Analytic analysis of single- and three-phase induction motors," *IEEE Trans. Magn.*, vol. 34, no. 5, pp. 3721–3727, Sep. 1998.

3-2-3-2 Rotational Eddy Current Speed Sensor [J5]

A novel eddy current speed sensor is developed to measure the rotational speed of conductive objects. The sensor consists of one excitation coil and two pick-up coils around a rotating cylinder or rod. The sensor does not use magnetic yoke. For the analysis and experimental verification, we used 30 mm diameter non-magnetic aluminum and also magnetic solid iron cylinders. The calculated and measured speed ranges are up to 1200 r/min. A 2-D analytical method is developed to calculate sensor performance. A 2-D finite element model is also used for simulations to compare results with the 2-D analytical method. A 3-D finite-element analysis is required to take into account significant 3-D effects due to the air coil configuration. The experimental results are presented at different steady-state speeds. The calculation results are compared with measurements to validate theoretical models and sensor performance.

The eddy current speed sensor shows high linearity even at low speeds. For ferromagnetic rods, we suggest a novel double-layer configuration: non-magnetic conductive ring or shell on top of the iron rod minimizes the influence of the permeability changes. The main advantage of the novel sensor is that it has neither mechanical nor electrical contact to the rotating rod.

Different configurations of rotational speed sensor and parameters were evaluated in this paper. The measurements and calculations have been done up to 1200 r/min but the proposed speed sensor is also suitable for higher speeds as it does not have mechanical and electrical limitations. The whole coils span is less than 180 deg**,** which allows installing them on one side of the rotating rod and the sensor is contactless. The double-layer rod can significantly improve eddy current speed sensor performance when the rotating rod must be from magnetic steel. By using the highly conductive non-magnetic shell, the sensitivity is improved, and it becomes less susceptible to permeability changes.

Rotational Eddy Current Speed Sensor

Mehran Mirzaei, Pavel Ripka, Jan Vyhnanek, Andrey Chirtsov, and Vaclav Grim

Faculty of Electrical Engineering, Czech Technical University in Prague, 16627 Prague, Czech Republic

A novel eddy current speed sensor is developed to measure the rotational speed of conductive objects. The sensor consists of one excitation coil and two pick-up coils around a rotating cylinder or rod. The sensor does not use magnetic yoke. For the analysis and experimental verification, we used 30 mm diameter non-magnetic aluminum and also magnetic solid iron cylinders. The calculated and measured speed ranges are up to 1200 r/min. A 2-D analytical method is developed to calculate sensor performance. A 2-D finite element is also used for simulations to compare results with the 2-D analytical method. A 3-D finite-element analysis is required to take into account significant 3-D effects due to the air coil configuration. The experimental results are presented at different steady-state speeds. The calculation results are compared with measurements to validate theoretical models and sensor performance. The eddy current speed sensor shows high linearity even at low speeds. For ferromagnetic rods, we suggest a novel double-layer configuration: non-magnetic conductive ring or shell on top of the iron rod minimizes the influence of the permeability changes. The main advantage of the novel sensor is that it has neither mechanical nor electrical contact to the rotating rod.

Index Terms— **2-D analytical method, 2-D and 3-D finite-element method (FEM), air coil, eddy current, rotational speed sensor.**

I. Introduction

SPEED sensors are a key component of control and monitoring systems in linear and rotating machines [1], [2]. Optical speed sensors are representatives of the well-established non-magnetic technology. Magnetic speed sensors utilize variable reluctance effect, eddy current effect, and Hall effect [3]. The contactless magnetic speed sensors are a better option for industrial speed sensors application in a harsh environment with a high probability of dirt and dust in comparison with non-magnetic speed sensors. Existing magnetic speed sensors usually use permanent magnets or current-carrying coils as the excitation source. Permanent magnets are either mounted on the moving part or stationary—in both cases, the sensors suffer from the temperature dependence of the magnet properties and they are also sensitive to the change in the distance between the moving and stationary parts [4], [5].

Speed probe based on eddy currents and reluctance variations in a metallic body moving in the field of the permanent magnet using the Hall sensor or pick-up coil was presented for some applications in [5] and [6]. A speed sensor based on high sensitivity of an amorphous core with ring shape mounted on a solid iron E-shape core for magnetic field excitation was shown in [7], which has the disadvantage of the necessity of using amorphous core with zero-magnetostriction and sharp rectangular $B-H$ curve. Different structures of eddy current speed sensor with non-perpendicular and perpendicular coils were presented with analytical models based on Fourier transform in [8]–[10]. Speed sensor based on the linear variable differential transformer (LVDT) configuration with ferrite yoke is presented in [11], which was presented for flat type moving part using outcomes in [8]–[10]. Non-ferromagnetic moving conductors such as aluminum are only used in [5]–[11], which are not complicated for measurement and simulations. An eddy current linear speed sensor with axisymmetric structure was developed and measured at variable linear speeds with a ferromagnetic iron rod [12], whose magnetic relative permeability was measured and estimated for precise simulations and analysis. Rotational eddy current speed sensor could be a very appropriate option for some applications such as turbochargers [13]–[15], which is problematic for the conventional speed sensor.

In our linear speed sensor, we use single-coil excitation coil with ac current and two antiserially connected pick-up coils for the measurement [12] without using ferromagnetic yoke as back iron for flux. In this paper, we suggest a similar scheme for rotational speed sensing. Despite the similar principle, the description of the rotational sensor requires a different approach.

Fast and precise 2-D analytical methods are presented to calculate coupling inductances and induced voltages into the pick-up coils taking into account eddy currents in the rotating conductive rod caused by alternating current and moving conductive rod speed for a rotating model using Fourier series. General closed-form equations are also obtained for output results. 2-D and 3-D finite-element method (FEM) simulations with consideration of rotating part speed are also presented to compare with analytical calculations and consider 3-D effects. Different relative magnetic permeabilities are considered for the rotating solid iron part. Cylindrical aluminum rod and solid ferromagnetic iron rod are both used in the measurement for the rotating part, and the experimental results are compared with the analytical and FEM calculations. The induced voltages of pick-up coils are measured with a lock-in amplifier.

The main novelty of this paper is double-layer configuration: non-magnetic conductive ring on top of the iron rod minimizes the influence of the permeability changes of the rod.

II. Model and Coils Configurations

Fig. 1 shows the 3-D model of the rotating rod and speed sensor coils. The middle coil is considered as excitation coil

Manuscript received April 15, 2019; accepted May 14, 2019. Date of publication June 12, 2019; date of current version August 19, 2019. Corresponding author: M. Mirzaei (e-mail: mirzameh@fel.cvut.cz).

Color versions of one or more of the figures in this paper are available online at http://ieeexplore.ieee.org.

Digital Object Identifier 10.1109/TMAG.2019.2918163

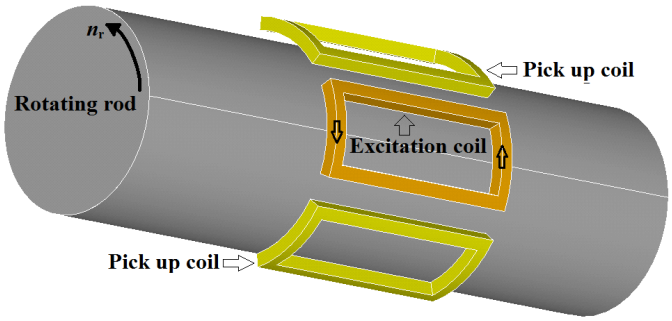

Fig. 1. 3-D model of rotating eddy current speed sensor—first configuration of coils: one excitation coil and two antiserially connected pick-up coils.

TABLE I
ROTATING SPEED SENSOR PARAMETERS

Parameters	Values
I	172.36 mA
N	50
$r_{\rm i}$	15 mm
$r_{\rm wi}$	16.25mm
$r_{\rm wo}$	18.25 mm
$g = r_{\rm wi} - r_{\rm i}$	1.25 mm
$\theta_{\rm o}$	46 Deg.
$\theta_{\rm i}$	33.4 Deg.
$L_{\rm i}$	30 mm
$\sigma_{\rm al}$	21.5 MS/m
$\sigma_{\rm i}$	5.54 MS/m
$\mu_{\rm ri}$	100

and left- and right-hand side coils are the pick-up coils in the first configuration. It is also possible to use left- and right-hand sides antiserially connected coils as excitation coils and the middle coil as a pick-up coil. The rotating rod is solid iron or aluminum. The axial length of the rotating rod is considered large enough in comparison with coil dimensions.

It is clear that the induced voltage in the pick-up coils in both the above-mentioned configurations is zero at zero speed because the net flux linkage is zero.

Fig. 2 and Table I show the parameters and dimensions of the rotational speed sensor. Parameters r_i, $r_{\rm wi}$, $r_{\rm wo}$, g, θ_o, θ_i, L_i, $\sigma_{\rm al}$, σ_i, and $\mu_{\rm ri}$ are the outer radius of rotating rod, inner radius of coils, outer radius of coils, gap between coils and rotating rod, outer angle of coils, inner angle of coils, straight part length of coils in the axial z-direction, aluminum electrical conductivity, iron electrical conductivity, and iron relative magnetic permeability, respectively.

III. 2-D MODELING

A. Analytical

The Maxwell equations are used to compute speed sensor performance [16], [17]. Final differential equations in the cylindrical coordinate have only axial z-component of magnetic vector potential A_z and current density J_z because of the 2-D configuration. Magnetic flux density and magnetic field strength have only radial and azimuthal components, B_r, B_θ,

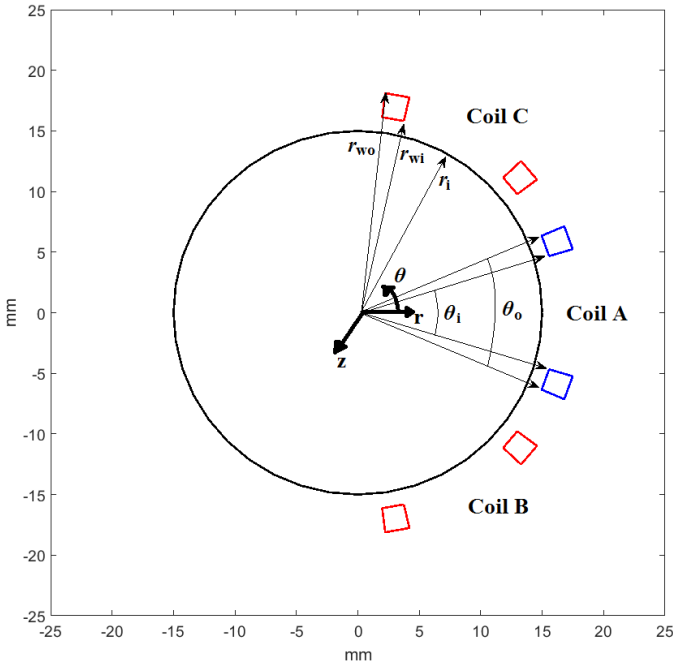

Fig. 2. 2-D model and dimensions.

H_r, and H_θ, respectively,

$$\begin{bmatrix} B_r \\ B_z \end{bmatrix} = \begin{bmatrix} \mu & 0 \\ 0 & \mu \end{bmatrix} \begin{bmatrix} H_r \\ H_z \end{bmatrix}$$

$$\frac{1}{r}\left(\frac{\partial (r H_\theta)}{\partial r} - \frac{\partial H_r}{\partial \theta}\right) = J_z, \quad \frac{1}{r}\left(\frac{\partial (r B_r)}{\partial r} + \frac{\partial B_\theta}{\partial \theta}\right) = 0$$

$$\begin{bmatrix} \frac{1}{r}\frac{\partial J_z}{\partial \theta} \\ -\frac{\partial J_z}{\partial r} \end{bmatrix} = \begin{bmatrix} -\sigma \frac{dB_r}{dt} \\ -\sigma \frac{dB_\theta}{dt} \end{bmatrix}, \quad \begin{bmatrix} B_r \\ B_\theta \end{bmatrix} = \begin{bmatrix} \frac{1}{r}\frac{\partial A_z}{\partial \theta} \\ -\frac{\partial A_z}{\partial r} \end{bmatrix} \tag{1}$$

where μ and σ are the magnetic permeability and electrical conductivity, respectively.

The induced eddy current in the rotating rod with electrical conductivity σ due to the iron rod speed ω_r must be considered in the equations [18], [19]

$$J_z = -\sigma\left(\frac{\partial A_z}{\partial t} + \frac{d\theta}{dt}\frac{\partial A_z}{\partial \theta}\right) = -\sigma\left(\frac{\partial A_z}{\partial t} + \omega_r \frac{\partial A_z}{\partial \theta}\right). \tag{2}$$

The computational model is divided into four parts. Parts 1–4 are the rotating rod region, air region between rotating rod and coils, coils region, and air region beyond coils, respectively,

$$\frac{1}{r}\frac{\partial}{\partial r}\left(r\frac{\partial A_{z,1}}{\partial r}\right) + \frac{1}{r^2}\frac{\partial^2 A_{z,1}}{\partial \theta^2} = \mu_1 \cdot \sigma\left(\frac{\partial A_{z,1}}{\partial t} + \omega_r \cdot \frac{\partial A_{z,1}}{\partial \theta}\right) \tag{3}$$

$$\frac{1}{r}\frac{\partial}{\partial r}\left(r\frac{\partial A_{z,3}}{\partial r}\right) + \frac{1}{r^2}\frac{\partial^2 A_{z,3}}{\partial \theta^2} = -\mu_3 \cdot J_s \tag{4}$$

$$\frac{1}{r}\frac{\partial}{\partial r}\left(r\frac{\partial A_{z,2,4}}{\partial r}\right) + \frac{1}{r^2}\frac{\partial^2 A_{z,2,4}}{\partial \theta^2} = 0 \tag{5}$$

where $J_{\rm s}$ is the source current density in the coils.

The method of separation of variables (method of Fourier) is used to solve (3)–(5) [16], [17].

It is assumed that magnetic fields change sinusoidally versus time and periodically in the θ-direction with a period length 2π. Therefore, derivations could be replaced as follows:

$$\begin{aligned} A_z &= \Theta(\theta)\cdot R(r)\cdot T(t) \qquad (6)\\ \Theta(\theta) &\propto \exp(-\mathrm{jm}\cdot\theta)\\ T(t) &\propto \exp(j\omega\cdot t)\\ \frac{\partial A_z}{\partial t} &= j\omega\cdot A_z\\ \frac{\partial A_z}{\partial \theta} &= -jm\cdot A_z,\quad \frac{\partial^2 A_z}{\partial \theta^2} = -m^2\cdot A_z \qquad (7)\end{aligned}$$

where ω is the angular frequency in rad/s.

The solutions versus radius r are as follows:

$$\begin{aligned} A_{z,1} &= \sum_{m=\pm1,\pm2,\ldots} (C_{11}\mathrm{BesselI}(m_1,\ \gamma\cdot r)\\ &\quad + C_{12}\mathrm{BesselK}(m_1,\gamma\cdot r))\\ \gamma &= \sqrt{j\mu_1\sigma(\omega - m\cdot\omega_r)}\\ A_{z,2} &= \sum_{m=\pm1,\pm2,\ldots} (C_{21}r^{m_1} + C_{22}r^{-m_1})\\ A_{z,3} &= \sum_{m=\pm1,\pm2,\ldots} (C_{31}r^{m_1} + C_{32}r^{-m_1} + A_{z,s})\\ A_{z,s} &= \frac{\mu_3 J_m}{m^2-4}\cdot r^2\ (m_1\neq 2),\ A_{z,s} = \frac{\mu_3 J_m}{16}\\ &\quad \cdot r^2(1-4\log(r))\quad (m_1 = 2)\\ A_{z,4} &= \sum_{m=\pm1,\pm2,\ldots} (C_{41}r^{m_1} + C_{42}r^{-m_1})\\ m_1 &= |m| \qquad (8)\end{aligned}$$

where C_{11}, C_{12}, C_{21}, C_{22}, C_{31}, C_{32}, C_{41}, and C_{42} are the constants and these are obtained by the following boundary conditions:

$$\begin{aligned} &A_{z,1}(r=0) = 0\\ &A_{z,1}(r=r_i) = A_{z,2}(r=r_i),\quad H_{\theta,1}(r=r_i) = H_{\theta,2}(r=r_i)\\ &A_{z,2}(r=r_{\mathrm{wi}}) = A_{z,3}(r=r_{\mathrm{wi}}),\ H_{\theta,2}(r=r_{\mathrm{wi}}) = H_{\theta,3}(r=r_{\mathrm{wi}})\\ &A_{z,3}(r=r_{\mathrm{wo}}) = A_{z,4}(r=r_{\mathrm{wo}}),\ H_{\theta,3}(r=r_{\mathrm{wo}}) = H_{\theta,4}(r=r_{\mathrm{wo}})\\ &A_{z,3}(r=\infty) = 0. \qquad (9)\end{aligned}$$

Parameter J_m in (8) for coils region for single-coil excitation and two antiserially connected coils could be calculated, respectively, as follows:

$$\begin{aligned} J_m &= \frac{j}{m\pi}C_J\cdot J_{\mathrm{s}}\\ J_m &= \frac{-1}{m\pi}C_J\cdot J_{\mathrm{s}}\cdot 2\cdot\sin\left(\frac{m\theta_d}{2}\right)\\ C_J &= \left(\cos\left(m\frac{\theta_i}{2}\right) - \cos\left(m\frac{\theta_o}{2}\right)\right),\ \theta_d = \frac{2\pi}{3}\\ J_s &= \frac{NI}{\frac{(\theta_o-\theta_i)}{4}\cdot\left(r_{\mathrm{wo}}^2 - r_{\mathrm{wi}}^2\right)} \qquad (10)\end{aligned}$$

where N and I are the number of turns per coil and current amplitude (Table I), respectively. The parameter θ_d is the angle between coils B and C centers, which is considered equal to 120°. It is considered that all coils have the same dimensions in this paper. Mutual-induced voltage V_M and mutual inductance L_M could be calculated as follows [18]:

$$V_M = -\frac{d\Psi_M}{dt} = -j\omega N\oint A_z\mathrm{dl} = -j\omega N\cdot L_i\cdot\left(A_z^+ - A_z^-\right) \qquad (11)$$

$$\begin{aligned} L_m &= \frac{\Psi_M}{I} = \frac{N\cdot L_i\cdot\int\left(A_z^+ - A_z^-\right)\cdot\mathrm{ds}}{I\cdot a_w}\\ a_w &= \frac{(\theta_o-\theta_i)}{4}\cdot\left(r_{\mathrm{wo}}^2 - r_{\mathrm{wi}}^2\right),\quad \mathrm{ds} = r\cdot\mathrm{dr}\cdot d\theta \qquad (12)\end{aligned}$$

where Ψ_M is the total average mutual flux linkage over coils a 2-D cross-sectional area. The surface integration in (12) is applied to each coil cross-sectional area. A_z^+ and A_z^- are the magnetic vector potentials in go and return paths of the coil. Integration in (11) is for the ideal case with an infinitesimal coil cross section. Integration in (12) is for the real case of the coil cross section, which is averaged over the coil cross-sectional area.

The differential voltage between the left- and right-side pick-up coils (B and C in Fig. 2) is presented in the following equations. The differential voltage polarity changes as speed direction changes according to

$$\begin{aligned} V_d &= V_{M,l} - V_{M,r} = j\omega\cdot(L_{M,r} - L_{M,l})\cdot I \qquad (13)\\ V_d &= V_{M,l} - V_{M,r} = \frac{j\omega N\ L_i}{a_w}\\ &\quad\times\sum_{m=\pm1,\pm2,\ldots}\left(C_V C_J\frac{4}{m}\sin\left(\frac{m\theta_d}{2}\right)\right)\\ C_V &= C_{31}\frac{r_{\mathrm{wo}}^{m_1+2} - r_{\mathrm{wi}}^{m_1+2}}{m_1+2} + C_{32}\frac{r_{\mathrm{wo}}^{-m_1+2} - r_{\mathrm{wi}}^{-m_1+2}}{-m_1+2} + \frac{\mu_3 J_m}{m^2-4}C\\ C &= \frac{r_{\mathrm{wo}}^4 - r_{\mathrm{wi}}^4}{4}\quad (m_1\neq 2),\\ C_V &= C_{31}\frac{r_{\mathrm{wo}}^{m_1+2} - r_{\mathrm{wi}}^{m_1+2}}{m_1+2} + C_{32}\log\left(\frac{r_{\mathrm{wo}}}{r_{\mathrm{wi}}}\right) + \frac{\mu_3 J_m}{16}C\\ C &= \frac{r_{\mathrm{wo}}^4 - r_{\mathrm{wi}}^4}{4}\\ &\quad - \left(r_{\mathrm{wo}}^4\cdot\left(\log(r_{\mathrm{wo}}) - \frac{1}{4}\right) - r_{\mathrm{wi}}^4\cdot\left(\log(r_{\mathrm{wi}}) - \frac{1}{4}\right)\right)\\ &\quad (m_1 = 2). \qquad (14)\end{aligned}$$

Magnetic flux penetration in the rotating rod decreases with ac excitation current [19] at 30 and 90 Hz and +1200 r/min speed due to the skin effect (Figs. 3 and 4). Less flux penetration in the rotating rod at higher frequency causes less differential mutual flux linkage and decreases speed sensitivity of the eddy current speed sensor (Table II).

B. FEM

A 2-D time-transient finite element with the consideration of motion is considered for numerical calculations [20]. Fig. 5 shows the differential voltage amplitude results of antiserially connected pick-up coils versus speed using 2-D analytical and 2-D FEM. The analytical calculations coincide well with 2-D FEM, which shows the accuracy of the analytical method. Excellent linearity is depicted in Fig. 5, which presents the suitability of the proposed sensor for speed measurement.

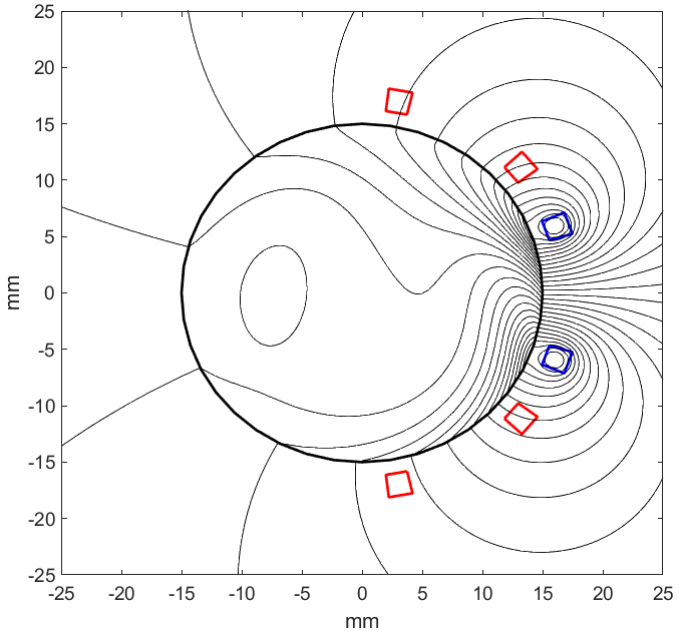

Fig. 3. Magnetic flux distribution at 30 Hz and +1200 r/min with rotating iron rod-first configuration of coils: one excitation coil and two antiserially connected pick-up coils—analytical method.

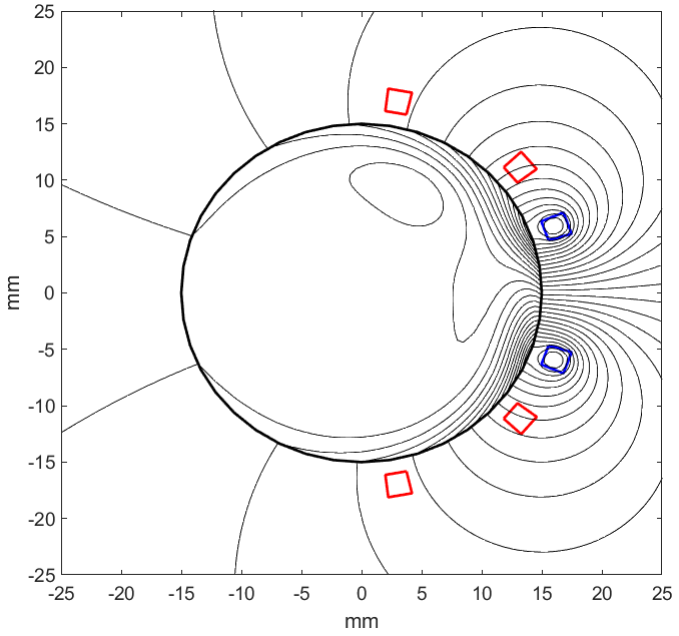

Fig. 4. Magnetic flux distribution at 90 Hz and +1200 r/min with rotating iron rod-first configuration of coils: one excitation coil and two antiserially connected pick-up coils—analytical method.

Higher frequency of 90 Hz is more suitable for differential voltage measurement despite lower flux linkage at higher frequencies.

C. Parameters Variation

Fig. 6 shows changing of magnetic flux distribution for a rotating iron rod at +1200 r/min and 90 Hz and flux linkage between pick-up coils and excitation coil with decreasing gap g (left) and increasing gap and coils angles θ_o and θ_i (right). The difference between the outer and inner angles of coils is considered to be constant in this paper. 3-D graphs shown in Figs. 7 and 8 related to variations in differential induced voltage amplitude versus gap and outer angle of coils show several tendencies. Increasing outer angle of coils to a maximum value of 60° increases the coupling between the excitation coil and pick-up coils and differential induced voltage.

Decreasing gap does not have the same effect for the iron and aluminum rods as the flux leakage (non-coupled flux between the excitation coil and the pick-up coils) increases with decreasing gap below 2 mm due to the high magnetic permeability of iron compared with aluminum. The maximum values of differential induced voltages are 30 μV for a rotating iron rod and 145 μV for an aluminum rod, respectively. Optimum and efficient gap for the rotating iron rod for the maximum differential voltage is calculated as 1.75–2 mm with the outer angle of coils 60° (Fig. 7). A larger air gap is mechanically better and coils are safer when the rod is rotating at high speeds. Fig. 9 presents the differential induced voltage versus relative permeability and conductivity for rotating iron

TABLE II
DIFFERENTIAL MUTUAL FLUX LINKAGE AT DIFFERENT FREQUENCIES—+1200 r/min

Frequency (Hz)	Flux linkage amplitude (nWb-t)-Iron / Aluminum
20	108.4 / 199.1
50	61.5 / 187.5
100	26.6 / 158.1
500	9.4 / 61.5
1000	5.7 / 34.3

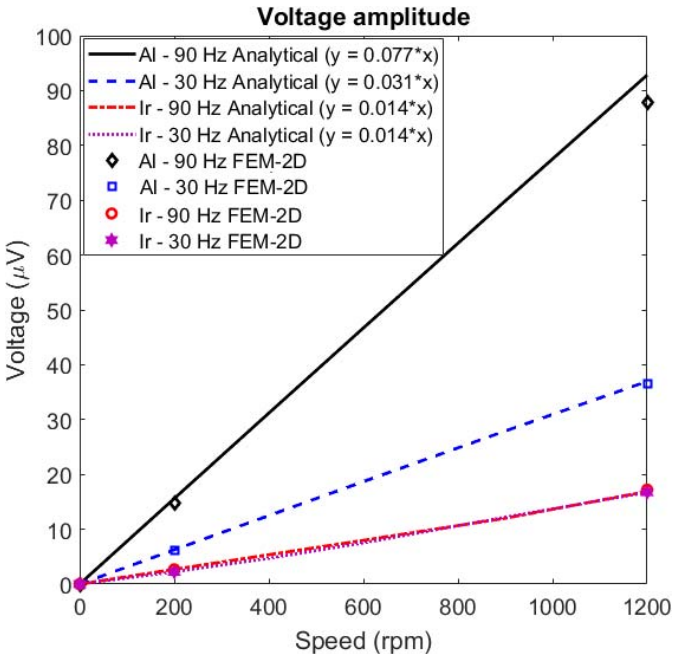

Fig. 5. Differential voltage versus speed for rotating aluminum rod (Al) and rotating iron rod (Ir)—analytical versus 2-D FEM.

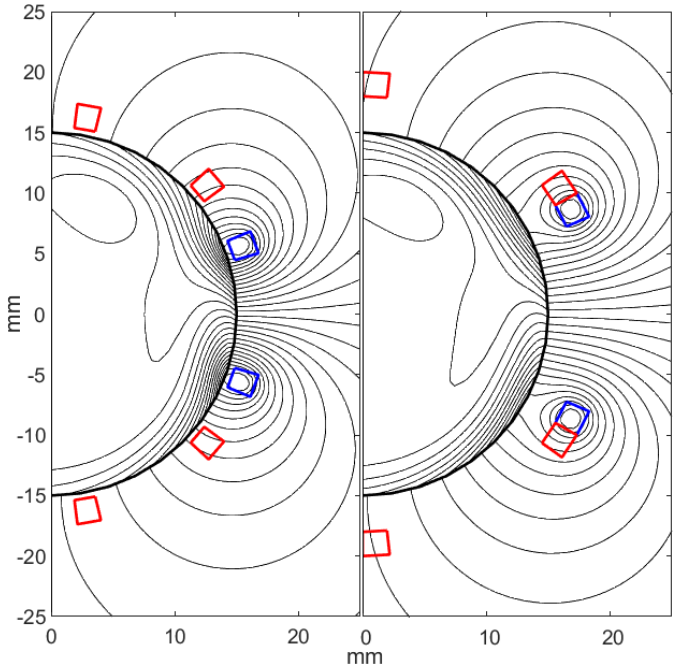

Fig. 6. Magnetic flux distribution at 90 Hz and +1200 r/min with rotating iron rod-modified gap (left) between coils and rod g to 0.5 mm ($r_{\rm wi} - r_i = 0.5$ mm) and modified gap (right) g to 3 mm and also modified coil inner angle $\theta_i = 47.4°$ and modified coil outer angle $\theta_o = 60°$ —analytical method.

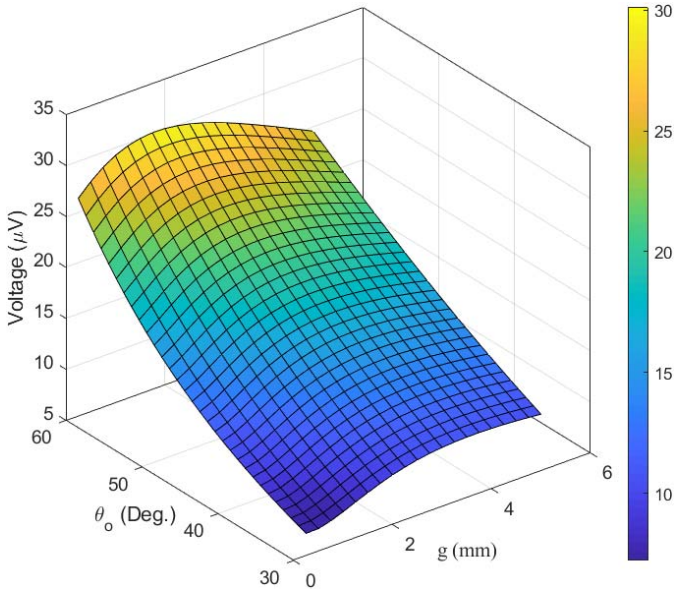

Fig. 7. Variation of differential voltage (amplitude) versus gap g and outer angle of coil θ_o for rotating iron rod at 90 Hz and 1200 r/min—analytical method.

rod. Decreasing magnetic relative permeability causes higher induced voltage similar to increasing iron electrical conductivity. It also shows that relative magnetic permeability has a higher influence than electrical conductivity. This is a weak point of such sensor, as permeability is temperature dependent. The differential induced voltage versus electrical conductivity for a non-magnetic rotating rod ($\mu_r = 1$) is shown in Fig. 10. It can be concluded that, for example, copper is more efficient than aluminum.

Increasing frequency up to 1000 Hz increases differential induced voltages for aluminum and iron rods, as shown

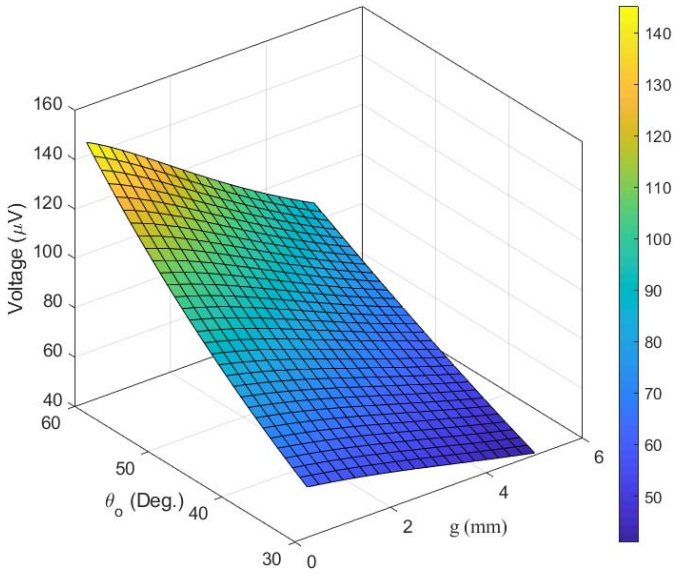

Fig. 8. Variation of differential voltage (amplitude) versus gap g and outer angle of coil θ_o for rotating aluminum rod at 90 Hz and 1200 r/min—analytical method.

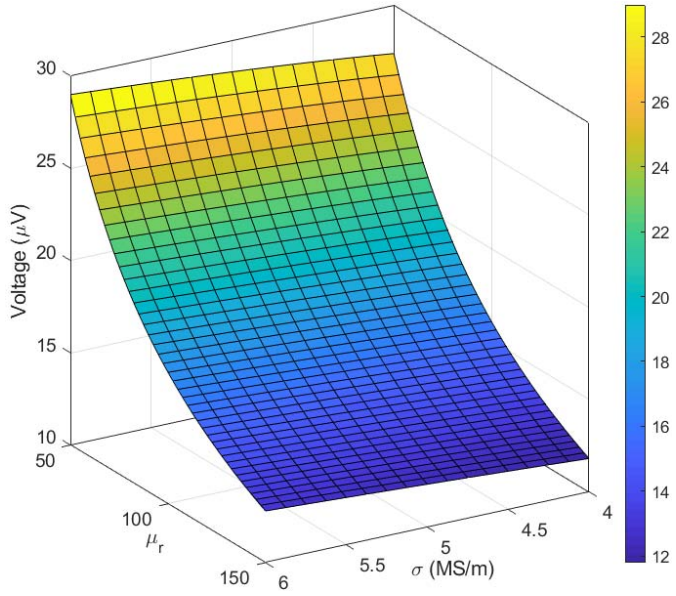

Fig. 9. Variation of differential voltage (amplitude) versus electrical conductivity and magnetic permeability for rotating iron rod at 90 Hz and 1200 r/min ($\theta_o = 46°$ and $g = 1.25$ mm)—analytical method.

in Fig. 11. The curves for rotating iron rod and aluminum rods do not have the same tendency versus frequency because of the high permeability of iron rod. Very high frequency is not recommended because the surface properties of conductive rods have large influence due to small penetration depth. The surfaces of conductive objects are usually more affected, for example, by manufacturing process and corrosion.

Skin depths are presented in Table III at different frequencies. Larger skin depths cause a higher differential flux linkage as shown in Table II and higher differential voltage.

Only linear magnetic modeling using initial permeability is considered in this paper due to the low magnetic fields in the sensor and nonlinearity and hysteresis effects are neglected. Relative magnetic permeability $\mu_{\rm ri} = 100$ (Table I) is selected for the used rotating iron rod in this paper.

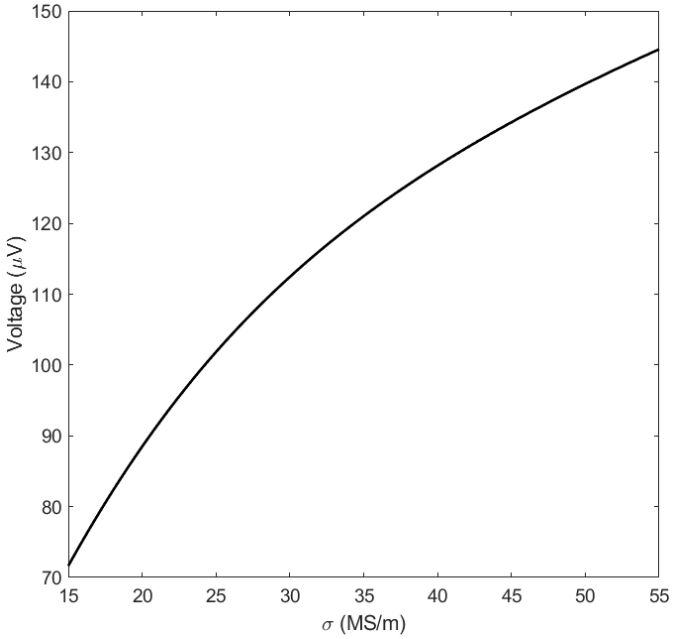

Fig. 10. Variation of differential voltage (amplitude) versus electrical conductivity for rotating aluminum rod at 90 Hz and 1200 r/min ($\theta_o = 46°$ and $g = 1.25$ mm)—analytical method.

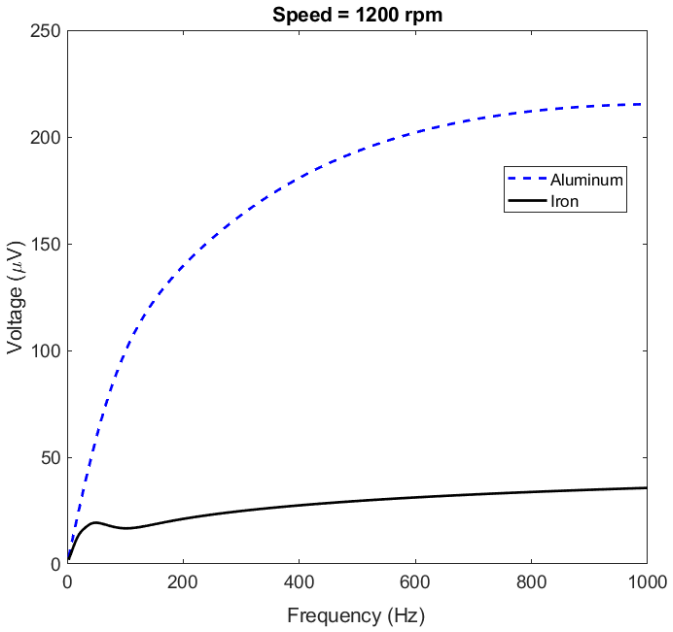

Fig. 11. Variation of differential voltage (amplitude) versus frequency at 1200 r/min ($\theta_o = 46°$ and $g = 1.25$ mm)—analytical method.

IV. 3-D FEM Modeling

A. Static Rotor

A 3-D analysis is required for more accurate analysis of air coil's eddy current speed sensor taking into account 3-D effects such as 3-D flux and eddy currents distributions in the conductive rotating rods. First, the 3-D eddy current analysis (time harmonic) was done using ANSYS/Maxwell software package [20] to evaluate the 3-D FEM model accuracy and parameters such as relative permeability of the iron rod as mentioned in Table I. Calculated self-inductance of the excitation coil and induced voltages in one of the pick-up coils at different frequencies is compared with experimental

TABLE III
Skin Depth at Different Frequencies

Frequency (Hz)	Skin depth, δ (mm)- Iron / Aluminum
20	4.8 / 24.3
50	3.0 / 15.4
100	2.1 / 10.9
500	1.0 / 4.9
1000	0.7 / 3.4

TABLE IV
Inductance of Excitation Coil at Different Frequencies-3-D FEM Versus Experiment

Frequency (Hz)	Inductance (μH) - 3D FEM / Exp.
20 (iron core)	137.2 / 135.0
50 (iron core)	136.6 / 134.2
100 (iron core)	135.8 / 132.4
100 (air core)	98.9 / 95.0
500 (iron core)	132.4 / 129.5
1000 (iron core)	130.5 / 127.0

TABLE V
Induced Voltages in One of the Pick-Up Coils at Different Frequencies—3-D FEM Versus Experiment

Frequency (Hz)	Induced voltage (mV) - 3D FEM / Exp.
1 (iron core)	0.0084 / 0.0076
100 (iron core)	0.91 / 0.85
100 (air core)	0.76 / 0.72
200 (iron core)	1.86 / 1.76

results in Tables IV and V. The calculated self-inductance shows high accuracy. Lower accuracy in the calculated mutual-induced voltage is due to the higher sensitivity to pick-up coils relative locations to the excitation coil and also probably manufacturing tolerance.

B. Rotating Rotor

3-D time transient FEM is used to take into account the rod rotating motion [20]. Fig. 12 shows the meshed model of conducting rods and coils. Half of the model is shown because of symmetry. Second-order elements are used. The sizes of elements are selected based on a compromise between the skin depth in the rotating rod and precise differential voltage calculations and also simulation time. The total axial length of rotating iron rod and rotating aluminum rod is considered as 100 mm in the 3-D FEM simulations.

V. Experiments

The experimental setup is shown in Figs. 13 and 14. Lock-in amplifier SR 830 is used to measure precisely small voltage of pick-up coils and to minimize noise effects. Signal generator Keithley 3390 50 MHz with an internal resistance of 50 Ω is connected to the excitation coil. The aluminum or iron rod is connected to the shaft of a dc motor. The speed range is between 0 and 1200 r/min. The axial length of rotating rods is considered 200 and 100 mm to evaluate its influence on the speed sensor performance.

Fig. 15 shows the experimental results and 3-D FEM calculations for differential induced voltage versus speed.

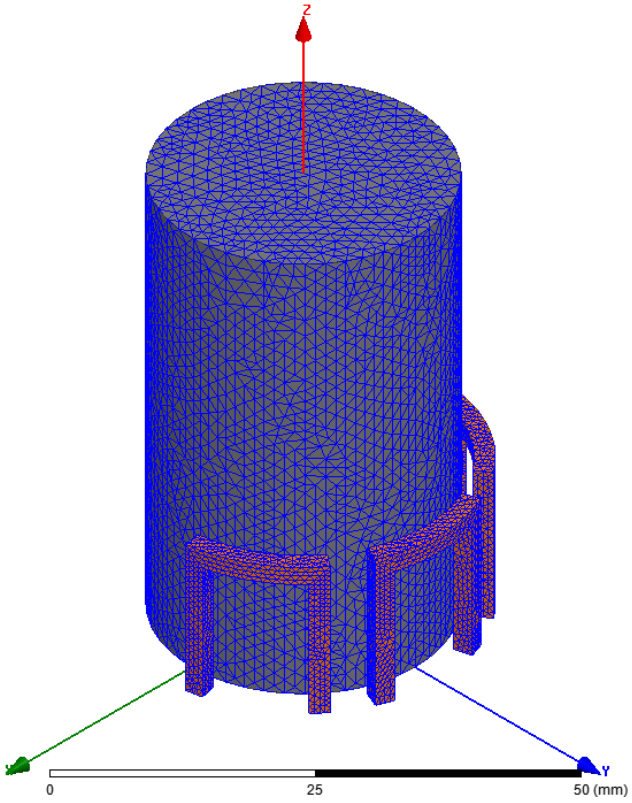

Fig. 12. Meshed model of the eddy current speed sensor.

Fig. 13. Experimental setup for rotational eddy current speed sensor—sensor mounted on rotating rod.

The 3-D FEM calculations coincide very well with experiments with small error (Fig. 16). Sensitivity of the speed sensor is higher for the rotating aluminum rod rather than the iron rod. The linearity of the eddy current speed sensor is excellent despite the simple structure of the proposed sensor. It has been verified that differential induced voltage is the same for two axial lengths of rotating rods, 100 and 200 mm.

The differential induced voltages are measured and calculated in 2-D and 3-D at 30 and 90 Hz, respectively. The 3-D FEM results are higher than 2-D analytical and 2-D FEM calculations (Fig. 5) due to the 3-D effects in the rotating iron rod. 3-D FEM is more precise in comparison

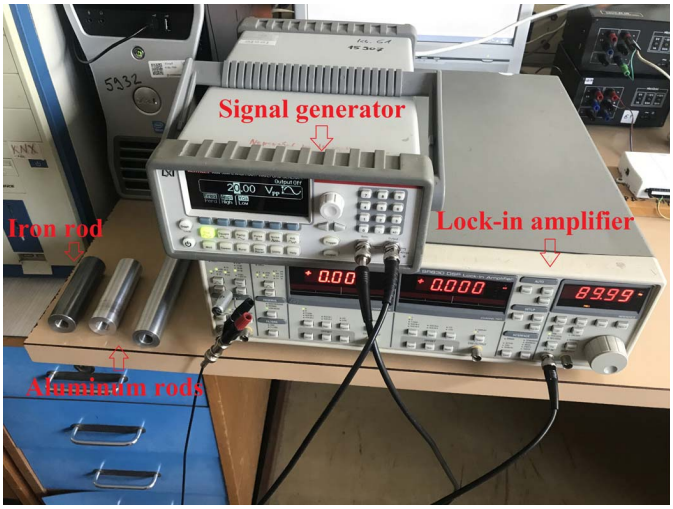

Fig. 14. Experimental setup for rotational eddy current speed sensor—signal generator and lock-in amplifier.

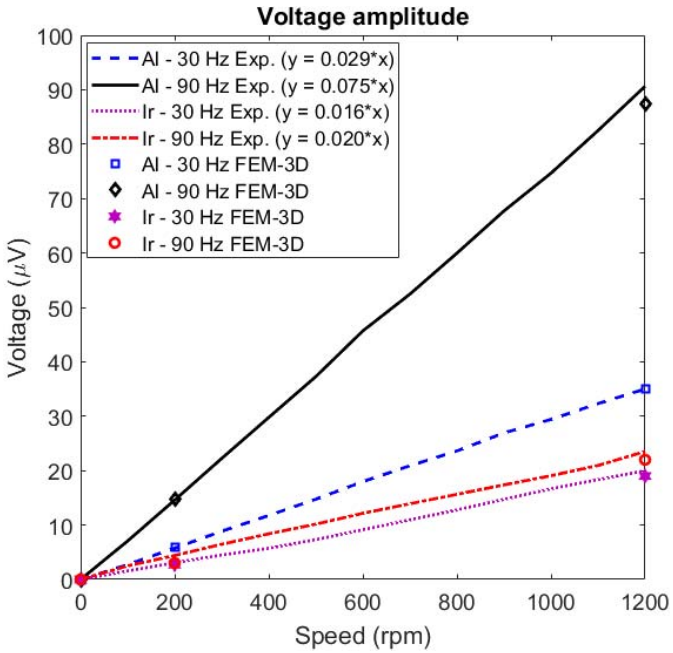

Fig. 15. Induced-voltage versus speed for rotating aluminum rod (Al) and rotating iron rod (Ir)—experiments versus 3-D FEM.

with measurement despite its longer simulations time. 3-D modeling is necessary for air coil or yokeless magnetic devices. Time-consuming 3-D FEM model simulations slow down fast optimization and analysis that is why 2-D models, especially analytical, are preferable at the design stage. Dynamic response of the eddy current speed sensor is higher at 90 Hz, which is important for acceleration and deceleration operations. The sensitivity of eddy current speed sensor for the iron rod should be improved as most of the industrial applications are made with solid iron rather than non-magnetic stainless steel or aluminum.

VI. Double-Layer Rod

Figs. 17 and 18 show a newly proposed double-layer rod with magnetic flux distribution. Center rod is solid iron and aluminum shell is the second layer. The second layer could be

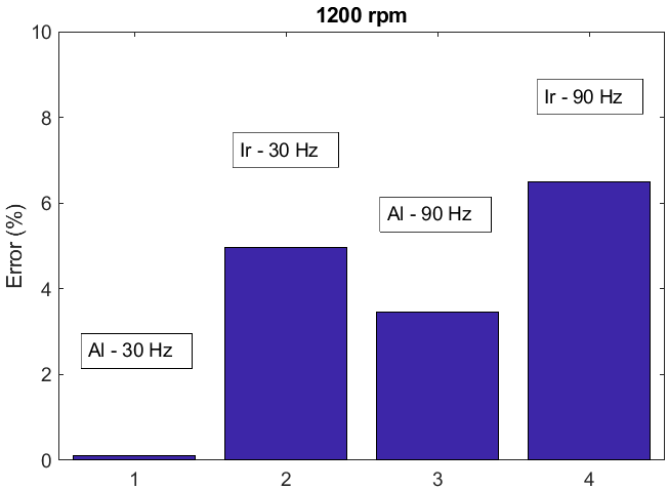

Fig. 16. Error of 3-D FEM results relative to measurements.

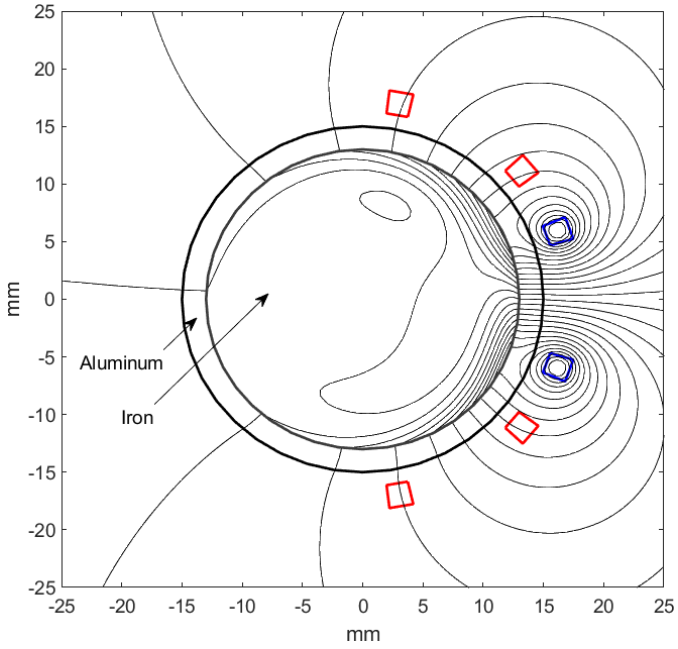

Fig. 17. Magnetic flux distribution at 90 Hz and +1200 r/min with double-layer rotating iron (outer radius 13 mm) and aluminum shell (with 2 mm thickness)—first configuration of coils: one excitation coil and two antiserially connected pick-up coils—analytical method.

any other non-magnetic metal such as copper or brass. Double-layer moving or rotating part is a well-known configuration to improve performance of the solid rotor rotating induction motor or solid secondary linear induction motors [21], [22]. It increases equivalent conductivity of rotating rod and causes low magnetic reluctance using high permeability iron part. The double-layer rotating rod can be easily manufactured by adding a simple shell or ring to the iron rod.

The rotating rod shown in Fig. 17 has a total outer radius of 15 mm with an iron rod radius of 13 mm. Iron rod radius is considered fixed, 15 mm, and the total outer radius is 16 mm, as shown in Fig. 18, with a 1.25 mm gap and same coil angle as Fig. 17. Both the models show improved flux linkages of the pick-up coils in comparison with a complete iron rod.

Differential voltage variations versus aluminum shell thickness for fixed rotating rod outer radius of 15 mm is shown

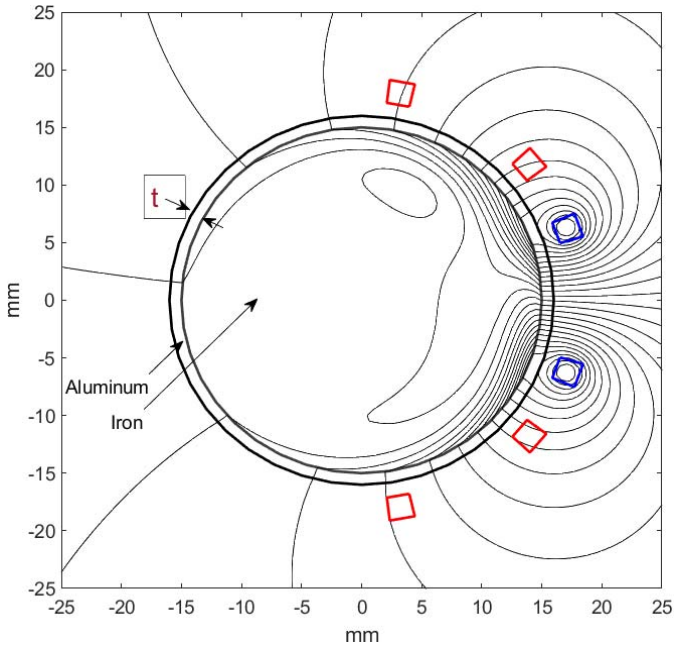

Fig. 18. Magnetic flux distribution at 90 Hz and +1200 r/min with double-layer rotating iron (with radius 15 mm) and aluminum shell (with 1 mm thickness)—first configuration of coils: one excitation coil and two antiserially connected pick-up coils—analytical method.

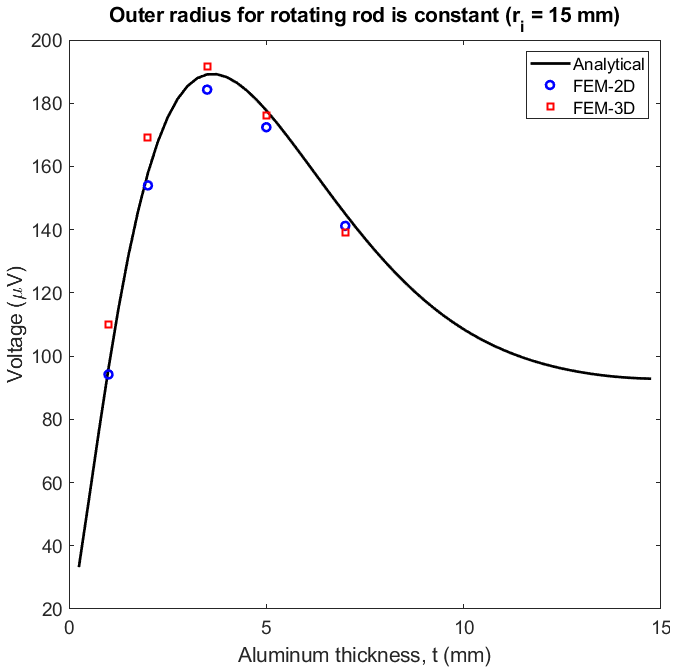

Fig. 19. Variation of differential voltage (amplitude) versus aluminum layer thickness with double-layer rotating iron and aluminum shell (with t mm thickness as shown in Fig. 18)—fixed total outer radius 15 mm.

in Fig. 19 at 90 Hz and 1200 r/min, which has a maximum value of 189 μV (analytical calculations) with an aluminum shell thickness of 3.5 mm. It shows considerable improvement in the speed sensor output and sensitivity. The 3-D and 2-D FEM results approve analytical estimation for the speed sensor performance improvement with the double-layer configuration.

Using higher conductivity, aluminum shell or copper shell could increase more the output differential voltage.

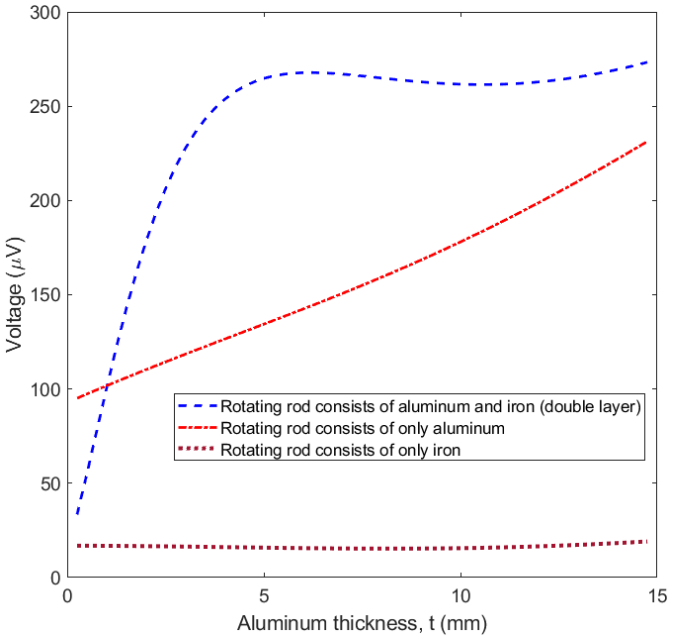

Fig. 20. Variation of differential voltage (amplitude) versus second layer shell thickness (with t mm thickness as shown in Fig. 18)—iron rod part has 15 mm radius—analytical method.

Fig. 20 shows the speed sensor output voltage for the double-layer rotating rod with a fixed rotating iron rod radius of 15 mm in comparison with completely aluminum rod and iron rod with the same outer radius at 90 Hz and 1200 r/min. The maximum value for induced voltage is 268 μV with the aluminum shell thickness of 6 mm, as shown in Fig. 20. The induced voltage in the double-layer rod is considerably higher than a complete aluminum rod. The induced voltage in a complete iron rod does not considerably increase even with much higher radius as shown in Fig. 20.

The effect of aluminum shell or ring height is evaluated, as shown in Figs. 21 and 22. Fig. 21 shows the eddy current distribution for long shell, and Fig. 22 shows the eddy current distribution for short shell. The calculated differential induced voltage is 110 μV in the long shell aluminum model and it becomes 66 μV in the short shell aluminum model due to the modified path for induced eddy currents [23], [24].

Fig. 23 presents the induced voltage versus relative magnetic permeability μ_r for different aluminum shell thicknesses of the double-layer rotating rod with a fixed outer radius of 15 mm at 90 Hz and 1200 r/min. Induced voltages decrease 56% for full iron rotating rod with zero aluminum shell thickness and 6.1% with 1 mm aluminum shell thickness when μ_r changes from 50 to 150. However, induced voltages only increase 0.23% with 2.35 mm aluminum shell thickness and 1.23% with 3.5 mm aluminum shell thickness. It shows that the effect of relative magnetic permeability could be minimized by adjusting the aluminum shell thickness. Gradient of induced voltage versus relative magnetic permeability is negative at small aluminum shell thickness and it is positive at bigger aluminum shell thickness.

The voltages are rather low, but for only 50-turn coil. A real number of turns can be higher, and it is practically limited only

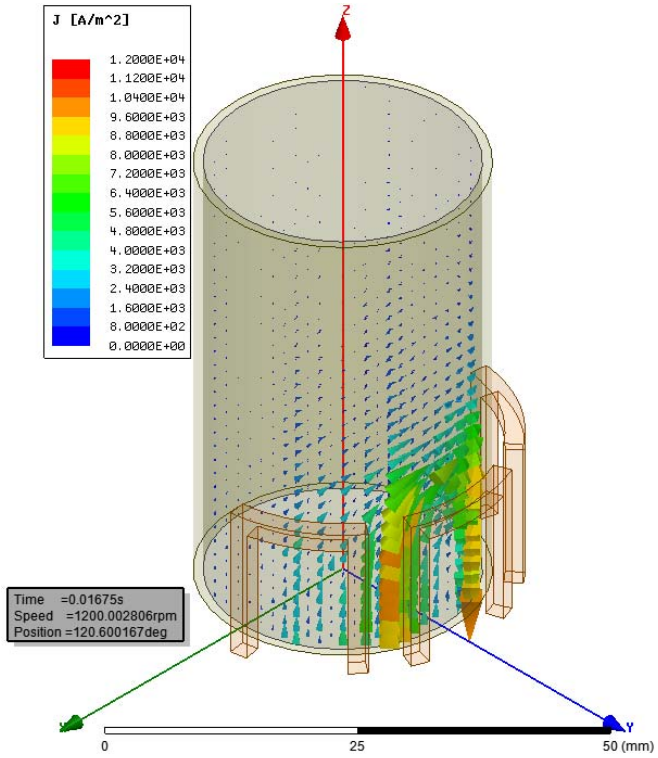

Fig. 21. Eddy currents distribution in the double-layer rotating iron + aluminum shell at 1200 r/min and 90 Hz (outer radius of iron is 14 mm and aluminum shell thickness is 1 mm)—long aluminum shell.

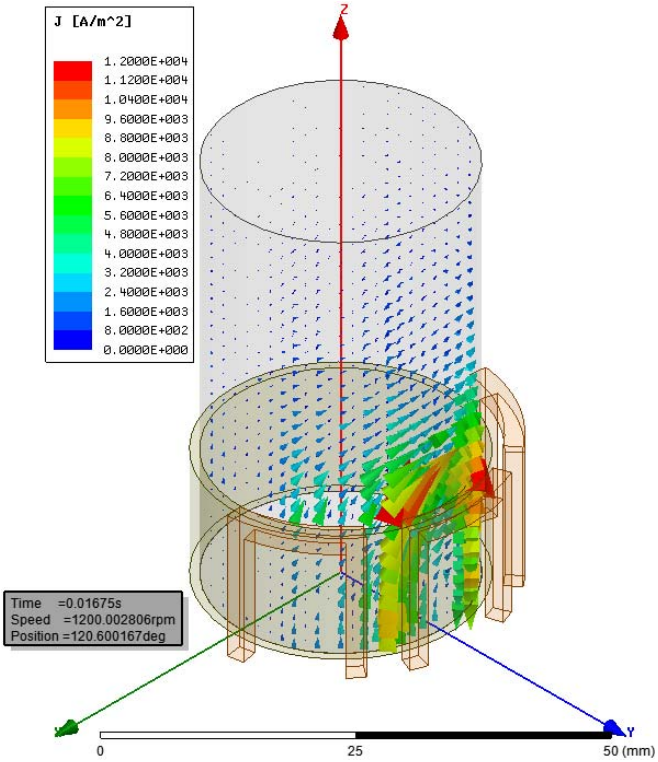

Fig. 22. Eddy currents distribution in the double-layer rotating iron + aluminum shell at 1200 r/min and 90 Hz (outer radius of iron is 14 mm and aluminum shell thickness is 1 mm)—short aluminum shell with 30 mm height.

by parasitic capacitances. For example, setting number of turns for the excitation coil and pick-up coils equal to 1000-turn can increase the eddy current speed sensor output with a gain

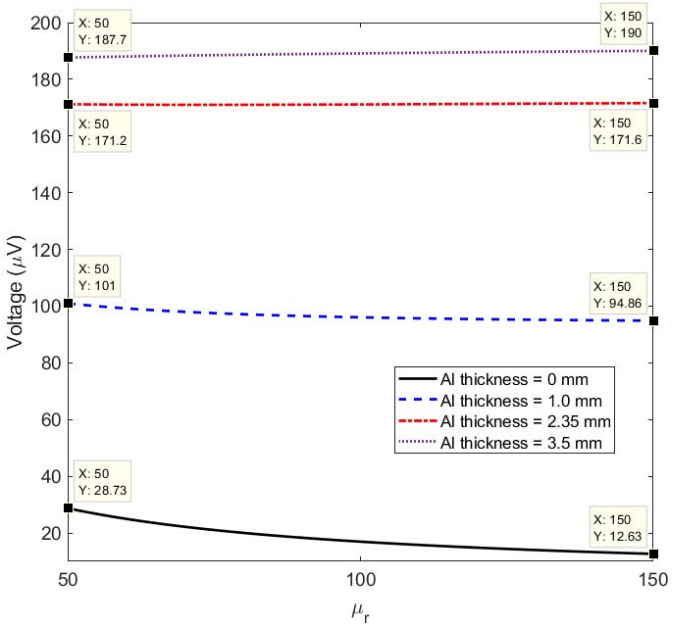

Fig. 23. Variation of differential voltage (amplitude) versus iron rod permeability at different aluminum layer thicknesses—1200 r/min and 90 Hz—analytical method.

of 400 for the same excitation current, as the induced voltage is proportional to the square of a number of turns.

VII. Conclusion

A novel rotational eddy current speed sensor was presented. Analytical and numerical FEM calculations were used to analyze and improve the performance of the proposed speed sensor. A 2-D analytical method is faster and more suitable for the design of eddy current speed sensor despite it being less precise in comparison with 3-D FEM for air coil configuration.

Different configurations of rotational speed sensor and parameters were evaluated in this paper. The measurements and calculations have been done up to 1200 r/min but the proposed speed sensor is also suitable for higher speeds as it does not have mechanical and electrical limitations. The whole coils span is less than 180°, which could be installed in one side of the rotating rod and it is mechanically contactless with rotating rod.

The double-layer rod can significantly improve eddy current speed sensor performance when the rotating rod must be from magnetic steel. It needs only high electrical conductivity non-magnetic ring, or shell, for example, made of aluminum or copper. By using the highly conductive non-magnetic shell, the sensitivity is improved, and it becomes less susceptible to permeability changes.

Acknowledgment

This work was supported by Czech Technical University in Prague under Grant SGS18/187/OHK3/3T/1. The authors would like to thank J. Cerny from the Department of Measurement, Faculty of Electrical Engineering, Czech Technical University in Prague, for his support in building rotational eddy current speed sensor components.

References

[1] T. Addabbo *et al.*, "Instantaneous rotation speed measurement system based on variable reluctance sensors for torsional vibration monitoring," *IEEE Trans. Instrum. Meas.*, to be published.

[2] N. Fernando, P. Arumugam, and C. Gerada, "Design of a stator for a high-speed turbo-generator with fixed permanent magnet rotor radius and volt–ampere constraints," *IEEE Trans. Energy Convers.*, vol. 33, no. 3, pp. 1311–1320, Sep. 2018.

[3] P. Ripka, *Magnetic Sensors and Magnetometers*. Norwood, MA, USA: Artech House, 2001.

[4] J. J. Costello and A. C. Pickard, "A novel speed measurement system for turbomachinery," *IEEE Sensors Lett.*, vol. 2, no. 4, Dec. 2018, Art. no. 2501204.

[5] E. Cardelli, A. Faba, and F. Tissi, "Contact-less speed probe based on eddy currents," *IEEE Trans. Magn.*, vol. 49, no. 7, pp. 3897–3900, Jul. 2013.

[6] T. J. Rocha, H. G. Ramos, A. L. Ribeiro, and D. J. Pasadas, "Evaluation of subsurface defects using diffusion of motion-induced eddy currents," *IEEE Trans. Instrum. Meas.*, vol. 65, no. 5, pp. 1182–1187, May 2016.

[7] T. Sonoda, R. Ueda, K. Fujitani, T. Irisa, and S. Tatata, "DC magnetic field type eddy current speed sensor detecting cross magnetization field with amorphous core," *IEEE Trans. Magn.*, vol. MAG-21, no. 5, pp. 1732–1734, Sep. 1985.

[8] N. Takehira and A. Tanaka, "Analysis of a perpendicular-type eddy-current speed meter," *IEE Proc. A-Phys. Sci., Meas. Instrum., Manage. Educ.-Rev.*, vol. 135, no. 2, pp. 89–94, Feb. 1988.

[9] T. Itaya, K. Ishida, A. Tanaka, N. Takehira, and T. Miki, "Eddy current distribution for a rectangular coil arranged parallel to a moving conductor slab," *IET Sci., Meas. Technol.*, vol. 6, no. 2, pp. 43–51, Mar. 2012.

[10] T. Itaya, K. Ishida, A. Tanaka, and N. Takehira, "Analysis of a fork-shaped rectangular coil facing moving sheet conductors," *IET Sci., Meas. Technol.*, vol. 3, no. 4, pp. 279–285, Jul. 2009.

[11] A. Tüysüz, M. Flankl, J. W. Kolar, and A. Mütze, "Eddy-current-based contactless speed sensing of conductive surfaces," in *Proc. IEEE 2nd Annu. Southern Power Electron. Conf.*, Dec. 2016, pp. 1–6.

[12] M. Mirzaei, P. Ripka, A. Chirtsov, and J. Vyhnanek, "Eddy current linear speed sensor," *IEEE Trans. Magn.*, vol. 55, no. 1, Jan. 2019, Art. no. 4000304.

[13] J. Rickman, "Eddy current turbocharger blade speed detection," *IEEE Trans. Magn.*, vol. MAG-18, no. 5, pp. 1014–1021, Sep. 1982.

[14] D. Gerada, X. Huang, C. Zhang, H. Zhang, X. Zhang, and C. Gerada, "Electrical machines for automotive electrically assisted turbocharging," *IEEE/ASME Trans. Mechatronics*, vol. 23, no. 5, pp. 2054–2065, Oct. 2018.

[15] M.-S. Lim, J.-M. Kim, Y.-S. Hwang, and J.-P. Hong, "Design of an ultra-high-speed permanent-magnet motor for an electric turbocharger considering speed response characteristics," *IEEE/ASME Trans. Mechatronics*, vol. 22, no. 2, pp. 774–784, Apr. 2017.

[16] K. J. Binns, P. J. Lawrenson, and C. W. Trowbridge, *The Analytical and Numerical Solution of Electric and Magnetic Fields*. Hoboken, NJ, USA: Wiley, 1992.

[17] M. N. O. Sadiku, *Numerical Techniques in Electromagnetics with MATLAB*, 2nd ed. Boca Raton, FL, USA: CRC Press, 2000.

[18] K. R. Davey, "Analytic analysis of single- and three-phase induction motors," *IEEE Trans. Magn.*, vol. 34, no. 5, pp. 3721–3727, Sep. 1998.

[19] D. Schieber, *Electromagnetic Induction Phenomena*. New York, NY, USA: Springer-Verlag, 1986.

[20] *ANSYS Maxwell*. Accessed: Jan. 23, 2019. [Online]. Available: https://www.ansys.com/products/electronics/ansys-maxwell

[21] S. A. Nasar and L. del Cid, "Certain approaches to the analysis of single-sided linear induction motors," *Proc. Inst. Elect. Eng.*, vol. 120, no. 4, pp. 477–483, Apr. 1973.

[22] J. F. Gieras and J. Saari, "Performance calculation for a high-speed solid-rotor induction motor," *IEEE Trans. Ind. Electron.*, vol. 59, no. 6, pp. 2689–2700, Jun. 2012.

[23] H. Bolton, "Transverse edge effect in sheet-rotor induction motors," *Proc. Inst. Elect. Eng.*, vol. 116, no. 5, pp. 725–731, May 1969.

[24] H. Seo, J. Lim, G.-H. Choe, J.-Y. Choi, and J.-H. Jeong, "Algorithm of linear induction motor control for low normal force of magnetic levitation train propulsion system," *IEEE Trans. Magn.*, vol. 54, no. 11, Nov. 2018, Art. no. 8207104.

3-2-3-3 Design and Modeling of A Linear Speed Sensor with A Flat Type Structure and Air Coils [J7]

This paper presents the design and modeling of a linear eddy current speed sensor with a flat type structure and an air coil configuration. The theory of the eddy current speed sensor is based on utilizing the speed component of the induced currents in a solid moving conductor under stationary or alternating source fields. The stationary part comprises one rectangular excitation coil and two antiserially connected rectangular pick-up coils on the left and right sides of the excitation coil in the direction of the trajectory of the moving part. The moving part is considered firstly as a rectangular conductive ferromagnetic solid iron plate, and secondly as a rectangular aluminum plate. A 3D analytical model using Fourier series is developed to analyze the linear speed sensor in Cartesian coordinates. In addition, the 3D numerical finite element method is used for simulations of the linear speed sensor, and the results are compared with the results for analytical methods. The effects of iron permeability on the speed sensor are calculated for a rectangular ferromagnetic solid iron bar or conductor. The experimental results are presented for a linear speed sensor for a rectangular ferromagnetic solid iron plate and also for a rectangular aluminum plate, at variable speeds.

The core of this paper is precise analysis method allowing fast design and suitability evaluations of eddy current speed sensors with both non-ferromagnetic and ferromagnetic materials for moving parts, which were overlooked in the literature. The performance and the design of a flat type eddy current speed sensor with air coils have been analyzed. The linearity of the proposed speed sensor is excellent, despite its simple configuration. The calculated and measured speed range has been considered up to 2 m/s, but it can be extended for higher translational speed. The proposed eddy current speed sensor could be used for all types of linear machines, as it has a simple structure and precise performance. The air coil configuration enables the proposed eddy current speed sensor to be very compact and cost-effective. The effects of the material of the conductive moving parts have been evaluated. They have been shown to have a very critical influence on the design and analysis of eddy current speed sensors, and they must be taken into account. The output results and the performance of an eddy current speed sensor with a ferromagnetic moving part differ greatly from the results and the performance with a non-magnetic moving part. It is critical to compensate the magnetic permeability and also the conductivity of the moving part in the design of this sensor. Temperature stability and the effects on the conductive moving part must also be taken into consideration, as the conductivity and even the magnetic permeability of the moving part are affected by temperature.

Journal of Magnetism and Magnetic Materials 495 (2020) 165834

Contents lists available at ScienceDirect

Journal of Magnetism and Magnetic Materials

journal homepage: www.elsevier.com/locate/jmmm

Research articles

Design and modeling of a linear speed sensor with a flat type structure and air coils

Mehran Mirzaei*, Pavel Ripka, Andrey Chirtsov, Jan Vyhnanek, Vaclav Grim

Faculty of Electrical Engineering, Czech Technical University, Prague 16627, Czech Republic

ARTICLE INFO

Keywords:
Flat type
Linear speed sensor
Eddy current
Aluminum
Iron
Analytical method and finite element method

ABSTRACT

This paper presents the design and modeling of a linear eddy current speed sensor with a flat type structure and an air coil configuration. The theory of the eddy current speed sensor is based on utilizing the speed component of the induced currents in a solid moving conductor under stationary or alternating source fields. The stationary part comprises one rectangular excitation coil and two antiserially connected rectangular pick-up coils on the left and right sides of the excitation coil in the direction of the trajectory of the moving part. The moving part is considered firstly as a rectangular conductive ferromagnetic solid iron plate, and secondly as a rectangular aluminum plate. A 3D analytical model using Fourier series is developed to analyze the linear speed sensor in Cartesian coordinates. In addition, the 3D numerical finite element method is used for simulations of the linear speed sensor, and the results are compared with the results for analytical methods. The effects of iron permeability on the speed sensor are calculated for a rectangular ferromagnetic solid iron bar or conductor. The experimental results are presented for a linear speed sensor for a rectangular ferromagnetic solid iron plate and also for a rectangular aluminum plate, at variable speeds. The calculation and the experimental results show that the speed sensor outputs differ completely for solid iron conductive plates and for aluminum conductive plates, due to the different electrical conductivities and magnetic permeabilities.

1. Introduction

Speed sensors are needed for rotating and translational energy converters [1–5]. Non-magnetic optical sensors, variable reluctance sensors, eddy current-based sensors and Hall effect magnetic sensors can be developed for speed measurements. Magnetic sensors could have a moving or stationary permanent magnet or coil as the excitation source. The principles of magnetic sensors are based on the magnetic properties of the sensing material, or on a change in the parameters of the magnetic circuit [6]. Magnetic sensors are more reliable and more robust to dust and dirt than non-magnetic sensors [7,8], especially when the position and the speed of moving objects are being measured.

Eddy current-based speed sensors are widely used for various configurations and applications [6] and [9–15]. For example, the Faraday generator, the homopolar generator and magnetic flowmeters [6] and [15] are the earliest utilization of the speed effect in moving conductive objects subjected to magnetic fields. Perpendicular and non-perpendicular pick-up coils for eddy current speed sensors are analyzed using the Fourier transform in [9–11], as is presented later using a ferrite core in [12]. Aluminum moving part is used in [9–12], which has relative magnetic permeability equal to 1. An eddy current speed sensor with an axisymmetric structure was developed and measured at variable speeds with a ferromagnetic iron rod [13]. It has three coils for excitation and pick-up voltage. The eddy current-based speed sensor has a quite simple and cost-effective structure, which is an essential consideration for industrial applications.

Our solution for flat type linear speed measurements is based on a single coil excitation coil with an AC current and two pick-up coils for measurements without using a ferromagnetic yoke. In order to analyze the eddy current speed sensor, a fast and precise 3D analytical method is presented for calculating the coil inductance and the induced voltages in the pick-up coils. This method takes into account the eddy currents in the moving conductive part caused by alternating current and the speed of the moving current part for a flat shape model, using Fourier series. General closed-form equations are also obtained for the output results. A 3D time-stepping finite element method (FEM) simulation taking into account the speed of the moving part is also presented for a comparison with analytical calculations. Various relative magnetic permeabilities and conductivities are considered for the solid iron moving part in order to evaluate the effects of the electrical and magnetic parameters on the performance of the eddy current speed sensor. The sensitivity of the eddy current speed sensor versus the gap between coils and moving

* Corresponding author.
E-mail address: mirzameh@fel.cvut.cz (M. Mirzaei).

https://doi.org/10.1016/j.jmmm.2019.165834
Received 26 June 2019; Received in revised form 23 August 2019; Accepted 10 September 2019
Available online 20 September 2019

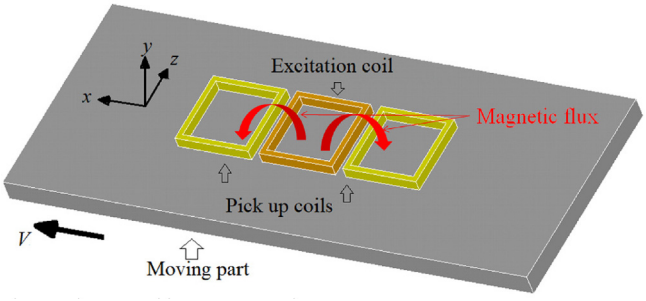

Fig. 1. Flat type eddy current speed sensor.

plate is also evaluated. Flat shape aluminum rectangular plates and solid ferromagnetic iron rectangular plates are both used in the measurements for the moving part, and the experimental results at variable speeds are compared with analytical calculations.

2. Model and coil configurations

Fig. 1 shows a 3D model of a flat type eddy current speed sensor coils and solid conductor moving part. The middle coil is the excitation coil, and the coils on the left and right sides are the pick-up coils, which are connected antiserially. The moving part is made of solid iron or of aluminum. Only 1-D movement is considered with speed, V in the direction of the x-axis (Fig. 1).

It is obvious that the induced voltage in the pick-up coils is zero at zero speed, because the net flux linkage is zero in the antiserially connected pick-up coils (Fig. 1).

Fig. 2 and Table 1 show the parameters and the dimensions of a linear speed sensor. Parameters d, h, t, g, w_1, w_2, σ_{al}, σ_i and μ_{ri} are the thickness of the moving part, the coil height, the coil thickness, the gap between the coils and the moving part (the air gap), the inner width of the coils in the x-direction, the inner width of the coils in the z-direction, the electrical conductivity of aluminum, the electrical conductivity of iron, and the relative magnetic permeability of iron, respectively. Regions 1, 2, 3, 4 and 5 in Fig. 2 (above) are the region

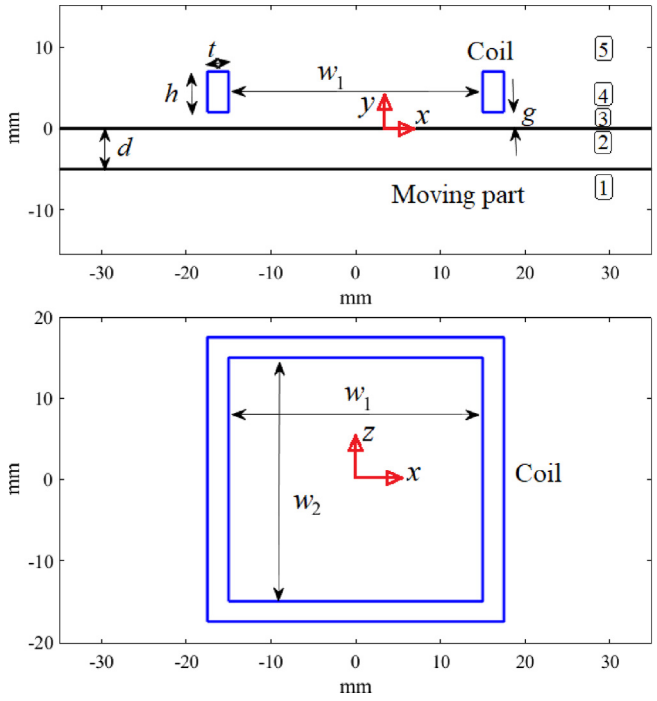

Fig. 2. Computational models – in the x-y plane (above) and in the x-z plane (below).

Table 1
Linear speed sensor parameters.

Parameters	Values
I	154 mA
N	100
d	5 mm and 10 mm
h	5.0 mm
t	2.5 mm
g	2 mm
w_1	30 mm
w_2	30 mm
σ_{al}	30.3 MS/m
σ_i	5.24 MS/m
μ_{ri}	100

below the moving part, in the moving part, the air region between the coils and the moving part, in the region of the coils, and the air region above the coils, respectively.

3. 3D modeling

3.1. Analytical

3D modeling and analysis is required for the proposed eddy current speed sensor, because the air coil configuration is used. 2D analysis is not accurate enough to take the 3D fluxes into account. The general partial differential equations in 3D, using the Maxwell equations, are as follows [16–18]:

$$\nabla \times H = J,\ B = \mu H,\ \nabla \times J = -\sigma\frac{dB}{dt}$$
$$\nabla\cdot B = 0 \rightarrow B = \nabla \times A,\ \nabla\cdot A = 0 \rightarrow \frac{\partial A_x}{\partial x} + \frac{\partial A_z}{\partial z} = 0$$
$$\nabla^2 A_x - \mu\sigma\frac{dA_x}{dt} = -\mu J_{s,x}$$
$$\frac{dA_x}{dt} = \frac{\partial A_x}{\partial t} + \frac{dx}{dt}\cdot\frac{\partial A_x}{\partial x} = \frac{\partial A_x}{\partial t} + V\cdot\frac{\partial A_x}{\partial x}$$
$$\frac{\partial^2 A_x}{\partial x^2} + \frac{\partial^2 A_x}{\partial y^2} + \frac{\partial^2 A_x}{\partial z^2} - \mu\sigma\left(\frac{\partial A_x}{\partial t} + V\cdot\frac{\partial A_x}{\partial x}\right) = -\mu J_{s,x}$$
$$\nabla^2 A_z - \mu\sigma\frac{dA_z}{dt} = -\mu J_{s,z}$$
$$\frac{dA_z}{dt} = \frac{\partial A_z}{\partial t} + \frac{dx}{dt}\cdot\frac{\partial A_z}{\partial x} = \frac{\partial A_z}{\partial t} + V\cdot\frac{\partial A_z}{\partial x}$$
$$\frac{\partial^2 A_z}{\partial x^2} + \frac{\partial^2 A_z}{\partial y^2} + \frac{\partial^2 A_z}{\partial z^2} - \mu\sigma\left(\frac{\partial A_z}{\partial t} + V\cdot\frac{\partial A_z}{\partial x}\right) = -\mu J_{s,z} \quad (1)$$

where H is magnetic field strength, B is magnetic flux density, J is current density, A is magnetic vector potential, μ is relative magnetic permeability, σ is electrical conductivity, A_x and A_z are the x-axis and z-axis components of the magnetic vector potentials, and $J_{s,x}$ and $J_{s,z}$ are the x-axis and z-axis components of the source current densities in the excitation coil.

Only linear magnetic modeling using the initial permeability is considered here, due to the low magnetic fields in the sensor, and nonlinearity and hysteresis effects are neglected.

The y-component of the magnetic vector potential is assumed to be zero, because the excitation coil is parallel to the x-z plane, and the y-component of the source current density is therefore zero [9] and [16] and also the dimensions of conducting object are enough large in comparison with excitation coil. This assumption helps to solve analytically computational model of the eddy current sensor.

The method of separation of variables (the Fourier method) is used to solve (1) [16] and [19]. It is assumed that the magnetic fields change sinusoidally against time and anti-periodically in the x-direction with period length $2l$ and in the z-direction with period length $2L$. It is assumed that the computational model of eddy current sensor is artificially repeated in longitudinal direction and transversal direction as shown in Fig. 3. Therefore the derivations in (1) can therefore be replaced as follows using the method of separation of variables:

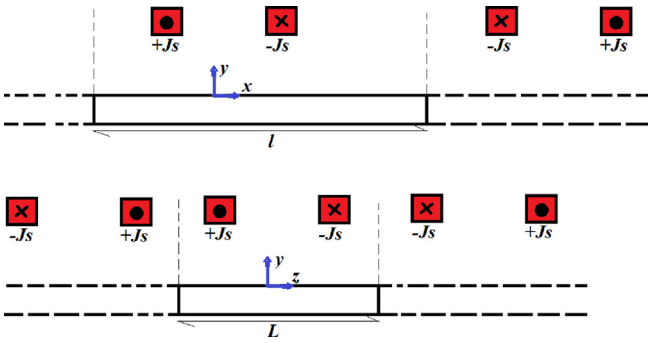

Fig. 3. Longitudinal view of anti-periodically repetition (above) and transversal view of anti-periodically repetition.

$$A_{x,z} = \sum_n \sum_m X_{x,z}^m(x)\cdot Y_{x,z}^{m,n}(y)\cdot Z_{x,z}^n(z)\cdot T(t) \tag{2}$$

$$\begin{gathered} X_{x,z}^m(x) \propto \exp(-jk_m\cdot x),\ \ k_m = m\frac{\pi}{l},\ \ \ m = \pm1, \pm3, \pm5, \ldots \\ Z_{x,z}^n(z) \propto \exp(-jk_n\cdot z),\ \ k_n = n\frac{\pi}{L},\ \ \ n = \pm1, \pm3, \pm5, \ldots \\ T(t) \propto \exp(j\omega\cdot t) \\ \frac{\partial A_{x,z}}{\partial t} = j\omega\cdot A_{x,z} \\ \omega = 2\pi f \\ \frac{\partial A_{x,z}^{m,n}}{\partial x} = -jk_m\cdot A_{x,z}^{m,n},\ \ \frac{\partial^2 A_{x,z}^{m,n}}{\partial x^2} = -k_m^2\cdot A_{x,z}^{m,n} \\ \frac{\partial^2 A_{x,z}^{m,n}}{\partial z^2} = -k_n^2\cdot A_{x,z}^{m,n} \end{gathered} \tag{3}$$

$$-k_m^2 A_{x,z}^{m,n} + \frac{\partial^2 A_{x,z}^{m,n}}{\partial y^2} - k_n^2 A_{x,z}^{m,n} - j\mu\sigma(\omega - V\cdot k_m)A_{x,z}^{m,n} = -\mu J_{s,x,z}^{m,n} \tag{4}$$

where f is frequency. m and n are harmonic orders. The magnetic flux densities and eddy current densities are forced to be zero at boundaries $x = \pm l/2$ and $z = \pm L/2$ using assumptions of the model in Fig. 3. The solutions of (1) versus y for regions 1 ($A_{z,1}$, $A_{x,1}$), 2 ($A_{z,2}$, $A_{x,2}$), 3 ($A_{z,3}$, $A_{x,3}$), 4 ($A_{z,4}$, $A_{x,4}$) and 5 ($A_{z,5}$, $A_{x,5}$) are presented in (5).

Harmonic orders are only odd numbers as the computational model is symmetric and it is anti-periodically repeated.

$$\begin{gathered} A_{z,1} = \sum_n \sum_m (C_{11}\exp(\gamma_1 y) + C_{12}\exp(\gamma_1 y)) \\ \times \exp(j(\omega t - k_m x - k_n z)),\quad \sigma = 0,\ J_{s,z} = 0 \\ \gamma_1 = \gamma,\ \ (\gamma = \sqrt{k_m^2 + k_n^2}),\ \ A_{x,1} = -\frac{k_n}{k_m}A_{z,1} \\ A_{z,2} = \sum_n \sum_m (C_{21}\exp(\gamma_2 y) + C_{22}\exp(\gamma_2 y)) \\ \times \exp(j(\omega t - k_m x - k_n z)),\quad \sigma \neq 0,\ \mu = \mu_2,\ J_{s,z} = 0 \\ \gamma_2 = \sqrt{\gamma^2 + j\mu_2\sigma(\omega - k_m\cdot V)},\ \ A_{x,2} = -\frac{k_n}{k_m}A_{z,2} \\ A_{z,3} = \sum_n \sum_m (C_{31}\exp(\gamma_3 y) + C_{32}\exp(\gamma_3 y)) \\ \times \exp(j(\omega t - k_m x - k_n z)),\quad \sigma = 0,\ J_{s,z} = 0 \\ \gamma_3 = \gamma,\ \ A_{x,3} = -\frac{k_n}{k_m}A_{z,3} \\ A_{z,4} = \sum_n \sum_m \left(C_{41}\exp(\gamma_4 y) + C_{42}\exp(\gamma_4 y) + \frac{\mu_4 J_p^{m,n}}{\gamma_4^2}\right) \\ \times \exp(j(\omega t - k_m x - k_n z)),\quad \sigma = 0,\ \mu = \mu_4,\ J_{s,z} \neq 0 \\ \gamma_4 = \gamma,\ \ A_{x,4} = -\frac{k_n}{k_m}A_{z,4} \\ A_{z,5} = \sum_n \sum_m (C_{51}\exp(\gamma_5 y) + C_{52}\exp(\gamma_5 y)) \\ \times \exp(j(\omega t - k_m x - k_n z)),\quad \sigma = 0,\ J_{s,z} = 0 \\ \gamma_5 = \gamma,\ \ A_{x,5} = -\frac{k_n}{k_m}A_{z,5} \end{gathered} \tag{5}$$

where C_{11}, C_{12}, C_{21}, C_{22}, C_{31}, C_{32}, C_{41}, C_{42}, C_{51} and C_{52} are constants, and they are calculated by the boundary conditions between regions 1 to 5 in (6).

$$\begin{gathered} A_{z,1}(y = -\infty) = 0 \\ A_{z,1}(y = -d) = A_{z,2}(y = -d) \\ H_{x,1}(y = -d) = H_{x,2}(y = -d) \\ A_{z,2}(y = 0) = A_{z,3}(y = 0) \\ H_{x,2}(y = 0) = H_{x,3}(y = 0) \\ A_{z,3}(y = g) = A_{z,4}(y = g) \\ H_{x,3}(y = g) = H_{x,4}(y = g) \\ A_{z,4}(y = g + h) = A_{z,5}(y = g + h) \\ H_{x,4}(y = g + h) = H_{x,5}(y = g + h) \\ A_{z,5}(y = \infty) = 0 \\ H_x = \frac{B_x}{\mu} = \frac{1}{\mu}\frac{\partial A_z}{\partial y} \end{gathered} \tag{6}$$

where H_x are B_x are the x-component of the magnetic flux density and magnetic field strength, respectively. Parameter $J_p^{m,n}$ in (5) for coil excitation is obtained as follows:

$$\begin{gathered} J_p^{m,n} = 4\frac{j}{n\pi l}C_J\cdot J_s \\ C_J = \frac{1}{k_m + k_n}C_{J,1}\cdot C_{J,2} - \frac{1}{k_m - k_n}C_{J,3}\cdot C_{J,4} \\ C_{J,1} = \cos\left(k_m\frac{w_1 + t}{2} + k_n\frac{w_2 + t}{2}\right) \\ C_{J,2} = \sin\left(k_m\frac{t}{2} + k_n\frac{t}{2}\right) \\ C_{J,3} = \cos\left(k_m\frac{w_1 + t}{2} - k_n\frac{w_2 + t}{2}\right) \\ C_{J,4} = \sin\left(k_m\frac{t}{2} - k_n\frac{t}{2}\right) \\ J_s = \frac{N\cdot I}{h\cdot t} \end{gathered} \tag{7}$$

where N and I are the number of turns per coil and the current amplitude (Table 1), respectively.

In this paper, it is considered that the excitation coil and the pickup coils have same dimensions and number of turns. The mutually-induced voltage, U_M, and the mutual inductance, L_M, can be calculated as follows [16,20,21]:

$$L_M = \frac{\Psi_M}{I} = \frac{N\int(\int A_4\cdot dl)ds}{I\cdot h\cdot t},\ \ U_M = -j\omega\cdot I\cdot L_M \tag{8}$$

where Ψ_M is the total average mutual flux linkage over the volume of the coils. Line integration of A_4 (magnetic vector potential in the coil region 4 in (5) is applied to each coil in the current flow direction, as in an excitation coil. The surface integration in (8) is for the coil cross-section area, which is averaged over the coil cross-section area, $h{\cdot}t$.

The differential voltage between the left and right side pick-up coils (Fig. 1) is presented in (9) and (10). The polarity of the differential voltage changes with the changes in speed direction, according to (9) and (10).

$$U_d = U_{M,l} - U_{M,r} = j\omega\cdot(L_{M,r} - L_{M,l})\cdot I \tag{9}$$

$$\begin{gathered} U_d = U_{M,l} - U_{M,r} = \frac{2\omega N\cdot L\cdot l}{h\cdot t}\sum_n \sum_m (C_U C_J \sin(k_m w_3)) \\ C_U = \frac{4j}{n\pi l}\left(1 + \left(\frac{k_n}{k_m}\right)^2\right)\cdot(C_{U,1} + C_{U,2} + C_{U,3}) \\ C_{U,1} = \frac{C_{41}}{\gamma_4}\cdot(\exp(\gamma_4\cdot(h + g)) - \exp(\gamma_4\cdot g)) \\ C_{U,2} = -\frac{C_{42}}{\gamma_4}\cdot(\exp(-\gamma_4\cdot(h + g)) - \exp(-\gamma_4\cdot g)) \\ C_{U,3} = \frac{\mu_0 J_m}{\gamma_4^2}\cdot h \end{gathered} \tag{10}$$

where w_3 is the distance between the centers of pick-up coils and the center of the excitation coil.

The magnetic flux lines distribution and the eddy current distribution for iron and aluminum moving parts at 100 Hz and 2 m/s are shown in Figs. 4–7. The magnetic flux lines distribution is corresponding to the contour plot of z-component of magnetic vector potential, A_z in the x-y plane (z = 0), which A_x is zero. The eddy current distribution is contour plot of streamline function, I_y in (11) in x-z plane

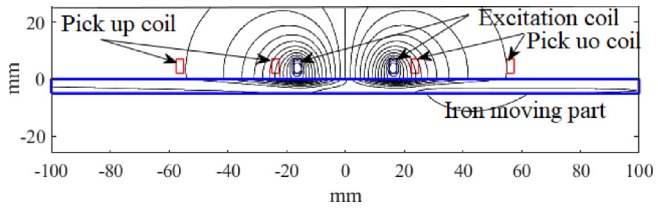

Fig. 4. Magnetic flux distribution in the *x-y* plane for the iron moving part at 100 Hz and 2 m/s.

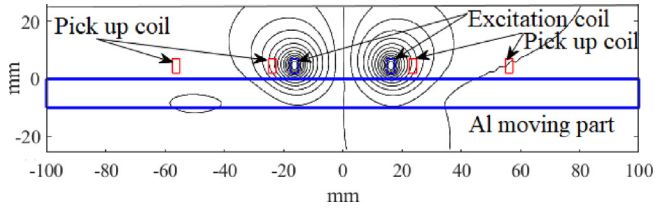

Fig. 5. Magnetic flux distribution in the *x-y* plane for the aluminum moving part at 100 Hz and 2 m/s.

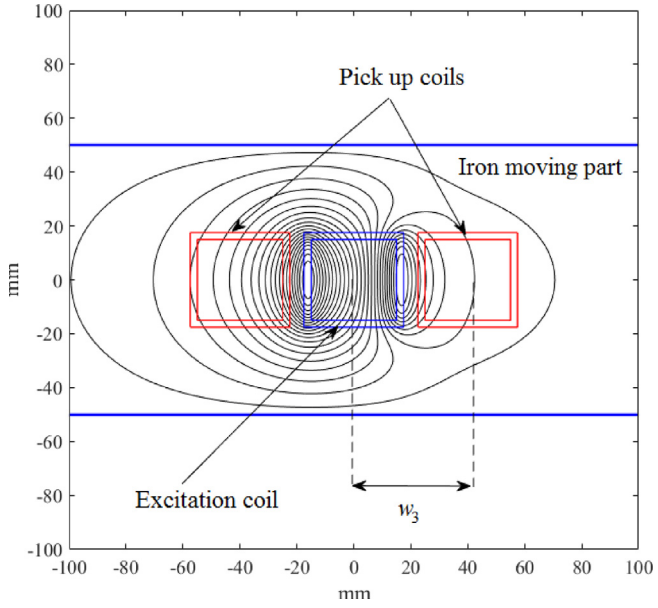

Fig. 6. Eddy current distribution in the *x-z* plane on the surface of the solid iron moving part at 100 Hz and 2 m/s – analytical method.

[19].

$$J = \nabla \times I_y$$

$$J_{x,2} = -\sigma\left(\frac{\partial A_{x,2}}{\partial t} + V\cdot\frac{\partial A_{x,2}}{\partial x}\right),\ I_y = -\int J_{x,2}\,dz$$

$$J_{z,2} = -\sigma\left(\frac{\partial A_{z,2}}{\partial t} + V\cdot\frac{\partial A_{z,2}}{\partial x}\right),\ I_y = \int J_{z,2}\,dx$$

$$I_y = \frac{\sigma(\omega - V\cdot k_m)}{k_m}\times \sum_n \sum_m \left(C_{21}\exp(\gamma_2 y) + C_{22}\exp(\gamma_2 y)\right) \times \exp(j(\omega t - k_m x - k_n z)) \quad (11)$$

The iron moving part is 5 mm in thickness, and the aluminum moving part is 10 mm in thickness (Table 1). The skin depths are 2.2 mm for the iron moving part, and 9.1 mm for the aluminum moving part, at 100 Hz. The speed effect on the differential induced voltage could be higher for an aluminum moving part than for an iron moving part, as the skin depth is greater in aluminum (Fig. 5). The deformation and the extension of the induced eddy currents in the iron moving part due to the speed effect is larger, because of the higher relative

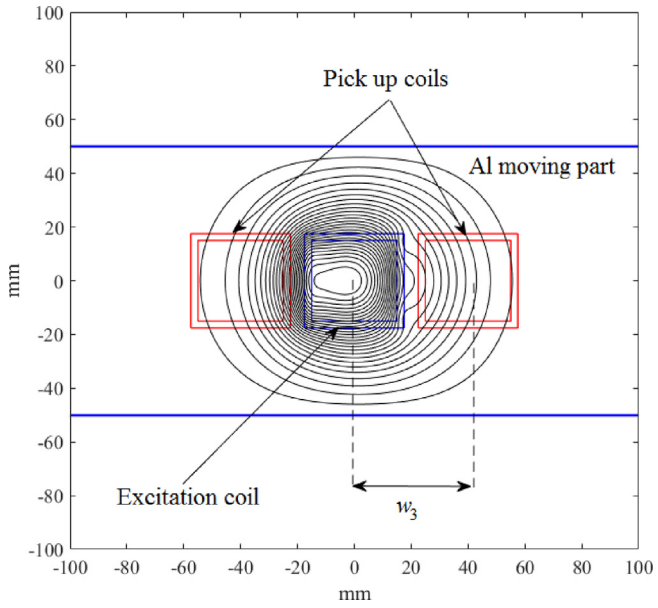

Fig. 7. Eddy current distribution in the *x-z* plane on the surface of the aluminum moving part at 100 Hz and 2 m/s – analytical method.

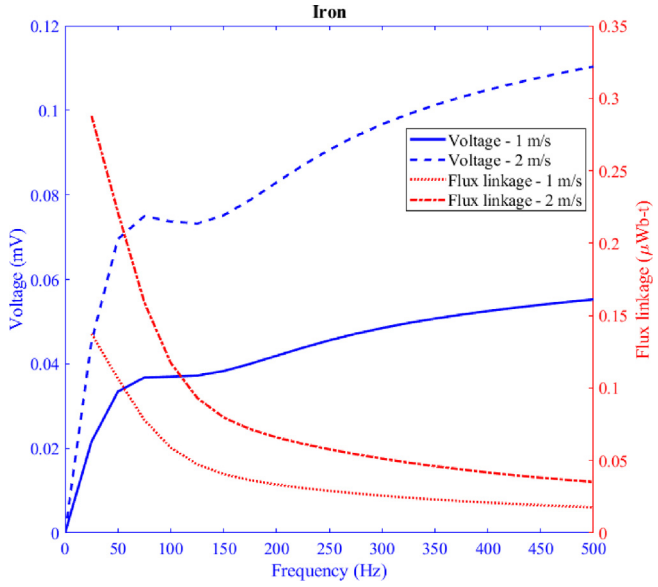

Fig. 8. Amplitude of differential induced voltage and flux linkage versus frequency for the iron moving part – airgap, $g = 2$ mm ($\mu_{ri} = 100$).

permeability. Figs. 8 and 9 show differential voltages and flux linkages versus frequency for iron and aluminum moving parts. The differential voltage for the iron moving part increases with frequency, with the exception of some fluctuation between 75 Hz and 125 Hz (Fig. 8). The maximum differential voltage value for the aluminum moving part is located at 75 Hz in Fig. 9, and the differential voltage decreases continuously at higher frequencies for the aluminum moving part. The flux linkages decrease at higher frequencies, which shows that lower frequencies or DC are best for obtaining maximum flux linkage or magnetic flux density, and the flux linkages are more sensitive to speed at lower frequencies.

The differential voltages and flux linkages versus the gap between the coils and the moving part are shown in Fig. 10. The differential voltage and the flux linkage decreases monotonically in the case of the aluminum moving part. The differential voltages and the flux linkages for the iron moving part have maximum values for a 3.5 mm gap. This is

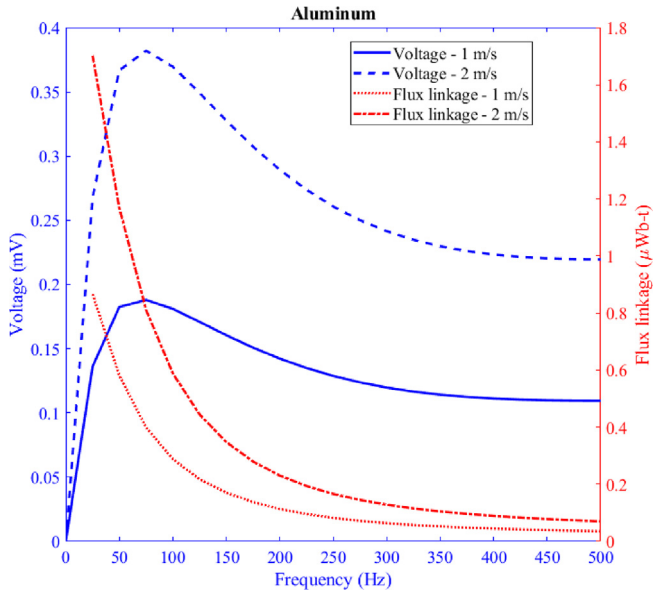

Fig. 9. Amplitude of the induced differential voltage and flux linkage versus frequency for the aluminum moving part – airgap, $g = 2$ mm.

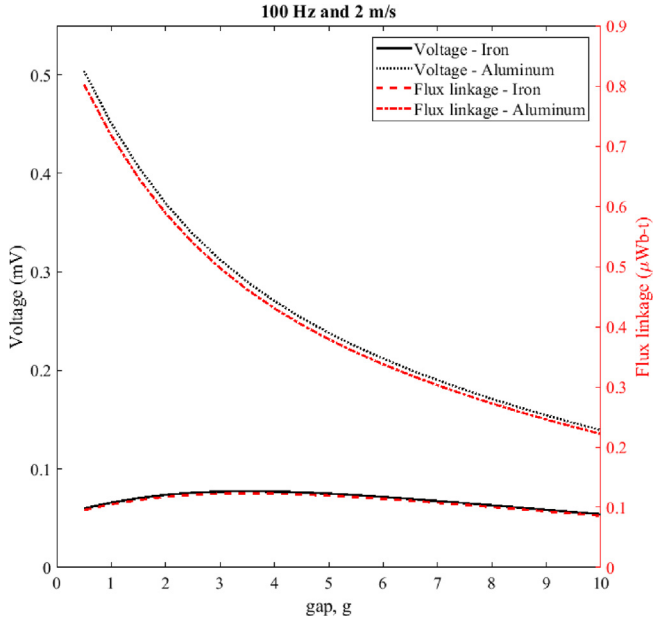

Fig. 10. Amplitude of the induced differential voltage and flux linkage versus gap, g ($\mu_{ri} = 100$).

due to the high permeability of the iron moving part. The differential voltage and the flux linkage are higher for an aluminum moving part than for an iron moving part for different gaps and frequencies, see in Figs. 8–10.

The differential voltage for a non-magnetic moving part (for example in this paper, aluminum) versus conductivity is shown in Fig. 11. The maximum value is at 22.0 MS/m.

The differential voltage for a magnetic moving part versus conductivity and relative magnetic permeability is presented as a 3D plot in Fig. 12. The relative magnetic permeability varies between 50 and 150, which is an acceptable range for low magnetic fields. Nonlinearity is neglected in the simulations, and constant magnetic permeability is used in the simulations as the magnetic field in the eddy current speed sensor is small. The assumed range of conductivity is between 4 MS/m and 6 MS/m, which is an expected range for construction steels and

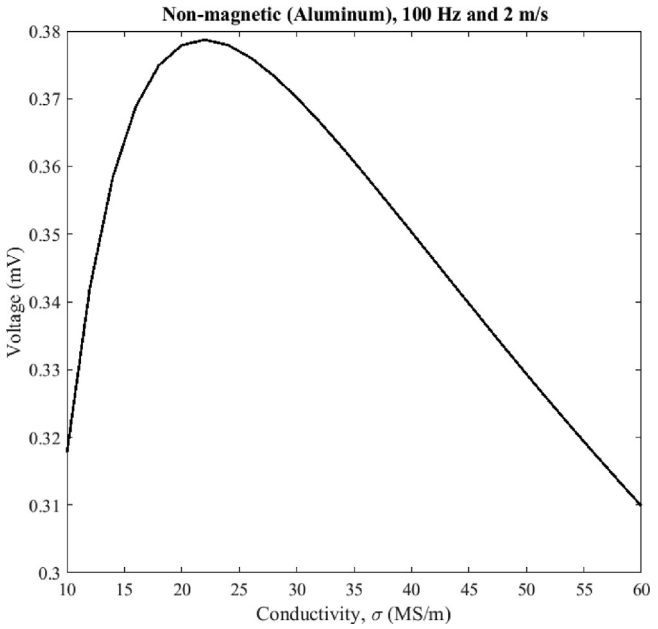

Fig. 11. Amplitude of the induced differential voltage versus conductivity for a nonmagnetic moving part, e.g. aluminum.

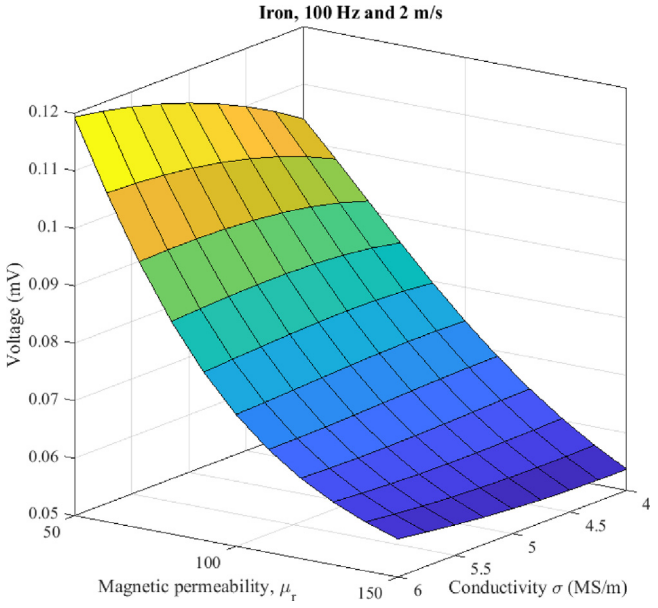

Fig. 12. Amplitude of the induced differential voltage versus conductivity and magnetic relative permeability for a magnetic moving part.

irons. The maximum and minimum differential voltage values for iron moving parts are located at conductivity = 6 MS/m, relative magnetic permeability = 50 and conductivity = 4 MS/m, relative magnetic permeability = 150, respectively. The sensitivity of the eddy current speed sensor to variations in magnetic permeability is much higher. The sensitivity for an aluminum moving part to variations in conductivity are much lower than for an iron moving part within the same range of conductivity variations (Fig. 11).

The sensitivity of an eddy current speed sensor to the thickness of the moving parts is dependent on the material of the moving part and on the excitation frequency (Fig. 13), because of the skin effects and the flux penetration depth in the conductive moving parts. The maximum values of the differential voltages for iron moving parts are located at a thickness of 4 mm for 100 Hz and at a thickness of 2 mm for 200 Hz. Thicknesses of 6 mm and 3 mm are the positions of the maximum values

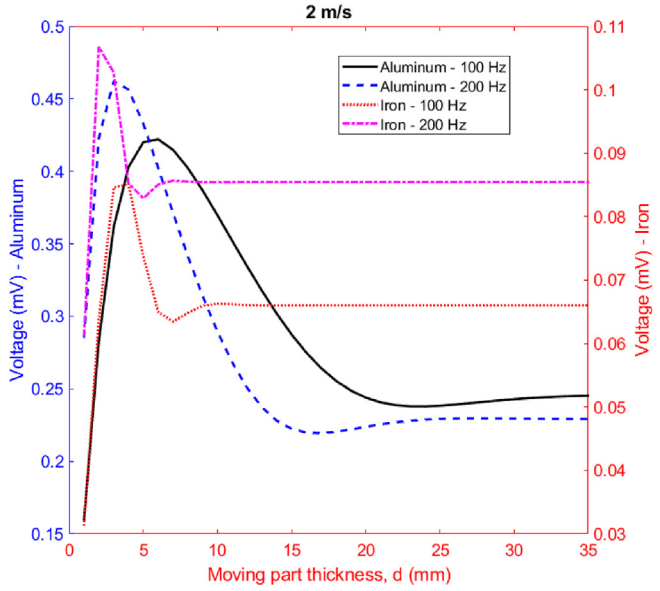

Fig. 13. Amplitude of the induced differential voltage versus moving part thickness – airgap, $g = 2$ mm ($\mu_{ri} = 100$).

of the differential voltages for an aluminum moving part at 100 Hz and 200 Hz, respectively.

Excellent linearity characteristics of a flat type eddy current speed sensor up to 2 m/s is shown in Fig. 14. The linear function equations between the differential voltage, U_d, and the moving part speed, V, are shown as follows:

$$U_d = K \cdot V \tag{12}$$

$$V = K' \cdot U_d \ , \quad K' = K^{-1} \tag{13}$$

Constant K is calculated in Fig. 14. An eddy current speed sensor with an iron moving part has greater sensitivity at 1000 Hz than at 100 Hz. However, it is not recommended to operate the sensor at very high frequencies due to the smaller skin depth and the greater sensitivity to the surface of an iron moving part, because iron and steel surfaces are affected by corrosion.

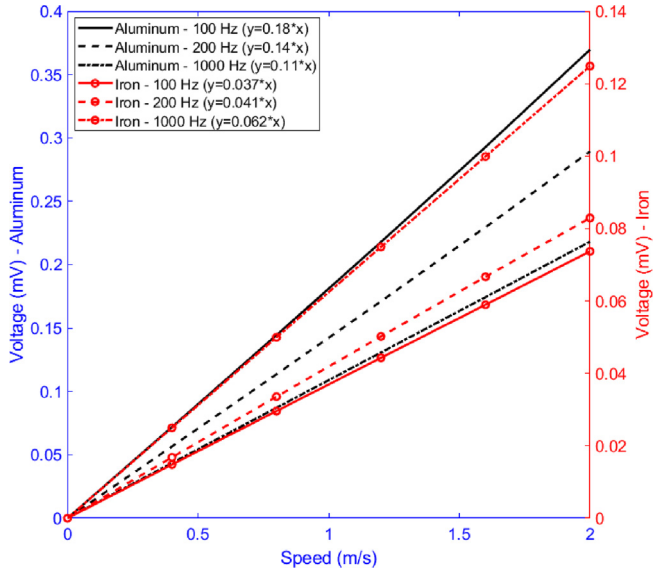

Fig. 14. Amplitude of induced differential voltage versus moving part thickness – airgap, $g = 2$ mm ($\mu_{ri} = 100$).

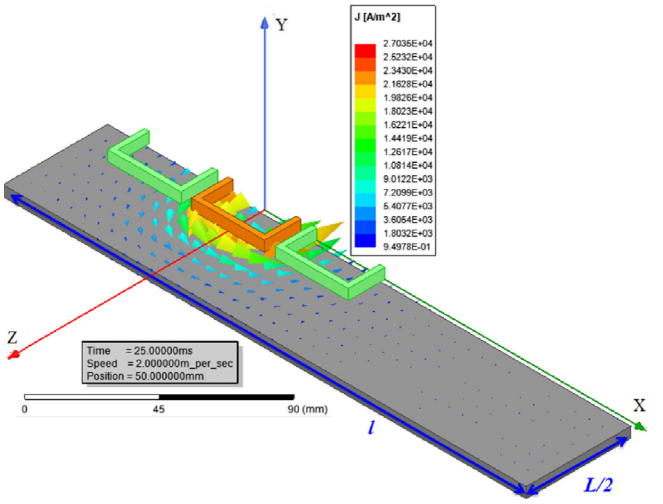

Fig. 15. Eddy current distribution in the x-z plane on the surface of a solid iron moving part at 100 Hz and 2 m/s ($\mu_{ri} = 100$) – FEM.

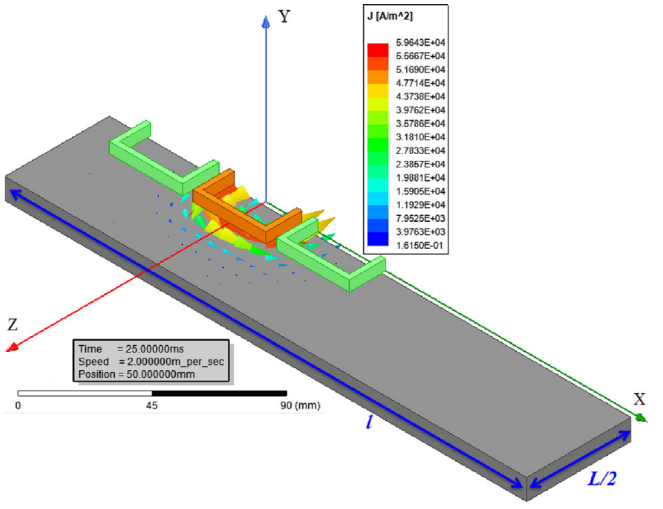

Fig. 16. Eddy current distribution in the x-z plane on the surface of an aluminum moving part at 100 Hz and 2 m/s – FEM.

3.2. FEM

Time-stepping 3D FEM is used to model a flat type eddy current speed sensor, taking into account the speed of the moving part. Figs. 15 and 16 show the eddy current distributions in the iron and aluminum moving parts. The eddy currents are weaker in the iron moving part, and they are located closer to the surface than in the case of the aluminum moving part. Only one half of the FEM model is analyzed, as the model is symmetric to the X-Y plane. A comparison between 3D FEM and the 3D analytical calculations shows that the 3D analytical calculations, which are much faster than 3D FEM, are highly accurate (Tables 2–6). The difference between 3D FEM and the 3D analytical

Table 2
Comparison between analytical and 3D FEM at different speeds – differential voltage (amplitude).

$g = 2$ mm $f = 100$ Hz	Iron ($d = 5$ mm) Analytical/FEM	Aluminum ($d = 10$ mm) Analytical/FEM
$V = 0.5$ m/s	0.019/0.017 mV	0.090/0.080 mV
$V = 1.0$ m/s	0.037/0.034 mV	0.181/0.161 mV
$V = 2.0$ m/s	0.074/0.069 mV	0.370/0.333 mV

Table 3
Comparison between analytical and 3D FEM at higher frequency – differential voltage (amplitude).

g = 2 mm V = 2.0 m/s	Iron (d = 5 mm) Analytical/FEM	Aluminum (d = 10 mm) Analytical/FEM
f = 200 Hz	0.083/0.078 mV	0.289/0.263 mV

Table 4
Comparison between analytical and 3D FEM for higher gap – differential voltage (amplitude).

V = 2.0 m/s f = 100 Hz	Iron (d = 5 mm) Analytical/FEM	Aluminum (d = 10 mm) Analytical/FEM
g = 4 mm	0.077/0.075 mV	0.27/0.247 mV

Table 5
Comparison between analytical and 3D FEM for different moving part thickness – differential voltage (amplitude).

g = 2 mm f = 100 Hz V = 2.0 m/s	Iron Analytical/FEM	Aluminum Analytical/FEM
d = 5 mm	–	0.42/ 0.376 mV
d = 10 mm	0.066/0.064 mV	–

Table 6
Comparison between analytical and 3D FEM for different material data – differential voltage (amplitude).

g = 2 mm f = 100 Hz V = 2.0 m/s	Iron (d = 5 mm) Analytical/FEM	Aluminum (d = 10 mm) Analytical/FEM
σ_{al} = 58 MS/m	–	0.314/0.286 mV
σ_{al} = 22 MS/m	–	0.379/0.342 mV
σ_i = 4.0 MS/m (μ_{ri} = 150)	0.054/0.051 mV	–
σ_i = 6.0 MS/m (μ_{ri} = 50)	0.119/0.108 mV	–

calculations can be reduced by using a finer mesh and a larger number of mesh elements and a smaller time step for the simulations. However, this significantly increases the 3D FEM simulation time. The relative magnetic permeability of iron is considered to be equal to 100 in the simulations.

Parameters l and L in Figs. 15 and 16 correspond to the parameters for the analytical calculations, which are mentioned in (3) and Fig. 3. These parameters are used in the analytical calculations. Parameter l is selected equal to 250 mm, and parameter L is 100 mm, which is similar to the width of the iron and aluminum plates. The maximum values for harmonic orders m and n are selected to be 200 and 100, respectively. These values are a compromise between accuracy and simulation time for the analytical method.

4. Experiments

Figs. 17 and 18 show the experiment set-up elements with the coils and with iron and aluminum moving parts and measurement devices, oscilloscope, reference position sensor and signal generator. The high accuracy of the analytical method for calculating the mutual induced voltage in one of the pick-up coils using (14) is shown in Table 7, in comparison with measurements at zero speed of the moving part. Table 8 also presents a comparison between the analytical calculations using (15) and (16) and the experimental values for the self- inductances of the excitation coil. This illustrates the high precision of the proposed analytical method.

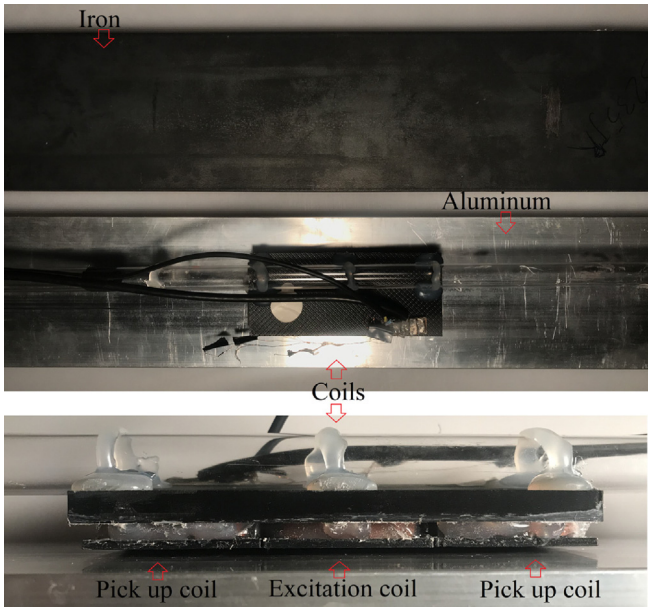

Fig. 17. Experiments elements – excitation and pick-up coils and aluminium plate (10 mm in thickness) and iron plate (5 mm in thickness).

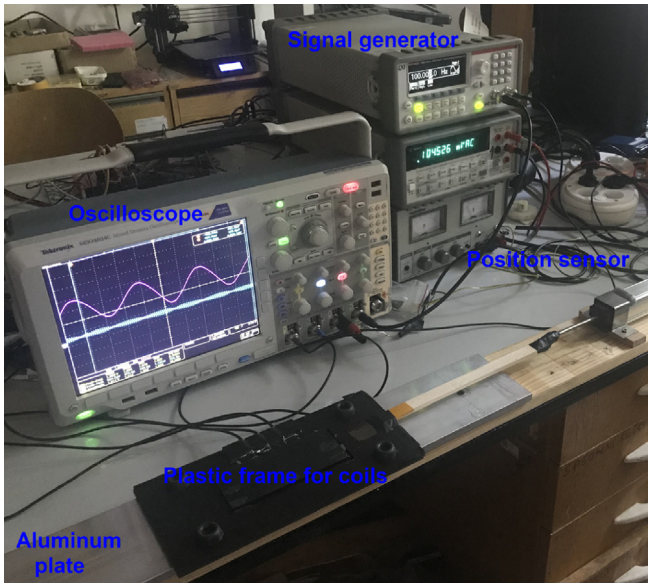

Fig. 18. Measurement devices – oscilloscope, signal generator and reference position sensor.

Table 7
Comparison between the analytical and experimental – induced voltage of one of the pick-up coils (rms value).

	Iron (g = 2 mm) Analytical/Exp.	Air Analytical/Exp.
f = 100 Hz	3.320/3.488 mV	2.192/2.253 mV

$$U_{M,l} = U_{M,r} = \frac{j\omega N \cdot L \cdot l}{h \cdot t} \sum_n \sum_m (C_U C_J \exp(jk_m w_3)) = \frac{j\omega N \cdot L \cdot l}{h \cdot t} \sum_n \sum_m (C_U C_J \exp(-jk_m w_3)) \quad (14)$$

$$L_S = \frac{\Psi_S}{I} = \frac{N \int (\int A_4 \cdot dl) ds}{I \cdot h \cdot t} \quad (15)$$

Table 8
Comparison between analytical and experimental – self inductances.

f = 100 Hz	Iron Analytical/Exp.	Air Analytical/Exp.
g = -	–	583.3/613.0 μH
g = 1.0 mm	820.8/843.0 μH	–
g = 2.0 mm	771.6/785.0 μH	–
g = 6.0 mm	673.0/698.0 μH	–
g = 7.0 mm	659.8/682.0 μH	–

$$L_S = \frac{N \cdot L \cdot l}{h \cdot t \cdot I} \sum_n \sum_m (C_U C_J) \tag{16}$$

In Tables 7 and 8, 'Air' means that there is no conductive moving part, 'Iron' means that the iron moving part is located in the gap, g and g is the distance between coils and iron moving part.

Eqs. (17) and (18) are used for the analytical calculations of transient differential voltages at variable speeds. Acceleration effects (the second term in (17)) are neglected in (18). The parameter, K in (18) at 100 Hz are calculated equal to 0.18 mV/m/s for the aluminum moving part and 0.037 mV/m/s for the iron moving part as presented in Fig. 14.

$$U_d = \frac{d((L_{M,r} - L_{M,l}) \cdot I_s)}{dt} = \frac{\partial((L_{M,r} - L_{M,l}) \cdot I \cdot \sin(\omega t))}{\partial t} + \frac{\partial((L_{M,r} - L_{M,l}) \cdot I_s)}{\partial V} \cdot \frac{dV}{dt} \tag{17}$$

$$U_d \approx \frac{\partial((L_{M,r} - L_{M,l}) \cdot I \cdot \sin(\omega t))}{\partial t} = \omega \cdot (L_{M,r} - L_{M,l}) \cdot I \cdot \cos(\omega t) = K \cdot V \cdot \cos(\omega t) \tag{18}$$

The analytically calculated results and the experimental values for differential voltages versus time at various speeds (Fig. 19 and Fig. 22) are shown in Figs. 20, 21 and Figs. 23, 24. The relative instantaneous positions of coils and moving parts are measured by a Senpos MRTM500 type potentiometric linear position sensor (Fig. 18) with a measurement range of 500 mm and linearity error of 0.05%.

The relative speed is calculated numerically using differentiation of relative positions of moving part and the coils versus time. The experimental differential voltage results and instantaneous relative positions of moving part and the coils are saved by a digital oscilloscope as shown in Fig. 18. Signal generator (Fig. 18) with internal resistance 50 Ω and voltage amplitude 10 V is connected to the excitation coil. The speed is variable function versus time, which affects the differential voltage of eddy current speed sensor. The analytical induced voltages coincide well with the experimental results, showing the accuracy of the proposed analytical method. The main sources of differences between the experimental calculations and the analytical calculations may be the tolerances of the elements in the experimental set up, for example, the gap (lift off) between the coils and the moving parts and the relative magnetic permeability for the iron moving part (Fig. 24).

The direction (sign) of the speed could not be calculated from the amplitude of the induced voltage, but it could be obtained by calculating the phase angle relative to the excitation current. The speed values could be calculated by the voltage peaks or by the voltage RMS

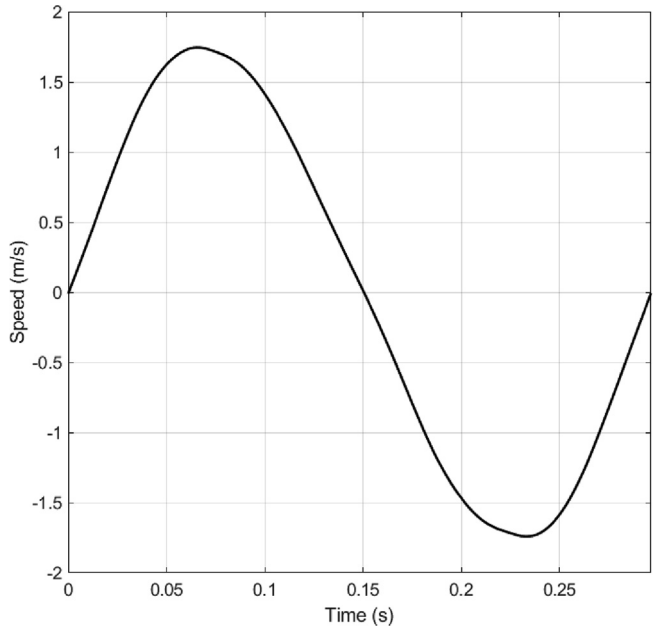

Fig. 19. Applied experimental speed versus time for an aluminium moving part.

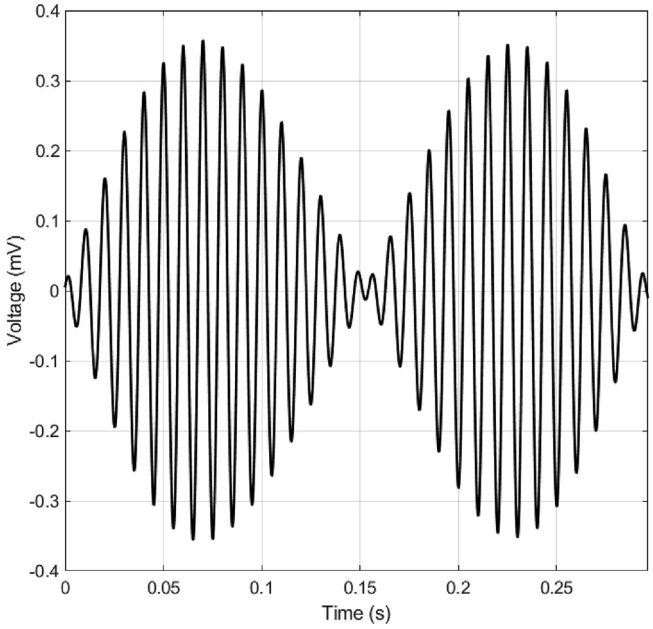

Fig. 20. Experimental differential voltage versus time for an aluminium moving part – 100 Hz.

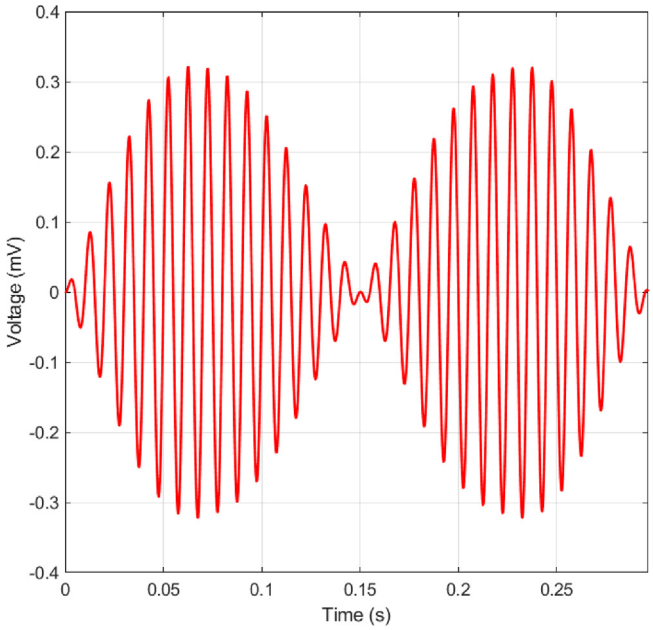

Fig. 21. Analytically calculated differential voltage versus time for an aluminium moving part – 100 Hz.

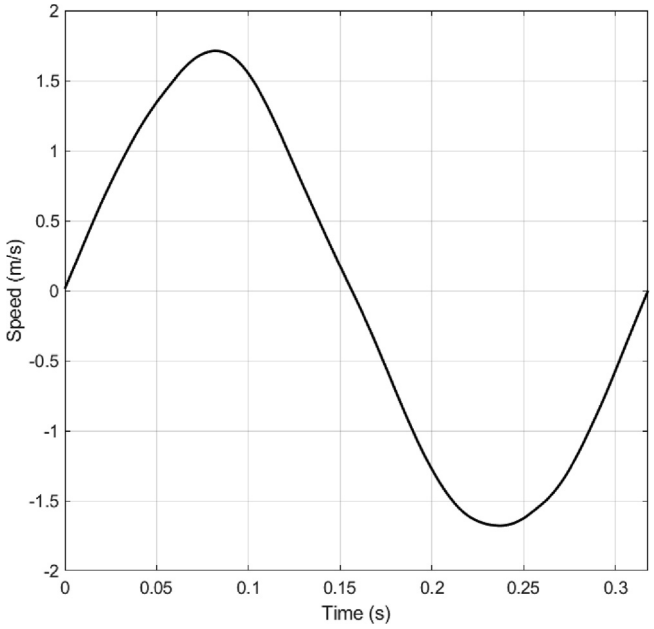

Fig. 22. Applied experimental speed versus time for an iron moving part.

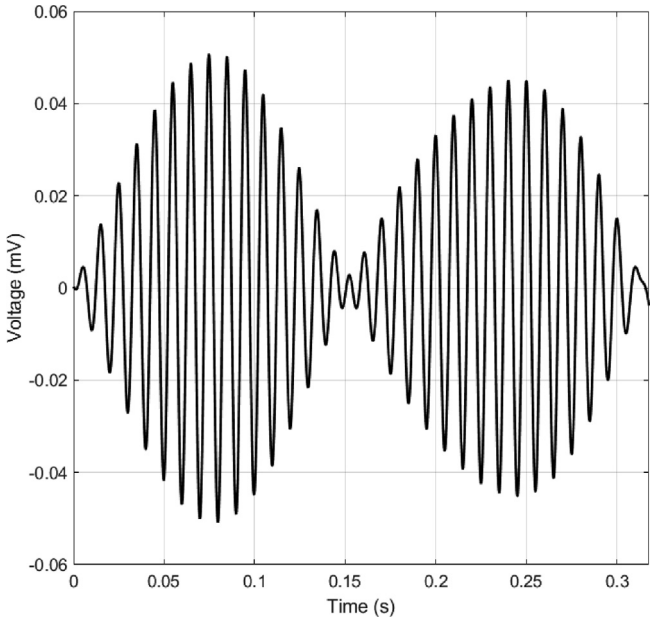

Fig. 23. Experimental differential voltage versus time for an iron moving part – 100 Hz.

or the rectified DC value in each half period can be used. Minima and maxima of the differential voltage in Figs. 20 and 23 correspond to the zero crossing and maximums of speed in Figs. 19 and 20.

The parameter, K in (18) for iron moving part changes from 0.037 mV/m/s for relative magnetic permeability, $\mu_{ri} = 100$ to 0.027 mV/m/s for $\mu_{ri} = 150$ at 100 Hz. The parameter, K (=0.18 mV/m/s) for the aluminum moving part is a fixed value for constant gap. The speeds of moving parts in Figs. 19 and 22 are changing between −1.75 m/s to +1.75 m/s. The induced voltage is higher for aluminum moving part in the same speed range in comparison with iron moving part.

Using ratiometric output $U_1 - U_2/(U_1 + U_2)$ would be the first choice to compensate lift off changing and materials effects of moving part. This technique is successfully utilized in LVDT sensors. However, verification of such compensation is out of the scope of the present

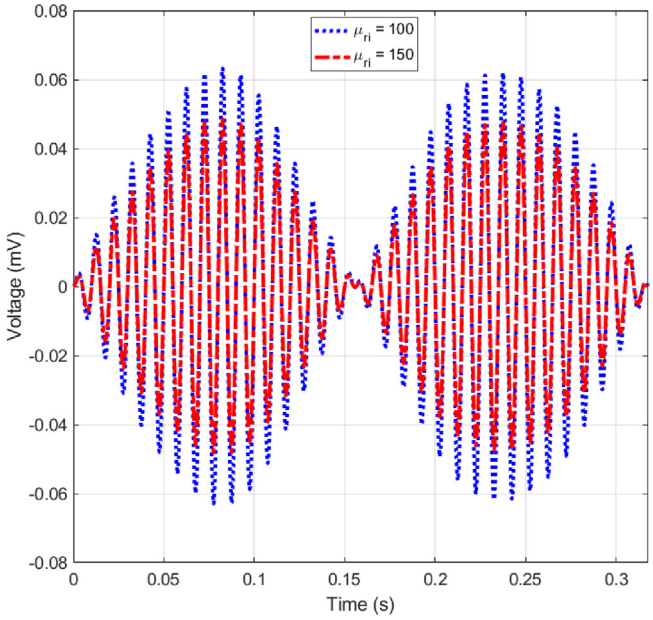

Fig. 24. Analytically calculated differential voltage versus time for an iron moving part – 100 Hz.

paper and will be a subject of the future study

Second potential approach to compensate the lift off changing and materials effects is using multi-frequency sensor technique, which is well proved in [22]; we also plan to examine this method in our future work.

Time stepping 3D FEM with motion consideration was implemented to analyze eddy current speed sensor, where sliding mesh is utilized to model moving part motion. Two fixed meshes are considered for stationary part and moving part and they are linked to each other by sliding mesh technique. Analysis of eddy current speed sensor using time stepping 3D FEM with motion is especially time consuming and complicated process and also with high probability of numerical errors, which could be mitigated using presented precise analytical method.

The methodology utilized in this paper to evaluate speed effect is also used, for example, for non-destructive testing (NDT) of metallic bodies [23–25]. Motion-induced eddy current thermography for high-speed inspection has been presented in [23] using equivalent rotating (travelling) magnetic field generated by three phase windings. The evaluation of effects of speed component of eddy current on the magnetic flux leakage inspection for non destructive testing of thick-wall steel pipe has been published in [24]. Utilizing speed effects on the induced eddy current in the conductive moving bodies with perpendicular configuration of coils relative to the moving body for non-destructive testing was presented in [25].

The presented contactless speed sensor shows better fittingness in terms for robustness and structure simplicity for practical applications in comparison with other contactless speed sensor [26].

5. Conclusion

The core of this paper is precise analysis method allowing fast design and suitability evaluations of eddy current speed sensors with both non-ferromagnetic and ferromagnetic materials for moving parts, which were overlooked in the literatures.

The performance and the design of a flat type eddy current speed sensor with air coils have been analyzed. Analytical models and 3D FEM calculations have been presented. The use of a fast and precise 3D analytical method is essential for the fast design and optimization of an air coil eddy current speed sensor. The linearity of the proposed speed sensor is excellent, despite its simple configuration. The calculated and

measured speed range has been considered up to 2 m/s, but it can be extended for higher translational speed. The proposed eddy current speed sensor could be used for all types of linear machines, as it has a simple structure and precise performance. The air coil configuration enables the proposed eddy current speed sensor to be very compact and cost-effective.

The effects of the material of the conductive moving parts have been evaluated. They have been shown to have a very critical influence on the design and analysis of eddy current speed sensors, and they must be taken into account. The output results and the performance of an eddy current speed sensor with a ferromagnetic moving part differ greatly from the results and the performance with a non-magnetic moving part. It is critical to compensate the magnetic permeability and also the conductivity of the moving part in the design of an eddy current speed sensor. Temperature stability and the effects on the conductive moving part must also be taken into consideration for an eddy current speed sensor. The conductivity and even the magnetic permeability of the moving part are affected by temperature.

The proposed configuration is without the use of a magnetic yoke for the coils, and without magnetic shielding. Adding a magnetic yoke to the sensor configuration could increase the output and the sensitivity of the sensor, and would shield the sensor from magnetic parasitic effects. Perpendicular configurations of the pick-up coils are alternatives to the flat type configuration aimed at reducing the longitudinal length of the sensor. However, perpendicular configurations would reduce the sensitivity of the sensor, and would decrease the magnetic coupling between the excitation coil and the pick-up coils.

Declaration of Competing Interest

No conflict of interest.

References

[1] C.-T. Liu, S.-Y. Lin, Y.-Y. Yang, Flux modeling and analysis of a linear induction motor for steel mill non-contacting conveyance system application, J. Magn. Magn. Mater. 290–291 (2005) 1359–1362.

[2] C.-T. Liu, S.-Y. Lin, Y.-Y. Yang, C.-C. Hwang, Analytical model development of an eddy-current-based non-contacting steel plate conveyance system, J. Magn. Magn. Mater. 320 (2008) 291–295.

[3] Z. Zhang, C. Xi, Y. Yan, Q. Geng, T. Shi, A hybrid analytical model for open-circuit field calculation of multilayer interior permanent magnet machines, J. Magn. Magn. Mater. 435 (2017) 136–145.

[4] D. Zeng, G. Lv, T. Zhou, Equivalent circuits for single-sided linear induction motors with asymmetric cap secondary for linear transit, IEEE Trans. Ener. Conv. 33 (4) (2018) 1729–1738.

[5] N. Fernando, P. Arumugam, C. Gerada, Design of a stator for a high-speed turbo-generator with fixed permanent magnet rotor radius and volt–ampere constraints, IEEE Trans. Ener. Conv. 33 (3) (2018) 1311–1320.

[6] P. Ripka, Magnetic Sensors and Magnetometers, Artech House, Jan 1, 2001 – Technology & Engineering.

[7] X. Ge, Z.Q. Zhu, R. Ren, J.T. Chen, A novel variable reluctance resolver with non-overlapping tooth–coil windings, IEEE Trans. Ener. Conv. 30 (2) (2015) 784–794.

[8] X. Ge, Z.Q. Zhu, A novel design of rotor contour for variable reluctance resolver by injecting auxiliary air-gap permeance harmonics, IEEE Trans. Ener. Conv. 31 (1) (2016) 345–353.

[9] N. Takehira, A. Tanaka, Analysis of a perpendicular-type eddy-current speed meter, IEE Proc. A – Phys. Science, Meas. Instr., Manag. Educ. Rev. 135 (2) (1988) 89–94.

[10] T. Itaya, K. Ishida, A. Tanaka, N. Takehira, T. Miki, Eddy current distribution for a rectangular coil arranged parallel to a moving conductor slab, IET Science, Meas. Tech. 6 (2) (2012) 43–51.

[11] T. Itaya, K. Ishida, A. Tanaka, N. Takehira, Analysis of a fork-shaped rectangular coil facing moving sheet conductors, IET Sci., Meas. Tech. 3 (4) (2009) 279–285.

[12] A. Tuysuz, M. Flankl, J.W. Kolar, A. Mutze, Eddy-current-based contactless speed sensing of conductive surfaces, IEEE 2nd Annual Southern Power Electronics Conference (SPEC), pp. 1–6, Dec. 2016.

[13] M. Mirzaei, P. Ripka, A. Chirtsov, J. Vyhnanek, Eddy current linear speed sensor, IEEE Trans. Mag. 55 (1) (2019) 1–4.

[14] H.H. Woodson, J.R. Melcher, Electromechanical Dynamics, Part II, John Wiley & Sons, Inc., 1968.

[15] J.A. Shercliff, The Theory of Electromagnetic Flow Measurement, Cambridge University Press, 1962.

[16] K. Yoshida, New transfer-matrix theory of linear induction machines, taking into account longitudinal and transverse ferromagnetic end effects, IEE Proc. B – Elect. Power Appl. 128 (5) (1981) 225–236.

[17] S. Yamamura, Theory of Linear Induction Motors, second ed., John Wiley & Sons, 1979.

[18] M. Poloujadoff, The Theory of Linear Induction Machinery, Clarendon Press, 1980.

[19] D. Schieber, Electromagnetic Induction Phenomena, Springer-Verlag, 1986 Science.

[20] K. Davey, Analytic analysis of single- and three-phase induction motors, IEEE Trans. Mag. 34 (5) (1998) 3721–3727.

[21] S. Salon, Finite Element Analysis of Electrical Machines, Springer US, 1995.

[22] M. Lu, Y. Xie, W. Zhu, A. Peyton, W. Yin, Determination of the magnetic permeability, electrical conductivity, and thickness of ferrite metallic plates using a multifrequency electromagnetic sensing system, IEEE Trans. Ind. Inf. 15 (7) (2019) 4111–4119.

[23] G. Piao, J. Guo, T. Hu, H. Leung, The effect of motion-induced eddy current on high-speed magnetic flux leakage (MFL) inspection for thick-wall steel pipe, Res. Nondest. Eval. (2019) 1–20.

[24] J. Wu, K. Li, G. Tian, J. Zhu, Y. Gao, C. Tang, X. Chen, Motion-induced eddy current thermography for high-speed inspection, AIP Adv. 7 (2017) 085105.

[25] T. Itaya, K. Ishida, A. Tanaka, N. Takehira, T. Miki, Analysis of a fork-shaped rectangular coil oriented perpendicular to moving conductor slabs, NDT E Int. 44 (5) (2011) 413–420.

[26] C. Moron, E. Suarez, Non-contact digital speed sensor, J. Magn. Magn. Mater. 133 (1994) 610–612.

3-2-3-4 Eddy Current Speed Sensor with Magnetic Shielding [J9]

This paper presents the design and analysis of a new eddy current speed sensor with ferromagnetic shielding. Aluminum and solid iron are considered for the moving part. One excitation coil and two antiserially connected pick up coils are shielded by a thin steel lamination. 3D time stepping finite element analysis is used to analyze the sensor performance with different magnetic materials and compare with experimental results. The compactness, simplicity and excellent linearity with different magnetic materials for the moving part show uniqueness of the proposed speed sensor.

The proposed shielded eddy current speed sensor has sensitivity 110 μV/m/s for iron rotating disk at 300 Hz and 210 μV/m/s for aluminum rotating disk at 120 Hz. The magnetic shielding acts also as magnetic yoke and it increases the sensor sensitivity as it decreases magnetic reluctance for the magnetic flux. The 3D FEM calculations show that the shielding increases sensitivity by a factor over 2, but its main role is to suppress sensitivity to external magnetic fields and ferromagnetic objects. The linearity error is 0.26% for iron moving part at 300 Hz. The sensitivity can be increased several times by increasing the number of turns of all coils; the limitations are the parasitic capacitances and shielding saturation. The sensor can be optimized in terms of linearity and sensitivity using 3D FEM as the simulation results fit well with the measured values. The sensor requires temperature compensation of the material properties and also compensation for the changes of lift-off: using ratiometric output (V1 – V2)/(V1 + V2) would be the first choice. This technique is successfully utilized in LVDT sensors. However, verification of such compensation is out of the scope of the present paper.

Journal of Magnetism and Magnetic Materials 502 (2020) 166568

Contents lists available at ScienceDirect

Journal of Magnetism and Magnetic Materials

journal homepage: www.elsevier.com/locate/jmmm

Research articles

Eddy current speed sensor with magnetic shielding

Mehran Mirzaei*, Pavel Ripka, Andrey Chirtsov, Vaclav Grim

Faculty of Electrical Engineering, Czech Technical University, Prague 16627, Czech Republic

ARTICLE INFO

Keywords:
Eddy current speed sensor
Aluminum
Iron
Shielding
Magnetic permeability and finite element method

ABSTRACT

This paper presents the design and analysis of a new eddy current speed sensor with ferromagnetic shielding. Aluminum and solid iron are considered for the moving part. One excitation coil and two antiserially connected pick up coils are shielded by a thin steel lamination. 3D time stepping finite element analysis is used to analyze the sensor performance with different magnetic materials and compare with experimental results. The compactness, simplicity and excellent linearity with different magnetic materials for the moving part show uniqueness of the proposed speed sensor. The shielding increases sensitivity and reduces the influence of close ferromagnetic objects and interferences on the sensor performance.

1. Introduction

Speed sensors are vital parts of linear and rotating machines for control and protection purposes [1–3]. Contactless magnetic speed sensors are resistant against dust and oil, which brings them advantage over optical sensors [4]. The most popular sensor type is based on the reluctance variation. Eddy current speed sensors work for all conducting moving bodies including those with smooth surface. They have simple construction and present favorable solution especially at high speeds. Longitudinal and perpendicular configurations of eddy current speed sensors and speed effects utilizations were presented in [5–11]. The presented models in [5–11] had only nonmagnetic aluminum moving part. However, they are simpler for analysis and impractical for industry in comparison with solid iron moving part. The authors analyzed and tested eddy current speed sensors for solid iron moving parts with linear configuration [12] and rotational configuration [13] without magnetic yoke and shield. These sensors suffered from sensitivity to magnetic interference and also to the presence of ferromagnetic materials from their vicinity. The magnetic shielding acts also as a yoke and it can increase the sensitivity of eddy current speed sensors as it provides low magnetic reluctance for the magnetic flux. The eddy current speed sensors are more reliable and mechanically stable in comparison with other speed sensors [14,15].

In this paper, a linear eddy current speed sensor with magnetic shielding using 0.5 mm silicon steel lamination is presented. Aluminum and solid iron moving bodies are both used in the finite element method (FEM) modeling and measurements. The effects of magnetic materials of the shielding are also investigated. Different excitation frequencies and speeds are considered in the measurements and analysis to obtain best sensor output linearity and sensitivity.

2. Eddy current speed sensor

2.1. Model

Table 1 and Fig. 1 present the eddy current speed sensor model and parameters. Parameter, V is the speed in Fig. 1.

2.2. Operation theory

Two pick up coils (Figs. 1 and 2) are antiserially connected. Ideally induced voltage and net flux in the antiserially pick up coils are zero at zero speed because left and right side coils have same flux linkage with the excitation coil. The net total flux of antiserially connected pick up coils is nonzero at nonzero speed because pick up coils sense different flux linkages due to the induced eddy currents as shown in Fig. 2. The flux linkages of pick up coils are affected unevenly by motion component of induced eddy current [5,16]. As speed increases, the difference between induced voltages of left and right side coils increases, which is utilized for the speed sensing for the solid conductive moving objects.

3. Speed sensor measurements

3.1. Experimental setup

Experimental set up and measurement devices are shown in Fig. 3. A rotating disk (aluminum and iron) with thickness 5 mm is considered as

* Corresponding author.
E-mail addresses: mirzameh@fel.cvut.cz (M. Mirzaei), ripka@fel.cvut.cz (P. Ripka).

https://doi.org/10.1016/j.jmmm.2020.166568
Received 15 August 2019; Received in revised form 5 February 2020; Accepted 5 February 2020
Available online 06 February 2020
0304-8853/

Table 1
Eddy current speed sensor parameters.

Parameters		Values
I	excitation coil current amplitude	166 mA
N	number of turn in all coils	100
L	moving part width	100 mm
h_m	moving part thickness	5.0 mm
h_c	coils thickness	4.7 mm
$w_{c,\,o}$	outer coil width	29.0 mm
$w_{c,\,i}$	inner coil width	25.0 mm
w_s	ferromagnetic shield width	30 mm
l_s	ferromagnetic shield length	90 mm
σ_{al}	moving part aluminum conductivity at room temperature	33.5 MS/m
σ_i	moving part solid iron conductivity at room temperature	6.0 MS/m
μ_{ri}	relative magnetic permeability of moving part solid iron	100
σ_s	silicon steel shield conductivity	3.1 MS/m
μ_{rs}	relative magnetic permeability of silicon steel shield	1000

moving part. The disk rotates between −500 rpm up to +500 rpm and center of eddy current speed sensor is located 22.5 cm distance from disk center.

The dimensions of eddy current speed sensor are reasonably small in comparison with rotating disk. Therefore, it can be assumed that eddy current speed sensor sense linear speed relative to the rotating disk. The electrical conductivities of iron and aluminum disk were measured and mentioned in Table 1 at room temperature. A lock-in amplifier is used for precise measurements of the pick up coils voltage. A signal generator with internal resistance 50 Ω is connected to the excitation coil.

Fig. 4 shows a schematic block diagram, which can be considered for possible electronic design for the sensor.

3.2. Speed sensor results

Figs. 5 and 6 present measured absolute value of measured voltage, V_a of pick up coils:

$$V_a = \sqrt{V_r^2 + V_i^2} \tag{1}$$

where V_r and V_i are real component and imaginary components of induced voltage in the antiserially connected pick up coils relative to the excitation coil current as reference signal. The polarity of absolute value of voltage is calculated using phase angle shift relative to the

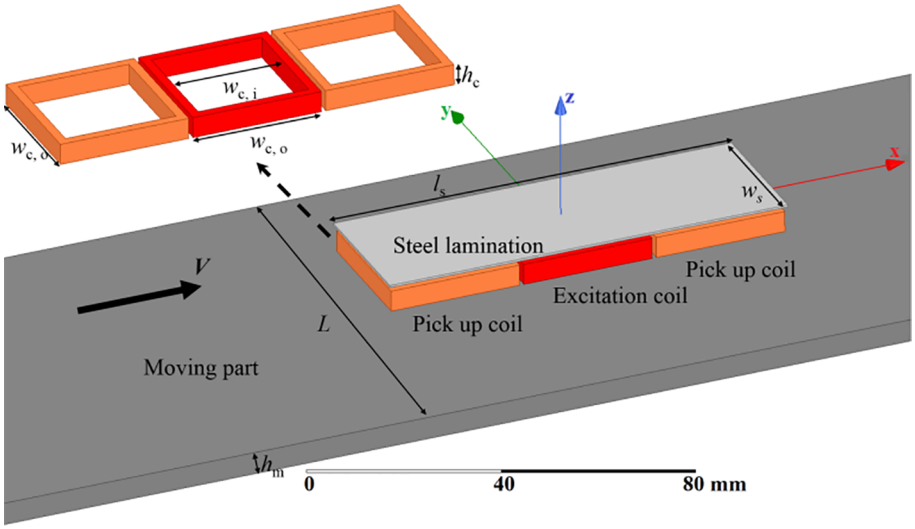

Fig. 1. Eddy current speed sensor with steel lamination for shielding.

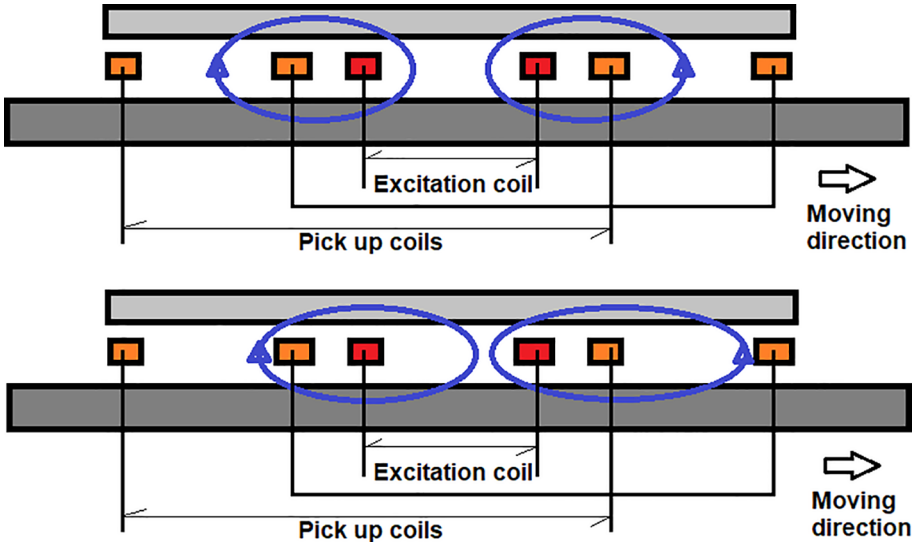

Fig. 2. 2D schematic models of eddy current speed sensor and moving part with single excitation coil and antiserially connected pick up coils – at zero speed (up) and nonzero speed (bottom).

Fig. 3. Experimental set up – rotating disk (aluminum and solid iron) as moving part and eddy current based speed sensor (left) and signal generator and lock-in amplifier (right).

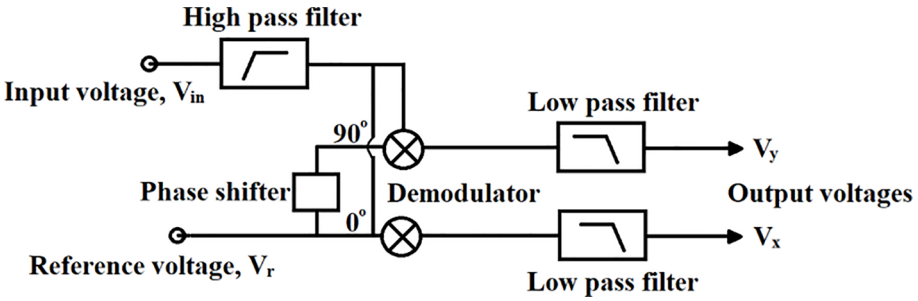

Fig. 4. Schematic block diagram to demonstrate the possible electronics diagram to process speed sensor output signal.

excitation coil current.

Pick up induced voltages for the iron rotating disk increase with increasing excitation coil frequency, which is different to the aluminium rotating disk. Linearity of induced voltage versus linear speed for iron rotating rod is the best at 300 Hz and it is the best between 120 Hz and 180 Hz for aluminium rotating disk. The gap between coils of eddy current speed sensor and rotating disk is about 6.25 mm, which is sufficient reasonable value for many industrial applications. High linearity of induced voltage curve versus speed makes the proposed sensor to be suitable device for speed measurement. The real and imaginary components of induced voltages show different tendency versus speed (Figs. 7 and 8).

Real component of induced voltage is more linear versus speed for all frequencies in comparison with imaginary component and its linearity is less dependent on the excitation frequency. Real component of

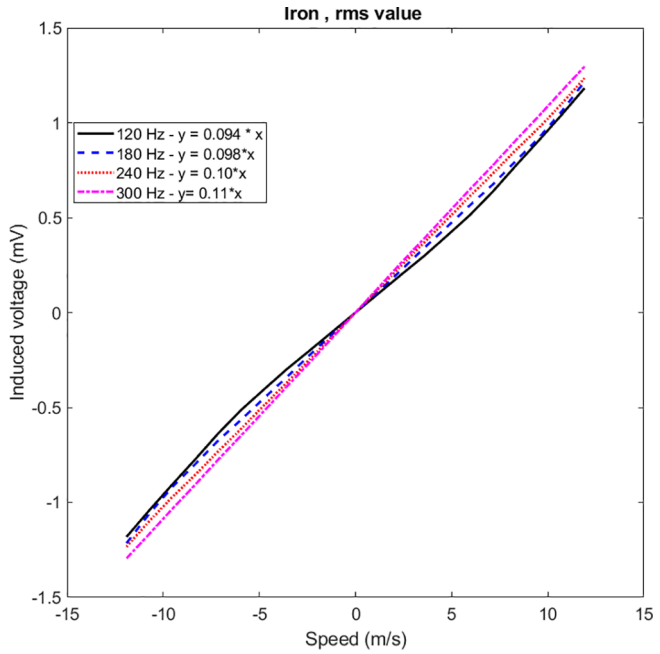

Fig. 5. Measured voltage of pick up coils for iron rotating disk at different frequencies – absolute value.

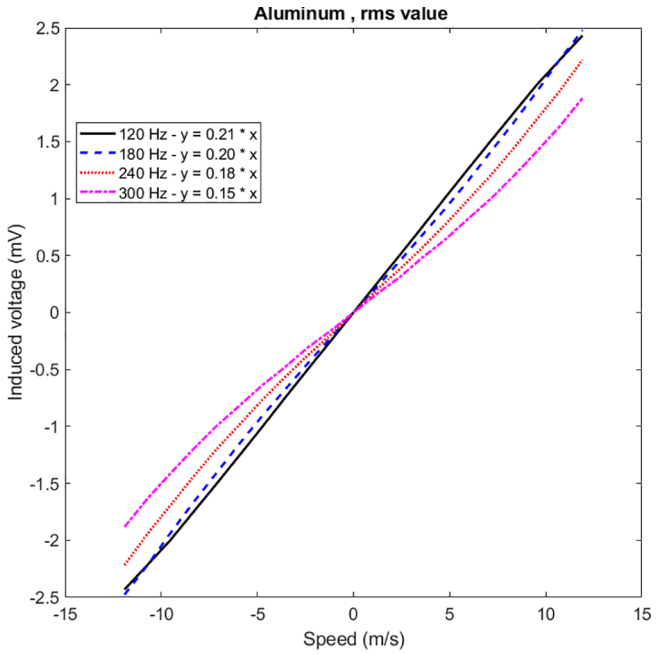

Fig. 6. Measured voltage of pick up coils for aluminum rotating disk at different frequencies – absolute value.

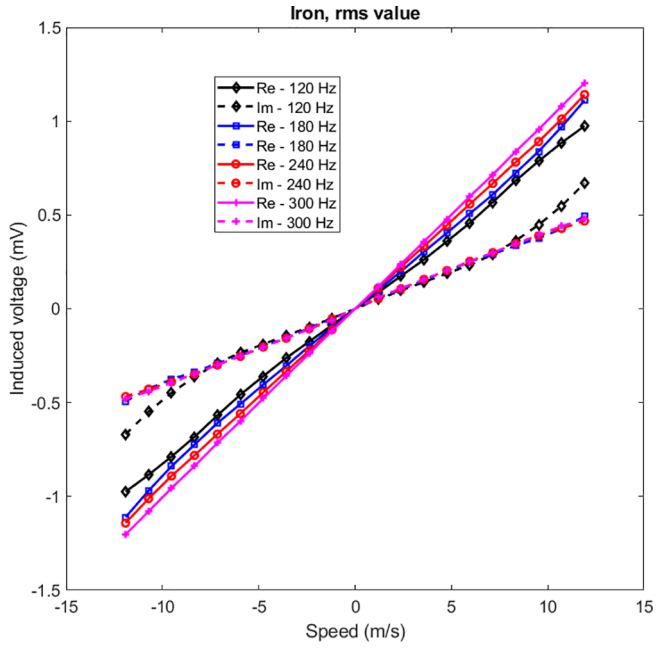

Fig. 7. Measured real component (Re) and imaginary component (Im) of induced voltage of pick up coils for iron rotating disk.

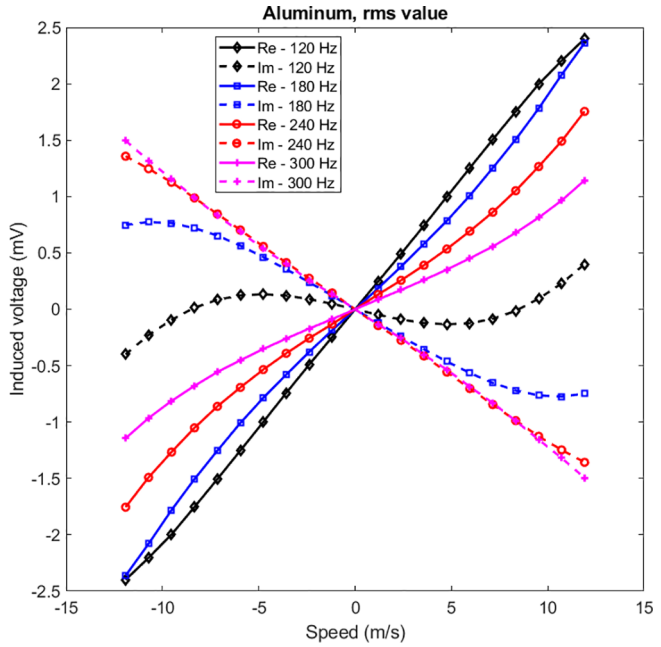

Fig. 8. Measured real component (Re) and imaginary component (Im) of induced voltage of pick up coils for aluminium rotating disk.

induced voltage is proportional to the losses component in the rotating disk, which could be more reluctant to the speed sensor lift off.

It is shown that eddy current speed sensor sensitivity is highly dependent on the moving part material properties. Conductivity of aluminum and iron moving part and relative permeability of iron moving part could change eddy current speed sensor outputs [13]. Compensating moving part material properties on the eddy current speed sensor output is a challenging issue and it must be addressed.

The root mean square error (RMSE) for linearity in percentage value as an indicator [17] is calculated about 0.26% for iron rotating disk at 300 Hz. It is representation of the fitness of the measured values to the linear approximation.

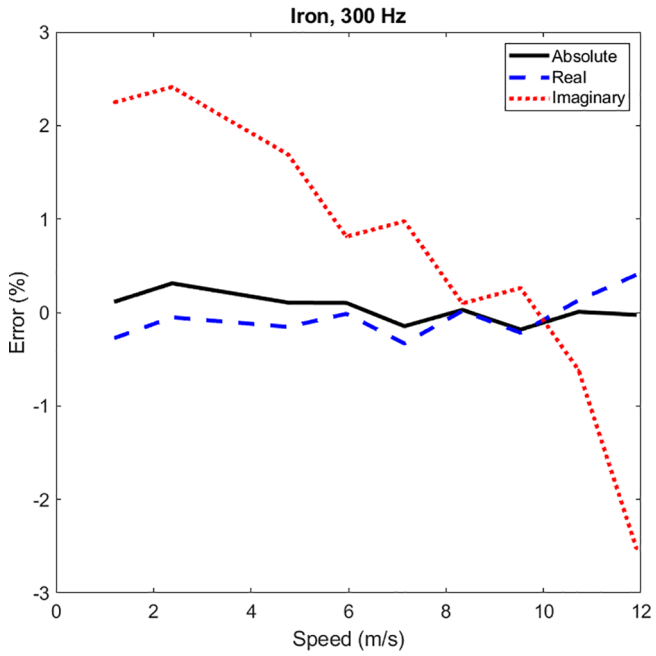

Fig. 9. Linearity error versus speed for absolute, real and imaginary components of induced voltages.

Fig. 9 shows the error in percent of full range as an alternative approach for linearity error evaluation of speed sensor. It shows that real component of induced voltage is more linear than imaginary component of induced voltage: the maximum error of the real part is only 0.3%, while it is 2.5% for the imaginary part.

4. 3D FEM analysis

The performance of eddy current speed sensor is analyzed using time stepping 3D FEM tool [18]. The motion of moving part is considered at different speeds. Sliding mesh method is used in the FEM tool to model motion of moving part. The eddy current effects are taken into account in the shielding too as well as conductive moving part. In order to model accurately the skin effects in the moving part and shielding, the mesh sizes are adjusted accordingly. Second order elements are utilized in the FEM tool. Therefore, high accuracy analysis could be achieved.

Only half of model is analyzed because of symmetry to save simulation time. Eddy current distribution in the aluminum moving part at zero speed and 10 m/s are shown in the Figs. 10 and 11. Eddy current distribution changes from symmetric form (Fig. 10) to asymmetric form (Fig. 11) due to the speed effect, which causes different induced voltage in the left and right side pick up coils.

4.1. Comparison between experiments and FEM

Table 2 presents comparison between 3D FEM analysis and measurements at 2 m/s, 5 m/s and 10 m/s for aluminum and iron rotating disks. 3D FEM results coincide very well with measurements, which show accuracy of 3D FEM. And its suitability is shown for further steps, for example, eddy current speed sensor optimization and material effects evaluations. Fig. 12 shows comparison between experimental and 3D FEM results versus time for rotating iron disk at 10 m/s. Linear model is used for the simulation as sensor size and dimensions are very small in comparison with rotating disk. It is convenient to use disk or cylinder as a fine approximation for linear motion [19–22].

4.2. Ferromagnetic materials evaluation of magnetic shield and moving part

Table 3 presents effect of relative magnetic permeability of iron

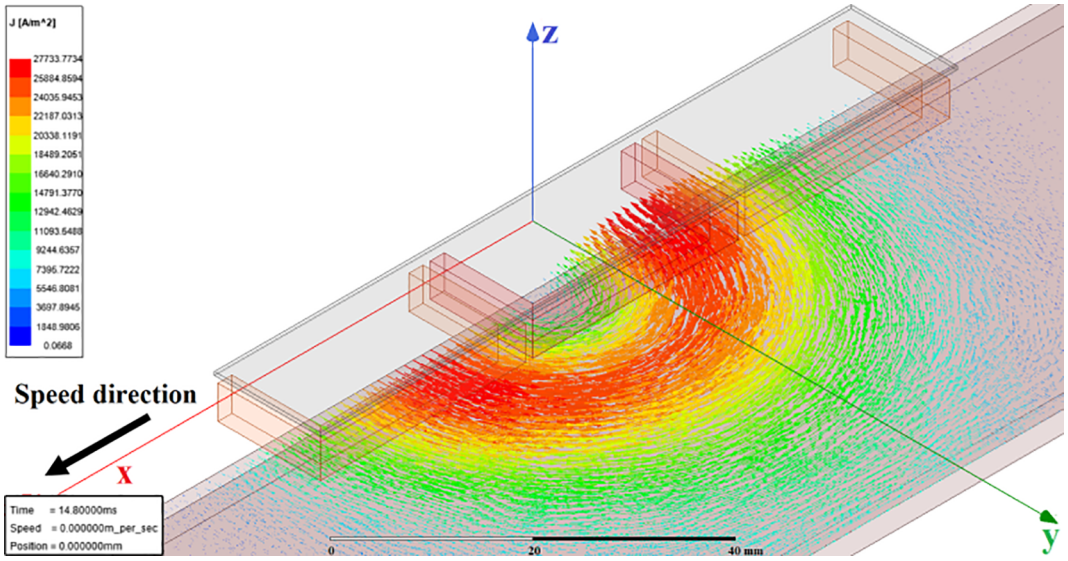

Fig. 10. Eddy current distribution in the aluminium moving part at zero speed.

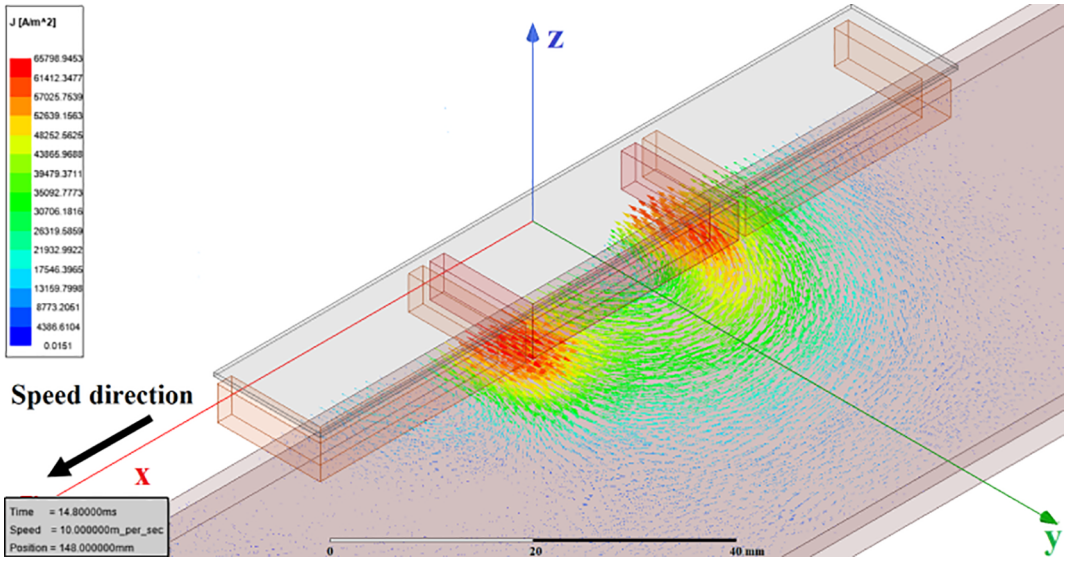

Fig. 11. Eddy current distribution in the aluminium moving part at 10 m/s.

moving part on the sensor output. With increasing permeability, the sensitivity is decreasing due to the decreasing of the penetration depth. Relative magnetic permeability varies for different steels and irons [23,24].

Effect of magnetic shielding is evaluated in the Table 4. First case is silicon steel with 0.5 mm thickness and estimated relative magnetic permeability 1000. The relative magnetic permeability in the second case is changed to 100, which induced voltage decreases considerably because of higher reluctance in the magnetic flux path. Third case is Ferrite core with 5 mm thickness and relative magnetic permeability 2000 for magnetic shielding, which induced voltage increases. However, eddy current speed sensor becomes thicker and less compact.

Table 2
Comparison between experimental results and FEM for induced voltage (mV) –rms value.

	2 m/s Exp./FEM	5 m/s Exp./FEM	10 m/s Exp./FEM
Aluminum 120 Hz	0.42/0.429	1.057/1.075	2.085/2.185
Aluminum 240 Hz	0.318/0.294	0.815/0.845	1.793/1.889
Iron 120 Hz	0.168/0.17	0.427/0.446	0.959/0.99
Iron 240 Hz	0.207/0.212	0.514/0.513	1.022/1.0

5. Discussions

The mutual flux between excitation coil and pick up coils, λ is proportional to the number of turns of the excitation coil, N_e ($=N$) and the number of turns of pick up coils, N_p ($=N$):

$$\lambda \propto N_e \bullet N_p \tag{2}$$

Therefore, increasing number of turns could increase mutual flux linkage and induced voltage in the pick up coils. The limitations are two reasons: saturation of ferromagnetic shielding and parasitic capacitances of the multi-turn coils.

The proposed eddy current speed sensor has compact structure, it is cost effective, and requires no modifications for the moving parts. Therefore, it shows significant merits in comparison with electrostatic phenomena-based and saliency-based speed sensors [14,15].

The sensor output voltage contains noise mainly on power line

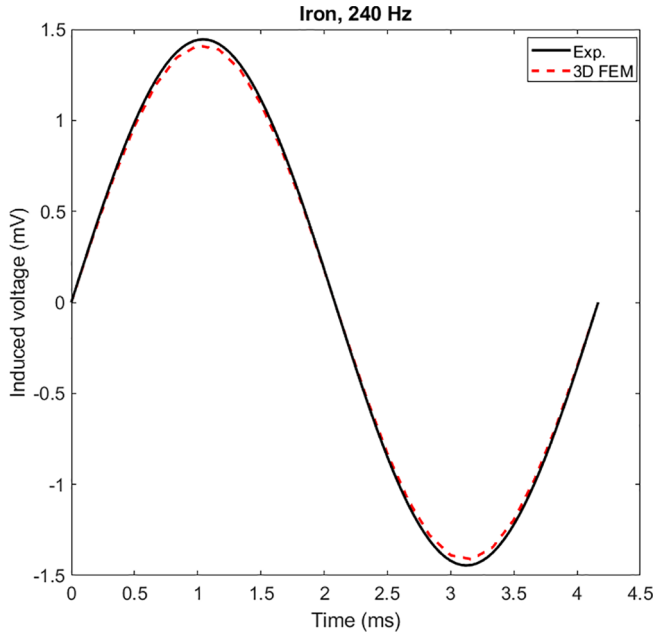

Fig. 12. Comparison between experimental and 3D FEM curves versus time at 10 m/s.

Table 3
FEM results of induced voltage (mV) for different iron moving part permeability –rms value.

10 m/s	μ_{ri} = 75	μ_{ri} = 100	μ_{ri} = 125
120 Hz	1.12	0.99	0.88
240 Hz	1.15	1.0	0.90

Table 4
FEM results of induced voltage (mV) for different magnetic shield materials –rms value.

10 m/s120 Hz	1 − μ_{rs} = 1000 σ_s = 3.14 MS/m	2 − μ_{rs} = 100 σ_s = 3.14 MS/m	3 − μ_{rs} = 2000 σ_s = 0 MS/m
Iron	0.99	0.838	1.66
Aluminum	2.185	1.641	2.404

frequency and its multiples mainly from electromagnetic interference. The lock-in amplifier which is based on the synchronous detection operation effectively suppresses these interferences and extracts clean signal. The disadvantage of this technique is the necessity of using the low pass filter (Fig. 4), which slows down the sensor response. Low interference is occurred due to the differential pick up coils connection.

6. Conclusions

The proposed shielded eddy current speed sensor has sensitivity 110 μV/m/s for iron rotating disk at 300 Hz and 210 μV/m/s for aluminum rotating disk at 120 Hz. The magnetic shielding acts also as magnetic yoke and it increases the sensitivity of eddy current speed sensors as it decreases magnetic reluctance for the magnetic flux. The 3D FEM calculations show that the shielding increases sensitivity by a factor over 2, but its main role is to suppress sensitivity to external magnetic fields and ferromagnetic objects. The linearity error is 0.26% for iron moving part at 300 Hz.

The sensitivity can be increased several times by increasing the number of turns of all coils; the limitations are the parasitic capacitances and shielding saturation. The sensor can be optimized in terms of linearity and sensitivity using 3D FEM as the simulation results fit well with the measured values.

The sensor requires temperature compensation of the material properties and also compensation for the changes of lift-off: using ratiometric output $V_1 - V_2/(V_1 + V_2)$ would be the first choice. This technique is successfully utilized in LVDT sensors. However, verification of such compensation is out of the scope of the present paper.

Declaration of Competing Interest

The authors declare that they have no known competing financial interests or personal relationships that could have appeared to influence the work reported in this paper.

References

[1] C. Moron, E. Suarez, Non-contact digital speed sensor, J. Magn. Magn. Mater. 133 (1994) 610–612.
[2] C.-T. Liu, S.-Y. Lin, Y.-Y. Yang, C.-C. Hwang, Analytical model development of an eddy-current-based non-contacting steel plate conveyance system, J. Magn. Magn. Mater. 320 (2008) 291–295.
[3] Z. Zhang, C. Xi, Y. Yan, Q. Geng, T. Shi, A hybrid analytical model for open-circuit field calculation of multilayer interior permanent magnet machines, J. Magn. Magn. Mater. 435 (2017) 136–145.
[4] P. Ripka, Magnetic Sensors and Magnetometers, Artech House, Jan 1, 2001 – Technology & Engineering.
[5] N. Takehira, A. Tanaka, Analysis of a perpendicular-type eddy-current speed meter, IEE Proc. A Phys. Sci. Meas. Instrum. Manage. Educ. Rev. UK 135 (2) (1988) 89.
[6] T. Itaya, K. Ishida, A. Tanaka, N. Takehira, T. Miki, Eddy current distribution for a rectangular coil arranged parallel to a moving conductor slab, IET Sci. Meas. Tech. 6 (2) (2012) 43–51.
[7] T. Itaya, K. Ishida, A. Tanaka, N. Takehira, Analysis of a fork-shaped rectangular coil facing moving sheet conductors, IET Sci. Meas. Technol. 3 (4) (2009) 279–285.
[8] T. Itaya, K. Ishida, Y. Kubota, A. Tanaka, N. Takehira, Visualization of eddy current distributions for arbitrarily shaped coils parallel to a moving conductor slab, Prog. Electromagn. Res. M 47 (2016) 1–12.
[9] Toshiya Itaya, Koichi Ishida, Akio Tanaka, Nobuo Takehira, Setsuo Yamamoto, Analysis of an eddy current speed meter by rectangular coil system, IEEJ Trans. Fundam. Mater. 133 (8) (2013) 416–423.
[10] T. Itaya, K. Ishida, A. Tanaka, N. Takehira, T. Miki, Analysis of a fork-shaped rectangular coil oriented perpendicular to moving conductor slabs, NDT&E Int. 44 (2011) 413–420.
[11] A. Tuysuz, M. Flankl, J. W. Kolar, and A. Mutze, "Eddy-current-based contactless speed sensing of conductive surfaces," IEEE 2nd Annual Southern Power Electronics Conference (SPEC), pp. 1 - 6, Dec. 2016.
[12] M. Mirzaei, P. Ripka, A. Chirtsov, J. Vyhnanek, Eddy current linear speed sensor, IEEE Trans. Mag. 55 (1) (2019) 1–4.
[13] M. Mirzaei, P. Ripka, J. Vyhnanek, A. Chirtsov, V. Grim, Rotational eddy current speed sensor, IEEE Trans. Mag. (Early access) (2019).
[14] L. Li, H. Hu, Y. Qin, K. Tang, Digital approach to rotational speed measurement using an electrostatic sensor, Sensors (Basel) 19 (11) (2019) 2540.
[15] T. Addabbo, M. Di Marco, A. Fort, E. Landi, M. Mugnaini, V. Vignoli, G. Ferretti, Instantaneous rotation speed measurement system based on variable reluctance sensors for torsional vibration monitoring, IEEE Trans. Instrum. Meas. 68 (7) (July 2019) 2363–2373.
[16] Tsih C. Wang, Linear induction motor for high-speed ground transportation, IEEE Trans. Ind. Gen. Appl. IGA-7 (5) (1971) 632–642.
[17] H. Sumali, E.P. Bystrom, G.W. Krutz, A displacement sensor for nonmetallic hydraulic cylinders, IEEE Sens. J. 3 (6) (2003) 818–826.
[18] Ansys-Maxwellsoftware (accessed 20.07.19): https://www.ansys.com/products/electronics/ansys-maxwell.
[19] O.C. Coho, G.B. Kliman, J.I. Robinson, Experimental evaluation of a high speed double sided linear induction motor, IEEE Trans. Power Apparatus Syst. 94 (1) (1975) 10–18.
[20] M. Iwamoto, S. Sakabe, K. Kitagawa, G. Utsumi, Experimental and theoretical study of high-speed single-sided linear induction motors, IEE Proc. B – Electric Power Appl. 128 (6) (1981) 306–312.
[21] T. Haller, W. Mischler, A comparison of linear induction and linear synchronous motors for high speed ground transportation, IEEE Trans. Magn. 14 (5) (1978) 924–926.
[22] Masatami Iwamoto, Eiichi Ohno, Toshio Itoh, Yoshiyuki Shinryo, End-effect of high-speed linear induction motor, IEEE Trans. Ind. Appli. IA-9 (6) (1973) 632–639, https://doi.org/10.1109/TIA.1973.349986.
[23] M. Lu, W. Zhu, L. Yin, A.J. Peyton, W. Yin, Z. Qu, Reducing the lift-off effect on permeability measurement for magnetic plates from multi frequency induction data, IEEE Trans. Instrum. Meas. 67 (1) (2018) 167–174.
[24] M. Lu, R. Huang, W. Yin, Q. Zhao, A. Peyton, Measurement of permeability for ferrous metallic plates using a novel lift-off compensation technique on phase signature, IEEE Sens. J. 19 (17) (2019) 7440–7446.

3-2-3-5 A Novel Eddy Current Speed Sensor with A Ferrite E-Core [J11]

This letter presents a novel speed sensor based on motion-induced eddy currents in conductive moving parts. The magnetic yoke is an E-shaped ferrite core. The excitation coil is on the center leg of the E-core, and two antiserially connected pick-up coils are on the side legs. Solid iron and aluminum materials are used for the moving part in the simulations and in the measurements. Two-dimensional and 3-D finite element methods are used for a detailed analysis and for the parametric calculations of the eddy current speed sensor. Despite its simple structure, the proposed eddy current speed sensor shows high linearity. The analysis and the measurements are performed at various speeds and excitation frequencies for an evaluation of the performance of the eddy current speed sensor. The minimum linearity error is less than 0.5%.

The merits of the proposed sensor that have motivated the authors are its cost-effectiveness, its compact and simple structure, and the possibility to use single-chip signal processing unit. The main limitation of the proposed speed sensor and challenge for the further development lie in temperature compensation for harsh and hot environments. Measurements and simulations of the eddy current speed sensor were performed for a speed range of ±14.1 m/s, at various frequencies from 100 to 800 Hz. The material of the moving part has a fundamental effect on the performance. The power consumption of the sensor at 30 mA excitation current is only 0.15 W. Compensation of the material effects, lift-off, and moving part temperature must be considered for industrial applications, but the study of these topics lies beyond the scope of this letter.

Magnetic Instruments

A Novel Eddy Current Speed Sensor With a Ferrite E-Core

Mehran Mirzaei, Pavel Ripka, and Vaclav Grim

Faculty of Electrical Engineering, Czech Technical University, Prague 16627, Czech Republic

Received 5 Apr 2020, revised 1 May 2020, accepted 4 May 2020, published 8 May 2020, current version 3 Jun 2020.

Abstract—This letter presents a novel speed sensor based on motion-induced eddy currents in conductive moving parts. The magnetic yoke is an E-shaped ferrite core. The excitation coil is on the center leg of the E-core, and two antiserially connected pick-up coils are on the side legs. Solid iron and aluminum materials are used for the moving part in the simulations and in the measurements. Two-dimensional and 3-D finite element methods are used for a detailed analysis and for the parametric calculations of the eddy current speed sensor. Despite its simple structure, the proposed eddy current speed sensor shows high linearity. The analysis and the measurements are performed at various speeds and excitation frequencies for an evaluation of the performance of the eddy current speed sensor. The minimum linearity error is less than 0.5%.

Index Terms—Magnetic instruments, eddy currents, speed sensor, ferrite E-core, iron, aluminum, finite element method, measurement.

I. INTRODUCTION

Speed measurements and speed assessments are vital in a range of applications with translational motion, e.g., on a railway line [see Fig. 1 (a)], and in applications with rotating motion for control, maintenance, and protection purposes [Addabbo 2019]. Various methods and technologies are currently used for speed measurements, e.g., optical sensors, capacitive sensors, and also magnetic reluctance and eddy current saliency-based sensors, which are, however, not resistant to dust and dirt or require modification of the moving part [Manyala 2013, Li 2019].

The use of an eddy current is a well-known technique for various electromagnetic applications [Gonen 1965, Gong 2019, Guilizzoni 2019, Tsukada 2019]. An eddy current speed sensor could be an appropriate option for speed measurements, as it is a nondestructive methodology with a cost-effective and simple configuration. Recent works [Sonoda 1985, Takehira 1988, Cardelli 2013, Itaya 2013] on eddy current speed sensors have focused on the nonferromagnetic moving conductive part, mainly aluminum, which is a less widely used material than solid iron and steel for moving objects. Speed measurements and performance analyses are much easier to make for nonferromagnetic moving parts than for an iron moving part, because not only the conductivity of the moving part but also its magnetic permeability has to be taken into account.

The authors of this letter have recently developed various types of eddy current speed sensors with iron and aluminum moving parts for rotating and translational motions [Mirzaei 2019a, 2019b, 2020a, 2020b]. These sensors have been designed and analyzed both with an air core and with a magnetic yoke. The magnetic yoke was used to improve the sensitivity of the sensor and for magnetic shielding purposes. The eddy current sensor proposed in this letter has a new configuration with a compact structure, using a ferrite E-core. This provides considerably greater sensitivity. The two-dimensional (**2-D**) time-stepping finite element method (**FEM**) is used for fast parametric calculations of the new eddy current speed sensor. Three-dimensional FEM is also used for precise calculation. Calculated results are verified by measurements at various speeds and frequencies.

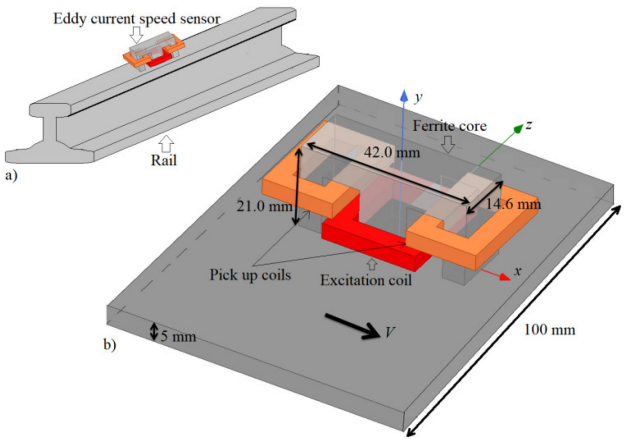

Fig. 1. (a) Eddy current speed sensor with linear translational motion for a railway application. (b) Detailed model.

II. EDDY CURRENT SPEED SENSOR MODEL

Fig. 1(b) shows a 3-D model of the proposed eddy current speed sensor for translational motion. The solid conducting moving part has speed V in the x-direction. The model shows three rectangular coils. The coil in the middle is the excitation coil, and the double side coils are antiserially connected pick-up coils. The induced voltage in the antiserially connected pick-up coils is zero at zero speed of the moving part, because the left and right coils have the same mutual magnetic flux linkage with the excitation coil. At nonzero speed, the differential induced voltage is proportional to the speed value.

Equation (1) presents the induced eddy current, J_e, in the conductive moving part with a smooth (not salient) surface in the direction of the translational motion [Hammond 1971, Binns 1992]. The first term and the second term in the right-hand side of the equality in (1) are the

Corresponding author: Mehran Mirzaei (e-mail: mirzameh@fel.cvut.cz).
Digital Object Identifier 10.1109/LMAG.2020.2993501

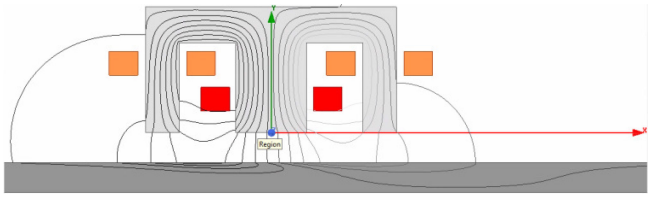

Fig. 2. Magnetic flux distribution at 120 Hz and 14.1 m/s for the moving iron part using 2-D FEM.

transformer component caused by the time variation of the source field, and the motional component proportional to the speed V, respectively [Hammond 1971]. Their reaction fields of the motional component of the induced eddy current, J_e, cause an unequal and asymmetric magnetic flux distribution in the left and right legs of the E-core and the corresponding pick-up coils

$$J_e = -\sigma \cdot \frac{\partial A}{\partial t} + \sigma \cdot V \times \nabla \times A, \quad B = \nabla \times A \tag{1}$$

where σ is the electrical conductivity of the moving conductive part, A is the magnetic vector potential, and B is the magnetic flux density.

III. PARAMETRIC ANALYSIS OF THE EDDY CURRENT SPEED SENSOR

The distribution of the induced eddy current in the conductive moving part has a 3-D configuration [Bolton 1969]. However, 2-D time-stepping FEM, taking into account the speed of the moving part, is used for the parametric calculations, although it is less accurate than time-stepping 3-D FEM. Two-dimensional FEM is faster, which makes it more suitable for parametric analysis. The maximum linear speed considered in this letter is 14.1 m/s. Fig. 2 shows the magnetic flux distribution at 14.1 m/s using 2-D time-stepping FEM [Ansys/Maxwell 2019], which is asymmetric due to the speed of the moving part. The asymmetric magnetic flux in the ferrite core causes different flux linkage and induced voltage in the pick-up coils. The third-dimension effects are neglected in the 2-D FEM analysis.

Fig. 3 presents the variations of the differential induced voltage of the pick-up coils versus the relative permeability μ_r and the electrical conductivity σ for the iron moving part and for the nonmagnetic moving part (for example, aluminum or copper). The induced voltage in the iron moving part increases with decreasing relative permeability and with increasing conductivity at 120 and 800 Hz. The induced voltage at 800 Hz is less sensitive to the material properties of the iron moving part (variations less than 15%) than the induced voltage at 120 Hz (variation less than 25%). The range of the variations for relative permeability is considered between 75 and 125, and for electrical conductivity the range is between 4 and 6 MS/m. These are quite common values for various construction irons and steels [Mirzaei 2020c]. The induced voltage is more sensitive to the conductivity at 800 Hz than at 120 Hz in the nonmagnetic moving part. The induced voltage increases with increasing frequency until 800 Hz for the iron moving part with relative permeability 100 and conductivity 6.0 MS/m (see Fig. 4). However, the induced voltage has a maximum value at about 200 Hz, and the value decreases for the aluminum moving part with conductivity 33.5 MS/m. The flux linkages decrease versus frequency for both the iron moving part and the aluminum moving part. This shows that the difference in the magnetic flux densities on

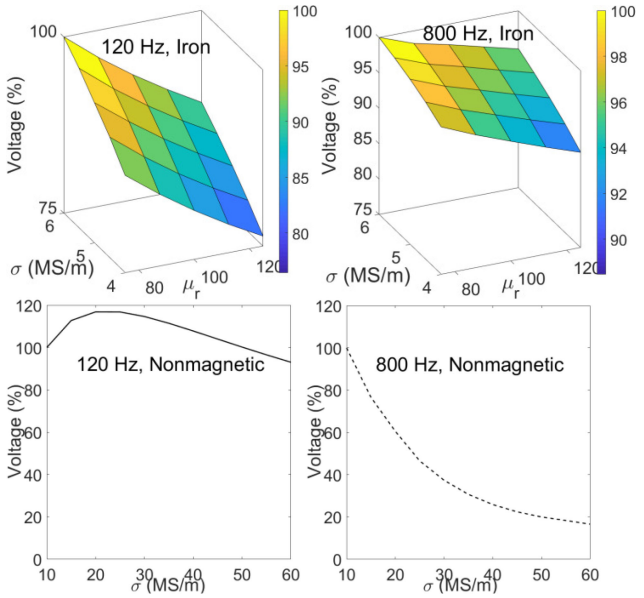

Fig. 3. Variation of the induced voltage versus the material properties of the moving part at 14.1 m/s for ferromagnetic iron and for nonmagnetic moving parts.

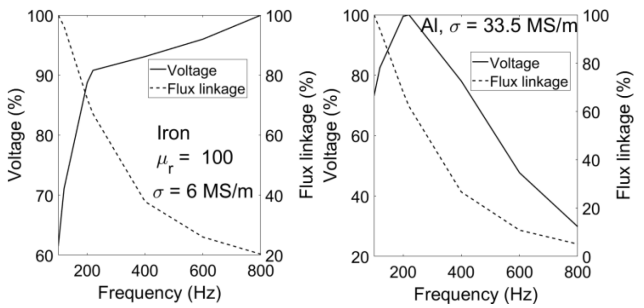

Fig. 4. Variation of the induced voltage and the flux linkage versus frequency at 14.1 m/s.

the left and right sides of the excitation coil is most sensitive at low frequencies or for dc. This contrasts with the variation of the induced voltage versus frequency, which in the ideal case is linear due to the induction law.

IV. EXPERIMENTAL RESULTS

The structure and the measurement elements of the eddy current sensor are shown in Fig. 5. Rotating iron and aluminum disks are used to model the moving part in the experimental setup [Iwamoto 1973, Coho 1975]. A signal generator with internal resistance $R_{\text{in}} = 50\ \Omega$ is used as a source for the excitation coil. The induced voltages are measured using an SR 860 lock-in amplifier. The real and imaginary components of the induced voltage are measured with phase relative to the excitation coil current. The number of turns per coil is 1000. The resistance and the inductance of the excitation coil mounted on the ferrite core without a conductive moving part nearby are measured as $R_c = 166\ \Omega$ and $L_c = 89.25$ mH, respectively. The variation of the inductance of the excitation coil versus frequency is shown in Fig. 6, with a magnetic gap of 5 mm between the ferrite core and the moving part. The inductance decreases with frequency due to the reaction fields

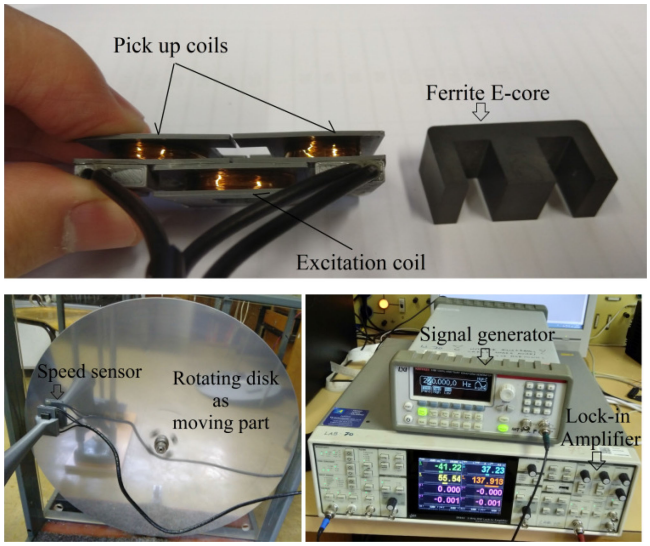

Fig. 5. Experimental setup. A speed sensor with a ferrite E-core and coils, rotating disk to model linear speed and signal generator, and lock-in amplifier.

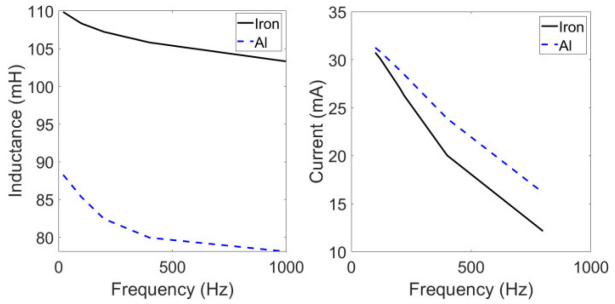

Fig. 6. Excitation coil inductance and excitation current (rms) versus frequency at a constant input source voltage of 7.07 V (rms).

of the induced eddy current. The measured current of the excitation coil $I_{\rm rms}$ decreases with frequency f as the source voltage U_s is constant $I_{\rm rms} = U_s/\sqrt{(R_{\rm in} + R_c)^2 + (2\pi f L_c)^2}$.

The measured induced voltages of the antiserially connected pick-up coils are shown in Figs. 7 and 8 at various frequencies between -14.1 and $+14.1$ m/s for the moving part. The sensitivity and the linearity of the real and imaginary induced voltage of the eddy current speed sensor show different tendencies for the iron and aluminum moving parts. All results for the real and imaginary components of the induced voltage show a roughly ideal linear curve versus speed between -5 and $+5$ m/s. The real component (Re) of the induced voltage for the iron moving part has the finest linearity at higher frequencies for the whole speed range of ± 14.1 m/s. The sensitivity of the eddy current speed sensor increases versus speed for the iron moving part with the same excitation coil current. The sensitivity is higher for the aluminum moving part at low frequencies, and it is higher for the iron moving part at higher frequencies. The absolute (Abs) component of the induced voltage U_a is calculated with an imaginary value U_i and with a real value U_r: $U_a = \sqrt{U_r^2 + U_i^2}$. Table 1 presents the sensitivity coefficient C mV/m/s for the iron moving part, using Fig. 7.

Fig. 9 shows the induced eddy current distributions, depicting an asymmetric shape because of the speed effects of the moving part. The calculated results using 2-D and 3-D time-stepping FEM in comparison

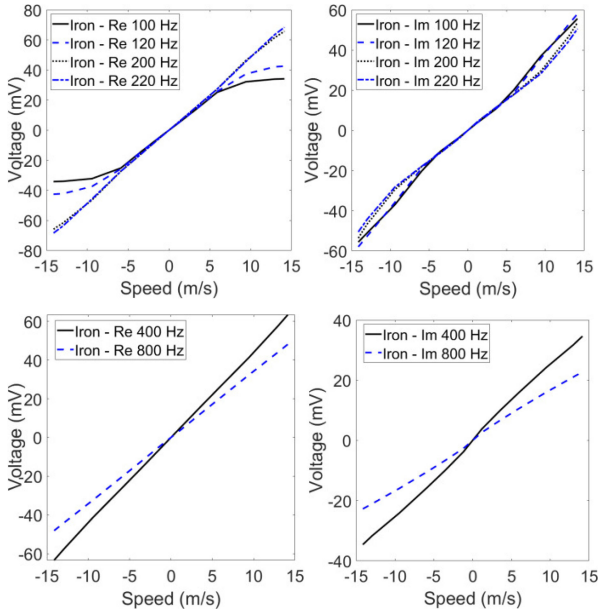

Fig. 7. Real and imaginary components of induced voltages (rms) versus speed at various frequencies. Iron moving part.

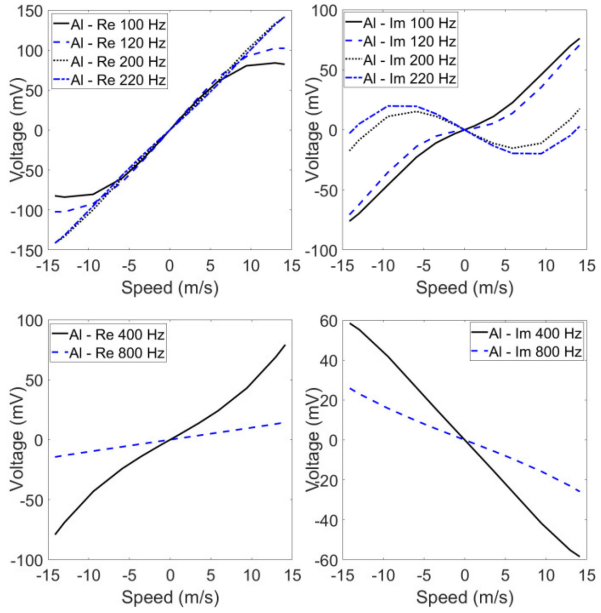

Fig. 8. Real and imaginary components of induced voltages (rms) versus speed at various frequencies. Aluminum moving part.

Table 1. Sensitivity coefficients at 400 and 800 Hz, $U = C \cdot V$.

Case for the iron moving part	400 Hz	800 Hz
Real	4.45 mV/m/s	3.41 mV/m/s
Imaginary	2.50 mV/m/s	1.65 mV/m/s
Absolute	5.10 mV/m/s	3.79 mV/m/s

with measurements are presented in Table 2. The measured conductivities of the material of the iron moving part and of the aluminum moving part are 6.0 and 33.5 MS/m, respectively. The 3-D FEM results are closer to the experimental results, especially for the aluminum moving part. The discrepancies for the iron moving part could be due

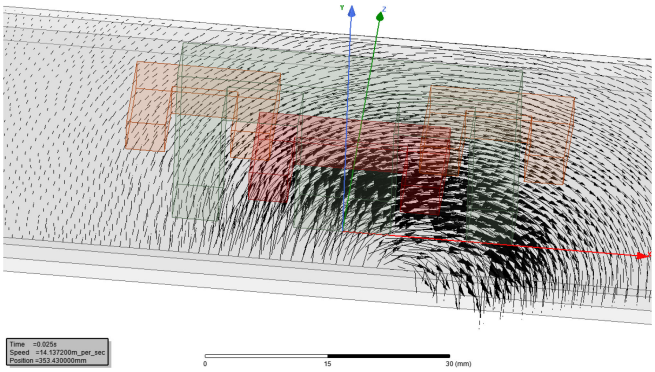

Fig. 9. Eddy current distribution in the moving part of a half model at 120 Hz and 14.1 m/s.

Table 2. Comparison between experimental results and 2-D and 3-D FEM for iron moving parts ($\mu_r = 100, \sigma = 6$ MS/m) and for aluminum moving parts ($\sigma = 33.5$ MS/m).

Case	Iron (Ir) Exp. 2D FEM/3D FEM	Aluminum (Al) Exp. 2D FEM/3D FEM
120 Hz, 14.1 m/s	71.9	124.2
	84.9 / 76.2	77.4 / 122.5
120 Hz, 5.9 m/s	31.7	66.8
	37.6 / 35.0	43.6 / 67.3
220 Hz, 14.1 m/s	85.1	141.5
	94.7 / 92.0	86.6 / 143.9
220 Hz, 5.9 m/s	32.5	60.1
	34.5 / 33.4	35.9 / 61.6

to the relative magnetic permeability, which may be different from the estimated $\mu_r = 100$.

V. LINEARITY ANALYSIS

Fig. 10 presents the linearity error as a percentage of the full range of real, imaginary, and Abs components of the induced voltage for the iron moving part at 400 and 800 Hz. The minimum linearity error is obtained less than 0.5% for the real component of the induced voltage at 800 Hz. The linearity error is higher in the imaginary component of the induced voltage, as it is more sensitive to the magnetic coupling variation between the magnetic core and the moving part, which might be caused by vibration of the moving disk [Mirzaei 2020a]. The magnetic gap variation is a common problem in practical applications, e.g., in speed measurements in railway transportation. It could be suggested that the real component of the induced voltage be utilized for speed measurements, and the imaginary component for compensating the variation in the gap.

The methodologies for compensating for the variation in the gap and the temperature were investigated in [Lu 2018, 2019]. The use of simultaneous double frequency excitation of 400 and 800 Hz can be proposed, as one frequency is utilized for the speed meter and another frequency is used for compensation.

High linearity in the full speed range is preferred for the good performance of the sensor. This avoids the need to improve the linearity, e.g., with the use of software. It also simplifies the signal processing of

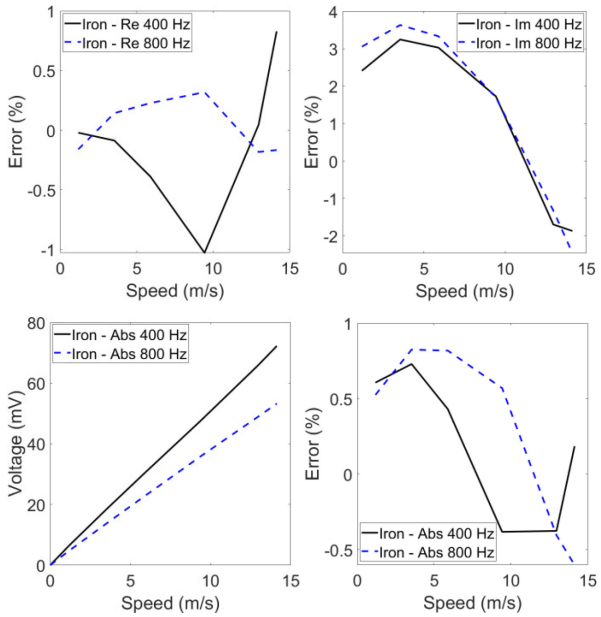

Fig. 10. Linearity error versus speed at various frequencies. Iron moving part.

the sensor. It has been observed that higher frequency is more suitable for the higher speed range because there is greater linearity in the full range of speeds.

VI. CONCLUSION

The linear eddy current speed sensor that has been presented here shows promising performance in terms of sensitivity and linearity.

A detailed linearity analysis has been made only for the iron moving part, as iron is the most widely used material in industrial applications, especially for high speeds. It has been observed that higher excitation frequency is more suitable for the higher speed range, because of better linearity.

The merits of the proposed sensor that have motivated the authors are its cost-effectiveness, its compact and simple structure, and the possibility to use single-chip signal processing unit. The main limitation of the proposed speed sensor and challenge for the further development lie in temperature compensation for harsh and hot environments.

Measurements and simulations of the eddy current speed sensor were performed for a speed range of ± 14.1 m/s, at various frequencies from 100 to 800 Hz. The material of the moving part has a fundamental effect on the performance.

The power consumption of the sensor at 30 mA excitation current is only 0.15 W. Compensation of the material effects, lift-off, and moving part temperature must be considered for industrial applications, but the study of these topics lies beyond the scope of this letter.

ACKNOWLEDGMENT

The authors thank A. Chirtsov and J. Vyhnanek from the Department of Measurement, Faculty of Electrical Engineering, Czech Technical University for their support in building the sensor components and in preparing the measurement elements. This work was supported by the Czech Technical University under Grant SGS18/187/OHK3/3T/1.

REFERENCES

Addabbo T, Di Marco M, Fort A, Landi E, Mugnaini M, Vignoli V, Ferretti G (2019), "Instantaneous rotation speed measurement system based on variable reluctance sensors for torsional vibration monitoring," *IEEE Trans. Instrum. Meas.*, vol. 68, pp. 2363–2373, doi: 10.1109/TIM.2018.2877808.

Ansys/Maxwell Software (2019), [Online]. Available: https://www.ansys.com/products/electronics/ansys-maxwell. Accessed on: Apr. 27, 2020.

Binns K J, Lawrenson P J, Trowbridge C W (1992), *The Analytical and Numerical Solution of Electric and Magnetic Fields*. Hoboken, NJ, USA: Wiley-Blackwell.

Bolton H (1969), "Transverse edge effect in sheet-rotor induction motors," *Proc.—Inst. Elect. Eng.*, vol. 116, pp. 725–731, doi: 10.1049/piee.1969.0144.

Cardelli E, Faba A, Tissi F (2013), "Contact-less speed probe based on eddy currents," *IEEE Trans. Magn.*, vol. 49, pp. 3897–3900, doi: 10.1109/TMAG.2013.2248701.

Coho O C, Kliman G B, Robinson J I (1975), "Experimental evaluation of a high speed double sided linear induction motor," *IEEE Trans. Power App. Syst.*, vol. PAS-94, pp. 10–18, doi: 10.1109/T-PAS.1975.31818.

Gonen D, Stricker S (1965), "Analysis of an eddy-current brake," *IEEE Trans. Power App. Syst.*, vol. PAS-84, pp. 357–361, doi: 10.1109/TPAS.1965.4766206.

Gong C, Tuysuz A, Flankl M, Stolz T, Kolar J, Habetler T (2019), "Experimental analysis and optimization of a contactless eddy-current-based speed sensor for smooth conductive surfaces," *IEEE Trans. Ind. Electron.*, to be published, doi: 10.1109/TIE.2019.2946547.

Guilizzoni R, Finch G, Harmon S (2019), "Subsurface corrosion detection in industrial steel structures," *IEEE Magn. Lett.*, vol. 10, 2108005, doi: 10.1109/LMAG.2019.2948808.

Hammond P (1971), *Applied Electromagnetism*. Oxford, U.K.: Pergamon.

Itaya T, Ishida K, Tanaka A, Takehira N (2013), "Analysis of an eddy current speed meter by rectangular coil system," *IEEJ Trans. Fundam. Mater.*, vol. 133, pp. 416–423, doi: 10.1541/ieejfms.133.416.

Iwamoto M, Ohno E, Itoh T, Shinryo Y (1973), "End-effect of high-speed linear induction motor," *IEEE Trans. Ind. Appl.*, vol. IA-9, pp. 632–639, doi: 10.1109/TIA.1973.349986.

Li L, Hu H, Qin Y, Tang K (2019), "Digital approach to rotational speed measurement using an electrostatic sensor," *Sensors (Basel)*, vol. 19, 2540, doi: 10.3390/s19112540.

Lu M, Zhu W, Yin L, Peyton A J, Yin W, Qu Z (2018), "Reducing the lift-off effect on permeability measurement for magnetic plates from multi frequency induction data," *IEEE Trans. Instrum. Meas.*, vol. 67, pp. 167–174, doi: 10.1109/TIM.2017.2728338.

Lu M, Huang R, Yin W, Zhao Q, Peyton A (2019), "Measurement of permeability for ferrous metallic plates using a novel lift-off compensation technique on phase signature," *IEEE Sensors J.*, vol. 19, pp. 7440–7446, doi: 10.1109/JSEN.2019.2916431.

Manyala J O, Fritz T, Atashbar M Z (2013), "Gearbox speed sensor design and performance optimization," *IEEE Sensors J.*, vol. 13, pp. 629–636, doi: 10.1109/JSEN.2012.2224862.

Mirzaei M, Ripka P, Chirtsov A, Vyhnanek J (2019a), "Eddy current linear speed sensor," *IEEE Trans. Magn.*, vol. 55, 4000304, doi: 10.1109/TMAG.2018.2872123.

Mirzaei M, Ripka P, Vyhnanek J, Chirtsov A, Grim V (2019b), "Rotational eddy current speed sensor," *IEEE Trans. Magn.*, vol. 55, 4003710, doi: 10.1109/TMAG.2019.2918163.

Mirzaei M, Ripka P, Chirtsov A, Vyhnanek J, Grim V (2020a), "Design and modeling of a linear speed sensor with a flat type structure and air coils," *J. Magnetism Magn. Mater.*, vol. 495, 165834, doi: 10.1016/j.jmmm.2019.165834.

Mirzaei M, Ripka P, Chirtsov A, Grim V (2020b), "Eddy current speed sensor with magnetic shielding," *J. Magnetism Magn. Mater.*, vol. 502, 166568, doi: 10.1016/j.jmmm.2020.166568.

Mirzaei M, Ripka P, Chirtsov A, Grim V (2020c), "Temperature stability of the transformer position transducer for pneumatic cylinder," *J. Magnetism Magn. Mater.*, vol. 503, 166636, doi: 10.1016/j.jmmm.2020.166636.

Sonoda T, Ueda R, Fujitani K, Irisa T, Tatata S (1985), "DC magnetic field type eddy current speed sensor detecting cross magnetization field with amorphous core," *IEEE Trans. Magn.*, vol. MAG-21, pp. 1732–1734, doi: 10.1109/TMAG.1985.1064042.

Takehira N, Tanaka A (1988), "Analysis of a perpendicular-type eddy-current speed meter," *IEE Proc. A—Phys. Sci., Meas. Instrum., Manage. Educ. Rev.*, vol. 135, pp. 89–94, doi: 10.1049/ip-a-1.1988.0014.

Tsukada K, Shobu H, Goda Y, Kobara T, Sakai K, Kiwa T, Saari M M (2019), "Integrated magnetic sensor probe and excitation wire for nondestructive detection of submillimeter defects," *IEEE Magn. Lett.*, vol. 10, 8105105, doi: 10.1109/LMAG.2019.2936392.

3-2-3-6 Design and Optimization of an Eddy Current Speed Sensor for Rotating Rods [J13]

This paper presents the design and optimization of a novel eddy current speed sensor for rotating rods and cylindrical shafts. The sensor consists of one excitation coil and two pick-up coils. All coils are stationary; we consider air coils, and we also use a magnetic yoke. We utilize a copper coating on an iron rod to increase the sensitivity, and we compare the performance with the performance achieved for an uncoated iron rod. 3D FEM is utilized for analyzing and for optimizing the design of the proposed sensor. The main advantages of the novel sensors are their simplicity, their low cost and their robust configuration. A linearity error of 0.5% has been achieved. The level of accuracy is limited by mechanical factors. A 1D analytical model has also been developed for rapid analysis and optimization of the sensor. An aluminum rod was also used in the measurements for a comparison with the results achieved with the iron rod.

Various rotating rods with an only iron rod, with a copper-coated iron rod, and with an only aluminum rod have been considered in the measurements and in the analysis. The optimum angle of the coil span was obtained, i.e. 120 deg., which is identical for an excitation coil and for pick-up coils. The tested eddy current speed sensor was manufactured with the optimum coil span angle. The presented eddy current speed sensor is an appropriate selection for speed measurements of any type of rotating machines, for example, turbines, motors, pumps, fans and turbochargers. This is an advantage of the sensor, which, unlike the conventional speed sensor, does not need additional space in the end shaft space. Operating an eddy current speed sensor at higher frequencies is an efficient method for obtaining greater sensitivity. However, the skin depth is smaller at high frequency. Surface cracks and defects and corrosion on the conductive rod could have a greater effect on the performance of eddy current speed sensors at high frequencies, if the radial thickness of the cracks or the corrosion depth is considerable in comparison with the magnetic flux penetration depth. Even a small crack on the conductive rotating rod could cause an accuracy error and noise in the speed sensor output, as an eddy current speed sensor is sensitive to the smoothness of the surface of the rotating rod. The use of a copper coating can minimize the effect of cracks in the solid rotating rod.

This article has been accepted for publication in a future issue of this journal, but has not been fully edited. Content may change prior to final publication. Citation information: DOI 10.1109/JSEN.2020.3000442, IEEE Sensors Journal

Design and Optimization of an Eddy Current Speed Sensor for Rotating Rods

Mehran Mirzaei, Pavel Ripka, Vaclav Grim, and Andrey Chirtsov

***Abstract*—This paper presents the design and optimization of a novel eddy current speed sensor for rotating rods and cylindrical shafts. The sensor consists of one excitation coil and two pick-up coils. All coils are stationary; we consider air coils, and we also use a magnetic yoke. We utilize a copper coating on an iron rod to increase the sensitivity, and we compare the performance with the performance achieved for an uncoated iron rod. 3D FEM is utilized for analyzing and for optimizing the design of the proposed sensor. The main advantages of the novel sensors are their simplicity, their low cost and their robust configuration. A linearity error of 0.5% has been achieved. The level of accuracy is limited by mechanical factors. A 1D analytical model has also been developed for rapid analysis and optimization of the sensor. An aluminum rod was also used in the measurements for a comparison with the results achieved with the iron rod.**

***Index Terms*—Eddy current speed sensor, optimization, copper coating, electrical steel lamination, rotating rods, 3D FEM.**

I. Introduction

THE electrification of transportation, e.g., electric cars, railways and airplanes, and also renewable energies are continuously increasing, and this especially involves replacing rotating mechanical elements with their electrical counterparts. Traction motors, electrically-assisted turbo chargers and other rotating elements need speed sensing for control purposes, and for diagnosing and preventing mechanical and electrical faults [1]-[8]. The simplicity of the sensor is of no less importance than its precision. Speed and position sensors often need compensation of mechanical issues, e.g., lift off and eccentricity. It is therefore a key advantage to use a sensor with a simple design for speed measurements.

Sensorless speed measurement methods for rotating electrical machines are well developed, although their signal processing is complex and time-consuming, and may not be rapid enough for control purposes [9]-[10]. Optical sensors are also widely used for speed measurements, but they may not be appropriate for harsh and dusty environments, and they often need maintenance to clean out dust and dirt [11]. The use of an external magnetic field sensor mounted on the housing of a machine was presented in [12]. Since it is not non-destructive, it needs magnetic shielding against external magnetic fields. Implementing a Hall sensor in the stator or inside the end windings to measure the speed of the rotating rotor was presented in [13]-[14]. However, this may be unreliable, e. g. in conditions where the winding becomes overheated. Variable reluctance (VR) or saliency-based speed measurements with pick-up coils or Hall sensors have also been used in industry for rotating machines. However, a non-salient magnetic surface needs to be built for operating reluctance variations or for changing the induced eddy current [15]-[18]. Recent works using electrostatic phenomena to measure speed were published in [19]-[20]. However, these sensors will be quite sensitive to dirt and dust, and they therefore need to be capsulated.

There is a long history in electrical engineering of utilizing the speed component of an induced eddy current, going back to the Faraday generator and the unipolar generator. The eddy current brake is another use of the speed component of the eddy current [21]-[22]. A non-destructive testing method for metals utilizes the same principle, as has been reported in [23]-[24].

Magnetic flow meters are used to measure the speed of fluids by reading the voltage caused by speed effects with electrodes in contact with the fluid across the fluid flowing in magnetic fields perpendicular to the direction of the flowing fluid [11] and [25]. A speed sensor using the fluxgate effect in an amorphous ring core to measure the field of eddy currents was presented in [26]. This rather complicated sensor has a poor linearity error of approx. 5%. A rotating permanent magnet rotor for contactless eddy current speed sensing was tested and analyzed in [27]; this type of sensor is not easy to manufacture and use because of the moving part. A Hall sensor with permanent magnet excitation was presented in [28]; however, this sensor shows poor offset stability.

Parallel and perpendicular types of eddy current-based speed sensors with air coils for excitation and pick-up voltage were analyzed and measured in detail in [24] and in [29]-[33]. The same parallel configuration as in [33], with one excitation coil and two pick-up coils using a ferrite magnetic yoke, was measured in [34]. These sensors use only aluminum for the moving part, though iron is a material typically used for shafts. The authors recently investigated linear speed sensors for variable speeds and a rotational speed sensor for constant speeds, using solid irons and steels for the moving part, taking into account the effects of the materials of the moving parts on the performance of the eddy current speed sensor [35]-[37].

This work was supported in part by the Czech Technical University in Prague under Grant SGS18/187/OHK3/3T/1.

M. Mirzaei is with the Faculty of Electrical Engineering, Czech Technical University, Prague 16627, Czech Republic (e-mail: mirzameh@fel.cvut.cz).

P. Ripka is with the Faculty of Electrical Engineering, Czech Technical University, Prague 16627, Czech Republic (e-mail: ripka@fel.cvut.cz).

V. Grim is with the Faculty of Electrical Engineering, Czech Technical University, Prague 16627, Czech Republic (e-mail: vaclav.grim@fel.cvut.cz).

A. Chirtsov is with the Faculty of Electrical Engineering, Czech Technical University, Prague 16627, Czech Republic (e-mail: chirtand@fel.cvut.cz).

This article has been accepted for publication in a future issue of this journal, but has not been fully edited. Content may change prior to final publication. Citation information: DOI 10.1109/JSEN.2020.3000442, IEEE Sensors Journal

Our new eddy current speed sensor for measuring the speed of rotating ferromagnetic bodies is based on an optimized single excitation coil with an AC current and two pick-up coils for measurements without a magnetic yoke. This sensor has high sensitivity with the air coils configuration. The time stepping 3D finite element method (FEM) simulation, taking into account the speed of the rotating part, is also presented for a comparison with measurements that could be used to estimate and optimize the performance of the eddy current speed sensor. A one-dimensional analytical model has also been developed and utilized for optimizing the design of eddy current speed sensors. A copper coating, which provides increased sensitivity, is applied to the rotating iron rod. A study of the magnetic shield and the magnetic yoke for the eddy current speed sensor, using various thicknesses and magnetic materials for the shield, is also presented in this paper.

II. Model and Performance

Fig. 1 shows the configuration and the structure of the proposed eddy current speed sensor with an air core structure for a rotating conductive rod. The total coils span is 360 deg., in order to provide increased sensitivity. One excitation coil and two antiserially connected pick-up coils are used.

The magnetic flux linkages of the pick-up coils diverge from each other if the rotating rod speed is nonzero (Fig. 2). The difference in flux linkage between the left side and the right side pick-up coils is proportional to the speed of the rotating conductive rod, and it can be measured in the case of AC current for the excitation coil as the differential induced voltage.

A simplified 1D analytical model is developed in appendix A for general analysis and for fast optimization of an eddy current speed sensor for rotating bodies (Fig. A1 (a)). The total angle span of the excitation coil and the pick-up coils covers the whole 360 deg. range, in order to achieve maximum sensitivity for the sensor ($\theta_{p1}=\theta_e$, $\theta_{p2}=180$ deg. in Fig. A1 (a)). Fig. 3 (a) shows that the optimum excitation coil angle span, $2\theta_e$, is 120 deg. in order to obtain the maximum voltage difference between the pick-up coil voltages. However, the maximum pick-up coil voltage values are obtained when the excitation coil angle span, $2\theta_e$, is 180 deg.

The induced eddy current in the rotating rod weakens the magnetic fields under the excitation coil and the pick-up coils, as shown in Fig. 4. The rotating rod speed effect causes the asymmetric distribution of the magnetic fields shown in Fig. 4, which causes the different flux linkage and the different induced voltage in the two pick-up coils (Fig. 3 (a)).

Fig. 3 (b) presents a linear curve for the real, imaginary and absolute components of the differential voltage (relative to the excitation coil current as a reference signal) versus speed, which can be utilized as a speed meter. The phase (the "polarity") of the induced voltage in the pick-up coils changes as the speed direction changes. The excitation current amplitude is considered constant at different speeds and frequencies in all simulations in this paper.

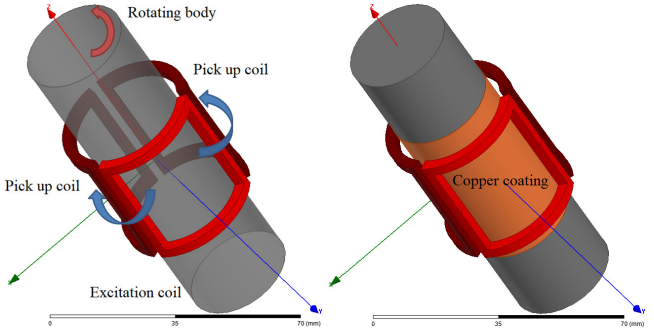

Fig. 1. 3D model of an eddy current speed sensor, a) a rotating rod with only a solid iron rod (left), and b) a rotating rod with a solid iron rod coated with a copper layer (right)

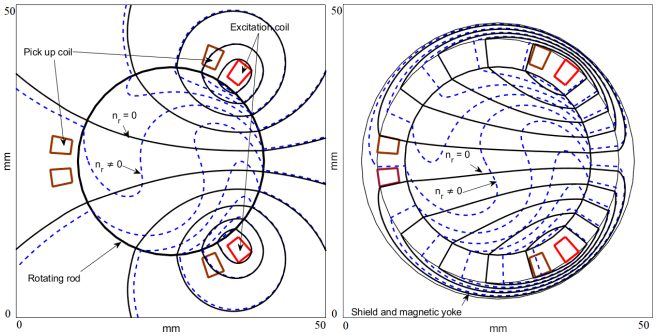

Fig. 2. General view of the magnetic flux distribution in the air core eddy current speed sensor a) without a shield (left) and b) with a shield and a magnetic yoke (right)

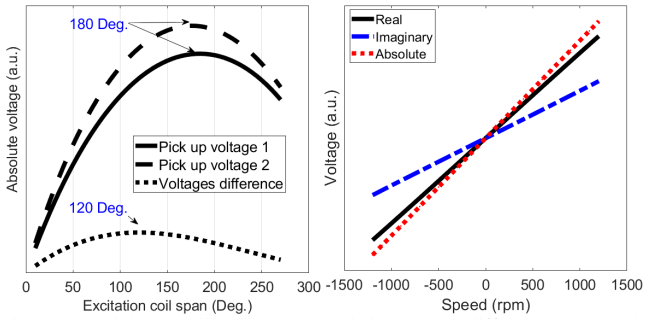

Fig. 3. a) Pick-up coil voltages and their voltage difference versus the excitation coil span (left) b) differential voltage variations versus rotating rod speed (right)- values calculated by the simplified 1D analytical model described in Appendix A

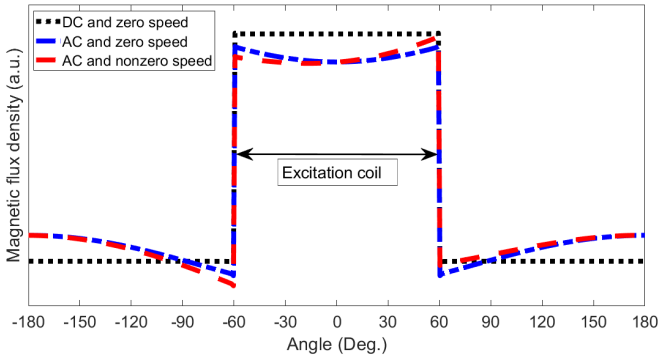

Fig. 4. Variations in magnetic flux density under an excitation coil and pick-up coils – the dotted line is for DC and zero speed, the dot-dashed line is for AC and zero speed, and the dashed line is for AC and nonzero speed. Values calculated by the simplified 1D analytical model described in Appendix A

This article has been accepted for publication in a future issue of this journal, but has not been fully edited. Content may change prior to final publication. Citation information: DOI 10.1109/JSEN.2020.3000442, IEEE Sensors Journal

The excitation and pick up coils have a smaller area in the case of a rotating rod than in the case of a similar linear speed sensor [35] and [37], and in addition the equivalent linear speed is rather low: for example, with 3 cm diameter, the surface linear speed of the rotating rod at 1200 rpm is less than 2 m/s. Therefore, the sensitivity of the speed sensor for a rotating rod is low for low speeds, and it is more difficult to measure rotating speeds than linear speeds.

III. Experimental Results

Fig. 5 and Fig. 6 show the experimental element, the eddy current speed sensor element, measurement instruments and schematic block diagram for speed measurements. A Keithley 3390 signal generator with amplitude accuracy 1% of the setting and internal resistance of 50 Ω is used to supply the excitation coil. A SR 830 lock-in amplifier with gain accuracy ±1% is utilized for the voltage measurements, in order to measure the voltage of the pick-up coils with minimum noise effects. The full scale sensitivity is 2 nV to 10 V.

Iron rods 100 mm and 200 mm in axial length are used for the measurements (Fig. 5), which showed a negligible effect of the axial length on the sensitivity of the speed sensor. The outer diameter of the iron rod is 30 mm, the inner diameter of the coils is 33.5 mm, and the outer diameter of the coils is 39.5 mm. All three coils are identical and have 100 turns per coil. The rods are connected to the shaft of the DC motor as the prime mover in the test bench. The measured speed range is between -1200 rpm and +1200 rpm.

Fig. 7 and Fig. 8 show the measured differential voltages of the eddy current speed sensor versus the speed only for the iron rod and for the iron rod with a copper coating, at 120 Hz and at 180 Hz. The real (U_r), imaginary (U_i) and absolute (U_a) components of the differential voltage are presented:

$$U_a = \sqrt{U_r^2 + U_i^2} \quad (1)$$

The applied current in the excitation coil is considered as the reference signal for calculating the real (Re) and imaginary (Im) components of the differential voltage. The polarity of the absolute values of the induced (differential) voltage is calculated using the phase shift between the induced voltage and the excitation coil current. Table I presents the linear curve parameters (induced voltage U, constant K, and speed S, using (2) fitted to the measurements in Fig. 7 and Fig. 8). The offset values for the voltage (U_{offset}) are removed numerically in the absolute values of the induced voltage in Figs. 7 and 8.

$$U = K \cdot S + U_{\text{offset}} \quad (2)$$

TABLE I
Linear Curve Parameters Fitted to The Measurements

Case	K (nV/rpm) 120 Hz / 180 Hz	U_{offset} (nV) 120 Hz / 180 Hz
Only iron - Re	110.92 / 133.38	13275 / 22417
Only iron - Im	73.09 / 79.86	-32687 / -54542
Only iron - Abs	132.85 / 155.47	0
With copper - Re	152.68 / 204.98	15333 / 29646
With copper - Im	144.97 / 169.15	-40313 / -63229
With copper - Abs	210.54 / 265.77	0

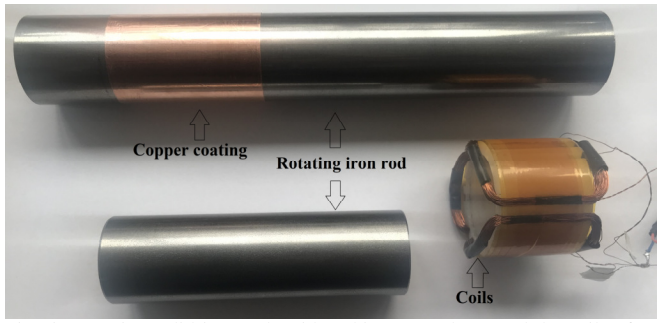

Fig. 5. Rotating solid iron rods with a thin copper layer and the coils of an eddy current speed sensor

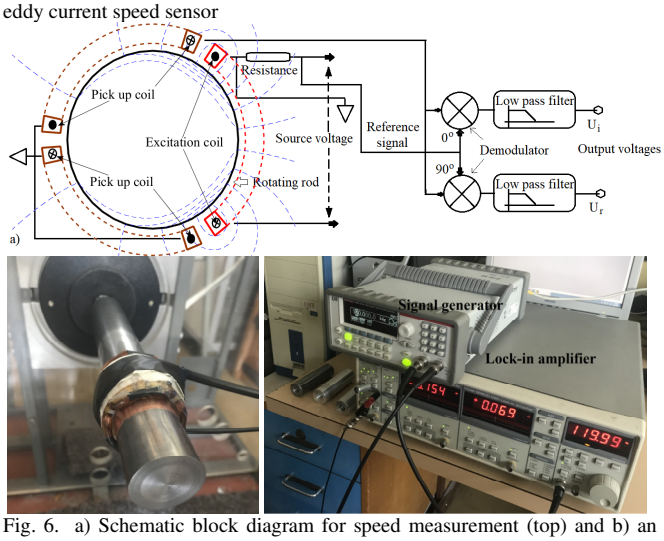

Fig. 6. a) Schematic block diagram for speed measurement (top) and b) an eddy current speed sensor mounted on the rotating solid iron rod and a signal generator and a lock-in amplifier (bottom)

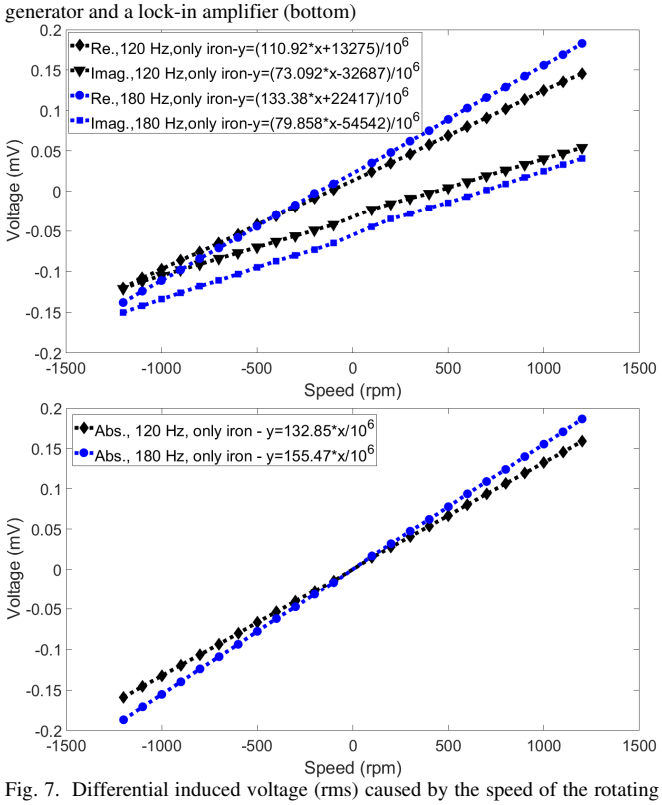

Fig. 7. Differential induced voltage (rms) caused by the speed of the rotating rod for only a solid iron rod, a) for the real and imaginary components of the voltage (top), and b) the absolute value of the voltage (bottom) -experimental results

This article has been accepted for publication in a future issue of this journal, but has not been fully edited. Content may change prior to final publication. Citation information: DOI 10.1109/JSEN.2020.3000442, IEEE Sensors Journal

The offset values are mainly caused by eccentricity, by prime mover or motor vibrations and the slightly asymmetric positions of the pick-up coils with a different magnetic coupling between the excitation coil and the pick-up coils. These offset values can easily be minimized by providing a more precise mechanical set-up. It is shown that the offset values are lower in the real component than in the imaginary component of the induced voltage, as the imaginary component is proportional to the magnetic gap, ($g\pm\Delta g$), and the real component is not roughly proportional to ($g\pm\Delta g$) according to (A8). Any fractional change in magnetic gap Δg can have a greater influence on the imaginary component of the induced voltage. The sensitivity of the eddy current speed sensor is higher for the real component of the induced voltage than for the imaginary component of the induced voltage.

Increasing the excitation frequency from 120 Hz to 180 Hz improves the sensitivity of the eddy current speed sensor by about 17.4% in the only iron rod and by 26.2% in the copper-coated iron rod for absolute values of the induced voltages. The copper coating is 70 μm in thickness and 50 mm in height, see the measured results in Fig. 8. When a copper coating is used for the absolute values of the induced voltages, the sensitivities increase by 59% at 120 Hz, and by 71% at 180 Hz, in comparison with the only iron rod.

The amplitude of current in the excitation coil is 150 mA in all measurements. The influence of the excitation coil reactance on the excitation coil current is negligible because the air coil inductive reactance is small.

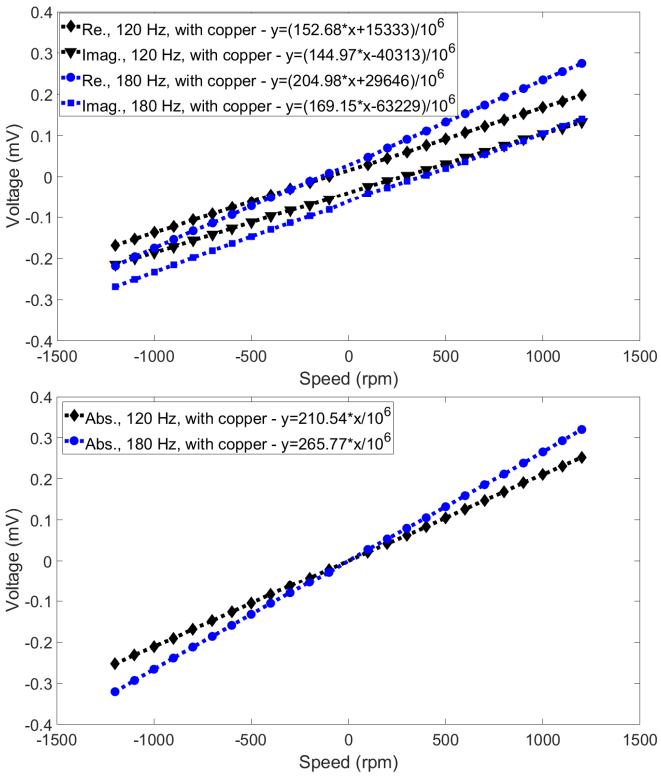

Fig. 8. Differential induced voltage (rms) caused by the speed of the rotating rod for a copper-coated solid iron rod, a) real and imaginary components of the voltage (top), and b) absolute value of the voltage (bottom)) -experimental results

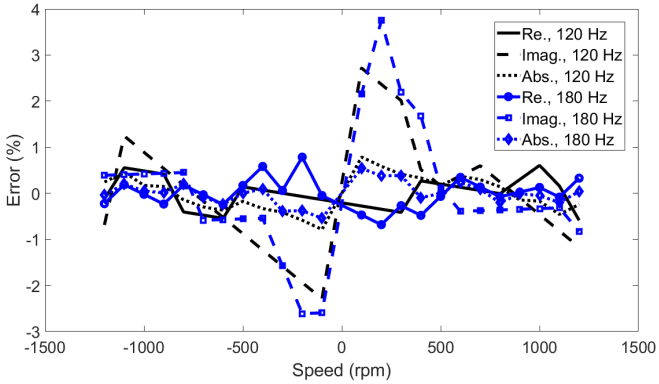

Fig. 9. Measured linearity errors for the only solid iron rod

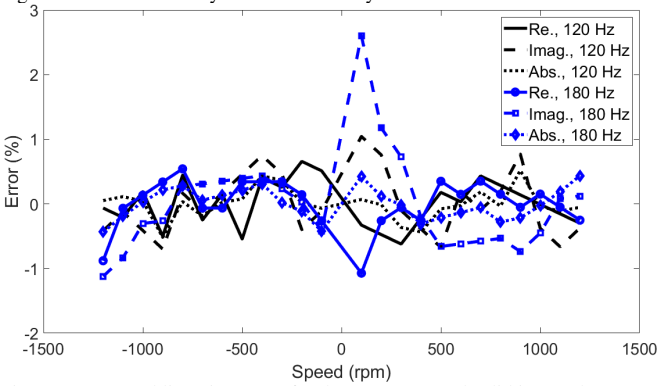

Fig. 10. Measured linearity errors for the copper-coated solid iron rod

The linearity error curves versus speed for different components of the induced voltage are shown in Fig. 9 and Fig. 10, using the linear curve fit parameters in Table I. The maximum error is about 0.5%, except at low speeds for imaginary components of the induced voltage. The peaks in the error curves for the imaginary component are mainly caused by vibration of the motor shaft or by the external resonance effect at low speeds, which can be avoided in a better experimental set-up. Similar reasons as for the higher offset errors can provide an explanation for the higher linearity errors for the imaginary component of the induced voltage, due to higher dependency on the magnetic gap variations and eccentricity.

IV. FEM Analysis

Only linear magnetic modeling using the initial permeability is considered here. Due to the low magnetic fields in the sensor, nonlinearity effects and hysteresis effects are neglected. The first estimate for the relative magnetic permeability of the iron rod is $\mu_{r\text{-}i}$=100, and this value was used in the simulations. The electrical conductivity is measured as σ_i=5.54 MS/m for the iron rod. The eddy current distributions in the half model of the speed sensor are depicted in Fig. 11 using time-stepping 3D FEM. The current amplitude is considered 150 mA in all simulations equal to the measured value.

Tables II and III show a comparison between the 3D FEM results and the experimental results for the only iron rod and for the copper-coated iron rod. The 3D FEM results coincide better with the measurements in the copper-coated

This article has been accepted for publication in a future issue of this journal, but has not been fully edited. Content may change prior to final publication. Citation information: DOI 10.1109/JSEN.2020.3000442, IEEE Sensors Journal

iron rod than with the measurements in the only iron rod. This is because the permeability of the iron rod plays a less important role in the performance of the eddy current speed sensor. Table IV presents the effects of the permeability of the iron rod on the sensitivity of the eddy current speed sensor, confirming that it has a greater influence on the only iron rod. Lower relative magnetic permeability causes higher sensitivity because of the greater magnetic flux penetration depth and greater skin depth.

TABLE II
A COMPARISON BETWEEN MEASUREMENTS AND 3D FEM - ONLY IRON AND WITHOUT A SHIELD

	120 Hz 3D FEM / Exp.	180 Hz 3D FEM / Exp.
300 rpm	34.5 / 40.5 μV	39.8 / 47.4 μV
600 rpm	71.1 / 80.3 μV	80.6 / 93.7 μV
1200 rpm	144.8/159.0μV	169.7 /186.6 μV

The higher electrical conductivity of the iron rod increases the sensor output voltage (Table V).

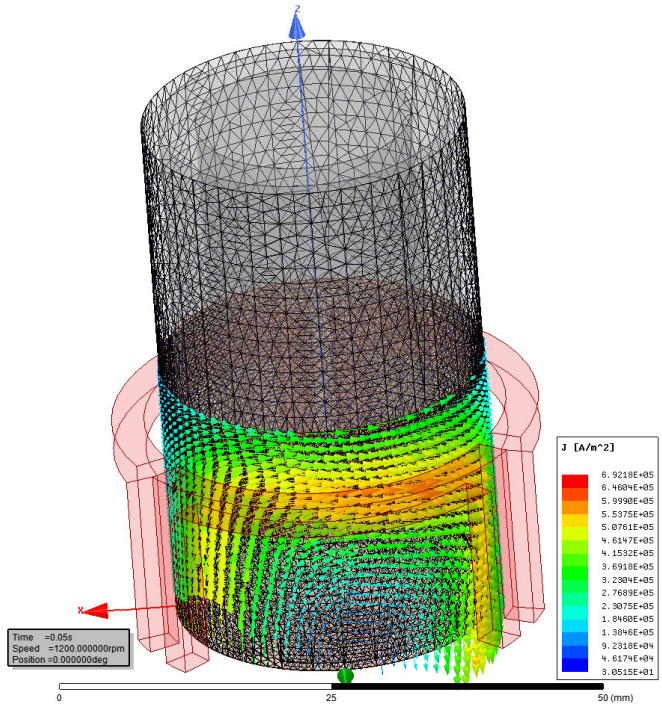

Fig. 11. Eddy current distribution in the copper-coated iron rod at 120 Hz and 1200 rpm

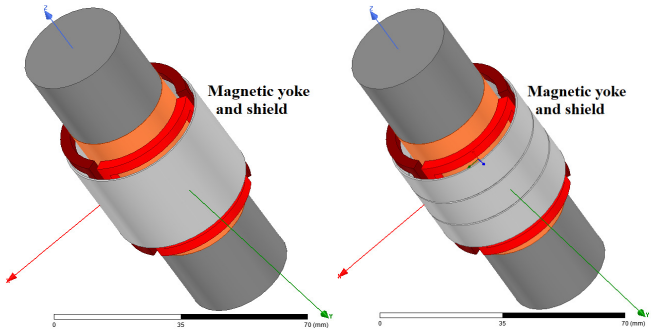

Fig. 12. A magnetic yoke and a shield in the eddy current speed sensor - shield height = 30 mm

TABLE III
A COMPARISON BETWEEN MEASUREMENTS AND 3D FEM - WITH COPPER AND WITHOUT A SHIELD

	120 Hz 3D FEM / Exp.	180 Hz 3D FEM / Exp.
300 rpm	61.5 / 62.2 μV	80.0 / 79.7 μV
600 rpm	126.3 / 126.3 μV	160.5 / 159.0 μV
1200 rpm	255.4 /252.5 μV	324.6 /320.3 μV

TABLE IV
3D FEM - WITHOUT A SHIELD

120 Hz and 1200 rpm	Only Iron	With copper
$\mu_{r\text{-}i}$=75	163.7 μV	271.2 μV
$\mu_{r\text{-}i}$=100	144.8 μV	255.4 μV
$\mu_{r\text{-}i}$=125	131.4 μV	245.2 μV

TABLE V
3D FEM - WITHOUT A SHIELD

120 Hz and 1200 rpm, $\mu_{r\text{-}i}$=100	Only Iron	With copper
σ_i=4.0 MS/m	127.9 μV	244.3 μV
σ_i=5.0 MS/m	139.3 μV	251.9 μV
σ_i=5.54 MS/m	144.8 μV	255.4 μV

A magnetic shield/yoke is used to increase the sensitivity and to shield the sensor from external interference (Fig. 2 b)). A magnetic shield made of high permeability ferromagnetic material such as electrical silicon steel lamination, a permalloy sheet or a Ferrite core [11] surrounds the magnetic sensor. The external field cannot get into magnetic sensor due to the shielding effect. The shield yoke also concentrates and amplifies the working magnetic field of the sensors. Fig. 12 shows the configurations of the magnetic yoke/shields. Tables VI – IX present the results with magnetic shields. The magnetic shield (0.5 mm in thickness with $\mu_{r\text{-}s}$ =1000) increases the sensitivity by about 700% (Table VI).

The variations in the sensitivity of an eddy current speed sensor versus the magnetic permeability of a solid iron rod are lower for sensors with a magnetic shield (Table VIII) than for sensors without a magnetic shield (Table IV). Approaches aimed at compensating and minimizing the effect of the permeability of the iron rod on the performance of the sensor should simultaneously use a thick enough copper coating and a magnetic shield.

The use of high permeability thin permalloy sheets could significantly increase the output of the sensor, as shown in Table IX. The use of a thinner permalloy sheet also helps toward compactness, and toward an easy and cost-effective manufacturing process for the eddy current speed sensor.

TABLE VI
3D FEM - ONLY IRON AND WITH A SHIELD

0.5 mm, $\mu_{r\text{-}s}$ =1000	120 Hz 3D FEM	180 Hz 3D FEM
300 rpm	262.3 μV	293.8 μV
600 rpm	530.3 μV	585.5 μV
1200 rpm	1070.6 μV	1204.9 μV

This article has been accepted for publication in a future issue of this journal, but has not been fully edited. Content may change prior to final publication. Citation information: DOI 10.1109/JSEN.2020.3000442, IEEE Sensors Journal

TABLE VII
3D FEM - WITH COPPER AND WITH A SHIELD

0.5 mm, $\mu_{r\text{-}s}$=1000	120 Hz 3D FEM	180 Hz 3D FEM
300 rpm	435.6 μV	519.4 μV
600 rpm	894.8 μV	1055.6 μV
1200 rpm	1799.2 μV	2135.5 μV

TABLE VIII
3D FEM - WITH A SHIELD

120 Hz and 1200 rpm, $\mu_{r\text{-}s}$=1000	Only Iron	With copper
$\mu_{r\text{-}i}$=75	1171.7 μV	1847.7 μV
$\mu_{r\text{-}i}$=100	1070.6 μV	1799.2 μV
$\mu_{r\text{-}i}$=125	994.6 μV	1760.0 μV

TABLE IX
3D FEM - ONLY IRON AND WITH A SHIELD

Shield thickness and relative permeability	120 Hz 1200 rpm
0.5 mm, $\mu_{r\text{-}s}$=1000	1069.9 μV
0.5 mm, $\mu_{r\text{-}s}$=2000	1251.6 μV
0.1 mm, $\mu_{r\text{-}s}$=10000	1274.6 μV
0.1 mm, $\mu_{r\text{-}s}$=20000	1366.8 μV

V. AN ALUMINUM ROD

Fig. 13 shows the real, imaginary and absolute components of differential voltage versus speed for a rotating aluminum rod. Table X presents the parameters of the linear curve fitting according to (2). The induced voltage is considerably higher in the aluminum rod than in the iron rod because of the greater magnetic flux penetration depth and the greater skin depth [37]. The sensitivity coefficients K in (2) are about 0.5 μV/rpm at 120 Hz and 0.54 μV/rpm at 180 Hz for an aluminum rod, while the sensitivity coefficients for the only iron rod are 0.13 μV/rpm at 120 Hz and 0.16 μV/rpm at 180 Hz. The linearity errors for the only aluminum rod show higher nonlinearity in the imaginary component of the induced voltage, as in the case of the iron rod.

A comparison between the 3D FEM results and the experimental results is presented in Table XI, which depicts higher matching than in the results for the only iron rod. The measured conductivity of the aluminum rod is 21.5 MS/m. The effects of the material properties of the aluminum rod on the eddy current speed sensor are limited to the electrical conductivity, which is easier to compensate than in the case of iron rods with two properties - magnetic permeability and electrical conductivity.

TABLE X
LINEAR CURVE PARAMETERS FITTED TO THE MEASUREMENTS

Case	K (nV/rpm) 120 Hz / 180 Hz	U_{offset} (nV) 120 Hz / 180 Hz
Only aluminum - Re	-496.65 / -403.3	-7333 / -14292
Only aluminum - Im	63.63 / 354.03	108850 / 163040
Only aluminum - Abs	500.72 / 536.65	0

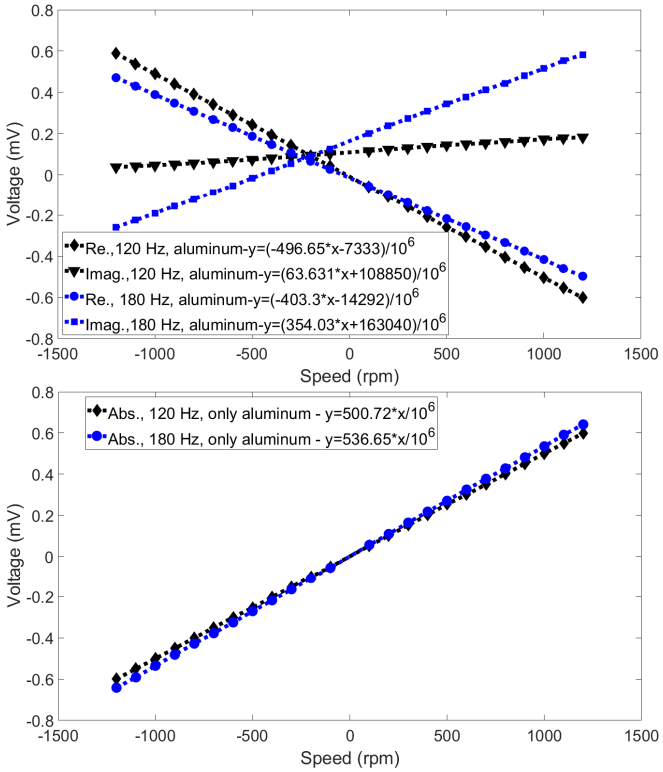

Fig. 13. Differential induced voltage (rms) caused by the rotating rod speed for an only aluminum rod, a) real and imaginary components of the voltage (top) and b) the absolute voltage value (bottom) - experimental results

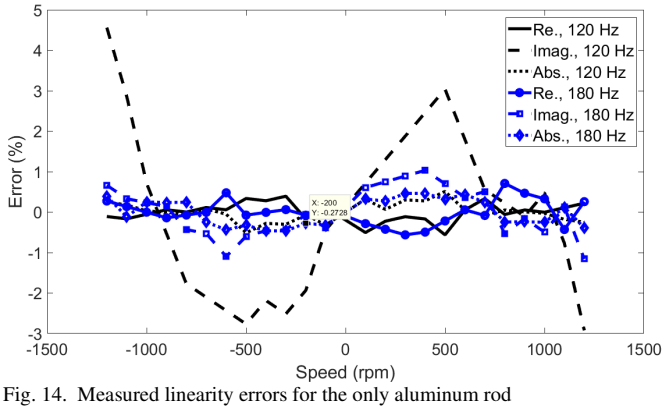

Fig. 14. Measured linearity errors for the only aluminum rod

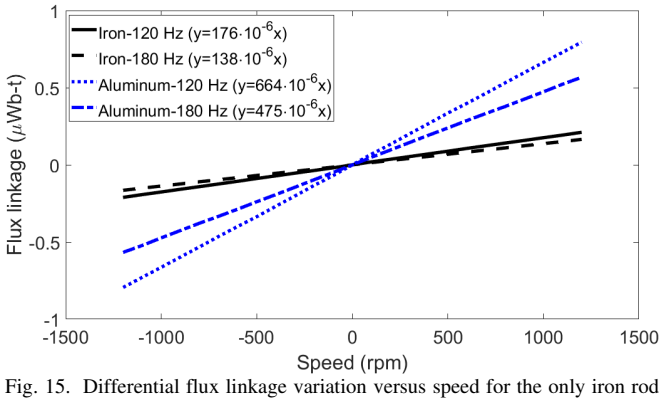

Fig. 15. Differential flux linkage variation versus speed for the only iron rod and for the only aluminum rod

This article has been accepted for publication in a future issue of this journal, but has not been fully edited. Content may change prior to final publication. Citation information: DOI 10.1109/JSEN.2020.3000442, IEEE Sensors Journal

TABLE XI
A COMPARISON BETWEEN MEASUREMENTS AND 3D FEM - ONLY ALUMINUM AND WITHOUT A SHIELD

	120 Hz 3D FEM / EXP.	180 Hz 3D FEM / EXP.
600 rpm	288.0 / 300.7 μV	305.3 / 324.8 μV
1200 rpm	574.9 / 599.4 μV	612.2 / 641.5 μV

VI. DISCUSSION

Compensating the effects of material properties and temperature on the material properties of a conductive rotating rod is a key issue in the final design of an eddy current speed sensor for industrial applications. Recent non-destructive smart methods for estimating electrical conductivity and relative magnetic permeability using multi-frequency and phase signature techniques could be utilized for eddy current speed sensors [38]-[40]. However, this topic lies beyond the scope of this paper. The temperature of rotating rod is a critical factor for the sensor performance, as the electrical conductivity and the magnetic permeability of a rotating rod change with temperature [41]. For example, a 10% decrease in the conductivity of the iron rod causes a 4% reduction in sensor sensitivity (Table V), and a 25% increase in permeability causes a 7% reduction in sensor sensitivity (Table VIII). The self-heating of the coil is negligible, as the power consumption in the excitation coil of the proposed speed sensor is less than 0.2 W.

The eddy current speed sensor proposed in this paper could also be used as a non-destructive method for making azimuthal vibration measurements. Measurements are made of the perpendicular vibrations and movements [42], and this is a convenient method.

The proposed speed sensor theoretically does not have maximum speed constraints. Only the linearity of the eddy current speed sensor could limit the applicable maximum speed range. It is suggested to use a higher operating frequency for higher speed ranges in order to keep the sensor linearity error as low as possible, as shown in Fig. 9 and in Fig. 10 for absolute values of the induced voltage at 120 Hz in comparison with 180 Hz. The minimum measurable speed and sensor sensitivity depends on the rod material, the number of turns and the configuration of the coils, and especially on the sensitivity of the lock-in amplifier that is used. A minimum measurable speed of less than 0.1 rpm can be achieved in the proposed eddy current sensor with the lock-in amplifier used in this paper with minimum sensitivity of 2 nV. The ability to reduce the offset and the ability to reduce the noise are also the most important factors for reducing the minimum measurable speed. Selection of the operating frequency depends on the maximum sensitivity, the minimum linearity error and the fast dynamic response of the speed sensor. The results show that higher excitation frequencies cause higher sensitivity and relatively higher linearity. However, rod surface imperfections can reduce the sensor performance, as the flux concentrates closer to the surface of the rod, and it is more sensitive to non-visible small cracks and defects [23] and non-uniformity surface. A compromise is therefore required when selecting the optimum frequency for a speed range.

It is clear that increasing the excitation frequency decreases the differential flux linkages of pick-up coils due to smaller magnetic flux penetration (Fig. 15). However, the induced differential voltage, and therefore the sensitivity increase with the frequency, as the induced voltage is proportional to the multiple of the flux linkage and the frequency.

A commercial magnetic speed sensor with a tachometer configuration reports a 1% linearity error [43], which is higher than the maximum linearity error of the speed sensor proposed in this paper, which is 0.5%. The maximum achievable resolution is 4.0 rpm.

Modeling and analyzing the eddy current speed sensor forms an important part of this paper, as it helps to analyze its performance and to optimize its parameters. The exact model for analysis should be three-dimensional, because the exact 3D distribution of the induced eddy currents is considered. A numerical method such as 3D FEM [44] is the first option, but it suffers from numerical errors, which are caused by insufficient mesh density, the motion of the rotating rod, and inadequate time steps. Increasing the mesh density and decreasing the time step could be a solution, but the simulation time will increase drastically, especially for a 3D model with eddy current effects in the solid conductive parts. The optimum solution is to develop an analytical model (appendix A). The equations in appendix A are extracted from the Maxwell equations as 3D FEM, but they are simplified for an analytical solution.

The equivalent circuit of antiserially connected pick up coils including the self-capacitance and the capacitance between the coil and the ground and the conductive rod are shown in Fig. 16. Equation (3) presents the relationship between the internal induced voltage and the output voltage of the pick-up coil. The output voltage is equal to the internal voltage, because the capacitive reactance is much higher than the resistance and the inductive reactance at low frequencies, 120 Hz and 180 Hz, as shown in (3). The output voltage could be distorted at the resonance frequency, which is much higher than the level of 180 Hz used in this paper. For the case of our 100-turns pick up coils, the measured resistance, R= 15.4 Ω, the inductance L= 1.545 mH and the self-capacitance, C_c= 30.5 pF, the resonance frequency can be calculated equal to $f_r = 1/2\pi/\sqrt{LC_c} = 733$ kHz.

$$U_o = \frac{1}{j(C_c + C_e/2)\omega} \Big/ \left(R + j\omega L + \frac{1}{j(C_c + C_e/2)\omega}\right) U_i \approx U_i \ , \omega = 2\pi f \quad (3)$$

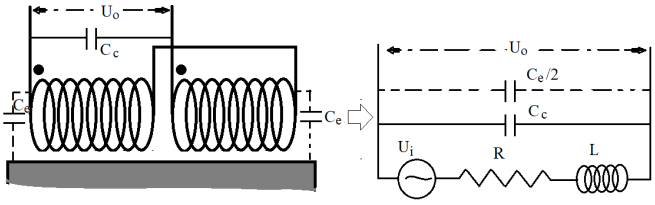

Fig. 16. A schematic model of pick-up coils with self-capacitance and capacitance between coil and ground and rod, and its equivalent circuit

However, if we increase the number of turns of this coil in an attempt to increase the sensitivity, the resonant frequency can be much lower. The capacitance between coils and rod and ground, C_e /2 is not considered for simplicity (Fig. 16).

A current-to-voltage converter could be used if the resonance frequency is close to the operating frequency of the eddy current speed sensor to avoid the effects of resonance on the performance of the sensor [45].

VII. Conclusion

An eddy current sensor with a new structure for measuring the speed of a rotating rod has been presented. Various rotating rods with an only iron rod, with a copper-coated iron rod, and with an only aluminum rod have been considered in the measurements and in the analysis. The optimum angle of the coil span was obtained, i.e. 120 deg., which is identical for an excitation coil and for pick-up coils. The tested eddy current speed sensor was manufactured with the optimum coil span angle.

The presented eddy current speed sensor is an appropriate selection for speed measurements of any type of rotating machines, for example, turbines, motors, pumps, fans and turbochargers. For example, it is appropriate for speed measurements for compact rotating electric devices in electric vehicles with limited space and weight for the powertrain, as the proposed eddy current speed sensor can be integrated with a rotating device and mounted on the shaft. This is an advantage of the sensor, which, unlike the conventional speed sensor, does not need additional space in the end shaft space.

Operating an eddy current speed sensor at higher frequencies is an efficient method for obtaining greater sensitivity. However, the skin depth is smaller at high frequency. Surface cracks and defects and corrosion on the conductive rod could have a greater effect on the performance of eddy current speed sensors at high frequencies, if the radial thickness of the cracks or the corrosion depth is considerable in comparison with the magnetic flux penetration depth. Even a small crack on the conductive rotating rod could cause an accuracy error and noise in the speed sensor output, as an eddy current speed sensor is sensitive to the smoothness of the surface of the rotating rod. The use of a copper coating can minimize the effect of cracks in the solid rotating rod.

A simplified 1D analytical method has been developed for a general analysis of the eddy current speed sensor and for optimizing the sensor. An analytical method is used to facilitate rapid analysis and rapid parametric calculations. The method is effective in terms of providing an analytical understanding of the performance of the eddy current speed sensor. 3D time stepping FEM, taking into account the rotating speed, was utilized for a detailed analysis and for further optimizations, including the effects of a magnetic yoke and a shield on the performance of the eddy current speed sensor.

It has been shown that a magnetic yoke has a big influence on the sensitivity of the eddy current speed sensor. The use of a magnetic yoke can affect the linearity of the sensor. In addition, the magnetic properties of the yoke materials can be altered by ageing and by external fields. This is a drawback that should be taken into account in the design of the sensor.

The linearity error is lower, the sensitivity is considerably higher, and the offset is lower for the real component of the induced voltage than for the imaginary component. The calculations indicate that the real component is also less sensitive to variations of the airgap. Using the experimental set-up presented in this paper, we evaluated the linear error and made a comparison between the real and imaginary components of the induced voltage. The linearity error is about 0.5% and less, and this can be reduced by adjusting the experimental set-up to avoid shaft vibrations of the prime mover.

A copper coating or any non-magnetic conductive coating is an effective method for increasing the sensitivity and for reducing the effect of the magnetic permeability of solid iron. Selecting the optimum thickness of the non-magnetic conductive coating can drastically reduce the effect of the magnetic permeability of solid iron.

The real component of the induced voltage is more linear than the imaginary component of the induced voltage. It has also been shown that the real component of the induced voltage is less sensitive to eccentricity and to vibrations, as it is caused by induced eddy current losses in the solid conductive rod.

Planned future work will be on compensating the temperature dependencies of the rotating rid and yoke properties, and on variations of the airgap.

Acknowledgment

The authors thank Mr. J. Cerny and Dr. J. Vyhnanek, from the Department of Measurement, Faculty of Electrical Engineering of the Czech Technical University, for their support in building the rotational eddy current speed sensor components and in preparing the measurement elements.

Appendix A

A 1D simplified computational model is presented to justify the performance of the rotating eddy current speed sensor. Fig. A1 (a) shows the 1D computational model. For the sake of simplicity, only the magnetic fields in the air gap and the conductive non-magnetic coating are considered here. Therefore, the following assumptions are made:

1) It is assumed that the coils are shielded by a non-conductive (or laminated) magnetic material with infinite magnetic permeability.

2) The magnetic core of the rotor has the same properties as the magnetic shield.

3) Only the radial component of the magnetic flux density is considered in the modeling and in the simulations.

4) Only azimuthal variations ($\partial\theta$) of the fields are considered, and radial variations (∂r) are set to zero.

5) Only the axial component of the induced eddy current (the z-axis) in the conductive coating is considered.

This article has been accepted for publication in a future issue of this journal, but has not been fully edited. Content may change prior to final publication. Citation information: DOI 10.1109/JSEN.2020.3000442, IEEE Sensors Journal

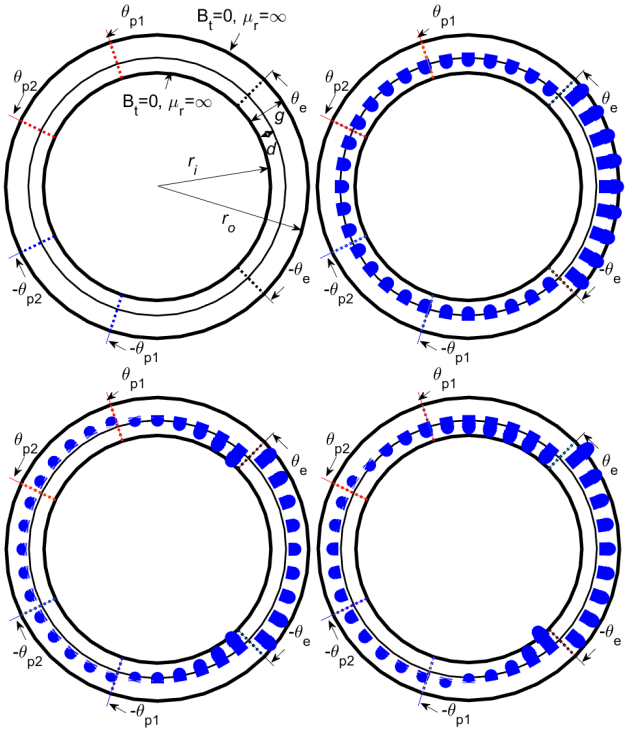

Fig. A1. a) 2D computational model (top-left), b) magnetic flux distribution for DC and zero speed (top-right), c) magnetic flux distribution for AC (100 Hz) and zero speed (bottom-left), d) magnetic flux distribution for AC (100 Hz) and nonzero speed (bottom-right),

6) The source coils are modeled by two current sheets with infinitesimal thickness at angles of $-\theta_e$ and $+\theta_e$ (Fig. A1).

7) Two pick-up coils are positioned at angles of $+\theta_{p1}$ and $+\theta_{p2}$ for pick-up coil 1 and at angles of $-\theta_{p1}$ and $-\theta_{p2}$ for pick-up coil 2.

The equations in (A1) can be derived using Ampere's law and Ohm's law, respectively [46]-[47]:

$$g\frac{\partial B_r}{\partial \theta} = -\mu_0 \cdot J_z \cdot d \cdot r_d, \qquad r_d = r_i + \frac{d}{2}, \qquad g = r_o - r_i$$
$$\frac{1}{r_d}\frac{\partial J_z}{\partial \theta} = -\sigma\left(\frac{\partial B_r}{\partial t} + \omega_r \frac{\partial B_r}{\partial \theta}\right), \quad \omega_r = 2\pi\frac{n_r}{60} \tag{A1}$$

where, B_r, is the radial component of the flux density, J_z is the axial component of the induced eddy current in the conductive coating, d is the radial thickness of the conductive coating, r_i is the inner radius of the conductive coating, r_o is the outer radius of the airgap region, n_r is the rotational speed of the rotating part in rpm, and f is the electrical frequency.

The induced eddy current has two components. The first term, $\partial B_r/\partial t$ and the second term, $\omega_r \cdot \partial B_r/\partial \theta$ on the right side of the equality in (A1) are the transformer component caused by the time variation of the source field and the motional (speed) component, respectively [48]. The speed component of the induced eddy current is linearly proportional to the speed. Equation (A2) is extracted by substituting the first differential term in the second differential term of (A1):

$$\frac{\partial^2 B_r}{\partial \theta^2} - \omega_r \frac{d}{g}\mu_0 \sigma r_d^2 \frac{\partial B_r}{\partial \theta} - j\omega \frac{d}{g}\mu_0 \sigma r_d^2 B_r = 0, \frac{\partial}{\partial t} = j\omega,$$
$$\omega = 2\pi f \tag{A2}$$

The magnetic flux density has two components, $B_r = B_{r,s} + B_{r,r}$:

1) The source field caused by the source current sheets at angles of $-\theta_e$ and $+\theta_e$: $B_{r,s}$

2) The reaction field caused by the induced eddy current in the conductive coating: $B_{r,r}$

The source magnetic field, $B_{r,s}$ can be written using Ampere's law and Gauss's law:

$$B_{r,s,1} = \frac{\pi - \theta_e}{\pi} N_e I_s \frac{\mu_0}{g}, -\theta_e \le \theta \le \theta_e$$
$$B_{r,s,2} = \frac{-\theta_e}{\pi} N_e I_s \frac{\mu_0}{g}, \theta \le -\theta_e, \theta \ge \theta_e \tag{A3}$$

The Fourier series method is used to solve (A2) [35]-[37] and [49]. The source can therefore be written in Fourier series format in (A4), using (A3):

$$B_{r,s} = \sum_{n=\pm1,\pm2,\cdots} C_n e^{j(\omega t - n\theta)}$$
$$C_n = \frac{1}{n\pi}\left(B_{r,s,1} - B_{r,s,2}\right)\sin(n\theta_e) \tag{A4}$$

Now the solution of (A2) is calculated as follows for the reaction field component of the magnetic flux density, $B_{r,r}$:

$$B_{r,r} = \sum_{n=\pm1,\pm2,\cdots} C_n C_n' e^{j(\omega t - n\theta)}$$
$$C_n' = -jC_{n-1}' / (n^2 + jC_{n-1}'), \quad C_{n-1}' = \omega \frac{d}{g}\mu_0 \sigma r_d^2 - n\omega_r \frac{d}{g}\mu_0 \sigma r_d^2, \tag{A5}$$

The flux linkage, λ and the induced voltage, U of the pick-up coils on the left side and on the right side of the excitation coil are as follows:

$$\lambda_l = N_p r_m \sum_{n=\pm1,\pm2,\cdots} \frac{C_n(1 + C_n')}{-jn}\left(e^{-jn\theta_{p2}} - e^{-jn\theta_{p1}}\right)e^{j(\omega t)}$$
$$\lambda_r = N_p r_m \sum_{n=\pm1,\pm2,\cdots} \frac{C_n(1 + C_n')}{-jn}\left(e^{jn\theta_{p1}} - e^{jn\theta_{p2}}\right)e^{j(\omega t)}$$
$$U_l = -\frac{\partial \lambda_l}{\partial t} = -j\omega\lambda_l, \; U_r = -\frac{\partial \lambda_r}{\partial t} = -j\omega\lambda_r, \quad r_m = \frac{r_o + r_i}{2} \tag{A6}$$

The flux linkage difference, λ_d, and the voltage difference, U_d,, between the left pick-up coil and the right pick-up coil are calculated:

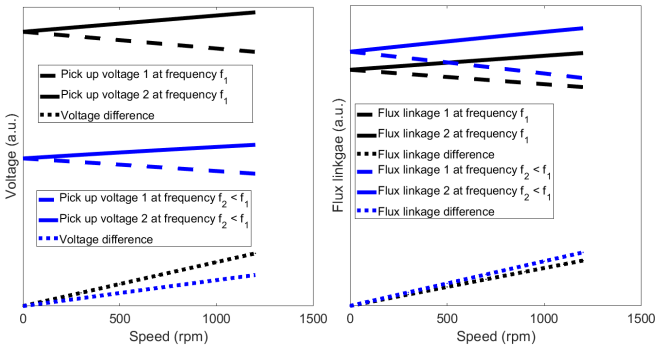

Fig. A2. a) Pick-up coil voltages and their voltage difference versus rotating rod speed (left) b) flux linkage variations versus rotating rod speed (right)

$$\lambda_d = \lambda_l\text{-}\lambda_r = N_p r_m \sum_{n=\pm1,\pm2,\cdots} \frac{2C_n C_n'}{-jn}\left(\cos\left(n\theta_{p2}\right) - \cos\left(n\theta_{p1}\right)\right) e^{j(\omega t)} \quad \text{(A7)}$$

$$U_d = -\frac{\partial \lambda_d}{\partial t} = -j\omega\lambda_d = (\, U_{d-r} + j\, U_{d-i}) e^{j(\omega t)}$$

$$U_{d-r} = -\omega N_p r_m \sum_{n=\pm1,\pm2,\cdots} \frac{2C_n C_{n-1}'^2}{n} \frac{\left(cos\left(n\theta_{p2}\right) - cos\left(n\theta_{p1}\right)\right)}{n^4 + C_{n-1}'^2}$$

$$U_{d-i} = -\omega N_p r_m \sum_{n=\pm1,\pm2,\cdots} n^2 \frac{2C_n C_{n-1}'}{n} \frac{\left(cos\left(n\theta_{p2}\right) - cos\left(n\theta_{p1}\right)\right)}{n^4 + C_{n-1}'^2} \quad \text{(A8)}$$

The voltage difference equation in (A8) depends on the angles of θ_{p1} and θ_{p2}, which could show the effect of the misalignments of the pick-up coils on the performance of the sensor. For example, any difference in the pick up coils span and relative position of them to the excitation coil could cause offset errors because mutual flux linkages between excitation coil and pick up coils become non-identical at zero speed. Also, the gap between the rotating rod and the coils, g, has a considerable effect on the performance of the sensor, as it affects the source field in (A3) and the reaction fields in (A5).

Fig. A1 b), c) and d) shows the magnetic flux density distribution in vector form for different electric sources (DC and AC) and for different speeds. It is obvious that the speed effect causes the flux linkages in the pick-up coil on the left side and the pick-up coil on the right side to diverge from each other. The voltages and the flux linkages of the two pick-up coils diverge from each other, and the difference in their voltage and flux linkage increases as the speed increases (Fig. A2). The flux linkage decreases with increasing frequency, because the reaction fields of the transformer component of the induced eddy current are stronger at higher frequencies.

REFERENCES

[1] M. Novak and J. Novak, "Test setup with a permanent magnet synchronous machine for efficiency maps of an electric vehicle," *XIII Int. Conf. on Elec. Machines (ICEM)*, pp. 1698-1703, 2018

[2] H. Chen, W. Yan, J. J. Gu , and M. Su, "Multiobjective optimization design of a switched reluctance motor for low-speed electric vehicles with a Taguchi–CSO algorithm," *IEEE/ASME Trans. Mechatronics*, vol. 23, no. 4, pp. 1762-1774, August 2018

[3] M.-S. Lim, J.-M. Kim, Y.-S. Hwang, and J.-P. Hong, "Design of an ultra-high-speed permanent-magnet motor for an electric turbocharger considering speed response characteristics," *IEEE/ASME Trans. Mechatronics*, vol. 22, no. 2, pp. 774–784, Apr. 2017.

[4] Y. J. Oh, H.-C. Liu, S. Cho, J. H. Won, H. Lee, and Ju Lee, "Design, modeling, and analysis of a railway traction motor with independently rotating wheelsets," *IEEE Trans. Magn.*, vol. 54, no. 11, 8205305, November 2018

[5] D.-K. Hong, T.-W. Lee, and Y.-H. Jeong, "Design and experimental validation of a high-speed electric turbocharger motor considering variation of the L/D ratio," *IEEE Trans. Magn.* ,vol. 54, no. 11, 2801904, November 2018

[6] S.S. Kalsi, J.G. Storey, K.A. Hamilton, R.A. Badcock, "Propulsion motor concepts for airplane,"*2019 AIAA/IEEE Electric Aircraft Technologies Symposium (EATS)*, 2019

[7] Y. Terao, A. Seta, H. Ohsaki, H. Oyori, and N. Moriok, "Lightweight design of fully superconducting motors for electrical aircraft propulsion systems," *IEEE Trans. on Applied Superconductivity*, vol. 29, no. 5, 5202305, August 2019

[8] S. S. Kalsi, "Superconducting wind turbine generator employing MgB2 windings both on rotor and stator," *IEEE Trans. on Applied Superconductivity*, vol. 24, no. 1, 5201907, February 2014

[9] X. Wu, S. Huang, K. Liu, K. Lu, Y. Hu , W. Pan, and X. Peng, "Enhanced position sensorless control using bilinear recursive least squares adaptive filter for interior permanent magnet synchronous motor," *IEEE Trans. on Power Electronics*, vol. 35, no. 1, pp. 681-698,January 2020

[10] Z. Xu, T. Zhang, Y. Bao, H. Zhang, and C. Gerada, "A nonlinear extended state observer for rotor position and speed estimation for sensorless IPMSM drives," *IEEE Trans. on Power Electronics*, vol. 35, no. 1, pp. 733-743,January 2020

[11] P. Ripka, *Magnetic Sensors and Magnetometers*, Artech House, Jan. 1,2001

[12] X. Liu, C. Liu, and P. W. T. Pong, "Velocity measurement technique for permanent magnet synchronous motors through external stray magnetic field sensing," *IEEE Sensors J.*, vol. 18, no. 10, pp. 4013-4021, May 15, 2018

[13] G. Liu, B. Chen, and X. Song, "High-precision speed and position estimation based on Hall vector frequency tracking for PMSM with bipolar Hall-effect sensors," *IEEE Sensors J.*, vol. 19, no. 6, pp.2347-2355, March 15, 2019

[14] V. Petrucha and P. Ripka, "Rotational speed measurement and angular position reference for a cryogenic propellant electric pump," *J. of Elec. Eng.*, vol. 66, no. 7/s, pp. 199-202, 2015

[15] J. Rickman, "Eddy current turbocharger blade speed detection," *IEEE Trans. Magn.*, vol. MAG-18, no. 5, pp. 1014–1021, Sep. 1982

[16] T. Addabbo, M. Di Marco, A. Fort, E. Landi, M. Mugnaini, V. Vignoli, and G. Ferretti, "Instantaneous rotation speed measurement system based on variable reluctance sensors for torsional vibration monitoring," *IEEE Trans. Instrum. Meas.*, vol. 68, no. 7, pp. 2363-2373, July 2019

[17] J. O. Manyala, T. Fritz, and M. Z. Atashbar, "Gearbox speed sensor design and performance optimization," *IEEE Sensors J.*, vol. 13, no. 2, pp. 629-636, February 2013

[18] W. Li, Z. Hua, W. Qian, L. Jianxuan, T. Jian, "Some considerations of eddy current proximity sensor applied for motor speed measurement," *Int. Conf. on Elec. Machines and Systems*, 2008

[19] L. Li, H. Hu, Y. Qin, and K. Tang, "Digital approach to rotational speed measurement using an electrostatic sensor," *Sensors (Basel)*, vol. 19, no. 11, 2540, 2019

[20] C. Wu, C. Fan and G. Wen, "Self-powered speed sensor for turbo drills based on triboelectric nanogenerator," *Sensors*, vol. 19, no. 22, 4889, 2019

[21] D. Gonen, S. Stricker, "Analysis of an eddy-current brake," *IEEE Trans. on Power App.& Syst.*, vol. 84, no. 5, pp. 357-361, 1965

[22] S. Cho, H.-C. Liu, H. Ahn, J. Lee, and H.-W. Lee, "Eddy current brake with a two-layer structure: calculation and characterization of braking performance," *IEEE Trans. on Mag.*, vol. 53, no. 11, 8110205, November 2017

[23] T. J. Rocha, H. G. Ramos, A. L. Ribeiro, and D. J. Pasadas, "Evaluation of subsurface defects using diffusion of motion-induced eddy currents," *IEEE Trans. Instrum.* Meas., vol. 65, no. 5, pp. 1182–1187, May 2016

[24] T. Itaya, K. Ishida, A. Tanaka, N. Takehira, and T. Miki, "Analysis of a fork-shaped rectangular coil oriented perpendicular to moving conductor slabs," *NDT&E International*, 44, 413–420, 2011
[25] J.A. Shercliff, *The Theory of Electromagnetic Flow Measurement*, Cambridge University Press, 1962.
[26] T. Sonoda, R. Ueda, K. Fujitani, T. Irisa, and S. Tatata, "DC magnetic field type eddy current speed sensor detecting cross magnetization field with amorphous core," *IEEE Trans. Magn.*, vol. MAG-21, no. 5, pp. 1732–1734, Sep. 1985
[27] C. Gong, A. Tuysuz, M. Flankl, T. Stolz, J. Kolar, T. Habetler, "Experimental analysis and optimization of a contactless eddy-current-based speed sensor for smooth conductive surfaces," *IEEE Trans. on Industrial Electronics*, Early Access, 2019
[28] E. Cardelli, A. Faba, and F. Tissi, "Contact-less speed probe based on eddy currents," *IEEE Trans. Magn.*, vol. 49, no. 7, pp. 3897–3900, Jul. 2013.
[29] N. Takehira, and A. Tanaka, "Analysis of a perpendicular-type eddy-current speed meter," *IEE Proc. A – Phys. Science, Meas. and Instr., Manag. and Educ.- Rev.* , vol. 135 ,no. 2, pp. 89 - 94, Feb. 1988
[30] T. Itaya, K. Ishida, A. Tanaka, N. Takehira, and T. Miki, "Eddy current distribution for a rectangular coil arranged parallel to a moving conductor slab," *IET Science, Meas. & Tech.*, vol. 6, no. 2, pp. 43 - 51, Mar. 2012
[31] T. Itaya, K. Ishida, A. Tanaka, and N. Takehira, "Analysis of a fork-shaped rectangular coil facing moving sheet conductors," *IET Science, Meas. & Tech.* , vol. 3 , no. 4, pp. 279 - 285, Jul. 2009
[32] T. Itaya, K. Ishida, Y. Kubota, A. Tanaka, and N. Takehira, "Visualization of eddy current distributions for arbitrarily shaped coils parallel to a moving conductor slab," *Prog. In Electromag. Research M*, Vol. 47, 1–12, 2016
[33] T. Itaya, K. Ishida, A. Tanaka, and N. Takehira, "Analysis of an eddy current speed meter by rectangular coil system," *IEEJ Trans. on Fund. and Mat.* 133(8),416-423 , January 2013
[34] A. Tuysuz, M. Flankl, J. W. Kolar, and A. Mutze, "Eddy-current-based contactless speed sensing of conductive surfaces," *IEEE 2nd Annual Southern Power Electronics Conf. (SPEC)*, pp. 1 - 6, Dec. 2016
[35] M. Mirzaei, P. Ripka, A. Chirtsov, and J. Vyhnanek, "Eddy current linear speed sensor," *IEEE Trans. Mag.*, vol. 55 , no. 1 , pp. 1-4, 2019
[36] M. Mirzaei, P. Ripka, J. Vyhnanek, A. Chirtsov and V. Grim, "Rotational eddy current speed sensor," *IEEE Trans. Mag.*, vol. 55, no. 9, 4003710, September 2019
[37] M. Mirzaei, P. Ripka, A. Chirtsov, J. Vyhnanek, and V. Grim, "Design and modeling of a linear speed sensor with a flat type structure and air coils," *J. of Magnetism and Magnetic Materials*, vol. 495, 165834, 2020
[38] M. Lu, Y. Xie, W. Zhu, A. Peyton, W. Yin, "Determination of the magnetic permeability, electrical conductivity, and thickness of ferrite metallic plates using a multifrequency electromagnetic sensing system," *IEEE Trans. Ind. Inf.*, vol. 15, no. 7, pp. 4111-4119, 2019
[39] W. Yin, J. Tang, M. Lu, H. Xu, R. Huang, Q. Zhao, Z. Zhang, and A. Peyton, "An equivalent-effect phenomenon in eddy current non-destructive testing of thin structures," *IEEE Access*, vol. 7, pp. 70296-70307, 2019
[40] M. Lu, R. Huang, W. Yin, Q. Zhao, and A. Peyton, "Measurement of permeability for ferrous metallic plates using a novel lift-off compensation technique on phase signature," *IEEE Sensors J.*, vol. 19, no. 17, pp. 7440-7446, 2019
[41] M. Mirzaei, P. Ripka, A. Chirtsov, and V. Grim, "Temperature stability of the transformer position transducer for pneumatic cylinder," *J. of Magnetism and Magnetic Materials*, vol. 503, 166636, 2020
[42] X. Xue, Y. Dong, and X. Wu, "Motion induced eddy current sensor for non-intrusive vibration measurement," *IEEE Sensors J.*, vol. 20, no. 2, pp. 735-744 ,2020
[43] Handheld tachometer, contact type, https://www.onosokki.co.jp/English/hp_e/whats_new/Catalog/PDF/digital_tachometers.pdf
[44] K.J.Binns, P. J.Lawrenson, and C. W.Trowbridge, *The Analytical and Numerical Solution of Electric and Magnetic Fields*. Wiley-Blackwell, 1992
[45] P. Kaspar, P. Ripka, "Induction Coils: voltage versus current output," Imeko World Congress, vol. 5, pp. 55-60. 2000
[46] S. A. Nasar, and I. Boldea, *Linear Motion Electric Machines*, John Wiley & Sons Inc; 1st Printing edition, August 1976
[47] C. H. Lee, C. Y. Chin, "A theoretical analysis of linear induction motors," *IEEE Trans. Power App. &Syst.*, vol. 98, no. 2, pp. 679-688, Mar. 1979
[48] P. Hammond, *Applied Electromagnetism*, Pergamon Press Ltd., Headington Hill Hall, Oxford, 1971
[49] M. N. O. Sadiku, *Numerical Techniques in Electromagnetics with MATLAB*, 2nd ed. Boca Raton, FL, USA: CRC Press, 2000.

4- Conclusions

Magnetic materials modeling and their effects in position sensors and eddy current speed sensors applications were presented in this thesis. All goals mentioned in the Chap. 2 of Thesis Objectives were successfully fulfilled. Results of individual tasks follow:

A novel approach for analytical modeling of magnetization curves using combined rational and power functions was presented, which shows high precision for *B-H* curves modeling of high permeability materials as well as other types of soft magnetic materials. It was presented that the proposed combined rational and power functions can model DC magnetization curves with minimum number of unknown parameters, which could be easily calculated using curve fitting. Hysteresis loops were also modeled using combined rational and power functions with applying a phase shift between magnetic flux density, *B,* and magnetic field strength, *H*, which presents excellent coincidence with measurements. The developed model was used and verified for different soft magnetic materials, which are used for sensor and magnetic measurements applications. The main advantages of proposed function for hysteresis loops modeling are simplicity, fast calculations of parameters in the proposed function and adequate precision. Therefore this function is very powerful and convenient tool for use in FEM analysis packages. (see 3-1)

Impedance analysis of solid iron conductors with different shapes was presented, which analysis results using FEM and analytical method were compared with measurements at low and high frequencies. The behavior of solid iron conductors was studied at different currents and frequencies. The effects of magnetic characteristics and electrical conductivity of solid irons and steels used for solid conductors and rails were evaluated in the wide frequency range. (see 3-2-1)

Two types of position sensors for the pneumatic cylinders were presented, and their magnetic materials effects were evaluated. The first type of position sensor for the pneumatic cylinders uses axisymmetric coils around an aluminum cylinder, which inductance and pick up voltage is sensitive to the piston and iron rod position. The second type of position sensor for pneumatic cylinders uses a conical iron rod instead of a cylindrical iron rod, which inductance and the pick up voltage of axisymmetric coils wound around conical iron rod are sensitive to conical iron movement. A flat type position sensor with LVDT configuration was also introduced and designed with different magnetic materials for the armature. A finite-difference model with taking into account materials effects was developed for design and analysis of this sensor. Also analytical models and 2D and 3D finite element method were utilized for detailed performance analysis of the positions sensors. Different soft magnetic materials such as solid irons and silicon steel laminations were used in the position sensor for pneumatic cylinder and flat type position sensor (see 3-2-2)

Translational and rotational eddy current speed sensors were designed and investigated by taking into account the material effects of the moving part. 2D and 3D developed analytical methods and FEM were utilized for optimization and material effects analysis of eddy current speed sensors. Excellent linearity for the proposed eddy current speed sensors was depicted. The presented eddy current speed sensors were considered with an air core and iron core or magnetic yoke and shielding. One excitation coil and two differentially connected pick-up coils were used in the presented eddy current speed sensors in this thesis. Translational or linear eddy current speed sensors with flat and axisymmetric configurations were both evaluated in this thesis. Transient and steady-state performance analysis of eddy current speed sensors was investigated and an analytical formula was extracted to model the transient operation. The materials effects

were clearly investigated in the developed 2D and 3D analytical models as well as 2D and 3D time stepping FEM with taking into account moving part motion. We found that the behavior of eddy current speed sensors with magnetic iron moving part is completely different from sensors using nonmagnetic aluminum moving part. A novel configuration of moving part for rotation speed sensor was proposed in this thesis with double layer structure using nonmagnetic aluminum or copper shell, which improves sensitivity of eddy current speed sensor. (see 3-2-3)

4-1 Specification of My Own Contribution to The Published Papers

I was the main author for publications J1, J3-J5, J7-J13, C1-C3 and S1-S2 in section 6. These papers are based on my ideas and I wrote the first version of the paper. I also made all simulations and analytical calculations.

For the rest of the papers I was co-author. I contributed with FEM analysis and analytical modeling and I also participated in the writing of the paper.

4-2 Future Works

Precise measurements of magnetization curves and hysteresis loops of different types of high permeability magnetic materials and also different solid irons could be planned for future works, which to be used for theoretical modeling and analysis of magnetic sensors and magnetic measurements. Measuring DC magnetization curves and hysteresis loops at low fields will be useful to evaluate the effects of magnetic characteristics of used soft magnetic materials on the performance of position sensors and eddy current speed sensors, which are operated at low fields.

Replacement of pick up coils with AMR and Fluxgate magnetic sensors could be considered as future plans to evaluate different measurements systems for the position sensors and eddy current speed sensors. Also using AMR and Fluxgate magnetic sensors allow us to evaluate the performance of position sensors and eddy current speed sensors with DC excitation and to compare their performance when they are operated with AC excitations.

5- References

[1] C. W. Chen, *Magnetism And Metallurgy Of Soft Magnetic Materials*, North Holland , 1st January 1977

[2] P. Ripka, *Magnetic Sensors and Magnetometers*, Artech House, Jan 1, 2001 - Technology & Engineering - 494 pages

[3] S. Tumanski, *Handbook of Magnetic Measurements*, June 23, 2011 by CRC Press Reference - 404 Pages

[4] F. C. Trutt, E. A. Erdélyi, and R. E. Hopkins, "Representation of the magnetization characteristic of dc machines for computer use," *IEEE Trans. Power App. Syst.*, vol. 87, no. 3, pp. 665–669, Mar. 1968

[5] G. F. T. Widger, "Representation of magnetization curves over extensive range by rational-fraction approximations," *Proc. Inst. Elect. Eng.*, vol. 116, no. 1, pp. 156–160, Jan. 1969

[6] J. Rivas, J. M. Zamarro, E. Martín, and C. Pereira, "Simple approximation for magnetization curves and hysteresis loops," *IEEE Trans. Magn.*, vol. 17, no. 4, pp. 1498–1502, Jul. 1981.

[7] Patrick Diez and J. P. Webb, "A Rational approach to B–H curve representation," *IEEE Trans. on Magn.*, vol. 52, no. 3, 2016

[8] M. K. El-Sherbiny, "Representation of the magnetization characteristic by a sum of exponentials," *IEEE Trans. Magn.*, vol. MAG-9, no. 1, pp. 60-61, Mar. 1973.

[9] W. K. Macfadyen, R. R. S. Simpson, R. D. Slater, W. S. Wood, "Representation of magnetization curves by exponential series", *Proc. IEE*, vol. 120, no. 8, pp. 902-904, 1973.

[10] J. R. Brauer, "Simple equations for the magnetization and reluctivity curves of steel," *IEEE Trans. Magn.*, vol. 11, no. 1, pp. 81, Jan. 1975

[11] P. Diez, "Symmetric Invertible B–H Curves Using Piecewise Linear Rationals," *IEEE Trans. on Magn.*, vol. 53, no. 6, 2017

[12] L. R. Nejman, *Skin effect in ferromagnetic bodies*, GEI, Moscow-Leningrad, 1949

[13] J. Lammeraner, and M. Stafl, *Eddy Currents*, Published by Iliffe, 1967

[14] S. A. Nasar, G. Y. Xiong, Z. X. Fu, "Eddy-current losses in a tubular linear induction motor," *IEEE Trans. on Magn.*, vol. 30, no. 4, pp. 1437 – 1445, 1994

[15] D.C. Jiles, D.L. Atherton, "Theory of ferromagnetic hysteresis," *J. Mag. Mag. Mater.*, vol. 61, pp. 48–60, 1986

[16] M. A. Mel'gui, "Formulas for describing nonlinear and hysteretic properties of ferromagnets," *Defektoskopiya* 11, pp. 3–10, 1987 (Translated from Russian)

[17] A. Skarlatos, A. Martínez-de-Guerenu, R. Miorelli, A. Lasaosa, C. Reboud, "Use of meta-modelling for identification and interpolation of parametric hysteresis models applied to the characterization of carbon steels," *Physica B: Condensed Matter*, 549, pp. 122–126, 2018

[18] S. E. Zirka, Y. I. Moroz, R. G. Harrison, and K. Chwastek, "On physical aspects of the Jiles-Atherton hysteresis models," *J. Appl. Phys.* 112, 043916, 2012

[19] A. P. S. Baghel and S. V. Kulkarni, "Hysteresis modeling of the grain-oriented laminations with inclusion of crystalline and textured structure in a modified Jiles-Atherton model, " *J. Appl. Phys.* 113, 043908, 2013

[20] I. D. Mayergoyz, *Mathematical models of hysteresis*, New York: Springer-Verlag, 1991.

[21] H. Hauser, "Energetic model of ferromagnetic hysteresis: Isotropic magnetization," *Journal of Applied Physics*, vol.96, no.5, pp.2753-2767, Sep 2004.

[22] Z. Wlodarski, "Analytical description of magnetization curves," *Physica B*, 373, (2006), 323–327.

[23] M.L. Hodgdon, "Mathematical theory and calculations of magnetic hysteresis curves," *IEEE Transactions on Magnetics*, vol. 24, no. 6, pp. 3120-3122, Nov 1988.
[24] B. Sai Ram, S.V. Kulkarni, "An isoparametric approach to model ferromagnetic hysteresis including anisotropy and symmetric minor loops," *J. Magn. Magn. Mater.*, 474, 2019, pp. 574–584, 2019
[25] L. Battistelli, G. Gentile, A. Piccolo, "Representation of hysteresis loops by rational fraction approximations," *Physica Scripta*. 40, pp. 502-507, 1989
[26] I. Nova, V. Havlicek, I. Zemanek, "Dynamic hysteresis loops modeling by means of extended hyperbolic model," *IEEE Trans. Mag.* vol. 49, no. 1, pp. 148-151, 2013
[27] I. Nova, I. Zemanek, "Analytical model with flexible parameters for dynamic hysteresis loops modeling," J. of Elec. Eng., 61, (7/s), pp. 46-49, 2010
[28] I. Nova, I. Zemanek, "Analytical inverse model with flexible parameters for dynamic hysteresis loops modeling," *Prz. Elek.* (9b), pp. 89-92, 2011
[29] M. K. Gohar, "The A-C resistance of solid magnetic wires," *Transactions of the American Institute of Electrical Engineers, Part I: Communication and Electronics* , vol. 78, no. 6,pp. 912 - 916, 1960
[30] P.K. Rajagopalan , D.V.S. Murty, "Internal impedance of solid ferromagnetic conductors," *Proceedings of the Institution of Electrical Engineers* , vol. 112, no. 7, pp. 1449 - 146, 1965
[31] B. Béland and D. Gamache, "Impedance and losses in magnetic cylindrical conductors", *Electromagnetic Fields in Electrical Engineering*, pp. 39-43, Springer-Verlag US, 1988
[32] B. Beland and D. Gamache, "The impedance of flat plate steel conductors," *Proceedings of the International Conference on Electrical Machines*, Part I, Lausanne, Switzerland, 18-21, pp. 5-8, 1984
[33] A. Alberto Dolara and S. Leva, "Calculation of rail internal impedance by using finite elements methods and complex magnetic permeability," *International Journal of Vehicular Technology*, Article ID 505246, pp. 1-10, 2009
[34] R. J. Hill; D. C. Carpenter, "Modeling of nonlinear rail impedance in AC traction power systems," *IEEE Transactions on Power Delivery*, vol. 6, no. 4. pp. 1755 - 1761, 1991
[35] R. L. Stoll, *Analysis of Eddy Currents*, Oxford University Press, 1974
[36] J. F. Gieras, "Analytical method of calculating the electromagnetic field and power losses in ferromagnetic halfspace, taking into account saturation and hysteresis," *Proc. of the Institution of Electrical Engineers*, vol. 124, pp. 1098 –1104, 1977
[37] A. L. Bowden, E.J. Davies, "Analytic separation of the factors contributing to the eddy-current loss in magnetically nonlinear steel," *Proc. of the Institution of Electrical Engineers*, vol. 130, pp. 364-372, 1983
[38] P. D. Agarwal, "Eddy current losses in solid and laminated iron," *Transactions of the American Institute of Electrical Engineers, Part I: Communication and Electronics*, vol. 78, pp. 169-181, 1959
[39] J. Penman, B. J. Chalmers, A. M. A. Kamar, R. N. Tuncay, "The performance of solid steel secondary linear induction machines," *IEEE Trans. on Power Apparatus and Systems*, vol. 100, no. 6, pp. 2927-2935, 1981
[40] J. Penman and A. M. A. Kamar, "Linearization of saturable magnetic field problems, including eddy currents," *IEEE Trans. Mag.*, vol.18, no. 2, pp. 563-566, 1982
[41] A. E. Emanuel, "The effect of nonsinusoidal excitation on eddy current losses in saturated iron," IEEE Transactions on Power Delivery, vol. 3, no. 2, pp. 662– 671, 1988

[42] R. Escarela-Perez, S. Maximov, J. C. Olivares-Galvan1, E. Melgoza, and M. A. Arjona, "Effective nonlinear surface impedance of conductive magnetic slabs," *IEEE Trans. Mag.*, vol.53, no. 5, pp. 563-566, 6300212, 2017

[43] S. C. Bera, R. Sarkar, M. Bhowmick, "Study of a modified differential inductance measurement circuit as position transducer of a power cylinder," *IEEE Trans. Instr. & Meas.*, vol. 61, no. 2, pp. 530-538, 2012

[44] P. Ripka, A. Chirtsov, V. Grim, "Contactless piston position transducer with axial excitation," *IEEE Trans. Mag.*, vol. 53, no. 11, 4002504, 2017

[45] A. Kumar A. S., B. George, "A noncontact angle sensor based on eddy current technique," *IEEE Trans. Instr.& Meas.*, vol. 69, no. 4, pp. 1275-1283, 2020

[46] S. Fericean, A. Hiller-Brod, A. D. Dorneich, M. Fritton, "Microwave Displacement Sensor for Hydraulic Devices," *IEEE Sens. J.*, vol. 13, no. 12, pp. 4682 - 4689, 2013

[47] L. Shih-Yuan, L. Jyun, S. S. Lee, "The study of the piston driving and position sensing for a linearly moving piston pump," *Automatic Control Conference* (CACS), 2014 CACS International, Kaohsiung, pp. 287-291, 2014

[48] K. Suzumori, J. Tanaka, T. Kanda, ""Development of an intelligent pneumatic cylinder and its application to pneumatic servo mechanism," Proceedings, 2005 *IEEE/ASME International Conference on Advanced Intelligent Mechatronics*., Monterey, CA, pp. 479-484, 2005

[49] A. A. M. Faudzi, K. Suzumori, S. Wakimoto, "Design and control of new intelligent pneumatic cylinder for intelligent chair tool application," 2009 *IEEE/ASME International Conference on Advanced Intelligent Mechatronics*, Singapore, pp. 1909-1914, 2009

[50] J. Vyhnanek, P. Ripka, A. Chirtsov, "Linear position sensing through conductive wall without permanent magnet," *Proceedings*, vol. 1, no. 4, 390, 2017

[51] H. Sumali, E. P. Bystrom, G.W. Krutz, "A displacement sensor for nonmetallic hydraulic cylinders," *IEEE Sens. J.*, vol. 3, no. 6, pp. 818 – 826, Dec. 2003

[52] B. Legrand, Y. Dordet, J. Y. Voyant, J. P. Yonnet, "Contactless position sensor using magnetic saturation," *Sens. &Act. A, Phys.*, vol. 106, no. 1–3, pp. 149–154, Sep. 2003

[53] Y. Kano, S. Hasebe, C. Huang, and T. Yamada, "New type linear variable differential transformer position transducer," *IEEE Trans. Instr.& Meas.*, vol. 38, no. 2, pp. 407 - 409, April 1989

[54] S. C. Saxena, S. B. L. Seksena, "A self-compensated smart LVDT transducer," *IEEE Trans. Instr.& Meas.*, vol. 38, no. 3, pp. 748-753, 1989

[55] G .Y. Tian, Z.X. Zhao, R.W. Baines, N. Zhang, "Computational algorithms for linear variable differential transformers (LVDTs)," *IEE Proc.-Scie. Meas. Technol.*, vol. 144, no. 4, pp. 189-192, 1997

[56] S. K. Mishra, G. Panda, D. P. Das, "A novel method of extending the linearity range of linear variable differential transformer using artificial neural network," *IEEE Trans. Instr. & Meas.*, vol. 59, no. 4, pp. 947-953, 2010

[57] S.-H. Yang, K. Hirata, T. Ota, and Y. Kawase, "Impedance linearity of contactless magnetic-type position sensor," *IEEE Trans. Mag.*, vol. 53, no. 6, pp. 1-4, June 2017

[58] A. Grima, M. D. Castro, A. Masi, N. Sammut, "Design enhancements of an ironless inductive position sensor," *IEEE Trans. Instr. & Meas.*, vol. 69, no. 4, pp. 1362-1369, 2020

[59] B. Reinholz, R. J. Seethaler, "Design and validation of a variable reluctance differential solenoid transducer," *IEEE Sens. J.*, vol 19, no. 23, pp. 11063-11071, 2019

[60] X. Wu, S. Huang, K. Liu, K. Lu, Y. Hu , W. Pan, and X. Peng, "Enhanced position sensorless control using bilinear recursive least squares adaptive filter for interior permanent

magnet synchronous motor," *IEEE Trans. on Power Electronics*, vol. 35, no. 1, pp. 681-698, January 2020

[61] Z. Xu, T. Zhang, Y. Bao, H. Zhang, and C. Gerada, "A nonlinear extended state observer for rotor position and speed estimation for sensorless IPMSM drives," *IEEE Trans. on Power Electronics*, vol. 35, no. 1, pp. 733-743,January 2020

[62] X. Liu, C. Liu, and P. W. T. Pong, "Velocity measurement technique for permanent magnet synchronous motors through external stray magnetic field sensing," *IEEE Sensors J.*, vol. 18, no. 10, pp. 4013-4021, May 15, 2018

[63] G. Liu, B. Chen, and X. Song, "High-precision speed and position estimation based on Hall vector frequency tracking for PMSM with bipolar Hall-effect sensors," *IEEE Sensors J.*, vol. 19, no. 6, pp.2347-2355, March 15, 2019

[64] V. Petrucha and P. Ripka, "Rotational speed measurement and angular position reference for a cryogenic propellant electric pump," *J. of Elec. Eng.*, vol. 66, no. 7/s, pp. 199-202, 2015

[65] J. Rickman, "Eddy current turbocharger blade speed detection," *IEEE Trans. Magn.*, vol. MAG-18, no. 5, pp. 1014–1021, Sep. 1982

[66] T. Addabbo, M. Di Marco, A. Fort, E. Landi, M. Mugnaini, V. Vignoli, and G. Ferretti, "Instantaneous rotation speed measurement system based on variable reluctance sensors for torsional vibration monitoring," *IEEE Trans. Instrum. Meas.*, vol. 68, no. 7, pp. 2363-2373, July 2019

[67] J. O. Manyala, T. Fritz, and M. Z. Atashbar, "Gearbox speed sensor design and performance optimization," *IEEE Sensors J.*, vol. 13, no. 2, pp. 629-636, February 2013

[68] W. Li, Z. Hua, W. Qian, L. Jianxuan, T. Jian, "Some considerations of eddy current proximity sensor applied for motor speed measurement," *Int. Conf. on Elec. Machines and Systems*, 2008

[69] L. Li, H. Hu, Y. Qin, and K. Tang, "Digital approach to rotational speed measurement using an electrostatic sensor," *Sensors* (Basel), vol. 19, no. 11, 2540, 2019

[70] C. Wu, C. Fan and G. Wen, "Self-powered speed sensor for turbo drills based on triboelectric nanogenerator," *Sensors*, vol. 19, no. 22, 4889, 2019

[71] D. Gonen, S. Stricker, "Analysis of an eddy-current brake," *IEEE Trans. on Power App.& Syst.*, vol. 84, no. 5, pp. 357-361, 1965

[72] S. Cho, H.-C. Liu, H. Ahn, J. Lee, and H.-W. Lee, "Eddy current brake with a two-layer structure: calculation and characterization of braking performance," *IEEE Trans. on Mag.*, vol. 53, no. 11, 8110205, November 2017

[73] T. J. Rocha, H. G. Ramos, A. L. Ribeiro, and D. J. Pasadas, "Evaluation of subsurface defects using diffusion of motion-induced eddy currents," *IEEE Trans. Instrum. Meas.*, vol. 65, no. 5, pp. 1182–1187, May 2016

[74] T. Itaya, K. Ishida, A. Tanaka, N. Takehira, and T. Miki, "Analysis of a fork-shaped rectangular coil oriented perpendicular to moving conductor slabs," *NDT&E International*, 44, 413–420, 2011

[75] J. A. Shercliff, *The Theory of Electromagnetic Flow Measurement*, Cambridge University Press, 1962.

[76] T. Sonoda, R. Ueda, K. Fujitani, T. Irisa, and S. Tatata, "DC magnetic field type eddy current speed sensor detecting cross magnetization field with amorphous core," *IEEE Trans. Magn.*, vol. MAG-21, no. 5, pp. 1732–1734, Sep. 1985

[77] C. Gong, A. Tuysuz, M. Flankl, T. Stolz, J. Kolar, T. Habetler, "Experimental analysis and optimization of a contactless eddy-current-based speed sensor for smooth conductive surfaces," *IEEE Trans. on Industrial Electronics*, Early Access, 2019

[78] E. Cardelli, A. Faba, and F. Tissi, “Contact-less speed probe based on eddy currents,” *IEEE Trans. Magn*., vol. 49, no. 7, pp. 3897–3900, Jul. 2013.

[79] N. Takehira, and A. Tanaka, “Analysis of a perpendicular-type eddy-current speed meter,” *IEE Proc. A – Phys. Science, Meas. and Instr., Manag. and Educ.- Rev.* , vol. 135 ,no. 2, pp. 89 - 94, Feb. 1988

[80] T. Itaya, K. Ishida, A. Tanaka, N. Takehira, and T. Miki, “Eddy current distribution for a rectangular coil arranged parallel to a moving conductor slab,” *IET Science, Meas. & Tech.*, vol. 6, no. 2, pp. 43 - 51, Mar. 2012

[81] T. Itaya, K. Ishida, A. Tanaka, and N. Takehira, “Analysis of a fork-shaped rectangular coil facing moving sheet conductors,” *IET Science, Meas. & Tech.* , vol. 3 , no. 4, pp. 279 - 285, Jul. 2009

[82] T. Itaya, K. Ishida, Y. Kubota, A. Tanaka, and N. Takehira, “Visualization of eddy current distributions for arbitrarily shaped coils parallel to a moving conductor slab,” *Prog. In Electromag. Research M,* Vol. 47, 1–12, 2016

[83] T. Itaya, K. Ishida, A. Tanaka, and N. Takehira, “Analysis of an eddy current speed meter by rectangular coil system,” *IEEJ Trans. on Fund. and Mat.* 133 (8), 416-423 , January 2013

[84] A. Tuysuz, M. Flankl, J. W. Kolar, and A. Mutze, “Eddy-current-based contactless speed sensing of conductive surfaces,” *IEEE 2nd Annual Southern Power Electronics Conf.* (SPEC), pp. 1 - 6, Dec. 2016

6- List of Selected Publications

6-1 Publications in Journals with Impact Factor

[J1] M. Mirzaei, P. Ripka, A. Chirtsov, P. Kaspar, and J. Vyhnanek, "The effect of conductor permeability on electric current transducers," *AIP Advances*, 2018, 8 ISSN 2158-3226. DOI 10.1063/1.4994195. ***co-authorship* 40 %**

[J2] P. Ripka, A. Chirtsov, M. Mirzaei, and J. Vyhnanek, "Inductance position sensor for pneumatic cylinder." *AIP Advances,* 2018, 8(4), ISSN 2158-3226. DOI 10.1063/1.4993559. ***co-authorship* 25 %**

[J3] M. Mirzaei, P. Ripka, "Analytical functions of magnetization curves for high magnetic permeability materials," *IEEE Transactions on Magnetics*, 2018, 54(11), ISSN 0018-9464. DOI 10.1109/TMAG.2018.2827932. ***co-authorship* 70 %**

[J4] M. Mirzaei, P. Ripka, A. Chirtsov, and J. Vyhnanek, "Eddy current linear speed sensor," *IEEE Transactions on Magnetics*, 2019, 55(1), ISSN 0018-9464. DOI 10.1109/TMAG.2018.2872123. ***co-authorship* 25 %**

[J5] M. Mirzaei, P. Ripka, J. Vyhnanek, A. Chirtsov, and V. Grim, "Rotational eddy current speed sensor." *IEEE Transactions on Magnetics*, 2019, 55(9), 1-10. ISSN 0018-9464. DOI 10.1109/TMAG.2019.2918163. ***co-authorship* 45 %**

[J6] P. Ripka, M. Mirzaei, A. Chirtsov, and J. Vyhnanek, "Transformer position sensor for a pneumatic cylinder," *Sensors and Actuators A: Physical*, 2019, 294 91-101. ISSN 0924-4247. DOI 10.1016/j.sna.2019.04.046. ***co-authorship* 40 %**

[J7] M. Mirzaei, P. Ripka, A. Chirtsov, J. Vyhnanek, and V. Grim, "Design and modeling of a linear speed sensor with a flat type structure and air coils" *Journal of Magnetism and Magnetic Materials*, 2020, 495 1-10. ISSN 0304-8853. DOI 10.1016/j.jmmm.2019.165834. ***co-authorship* 20 %**

[J8] M. Mirzaei, J. Machac, P. Ripka, A. Chirtsov, J. Vyhnanek, and V. Grim, "Design of a flat-type magnetic position sensor using a finite-difference method", *IET Science, Measurement & Technology*, 2020, 1-11. ISSN 1751-8822. DOI 10.1049/iet-smt.2019.0197. ***co-authorship* 25 %**

[J9] M. Mirzaei, P. Ripka, A. Chirtsov, V. Grim, "Eddy current speed sensor with magnetic shielding", *Journal of Magnetism and Magnetic Materials*, 2020, 502 1-6. ISSN 1873-4766. DOI 10.1016/j.jmmm.2020.166636. ***co-authorship* 40 %**

[J10] M. Mirzaei, P. Ripka, A. Chirtsov, and V. Grim, "Temperature stability of the transformer position transducer for pneumatic cylinder," *Journal of Magnetism and Magnetic Materials*, 2020, 503 1-4. ISSN 0304-8853. DOI 10.1016/j.jmmm.2020.166636. ***co-authorship* 40 %**

[J11] M. Mirzaei, P. Ripka, and V. Grim, "A novel eddy current speed sensor with a Ferrite E-core", *IEEE Magnetics Letters,* 2020, 11, 1-5. ISSN 1949-3088. DOI 10.1109/LMAG.2020.2993501. ***co-authorship* 50 %**

[J12] M. Mirzaei, P. Ripka, and V. Grim, "A novel position sensor with conical iron core," *IEEE Transactions on Instrumentation and Measurement* (Early Access), 2020, ISSN 1557-9662. DOI 10.1109/TIM.2020.2999691. ***co-authorship* 50 %**

[J13] M. Mirzaei, P. Ripka, V. Grim, and A. Chirtsov, "Design and optimization of an eddy current speed sensor for rotating rods," *IEEE Sensors Journal* (Early Access). 2020, ISSN 1558-1748. DOI 10.1109/JSEN.2020.3000442. ***co-authorship* 50 %**

6-2 Publications in Conference Proceedings

[C1] M. Mirzaei, P. Ripka, "Analysis of material effect on rail impedance," In: Proceedings - 2018 53rd *International Universities Power Engineering Conference*, UPEC 2018, Glasgow, 2018-09-04/2018-09-07. Piscataway: IEEE, 2018. ISBN 978-1-5386-2910-9. DOI 10.1109/UPEC.2018.8541860. ***co-authorship* 70 %**

[C2] M. Mirzaei, P. Ripka, A. Chirtsov, and J. Vyhnanek, "Impedance of iron conductors with circular and rectangular shapes," *IECON* 2018 - 44th Annual Conference of the IEEE Industrial Electronics Society, 2018. ***co-authorship* 25 %**

[C3] M. Mirzaei, P. Ripka, A. Chirtsov, and J. Vyhnanek, "Temperature influence on position transducer for pneumatic cylinder," In: Proceeding - 2018 *IEEE SENSORS*. 2018 IEEE SENSORS, Delhi, 2018-10-28/2018-10-31. ***co-authorship* 25 %**

6-3 Submitted Papers

[S1] M. Mirzaei, P. Ripka, "Impedance analysis of solid iron conductors at high frequencies for power systems," Submitted to *International Journal of Electrical Power & Energy Systems.* ***co-authorship* 50 %**

[S2] M. Mirzaei, P. Ripka, J. Vyhnanek, A. Chirtsov, and V. Grim, "Modeling of hysteresis loops using rational and power functions," Submitted to *Journal of Magnetism and Magnetic Materials.* ***co-authorship* 40 %**

[S3] P. Ripka, V. Grim, M. Mirzaei "The apparent permeability and the amplification factor of magnetic wires and wire arrays," Submitted to *Journal of Magnetism and Magnetic Materials,* ***co-authorship* 10 %**

7- List of Citations to Author's Publications

[J2] P. Ripka, A. Chirtsov, M. Mirzaei, and J. Vyhnanek, "Inductance position sensor for pneumatic cylinder." *AIP Advances,* 2018, 8(4), ISSN 2158-3226. DOI: 10.1063/1.4993559.

- Y. Jiang, X. He, "Overview of applications of the sensor technologies for construction machinery," IEEE Access, vol. 8, 2020, DOI: 10.1109/ACCESS.2020.3001968
- M. Deguchi, "A simple method for detecting very small changes in capacitance or inductance," Microelectronics Journal, vol. 101, July 2020, 104802, DOI: 10.1016/j.mejo.2020.104802

[J3] M. Mirzaei, P. Ripka, "Analytical functions of magnetization curves for high magnetic permeability materials," *IEEE Transactions on Magnetics*, 2018, 54(11), ISSN 0018-9464. DOI 10.1109/TMAG.2018.2827932.

- B. Boomiraja and R. Kanagaraj, "Convergence behaviour of newton-raphson method in node- and loop-based non-linear magnetic equivalent circuit analysis," 2020 *IEEE International Conference on Power Electronics, Smart Grid and Renewable Energy* (PESGRE2020), DOI: 10.1109/PESGRE45664.2020.9070682

[J5] M. Mirzaei, P. Ripka, J. Vyhnanek, A. Chirtsov, and V. Grim, "Rotational eddy current speed sensor." *IEEE Transactions on Magnetics*, 2019, 55(9), 1-10. ISSN 0018-9464. DOI 10.1109/TMAG.2019.2918163.

- C. Wu, C. Fan, G. Wen, "Self-powered speed sensor for turbodrills based on triboelectric nanogenerator," *Sensors*, 2019, DOI: 10.3390/s19224889
- W. Chuan, W. Guojun, H. Lei, "Research on rotating speed measurement method of turbodrill based on tilt sensor," Proceedings of the Institution of Mechanical Engineers, Part C: Journal of Mechanical Engineering Science, July 22, 2020, DOI: 10.1177/0954406220944431

[J9] M. Mirzaei, P. Ripka, A. Chirtsov, V. Grim, "Eddy current speed sensor with magnetic shielding", *Journal of Magnetism and Magnetic Materials*, 2020, 502 1-6. ISSN 1873-4766. DOI 10.1016/j.jmmm.2020.166636.

- W. Chuan, W. Guojun, H. Lei, "Research on rotating speed measurement method of turbodrill based on tilt sensor," Proceedings of the Institution of Mechanical Engineers, Part C: Journal of Mechanical Engineering Science, July 22, 2020, DOI: 10.1177/0954406220944431
- S. She, Y. Chen, Y. He, Z. Zhou, and X. Zou, "Optimal design of remote field eddy current testing probe for ferromagnetic pipeline inspection," Measurement, vol. 168, 15 January 2021, 108306, DOI:10.1016/j.measurement.2020.108306

[C1] M. Mirzaei, P. Ripka, "Analysis of material effect on rail impedance," In: Proceedings - 2018 53rd *International Universities Power Engineering Conference*, UPEC 2018. Glasgow,

2018-09-04/2018-09-07. Piscataway: IEEE, 2018. ISBN 978-1-5386-2910-9. DOI 10.1109/UPEC.2018.8541860.

- I. Ignatenko, E. Tryapkin, S. Vlasenko, “Impact of return traction current harmonics on the value of the potential of the rail ground for the AC power supply system,” *International Scientific Siberian Transport Forum, TransSiberia* 2019: VIII, DOI: 10.1007/978-3-030-37916-2_13
- A. Mariscotti, “Impact of rail impedance intrinsic variability on railway system operation, EMC and safety,” *International Journal of Electrical and Computer Engineering* (IJECE) vol. 9, no. 4, August 2020, DOI: 10.11591/ijece.v9i4